THÈSE DE DOCTORAT

Université de Lille

Intelligent End-of-Pipe Catalytic Systems Suited for Alternative Fuels

PhD Candidate: **Mr. Yuanshuang ZHENG**

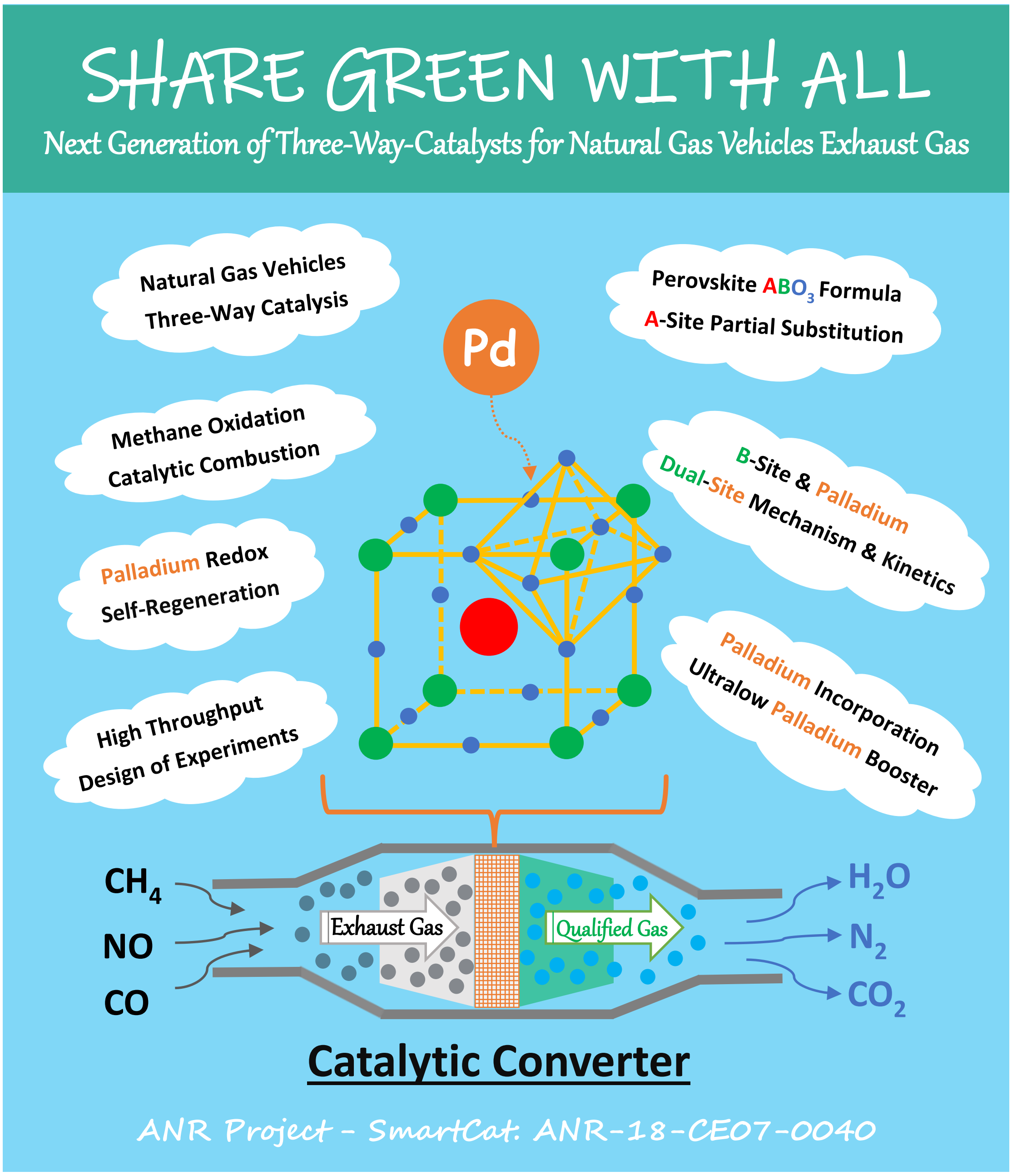

THÈSE

Pour l'obtention du Grade de

DOCTEUR EN CHIMIE

Ecole Doctorale :
Sciences de la Matière, du Rayonnement et de l'Environnement

Secteur de Recherche : Chimie Théorique, Physique, Analytique

Présentée et soutenue par

Yuanshuang ZHENG

Le 18 octobre 2022

Catalyseurs de post-traitement intelligent adaptés à l'usage de carburants alternatifs

Directeur de thèse : Pascal GRANGER

JURY

Mme. Valérie KELLER	Directrice de Recherche, Université de Strasbourg	Rapporteuse
M. Philippe VERNOUX	Directeur de Recherche, Université de Lyon	Rapporteur
Mme. Catherine ESPECEL	Professeure des Universités, Université de Poitiers	Présidente du Jury Examinatrice
M. Xavier COURTOIS	Maître de conférences HDR, Université de Poitiers	Examinateur
M. Pascal GRANGER	Professeur des Universités, Université de Lille	Directeur de thèse

Table of Contents

Résumé

L’objectif de ces travaux de thèse est pour développer les catalyseurs à base de pérovskite et palladium pour le traitement des traces de méthane issues des véhicules fonctionnant au gaz naturel. Plus en détail, l’étude est basée sur la combinaison de deux catalyseurs actifs ayant chacun un rôle dans la réaction visée sur la combustion catalytique de méthane. Les pérovskites à base de composition $LaMnO_3$ avec une excellente activité d'oxydation du méthane à haute température sont utilisées comme supports. Parmi eux, l’étude non-stœchiométrique du lanthane et les substitutions partielles du lanthane par le potassium et le strontium ont été utilisés pour modifier la structure de la pérovskite afin de générer des distorsions pour une meilleure activité catalytique et une meilleure mobilité de l'oxygène. Le palladium, reconnu comme un métal noble avec d'excellentes performances catalytiques du méthane à basse température, a été incorporé aux catalyseurs pérovskites par différentes méthodes de calcination (c'est-à-dire la méthode one-pot et la méthode séquentielle par la voie de synthèse de la méthode sol-gel de l’acide citrique). Compte tenu de la prise en compte de la maîtrise des coûts, l’objectif est de réduire au maximum l'utilisation du palladium, de 1% à 0.5% en masse dans l’expérimentation. Par conséquent, le système catalytique composite de pérovskite boosté par la faible teneur en palladium est la stratégie de recherche de ce sujet autour de la combustion catalytique de méthane.

Afin d'étudier les propriétés physico-chimiques des catalyseurs, les méthodes de caractérisation telles que l’analyse thermogravimétrique, la diffractométrie de rayons X, la N_2-physisorption, la H_2-réduction en température programmée, la O_2-oxidation en température programmée, la O_2-désorption programmée en température combiné par spectrométrie de masse, la microscopie électronique à balayage combiné par spectroscopie de rayons X à dispersion d'énergie, la microscopie électronique en transmission combiné par spectroscopie de rayons X à dispersion d'énergie, la spectrométrie photo-électronique X, la spectrométrie de masse à plasma à couplage inductif et la conductivité sont utilisées pour analyser les propriétés de surface et de bulk des catalyseurs cibles.

La deuxième partie de cette thèse a été consacrée à la cinétique de l’oxydation de méthane par la route de réactions à haut débit. L’étude de la cinétique a été effectuée par l’approche à travers la combinaison théorique et expérimentale pour étudier les mécanismes des différentes propositions des sites actifs et la source d'espèces réactives de l'oxygène actif avant et après vieillissement. De plus, dans tout le processus de réaction, les catalyseurs avec différentes méthodes d’incorporation de palladium présentent les mécanismes de réaction différents. Cette étude est instructive pour d'étudier la nature et la synergie de l'oxydation de méthane sur la pérovskite boostée par palladium et les facteurs influençant la conception des catalyseurs.

En pratique, cette combinaison des catalyseurs a été utilisée comme catalyseurs à trois voies pour le post-traitement de gaz d'émission simulé des véhicules à gaz naturel. Les catalyseurs ont été testé dans le réacteur de plug-flow à l'échelle du laboratoire selon le même plan expérimental comme la partie cinétique. Dans le courant des traces de méthane, la réaction devient plus difficile et plus compliquée en présence de NO, CO, vapeur d'eau et CO_2. L'oxydation complète du méthane, l'oxydation partielle du méthane, la réduction du NO à l'azote et même à l'ammoniac ont été découvert et investigué par le bilan de réaction.

Mots-clés : Pérovskite / Combustion catalytique du méthane / Palladium / Catalyse à trois voies / Émission des véhicules au gaz naturel

Abstract

The objective of this thesis work is to develop catalysts based on perovskite and palladium for the treatment of traces of methane from vehicles running on natural gas. In more detail, the study is based on the combination of two active catalysts, each having a role in the targeted reaction of the catalytic combustion of methane. Perovskites based on $LaMnO_3$ composition with excellent high temperature methane oxidation activity are used as carriers. Among them, the non-stoichiometric study of lanthanum and the partial substitutions of lanthanum by potassium and strontium have been used to modify the structure of perovskite to generate distortions for better catalytic activity and mobility of the oxygen. Palladium, recognized as a noble metal with excellent low temperature methane catalytic performance, has been incorporated into perovskite catalysts by different calcination methods (i.e. one-pot method and sequential method by synthesis of the sol-gel method of citric acid). Given the consideration of cost control, the objective is to reduce the use of palladium as much as possible, from 1% to 0.5% by mass in the experiment. Therefore, low palladium boosted perovskite composite catalytic system is the research strategy of this topic around catalytic methane combustion.

In order to study the physicochemical properties of catalysts, characterization methods such as thermogravimetric analysis, X-ray diffractometry, N_2-physisorption, H_2-temperature-programmed reduction, O_2-temperature-programmed oxidation, O_2-temperature-programmed desorption combined with mass spectrometry, scanning electron microscopy combined with energy dispersive X-ray spectroscopy, transmission electron microscopy combined with energy dispersive X-ray spectroscopy, X-ray photoelectron spectrometry, inductively coupled plasma mass spectrometry and conductivity properties are used to analyze bulk and surface properties of target catalysts.

The second part of this thesis was dedicated to the kinetics of methane oxidation by the high-throughput reaction method. The study of the kinetics was carried out by the approach through the theoretical and experimental combination to study the mechanisms of the different proposals of the active sites and the source of reactive species of active oxygen before and after aging. Moreover, in the whole reaction process, the catalysts with different palladium incorporation methods exhibit the different reaction mechanisms. This study is instructive to investigate the nature and synergy of methane oxidation on palladium-boosted perovskite and the factors influencing catalyst design.

In practice, this combination of catalysts has been used as three-way catalysts for simulated gas aftertreatment of natural gas engines. The catalysts were tested in the laboratory-scale plug-flow reactor according to the same experimental plan as the kinetic part. In the current of methane traces, the reaction becomes more difficult and more complicated in the presence of NO, CO, water vapor and CO_2. The complete oxidation of methane, the partial oxidation of methane, the reduction of NO to nitrogen and even to ammonia have been discovered and investigated by the reaction balance.

Keywords: Perovskite / Methane catalytic combustion / Palladium / Three-way catalysis / Natural gas vehicles emission

Chapter I. General Introduction

1. General introduction

Regulations on pollution and greenhouse gas emission are becoming more stringent on the issue of climate change. Humans impact the environments in many ways, environmental pollution, global warming and climate change could be regarded as a formula for multifactorial combination hazards on environmental and energy issues. The damages caused by their interaction are real and affect all living things on the earth.

Natural gas or biogas, as alternative fuels, is seen as a cleaner energy source than conventional petroleum fuels. However, as methane is 28 times more potent than carbon dioxide at trapping heat in the atmosphere, the removal of trace methane from complex automobile exhaust emissions become very necessary, but it is still a technological challenge when considering the overall cost-effectiveness and economizing precious metal resource. In the context of intense international attention on environmental and climate issues, scientific research and technological progress in the field of the environment are given greater responsibility. Therefore, the objective of the short overview is to present and compare recent major strategies and novel potential trends on three-way catalysts for methane combustion with the purpose of reducing cost of end-of-pipe catalytic system and effectively improving hydrothermal stability, resistance to aging and poisoning. Particular attention has been paid in this manuscript to palladium-based catalysts and mixed metal oxides, such as perovskite type oxides and multi-element oxide materials. Excellent oxygen exchange capacity and their synergistic effects with precious metals promote methane oxidation process while lowering content of noble metal.

2. Background and significance

Climate change and the increase of extreme disasters caused by anomalies are constantly threatening the survival of mankind and the earth home on which human beings live [1]. Therefore, human beings continue to make efforts under the United Nations Framework Convention on Climate Change, the Kyoto Protocol and the Signing of the Paris Agreement have brought a clear outlook on climate change [2] which is urged to be implemented during the COP26 in 2021. Traditional fossil fuels, such as coal and oil, as the most important energy source, are not only non-renewable energy, but also bring various serious environmental pollution. In the field of transportation, the environmental problems associated with the use of petroleum and its derivatives as fuels have been always seriously concerned. Aiming at major pollutants, such as CO, NO_x, unburned HC and particulate matters [3], increasingly strict environmental protection laws and regulations put forward higher requirements on the end-of-pipe technology of exhaust gas emission of internal combustion engine [4]. Especially in the context of the global Covid-19 pandemic, the instability of oil and coal markets is further driving the development of alternative energy [5].

Methane, as the main component of natural gas and biogas, is treated as a pivotal alternative energy source with abundant supplies because of its clean and renewable properties [6]. However, methane, which is gaining more attention lately, is the second most abundant anthropogenic greenhouse gas (GHG) after carbon dioxide (CO_2), accounting for about 20 percent of global emissions [7]. Moreover, 28 times as potent as carbon dioxide at trapping heat in the atmosphere is a thorny issue, and its concentration in the atmosphere have more than doubled over the last two centuries, which rapidly and powerfully affects the earth’s temperature and climate system [8].

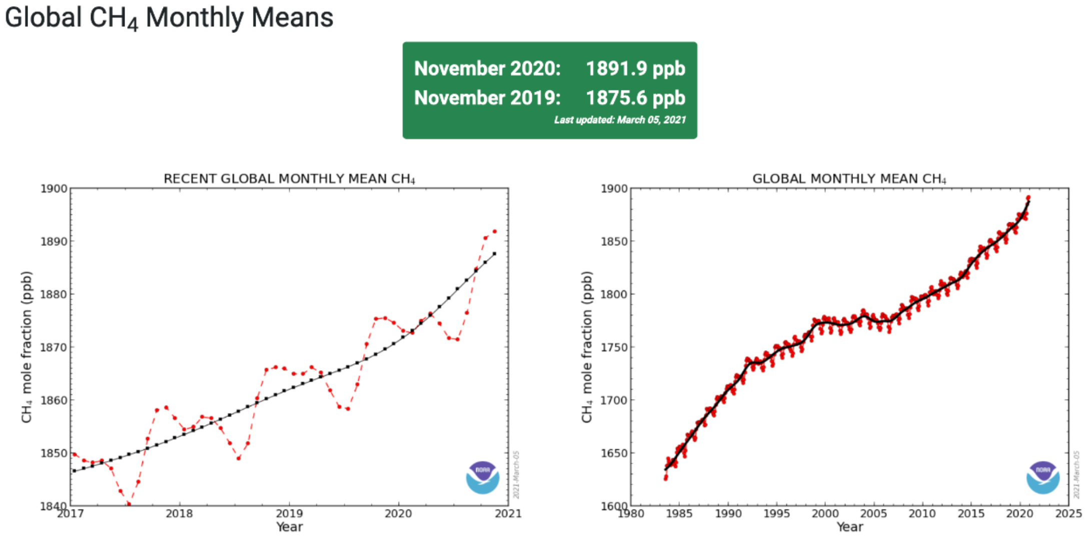

Fig. 1.1 Global CH_4 Monthly Means

Concentrations of methane have increased by more than 150% since industrial activities and intensive agriculture began [9] because methane, as an energy source with easily accessible feature, can be produced by various routes, such as natural, agricultural and industrial production activities. After carbon dioxide, methane is responsible for about 23% of climate change in the twentieth century [10]. The measurements from Global Greenhouse Gas Reference Network, as a vital reference widely used by international climate researchers, presents the analysis of samples from 2020 with a significant jump about 6% (Fig.1.1) in the first two decades of this century [11] in the atmospheric burden of methane. Scientists around the world therefore make efforts to better understand the budget of methane with the ultimate objectives of reducing GHG emissions and improving prediction of environmental change. The Global Methane Budget [12] shows the distribution of sources of methane emissions during recent years: about 30% of methane emissions are produced by wetlands, including ponds, lakes and rivers; Another 20% is produced by agriculture, due to a combination of livestock, waste management and rice cultivation; Activities related to oil, gas, and coal extraction release an additional 30%; The remainder of methane emissions come from minor sources such as wildfire, biomass burning, permafrost, termites, dams, and the ocean (Fig.1.2).

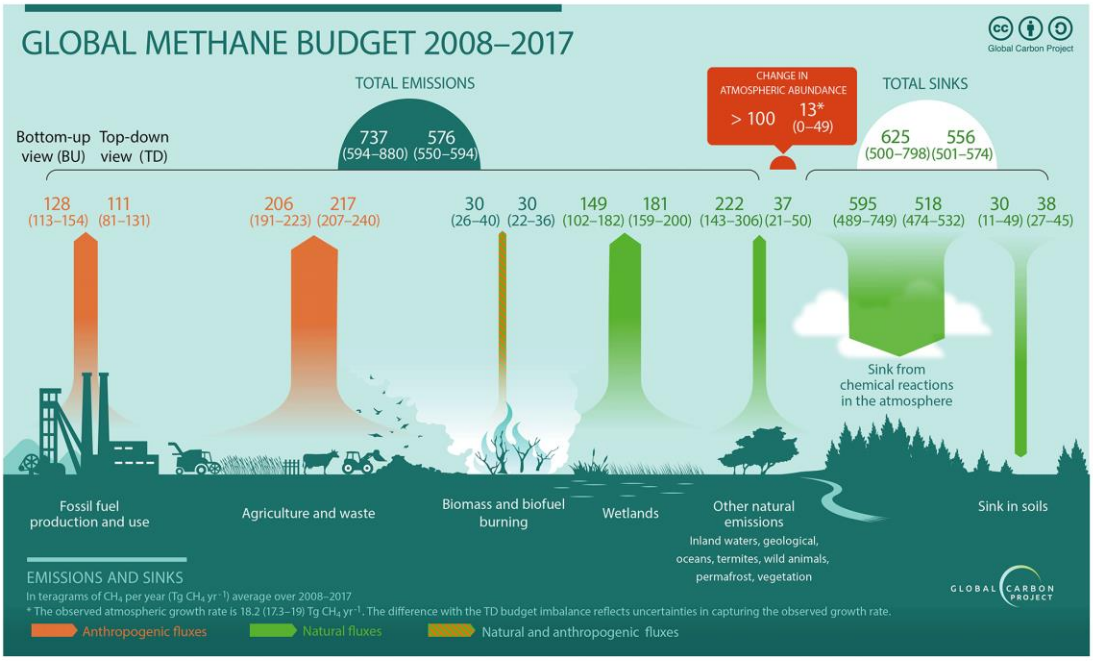

Fig. 1.2 Global Methane Budget 2008-2017.

As a result, regulations and policies on environmental issues [13] have become increasingly strict and global climate governance has become more and more clear after countries have committed to peak carbon dioxide emissions in recent years and carbon neutrality [14]. In order to achieve the ambitious issue on Environment and Climate, European Commission has set a 2050 long-term strategy to reach carbon neutrality [15], United States announce a 50-52 percent reduction in GHG emissions by 2030 [16], while China, under the guidance of the Two Mountain Theory [17], plans to reach the peak carbon emission and carbon neutral targets respectively by 2030 and by 2060 [18]. Hence, the widespread use of renewable clean energy has become an international reality in the coming decades [19] with the efforts of all parties and methane, as a promising renewable source of clean energy, holds the promise of a bright future of diverse energy sources under control of emission regulations [20].

3. Coexistence of opportunities and challenges for methane use

Methane “flaring” provides a significant fraction of the world's primary energy, and is used for heating, electrical generation and energy for transportation. Opportunities and challenges coexist in the use of natural gas or biogas. A study from Environmental Defence Fund found that cutting methane emissions now could slow the near-term rate of global warming by as much as 30% [21]. In addition to the greenhouse effect of methane itself, the by-product is N_2O and the formation of underlying ozone. Besides, main applications involve the reaction of methane combustion in air, and hence that brings up an additional problem of GHG emissions because the greenhouse gas emissions are not only methane but also trace amounts of nitrous oxide (N_2O) during transient combustion events such as ignition and blowoff [19], which has an even longer lifetime and its greenhouse effect is 300 times higher than carbon dioxide (CO_2) [20]. Therefore, with the increase consumption demand of natural gas and biogas as alternative fuel [21], these negative effects of methane combustion come from both stationary and mobile sources [22] involving natural gas. In consequence, the review mainly focuses on methane abatement and also the corresponding removal of greenhouse effect by-products is under consideration among the different scientific and technological routes.

4. Natural gas as alternative in transportation

An end-of-pipe technology, according to the term given by European Environment Agency, is an approach to pollution control which concentrates upon effluent treatment or filtration prior to discharge into the environment, as opposed to changes in the process giving rise to the wastes [15]. “SmartCat” concentrates mainly on vehicles of natural gas or biogas powered engines, methane oxidation is our concerns and the foundation to extend materials research and catalytic system design.

The research objectives in this manuscript are focused on new Three-Way-Catalyst composition for methane catalytic combustion. Up to now, Pd supported on alumina can be regarded as a benchmark. However, this formulation is strongly subjected to deactivation at high temperature due to particle sintering. A current strategy is to force palladium composition to preserve in severe conditions significant residual catalytic activity. This option is not cost-efficient and does not fulfill the European recommendations to reduce the use of materials of strategic importance.

An alternative is to lower thermal sintering by strengthening the metal support interaction. Previous investigations revealed successful achievements even though the explanations diverge regarding the origin of improved thermal stability. Indeed, dynamic changes typically under cycling lean/reach conditions can protect PGM to coalescence then preserving high degree of dispersion. This concept has been widely discussed and largely questioned as these dynamic changes require large amount of surface defects. Alternative explanation led to the conclusion that the strength of interaction can be associated to the formation of two-dimensional aggregates that wet the surface of perovskite.

Different scenarios have been envisioned by modifying the perovskite composition through partial substitution of A-site, La-deficiency and well as the strategy for Pd incorporation, e.g. one-pot vs. sequential method. A proposal consisting in lowering the Pd content has been suggested. Based on this the manuscript has been divided in 8 chapters. The state-of-the art reviewed the main achievements in automotive exhaust depollution especially when engines are powered by natural gas. Three chapter detailed the experimental protocols as well as the techniques used for physicochemical characterization, and a chapter focused on methane oxidation kinetics. In simulated condition, kinetic approaches have been developed with the aim to establish relevant comparison with surface properties. Particular attention was paid to the evaluation of the catalytic measurement in simplified and complex composition more representative of the exhaust gas composition.

Experimental results and their discussion have been distribution in 4 chapters entitled: (i.) Impact of elemental composition of perovskites on bulk and surface properties, (ii.) Impact of palladium incorporation on bulk and surface properties of perovskites, (iii.) Methane oxidation kinetic study from high-throughput experimentations, (iv.) Catalytic measurement in real exhaust gas composition of NGVs engine. A general conclusion emphasized the most relevant information to conclude this thesis and an outlook to guide for a future optimization of three-way catalysis for natural gas vehicles exhaust gas.

References

1. Welcome to the Anthropocente, The UNESCO Courier, e-ISSN 2220-2293, 2018. https://en.unesco.org/courier/2018-2.
2. The European Green Deal. COM/2019/640 final. https://ec.europa.eu/info/strategy/priorities-2019-2024/european-green-deal_en#thematicareas.
3. P. Granger, Challenges and breakthroughs in post-combustion catalysis: how to match future stringent regulations. Catal. Sci. Technol., 2017,7, 5195-5211. https://doi.org/10.1039/C7CY00983F.
4. Emission in the automobile sector, Environmental Protection, Automobile Industry, Sectors, Internal Market, Industry, Entrepreneurship and SMEs, European Commission, 2016. https://ec.europa.eu/growth/sectors/automotive-industry/environmental-protection/emissions-automotive-sector_en.
5. Yilin Wu, Shiyu Ma. Impact of COVID-19 on energy prices and main macroeconomic indicators—evidence from China's energy market[J]. Green Finance, 2021, 3(4): 383-402. http://doi.org/10.3934/GF.2021019.
6. French strategy for energy and climate, Multi annual energy plan 2019-2023 2024-2028. Ministère de la Transition Ecologique, 2017. https://www.ecologie.gouv.fr/sites/default/files/PPE-Executive%20summary.pdf.
7. An EU strategy to reduce methane emissions COM (2020) 663 final, European Comission, 2020. https://ec.europa.eu/energy/topics/oil-gas-and-coal/methane-emissions_en.
8. Importance of Methane, Global Methane Initiative, United States Environmental Protection Agency. https://www.epa.gov/gmi/importance-methane.
9. Climate Change Indicators: Atmospheric Concentrations of Greenhouse Gases, United States Environmental Protection Agency, 2021. https://www.epa.gov/climate-indicators/climate-change-indicators-atmospheric-concentrations-greenhouse-gases#ref6.
10. Sources of Methane, United States National Aeronautics and Space Administration, 2020. https://svs.gsfc.nasa.gov/4799.
11. Despite pandemic shutdowns, carbon dioxide and methane surged in 2020, United States National Oceanic and Atmospheric Administration, 2021.

https://research.noaa.gov/article/ArtMID/587/ArticleID/2742/Despite-pandemic-shutdowns-carbon-dioxide-and-methane-surged-in-2020.

12. Marielle Saunois, Earth Syst. Sci. Data, 12, 1561–1623, 2020. https://doi.org/10.5194/essd-12-1561-2020.
13. Joint EU-US Press Release on the Global Methane Pledge, European Comission, 2021. https://ec.europa.eu/commission/presscorner/detail/en/IP_21_4785.
14. Natural Gas Development Report (2021), National Energy Administration, Development Research Center of the State Council, Ministry of Natural Resources of the P.R. of China. ISBN 978-7-5183-4800-8. http://www.nea.gov.cn/1310139334_16294604014501n.pdf.
15. 2050 long-term strategy, Climate Action, European Comission, 2018. https://ec.europa.eu/clima/eu-action/climate-strategies-targets/2050-long-term-strategy_en.
16. The White House, FACT SHEET: President Biden Sets 2030 Greenhouse Gas Pollution Reduction Target Aimed at Creating Good-Paying Union Jobs and Securing U.S. Leadership on Clean Energy Technologies, 2021. https://www.whitehouse.gov/briefing-room/statements-releases/2021/04/22/fact-sheet-president-biden-sets-2030-greenhouse-gas-pollution-reduction-target-aimed-at-creating-good-paying-union-jobs-and-securing-u-s-leadership-on-clean-energy-technologies/.
17. “Province turns green into gold”, Ministry of Ecology and Environment of the P.R. of China, 2020. http://english.mee.gov.cn/News_service/media_news/202008/t20200813_793530.shtml.
18. An energy sector roadmap to carbon neutrality in China, IEA, 2021. https://www.iea.org/reports/an-energy-sector-roadmap-to-carbon-neutrality-in-china.
19. Smriti Mallapaty, How China could be carbon neutral by mid-century, p482, vol 586, Nature 2020. https://doi.org/10.1038/d41586-020-02927-9.
20. A. Raj, Methane emission control. Johnson Matthey Technology Review, vol60, 4, 1, 2016. https://doi.org/10.1595/205651316X692554.
21. I-B Ockol, T Sun, D Shindell, M Oppenheimer, A-N Hristov, S-W Pacala, D-L Mauzerall, Y Xu and S-P Hamburg, Environ. Res. Lett. 16 054042, 2021. https://doi.org/10.1088/1748-9326/abf9c8.
22. "BP Statistical Review of World Energy 2016," British Petroleum, Jun 2016. http://large.stanford.edu/courses/2016/ph240/yoon2/docs/bp-2016.pdf.
23. Andrés Colorado, Vincent McDonell, Scott Samuelsen, Direct emissions of nitrous oxide from

combustion of gaseous fuels, International Journal of Hydrogen Energy, Volume 42, Issue 1, 2017, Pages 711-719, ISSN 0360-3199. https://doi.org/10.1016/j.ijhydene.2016.09.202.

24. Y. Wu, C. Cordier, E. Berrier, N. Nuns, C. Dujardin, P. Granger, Surface reconstructions of $LaCo_{1-x}Fe_xO_3$ at high temperature during N_2O decomposition in realistic exhaust gas composition: Impact on the catalytic properties, Applied Catalysis B: Environmental, Volumes 140–141, 2013, Pages 151-163, ISSN 0926-3373, https://doi.org/10.1016/j.apcatb.2013.04.002.
25. Rafiu O. Yusuf, Zainura Z. Noor, Ahmad H. Abba, Mohd Ariffin Abu Hassan, Mohd Fadhil Mohd Din, Methane emission by sectors: A comprehensive review of emission sources and mitigation methods, Renewable and Sustainable Energy Reviews, Volume 16, Issue 7, 2012, Pages 5059-5070, ISSN 1364-0321. https://doi.org/10.1016/j.rser.2012.04.008.
26. Earth Syst. Sci. Data, 12, 1561–1623, 2020. https://doi.org/10.5194/essd-12-1561-2020.
27. In focus: Methane - what’s the deal?, European Comission, 2021. https://ec.europa.eu/info/news/focus-methane-whats-deal-2021-oct-14_en.

Chapter II. Literature Review

1. Introduction

The realization of effective sophisticated end-of-pipe technology is expensive because of requiring an extensive use of critical materials of strategic importance, such as platinum group metals and rare earths metals. In addition, the efficiency of current processes in terms of selectivity and energy consumption and, most importantly, the development of alternative routes has become a priority for modern and particularly future industry because of limited natural oil reserves and stringent environmental legislation [1].

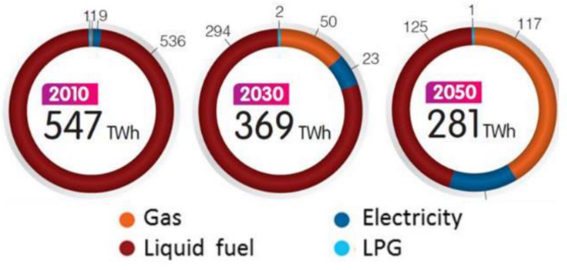

Fig.2.1. Scenario on the consumption of energy in the transport sector in France. [2]

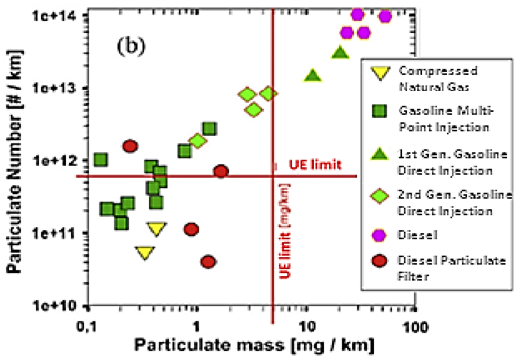

Fig.2.2. Comparison of particulate matter number and particulate matter mass emissions from various engines. [3]

According to the related French energy development plan, the energy consumption of liquid fossil fuel in transport is expected to reduce by 50% [2] in the next 30 years (Fig.2.1), which can be an exalting occasion to diversify energy sources by adopting simpler and more compact end-of-pipe technologies.

One of the most promising alternative and green carbon feedstock is methane with their reserves significantly exceeding those of crude oil. Moreover, methane can also be considered as a renewable energy source which is also called biogas. Compared to traditional liquid fossil fuel powered engines, the emergence of natural gas or biogas powered engines afford an alternative option with lower greenhouse gas and nitrogen oxide (NO_x) emissions, as well as much lower particulate matter formation (Fig.2.2) [3]. Nevertheless, methane, as the main gas in natural gas and biogas, has 23 times higher global warming potential than carbon dioxide although it has the above advantages. Therefore, the relevance of the option resides in the abatement of unburnt methane in the exhaust gas.

In consequence, how to decrease or substitute the use of cost-effectiveness active materials to remove residual traces of refractory methane in the exhaust stream is the main technological challenge.

2. Scientific hypotheses and objectives

Currently, methane treatment systems involve highly loaded palladium-based catalysts [4] with a content greater than 200 g/ft [5], which is more than twice the amount used in conventional Three-Way-Catalysts (Fig.2.3) with high running temperature range between 400 °C and 500 °C [5,6].

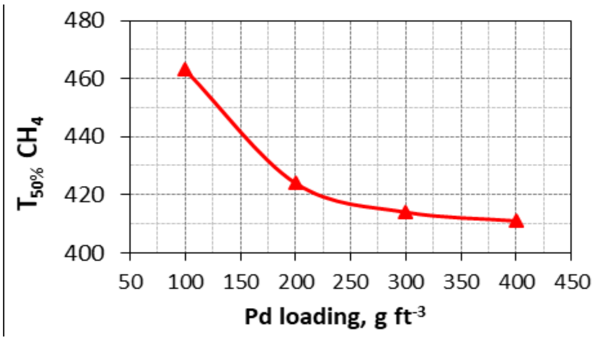

Fig.2.3. Effect of Pd loading on methane conversion [3].

Besides, the thermal resistance of catalysts, which should be adequately taken into account to prevent deactivation, is a critical and crucial issue at high temperature. In spite of numerous researches reporting various active materials for methane oxidation such as supported transition metal, noble metals and partially reduced mixed metal oxides [7-10], highly loaded palladium-based catalysts are still mainly used as reference in industry. The choice of highly loaded precious metal is dictated to attenuate the deactivation effects by thermal sintering.

According to the above, "SmartCat" will tackle main issues related to the innovative development cost-effective end-of-pipe technologies, in matter of the use of methane considered as less harmful in terms of atmospheric pollution as alternative fuels and in connection with the reduction of strategically critical materials such as platinum group and rare earths metals.

In order to avoid the impact of the greenhouse effect by methane, eliminating the residue of methane in the exhaust gas lays our fingers on the development of a new applicable exhaust gas cleaning technology. Recently, M. Richard et al. [10,11]

proposed a new conception based on a catalytic dual bed concept in order to boost methane oxidation. A significant enhancement of methane conversion rate (Fig.2.4) was researched and observed on a low palladium loading (≤ 0.2% wt). by a catalytic dual bed configuration ($LaMnO_3$-Pd/YSZ). The former is perovskite-type material for the sake of generating active oxygen species, the latter is yttria-stabilized zirconia ceramic material or with low palladium-loaded framework. Besides, the active oxygen species boost the reaction more readily with methane on second catalytic portion. A synergetic catalytic effect showed a positive and remarkable result but without well understanding the chemical kinetic nature of oxygen.

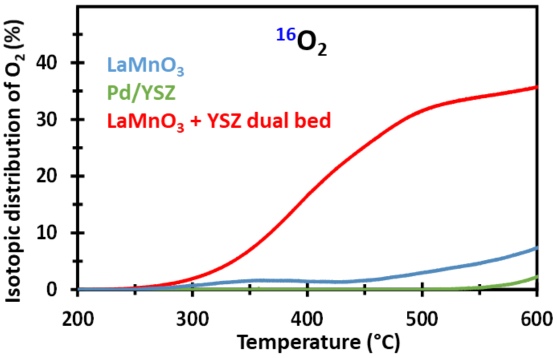

Fig. 2.4. Effect of the $LaMnO_3$ + YSZ dual bed on the $^{16}O_2$ formation from isotopic exchange of $^{18}O_2$ (gas) with $^{16}O_2$ (solid) [12]

By the new design of dual bed, a new concept of single bed is also under consideration, which is aimed at loading precious metals on perovskites materials. In this case, integrating perovskites materials with low palladium loading becomes the main effort. Whether the single bed concept or dual bed design, the research on new formulation of perovskite-based materials is our premier importance.

To overcome scientific and practical issues in the face of catalysts with low amount precious metals and without noble metals, our attention has been paid on stoichiometric and non-stoichiometric perovskites and related mixed oxides materials by doping and substitution concepts with the purpose of adjusting perovskite ABO_3 formula to modulate lattice oxygen in metal oxides. Exceptional redox and oxygen storage capacity could be activated by structural distortion and relevant oxygen quantum states.

Therefore, to well control perovskite valency and the related oxygen vacancy is principal for generating specific active oxygen species and maintaining a high Pd dispersion at relative high temperature to activate methane. Y. Nishihata et al. researched the self-generation behavior of such materials [13], e.g. the ability to adjust their surface properties in complex conditions of exhaust gas, can be profitably applied to enhance the thermal sintering resistance and sulfur poisoning tolerance during the cold start of engines.

In spite of the above advantages, the poor specific surface area is treated as a serious obstacle in the face of bulk-type mixed oxides materials, which is one of the features of perovskite. A. Zaki et al. developed the moderate templating synthesis routes in mild conditions leading to unique two-dimensional porous structure [14] with a considerable outcome concerning the porous structure preservation at high temperature, related oxygen storage capacity and redox properties. A significant reduction of catalytic bed volume could be envisaged in case of improvement in mass transport phenomena owing to the optimization of bi-dimensional macro-mesoporous structure.

As a consequence, SmartCat project proposes innovative technological solutions by restudying the automotive exhaust systems on the basis of two complementary approaches, according to the self-regenerative behavior of doped and substituted spinel/perovskite-like structure and to the dual bed concept with more singlet oxygen species as more active intermediates issuing in the methane conversion at lower temperature to protect catalysts from deactivation such as thermal sintering.

According to the above introductions, the objectives mentioned covered such issues:

1. The development of hard templating methods for obtaining thermally resistant hierarchical porous structures in order to improve oxygen mobility, related oxygen storage capacity, specific surface area and mass transfer diffusion.
2. The development of innovative strategies: Introducing more resistant palladium species in case of thermal sintering and poisoning effects; Implementing advanced techniques for ex-situ and in-situ characterization on the catalytic system functionalities, such as redox and oxygen storage capacity properties.
3. The development of advanced spectroscopic instruments and proper in-situ methodologies for the characterization of reactive oxygen species and reactive intermediate species implying steady-state transient kinetic analysis.
4. The investigation of methane combustion kinetics at various richness. As well as the establishment of more relevant surface-reactivity relationships in agreement with a selected reaction mechanism for the sake of better optimizing catalytic functionalities.
5. The selection of appropriate formulation, compositions and structures in order to verify the concepts of catalytic single-bed and dual-bed reactors.
6. The validation of the single-bed and the dual-bed concepts at various richness approaching realistic conditions in a wide temperature range with the presence of sulfur material as contaminant.

3. Three-way catalytic system

Air pollution generated from mobile sources becomes an environmental problem and gains extensive public attention. “More than 1.1 billion cars were registered worldwide between the year of 1965 and 2018 and the world’s annual automobile production reached a peak of nearly 74 million in 2017” (Fig.2.5), reported by US Department of Energy on Transportation Energy Data Book [16]. Just in the European Union, the passenger car production is close to 20 million in 2019 [17] on the basis of investigation of European Automobile Manufacturers Association. In the context, emission control of automotive exhaust is of great importance on a global level to tackle the problem of air pollution and it is crucial to address the environmental problems caused by vehicle exhaust emissions. The environmental concern by mobile sources is due to the fact that the majority of engines employ combustion of liquid fuels derived from crude oil.

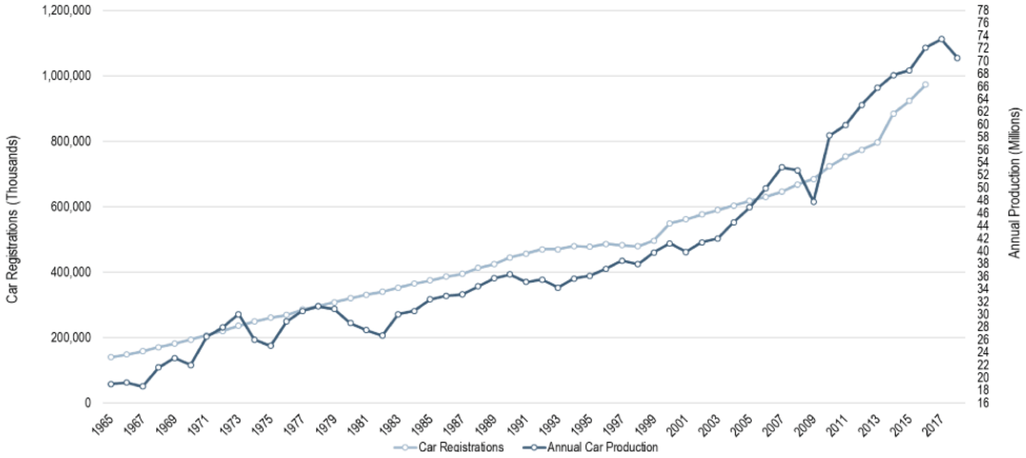

Fig.2.5. World Automobile Production and Fleet, 1965-2018 [17]

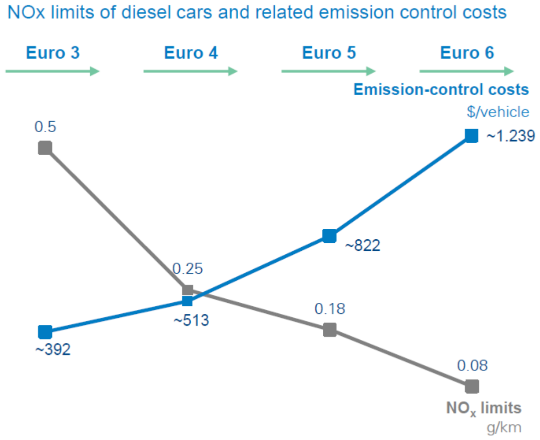

Fig.2.6. NO_x limits of Diesel cars and related emission control costs [18]

For the past few years, there are two contradictory trends that automobile manufacturers have to face with the development of efficient end-of-pipe technology: cost investments and preservation of the competitiveness vs. the implementation of more stringent standard regulations with respect to atmospheric pollutants, *e.g.* NO_x and particulate matter from gasoline and Diesel engines. Automotive industry already mobilized a lot of investments to match the increasingly strict standards about the atmospheric pollutant emissions (Fig.2.6) [18]. Particular attention was paid to Diesel engines compared to gasoline engines utilizing a mature technology. The catalytic exhaust gas treatments for mobile sources are becoming more and more sophisticated, with consequently an extensive use of critical materials such as precious metals and rare earth elements.

Engine exhausts consist of a complex mixture, the composition depending on a variety of factors such as: type of engine (two- or four-stroke, spark- or compression (diesel)-ignited), driving conditions, cold start, vehicle speed, acceleration/deceleration, etc. Kaspar et al. [19] summarized typical compositions of exhaust gases for some common engine types.

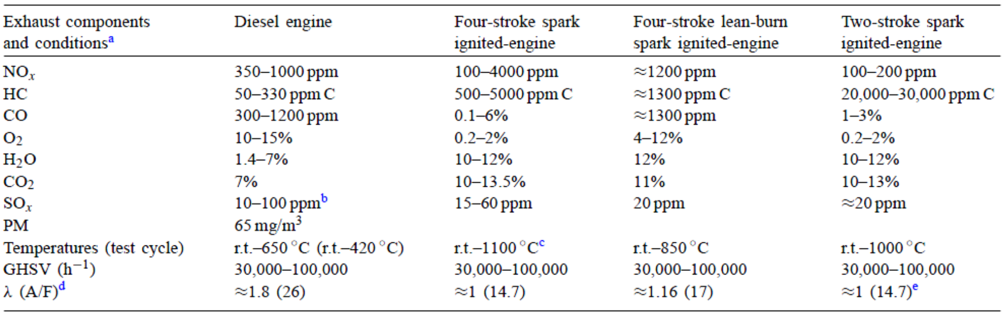

Exhaust components and conditions[a]	Diesel engine	Four-stroke spark ignited-engine	Four-stroke lean-burn spark ignited-engine	Two-stroke spark ignited-engine
NO_x	350–1000 ppm	100–4000 ppm	≈1200 ppm	100–200 ppm
HC	50–330 ppm C	500–5000 ppm C	≈1300 ppm C	20,000–30,000 ppm C
CO	300–1200 ppm	0.1–6%	≈1300 ppm	1–3%
O_2	10–15%	0.2–2%	4–12%	0.2–2%
H_2O	1.4–7%	10–12%	12%	10–12%
CO_2	7%	10–13.5%	11%	10–13%
SO_x	10–100 ppm[b]	15–60 ppm	20 ppm	≈20 ppm
PM	65 mg/m^3			
Temperatures (test cycle)	r.t.–650 °C (r.t.–420 °C)	r.t.–1100 °C[c]	r.t.–850 °C	r.t.–1000 °C
GHSV (h^{-1})	30,000–100,000	30,000–100,000	30,000–100,000	30,000–100,000
λ (A/F)[d]	≈1.8 (26)	≈1 (14.7)	≈1.16 (17)	≈1 (14.7)[e]

Table.2.1. Exhaust compositions for two-/four-stroke, diesel and lean-four-stroke engines [19].

[a] *N_2 is remainder.*

[b] *For comparison: diesel fuels with 500 ppm of sulfur produce about 20 ppm of SO_2* [20].

[c] *Close-coupled catalyst.*

[d] *λ defined as ratio of actual A/F to stoichiometric A/F, λ = 1 at stoichiometry (A/F = 14.7).*

[e] *Part of the fuel is employed for scavenging of the exhaust, which does not allow to define a precise*

In the exhaust mixture of gasoline powered engine, nitrogen oxides (NO_x), mostly NO, unburned or partially burned hydrocarbons (HCs) and carbon monoxide (CO) are the most harmful and principal gaseous pollutants (as shown in Table.2.1) and the name of TWCs is derived from the ability to eliminate simultaneously the three main atmospheric pollutants existing emission. In addition to the other pollutant components such as water, hydrogen, nitrogen, oxygen, etc., sulfur oxides are normally unremoved by the post-combustion treatments because the only effective way is to reduce them to elemental sulfur which would accumulate in the system [19]. Besides, the prevention of catalyst sulfur poisoning is also a point that we need to seriously consider when dealing with methane by perovskite-type catalysts. Accordingly, diminishing sulfur content in fuel is the way to minimize sulfur emissions.

Besides, the variability of the exhaust emissions with the air/fuel ratio (A/F) is illustrated in Fig.2.7., where A/F is expressed as the sometimes-used equivalence ratio (λ). The value is defined as the ratio of the total oxygen in the air-fuel mixtures burning in the engine to the amount of oxygen required for the complete combustion of the fuel. It can also be conveniently measured as a ratio of the actual A/F to the stoichiometric A/F. An A/F of 14.6 corresponds to an equivalence ratio of λ=1, which is also referred to as the stoichiometric point [22]. Therefore, rich burn and lean burn is defined respectively as $\lambda<1$ and $\lambda>1$.

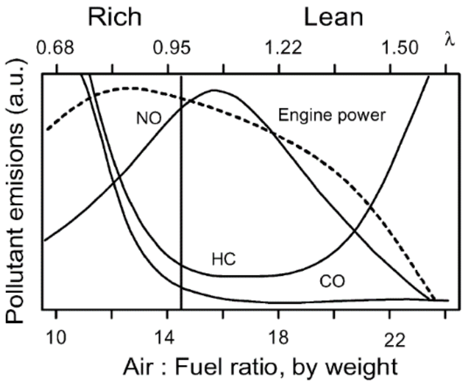

Fig.2.7. The effect of the air/fuel (A/F) ratio (w/w) on automotive gasoline engine emissions. [19, 22]

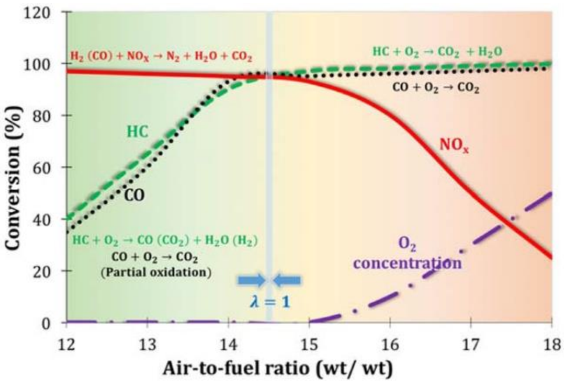

Fig.2.8. Three-way catalytic (TWC) converter profile for conversion vs. air-to-fuel ratio. [21]

The main reactions on TWC converter are listed on the Table.2.2 below [19, 22]:

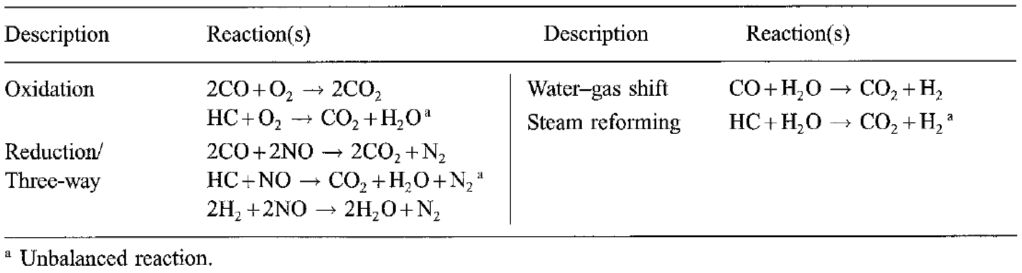

Description	Reaction(s)	Description	Reaction(s)
Oxidation	$2CO + O_2 \rightarrow 2CO_2$ $HC + O_2 \rightarrow CO_2 + H_2O$ ᵃ	Water–gas shift Steam reforming	$CO + H_2O \rightarrow CO_2 + H_2$ $HC + H_2O \rightarrow CO_2 + H_2$ ᵃ
Reduction/ Three-way	$2CO + 2NO \rightarrow 2CO_2 + N_2$ $HC + NO \rightarrow CO_2 + H_2O + N_2$ ᵃ $2H_2 + 2NO \rightarrow 2H_2O + N_2$		

ᵃ Unbalanced reaction.

Table.2.2. Reactions occurring on automotive exhaust catalysts, which may contribute to exhaust removal [22].

Zheng et al. [21] also shows the TWC conversion profile (Fig.2.8) which extends the former figure in detail. CO and HCs are essentially fully oxidized at lean (excess

O_2) of the stoichiometric air-to-fuel ratio (right side of stoichiometric, $\lambda>1$). NO_x reduction occurs when little or no O_2 is present, as in the rich operating mode (left side of stoichiometric, $\lambda<1$). The λ value is controlled via a feedback control system through a signal received from the O_2 sensor as shown in Fig.1.4.

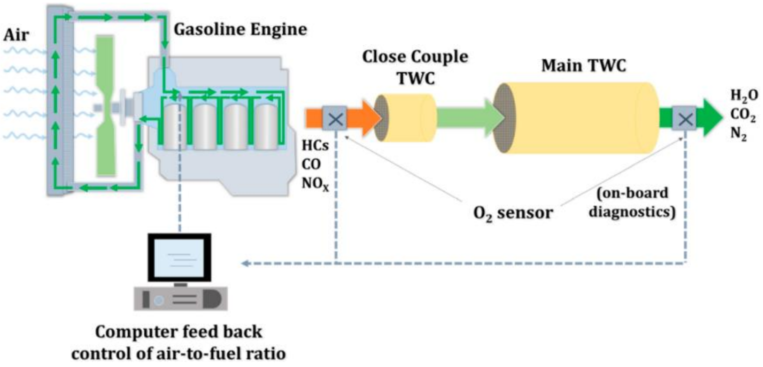

Fig.2.9. A schematic of the unit operations in the exhaust system for a TWC with feedback control of air-to-fuel ratio [21].

Two λ sensors (oxygen quantity sensor) are installed in the closed-loop control system: one placed upstream and the other placed downstream of the catalytic converter. The quantity of air is constantly measured and the fuel injection is adjusted automatically by the electronic automation system which relies on the feedback signal from the λ sensor located upstream of the catalytic converter. A/F fluctuations can be detected by comparing the signal difference between the two λ sensors (Fig.2.9). However, in case of abnormal behavior of oxygen sensors leading to extensive variations of A/F ratio, an On-Board Diagnostics (OBD) ensures the exhaust emission under the limits with the coordination of each part [21].

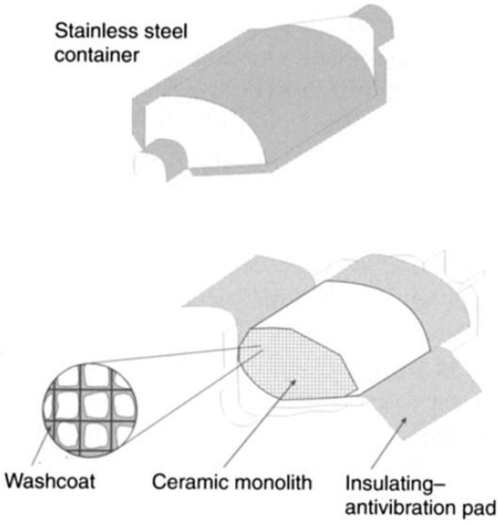

Fig.2.10. A typical catalytic exhaust converter. [22].

For the composition of three-way catalytic converter (Fig.2.10), the monolith (honeycomb) and the active phase (washcoat) are the two main components. The monoliths are made of ceramic materials, which is cheaper and readily available materials conferring sufficient thermal resistance under normal engine running conditions and a good thermal shock resistance. Typically, a density of 46-62 cells per cm^2 with a wall thickness of 0.10-0.30 mm is employed. This allows the exhaust gases to pass through the honeycomb with a small pressure drop, keeping a good contact between the active phase and the gas phase. The active phase (washcoat) is a mixture of noble metals, promoters, surface area stabilisers, high-surface-area support as well as proprietary additives to improve the activity of the TWCs. The active phase is supported (washcoated) from slurry onto the monoliths by dipping method [22].

4. Four-way catalytic system

Compared to three-way catalytic system (TWC), the four-way converter (FWC) is aimed at treat diesel powered engine emission pollution. Besides the normal pollutants carbon monoxide (CO) and hydrocarbon (HC), the emission contains significant amount of the nitrogen oxides (NO_x) as well as the particulate matters (PM) emitted from diesel engines. These primary pollutants are undesirable in the atmosphere as they cause health problems of living beings, global warming and climate change, pollution of water and soil, deterioration of buildings and monuments, negative impact on agricultural productivity and are known to be mutagenic and carcinogenic [23]. Furthermore, the pollutants react with atmospheric constituents photochemically to form much more dangerous secondary pollutants, such as peroxyacetyl nitrate (PAN), smog, ozone, etc. Thus, for maintaining air quality, European Emission Standards [18] have become increasingly stringent as mentioned in Table 2.3 for light-duty vehicles (LDVs) and heavy-duty vehicles (HDVs). It reflects lowering of NO_x emission threshold, on the order of 55–80%, and PM, on the order of 10–67% from Euro-5 to Euro-6 [24] (Table 2.3).

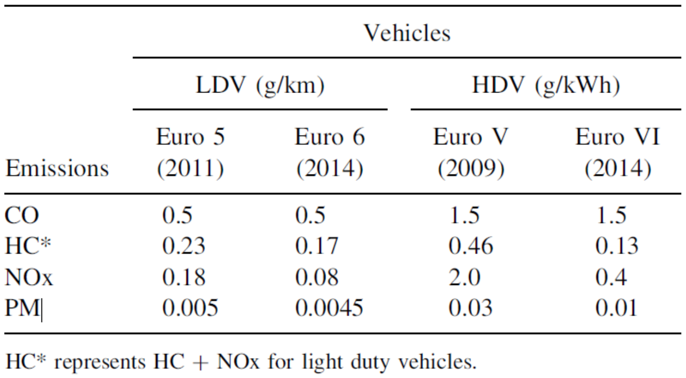

	Vehicles			
	LDV (g/km)		HDV (g/kWh)	
Emissions	Euro 5 (2011)	Euro 6 (2014)	Euro V (2009)	Euro VI (2014)
CO	0.5	0.5	1.5	1.5
HC*	0.23	0.17	0.46	0.13
NOx	0.18	0.08	2.0	0.4
PM	0.005	0.0045	0.03	0.01

HC* represents HC + NOx for light duty vehicles.

Table.2.3. Emission limits for light-duty vehicles (LDVs) and heavy-duty vehicles (HDVs)

Particulate matter, known as PM, is a complex mixture consisting of solid phase and condensate materials. The main components of solid phase are inorganic carbon and metal ashes, while condensate materials contain boiling hydrocarbons, water and sulfuric acid [25]. Burtscher et al. [26] researched particles from diesel as well as particles from other combustion sources are a complex mixture of elemental carbon (EC), a variety of hydrocarbons (HC), sulfur compounds, and other species. Particles differ in size, composition, solubility and therefore also in their toxic properties.

Zhu et al. [27] did an investigation on the morphology, internal macrostructure, and fractal geometry of particulate matter (PM) conducted for a 1.7-L light-duty diesel engine. A high-resolution transmission electron microscope (TEM) was used to observe and graphitic crystallite structures were found from these light-duty diesel particulates, particularly at high engine loads.

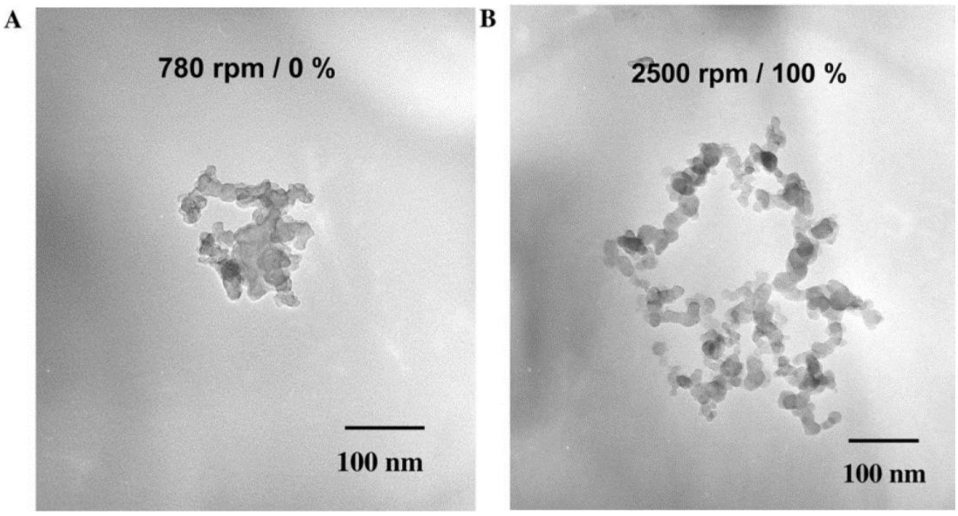

Fig.2.11. TEM photographs of diesel particulates sampled at (A) 780 rpm/0% load and (B) 2500 rpm/70% load (Magnification of 89,000) [27].

The particulates produced from diesel engines showed distinctive morphological differences. A and B (Fig.2.11) show the typical TEM images of diesel particulates sampled at 780 rpm/0% load (idling) and 2500 rpm/100% load, respectively. At the idling condition, many particles appeared to be nebulous in morphology (boundaries between primary particles were unclear). These amorphous soot particles are suspected to contain a significant amount of soluble organic compounds (SOCs) or other liquid phase chemicals. Further investigations into chemical compositions are needed to validate this observation. On the other hand, the particulates sampled at 100% load appeared to be quite distinctive [27]. Therefore, the engine load has a profound effect on particulate morphology. A similar trend has been found from heavy-duty diesel particulates [28-30].

To address the problem of particulate matter emission, a Diesel Particulate Filter (DPF) is inevitably required and has been proven to be quite effective in controlling PM emissions of diesel automobiles. Václavík et al. researched the structure of a wall-flow particulate filter (Fig.2.12) [31].

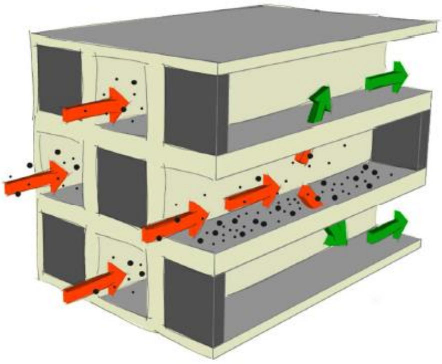

Fig.2.12. Structure of wall-flow particulate filter (PF) [31].

Therefore, after the investigations on PM treatment, for meeting the current emission standards of diesel-powered vehicles, the optimization of integral engine and post-treatment catalytic system has been taken into consideration. Up to now, an integration of separate technologies (Fig.2.13) is designed to control various pollutants in the exhaust emission of diesel engines, such as diesel oxidation catalyst (DOC), diesel particulate filter (DPF), selective catalytic reduction (SCR) and ammonia slip catalyst (ASC) [32].

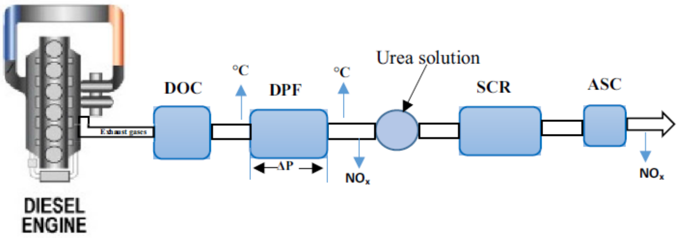

Fig.2.13. Diesel engine emission control technologies [32].

For the treatment of NO_x with relatively high content from the diesel engines, the selective catalytic reduction (SCR) technology develops progressively. In actual industry (Robert Bosch GmbH), Nova et al. [33] designed a sophisticated Urea-SCR with vanadium(V) oxide (V_2O_5)/WO_3 supported on titania catalyst technology. Similar as the concept presented in Fig.1.8, they put it into reality in order to control diesel vehicle exhaust gas emissions with a urea solution tank, dosing spray module and static mixer, temperature and NO_x sensors. Besides, increasing activity by using higher manganese loadings appears to result in the formation of more N_2O. It is noted perhaps the most successful development in this area was made by Shell who in the early 1990s developed a relatively low-temperature ammonia SCR process using a vanadium on titania catalyst promoted by transition metal species [33].

5. Three-way catalysts for natural-gas-vehicles

Compared to TWC and FWC end-of-pipe technologies for gasoline and diesel-powered vehicles, the emergence of engines powered by natural gas (NGV), or locally produced bio-gas, offers an alternative to liquid fossil engines with lower greenhouse gas and NO_x emissions combined with significantly lower amounts of particulate matters (PM) formation in exhaust emission [2]. However, the main obstacle of NGV lies in the residual emission of methane which is characteristically refractory to break down due to the high bond energy of CH_3-H(g) (439.3 kJ mol^{-1}) [34]. Heterogeneous catalysts have therefore been a key to the successful conversion of methane. The reason for this is that once methane is adsorbed on a metal surface the C-H bond dissociation energies depends on the hosting surface metal, and the total bond dissociation energy appears to be useful for identifying promising catalysts [35-37].

Although natural gas-powered engine has such mentioned advantages, these could be partly counterbalanced by the residual emissions of methane in the exhaust which is recognized as a potent greenhouse gas that is 23 times higher than CO_2. Raj [38] investigated the implementation of palladium–rhodium three-way catalysts and platinum–palladium oxidation catalysts respectively to regulate the emissions of NO_x and unburnt methane from stoichiometric ($\lambda = 1$) and lean-burn ($\lambda = 1.3$) NGV engines. Generally, stoichiometric conditions are advantageous because the simultaneous abatement of NO_x and methane is easier than under lean conditions, and greater resistance to poisoning effects in the presence of water (>10 vol%) and sulfur (<0.5 ppm) is observed. Till now, the majority of academic investigations have been performed under lean-burn conditions (excess of oxygen), being more favorable for combusting methane at lower temperature. Important technical issues are addressed by academia in order to stabilize the presence of oxidic palladium species responsible for the catalytic performances [39].

As to the function of palladium matter, Granger et al. [39, 40] researched the conversion between Pd^0 species and PdO. A critical aspect in the development of stoichiometric NGV catalysts is related to the low stability of PdO under these operating conditions, which decomposes to much less reactive Pd^0 species at high temperature. Hence, some thermodynamic constraints must be considered due to the equilibrium between PdO_x and Pd^0. Palladium in association with platinum was found to improve the thermal durability and the impact of sulfur poisoning [41]. For the methane abatement catalytic technologies, palladium is the metal chosen for highly loaded benchmark catalysts generally [38] (>200 g/ft, more than twice the amount used in conventional catalysts) to compensate the deactivation process due to thermal sintering. The investigation of Wang et al. [42] introduced that a high temperature in the range 400–500°C is needed to activate the cleavage of the C–H bond [34]. Gelin et al. [43] put forward such issues: (i) thermal deactivation at high temperature, (ii) design of catalytic systems more resistant to poisoning effects, especially sulfur compounds in the exhaust gas, and (iii) high activity at the lowest temperatures typically during the engine cold start. Activation of methane is supposed to take place on site pairs composed of surface PdO and surface Pd (Fig.2.14) [40, 43].

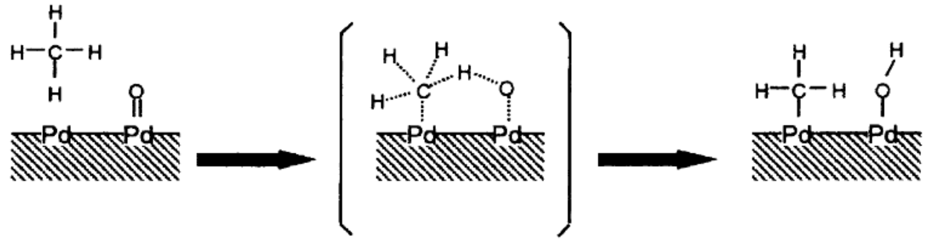

Fig.2.14. Reaction scheme for the activation of methane on a surface Pd–PdO site pair [40,

Lee et al. [44] studied methane oxidation on a plasma-catalysis hybrid system. According to the catalyst loading position, two different configurations of the hybrid system were proposed: (a) in-plasma catalysis (wherein the catalyst is placed in the discharge zone) and (b) post-plasma catalysis (wherein the catalyst is placed after the discharge zone) (Fig.2.15).

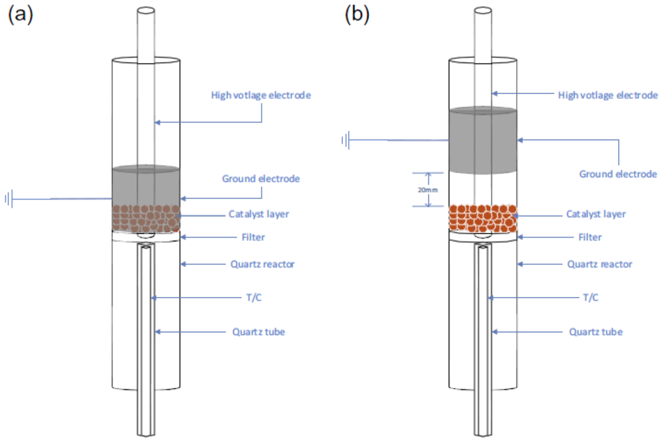

Fig.2.15. (a) In-plasma catalysis / (b) Post-plasma catalysis reactor configuration [44].

A synergistic effect was found for the in-plasma configuration [44], demonstrating a quicker “light-off” of methane oxidation and a lower CO selectivity. Consequently, complete methane oxidation was achieved even at room temperature when 2% wt Pd/A_2O_3 oxidation catalyst was employed. However, such synergy was not detected in the post-plasma configuration. In addition, electrochemical method has also introduced to assist the catalytic activity of methane oxidation. This method is based upon the concept of non-faradaic electrochemical promotion of catalysis (NEMCA) discovered by Stoukides et al. [45]. By applying a potential between the working electrode (consisting of the catalyst supported on a solid electrolyte) and the counter electrode (deposited on the same solid electrolyte), the metal-support interaction can be monitored [39]. Matei et al. [46] studied systematically the effect of electrochemical promotion of catalysis on methane combustion. It was established that impregnation of Pd on highly porous YSZ (Y_2O_3-stabilized-ZrO_2, an oxygen ion conductor) led to a much more active catalyst compared to that typically deposited on dense YSZ, with an increased catalytic rate as much as one order of magnitude (Fig.2.16). The author attributed the improvement of catalytic performance to the much higher dispersion of palladium on porous electrolytes.

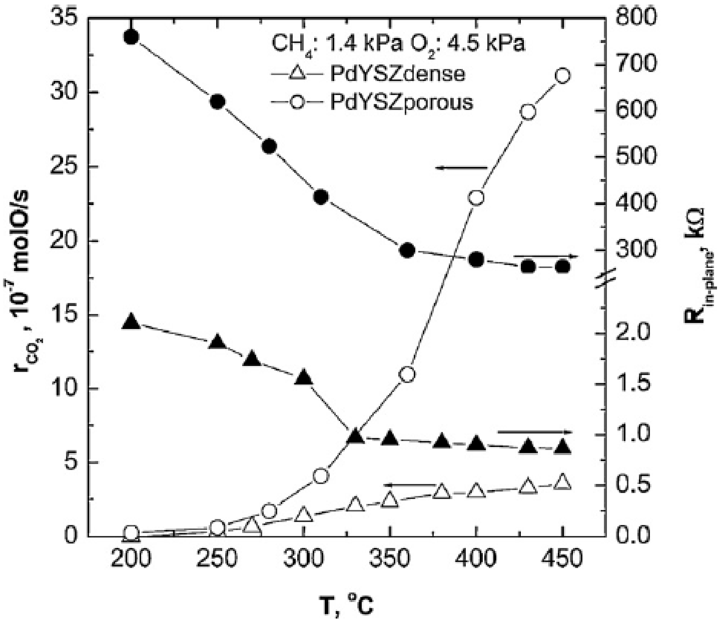

Fig.2.16. Effect of the temperature on methane conversion, CO_2 formation rate and in-plane resistance of the Pd catalyst deposited on dense and on porous YSZ [46].
$P_{CH_4} = 1.4\ kPa$, $P_{O_2} = 4.5\ kPa$, F = 200 ml/min.

Granger et al. [39] pointed out that one of the main obstacles in methane conversion consists in the deactivation caused by coke deposition, and that materials with excellent Oxygen Storage Capacity (OSC) properties could overcome the deactivation obstacle. Hence, perovskite-based materials, whose formula is well known as ABO_3 with OSC and intrinsic oxygen mobility, are taken into extensively investigations. Meanwhile, Eyssler et al. [47] have indicated the beneficial effect of perovskite-based material on stabilizing PdO and asserted that depending on the calcination temperature and reaction temperature, a delicate equilibrium existed between the fraction of active PdO exposed on the $LaFeO_3$ surface and the fraction of Pd^{n+} dissoluted in the Pd-$LaFeO_3$ solid solution. Eyssler et al. [47] further discovered that below 700 °C, catalytic activity was in accordance with Pd^{2+} species on the surface of $LaFeO_3$. The higher the thermal treatment temperature, the lower the Pd dispersion, these result in a diminished accessibility of PdO-surface and active centers. They concluded that 2 wt% Pd/$LaFeO_3$ outperformed the conventional Pd/Al_2O_3 in terms of stabilizing active PdO at high temperature [47]. It was widely recognized that the self-regenerative mechanism of perovskites can protect noble metals (i.e. Pt, Pd, Rh) from sintering by inhibiting the particle growth. Yoon et al. [48] studied the thermal stability of Pd-containing $LaAlO_3$ catalyst. A strong Pd-La interaction was clarified to induce the electron transfer from La to Pd. As a result, a higher electron density of Pd was identified, probably responsible for the enhancement of thermal stability of PdO when subjected to high temperature.

Besides, the solids exhibit remarkable catalytic properties on total oxidation reactions, especially methane combustion. However, their practical applications on an industrial scale are relatively insufficient. The most demonstrated in post-combustion catalysis are related to their development at the beginning of the 1970s as two-way catalysts [49, 50], and recently in three-way catalysis based on the fact that the self-regenerative behavior of perovskite-based materials could protect PGM particles from irreversible thermal sintering under airflow cycling conditions.

NGV is considered as alternative for conventional gasoline or diesel vehicles to meet future legislation requirements. The concept of NGV can be concretized through either CNG or LNG. Further amendments are still needed to be cost-efficient while improving the overall performance of the NGV prior to its large-scale application, in particular dealing with issues of deactivation caused by thermal ageing and sintering, water or sulfur poisoning as well as methane slip at low temperature [38].

6. Perovskite materials

Perovskite materials are mixed oxides and described by the general formula ABO_3. Besides, A and B are two cations and O being an oxygen anion. They represent probably the most studied mixed-oxide system in the field of heterogeneous catalysis due to their versatile properties to accommodate a wide range of cations. Because most of the oxides present a slightly lower or higher oxygen content compared to the theoretical formulation, $ABO_{3\pm\delta}$ is more accurate and the stoichiometric term δ means the differences from the theory. Here for easier readability, ABO_3 denotes $ABO_{3\pm\delta}$.

6.1. Structure

In the structure of perovskite, the A cation can be a lanthanide, alkaline, or alkaline-earth cation while the B cation is a metallic element from the 3d, 4d, or 5d configuration. Considering the possible valences of the cations and the electroneutrality of the structure, different charge distributions can be encountered in the structure [5].

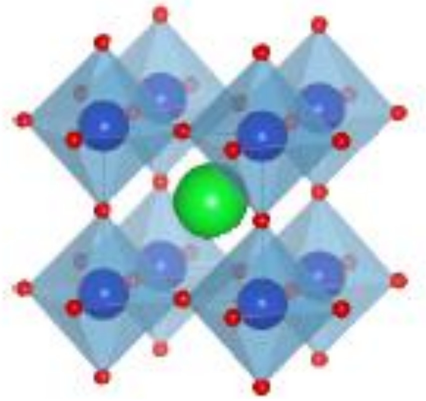

Fig.2.17. Perovskite structure [51].
A green; B blue; O red.

dodecahedral A site			octahedral B site		
ion	radius (Å)^a	radius (Å)^b	ion	radius (Å)^a	radius (Å)^b
Na^+	1.06	1.32? (IX)	Li^+	0.68	0.74
K^+	1.45	1.60?	Cu^{2+}	0.72	0.73
Rb^+	1.61	1.73	Mg^{2+}	0.66	0.72
Ag^+	1.40	1.30 (VIII)	Zn^{2+}	0.74	0.75
Ca^{2+}	1.08	1.35	Ti^{3+}	0.76	0.67
Sr^{2+}	1.23	1.44	V^{3+}	0.74	0.64
Ba^{2+}	1.46	1.60	Cr^{3+}	0.70	0.62
Pb^{2+}	1.29	1.49	Mn^{3+}	0.66	0.65
La^{3+}	1.22	1.32?	Fe^{3+}	0.64	0.64
Pr^{3+}	1.10	1.14 (VIII)	Co^{3+} (LS)		0.52
Nd^{2+}	1.09	1.12(VIII)	Co^{3+} (HS)	0.63	0.61
Bi^{3+}	1.07	1.11(VIII)	Ni^{3+} (LS)		0.56
Ce^{4+}	1.02	0.97(VIII)	Ni^{3+} (HS)	0.62	0.60
Th^{4+}	1.09	1.04(VIII)	Rh^{3+}	0.68	0.66
			Ti^{4+}	0.68	0.60
			Mn^{4+}	0.56	0.54
			Ru^{4+}	0.67	0.62
			Pt^{4+}	0.65	0.63
			Nb^{5+}	0.69	0.64
			Ta^{5+}	0.69	0.64
			Mo^{6+}	0.62	0.60
			W^{6+}	0.62	0.60

Table.2.4. Cations commonly found in perovskite structure.
List of Cations with Their Respective Radii, Found in ABO3-Type Perovskite [52].
^{a}From ref 53. ^{b}From ref 54.

The ideal crystalline unit cell of perovskite is described as cubic from the Pm3m space group (Fig.2.17), where the A cation is in the center of the cube, formed by the B cations, and the oxygen ions are located in the middle of the edges. The B cation is in octahedral coordination toward oxygen, while the A cation is in dodecahedral coordination [51, 52]. As such, more than 90% of the metallic elements from the periodic table can enter the perovskite structure.

Royer et al. [5] summarized that one of the advantages of the perovskite structure is thus the possibility to adopt a wide range of different compositions, changing either the A or the B cation or partially substituting each cation by other cations of the same or different valences, resulting in a general formula of $A_{1-x}A'_{x}B_{1-y}B'_{y}O_{3\pm\delta}$, to adjust its redox and surface properties (Table 2.4, Table 2.5). The stability of the structure depends directly on the geometrical constraints of octahedral and dodecahedral cavities. To have a stable BO_6 octahedron, the B^{x+} radii should be higher than 0.51 Å. Insertion of the A cation in the cube octahedral cavities of the BO_6 arrangement leads to distortion of the octahedrons and formation of more stable orthorhombic or rhombohedral structures.

The tolerance factor (or Goldschmidt factor) is an empirical factor introduced to indicate the ion accommodation capability of the perovskite structure [55, 56].

$$t = \frac{r_A + r_O}{\sqrt{2}(r_B + r_O)}$$

$r_A - \mathit{radius\ of\ A\ site\ cation}$

$r_B - \mathit{radius\ of\ B\ stie\ cation}$

$r_O - \mathit{radius\ of\ oxygen\ anion}$

	0.75 < t < 1.06 Perovskites			
$t < 0.75$ Ilmenite	$0.75 < t < 0.96$ *orthorhombic distorsion*	$0.96 < t < 0.99$ *Rhombohedral distorsion*	$0.99 < t < 1.06$ *cubic*	t > 1.06 hexagonal

Table.2.5. Tolerance factor with the corresponding structure.

Theoretically, perovskite structure could be maintained as long as the tolerance factor is kept within the range of $0.75 \leq t \leq 1$. The ideal cubic structure is characterized by a tolerance factor of 1; In the ideal cubic structure of highest symmetry, A cation, B cation and oxygen anion have contact with each other. The ideal structure occurs only when the tolerance factor gets close to 1.0 at high temperature. A t value lower than 1.0 gives rise to a structure with less symmetry. When t < 0.75 the crystal exists in the form of ilmenite structure ($FeTiO_3$). While when 1.00 < t < 1.13 the crystal becomes hexagonal symmetry such as calcite or aragonite [57]. Table.1.5 summarizes the range of tolerance factor corresponding to the relevant structure. Due to the role of the BO_6 octahedron on crystal unit cell formation, an octahedral factor (r_B/r_O) was also introduced, being as important as the tolerance factor [56].

The Ruddlesden-Popper phase (RP phase) is composed of n consecutive perovskite layers (ABO_3) alternating with rock-salt layer (AO) along the crystallographic c-axis direction [58]. A cation is located at the boundary between two types of layers with a coordination number of 9 while B cation is situated in the center of octahedron formed with nearby 6 oxygen anions. Lee et al. [58] researched the general formula of RP oxides expressed as $A_{n+1}B_nO_{3n+1}$ ($n\geq1$) or more specifically as $(AO)\cdot(ABO_3)$ where n represents the number of connected layers of vertex-sharing BO_6 octahedra [59]. When n=1, A_2BO_4 structure is formed, i.e. La_2CuO_4; When n>1 additional ABO_3 blocks are introduced between two rock-salt layers to form complex oxides with multiple stacked octahedral layers.

6.2. Related reactions and applications

Royer et al. [5] outlined four main kinds of perovskite-based materials reactions, which are oxidation reactions, reduction reactions, selective oxidation reactions and reactions for hydrogen and syngas production. Aiming at methane partial or total oxidation, such applications below are chosen to introduce.

For the oxidation reactions [5], owing to their exceptional redox properties (multiple valence states of the cations) coupled to a high oxygen mobility, perovskites can be remarkable oxidation catalysts, such catalysts are applied for CO oxidation at low-temperature [60], confirming that manganite and cobaltite perovskites were very active for CO oxidation, and CH_4 oxidation at high-temperature, explaining that perovskites and other mixed oxides such as hexa-aluminates are less active than Pd catalysts but are more stable at high temperatures [61, 62], which is a decisive advantage in natural gas combustion technology [63]. Even though cobaltites and manganites (and to a lesser extent, ferrites) dominate this application, the quasi-infinite possibilities to substitute A and B cations allowed us to tune the catalytic properties on demand. However, intrinsic activity of perovskites for most oxidation reactions remains 1 or 2 orders of magnitude lower than that of noble metals. Intensive research was performed to increase surface area (see section 2). Perovskites of 100 m^2/g can now compete with noble-metal catalysts having currently metallic surface areas of 1 m^2/g. Keeping a high surface area in oxidation reactions is however challenging. Higher stability could be obtained by supporting perovskite on other oxides such as zirconia and alumina. Finally, perovskites were proven to be excellent supports of metal catalysts: combining the two active materials (perovskite oxide and metal) gives rise to innovative catalysts in many applications [64-68].

Perovskites are good candidates for both decomposition (of N_2O or NO) and catalytic reduction of NO_x because of the wide range of composition and their modular properties [69]. Concerning N_2O decomposition [70], oxygen desorption is proposed to be the rate-determining step of the process. Perovskite has been studied for NO_x reduction in a continuous process (SCR) because of their ability to incorporate and combine many chemical elements, like precious metal, or to accommodate B-site cation substitution. NO decomposition, oxygen can act as an inhibitor. Adsorption of O_2 must be weakened, accompanied by an increase of NO adsorption capacity, which is achieved in the presence of reduced metallic sites and oxygen vacancies [71, 72]. At higher temperature, NO_x removal occurs through the nitrate route. Oxygen is involved in NO oxidation, and the improvement of both α-oxygen abundance and β-oxygen mobility help formation of nitrate species and results in high $DeNO_x$ efficiency. However, perovskite materials suffer from a lack of activity, mainly at low temperature. By the enhancement of lattice O_2 mobility and the increase in cationic defects, incorporation of Pd into the perovskite B site is an interesting option to improve the catalytic performance [10].

For the selective oxidation reactions [5], methane is often the feedstock of choice due to the abundance of natural gas and conversion of methane to syngas by partial oxidation of methane (POM). POM is more energy efficient compared to conventional steam reforming, and it produces synthesis gas with a H_2/CO ratio of 2 suitable for methanol synthesis and Fischer−Tropsch reactions [73]. At this temperature, total oxidation of methane is favored. Consequently, two different mechanisms have been proposed for the POM reaction: (i) CO and H_2 are produced directly from methane; (ii) CH_4 is oxidized into CO_2 and H_2O followed by steam or dry reforming of CH_4 to yield CO and H_2 [74, 75]. Oxidative coupling of methane (OCM) is an interesting route for direct conversion of natural gas to C_2 hydrocarbons, especially ethylene, which can then be converted to useful chemicals and fuels. The reaction is highly exothermic and requires high temperatures (>700 °C, necessary to activate methane). The catalysts are mostly supported metal oxides with basic properties such as alkali metals, alkaline-earth metals, and rare-earth metals [76].

6.3. Perovskites self-regenerative mechanism

Besides the excellent properties on oxygen mobility and oxygen storage capacity of perovskite materials, their self-regenerative behaviour is also recognised as “intelligent” performance (Fig.2.18). Daihatsu Motor developed the "Intelligent Catalyst" using perovskite oxide as a support instead of alumina materials in 2001 [77].

The coordination of Pd ions in a crystal perovskite oxide provided the active function for self-regeneration in automotive exhaust gas, resulting in long catalyst life and less use of Pd.

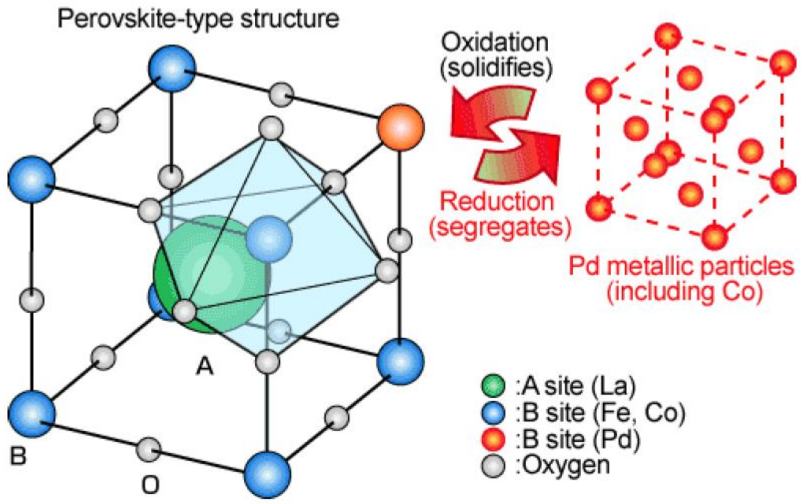

Fig.2.18. B site doped by Pd to exhibit self-regenerative property [77].

Self-regeneration is realized through a cycle between solid solution and segregation of Pd in a perovskite crystal. Namely, Pd atoms move back and forth between the inside and the outside of the perovskite crystal synchronized with the fluctuations of the real automotive exhaust gases. As a result, catalyst deactivation by the growth of Pd nanoparticles can be suppressed (Fig.2.19) [77].

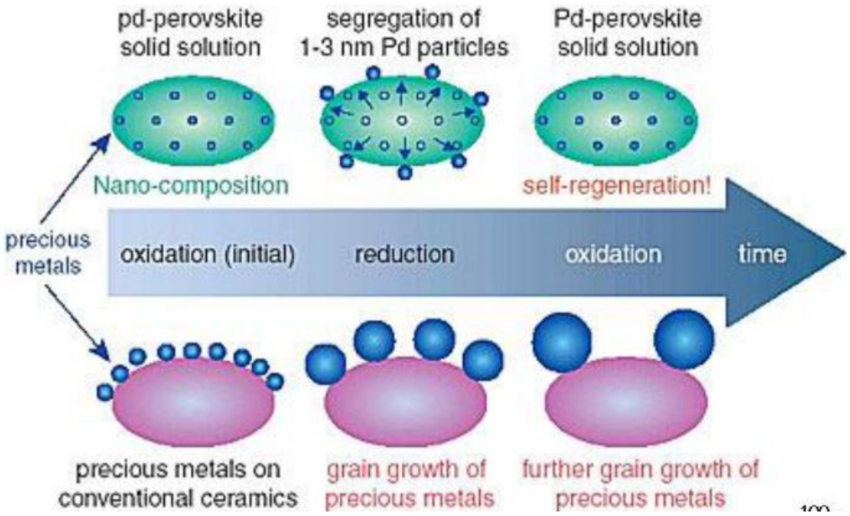

Fig.2.19. Self-regenerative mechanism of Pd doped perovskite in structure [77].

$LaFe_{0.57}Co_{0.38}Pd_{0.05}O$ was used as the so-called “intelligent catalyst” to compare with the conventional Pd-impregnated γ-Al_2O_3 catalyst (Fig.2.20) [77, 78]. Tolerance to aging as well as catalytic activity prior to and after aging of the as-mentioned catalysts were examined by a series of methods. It was manifested that perovskite-based $LaFe_{0.57}Co_{0.38}Pd_{0.05}O_3$ catalyst afforded an extraordinary heat resistance capability compared to Pd-impregnated γ-Al_2O_3 catalyst. From the images of transmission electron microscopy (Figure1.4 b), it was shown that after ageing at 900°C during 100 h, the particle size of palladium of perovskite-based catalyst increased only to a limited extent, evidenced by small metallic particles with diameters of 1-3 nm. On the contrary, an enormous increase of the particle size of the Pd/alumina catalyst was observed when exposed to the same ageing conditions, reaching up to 120 nm. The reason for this phenomenon was attributed by the authors to the capability of Pd-perovskite catalyst to suppress remarkably the growth of metallic particles. Furthermore, the aged Pd-perovskite catalyst displayed a much higher catalytic activity compared with the Pd/alumina one. After ageing at 900 °Cduring 100h, the Pd-perovskite catalyst retained high catalytic activity whilst catalytic activity of the Pd/alumina decreased dramatically by around 10% (Fig.2.20).

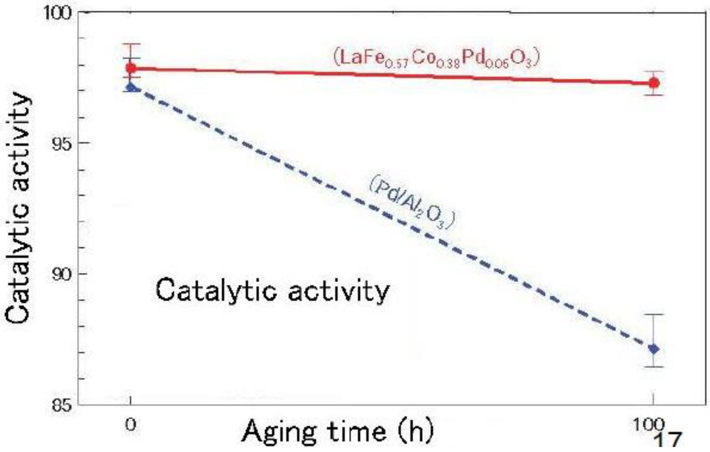

Fig.2.20. Catalytic activity of $LaFe_{0.57}Co_{0.38}Pd_{0.05}O_3$ (Pd-perovskite catalyst) and Pd-impregnated γ-Al_2O_3 (Pd/alumina catalyst) during the ageing at 900°C lasting 100h. [77].

Taniguchi et al. [79] extended the self-regeneration concept initially discovered in Pd-perovskite to other perovskite-type oxides. It was confirmed by author that self-regenerative function was observed not only in the Pd-perovskite, but also in the Rh-perovskite and the Pt-perovskite as well. Similar to palladium, rhodium and platinum exhibited a comparable pattern of moving in and segregating out of the perovskite lattice in a reversible way in a redox cycle as well as outstanding suppression effect on the agglomeration and growth of either rhodium or platinum grains, respectively (Fig.2.21). A universal technology was accordingly proposed for designing such a “Super intelligent catalyst” (Fig.2.22).

Therefore, precious metal-containing perovskite is labelled as “intelligent” by Tanaka et al. [80] as it maintains high catalytic activity even when subjected to harsh conditions thanks to its self-regeneration function. The core the self-regenerative technology lies in the formation of the metal-perovskite solid solution under oxidizing condition and the segregation of metal under reducing conditions to form either nanoparticles or metallic clusters. Hence, the self-regenerative mechanism is dependent heavily on the precious metal-perovskite interaction and some aspects should be taken into account when it comes to the design of an intelligent catalyst. That is to say, the oxide consisted of perovskite components should be able to capture and release precious metals in a reversible manner under redox environment and at the same time preserve the stability of the perovskite structure itself even at high temperature.

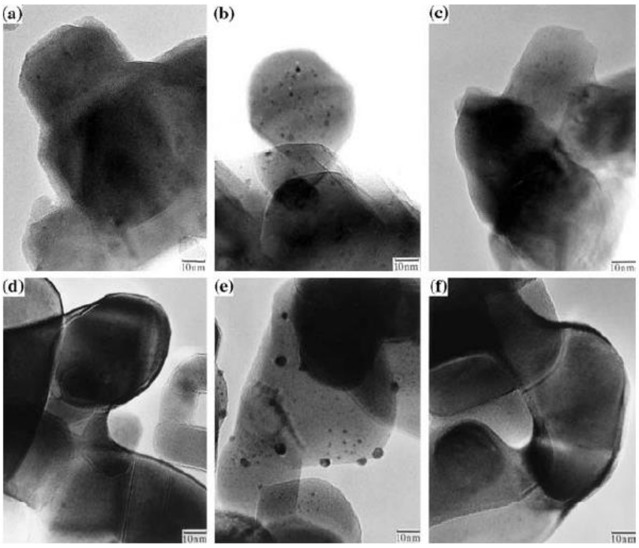

Fig.2.21. TEM photographs of Rh and Pt on perovskite: a) $CaTiRhO_3$ after oxidation; b) $CaTiRhO_3$ after reduction; c) $CaTiRhO_3$ after re-oxidation; d) $CaTiPtO_3$ after oxidation; e) $CaTiPtO_3$ after reduction; f) $CaTiPtO_3$ after re-oxidation, demonstrating the self-regeneration function of Rh and Pt perovskites [79].

Till now, self-regeneration function has been identified in lots of intelligent catalysts, most of which are based upon platinum, palladium or rhodium hosted in $LaFeO_3$, $LaAlO_3$, $CaTiO_3$, $CaZrO_3$, $SrTiO_3$, $SrZrO_3$, $BaTiO_3$, $BaZrO_3$ perovskite [80]. However, contrary to most previous claims, recent studies manifested that the dislodged noble metal is not completely reintegrated into the perovskite crystal, casting doubt on the self-regeneration theory [81]. Meanwhile, M. B. Katz et al. [82] found that the cyclical process of platinum-doped $CaTiO_3$ perovskite mostly arose from bulk rather than surface re-dispersion and only a few nanometers (measured from free surface) of perovskites with self-regeneration function are potentially useful as a host or support for precious metals in any practical embodiment of the original self-regenerating TWC concept. In our real planning, the catalysts impregnated or doped Pd is also considered to finish our future High-throughput screening at RealCat Advanced Laboratory under the references of Pd impregnated CeO_2 and ZrO_2 and $Ce_{0.5}Zr_{0.5}O_2$.

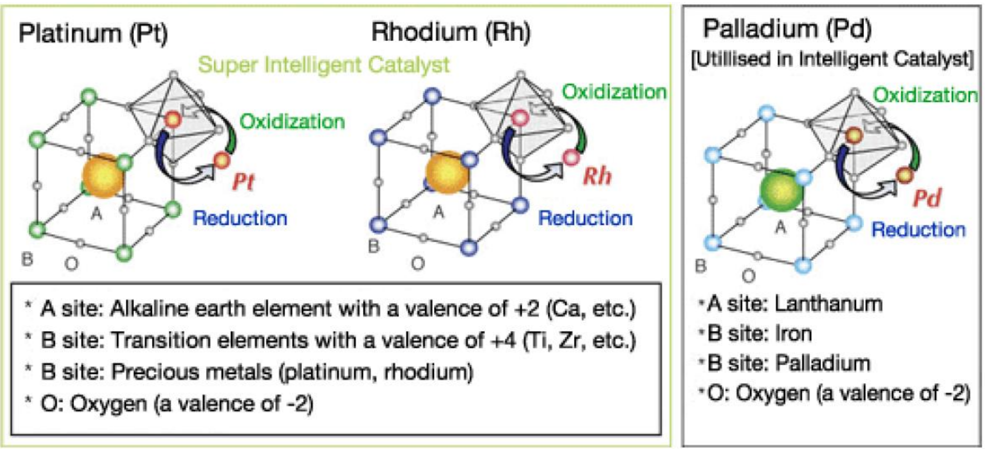

Fig.2.22. Self-regenerative scheme of Pd, Pt, Rh doped perovskite in structure [77]. "Super intelligent catalysts"

6.4. Synthesis of perovskite

Different synthesis methods were developed over the past years to prepare perovskites. Up to now, a multitude of various preparation routes of perovskite was proposed from solid state reactions, over co-precipitation to reverse micelles microemulsion [83] and microwave assisted method [84]. The non-exhaustive study can address but a limited overview and additional details can be found in a recent review by Zhu et al. [85].

6.4.1 Solid state process

6.4.1.1 Solid-solid method

Solid-solid method, also called ceramic method, was introduced in the 1970s as the first approach to prepare perovskite [86]. Oxides, hydroxides or carbonates solids are mixed together to undergo reactions through solid-solid diffusion. The obtained compounds are then subjected to heat treatment at high temperature (typically higher than 1000°C) [86]. This simple method requires high-temperature processing and long reaction time. It has thereby been considered not suitable for catalysis application owing to the poor textural properties of the products because of the growth and agglomeration of particles caused by thermal treatment at high temperature [87].

6.4.1.2. Reactive grinding method

Reactive grinding method refers to mechano-synthesis, known as mechano-chemical processing (MCP). The first systematic investigation on chemical effects of mechanical action was conducted [88, 89]. Mechano-synthesis starts with mixing the precursors (usually in the form of powder) with appropriate proportions and subsequent loading of the above powder mixture, together with grinding media (i.e. steel, zirconia or tungsten carbide) into a reactor in which reactants are subjected to repeated milling for the requisite length of time to get final products [90]. Mechano-synthesis is characterized by the implementation of mechanical energy provided by high-energy ball milling to trigger chemical reactions at quasi room temperature [91]. A low reaction temperature allows this technique to reduce significantly the particle size of products and consequently gives rise to higher specific surface area and enhanced density of surface defects expected to be active sites for redox reactions. It should be noticed that some key factors, including the ratio of ball-to-precursor, milling time, milling atmosphere etc. will have a great influence on the particle size of products. In most of the cases, a certain number of additives such as NaCl, LiCl, ZnO can be used for the purpose of further improving specific surface area of perovskite. In such circumstance, additional leaching steps become indispensable to remove additives by means of appropriate liquid solution depending on the nature of employed additives.

6.4.1.3 Microwave crystallization

Various perovskites synthesized by microwave crystallization have been reported [92, 93, 94]. The advantages of microwave can be exemplified: Firstly, a lot of reactions have been observed to occur faster under microwave irradiation and reaction kinetics could be increased by 1-2 orders of magnitude thanks to either the reduction of energy barrier or thermal effect [95, 96]. Secondly, the limited use of organic solvent makes it more ecologically friendly. In addition, since the initial heating is done rapidly, it consumes less energy and saves cost. Generally speaking, microwave synthesis is faster, cleaner and more energy efficient route compared to conventional methods. However, reagents must have a high dielectric constant or ionic conductivity in order to absorb microwave energy, restricting to a great extent the applicability of microwave technology [97].

6.4.2 Solution-based method

Wet-chemistry synthetic routes are believed to be approaches that are more convenient, more sustainable and less energy-consuming. Unlike solid-state methods, more precise process control is possible in wet-synthesis routes, which yields better textural properties and homogeneity of the products [98].

6.4.2.1 Sol-gel method

In his patent published in 1967, Pechini invented a method for the preparation of alkaline earth titanates, zirconates and niobates by way of resin intermediates [99]. The principle of this method is based on the ability of certain alpha-hydroxycarboxylic acids such as citric, lactic and glycolic acids to form stable polybasic acid chelates with several cations (i.e. titanium, zirconium and niobium) in an aqueous-organic medium. When heated with polyhydroxy alcohol (i.e. ethylene glycol), a polymeric gel with homogeneous distribution of cations is formed as a result of polyesterification of the above chelates. After a thermal treatment at relatively low temperature, excessive organic constituents are removed and desired oxides are obtained [99, 101]. The nature of gel varies depending on the method of drying step: a xerogel is the product of solvent extraction done through thermal evaporation. In contrast, supercritical conditions result in an aerogel (Fig.2.23).

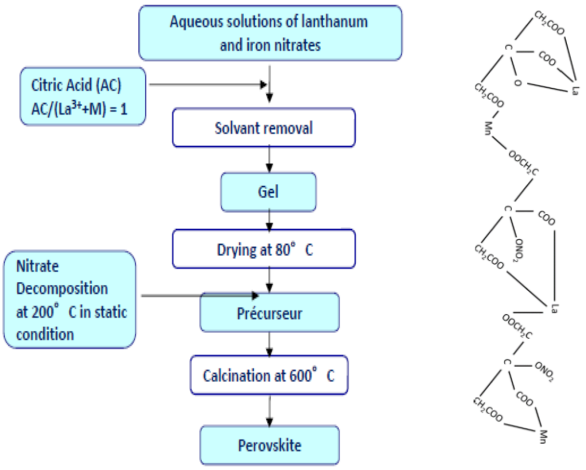

Fig.2.23. Graphic representation of Conventional Citric Method. [99-101]

6.4.2.2 Mechanism of sol-gel method

Various factors, such as the type of employed organic acid, the solution characteristic, the ratio of organic acid to metal ions and the decomposition/calcination temperature, have influences on the product properties. Among common organic acids capable of complexing metals, citric acid was known to be able to form the most stable precursors with metal ions and make them most resistant to autooxidation. Hence, citric acid is most widely used as the complexing agent in sol-gel route. In spite of the fact that specific surface area of perovskites prepared by citric acid complexation is a bit lower than those prepared by polyacrylic acid under same conditions, the enhanced homogeneity and uniformity of ions on the material surface often leads to better catalytic activity for CO oxidation [5]. What's more, it should be mentioned that the ratio of complexing agent to metal ions impacts greatly the composition and property of the product. The effect of CA/metal ions ratio on $LaMnO_{3+\delta}$ was studied by Taguchi et al. [100]. It was shown that gel formation was possible in the molar range from 0.0023 to 0.015 mol of citric acid and the composition of gel was dependent on the citric acid proportion in the initial mixture. Courty [102] discovered that the content of residual carbon in the final product was affected deeply by the citric acid proportion. The higher proportion of citric acid was, the lower content of residual carbon would be. The author attributed this phenomenon to the fact that the combustion of residual carbon was facilitated by higher citric acid proportion leading to diminished apparent density and subsequently augmented porosity. Besides, effect of thermal treatment temperature and time was also examined by the same author. It was found that higher temperature as well as longer treatment time gave rise to bigger size and better crystallinity of perovskite particles. Residual carbon content in the final product plummeted as the decomposition temperature rose in the range of 0-1000 degrees yet stabilized above 1000 degrees [102].

Another important factor during synthesis is the solvent utilized. As a matter of fact, the characteristic of solvent is linked directly to the dissolution of metallic salts as well as the following complexation and gelation process. A wide variety of solvents have been reported, including both inorganic (i.e. water) and organic ones (i.e. ethanol, propanol, ethylene glycol, diethylene glycol). A.Kahoul [103] gave a detailed comparison of water and propanol on the physico-chemical properties of $La_{1-x}Ca_xCOO_3$ perovskites. He claimed that cobaltite synthesized using propanol as solvent exhibited single perovskite phase, larger SSA and higher electrical conductivity values compared to those prepared using water. H. Aono et al. [104] prepared precursors of fine perovskite-type materials by using a series of complex solvents composed of water-organic solvent with various constituents and content. According to his result, pure $LaFeO_3$ perovskite phase was obtained even calcined at temperature as low as 350°C by using a water-ethylene glycol mixed solvent.

In some cases, Ethylene Glycol (EG) is employed to improve product property. EG has been proven as a stabilizer of the CA-metal chelate, leading to a lessened gel combustion rate. Surface crystallinity of material could be ameliorated due to the addition of EG, contributing to a better catalytic activity. Mohsennia [105] studied the impact of ethylene/citric acid ratio (EG/CA ratio) on the catalytic activity of $La_{0.7}Ba_{0.3}Co_xNi_{1-x}O_3$ nano-catalyst. The author argued that the catalytic activity of LBCNs can be strongly affected by the EG/CA ratio through distinctive complexing mechanism and a higher EG/CA ratio can result in a better catalytic activity for CO oxidation [105]. The main drawback of sol-gel route is, however, the release of undesired gases such as NO_x during nitrates decomposition and solvent evaporation and drying processes.

6.4.2.3 Co-precipitation method

The co-precipitation method is based on simultaneous precipitation of precursors in a liquid medium with the presence of precipitating agent. The advantages of co-precipitation lie in its simplicity, wide variability, low cost and easily scalable to industrial level [106]. Many metal salts could serve as precursors, such as hydroxides, carbonates and oxalates. Water, ammonia, urea and oxalic acid are often used as precipitating agents [107-111]. Driven by the principle of reduction of Gibbs free energy of a supersaturated solution, precursors will undergo nucleation, growth, coarsening and/or agglomeration processes, resulting in precipitates which are subjected to further processing (washing, drying, calcination) in order to get final products [112]. The simultaneous precipitation of multiple species present in the solution is a prerequisite for the success of synthesis. Moreover, pH value of solution and types of precipitating agent plays a decisive role in the precipitation process. By utilizing *N*, *N*-dimethylacetamide (DMAC) as solvent and tetramethylammonium hydroxide (TMAOH) as precipitating agent, Huang and co-workers [106] reported a facile co-precipitation method to synthesize $La_{0.6}Sr_{0.4}MnO_3$ perovskite catalyst with high surface area of 48 m^2/g and excellent catalytic activity for methane oxidation. The author ascribed the reason of this result to the better compositional homogeneity of precipitates caused by lower crystallization temperature. Djoudi [113] synthesized successfully $LaAl_{1-x}Ni_xO_{3-\delta}$ $(0 \leq x \leq 0.6)$ perovskite via co-precipitation method by employing nitrate salts of lanthanum, aluminum and nickel as cations precursors and sodium hydroxide as base precipitating agent. Final products showed pure perovskite phase and good crystallinity.

Nevertheless, this method has some inherent disadvantages: Firstly, the solubility and compatibility of precursors must be ensured to form oxides with expected compositions. Further, the quality of products is susceptible to many operational parameters such as pH value, co-precipitation rate, washing, drying and thermal treatment temperature. What’s more, addition of inappropriate precipitating agent or poor mixing may induce ununiformed temperature distribution in certain part of the solution, resulting in agglomeration of precipitates and heterogeneity in composition.

6.4.2.4 Auto-combustion method

In the past decade, auto-combustion method has been extensively applied as a reference method to synthesize numerous catalytic materials [114, 115]. This method is characterized by its merits in terms of simplicity, short synthesis time as well as the ease of up-scaling. Precursors can be nitrates or oxides. Organic reagents, such as citric acid, oxalic acid, tartaric acid, urea and glycine, are used as fuels [116]. Auto-combustion is triggered when the gel is heated by a heat source, resulting in the removal of organic matter. Perovskite phase is then formed either directly through heating or through further calcination.

3 atmospheric conditions are involved in auto-combustion: namely, oxidizing atmosphere (fuel-deficient), reducing atmosphere (fuel-rich) and stoichiometric atmosphere. It is worth mentioning that the ratio of fuel/oxidizer has a substantial influence on the released heat and subsequently maximum temperature of the combustion reaction process. Thus, a suitable fuel/oxidizer ratio is very essential to guarantee the purity of crystalline phase [117].

Despite the fact that the auto-combustion method has been used to synthesize a broad variety of materials, improvement of operational parameters is still demanded for commercial applications. Parameters influencing the combustion reaction, such as type of fuel, fuel/oxidizer ratio, use of excess oxidizer, and water content of the precursor mixture, need to be optimized towards desirable particle size distribution and crystallinity of products [118].

6.4.2.5 Flame spray pyrolysis method

Flame spray pyrolysis, also known as flame aerosol synthesis, is a technology consisting of producing nanoparticle aerosol by feeding either liquid or vapor precursors into a high-temperature flame. Some key parameters, including precursor concentration, flame temperature, fuel, mixing, oxidant, entrainment, precursor/dispersion flow rate ratio (P/D) and precursor solution composition, affect significantly product properties and particularly primary particle and crystallite sizes related directly to catalytic performance [119]. It is regarded as a time-saving, energy-efficient synthesis approach as it combines feeding of precursors, mixing, in-situ calcination in a fast single-step without neither the need of solvent-intensive washing nor post-thermal-treatment typical of those made by other wet-chemistry methods. Unlike batch process, it offers the possibility of continuous production of nanoparticles in industrial scale. Equally important, catalytic features of flame-made materials such as particle size and crystallinity, SSA could be tuned to achieve better performance. Synthesis of perovskite was first reported by J.H. Brewster [120]. By spraying an aqueous mixture comprising of barium acetate and titanium lactate into a H_2/air flame, $BaTiO_3$ perovskite was successfully synthesized. A series of $La_{1-x}M_xCoO_3$ (M=Ce, Eu) was prepared by spraying aqueous feed composed of metal acetate/nitrate/citrate into a H_2/O_2 flame, resulting in pure perovskite phase with SSA up to $25m^2/g$ [121]. The same methodology has been applied to the successful synthesis of a broader range of perovskites with formula of $LaBO_3$ (B=Co, Mn, Fe) [122]. Organic liquid feed has been reported to be effective to increase dramatically the SSA of products. Chiarello proposed a technique based on organic liquid feed to synthesize cobaltites. SSA of $LaCoO_3$ was improved to as high as 64 m^2/g by employing a mixed solvent of alcohols and propionic acid [123].

Notwithstanding, some disadvantages still existed, one of the mains shortcomings was from the high cost of suitable precursors and highly specialized facility. Since the synthesis is completed in a single step, it is sometimes not easy to get rid of the temples frequently used in the synthesis of macroporous material, thus not suitable for the preparation of materials with porous structure. In addition, conditions of precursor mixing must be well controlled as respect to explosive precursors and in certain cases an incomplete combustion could occur [124].

6.4.2.6 Solvothermal/Hydrothermal method

A solvothermal reaction refers to any chemical reaction which takes place under temperature and pressure above ambient temperature and pressure in a sealed vessel in the presence of a solvent. It is specifically called hydrothermal reaction in the case of water as solvent [125, 126]. It relies on the solvation of precursors (usually soluble metal salts) to form target product in an aqueous medium. Some mineralizers, such as hydroxides, carbonates and halides, are often added to assist the solubilization of precursor salts and have a considerable impact on the final particle size and morphology [126]. One of the biggest advantages of solvothermal method arises from the fact that it enables the preparation of inorganic materials at temperatures well below those required for solid-state or sol-gel method and in most of the cases post-annealing treatment could be omitted [125]. Application of hydrothermal method to the synthesis of titanate perovskites $ATiO_3$ (A = Ca, Sr, Ba, etc.) have been widely reported [127-130]. Furthermore, microwave has been reported beneficial to the improvement of physico-chemical and catalytic properties of perovskite-type oxides during hydrothermal aging step [131]. Kaddouri et al. [132] found that microwave-assisted hydrothermal synthesis led to enhanced methane combustion activity of La-Ce-Mn-O perovskite. The author claimed that the strong interaction between well dispersed cerium oxide species and $LaMnO_3$ host structure was responsible for the good performance of as-prepared material.

6.4.2.7 Spray/freeze drying method

Spray drying refers to a technique involving a rapid vaporization of the solvent contained in small droplets of required solutions of cations whilst slow sublimation of the solvent is employed in the case of freeze drying [133]. Freeze drying relies on spraying the solution in the form of fine droplets into liquid nitrogen followed by sublimation of the solvent in the absence of liquid phase [134]. The first step of freezing aims at a minimum segregation of diluted salts and as a consequence an intimate mixing of ions can be attained [135]. Both spray drying and freeze drying allow excellent control over purity levels and compositions, generating particles with adequate homogeneity [133]. Reports regarding perovskite preparation using these techniques are not scarce, exemplified by the synthesis of $La_{1-x}Sr_xCo_{1-y}Fe_yO_{3-\delta}$ [136] by spray drying and the synthesis of Sr_2CoTeO_6 and $La_{0.9}Sr_{0.1}Ga_{0.8}Mg_{0.2}O_{2.85}$ by freeze drying [137].

7. High-throughput and design of experiments

7.1. High-throughput experimentation

High-throughput experimentation (HTE) has developed from applications in the pharmaceutical industry [138]. High-throughput synthesis and testing of solid materials has recently gained special attention in heterogeneous catalysis. The basic concept for accelerating the development process comprises parallel synthesis, screening and testing of a large number of materials based on heuristic approaches, which, in tum, include fundamental and empirical knowledge on catalysis and appropriate optimization procedures when progressing in the development process. In high-throughput experimentation an extensive amount of data is being accumulated. For handling of these data and extraction of knowledge therefrom in the form of relationships between the chemical and physical properties of the materials and their catalytic performance suitable data storage and analysis capabilities are required [139].

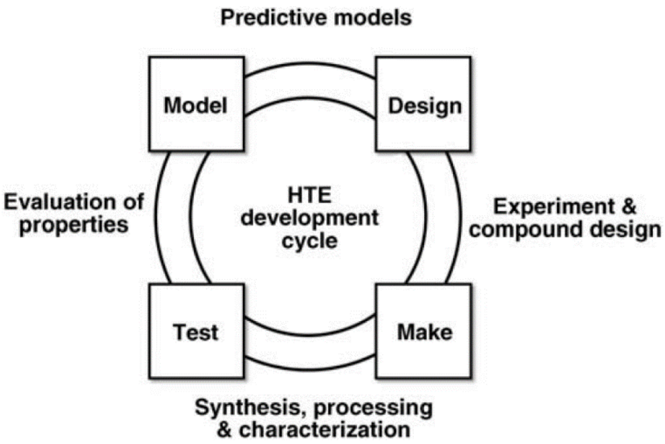

Fig.2.24. Graphic representation of the development cycle design-make-test-model [141].

Comprehensive HTE platforms are now available for conducting all stages in the R&D trajectory, from catalyst preparation and reaction screening of libraries of catalysts, to processing of the large volumes of data generated by high-throughput experimentation, and the derivation of useful knowledge from the results in the form of kinetic and process models. Maxwell et el. [140] classified concretely a HTE platform into hardware for reaction screening including software for design, simulation and modeling, as well as data handling. High throughput experimentation in heterogeneous catalysis provides an efficient solution to the generation of large datasets under reproducible conditions. Knowledge extraction from these datasets has mostly been performed using statistical methods, targeting the optimization of catalyst formulations. The effort to integrate the automated equipment by suitable software environments into efficient functional platforms and workflows for HTE has to be balanced in the light of desired throughput, required consumption of resources, and time for realization. Gordillo et al. [142] proposed the efficient and successful workflow in a fully closed HTE cycle that can be best visualized with design–make–test–model (Fig.2.24). Considering the amount of bigdata to handle, McCullough et al. [141] proposed a new pathway to HTE with the combination with advanced learning methodologies belonging to the artificial intelligence. By modifying the different reactive and catalytic condition, HTE could be widely used for synthesis and redox reactions.

7.2. Design of experiments

Design of experiments (DOE), as a methodology of statistical analysis, can be a vital tool for accelerating the discovery and creation of viable new chemical products, and for engineering the processes through which they can be delivered at scale. O'Neill [143] considered that competition and increased demand for product innovation are placing unprecedented pressures on chemical manufacturing. As well as a seemingly unquenchable need for new products and product variants, the industry as a whole is also burdened with the high cost of research and development, leading to a near constant search for lean and efficient solutions. Though statistical analysis has not always gone hand-in-hand with chemical development, it can be a vital tool for accelerating the discovery and creation of viable new products, and for engineering the processes through which they can be delivered at scale. This marriage is the way to get things "right first time", reducing development risks and relieving the pressures mentioned above. Design of experiments is a systematic method to determine the relationship between factors affecting a process and the output of that process.

Design of experiments (DOE) is a statistical approach to process optimization that is used across a variety of industries. It possesses a number of advantages over the traditionally employed "one variable at a time" (OVAT) approach, such as increased experimental efficiency as well as an ability to resolve factor interactions and provide detailed maps of a process's behavior. Bowden et al. [144] demonstrated the DoE approach to accelerate and to optimize their methodologies and new synthesis. Farrusseng [145] reviewed the relation between DOE method and high-throughput experimentation in heterogeneous catalysis by pointing out that DoE planning is very efficient for the fine optimization of both catalyst synthesis and process conditions. In this case, the most robust surface responses are generated as empirical models while minimizing the number of experiments. Recent publications illustrate the versatility and power of DOE applied to HT catalyst experimentation.

As a consequence, in the SmartCat project, the investigation to bridge DOE, as a statistic method, and high-throughput experimentation brings us a new effort not only in the catalytic performance planning but also could be considered further on catalytic result-oriented principle to design.

References

1. P. Granger et al., Recent Progress in Oxidative Conversion of Methane to Value-Added Products., P517-519., Perovskites and Related Mixed Oxides., 12 Nov. 2015.
2. http://www.grdf.fr/dossiers/gnv-biognv/vehicules-gnv-france-europe
3. P. Whitaker et al., Measures to Reduce Particulate Emissions from Gasoline DI engines, SAE Technical Paper 2011-01-1219. https://doi.org/10.4271/2011-01-1219.
4. A. Raj, Methane Emission Control, Johnson Matthey Technol. Rev., 2016, 60, (4), 228–235. https://doi.org/10.1595/205651316X692554.
5. S. Royer et al., Perovskites as Substitutes of Noble Metals for Heterogeneous Catalysis: Dream or Reality, Chem. Rev., 2014, 114, 10292–10368. https://doi.org/10.1021/cr500032a.
6. Y. Wang et al. Effects of ZnO content on the performance of $Pd/Zr_{0.5}Al_{0.5}O_{1.75}$ catalysts used in lean-burn natural gas vehicles, Chinese J. Catal., 2014, 35, 1157–1165. https://doi.org/10.1016/S1872-2067(14)60062-0.
7. D. Dissanayake et al., Partial oxidation of methane to carbon monoxide and hydrogen over a Ni/Al_2O_3 catalyst, J. Catal. 1991, 132, 117–127. https://doi.org/10.1016/0021-9517(91)90252-Y.
8. W.J.M. Vermeiren et al., Catalytic and thermodynamic approach of the oxyreforming reaction of methane, Catal. Today 1992, 13, 427–436. https://doi.org/10.1016/0920-5861(92)80168-M.
9. P.E. Marti et al., Methane Oxidation over Palladium on Zirconia Prepared from Amorphous Pd_1Zr_3 Alloy, J. Catal. 1993, 141, 494–509. https://doi-org/10.1006/jcat.1993.1158.
10. A.T. Ashcroft et al., Selective oxidation of methane to synthesis gas using transition metal catalysts, Nature 1990, 344(6264), 319–321. http://doi-org/10.1038/344319a0.
11. M. Richard et al., Remarkable Enhancement of O_2 Activation on Yttrium-Stabilized Zirconia Surface in a Dual Catalyst Bed, Angew. Chem., 2014, 53, 11342–11345. http://10.1002/anie.201403921.
12. M. Richard et al., Investigation of Methane Oxidation Reactions Over a Dual-Bed Catalyst System using ^{18}O Labelled DRIFTS coupling, ChemSusChem, 2017, 10, 210-219. http://10.1002/cssc.201601165.
13. Y. Nishihata, et al., Self-regeneration of a Pd-perovskite catalyst for automotive emissions control, Nature 2002, 418, 164–167. http://10.1038/nature00893.

14. A. Zaki et al., Tunable hierarchical porous silica materials using hydrothermal sedimentation-aggregation technique Micro. Meso. Mater., 2015, 208, 140–151. https://doi.org/10.1016/j.micromeso.2015.01.041; Z.X. Li et al., Controllable Assembly of Hierarchical Macroporous–Mesoporous $LnFeO_3$ and Their Catalytic Performance in the CO + NO Reaction, Langmuir,2015, 31, 8672–8679. http://10.1021/acs.langmuir.5b01519.
15. https://www.eea.europa.eu/help/glossary/gemet-environmental-thesaurus/end-of-pipe-technology
16. https://transportgeography.org/?page_id=1874
17. https://www.acea.be/statistics/article/economic-and-market-report-state-of-the-eu-auto-industry-full-year-2019
18. http://www.adlittle.com/downloads/tx_adlreports/ADL_The_Future_of_Diesel_Engines_updated.pdf
19. Jan Kašpar, Paolo Fornasiero, Neal Hickey. Automotive catalytic converters: current status and some perspectives. Catalysis Today, 2003, 77:419–449. https://doi.org/10.1016/S0920-5861(02)00384-X.
20. K.M. Adams, J.V. Cavataio, R.H. Hammerle, Lean NO_x catalysis for diesel passenger cars: Investigating effects of sulfur dioxide and space velocity, Appl. Catal. B. Environmental, 10 (1996) 157. https://doi.org/10.1016/0926-3373(96)00029-X.
21. Qinghe Zheng, Robert Farrauto, Michel Deeba, Ioannis Valsamakis. Part I: A comparative thermal aging study on the regenerability of Rh/Al_2O_3 and Rh/Ce_xO_y-ZrO_2 as model catalysts for automotive three-way catalysts. Catalysts, 2015, 5:1770-1796. https://doi.org/10.3390/catal5041770.
22. Jan Kašpar. Mauro Graziani. Paolo Fornasiero. Handbook on the Physics and Chemistry of Rare Earths, Chapter 184 Ceria-containing three-way catalysts. 2000, 29:159-267. http://dx.doi.org/10.1016/S0168-1273(00)29007-7.
23. Prasad R and Bella V R 2010 Review on diesel soot emission, its effect and control. Bull. Chem. React. Eng. Catal. 5: 69–86. https://doi.org/10.9767/bcrec.5.2.794.69-86.
24. Walker, A. Controlling Particulate Emissions from Diesel Vehicles. Topics in Catalysis 28, 165–170 (2004). https://doi-org/10.1023/B:TOCA.0000024346.29600.0e
25. B.Guan et al., Review of state of the art technologies of selective catalytic reduction of NO_x from diesel engine exhaust. Applied Thermal Engineering, 2014, 66, 395-414. https://doi.org/10.1016/j.applthermaleng.2014.02.021.

26. H.Burtscher., Physical characterization of particulate emissions from diesel engines: a review., Journal of Aerosol Science 36 (2005) 896–932. https://doi-org/10.1016/j.jaerosci.2004.12.001.
27. J.Zhu et al., Effects of engine operating conditions on morphology, microstructure, and fractal geometry of light-duty diesel engine particulates., Proceedings of the Combustion Institute 30 (2005) 2781–2789. https://doi-org/10.1016/j.proci.2004.08.232.
28. K.O. Lee, R. Cole, R. Sekar, M.Y. Choi, J. Zhu, in: Second Joint Meeting of the Combustion Institute, Oakland, CA, March 26–28, 2001.
29. K.O. Lee, R. Cole, R. Sekar, M.Y. Choi, J. Zhu, J. Kang, C. Bae, Detailed Characterization of Morphology and Dimensions of Diesel Particulates via Thermophoretic Sampling, SAE Technical Paper 2001-01-3572 (2001).
30. K.O. Lee, R. Cole, R. Sekar, M.Y. Choi, J. Kang, C.S. Bae, H.D. Shin, Proc. Combust. Inst. 39 (2002) 647–653. https://www.jstor.org/stable/44742453.
31. Marek Václavík, Marie Plachá, Petr Kočí, Miloš Svoboda, Thomas Hotchkiss,Vladimír Novák, David Thompsett. Structure characterisation of catalytic particulate filters for automotive exhaust gas aftertreatment. Materials Characterization. 2017, 134, 311-318. https://doi.org/10.1016/j.matchar.2017.11.011.
32. S.Trivedi et al., a four-way catalytic system for control of emissions from diesel engine, Sadhana(2018) 43:130. https://doi.org/10.1007/s12046-018-0884-0.
33. Isabella Nova and Enrico Tronconi., “Urea-SCR Technology for DeNOx After Treatment of Diesel Exhausts”., Johnson Matthey Technol. Rev., 2015, 59, (3), 221–232. http://dx.doi.org/10.1595/205651315X688280
34. Enger, B.C., Lødeng, R. and Holmen, A. (2008) A Review of Catalytic Partial Oxidation of Methane to Synthesis Gas with Emphasis on Reaction Mechanisms over Transition Metal Catalysts. Applied Catalysis A: General, 346, 1-27. http://dx.doi.org/10.1016/j.apcata.2008.05.018.
35. Chak-Tong Au, Ching-Fai Ng, Meng-Sheng Liao, Methane Dissociation and Syngas Formation on Ru, Os, Rh, Ir, Pd, Pt, Cu, Ag, and Au: A Theoretical Study, Journal of Catalysis, Volume 185, Issue 1, 1999, Pages 12-22, ISSN 0021-9517, https://doi.org/10.1006/jcat.1999.2498.
36. M.J. Hei, H.B. Chen, J. Yi, Y.J. Lin, Y.Z. Lin, G. Wei, D.W. Liao, CO_2-reforming of methane on transition metal surfaces, Surf. Sci. 417 (1998) 82. https://doi-org/10.1016/S0039-6028(98)00663-3.

37. T.V. Choudhary, D.W. Goodman, Methane activation on Ni and Ru model catalysts, J. Mol. Catal. A: Chem. 163 (2000) 9. https://doi.org/10.1016/S1381-1169(00)00395-2.

38. A. Raj, Methane Emission Control, A review of mobile and stationary source emissions abatement technologies for natural gas enginesJohnson Matthey Technol. Rev., 2016, 60(4), 228–235. http://doi-org/10.1595/205651316X692554.

39. P. Granger., Challenges and breakthroughs in postcombustion catalysis: how to match future stringent regulations Catal. Sci. Technol.2017, 017, 7:5195–5211. https://doi-org/10.1039/C7CY00983F.

40. J. Chen et al., New insights into the role of Pd-Ce interface for methane activation on monolithic supported Pd catalysts: A step forward the development of novel PGM Three-Way Catalysts for natural gas fueled engines., Applied Catalysis B: Environmental 264 (2020) 118475. https://doi-org/10.1016/j.apcatb.2019.118475.

41. G. Corro, C. Cano and J. L. G. Fierro, A study of Pt-Pd/gamma-Al_2O_3 catalysts for methane oxidation resistant to deactivation by sulfur poisoning, J. Mol. Catal. A: Chem., 2010, 315, 35–42. http://dx.doi.org/10.1016/j.molcata.2009.08.023.

42. Y. Wang, H. Shang, H. Xu, M. Gong and Y. Chen, Chin. Effects of ZnO content on the performance of $Pd/Zr_{0.5}Al_{0.5}O_{1.75}$ catalysts used in lean-burn natural gas vehicles, J. Catal., 2014, 35, 1157–1165. https://doi.org/10.1016/S1872-2067(14)60062-0.

43. P. Gelin and M. Primet, Complete oxidation of methane at low temperature over noble metal based catalysts: a review, Appl. Catal., B, 2002, 39, 1–37. https://doi.org/10.1016/S0926-3373(02)00076-0.

44. Heesoo Lee, Dae-Hoon Lee, Young-Hoon Song, Won Choon Choi, Yong-Ki Park, Do Heui Kim. Synergistic effect of non-thermal plasma–catalysis hybrid system on methane complete oxidation over Pd-based catalysts. Chemical Engineering Journal-Lausanne, 2015, 259:761–770. https://doi-org/10.1016/j.cej.2014.07.128.

45. M. Stoukides, C.G. Vayenas. Solid-electrolyte-aided study of the ethylene oxidation on polycrystalline silver. Journal of Catalysis, 1981, 69: 18-31. https://doi.org/10.1016/0021-9517(81)90124-X.

46. F. Matei, C. Jiménez-Borja, J. Canales-Vázquez, S. Brosda, F. Dorado, J.L. Valverde, D. Ciuparu. Enhanced electropromotion of methane combustion on palladium catalysts deposited on highly

porous supports. Applied Catalysis B: Environmental, 2013, 132–133: 80– 89. https://doi-org/10.1016/j.apcatb.2012.11.011.

47. Arnim Eyssler, Alexander Winkler, Peter Mandaliev, Paul Hug, Anke Weidenkaff, Davide Ferri. Influence of thermally induced structural changes of 2 wt% Pd/$LaFeO_3$ on methane combustion activity. Applied Catalysis B: Environmental, 2011, 106: 494–502. https://doi-org/10.1016/j.apcatb.2011.06.008.
48. Dal Young Yoon, Young Jin Kim, Ji Hyun Lim, Byong K. Cho, Suk Bong Hong, In-Sik Nam, Jin Woo Choung. Thermal stability of Pd-containing $LaAlO_3$ perovskite as a modern TWC. Journal of Catalysis, 2015, 330: 71–83. https://doi-org.ressources-electroniques.univ-lille.fr/10.1016/j.jcat.2015.07.013.
49. W. F. Libby, Promising Catalyst for Auto Exhaust, Science, 1971, 171, 499–500. https://doi.org/10.1126/science.171.3970.499.
50. R. J. H. Voorhoeve, J. P. Remeika Jr., P. E. Freeland and B. T. Mathias, Science, 1972, 177, 353–354. https://doi.org/10.1016/0920-5861(90)87017-W.
51. M. Becker et al., Formation of hybrid ABX_3 perovskite compounds for solar cell application: first-principles calculations of effective ionic radii and determination of tolerance factors., Dalton Trans., 2017, 46, 3500. https://doi-org/10.1039/C6DT04796C.
52. Properties and applications of perovskite-type oxides; Tejuca, L. G., Fierro, J. L. G., Eds.; Marcel Dekker Inc.: New York, 1993. https://nla.gov.au/nla.cat-vn2650903.
53. Magdalena Bosomoiu, Grigore Bozga, Daniela Berger, Cristian Matei, Studies on combustion catalytic activity of some pure and doped lanthanum cobaltites, Applied Catalysis B: Environmental,
54. Volume 84, Issues 3–4, 2008, Pages 758-765, ISSN 0926-3373, https://doi.org/10.1016/j.apcatb.2008.06.008.
55. Shannon, R. D.; Prewitt, C. T., Revised values of effective ionic radii, Acta Crystallogr., Sect. B 1969, 25, 925; 1970, 26, 1046. https://doi-org/10.1107/S0567740870003576.
56. V. M. Goldschmidt., The geometric blueprint of perovskites, Die Naturwissenschaften, 1926, 21:477−485. https://doi.org/10.1073/pnas.1719179115.
57. Reuben Rudman, Functional and Smart Materials: Structural Evolution and Structure Analysis By Z. L. Wang and Z. C. Kang. Plenum Press: New York and London. 1998. $125.00. xxiii + 514 pp. ISBN 0-306-45651-6. Journal of the American Chemical Society 1998 120 (38), 9976-9977.

http://10.1021/ja9856351.

58. M.A. Pena, J.L.G. Fierro. Chemical Structures and Performance of Perovskite Oxides. Chem. Rev., 2001, 101:1981−2017. https://doi-org/10.1021/cr980129f.
59. Dongkyu Lee and Ho Nyung Lee. Controlling Oxygen Mobility in Ruddlesden–Popper Oxides. Materials, 2017,10:368. https://doi.org/10.3390/ma10040368.
60. I.D. Brown. Modeling the structures of La_2NiO_4. Z. Kristallogr. 1992, 199:255–272. https://doi.org/10.1524/zkri.1992.199.3-4.255.
61. Royer, S.; Duprez, D., Catalytic Oxidation of Carbon Monoxide over Transition Metal OxidesChemCatChem 2011, 3, 24. https://doi.org/10.1002/cctc.201000378.
62. Royer, S.; Ayrault, C.; Carnevillier, C.; Epron, F.; Marécot, P.; Duprez, D. Enthalpy recovery of gases issued from H_2 production processes: Activity and stability of oxide and noble metal catalysts in oxidation reaction under highly severe conditions, Catal. Today 2006, 117, 543. https://doi-org/10.1016/j.cattod.2006.06.023.
63. Baylet, A.; Royer, S.; Marécot, P.; Tatibouët, J. M.; Duprez, D. High catalytic activity and stability of Pd doped hexaaluminate catalysts for the CH4 catalytic combustion, Appl. Catal., B 2008, 77, 237. https://doi-org/10.1016/j.apcatb.2007.07.031.
64. Cimino, S.; Pirone, R.; Russo, G., Thermal Stability of Perovskite-Based Monolithic Reactors in the Catalytic Combustion of Methane, Ind. Eng. Chem. Res. 2001, 40, 80. https://doi-org/10.1021/ie000392i.
65. Oliva, C.; Forni, L., EPR and XRD as probes for activity and durability of LaMnO3 perovskite-like catalysts, Catal. Commun. 2000, 1, 5. https://doi.org/10.1016/S1566-7367(00)00003-0.
66. Chen, L., Feng, T., Wang, P. et al. Catalytic properties of Pd supported on hexaaluminate coated alumina in low temperature combustion of coal mine ventilation air methane. Kinet Catal 54, 767–772 (2013). https://doi-org/10.1134/S0023158413060165.
67. Civera, A.; Pavese, M.; Saracco, G.; Specchia, V., Combustion synthesis of perovskite-type catalysts for natural gas combustion, Catal. Today 2003, 83, 199. https://doi-org/10.1016/S0920-5861(03)00220-7.
68. Xun Wei, Paul Hug, Renato Figi, Matthias Trottmann, Anke Weidenkaff, Davide Ferri, Catalytic combustion of methane on nano-structured perovskite-type oxides fabricated by ultrasonic spray combustion, Applied Catalysis B: Environmental, Volume 94, Issues 1–2, 2010, Pages 27-37, ISSN

0926-3373, https://doi.org/10.1016/j.apcatb.2009.10.017.

69. Hend Najjar, Jean-François Lamonier, Olivier Mentré, Jean-Marc Giraudon, Habib Batis, Optimization of the combustion synthesis towards efficient $LaMnO_{3+y}$ catalysts in methane oxidation, Applied Catalysis B: Environmental, Volume 106, Issues 1–2, 2011, Pages 149-159, ISSN 0926-3373, https://doi.org/10.1016/j.apcatb.2011.05.019.

70. Kim, C. H.; Qi, G. S.; Dahlberg, K., Strontium-Doped Perovskites Rival Platinum Catalysts for Treating NO_x in Simulated Diesel Exhaust, Science 2010, 327, 1624. https://doi.org/10.1126/science.1184087.

71. Kapteijn, F.; Rodiguez-Mirasol, J.; Moulijn, J., Heterogeneous catalytic decomposition of nitrous oxide, A. Appl. Catal., B 1996, 9, 25. https://doi.org/10.1016/0926-3373(96)90072-7.

72. Zhu, J. J.; Yang, X. G.; Xu, X. L.; Wei, K. M., Active Site Structure of NO Decomposition on Perovskite(-like) Oxides: An Investigation from Experiment and Density Functional Theory, J. Phys. Chem. C. 2007, 111, 1487. https://doi-org/10.1021/jp0662101.

73. Shin, S.; Arakawa, H.; Hatakeyama, Y.; Ogawa, K.; Shimomura, K., Absorption of NO in the lattice of an oxygen-deficient perovskite $SrFeO_{3-x}$ and the infrared spectroscopic study of the system NO - $SrFeO_{3-x}$, Mater. Res. Bull. 1979, 14, 633. https://doi-org.ressources-electroniques.univ-lille.fr/10.1016/0025-5408(79)90046-1.

74. Mihai, O.; Chen, D.; Holmen, A., Chemical looping methane partial oxidation: The effect of the crystal size and O content of $LaFeO_3$, J. Catal. 2012, 293, 175. https://doi.org/10.1016/j.jcat.2012.06.022.

75. Heitnes, K.; Lindberg, S.; Rokstad, O. A.; Holmen, A., Catalytic partial oxidation of methane to synthesis gas using monolithic reactors, Catal. Today 1994, 21, 471. https://doi.org/10.1016/0920-5861(94)80169-X.

76. Lyubovsky, M., Roychoudhury, S. & LaPierre, R. Catalytic partial “oxidation of methane to syngas” at elevated pressures. Catal Lett 99, 113–117 (2005). https://doi-org.ressources-electroniques.univ-lille.fr/10.1007/s10562-005-2103-y.

77. Kus, S.; Otrenba, M.; Taniewski, M. The catalytic performance in oxidative coupling of methane and the surface basicity of La_2O_3, Nd_2O_3, ZrO_2 and Nb_2O_5, Fuel 2003, 82, 1331. https://doi.org/10.1016/S0016-2361(03)00030-9.

78. H.Hamada., Novel Catalytic Technologies for Car Emission Reduction., OECD Conference on

Potential Environmental Benefits of Nanotechnology 15-17 July,2009 Clean Car Technology Session. https://www.oecd.org/chemicalsafety/nanosafety/43289415.pdf.

79. Y. Nishihata, J. Mizuki, T. Akao, H. Tanaka, M. Uenishi, M. Kimura, T. Okamoto, N. Hamada. Self-regeneration of a Pd perovskite catalyst for automotive emissions control. Nature ,2002, 418:164-167. https://doi.org/10.1038/nature00893.

80. Taniguchi, M., Tanaka, H., Uenishi, M. et al. The self-regenerative Pd-, Rh-, and Pt-perovskite catalysts. Top Catal 42, 367–371 (2007). https://doi-org.ressources-electroniques.univ-lille.fr/10.1007/s11244-007-0207-x.

81. Hirohisa Tanaka, Masashi Taniguchi, Mari Uenishi, Nobuhiko Kajita, Isao Tan, Yasuo Nishihata, Junichiro Mizuki, Keiichi Narita, Mareo Kimura, Kimiyoshi Kaneko. Self-Regenerating Rh- and Pt-Based Perovskite Catalysts for Automotive-Emissions Control. Angew. Chem. Int. Ed. 2006, 45:5998-6002. https://doi-org/10.1002/anie.200503938.

82. S. Keav,et al., Structured Perovskite-Based Catalysts and Their Application as Three-Way Catalytic Converters-A Review., Catalysts 2014, 4(3), 226-255; https://doi.org/10.3390/catal4030226.

83. Michael B. Katz, Shuyi Zhang, Yingwen Duan, Hongjie Wang, Minghao Fang, Kui Zhang, Baihai Li, George W. Graham, Xiaoqing Pan. Reversible precipitation/dissolution of precious-metal clusters in perovskite-based catalyst materials: Bulk versus surface re-dispersion. Journal of Catalysis, 2012, 293:145–148. https://doi.org/10.1016/j.jcat.2012.06.017.

84. A.E. Giannakas, A.A. Leontiou, A.K. Ladavos, P.J. Pomonis, Characterization and catalytic investigation of NO+CO reaction on perovskites of the general formula $La_xM_{1-x}FeO_3$ (M=Sr and/or Ce) prepared via a reverse micelles microemulsion route, Applied Catalysis A: General, Volume 309, Issue 2, 2006, Pages 254-262, ISSN 0926-860X, https://doi.org/10.1016/j.apcata.2006.05.016.

85. Rui Ran, Duan Weng, Xiaodong Wu, Jun Fan, Liang Qing, Rapid synthesis of $La_{0.7}Sr_{0.3}MnO_{3+\lambda}$ catalysts by microwave irradiation process, Catalysis Today, Volume 126, Issues 3–4, 2007, Pages 394-399, ISSN 0920-5861, https://doi.org/10.1016/j.cattod.2007.06.008.

86. J.Zhu et al., Perovskite Oxides: Preparation, Characterizations, and Applications in Heterogeneous Catalysis, ACS Catalysis 2014, 4, 2917-2940. https://doi-org/10.1021/cs500606g.

87. R.J.H.Voorhoeve., J.P.Remeika., L.E.Trimble., Defect Chemistry and Catalysis in Oxidation and Reduction over Perovskite-Type Oxides., Annuals of The New York Academy of Sciences., April 1976., https://doi.org/10.1111/j.1749-6632.1976.tb34221.x

88. Royer S., Bérubé F., Kaliaguine S. Effect of the synthesis conditions on the redox and catalytic properties in oxidation reactions of $LaCo_{1-x}Fe_xO_3$. Applied Catalysis A, 2005, 282(1):273-284. https://doi.org/10.1016/j.apcata.2004.12.018.

89. Laszlo Takacs. M.Carey Lea, the father of mechanochemistry. Bull. Hist. Chem., 2003, 28:26-34. http://acshist.scs.illinois.edu/bulletin_open_access/v28-1/v28-1%20p26-34.pdf.

90. Takacs, L. M. Carey Lea, the first mechanochemist. Journal of Materials Science 39, 4987–4993 (2004). https://doi-org/10.1023/B:JMSC.0000039175.73904.93.

91. J.Wu, Development of novel catalytic materials with low content of precious metals for the after-treatment of automobile exhaust gas, https://hal.archives-ouvertes.fr/tel-02337766/.

92. Baláž, P. (2008). Mechanochemistry in Minerals Engineering. In: Mechanochemistry in Nanoscience and Minerals Engineering. Springer, Berlin, Heidelberg. https://doi-org/10.1007/978-3-540-74855-7_5.

93. Ya-Fei Liu, Xing-Qin Liu, Guang-Yao Meng, A novel route of synthesizing $La_{1-x}Sr_xCoO_3$ by microwave irradiation. Materials Letters, 2001, 48:176–183. https://doi.org/10.1016/S0167-577X(00)00299-8.

94. A. Kaddouri, S. Ifrah. Microwave-assisted synthesis of $La_{1-x}B_xMnO_{3.15}$ (B = Sr, Ag; x = 0 or 0.2) via manganese oxides susceptors and their activity in methane combustion. Catalysis Communications, 2006, 7:109–113. https://doi.org/10.1016/j.catcom.2005.09.010.

95. Rui Ran, Duan Weng, Xiaodong Wu, Jun Fan, Liang Qing. Rapid synthesis of $La_{0.7}Sr_{0.3}MnO_{3+\lambda}$ catalysts by microwave irradiation process. Catalysis Today, 2007, 126:394–399. https://doi.org/10.1016/j.cattod.2007.06.008.

96. C. H. Lin, H. Y. Chang and I. N. Lin, "Densification behaviour of Y/sub 3/Fe/sub 5/O/sub 12/ materials prepared by microwave sintering process," in IEEE Transactions on Magnetics, vol. 33, no. 5, pp. 3415-3417, Sept. 1997, http://doi-org/10.1109/20.617962.

97. P.D. Ramesh, P. Sarin, S. Jeevan, K.J. Rao. Microwave Sintering Studies of ZrO_2–CeO_2 Ceramics," J. Mater. Synth. Process., 1996, 4:163–173. http://repository.ias.ac.in/91139/.

98. Yakovleva, I.S., Nadeev, A.N., Gerasimov, E.Y. et al. Microwave synthesis of $LaMO_3$ (M = Mn, Co, Fe) perovskites from crystalline hydrates of nitrates. Kinet Catal 54, 119–129 (2013). https://doi-org/10.1134/S002315841301014X.

99. Stefano Diodati, Luca Nodari, Natile Marta Maria et al. Coprecipitation of Oxalates: An Easy and

Reproducible Wet-Chemistry Synthesis Route for Transition-Metal Ferrites. European Journal of Inorganic Chemistry, 2014, Volume2014, Issue5, page:875-887. https://doi.org/10.1002/ejic.201301250.

100. Maggio P. Pechini. Method of preparing lead and alkaline earth titanates and niobates and coating method using the same to form a capacitor. 1967, U.S. Patent, Patent No. 3,330,697. https://patents.google.com/patent/US3330697A/en.

101. Hideki Taguchi, Shin-ichiro Matsu-ura, Mahiko Nagao et al. Synthesis of $LaMnO_{3+\delta}$ by Firing Gels Using Citric Acid. Journal of Solid-State Chemistry, 1997, 129:60-65. https://doi.org/10.1006/jssc.1996.7229.

102. A.M. Huízar-Félix, T. Hernández, S. de la Parra, J. Ibarra, B. Kharisov. Sol–gel based Pechini method synthesis and characterization of $Sm_{1-x}Ca_xFeO_3$ perovskite $0.1 \le x \le 0.5$. Powder Technology, 2012, 229:290–293. https://doi.org/10.1016/j.powtec.2012.06.057.

103. Ph. Courty, H. Ajot, Ch. Marcilly, B. Delmon. Oxydes mixtes ou en solution solide sous forme très divisée obtenus par décomposition thermique de précurseurs amorphes. Powder Technology, 1973, 7:21-38. https://doi.org/10.1016/0032-5910(73)80005-1.

104. A. Kahoul, A. Hammouche, F. Naamoune, P. Chartier, G. Poillerat, J.F. Koenig. Solvent effect on synthesis of perovskite-type $La_{1-x}Ca_xCoO_3$ and their electrochemical properties for oxygen reactions. Materials Research Bulletin, 2000, 35:1955–1966. https://doi.org/10.1016/S0025-5408(00)00395-0.

105. Hiromichi Aono, Jun Izumi, Musashi Tomida, Yoshihiko Sadaoka. Synthesis for fine perovskite-type materials using precursor prepared by metal nitrates solution mixed with organic solvent. Materials Chemistry and Physics, 2011, 130:973-979. https://doi.org/10.1016/j.matchemphys.2011.08.021.

106. Mohsennia, M., Niknahad, B. & Eliassi, A. Effect of polymerization/complexation agents molar ratio on structure and catalytic activity of $La_{0.7}Ba_{0.3}Co_{0.3}Ni_{0.7}O_3$ nanocatalyst in low-temperature CO oxidation. J Sol-Gel Sci Technol 82, 458–467 (2017). https://doi-org/10.1007/s10971-017-4331-1.

107. Fei Huang, Xiucheng Sun, Yong Zheng, Yihong Xiao, Ying Zheng, Facile coprecipitation synthesis of $La_{0.6}Sr_{0.4}MnO_3$ perovskites with high surface area, Materials Letters, Volume 210, 2018, Pages 287-290, ISSN 0167-577X, https://doi.org/10.1016/j.matlet.2017.09.048.

108. M.K. Mahata, K. Kumar, V.K. Rai. Structural and optical properties of Er^{3+}/Yb^{3+} doped barium titanate phosphor prepared by co-precipitation method. Spectrochimica Acta Part A: Molecular and Biomolecular Spectroscopy, 2014, 124:285–291. https://doi.org/10.1016/j.saa.2014.01.014.

109. Hsiang, HI., Yen, FS. & Chang, YH. Effects of doping with La and Mn on the crystallite growth and phase transition of $BaTiO_3$ powders. J Mater Sci 31, 2417–2424 (1996). https://doi-org/10.1007/BF01152955.

110. D.K. Patel, B. Vishwanadh, V. Sudarsan, R. Vatsa, S.K. Kulshreshtha. Hexagonal $BaTiO_3$:Eu^{3+} nanoparticles: a kinetically stable phase prepared at low temperatures. Journal of the American Ceramic Society, 2010, 94:482–487. https://doi-org/10.1111/j.1551-2916.2010.04077.x.

111. Yanan Hao, Xiaohui Wang and Longtu Li, Highly dispersed $SrTiO_3$ nanocubes from a rapid sol-precipitation method, Nanoscale, 2014, 6, 7940, http://doi-org/10.1039/c4nr00171k.

112. M.E.V. Costa, P.Q. Mantas. Dielectric properties of porous $Ba_{0.997}La_{0.003}Ti_{1.0045}O_3$ ceramics. Journal of the European Ceramic Society, 1999, 19:1077–1080. https://doi.org/10.1016/S0955-2219(98)00377-X.

113. Guozhong. Cao. Ying Wang. Nanostructures and nanomaterials—synthesis, properties, and applications. Imperial College Press, USA, 2004.

114. Djoudi, L., Omari, M. Synthesis and Characterization of Perovskite Oxides $LaAl_{1-x}Ni_xO_{3-\delta}$ ($0 \leq x \leq 0.6$) via Co-precipitation Method. J Inorg Organomet Polym 25, 796–803 (2015). https://doi-org/10.1007/s10904-014-0162-5.

115. K.C. Patil, S.T. Aruna, T. Mimani. Combustion synthesis: an update. Current Opinion in Solid State and Materials Science, 2002, 6:507–512. https://doi.org/10.1016/S1359-0286(02)00123-7.

116. Tyurkin, Y.V., Chesalov, L.A. & Luzhkova, E.N. Self-propagating high-temperature synthesis in the production of catalysts and supports. React Kinet Catal Lett 60, 279–284 (1997). https://doi-org/10.1007/BF02475689.

117. J. Chandradass, M. Balasubramanian, K.H. Kim. Synthesis and characterization of $LaAlO_3$ nanopowders by various fuels. Materials and Manufacturing Processes, 2010, 25:1449–1453. https://doi.org/10.1080/10426914.2010.508962.

118. J. Chandradass, M. Balasubramanian, K.H. Kim. Synthesis and characterization of $LaAlO_3$ nanopowders by various fuels. Materials and Manufacturing Processes, 2010, 25:1449–1453. https://doi.org/10.1080/10426914.2010.508962.

119. L.E. Shea, J. McKittrick, O.A. Lopez. Synthesis of red-emitting, small particle size luminescent oxides using an optimized combustion process. Journal of the American Ceramics Society, 1996, 79, 3257–3265. https://doi-org/10.1111/j.1151-2916.1996.tb08103.x.
120. Rajesh Koirala, Sotiris E. Pratsinis, Alfons Baiker. Synthesis of catalytic materials in flames: opportunities and challenges. Chemical Society Reviews, 2016, 45:3053-3068. https://doi-org/10.1039/C5CS00011D.
121. J.H. Brewster, T.T. Kodas. Generation of unagglomerated, dense, $BaTiO_3$ particles by flame-spray pyrolysis, AIChE Journal, 1997, 43:2665–2669. https://doi.org/10.1002/aic.690431310.
122. R. Leanza, I. Rossetti, L. Fabbrini, C. Oliva, L. Forni. Perovskite catalysts for the catalytic flameless combustion of methane: preparation by flame-hydrolysis and characterisation by TPD-TPR-MS and EPR. Applied Catalysis B: Environmental, 2000, 28:55–64. https://doi.org/10.1016/S0926-3373(00)00163-6.
123. I. Rossetti, L. Forni. Catalytic flameless combustion of methane over perovskites prepared by flame-hydrolysis. Applied Catalysis B: Environmental, 2001, 33:345–352. https://doi.org/10.1016/S0926-3373(01)00194-1.
124. G.L. Chiarello, I. Rossetti, L. Forni, P. Lopinto, G. Migliavacca. Solvent nature effect in preparation of perovskites by flame-pyrolysis: 2. Alcohols and alcohols + propionic acid mixtures. Applied Catalysis B: Environmental, 2007, 72:227-232. https://doi.org/10.1016/j.apcatb.2006.11.001.
125. Rajesh Koirala, Sotiris E. Pratsinis, Alfons Baiker. Synthesis of catalytic materials in flames: opportunities and challenges. Chemical Society Reviews, 2016, 45:3053-3068. https://doi-org/10.1039/C5CS00011D.
126. Gomes, M.A., Lima, Á.S., Eguiluz, K.I.B. et al. Wet chemical synthesis of rare earth-doped barium titanate nanoparticles. J Mater Sci 51, 4709–4727 (2016). https://doi-org/10.1007/s10853-016-9789-7.
127. K. Byrappa, M. Yoshimura. Handbook of hydrothermal technology. A technology of crystal growth and materials processing. Noyes Publications, New Jersey; William Andrew Publishing, New York, 2001.
128. H. Xu, S. Wei, H. Wang, M. Zhu, R. Yu, H. Yan. Preparation of shape controlled $SrTiO_3$ crystallites by sol–gel-hydrothermal method. Journal of Crystal Growth, 2006, 292:159-164. https://doi-org/10.1016/j.jcrysgro.2006.04.089.

129. J. Xu, Y. Wei, Y. Huang, J. Wang, X. Zheng, Z. Sun, L. Fan, J. Wu. Solvothermal synthesis nitrogen doped $SrTiO_3$ with high visible light photocatalytic activity. Ceramics International, 2014, 40:10583-10591. https://doi-org/10.1016/j.ceramint.2014.03.037.

130. Um, MH., Kumazawa, H. Hydrothermal synthesis of ferroelectric barium and strontium titanate extremely fine particles. Journal of Materials Science 35, 1295–1300 (2000). https://doi-org/10.1023/A:1004713226000.

131. Shicheng Zhang, Jiaxiang Liu, Yuexin Han, Bingchen Chen, Xingguo Li, Formation mechanisms of $SrTiO_3$ nanoparticles under hydrothermal conditions, Materials Science and Engineering: B, Volume 110, Issue 1, 2004, Pages 11-17, ISSN 0921-5107, https://doi.org/10.1016/j.mseb.2004.01.017.

132. N. Miniajluk, J. Trawczynski, M. Zawadzki, P.E. Tomaszewski, W. Mista. Solvothermal synthesis and characterization of mixed oxides with perovskite-like structure. Catalysis Today, 2015, 257:26–34. https://doi.org/10.1016/j.cattod.2015.03.029.

133. A. Kaddouri, P. Gelin, N. Dupont. Methane catalytic combustion over La–Ce–Mn–O- perovskite prepared using dielectric heating. Catalysis Communications, 2009, 10:1085–1089. https://doi.org/10.1016/j.catcom.2008.12.063.

134. P. Cousin, R.A. Ross. Preparation of mixed oxides: a review. Materials Science and Engineering: A, 1990, 130:119-125. https://doi.org/10.1016/0921-5093(90)90087-J.

135. D.M. Roy, S.O. Oyefesobi. Preparation of very reactive Ca_2SiO_4 powder. Journal of the American Ceramic Society-Discussions and Notes, 1977, 60 :178-180. https://doi-org/10.1111/j.1151-2916.1977.tb15506.x.

136. Daniel D. Athaydea, Douglas F. Souzaa, Alysson M.A. Silvaa, Daniela Vasconcelos, Eduardo H.M. Nunes, João C. Diniz da Costa, Wander L. Vasconcelos. Review of perovskite ceramic synthesis and membrane preparation methods. Ceramics International, 2016, 42:6555–6571. https://doi-org/10.1016/j.ceramint.2016.01.130.

137. O. Büchler, J.M. Serra, W.A. Meulenberg, D. Sebold, H.P. Buchkremer. Preparation and properties of thin $La_{1-x}Sr_xCo_{1-y}Fe_yO_{3-\delta}$ perovskitic membranes supported on tailored ceramic substrates, Solid State Ionics, 2007, 178:91–99. https://doi.org/10.1016/j.ssi.2006.11.015.

138. O.S.M. Luis, P,C. Jon, L. Luis, et al. Factors determining the effect of Co(II) in the ordered double perovskite structure: Sr_2CoTeO_6. Journal of Materials Chemistry, 2005, 15:183-193. https://doi-

org/10.1039/B413341B.

139. A. Metrick, A. Yasuda (eds.): Venture Capital and the Finance of Innovation, 2nd ed., J. Wiley & Sons, New York 2010

140. U.Rodemerck and M.Baerns., High-Throughput Experimentation in the Development of Heterogeneous Catalysts Tools for Synthesis and Testing of Catalytic Materials and Data Analysis., Basic principles in Applied Catalysis.. P259-280. http://10.1002/chin.200420260.

141. I.E.Maxwell., High-throughput technologies to enhance innovation in catalysis., Topics in Catalysis Vol. 24, No. 1–4, October 2003. https://schlr.cnki.net/Detail/doi/GARJ0010_2/SSJD00002820849.

142. K.McCullough et al., High-throughput experimentation meets artificial intelligence: a new pathway to catalyst discovery., Phys.Chem.Chem.Phys., 2020, 22, 11174. https://doi-org/10.1039/D0CP00972E.

143. A.Gordillo et al., High-Throughput Experimentation in Catalysis and Materials Science., 2014 Wiley-VCH Verlag GmbH & Co. KGaA, Weinheim http://doi-org/10.1002/14356007.s13_s01.

144. https://www.chemanager-online.com/en/topics/production/design-experiments

145. Bowden, G.D., Pichler, B.J. & Maurer, A. A Design of Experiments (DoE) Approach Accelerates the Optimization of Copper-Mediated ^{18}F-Fluorination Reactions of Arylstannanes. Sci Rep 9**,** 11370 (2019). https://doi.org/10.1038/s41598-019-47846-6

146. Farrusseng, D., High-throughput heterogeneous catalysis., Surface Science Reports 63 (2008) 487–513. https://doi.org/10.1016/j.surfrep.2008.09.001.

Chapter III. Experimental Measurements and Characterizations

1. Preparation of catalysts

1.1. Chemicals

Precursors

Lanthanum (III) nitrate hexahydrate [Ref-203548-500G, $La(NO_3)_3{\cdot}6H_2O$, 433.01 g/mol, 99.999% trace metals basis, Merck(Sigma-Aldrich)], Manganese (II) nitrate tetrahydrate [Ref-63547-100G, $Mn(NO_3)_2{\cdot}4H_2O$, 251.01 g/mol, purum p.a., ≥97.0% (KT), Merck(Sigma-Aldrich)], Palladium (II) nitrate dihydrate [Ref-76070-1G, $Pd(NO_3)_2{\cdot}2H_2O$, 266.46 g/mol, ~40% Pd basis, Merck(Sigma-Aldrich)], Strontium (II) nitrate [Ref-204498-10G, $Sr(NO_3)_2$, 211.63 g/mol, 99.995% trace metals basis, Merck(Sigma-Aldrich)], citric acid [Ref-791725-500G, $C_4H_8O_7$, $HOC(COOH)(CH_2COOH)_2$, anhydrous, free-flowing, Redi-Dri^{TM}, ACS reagent, ≥99.5%, Merck(Sigma-Aldrich)].

References

Commercial cerium zirconium mixed oxides with a stoichiometric ratio 1:1 and their impregnation oxides with 0.5%wt palladium are chosen as reference catalysts. One kind is from Lurederra (CeO_2/ZrO_2, 0.5%wt $Pd/(CeO_2/ZrO_2)$) and the other is from Johnson Matthey ($Ce_{0.5}Zr_{0.5}O_2$, 0.5%wt $Pd/Ce_{0.5}Zr_{0.5}O_2$).

1.2. Synthesis protocols

1.2.1 Synthesis of perovskite

Synthesis methods of perovskite materials can be generally be classified into three major routes: processes involving solid, processes involving liquid and processes involving gases or vapours [1]. Sol-gel method, which is one of processes involving liquid beginning with liquid reactants or solutions, is a relatively optimal option in the laboratory scale to prepare small particles in the nanoscale under lower temperature and short time [1]. The *Pechini route* is a modified sol-gel method and the so-called conventional citrate method is treated as the principle of synthesis to guide the way to parent and substituted perovskite materials [2].

Metal nitrate precursors are dissolved into ultrapure water to obtain the aqueous solution in first. Then add citric acid, as the chelating agent, until the corresponding quantity and therein molar ratio of metal ions to chelators is 1:1. Continue to stir the mixture till gel form, and then transfer the gel liquid into a flask. Attach the flask to the rotavapor instrument, the rotative evaporation condition has two parameters, constant temperature is set to 60 °C with water bath and rotation velocity could be between 30 rpm and 60 rpm to obtain moderate bubbles during the process of reducing the pressure in the flask. As rotative evaporation continues, the liquid gel viscosity increases and becomes viscous gel. Transfer the viscous gel onto culture dish and keep dry at 80 °C in thermostatic drying oven for 24 hours. During the drying process, residual moisture in gel is well evaporated till obtain a very dry gel. Grind and pulverize the dry gel in powder form in a mortar [3].

Depending on the thermo-gravimetric analysis on the dry gel powder, the nitrate dry gel could be decomposed around 300 °C with a violent reaction like explosion and the following calcination becomes smoothly above the nitrate decomposition temperature. The nitrate decomposition is treated in muffle furnace till 300 °C and then transfer the decomposed powder into a quartz tube reactor [4]. Assemble the quartz tube reactor into a tube furnace with constant air flow inside and finally calcined the pretreated powder at 600 °C or 800 °C in order to obtain the final perovskites. Therefore, the nitrate decomposition step, which is also named as pre-calcination below 300 °C, and the calcination step in tube furnace form the two-step calcination strategy. Besides, calcination heating rate is set to 2 °C/min and maintain the target calcination temperature for 8 hours (Fig. 3.1. and Fig. 3.2.).

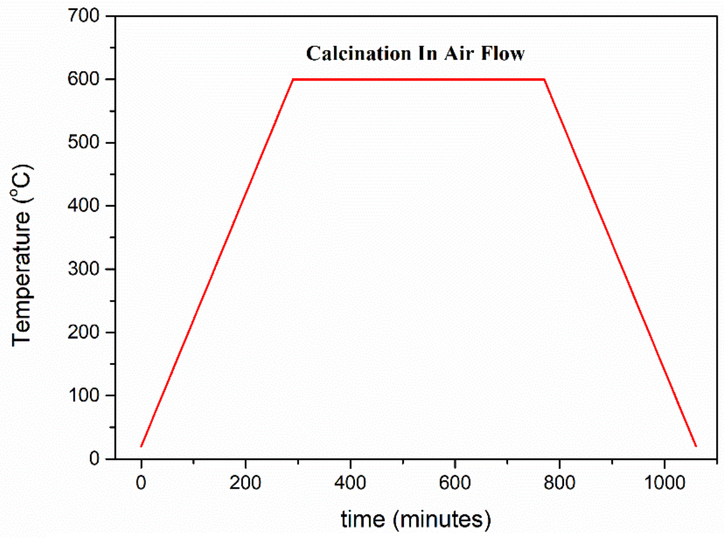

Fig. 3.1. Calcination Program for Perovskites at 600 ºC.

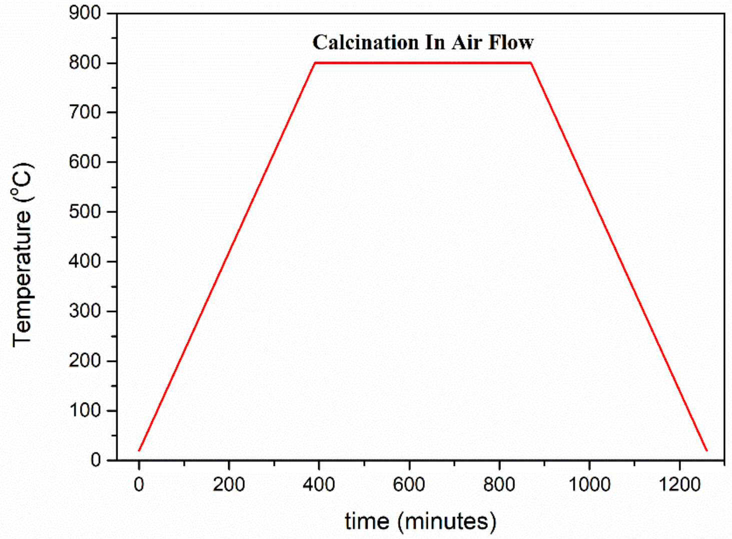

Fig. 3.2. Calcination Program for Perovskites at 800 ºC.

Citric acid as the nature of chelating agent is a conventional sol-gel route presenting an agreeable route to perovskite synthesis in laboratory scale with good homogeneity and suitable yield as mentioned in the beginning. However, low specific surface area and rare pore structure are the shortcomings to a certain extent. In addition, the higher the calcination temperature, the lower the specific surface area. The correlative characterizations are presented and analysed in subsequent chapters.

1.2.2 Incipient wet impregnation method

Incipient wet impregnation method is generally applied to load precious metal on support materials [5]. The perovskite synthesized in the previous step is treated as active catalytic support and impregnated by palladium nitrate precursor.

Firstly, weigh the palladium nitrate precursor and record the mass. Then transfer the precursor into a volumetric flask of 250 mL and add ultrapure water to dissolve the nitrate to an aqueous solution. The corresponding concentration in mass can be calculated by the palladium basis labelled 40%.

Weigh perovskites and calculate the related palladium nitrate volume. Transfer the weighed perovskite to a flask and the corresponding volume of precursor solution should be added with pipettor (Thermo-Scientific, Finnpipette F1 Single Channel Pipette, Variable volume).

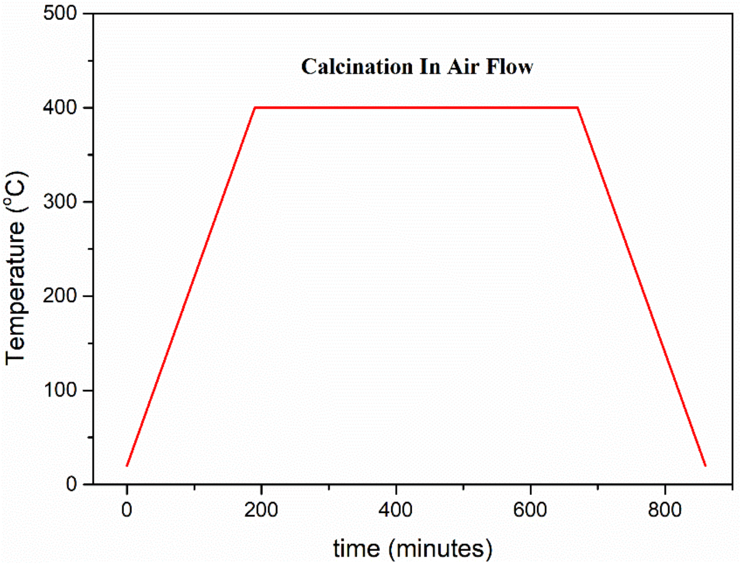

Fig. 3.3. Calcination Program for Perovskites at 400 °C.

Connect the flask with the rotavapor to evaporate the water and obtain the perovskite supported by palladium nitrate. Transfer the mixture powder into tube reactor and calcinate at 400 °C under air flow using tube furnace for 8 hours with heating rate of 2 °C/min (Fig. 3.3.).

1.2.3 Synthesis strategies

Depending on the mentioned route to perovskite synthesis as principle, two methods to reach palladium incorporation into perovskite materials have been investigated and developed: sequential method and one-pot method.

Sequential method

As the name suggests, the sequential method is done step by step in order realizing palladium incorporation in two stages. Firstly, synthesize perovskite active support by sol-gel route and then incorporate palladium on the surface of perovskite materials following incipient wet impregnation method (Fig. 3.4.). The sequential design is to realize a conception doping palladium species on the perovskite surface as far as possible.

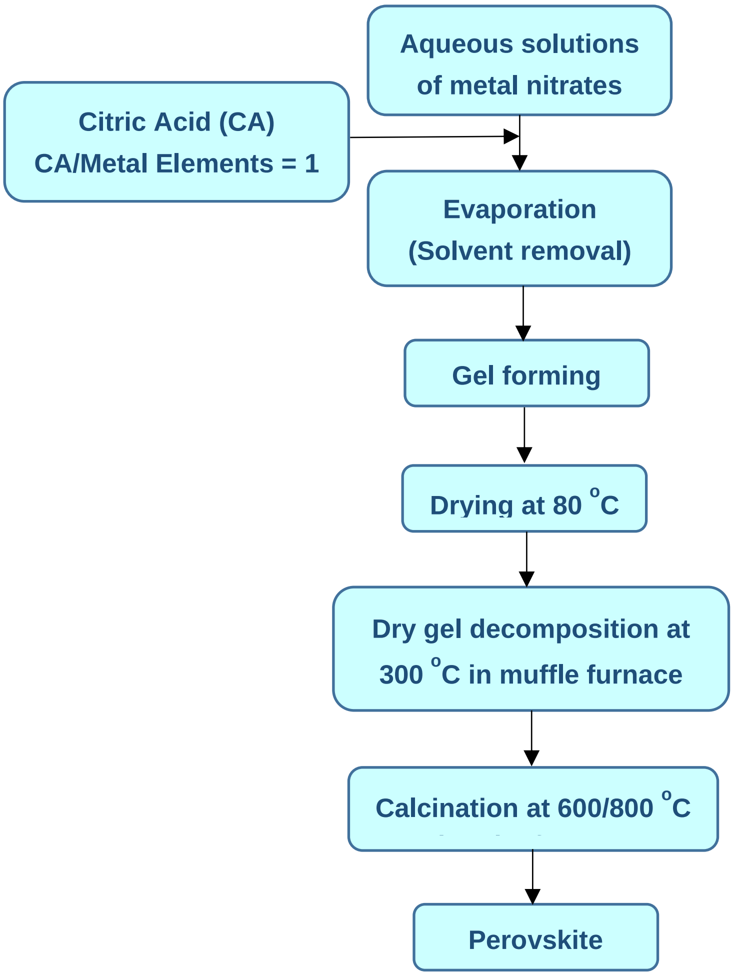

Sequential Stage 1: Protocol of Perovskite Support

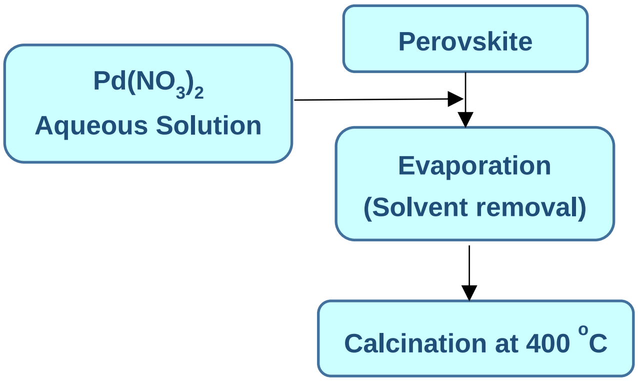

Sequential Stage 2: Protocol of Palladium Incorporation

Fig.3.4. Citric acid route of sequential method [2, 3].

One-Pot method

One-pot method is the combination of perovskite active support synthesis and the incorporation of noble metal active site. The route is designed to dope palladium into the perovskite structure co-existing with manganese element in the B position of perovskite ABO_3 structure (Fig. 3.5.).

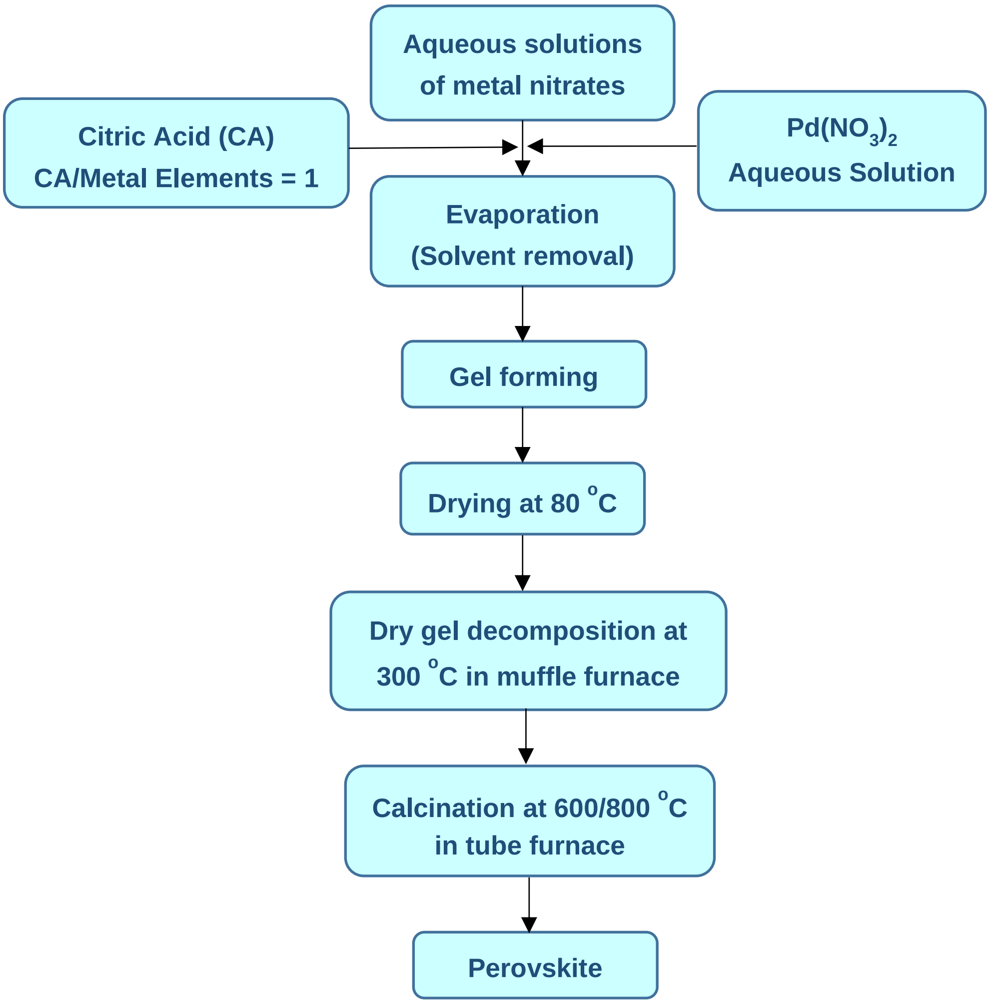

Fig.3.5. Citric acid route of one-pot method.

2. Catalyst characterisations

2.1. Thermalgravimetric analysis

Thermalgravimetric analysis (TGA) is thermal analysis method while measuring sample mass with the increase of temperature. The measurement provides relative physical and chemical information, such as phase transition and thermal decomposition. Quantitative and qualitative changes information and the corresponding influences can be obtained while combining other detection means. In our project, TGA is the technique to investigate nitrates decomposition and is carried out on a TA Instrument DSC-TGA SDT 2960 thermal analyser in the temperature range from room temperature to 1000 °C in air. Besides, the heating rate was kept constant to 10 °C/min [6].

2.2. X-ray diffraction

Powder X-ray diffraction is measured at *Chevreul Institute* and performed on Bruker AXS D8 advance diffractometer in Bragg-Brentanamo geometry fitted with a LynxEye Super Speed detector. Data are recorded with Cu Kα radiation (λ = 0.154 nm, 40 kV, 30 mA) on the 2θ range from 10° to 80° with 2θ step of 0.02° and calculated depending on Bragg equation (eq. 3.1).

Bragg equation:

$$2d\sin\theta = n\lambda \quad \textit{(eq. 3.1)}$$

Where the parameters mean:

d – Spacing between diffracting planes

θ – Incident angle of the incoming beam

λ – Wavelength of the beam

n – Integer

The Fullprof Suite Software is used for Rietveld refinement to analyse crystal structure parameters. Unit cell parameters are calculated by Williamson-Hall method with LaB_6 as reference standard.

2.3. Temperature programmed reduction

H_2 temperature programmed reduction (H_2-TPR) experiment is a thermal technique to evaluate reducibility of catalytic materials. Micromeritics AutoChem II 2920 apparatus is used to analyse samples with a constant heating rate of 10 ºC min^{-1} during heating process from ambient temperature to 1000 ºC. Besides, weigh 50 mg of catalyst and expose the samples to a flow of 5 vol.% hydrogen diluted in helium (5 vol.% H_2/He). A thermal conductive detector is carried out to monitor the evaluation of hydrogen concentration and hence the difference between reference and sample is calculated to obtain hydrogen consumption. A cold trap containing iso-ethanol is employed to trap the water produced by reaction.

2.4. Temperature programmed oxidation

O_2 temperature programmed oxidation (O_2-TPO) experiment is a thermal technique to evaluate oxidability of catalytic materials, which could be treated as reverse analysis of H_2-TPR. Therefore, Micromeritics AutoChem II 2920 apparatus is also used to analyse samples with a constant heating rate of 10 ºC min^{-1} during heating process from ambient temperature to 1000 ºC. Besides, weigh 50 mg of catalyst and expose the samples to a flow of 5 vol.% oxygen diluted in helium (5 vol.% O_2/He). A thermal conductive detector is carried out to monitor the evaluation of oxygen concentration and hence the difference between reference and sample is calculated to obtain oxygen consumption. A cold trap containing iso-ethanol is employed to catch the water produced by reaction.

Table. 3.1. Parameters of H_2-TPR and O_2-TPO Connection Program.

Process	**Step**	**Combined H_2-TPR/O_2-TPO Parameters**	**Unit**	**Note**
H_2-TPR	No.1	**Heating Rate**	°C/min	10
	No.2	**Temperature Range**	°C	From $T_{(ambient)}$ to 1000
	No.3	**Flow Rate**	ml/min	50
	No.4	**Sample Mass**	mg	~50
	No.5	**Gaz Composition**	%	5% H_2/Ar
Cooling	No.1	**Cooling Gaz Composition**	%	5%H_2/Ar (30 min)
	No.2		%	He (30 min)
O_2-TPO	No.1	**Heating Rate**	°C/min	10
	No.2	**Temperature Range**	°C	From $T_{(ambient)}$ to 1000
	No.3	**Flow Rate**	ml/min	50
	No.4	**Sample Mass**	mg	~50
	No.5	**Gaz Composition**	%	5% O_2/He

In our case of study, O_2-TPO is combined with H_2-TPR to study the re-oxidizing property of metal oxides and their interaction between perovskite support and palladium active site after reducing process (Table 3.1 and Fig. 3.6). In addition, the connection could provide details on metal valence to investigate metal re-oxidation capacity. Between the reducing and oxidizing process, helium is added to protect the catalysts in reducing state during the cooling procedure.

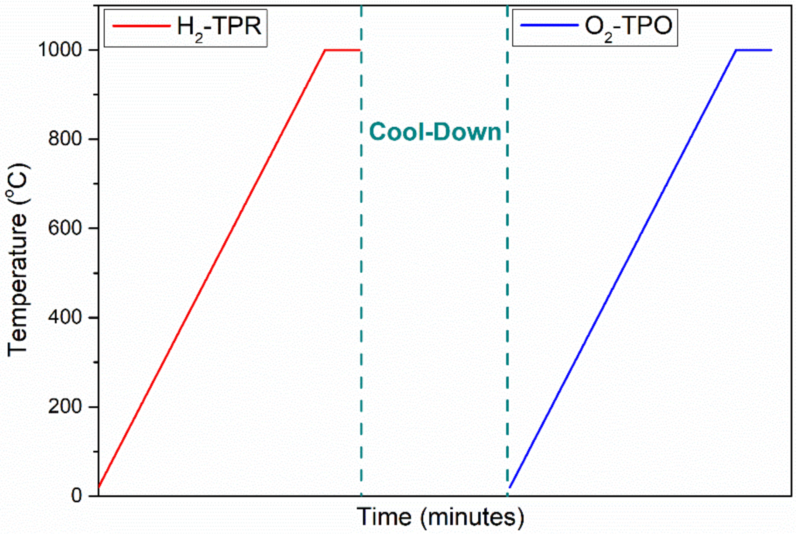

Fig.3.6. H_2-TPR and O_2-TPO Connection Schematic Program.

2.5. Temperature programmed desorption / mass spectroscopy

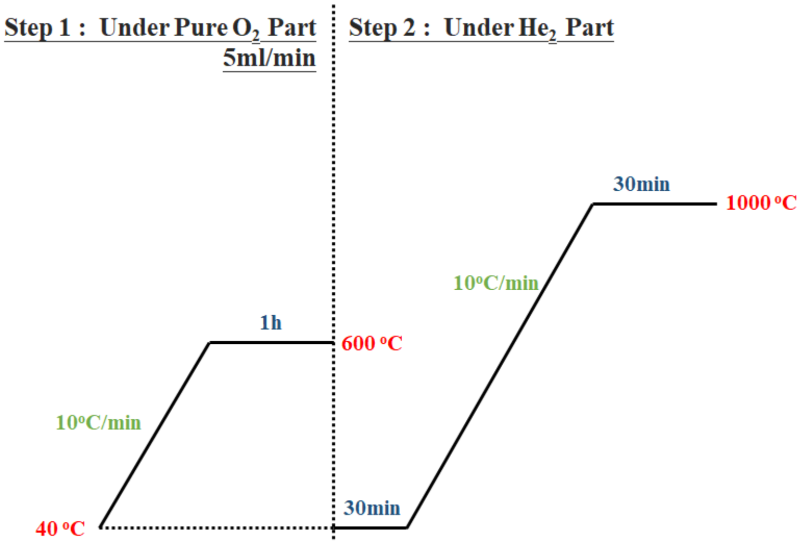

Fig.3.7. O_2-TPD Schematic Program.

O_2 Temperature Programmed Desorption (O_2-TPD) provides a route to investigate the oxygen mobility of catalytic materials. The experiment is also realized via

Micromeritics AutoChem II 2920 apparatus. 50 mg weighed catalyst sample is exposed to pure oxygen flow (5 ml/min) while heating from ambient temperature to 600 °C with a constant heating rate of 10 °C/min, and keep the sample in the same condition at 600 °C for 1 hour. Then cool-down to room temperature, and the following step is to change the circumstance from pure oxygen to pure helium and then heat to 1000 °C again with a rate of 10 °C/min and keep it at 1000 °C for 30 minutes (Fig. 3.7.).

During the process of oxygen desorption, the desorbed oxygen is detected by the thermal conductive detector. Meanwhile, the mass spectroscopy is connected to the detector to identify quantitatively in the process of desorption of oxygen species.

2.6. Nitrogen physisorption

Textural properties of catalytic materials are tested by nitrogen physisorption measurement with Micromeritics Tristar analyzer. In first, a degassing process under vacuum is put into effect aiming at removing impurities on the samples. Then setting up all device and fill an insulated container with liquid nitrogen. Pore size distribution, as a frequently used method to detect the surface properties of target materials, is an important parameter to characterize the corresponding porosity. According to the definition of International Union of Pure and Applied Chemistry (IUPAC), porous solid materials can be divided into three types according to the size of pore diameter (d): microporous materials ($d < 2$ nm), mesoporous materials ($2 \text{ nm} < d < 50$ nm) and macroporous materials ($d < 50$ nm). The specific surface area and the pore size/volume distribution were calculated according to and Brunauer-Emmett-Teller (BET) [10] and Barrett-Joyner-Halenda (BJH) [11] methods. Besides, the principle of measuring specific surface area by nitrogen gas adsorption method is based on the adsorption characteristics of gas on the solid surface. Under a certain pressure, the surface of the tested sample particle (adsorbent) has a reversible physical adsorption effect on gas molecules (adsorbate) at ultra-low temperature, and corresponds to There is a certain equilibrium adsorption capacity at a certain pressure. By measuring this equilibrium adsorption amount, the specific surface area of the sample is equivalently obtained by using a theoretical model. Due to the irregularity of the outer surface of the actual particle, strictly speaking, this method measures the sum of the total surface area of the outer surface of the particle and the internal through-holes that the adsorbate molecules can reach.

The updated IUPAC classification of physisorption isotherms is presented in Fig. 3.8 (relative pressure is X-axis; nitrogen adsorption capacity is Y-axis). The relative pressure of X-axis can be roughly divided into three stages: low pressure (0.0-0.1), medium pressure (0.3-0.8) and high pressure (0.9-1.0). The Y-axis deviation of the adsorption curve at the low-pressure end indicates that there is a strong force between the materials and nitrogen (type I, type II, type IV). When there are many micropores in the material, due to the strong adsorption potential in the micropores, the initial adsorption curve appears to be type I. The X-axis deviation of the low-pressure end indicates that the force between the material and nitrogen is weak (type III, type V). The middle pressure end is mostly the condensation and accumulation of nitrogen in the material channels, including the holes generated by particle accumulation of samples, and the pore structure within the range of ordered or gradient mesoporous. The high pressure can be used to roughly see the degree of particle accumulation. Besides, a relevancy between the shape of the hysteresis loop of a type IV(a) isotherm and the adsorbent texture has been widely confirmed, and IUPAC classified the hysteresis loops into types H1, H2(a), H2(b), H3, H4 and H5 [12].

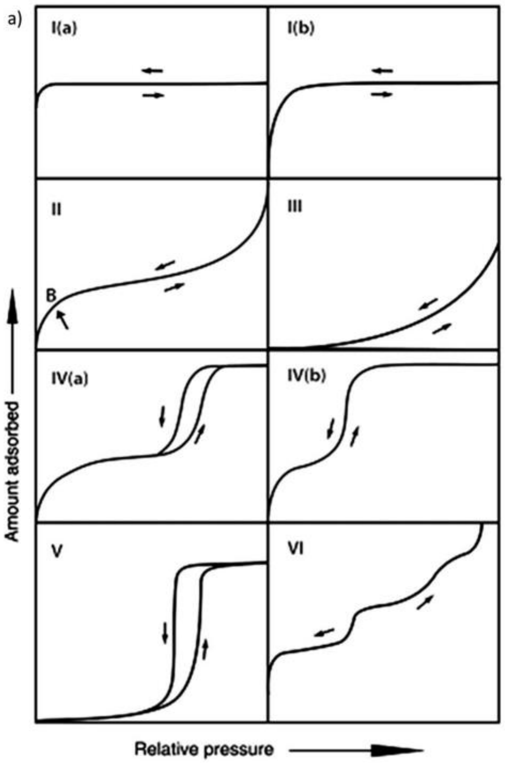

Fig.3.8. Types of nitrogen isotherm adsorption and desorption curves [12].

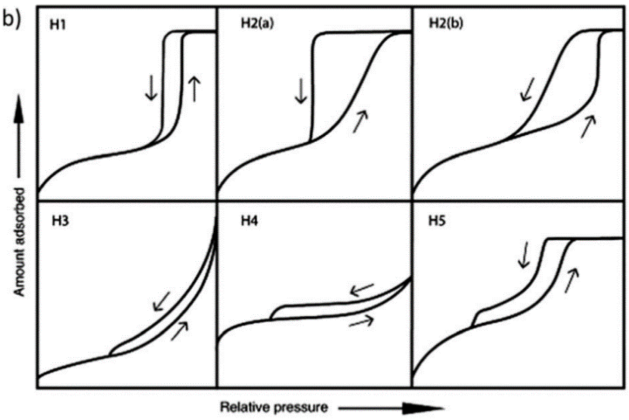

Fig.3.9. Types of hysteresis loops in type IV(a) of N_2 isotherm adsorption/desorption curves [12].

In addition, according to the shape of the adsorption isotherm and the analysis of hysteresis loop, the main information about pore structure and textural properties could be obtained. However, due to the complex pore structure of the actual adsorbent, the isotherms and hysteresis loops obtained from the experiments sometimes cannot be simply classified into a certain category, and they often reflect the "mixed" pore structure characteristics of the adsorbent [13]. Fig. 3.9 presents four types of hysteresis loops of adsorption isotherm. There are saturated adsorption plateaus on the adsorption isotherms of the H1 and H2 hysteresis loops, reflecting that the pore size distribution is relatively uniform. H1 is a uniform pore model, while H2 reflects a complex pore structure. The H3 and H4 type hysteresis loop isotherms do not have obvious saturation adsorption plateaus, indicating that the pore structure is very irregular.

2.7. X-ray photoelectron spectroscopy

X-ray photoelectron spectroscopy analysis, as an advanced technical detection means, is used for chemical valence investigation on materials surface. A Kratos Axis Ultra spectrometer as the apparatus at Chevreul Institute is equipped with a monochromatized Al Kα source (15 mA, 14 KV) and a charge compensation gun. The calibration of instrumental work function is modified to Au 4f7/2 metallic god with binding energy of 83.95 eV. The recorded spectra were charged corrected by attributing C 1s spectral component a binding energy of 285.0 eV. Spectra analysis was carried out using the scientific software CasaXPS which is specifically used in XPS Data analysis. Besides, the Gaussian(70)-Lorentzian(30) line profile was adopted for peak deconvolution because the symmetry of peaks are different: symmetric when it concerns about metal oxides, asymmetric to Pd metal as an example. Calculation of surface atomic composition is conducted by relative sensitivity factor analysis method with Shirley background.

2.8. Hydrogen chemisorption

Pulse technique is carried out for hydrogen chemisorption to measure the dispersion of precious metal on the surface of support materials. Catalyst mass of 200 mg is weighed for the test. In first, sample is heated from ambient temperature to 300 °C under diluted hydrogen (5 vol.% H_2/He) with a heating rate of 10 °C/min. This reduction process continues for 2 hours at 300 °C. Then a following step for purging sample with pure argon is operated for 1 hour at 300 °C. Finally, cool-down until ambient temperature. The hydrogen chemisorption is operated via injection of 10 pulses of hydrogen with an interval of 5 minutes under argon with a flowrate of 50 mL/min. The dispersion of precious metal on surface is assumed in first an overall stoichiometry of metal/H_2 ratio = 1:1. Besides, a hemispherical geometry is assumed to investigate the corresponding particle size.

2.9. Scanning electron microscopy / energy dispersive x-ray spectroscopy

The morphology of catalytic materials is investigated by scanning electron microscopy (SEM) with Hitachi S-4700 Cold Field Emission Gun Scanning Electron Microscopy operated at voltage acceleration of 15 kV with a resolution of 1.5 nm. Two secondary electron detectors are carried out, one is above the objective lens and the other is below the lens.

Energy dispersive X-ray spectroscopy (EDS or EDX) is combined with SEM to conduct elemental analysis or chemical characterization for elemental dispersion investigation. Oxford EDS instrument is connected to SEM to help us analyze elemental composition of metal oxide catalysts.

2.10. Inductively coupled plasma / atomic emission spectroscopy

Inductive coupled plasma atomic emission spectroscopy (ICP-AES) is operated at *RealCat Platform* in *Centrale Lille Institute*. The technique is to examine the corresponding elemental composition of materials in order to confirm the difference between theorical calculation and sample. 20 mg sample is dissolved into aqua regia and then heated to 120 ºC for 100 minutes. Then the following step is to dilute with ultra-pure water, the samples is pumped into a nebulizer and then introduced to the plasma flame. Intensity of the characteristic wavelength is emitted by a certain element and can be measured by a photomultiplier and concentration of the element was operated by comparing the intensities of the characteristic lines of the element with that of reference sample as standard.

2.11. *in situ* Electrical conductivity measurement

The *in situ* electrical conductivity measurements is considered as a remarkable technique to study the oxidation state of mixed metal catalysts for well knowing the corresponding catalytic behaviors [7]. The effects of oxidation–reduction cycle of the catalytic system can be followed by measuring the surface conductivity [8].

Besides, the characterization has been not only studied as a function of temperature and oxygen partial pressure, but also analyzed by temporal responses during sequential exposures to air, methane/nitrogen and methane/air mixture under reaction conditions.

Catalysts based on oxidized or reduced semiconductor oxides can be demonstrated by tracking the evolution of their electrical conductivity as a function of the nature of the gas phase in contact with the solid phase. Thus, exposure of p-type oxides to oxygen causes their conductivity to increase relative to that of inert atmospheres, according to the following equilibrium [9]:

$$O_{2(\mathrm{gas})} \leftrightarrow O_{2\ (ads)}^{-} + h^{\bullet} \leftrightarrow 2O_{(ads)}^{-} + h^{\bullet} \leftrightarrow 2O_{(ads)}^{2-} + 2h^{\bullet} \leftrightarrow O_{O}^{X}$$

where $h^{\bullet}$ represents a positive hole and O_{O}^{X} a lattice oxygen anion of the perovskites.

This characterization method presents a route to analyze oxygen vacancies by identifying conductor and semi-conductor types under different gas atmospheres in order to study the catalytic behavior of perovskites in the methane complete oxidation by *in situ* conductivity measurement.

3. Catalytic performance

3.1. Experimental setups

Two kinds of reaction have been carried out, one is high throughput reaction with recently popular high throughput screening techniques to investigate methane oxidation in rich, lean and stoichiometric conditions, the other is to simulate the real stoichiometric gas composition of methane engine emission.

3.1.1. High throughput reaction

High throughput technique is a screening process aiming at reducing time and error, and hence parallel synthesis and reactions can be obtained in the same condition. The experiments have been realized at RealCat Platform in Centrale Lille Institute. Implementation of screening method provides an efficient route to synthetize materials and to test the reaction activities of different materials in the parallel conditions. Therefore, large amount of data can be obtained in the same time to help scientists investigate the differences by comparing their performance and activities. In our project, *Flowrence 1220 instrument* at RealCat platform is used for methane conversion tests.

Reactor type:

- **Stainless steel reactors**
- narrow end stainless steel reactors tube with frit, internal diameter **2.6 mm**, external diameter 3 mm, length 30 cm, frit porosity 3 µm (ref AV2061)
- narrow end stainless steel reactors tube with frit, internal diameter **2 mm**, external diameter 3 mm, length 30 cm, frit porosity 3 µm (ref AV2060)
- NF 30 stainless steel reactors tube with frit, internal diameter **2.6 mm**, external diameter 3 mm, length 30 cm, frit porosity 3 µm (ref AV2059)
- NF 30 stainless steel reactors tube with frit, internal diameter **2 mm**, external diameter 3 mm, length 30 cm, frit porosity 3 µm (ref AV2058)

Be careful: Viton O-ring 2.85*2.62 mm for reactor tube (standard for all applications) (Ref AV2009) should be used

- **Quartz reactors**
- reactor tube quartz internal diameter **2 mm**, external diameter 3 mm, length 29.5 cm, end rounded (Ref AV2063) frit porosity 3 µm (ref AV2027)

Reactor filling (Fig. 3.10):

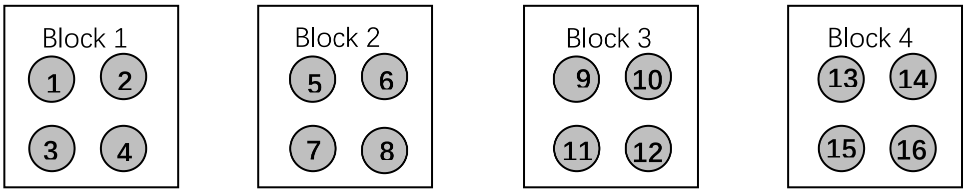

(Only catalyst and support with fraction of 50-250 μm particle size should be loaded in the reactors)

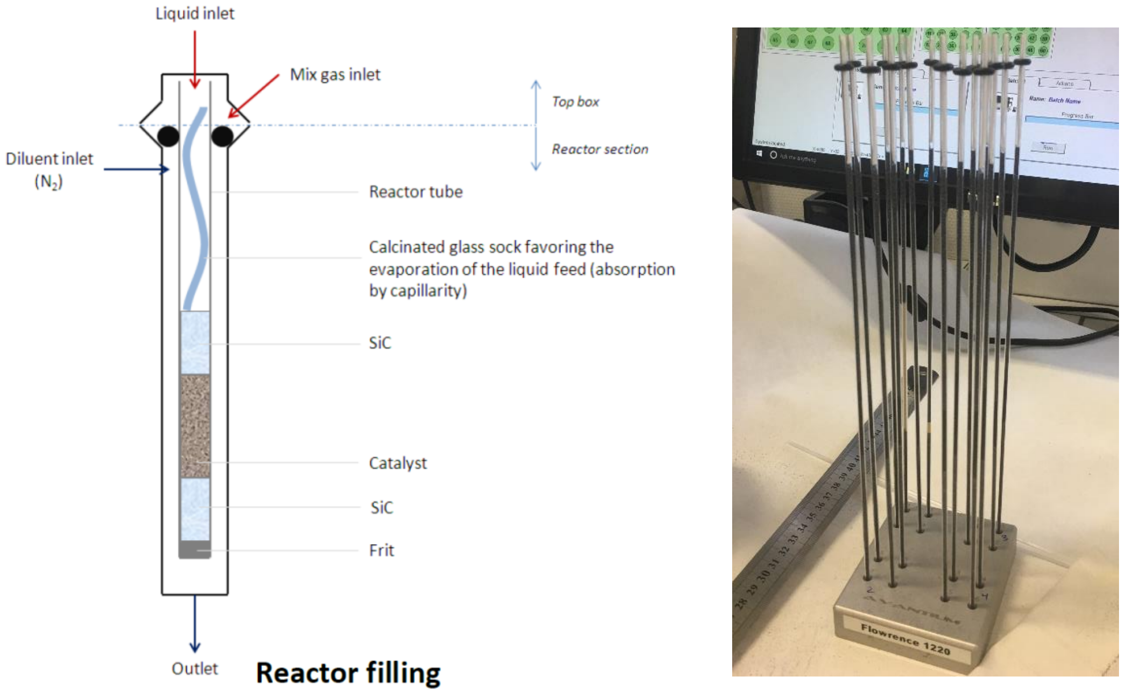

Fig.3.10. Reactor filling.

Table. 3.2. Catalyst information of first high throughput reaction.

Catalysts	Pd Position	Mass Percent of Pd/%	Reactor Number	Block Number
Pd/$Ce_{0.5}Zr_{0.5}O_2$	Surface	0.5	2	4
Pd/CeO_2ZrO_2	Surface	0.5	16	1
Pd/$LaMnO_3$ C600	Surface	1	6	2
Pd/$La_{0.7}MnO_3$ C600	Surface	1	7	2
Pd/$La_{1.3}MnO_3$ C600	Surface	1	8	2
$LaMn_{1-x}Pd_xO_3$ C600	Lattice	1	4	1
Pd/$LaMnO_3$ C800	Surface	1	5	2
$LaMn_{1-x}Pd_xO_3$ C800	Lattice	1	3	1
Pd/$La_{0.98}K_{0.02}MnO_3$ C600	Surface	1	9	3
Pd/$La_{0.95}K_{0.15}MnO_3$ C600	Surface	1	10	3
Pd/$La_{0.9}K_{0.1}MnO_3$ C600	Surface	1	11	3
Pd/$La_{0.85}K_{0.15}MnO_3$ C600	Surface	1	12	3
Pd/$La_{0.98}Sr_{0.02}MnO_3$ C600	Surface	1	13	4
Pd/$La_{0.95}Sr_{0.05}MnO_3$ C600	Surface	1	14	4
Pd/$La_{0.9}Sr_{0.1}MnO_3$ C600	Surface	1	15	4
Pd/$La_{0.85}Sr_{0.15}MnO_3$ C600	Surface	1	1	1

Two times high throughput reactions have been operated. From the 29th June 2020 to the 7th July 2020, the first series high throughput reactions have been carried out at Realcat Platform which is located in Centrale Lille Engineering School. During this time, 16 catalysts are been tested in the same conditions as parallel experiments. As the first high throughput reactions in the plan, 2 commercial catalysts are chosen as references: CeO_2/ZrO_2 and $Ce_{0.5}Zr_{0.5}O_2$ both impregnated with 0.5% mass of palladium from Luderra and Johnson Matthey respectively; and 14 catalysts with different perovskite formulas impregnated with 1% mass of palladium have been chosen as candidates (Table. 3.2)

Programming for reaction

The programming part follows our catalytic conditions and the software, combined with Flowrence 1220, is to control the high throughput reaction conditions involving pretreatment, before aging reaction condition, aging process and post-aging activity test. In addition, the program is designed to simulate the rich, lean and stoichiometric inlet gas composition. Besides, combined with gas spectroscopy instrument, the whole reaction system can be turned on once the preparation of reactors finish.

Fig. 3.11. Flowrence 1220 Programming.

Table. 3.2. presents the two references and fourteen candidates. The objective of the first high throughput reaction is to research the reactivities of the different formulations of perovskite catalysts impregnated with 1% mass percent of palladium in about 1% methane and inert gas flow.

Table. 3.3. gives the details of second time reaction, involving eight catalysts under reduced matrix using “design of experiments” technique aiming at investigating the impacts of the following four factors: calcination temperature, palladium loading content, palladium incorporation position and perovskite site A stoichiometry. The second reactions with four impacts depend on the first results and corresponding thinking. By controlling the four synthesis conditions, the eight catalysts are prepared to obtain different formulation and combination in order to investigate corresponding physicochemical properties.

Table. 3.3. Catalyst information of second high throughput reaction.

Catalysts and Preparation Conditions	Pd Postition	Pd Content/%	Site A	T (ºC)
0.5%Pd/($La_{0.55}Sr_{0.15}MnO_3$-C600)	Surface	0.5	0.7	600
$La_{0.55}Sr_{0.15}Mn_{0.9909}Pd_{0.0091}O_3$-C800	Lattice	0.5	0.7	800
$La_{0.55}Sr_{0.15}Mn_{0.9818}Pd_{0.0182}O_3$-C600	Lattice	1	0.7	600
1%Pd/($La_{0.55}Sr_{0.15}MnO_3$-C800)	Surface	1	0.7	800
$La_{0.85}Sr_{0.15}Mn_{0.9890}Pd_{0.0110}O_3$-C600	Lattice	0.5	1	600
0.5%Pd/($La_{0.85}Sr_{0.15}MnO_3$-C800)	Surface	0.5	1	800
1%Pd/($La_{0.85}Sr_{0.15}MnO_3$-C600)	Surface	1	1	600
$La_{0.85}Sr_{0.15}Mn_{0.9779}Pd_{0.0221}O_3$-C800	Lattice	1	1	800

3.1.2. Laboratory scale in real exhaust gas condition

Catalytic measurements were carried out in a fixed bed flow reactor on 200 mg of catalysts in powder form (average grain size of 150 µm sieved between 100 µm and 200 µm) mixed with silicon carbide. Catalytic performances were evaluated from successive Temperature-Programmed Reaction (TPR), in the temperature range from 120 °C to 550 °C (Fig. 3.12.). The total flow rate is adjusted to 333 ml/min (20 L/h) controlled by “Brooks Instrument Smart Mass Flowmeters”. The inlet gases are under stoichiometric condition and the outlet gases are monitored by a “Thermo Scientific Model 42i-HL chemiluminescence analyzer for NO_x” and an “Agilent Technologies 490 Micro Gas Chromatography (Mcrio GC)” for the detection and the quantification of H_2, N_2, N_2O, CO, CH_4 and CO_2.

Table. 3.4. Inlet gas composition for lab-scale temperature-programmed reaction.

Gas (Vol %)	CH_4	CO	NO	O_2	CO_2	He	H_2O
Stoichiometric	0.1 %	0.05 %	0.2 %	0.125 %	10 %	Balance	1 %

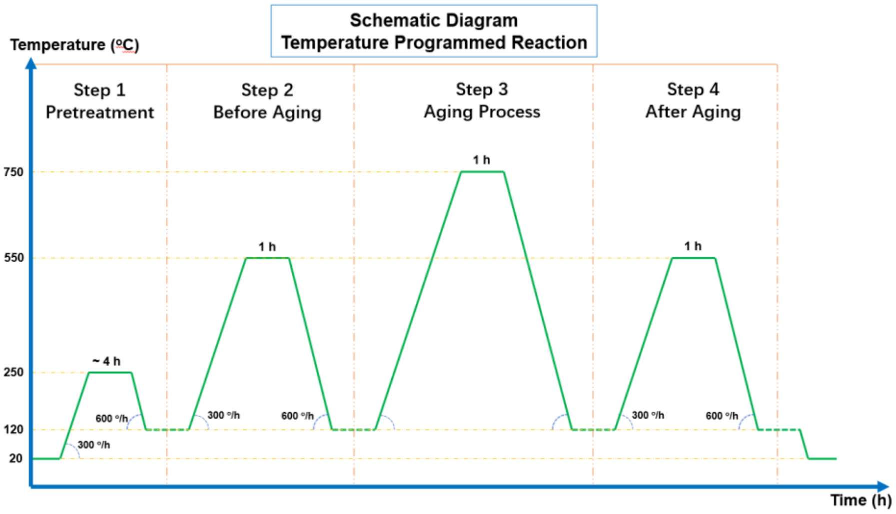

Fig.3.12. Schematic Program of Thermal Programmed Reaction.

Besides, catalytic reaction simulating methane engine emissions are performed by the laboratory scale experimental set-up (Fig. 3.13.). The body of the device involves 5 major sections: a pre-treatment section connecting four gases respectively; an air inlet system with 6 gas flowmeters; an evaporation system with a water reservoir, a liquid flowmeter and water evaporator; a high-temperature tube furnace and corresponding plug-flow reactor; a detection system with a micro gas chromatography and a NO_x analyser.

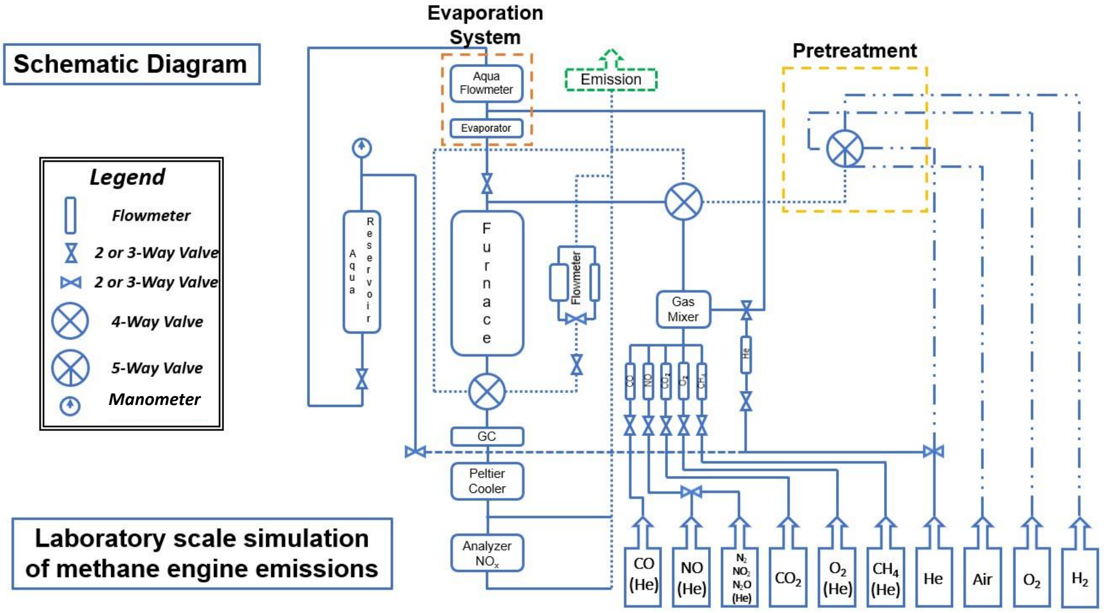

Fig.3.13. Schematic Program of Thermal Programmed Reaction Set-up in Laboratory Scale for Methane Catalytic Oxidation.

3.2. Catalyst performance and kinetic principal

3.2.1. Catalyst performance principal

Catalyst performance is investigated by conversion of methane under the complex condition. Due to the stoichiometric gas composition, high temperature range and water vapour, major reactions and side reactions should be taken into consideration. As illustrated parallel and sequential reaction can be envisioned taking place mostly at high temperature.

Major reactions:

$CH_4 + 4NO = 2N_2 + CO_2 + 2H_2O$,

$CH_4 + 2O_2 = CO_2 + 2H_2O$,

$2NO + 2CO = N_2 + 2CO_2$

$2CO + O_2 = 2CO_2$,

$CH_4 + H_2O = CO + H_2$

$H_2 + ½ O_2 = H_2O$

Side reactions:

$CH_4 + 8NO = 4N_2O + CO_2 + 2H_2O$,

$2NO + 5H_2 = 2NH_3 + 2H_2O$,

$2NO + CO = N_2O + CO_2$

Equations 3-1:

Conversion of CH_4: $C_{(CH4)} = \frac{[CH4]_0 - [CH4]}{[CH4]_0} \times 100\%$

Conversion of CO: $C_{(CO)} = \frac{[CO]_0 - [CO]}{[CO]_0} \times 100\%$

Conversion of NO (rich/near-stoichiometric condition): $C_{[NO]} = \frac{[NO]_0 - [NO]}{[NO]_0} \times 100\%$

Calculation of unreacted NO amount: $[NO]_{unreacted} = [NO]_0 – [NO]$

Calculation of NH_3 amount: $[NH_3] = [NO]_0 – [NO] – 2[N_2] – 2[N_2O]$

Yield of N_2: $Y_{(N2)} = \frac{2N_2}{2N_2+2N_2O+NH_3+NO_{unreacted}} \times 100\%$

Yield of N_2O: $Y_{(N2O)} = \frac{2N_2O}{2N_2+2N_2O+NH_3+NO_{unreacted}} \times 100\%$

Yield of NH_3: $Y_{(NH3)} = \frac{NH_3}{2N_2+2N_2O+NH_3+NO_{unreacted}} \times 100\%$

Where:

$[CH_4]_0$ – Inlet concentration of methane

$[CH_4]$ – Outlet concentration of methane

$[CO]_0$ – Inlet concentration of carbon monoxide

$[CO]$ – Outlet concentration of carbon monoxide

$[NO]_0$ – Inlet concentration of nitric oxide

$[NO]$ – Outlet concentration of nitric oxide

$[N_2]$ – Outlet concentration of nitrogen

$[N_2O]$ – Outlet concentration of nitrous oxide

$[NH_3]$ – Calculated outlet concentration of ammonia

3.2.2. Kinetic principal

Reaction rate of methane oxidation is calculated at each corresponding sampling temperature and plug-flow reactor model is assumed to investigate the kinetic research. Besides, first order reaction of methane oxidation on perovskite catalysts is adopted for kinetic properties [2, 3].

Rate constant of methane oxidation reaction can be calculated by equation 3-2:

$$k = \frac{Q_0}{W} \ln \frac{1}{1 - X_{CH4}} \qquad \text{(eq. 3-2)}$$

Where:

k – Rate constant for the corresponding temperature ($l \cdot g^{-1} \cdot s^{-1}$)

Q_0 – Total initial volumetric feed flowrate (l/h)

W – Catalyst weight (g)

X_{CH4} – Conversion of methane for the corresponding temperature (%)

Rate of methane oxidation reaction can be calculated by equation 3-3:

$$r = k[CH_4]_0(1 - X_{CH4}) = \frac{F_{CH_{4,0}}}{W}(1 - X_{CH4}) \ln \frac{1}{1 - X_{CH4}} \qquad \text{(eq. 3-3)}$$

Where:

k – Rate constant for the corresponding temperature ($l \cdot g^{-1} \cdot s^{-1}$)

$[CH_4]_0$ – Methane concentration

X_{CH4} – Conversion of methane for the corresponding temperature (%)

$F_{[CH4]0}$ – Inlet molar flowrate (mol/min)

$m_{(Catalyst)}$ – Catalyst weight (g)

Arrhenius plots and corresponding formula ($\ln r = ax + b$) are drawn by Excel depending on relation between ln r and 1/T. Apparent energy (E_{app}) and pre-exponential factor (A) can be deduced:

$$E_{app} = -a \times R \qquad \text{(eq. 3-4)}$$

$$A = e^{b} \qquad \text{(eq. 3-5)}$$

Where:

E_{app} – Apparent energy ($kj \cdot mol^{-1}$)

A – Pre-exponential factor ($l \cdot g^{-1} \cdot s^{-1}$)

R – Gas constant ($kj \cdot mol^{-1} \cdot k^{-1}$)

a – slope extrapolated from the corresponding Arrhenius plot

b – intercept extrapolated from the corresponding Arrehnius plot

The kinetic properties of corresponding catalysts based on temperature and pressure can be calculated and investigated by the above formulas and principals.

References

1. V. Rives, Chapter 1, From Solid-State Chemistry to Soft Chemistry Routes. P. Granger, V. I. Parvulescu, S. Kaliaguine, W. Prellier, Perovskites and Related Mixed Oxides, Concepts and Applications. 2016 Wiley-VCH Verlag GmbH & Co. KGaA, Boschstr. 12, 69469 Weinheim, Germany.
2. J. Wu, J.P. Dacquin, N. Djelal, C. Cordier, C. Dujardin, P. Granger, Calcium and copper substitution in stoichiometric and La-deficient LaFeO3 compositions: A starting point in next generation of Three-Way-Catalysts for gasoline engines, Applied Catalysis B: Environmental 282 (2021) 119621. https://doi.org/10.1016/j.apcatb.2020.119621.
3. A. Schön, J.P. Dacquin, P. Granger, C. Dujardin, Non-stoichiometric $La_{1-y}FeO_3$ perovskite-based catalysts as alternative to commercial three-way-catalysts? – Impact of Cu and Rh doping, Applied Catalysis B: Environmental 223 (2018) 167-176. https://doi.org/10.1016/j.apcatb.2017.06.026.
4. A. Schön, C. Dujardin, J.P. Dacquin, P. Granger, Enhancing catalytic activity of perovskite-based catalysts in three-way catalysis by surface composition optimization, Catalysis Today 258 (2015) 543-548. https://doi.org/10.1016/j.cattod.2014.11.002.
5. J. Wu, A. Glisenti, J.P. Dacquin, C. Dujardin, C. Fernandez Acevedo, C. Salazar Castro, P. Granger. $Ce_xZr_{1-x}O_2$ mixed oxide as OSC materials for supported Pd three-way catalysts: Flame-spray-pyrolysis vs. co-precipitation, Applied Catalysis A: General 598 (2020) 117527. https://doi.org/10.1016/j.apcata.2020.117527.
6. P. Granger, S. Troncéa, J.P. Dacquin, M. Trentesaux, V.I. Parvulescu, Support-induced effect on the catalytic properties of Pd particles in water denitrification: Impact of surface and structural features of mesoporous ceria-zirconia support. Applied Catalysis B: Environmental, (2018). https://doi.org/10.1016/j.apcatb.2017.11.007
7. Maeda. (2013). Generation of Oxygen Vacancies at Au/TiO_2 Perimeter Interface during CO Oxidation Detected by in Situ Electrical Conductance Measurement. Journal of the American Chemical Society, 135(2), 906–909. https://doi.org/10.1021/ja310999c
8. Anca Vasile, Veronica Bratan, Cristian Hornoiu, Monica Caldararu, Niculae I. Ionescu, Tatiana Yuzhakova, Ákos Rédey, Electrical and catalytic properties of cerium–tin mixed oxides in CO

depollution reaction, Applied Catalysis B: Environmental, Volumes 140–141, 2013, Pages 25-31, ISSN 0926-3373, https://doi.org/10.1016/j.apcatb.2013.03.042.

9. Ionel Popescu, Yihao Wu, Pascal Granger, Ioan-Cezar Marcu, An *in situ* electrical conductivity study of LaCoFe perovskite-based catalysts in correlation with the total oxidation of methane, Applied Catalysis A: General, Volume 485, 2014, Pages 20-27, ISSN 0926-860X, https://doi.org/10.1016/j.apcata.2014.07.025.
10. Stephen Brunauer, P. H. Emmett, and Edward Teller. Adsorption of gases in multimolecular layers [J]. Journal of the American chemical society, 1938, 60(2): 309-19. https://doi-org.ressources-electroniques.univ-lille.fr/10.1021/ja01269a023.
11. Elliott P. Barrett, Leslie G. Joyner, and Paul P. Halenda., The determination of pore volume and area distributions in porous substances. I. Computations from nitrogen isotherms [J]. Journal of the American Chemical society, 1951, 73(1): 373-80. https://doi-org.ressources-electroniques.univ-lille.fr/10.1021/ja01145a126.
12. Katie A. Cychosz, a Remy Guillet-Nicolas, a Javier Garcia-Martinez and Matthias Thommes, Recent advances in the textural characterization of hierarchically structured nanoporous materials, Chem. Soc. Rev., 2017, 46, 389, https://doi-org/10.1039/C6CS00391E.
13. Katie A. Cychosz, Matthias Thommes, Progress in the Physisorption Characterization of Nanoporous Gas Storage Materials, Engineering, Volume 4, Issue 4, 2018, Pages 559-566, ISSN 2095-8099, https://doi.org/10.1016/j.eng.2018.06.001.

Chapter IV. Elemental Composition of Perovskites on Bulk and Surface Properties

1. Introduction

Perovskite materials, as one of the most attractive mixed metal oxides systems since 1970s, are normally described in the form of a general $ABO_{3+\delta}$ formula. A and B represent two cations and O is oxygen anion in the perovskite composition. A cation is located in the centre of cube and surrounded by B cations while oxygen ions are located in the middle of edges. Furthermore, A cation is in dodecahedral coordination for oxygen while B cation is in octahedral coordination (Fig. 4.1.).

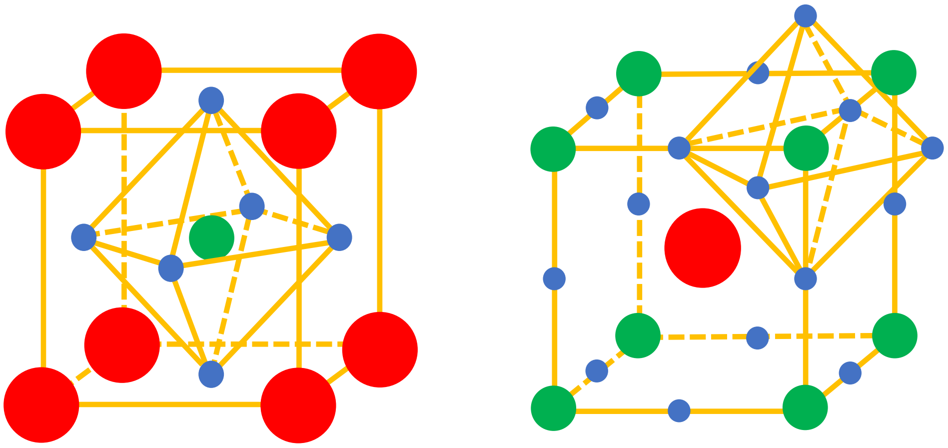

Fig. 4.1. Schematic illustration of ideal perovskite structure in the form of the formula $ABO_{3+\delta}$. (Cation A: Red; Cation B: Green; Anion O: Blue.)

Besides, lanthanide, alkaline and alkaline-earth cations can be located in site of cation A while the site of cation B situates a transition metal having 3d, 4d or 5d configuration. In view of the ionic valence state and electroneutral structure, various charge distributions are thus regulated by different metal compositions in perovskite structure. In addition, dodecahedral cation A and octahedral cation B can be partially substituted by other cations with the same or different valences. This advantage brings a broad composition as reported elsewhere in chapter 1 (see Table 1.4.) leading to various metal formulas related to corresponding redox and surface properties.

As an alternative for precious metal three-way catalyst, the stability of structure is a key parameter of the catalytic materials depending on the correlative geometrical constraints of octahedral and dodecahedral cavities. The radii of cation B should be higher than 0.51 Å in order to reach a stable structure of BO_6 octahedron. The insertion of cation A into the BO_6 octahedral cavities results in related structural distortion and more stable orthorhombic or rhombohedral structures [1].

Perovskite structure can be maintained theoretically as long as tolerance factor is kept within the range of $0.75 < t < 1.06$ (see Table 1.5. in chapter 1). Furthermore, the ideal cubic structure with the highest symmetry is characterized by a tolerance factor between 0.99 and 1.06, and the distortion of orthorhombic and rhombohedral structure is identified in the range of $0.75 < t < 0.96$ and $0.96 < t < 0.99$ respectively. Therefore, perovskite has a wide and flexible selection of elements under the constraint of tolerance factor.

According to the perovskite compositions, some advantages in terms of high temperature stability and resistance to reaction inhibitors such as water and sulfur species in the harsh environment of automobile exhaust gas can be obtained.

However, perovskites generally require a higher temperature to achieve the same catalytic activity as noble metals, which means higher energy consumption. Moreover, in consideration of their usual limited specific surface area, often less than 1 m^2/g with conventional high temperature preparation methods ($T \geq 1000$ °C), the catalytic results of the oxides are negligible.

Hence, since the first works in the 1970s reporting the remarkable catalytic properties of perovskite materials for oxidation and NO reduction reactions, their application has extended to a wide variety of catalytic reactions, thanks in particular to the development of new soft synthesis routes involving lower temperature to get the structure of the perovskite and then making it possible to significantly increase the specific surface of materials. Hence, coprecipitation, complexation and sol-gel routes or else rapid drying methods (lyophilization, spray) lead to sharp improvement in textural properties.

The heterogeneous catalysis performance of perovskites of formula LaA'BB'O_3 (A'= Sr^{2+}, Ce^{4+} and B or B' = Mn, Fe, Co, Ni) have been widely studied and reported in the literature. Cobaltites and manganites generally show better activities in oxidation catalysis, compared to other transition metals: $LaCoO_3 \approx LaMnO_3 > LaNiO_3 > LaFeO_3 \gg LaCrO_3$ [3]. Moreover, the substitution of La^{3+} by a cation of a different valence often results in further increase in catalytic activity. The rest of this chapter will be focused on perovskite compositions based on $LaMnO_3$ and optimized formulas depending on A-site stoichiometry, A-site substitution, palladium boosted perovskites and their related synergic effects. Therein, the bulk and surface properties of the related perovskites, involved in the reaction mechanisms of methane catalytic combustion, are detailed by various techniques of characterizations.

2. Impact of lanthanum stoichiometry and A-Site partial substitution on $La_xA_{1-x}MnO_{3+\delta}$ perovskites

The perovskite A-site investigation on stoichiometry and partial substitution were based on La-deficient and stoichiometric, i.e. the compositions of $La_xMnO_{3+\delta}$ and $La_xA_{1-x}MnO_{3+\delta}$ formulas respectively. A-site regulation of perovskite $LaMnO_3$ as basic composition is characterized on structural properties of bulk and related surface properties. In addition, the related electrical conductivity variation of prepared perovskites was tested and also discussed in lean conditions.

2.1. Bulk and structural properties

Bulk and structural properties reflect the physicochemical properties of catalytic materials through relevant physicochemical characterization, such as thermal gravimetric analysis (TGA), X-ray diffraction analysis (XRD), thermal-programmed reduction by hydrogen (H_2-TPR), thermal-programmed oxidation (O_2-TPO), thermal-programmed desorption of oxygen combined with mass spectrometry (O_2-TPD-MS).

2.2.1. Thermal gravimetric analysis

Thermal gravimetric analysis on perovskite materials investigates the chemical and physical processes taking place during the thermal decomposition of dried precursors to get the final structure of catalytic materials [4].

Thermalgravimetric analysis (TGA), differential scanning calorimetry (DSC) and differential thermal analysis (DTA) of the precursor decomposition were performed on TA Instrument SDT Q600. The thermal analysis is applied to three perovskite series of catalysts. Among them, $La_xMnO_{3+\delta}$ formula as the base to study the impact of lanthanum stoichiometry; $La_xK_{1-x}MnO_{3+\delta}$ and $La_xSr_{1-x}MnO_{3+\delta}$ as examples to study the impact of partial stoichiometric substitution of potassium and strontium at the A site of perovskite materials.

Figs. 4.2.-4.4. show the decomposition curves of $La_{0.7}MnO_{3+\delta}$, $LaMnO_{3+\delta}$ and $La_{1.3}MnO_{3+\delta}$ dry sol-gel or so-called xerogel precursor powder obtained by citrate acid

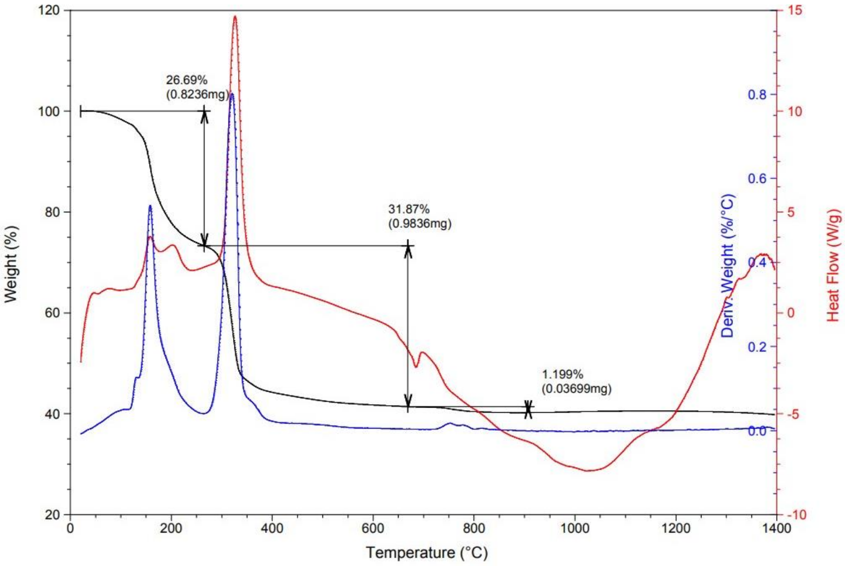

Fig. 4.2. TGA/DSC/DTA curves of $La_{0.7}MnO_{3+\delta}$ xerogel.
(Black: TGA; Blue: DSC; Red: DTA.)

route synthesis method.

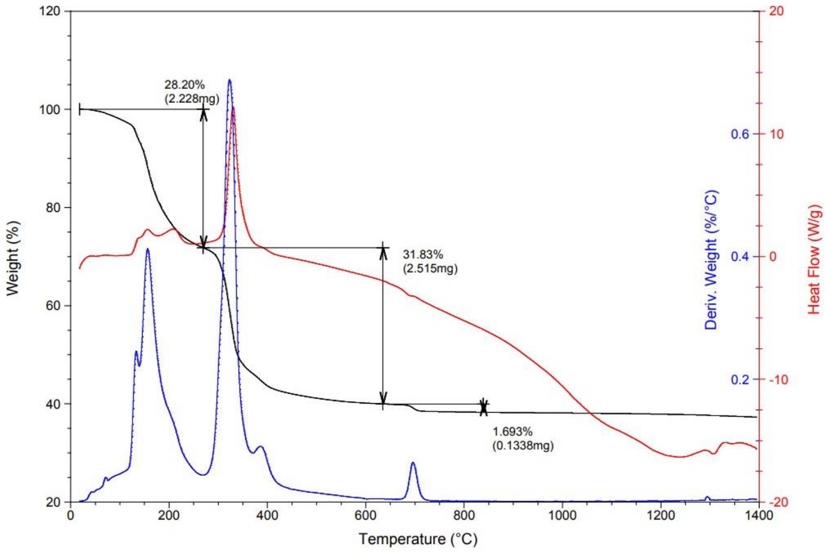

Fig. 4.3. TGA/DSC/DTA curves of LaMnO$_{3+\delta}$ xerogel.
(Black: TGA; Blue: DSC; Red: DTA.)

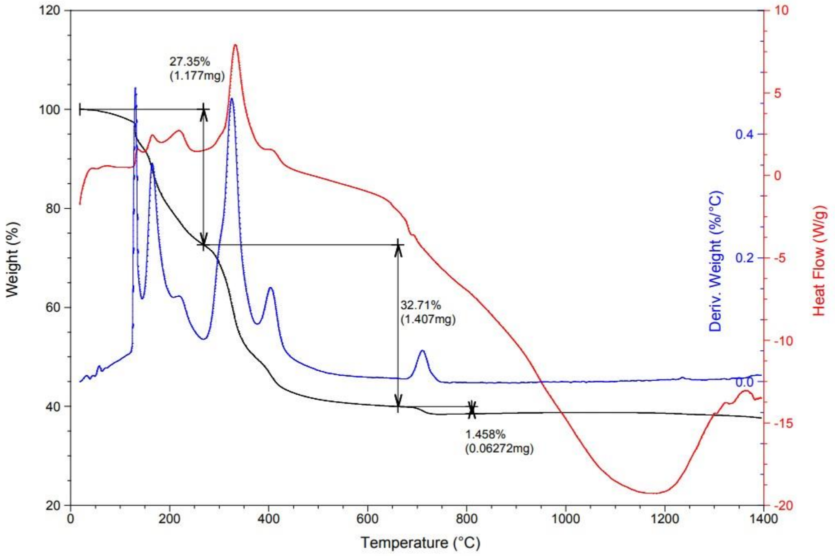

Fig. 4.4. TGA/DSC/DTA curves of La$_{1.3}$MnO$_{3+\delta}$ xerogel.
(Black: TGA; Blue: DSC; Red: DTA.)

The decomposition reaction of La$_x$MnO$_{3+\delta}$ composition precursors series obviously takes place in three stages. The first stage between 20 ºC and 280 ºC corresponds to a weight loss of about 27%. In this stage, the removal of physically adsorbed water from xerogel structure happens near 100 ºC and the exothermic range from 180 ºC to 280 ºC concerns the decomposition of lanthanum and manganese nitrates and some citrates with a mass of H_2O, CO_2 and NO_x gas production. The second mass loss stage from about 280 ºC to 400 ºC reflects thermal decomposition of the remaining citric acid complex and then the mixture of oxides begins the crystal formation stage to form perovskite at about 700 ºC [6, 7]. The third stage between 700 ºC and 750 ºC with a slight weight loss around 1.5% is considered as the step to eliminate the impurity oxides in order to obtain pure target perovskite [8].

Profiles for weight loss, heat flow reveal the same processes irrespective of La stoichiometry highlighting strong exothermic reaction, *i.e.* nitrate decomposition and citrate combustion. From the related thermal gravimetric analyses, 300 ºC can be regarded as the boundary temperature between the related citric acid organometallic complexes and the formation of metal oxides. Based on these observations a two-step calcination process was implemented as reported elsewhere [5]. A first ramp of temperature reaching isotherm at 300°C was performed in muffle furnace. Afterwards, a subsequent calcination in air was performed in a fixed bed flow reactor with a final isotherm at 600°C to obtain the perovskite structure. However, even though the calcination proceeded 8 hours in isothermal conditions at 600°C transient TGA analysis also emphasizes weak weight loss on La_xMnO_3, with $x = 1$ and 1.3, near 700°C suggesting incomplete conversion of single oxides to mixed oxide. Hence, a second series was prepared with calcination temperature at 800°C to get a pure structure.

2.2.2. Structural properties from XRD analysis

Calcined samples at 600°C and 800°C were characterized by XRD (X-ray diffraction) analysis in order to investigate the influence of calcination temperature on their structural properties. XRD pattern are reported in Figs 4.5-4.6.

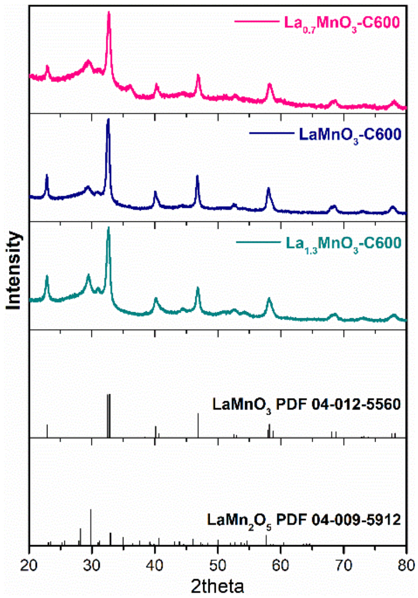

Fig.4.5. XRD profiles: (Red) $La_{0.7}MnO_3$-C600; (Blue) $LaMnO_3$-C600; (Olive) $La_{1.3}MnO_3$-C600 in the 2-theta range from 20° to 80°.

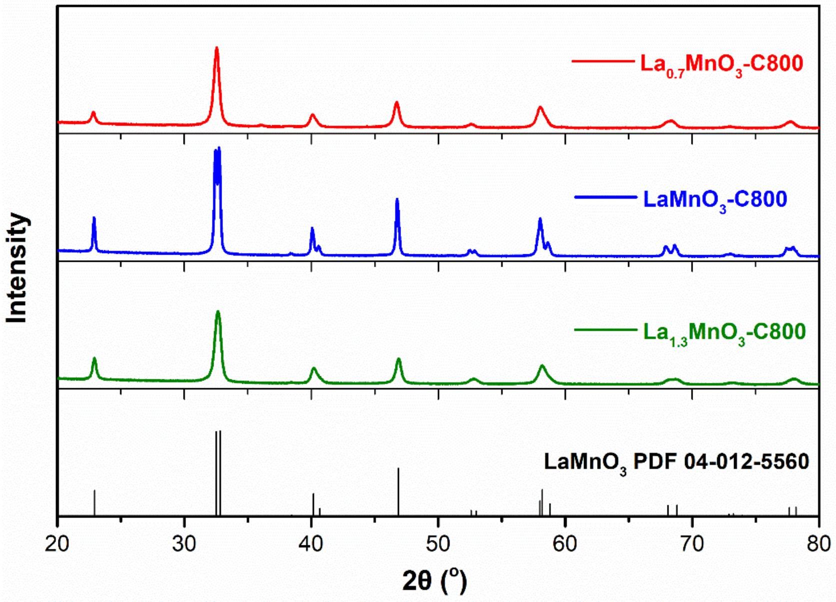

Fig.4.6. XRD profiles: (Red) $La_{0.7}MnO_3$-C800; (Blue) $LaMnO_3$-C800; (Olive) $La_{1.3}MnO_3$-C800 in the 2-theta range from 20° to 80°.

For the $La_xMnO_{3+\delta}$ series calcinated at 600 °C (see Fig. 4.5), $LaMnO_3$ served as benchmark composition characterized by a rhombohedral structure. with peak splitting at $2\theta = 32.5°$ and 32.8° for the most intense reflection characteristic of the rhombohedral structure (PDF 04-012-5560). As observed broad reflections appear for the calcined samples at 600°C which does not reveal the abovementioned peak splitting. The orthorhombic structure predominates but additional weak reflections appear at 2θ = 28.2°, 29.8° and 31° reflecting bulk detectable impurities assigned to $LaMn_2O_5$ (PDF 04-009-5912) composed by La_2O_3 and $Mn(NO_3)_2\cdot 2H_2O$ on the La_xMnO_3-C600. For the series of La_xMnO_3-C600, the low crystallinity of perovskite increases the surface valence of manganese metal, but also brings complex impurity phases.

The diffractograms recorded on samples calcined at 800°C exhibit narrower reflections which reflect improved crystallinity. Let us note that the peak splitting is observed on $LaMnO_3$ and no additional discernible reflection seems to appear assigned to bulk single oxide impurities. Hence, in contrast to calcination at 600°C, thermal treatment at 800°C leaded to the pure structure. Let us note similar observations for the composition *x* = 0.7 and 1.3 although these samples seem in lesser extent less crystallized.

Table 4.1. XRD Rietveld refinement results of lattice parameters
La_xMnO_3 series calcinated at 800 °C

Catalyst	Crystal system	Lattice system	a(Å)	b(Å)	c(Å)	Unit cell volume(Å^3)	α	β	γ
$LaMnO_3$	trigonal	rhombohedral	5.49008 (±0.00016)	5.49008 (±0.00016)	13.29487 (±0.00080)	347.034 (± 0.025)	90°	90°	120°
$La_{0.7}MnO_3$	trigonal	rhombohedral	5.48414 (±0.00030)	5.48414 (±0.00030)	13.33177 (±0.00159)	347.245 (± 0.049)	90°	90°	120°

As global tendencies, calcination at 600°C leads to sample exhibiting a lower crystallinity than those calcined at 800°C. For this latter series the absence of impurities is also noticeable. Based on this, the Rietveld refinement method has been implemented to determine the lattice parameters at the unit cell volume. Stoichiometric $LaMnO_{3+\delta}$ presents almost perfectly clear according with the reflection peak signals of reference than the non-stoichiometric $La_{0.7}MnO_{3+\delta}$. Both of them have the most intense signals at

2θ (32.811°) and h k l (1 0 4), but a small peak splitting at 2θ (32.503°) with h k l (1 1 0) which indicates the rhombohedral system and relatively intense peak at 2θ (22.934°) with h k l (0 1 2) indicating slightly more Lanthanum in stoichiometric structure. Besides, the pure manganite $La^{3+}Mn^{3+}O^{2-}{}_3$ is essentially antiferromagnetic with orthorhombic structure. $LaMnO_3$ could be orthorhombic, rhombohedral or cubic depending on their differences on Mn^{4+} concentration which presents about 0-12% (orthorhombic), 18-30% (rhombohedral) and more than 30% (cubic) respectively [9].

The results from Rietveld refinement analysis using Fullprof software present that all diffraction peak signals were well indexed in rhombohedral structure and lanthanum deficiency on perovskite A-site produced an obvious structure distortion with slightly bigger unit cell volumes. Combining with the peak splitting on stoichiometric $LaMnO_3$ but no obvious peak splitting on non-stoichiometric $La_{0.7}MnO_3$, this phenomenon may also indicate that the distortion of the latter is favorable for a larger contact area corresponding to the results of specific surface area, which is lanthanum deficiency sample has a relatively higher specific surface area than stoichiometric $LaMnO_3$ sample. The details of porosity will be illustrated in the following Brunauer-Emmett-Teller specific area investigation.

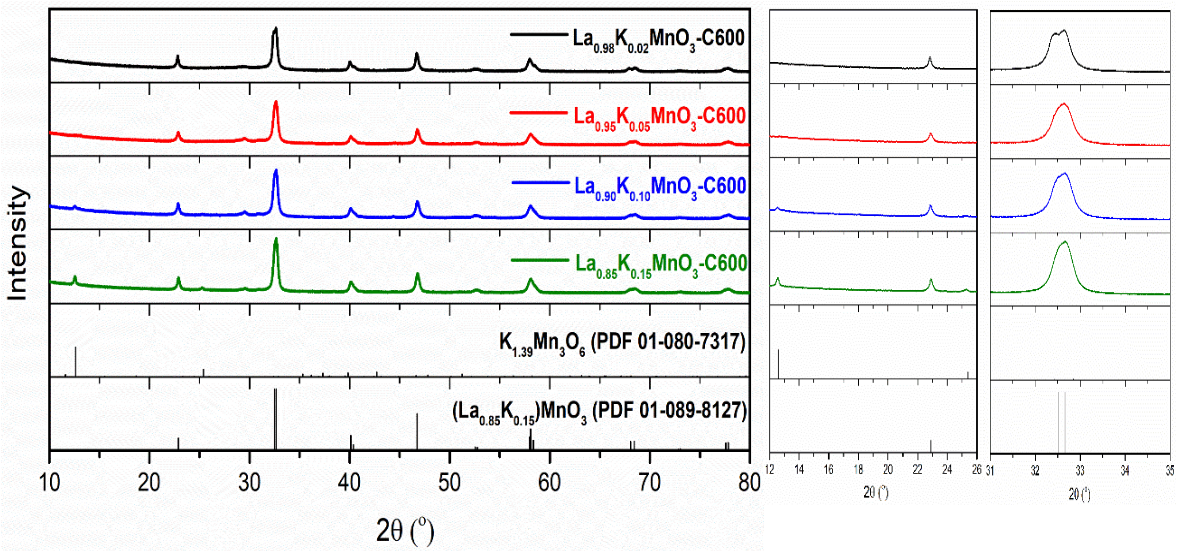

Fig.4.7. XRD profiles: (Black) $La_{0.98}K_{0.02}MnO_3$-C600; (Red) $La_{0.95}K_{0.05}MnO_3$-C600; (Blue) $La_{0.9}K_{0.1}MnO_3$-C600; (Olive) $La_{0.85}K_{0.15}MnO_3$-C600 in the 2-theta range from 10° to 80°.

With regard to $La_{1-x}K_xMnO_3$ samples calcinated at 600 °C, the four samples present a rhombohedral symmetry. Their main reflections, with peak splitting at 2θ = 32.5° and 32.7°, are characteristic of the rhombohedral structure (PDF 01-089-8127). Besides, as the K substitution content increases from 0.02 to 0.15 in perovskite formulation, monoclinic lattice structure $K_{1.39}Mn_3O_6$ (PDF 01-080-7317) arises with two increasingly intense peaks at 2θ = 12.6° and 25.4°, same as the work of adding potassium from K. Jiratova et al. [34]. the impurity could be attributed to relatively low calcination temperature at 600 °C.

To Sr-substituted $La_{1-x}Sr_xMnO_3$ samples calcinated at 600 °C, the absence of reflection for $x = 0.02$ clearly emphasize an amorphous structure. The crystallization is enhanced at increasing Sr content with the appearance of typical reflections of the rhombohedral $La_{0.8}Sr_{0.2}MnO_3$ structure (PDF 01-075-3215). No additional reflection assigned to SrO, La_2O_3 or MnO_x is distinguishable which suggest a preferential inclusion of Sr^{2+} cation in dodecahedral coordination [32].

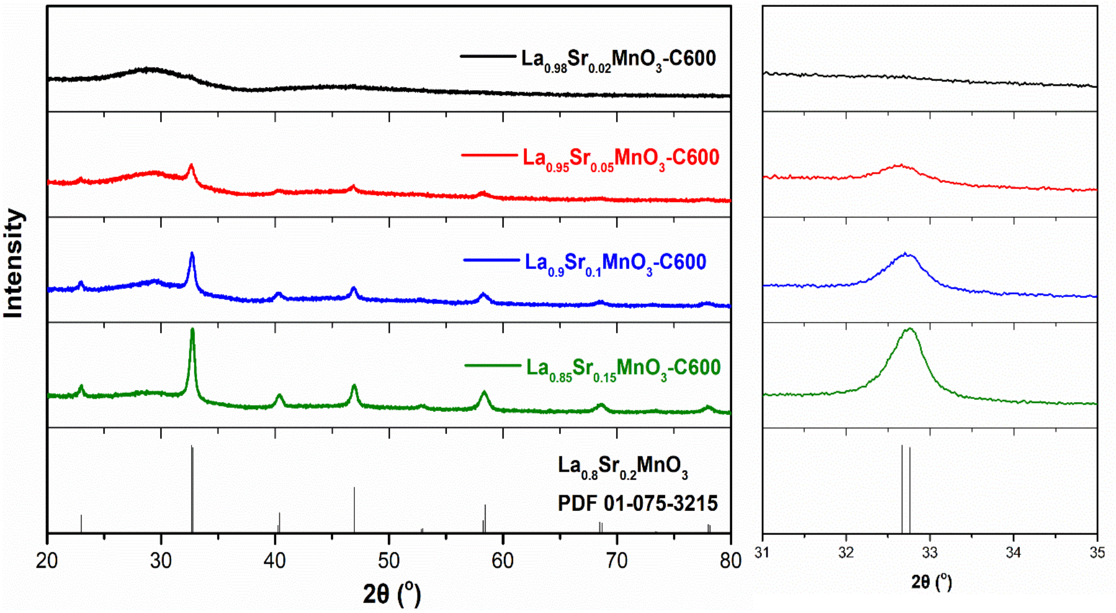

Fig.4.8. XRD profiles: (Black) $La_{0.98}Sr_{0.02}MnO_3$-C600; (Red) $La_{0.95}Sr_{0.05}MnO_3$-C600; (Blue) $La_{0.9}Sr_{0.1}MnO_3$-C600; (Olive) $La_{0.85}Sr_{0.15}MnO_3$-C600 in the 2-theta range from 20° to 80°.

2.2.3. Bulk reducibility from H_2-TPR experiments

H_2-TPR experiment (hydrogen thermal programmed reduction) is a useful thermal technique to evaluate reducibility of catalytic materials. Micromeritics AutoChem II 2920 apparatus was used to analyse samples with a constant heating rate of 10 ºC min^{-1} during a heating-process from ambient temperature to 1000 ºC. Typical H_2-consumption profiles vs. temperature are reported in Figs.4.9-4.12. H_2 uptakes were calculated by integration of the reduction peaks. A cold trap containing iso-ethanol was employed to trap water produced from the reduction process.

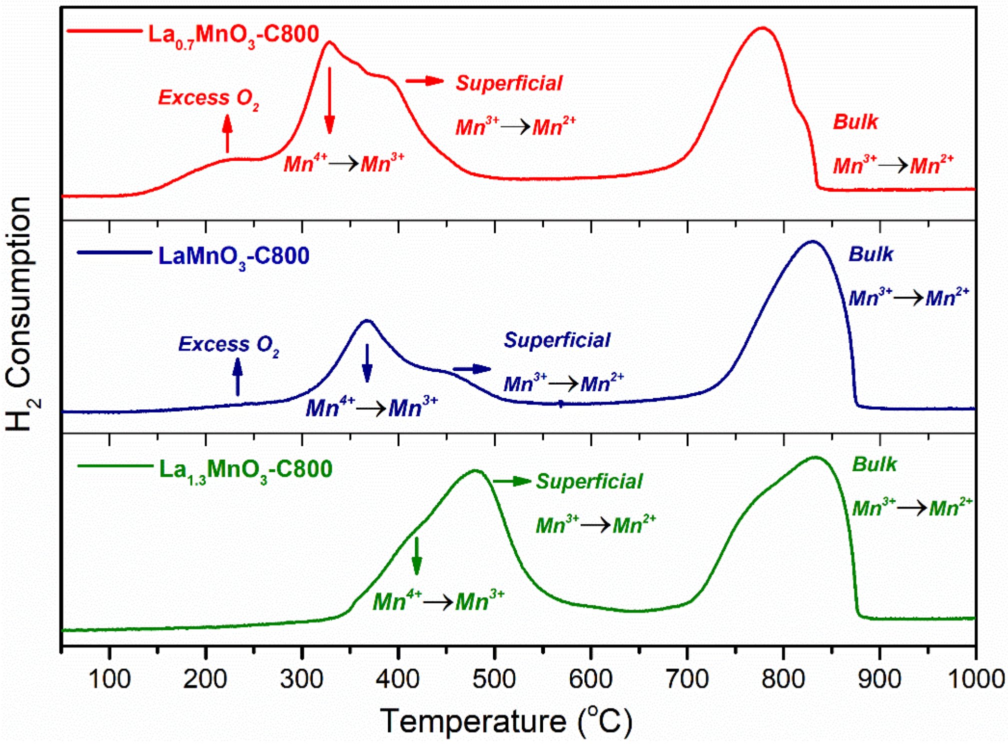

Fig.4.9. H_2-thermal-programmed reduction of La_xMnO_3 series calcinated at 800 ºC

The thermal-programmed reduction experiments were operated by above-mentioned conditions to investigate the reducibility of B-site adjusted perovskite materials as target based on $LaMnO_3$ formulation, and the results are illustrated and discussed from profile shape, peak region and the temperature at maximum peak in the following Figures and Tables. Particular attention was paid to the impact of lanthanide stoichiometry and Sr-substitution on the reducibility of framework and extra framework oxidic manganese species.

This study on impact of lanthanum stoichiometry is put into effect by heating from ambient temperature to 1000 °C and also by comparing the two calcination temperature series together in the same scale and conditions. The total reduction accounts for Eq. (1). Nonetheless, two sequential reduction processes appear distinctly corresponding to Eqs. (2) and (3).

$$LaMnO_3 + \frac{1}{2}H_2 = \frac{1}{2}La_2O_3 + MnO + \frac{1}{2}H_2O \text{ —— Eq. (1)}$$

$$Mn^{4+} \rightarrow Mn^{3+} \text{ —— Eq. (2)}$$

$$Mn^{3+} \rightarrow Mn^{2+} \text{ —— Eq. (3)}$$

Two major reduction regions, standing for two reduction steps, in bulk and on the surface, were expressly observed at temperatures below and above 550 °C respectively. A-site cations usually have stable valence states (e.g. La^{3+}, Sr^{2+}) and unreducible in the temperature range of the study. Hence, H_2-TPR profiles of $LaMnO_3$ composition perovskite is representative of the redox properties of manganese cation in B-site with adjustable valence state.

Besides, the number and sequence of reduction peaks are closely related to the valence state of the B-site metals which can be stabilized in unusual oxidation state then creating electronic imbalance. Subsequent restoration of the electroneutrality can be obtained by further adjustment on the oxygen stoichiometry and/or the oxidation state of manganese. A further reduction from Mn^{2+} cation to metallic Mn do not take place in this reduction process [10].

As to the La_xMnO_3-C800 samples, calcinated at 800 °C, shown in Fig.4.9, La deficiency sample $La_{0.7}MnO_3$-C800 generally presents characteristic peaks of reduction process at lower reduction temperature than $LaMnO_3$-C800 and $La_{1.3}MnO_3$-C800 samples. The phenomenon can be ascribed to the nonstoichiometric perovskite structure with segregation of more reducible cationic manganese species due to partial ex solution process as exemplified in Fig.4.6. and improved oxygen mobility due to vacancies formation.

Let us note that reduction profiles mimic those already reported by Y. Liu et al [11] on 3DOM $LaMnO_3$ perovskite and *y* wt% $MnO_x/LaMnO_3$ where MnO_x was incorporated by wet impregnation. They observed the growth of the lowest temperature reduction process assigned to the removal of a small amount of surface oxygen ads-species with an increase of *y* content. Hence the broad and weak contribution near 189 °C on $La_{0.7}MnO_3$-C800 seems consistent with previous assignment and would correspond to the slow segregation on MnO_x at the surface.

However, this contribution disappears for stoichiometric and over-stoichiometric lanthanum composition. With an increase of the amount of lanthanum, the following peak positions, between 300 °C and 400 °C on $La_{0.7}MnO_3$-C800, are shifted to higher temperature on $LaMnO_3$-C800 and $La_{1.3}MnO_3$-C800. Their relative intensity also varies while the latter contribution becoming prominent on $La_{1.3}MnO_3$-C800.

As a matter of fact, the evolution in relative intensity reflects changes in the relative concentration of Mn^{4+} and Mn^{3+}. The former contribution around 320 °C and 351 °C would be related to reduction of Mn^{4+} to Mn^{3+} and Mn^{3+} situated in a highly unsaturated coordination microenvironment. The latter peak about 379 °C belongs to the single electron reduction of Mn^{3+} to Mn^{2+} located in an unsaturated coordination microenvironment [12].

Therefore, it could be concluded that La-defiency would promote the formation of Mn^{4+} and Mn^{3+} in highly unsaturated coordination microenvironment at relatively lower temperature. At higher temperature, above 550 °C, the characteristic peak was due to the bulk lattice Mn^{3+} reduction to Mn^{2+} cation. In the second region, the bulk reduction of Mn^{3+} to Mn^{2+} of deficient and excess La cation samples occur at relatively lower calcination temperature than stoichiometric $LaMnO_3$-C800, which can be ascribed to the lattice structure distortion.

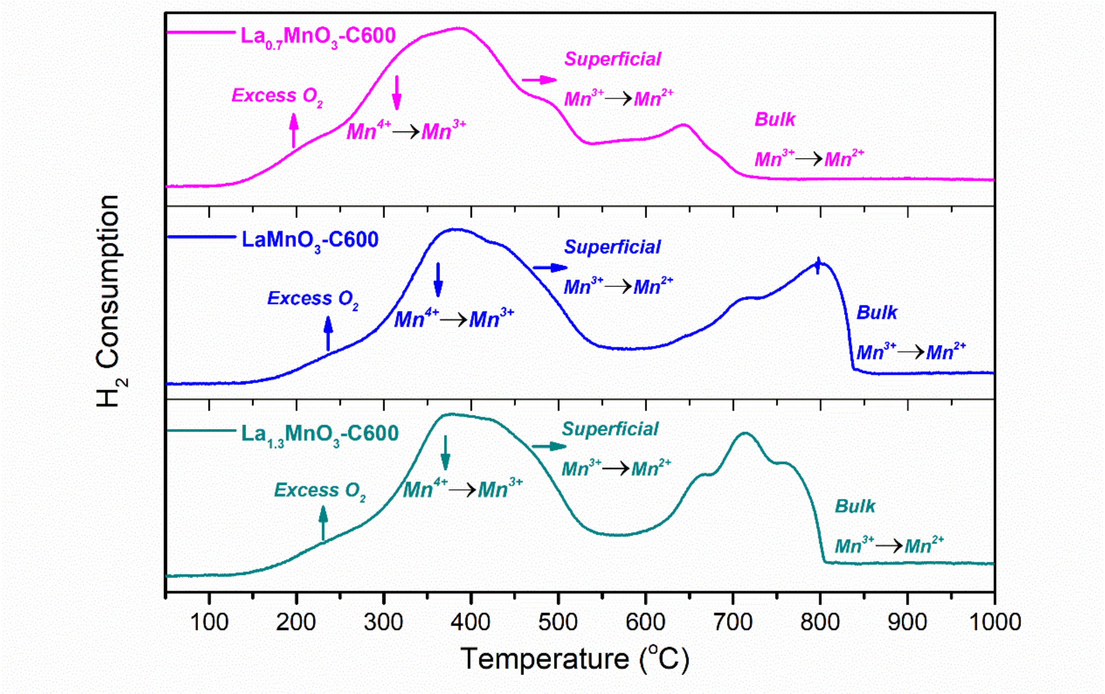

Fig.4.10. **H_2-thermal-programmed reduction of La_xMnO_3 series calcinated at 600 °C**

Quantitative analysis of hydrogen consumption can be estimated from the estimation of H_2 uptakes by integration of H_2 consumption profiles. The related atomic H/Mn can be deduced. In usual case, H/Mn=1 when the valence of manganese is Mn^{3+} in $LaMnO_3$ composition because the reduction of 1 mol Mn^{3+} of $LaMnO_3$ consumes 1 mol H (0.5 mol H_2) [13]. Hence, H/Mn value could reflect the valence of bulk oxidic manganese species, *i.e.* the relative composition of Mn^{4+} and Mn^{3+} species in calcined perovskite samples. Nonstoichiometric samples per unit mass calcinated at high temperature of 800 °C uptake more hydrogen than stoichiometric one, and under the same mass, the Mn content of stoichiometric sample is lower than that of deficient sample and higher than that of excess La sample because the corresponding molar mass is $La_{0.7}MnO_3 < LaMnO_3 < La_{1.3}MnO_3$. In addition, H_2 consumption on the surface of nonstoichiometric catalysts is obviously higher than $LaMnO_3$-C800, which reflects nonstoichiometric composition calcinated at high temperature promotes the surface reduction capacity. By examining the estimates of H/Mn ratio, one should mention that the values likely vary with the margin of error and did not indicate a significant impact of A-stoichiometry on the valence state of manganese in the bulk structure of manganese. Regarding the contribution of the surface reduction process, there is no clear tendency observed that would indicate a clear A-site stoichiometric dependency on oxidation state of manganese at the surface. The values emphasize a predominant stabilization of Mn^{3+}. This observation relativize previous evolution observed on the profiles which a priori emphasized changes in the bulk Mn^{4+} and Mn^{3+} distribution. Sharp changes are observable in the reduction profile vs. temperature recorded on perovskite calcined at 600°C. First, the low reduction process (< 550 ºC) becomes prominent notably on $La_{0.7}MnO_3$-C600. As seen a broader and intense signal appears in the temperature 150-500°C while a weak and broader high temperature signal shifted to much lower temperature arise in the range 500-700°C, which has the similar results as W. Yang et al. [14]. Generally, series calcinated at 600 ºC presented larger peaks than 800 ºC and different profiles, H. Zhu et al. attributed the phenomena to pore distributions and structure differences [21]. For $LaMnO_3$-C600 and $La_{1.3}MnO_3$-C600, a splitting of the high temperature signal appears with a shoulder near 700°C. In case of La_xMnO_3-C600 samples calcinated at 600 ºC (Fig.4.10.), lower calcination temperature leads to lower crystallization state depending on related XRD profiles (Fig.4.5.). Compared to former high calcination temperature, the wider range of characteristic peaks at both low and high temperature are observed and excess oxygen ad-species of all the three formulas occur nearly 200 ºC and clear wider signals reflect the reducibility of multiple undetected amorphous manganese oxide impurities. As the expected quantitative study (Table 4.2) on La deficient sample calcinated at 600 ºC, the one shows highest surface H_2 consumption of 75.6%. In addition, $La_{1.3}MnO_3$-C600 composition still holds the highest average oxidation state which is same as the samples calcinated at 800 ºC. It seems obvious that the stabilization of Mn^{4+} at the expense of Mn^{3+} does not seem sensitive to A-stoichiometry. On the other hand, the calcination temperature seems a more critical parameter. Indeed, calcination at 600°C is accompanied with significant increase of the H/Mn value that reflects a greater stabilization of Mn^{4+} species

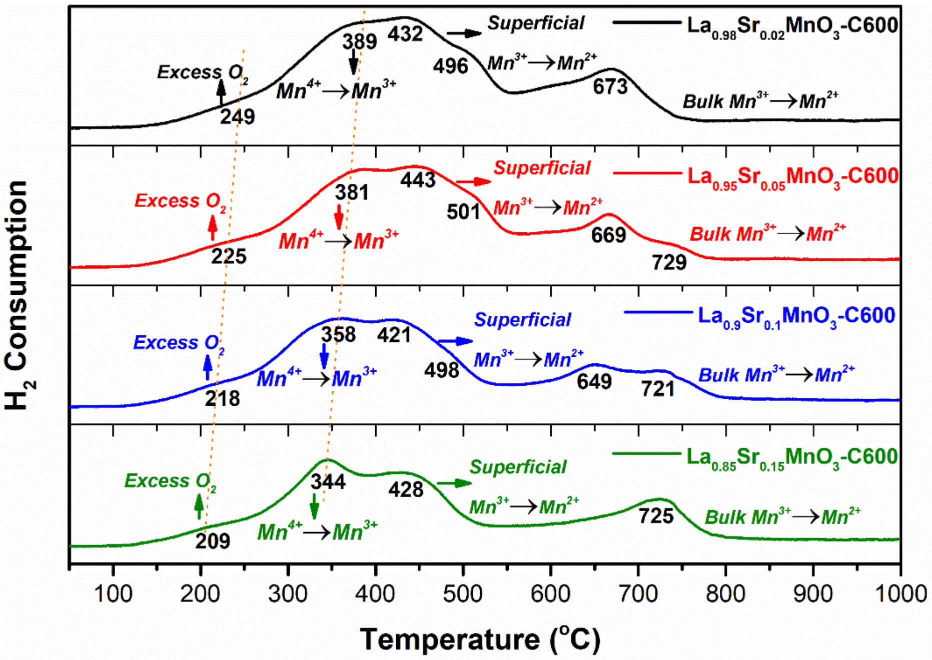

Fig.4.11. H_2-TPR profiles: (Black) $La_{0.98}Sr_{0.02}MnO_3$-C600; (Red) $La_{0.95}Sr_{0.05}MnO_3$-C600; (Blue) $La_{0.9}Sr_{0.1}MnO_3$-C600; (Olive)$La_{0.85}Sr_{0.15}MnO3$-C600 in overall temperature range.

As to $La_xSr_{1-x}MnO_3$-C600 series (Fig.4.11.) owning stochiometric composition and A-site partially substituted by Sr, the series can be generally divided into two regions bounded by 550 °C. With adding more Sr content, XRD profiles present that the samples become more and more crystallized which has an obvious impact on the corresponding reduction properties. Both La^{3+} and Sr^{2+} are nonreducible under the H_2-TPR condition, the reduction peaks should only root in the reduction of Mn species. However, partial substitution of La^{3+} by Sr^{2+} creates electronic imbalances. Subsequent equilibration can be restored by an increase of the valence state of manganese and/or an oxygen deficiency [32]. In the first region, the temperature of excess oxygen and of Mn^{4+} to Mn^{3+} and/or the single electron reduction of Mn^{3+} situated in a highly unsaturated coordination micro-environment decrease with better crystallinity and increasing Sr content which was investigated also by J.A. Onrubia et al. [32]. And the peaks about 430 °C may arise from a single electron reduction of Mn^{3+} in an unsaturated microenvironment [12]. Besides, the shoulder peaks around 500 °C and 650-670 °C disappear while perovskite crystals are fully formed, and appearing the peak around 725 °C indicating the reduction of perovskite bulk Mn^{3+} to Mn^{2+} [23].

With regard to K substitution series (Fig.4.12.), 550 °C could also be treated as the boundary temperature between the reduction on surface at low temperature and inside the bulk at high temperature. Considering the charge balance of perovskites, the valence state of potassium ion can theoretically partly stabilize the valence state of manganese from Mn^{3+} to Mn^{4+}. The hydrogen reduction process proceeds from the surface gradually to the interior. Excess oxygen species firstly reacted with hydrogen at around 260 °C for the series. $La_{0.98}K_{0.02}MnO_3$-C600 presented a similar characteristic reduction as $LaMnO_3$-C600 (Fig.4.11.). With K content increasing, a trend of Mn^{4+} predominance has taken place on surface, the relatively high quantity of superficial Mn^{3+} under unsaturated microenvironment [12] comes down significantly which corresponds to increasing Mn^{4+} species from XRD results [15]. Besides, the Mn^{4+} to Mn^{3+} characteristic peak became dominant which was investigated by Y. Xu et al. [33]. According to these authors, by adding more K content in the high temperature region (> 550 °C), the position of reduction peak deviates to slightly high temperature, which reflects the change of manganese valence state in the lattice structure.

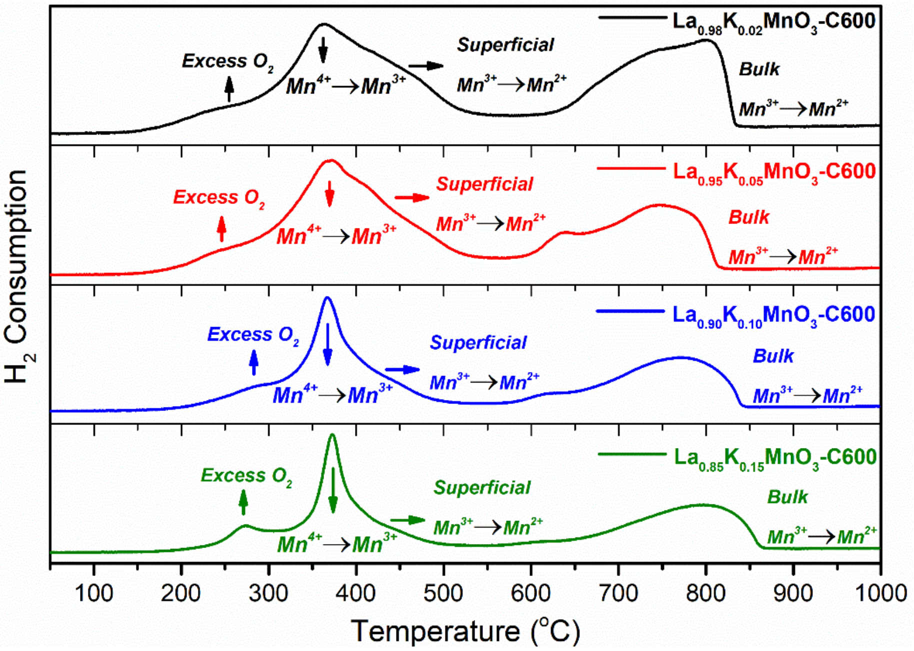

Fig.4.12. H_2-TPR profiles: (Black) $La_{0.98}K_{0.02}MnO_3$-C600; (Red) $La_{0.95}K_{0.05}MnO_3$-C600; (Blue) $La_{0.9}K_{0.1}MnO_3$-C600; (Olive)$La_{0.85}K_{0.15}MnO3$-C600 in overall temperature range.

With regard to relative quantitative analysis, the La_xMnO_3-C800 samples present globally higher H/Mn ratio than La_xMnO_3-C600 samples although their corresponding total and surface hydrogen consumption show the crosscurrents. In addition, La-deficiency provides a beneficial impact on surface H_2 consumption of both La_xMnO_3 composition. Sr partial substitution on A-site leads to higher H_2 surface reduction and H/Mn ratio (Table 4.2.). Hence, depending on the comparison of stoichiometric study and samples with same calcination temperature, nonstoichiometric composition and partial Sr substitution on A site provides a positive impact on obtention of relatively more Mn species with Mn^{4+} cation. As to K substitution, with increasing K substitution content, both total hydrogen consumption grew and increasing H/Mn presented relatively higher Mn^{4+} content.

In principle H_2-TPR experiments represent bulk phenomena. However, the initial stage concerns processes taking place at the surface while extensive bulk reduction will be governed by diffusion phenomena. Based on this, H_2-uptakes have been normalized taking the specific surface area into account.

As seen, the normalized H_2 consumptions provide a different perspective, the above-mentioned series show generally different trends depending on calcination temperature and crystallinity: 1) As to La_xMnO_3-C800 series, stoichiometry was a positive factor: stoichiometric sample expressed significant advantage compared to two non-stoichiometric ones. 2) For La_xMnO_3-C600 series, La-deficiency and La-excess show respectively positive and negative effects. 3) Relative to Sr samples calcinated at 600 °C, adding Sr from 0.02 wt.% to 0.15 wt.% presented a trend from amorphous state to the crystal formation from XRD information (Fig.4.8.) and the corresponding decreasing tendency on surface H_2 consumption indicated the formation of higher degree of crystallinity. 4) With regard to K series calcinated at 600 °C, adding K from 0.02 wt.% to 0.15 wt.% showed a stable rhombohedral structure feature with more and more obvious surface oxides of relative high Mn valence from XRD results (Fig.4.7.), which corresponds to the increasing hydrogen consumption while adding K content.

Table 4.2. H_2-TPR quantitative analysis.

Catalyst	Total H_2 Consumption (mmol/g)	H_2 Consumption < 550 °C (mmol/g)	Relative H_2 contribution (%) (< 550 °C)	H/Mn	SSA[1] (m^2/g)	Nomalized Consumption ($mmol/m^2$)
$La_{0.7}MnO_3$-C800	3.5	2.0	56.8	1.8	26.4	0.076
$LaMnO_3$-C800	2.9	1.1	37.9	1.7	7.5	0.147
$La_{1.3}MnO_3$-C800	2.8	1.4	50.5	1.9	17.9	0.078
$La_{0.7}MnO_3$-C600	4.5	3.8	84.2	1.4	29.4	0.129
$LaMnO_3$-C600	3.4	2.2	64.6	1.4	21.7	0.101
$La_{1.3}MnO_3$-C600	3.3	2.1	63.6	1.6	23.7	0.089
$La_{0.98}Sr_{0.02}MnO_3$-C600	4.1	3.4	82.9	2.0	21.3	0.160
$La_{0.95}Sr_{0.05}MnO_3$-C600	4.1	3.6	87.8	2.0	21.1	0.171
$La_{0.9}Sr_{0.1}MnO_3$-C600	3.8	3.1	81.6	1.8	26.3	0.118
$La_{0.85}Sr_{0.15}MnO_3$-C600	3.5	2.9	82.9	1.7	36.9	0.079
$La_{0.98}K_{0.02}MnO_3$-C600	3.5	2.0	57.1	1.7	26.9	0.074
$La_{0.95}K_{0.05}MnO_3$-C600	3.6	2.3	63.9	1.7	22.8	0.101
$La_{0.9}K_{0.1}MnO_3$-C600	3.8	2.1	55.3	1.7	20.1	0.104
$La_{0.85}K_{0.15}MnO_3$-C600	3.9	2.1	53.8	1.8	16.6	0.127

[1] SSA: Specific Surface Area.

2.2.4. Reoxidation of reduced sampled from O_2-TPO experiments

After H_2-TPR experiments till 1000°C, the samples were cooled down to room temperature in helium gas flow and then subjected to a same temperature ramp 10 °C/min in 5 vol.% O_2 in He to study reoxidation properties of perovskites (Fig.4.13.).

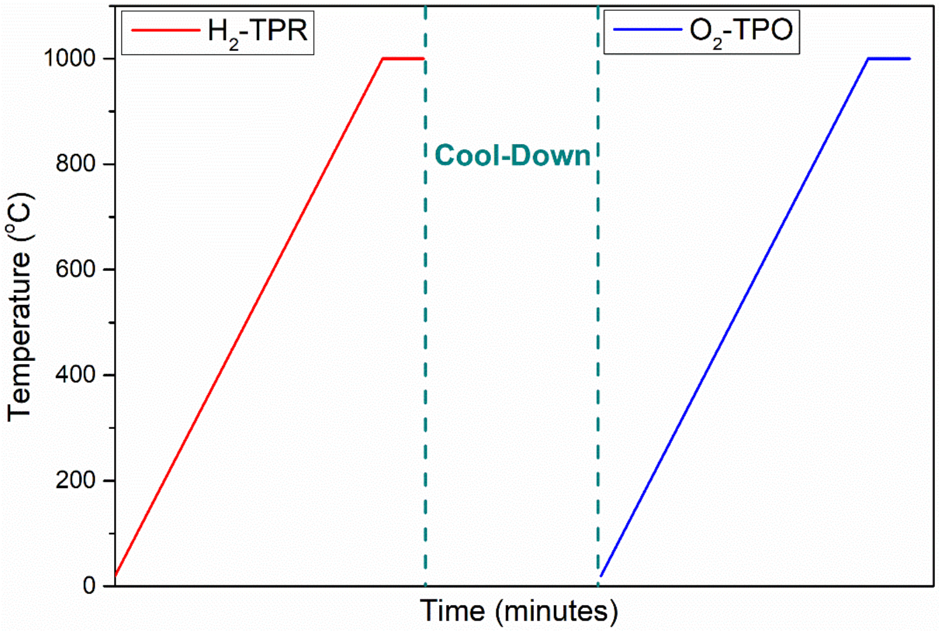

Fig.4.13. H_2-TPR and O_2-TPO combination schematic illustration.

Starting from the benchmark $LaMnO_3$ composition, extensive reduction of the perovskite into La_2O_3 and MnO is expected up to 1000°C in gaseous hydrogen. Previous investigations [12] shown that subsequent thermal treatment in oxidative conditions can retore the perovskite structure according to the following Eq. (4). Accordingly, the theoretical atomic O/Mn ratio should be equal to 0.5 which accounts for a preferential stabilization of Mn^{3+} in octahedral position in the perovskite structure. Hence, excess oxygen consumption ($O/Mn > 0.5$) indicates the formation of a higher valence state of Mn cation for the corresponding perovskite composition in the same re-oxidation conditions.

$$La_2O_3 + 2\ MnO + 1/2\ O_2 = 2\ LaMnO_3 \qquad \text{Eq. (4).}$$

As observed, a two-steps re-oxidation process takes place on reduced samples. At high temperature re-oxidation of pre-reduced La_xMnO_3-C600 and La_xMnO_3-C800 takes place at the same temperature above 750°C and should correspond to the restoration of the perovskite structure. A peculiarity appears near 925°C on La-deficient $La_{0.7}MnO_3$-C600 and La_xMnO_3-C800 compositions.

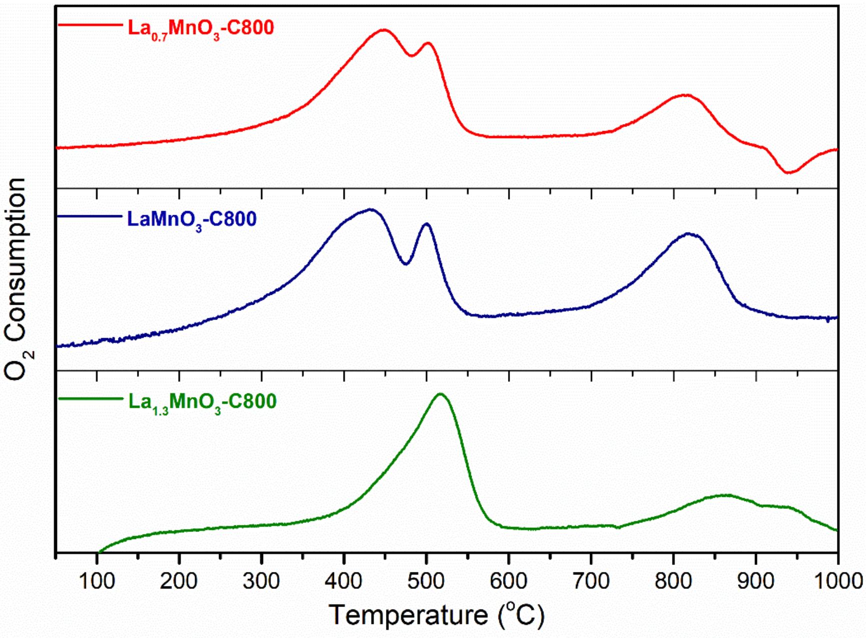

Fig.4.14. O_2-TPO profiles:

(Red) $La_{0.7}MnO_3$-C800; (Navy) $LaMnO_3$-C800; (Olive) $La_{1.3}MnO_3$-C800.

For the low temperature reduction process, no discernible change appears except on $La_{1.3}MnO_3$-C800. Clearly, the peak splitting, likely related to the re-oxidation of Mn^{2+} species in different chemical environments does not appear on this sample: O_2 consumption corresponding to this process is significantly delayed.

The corresponding quantitative analysis summarized in Table 4.3. is useful as the calculation of the atomic O/Mn ratio from O_2 uptake leads to values that exceed 0.5 underlining the formation of Mn^{4+} except for $La_{1.3}MnO_3$-C800. In that case, the value tends to the theoretical values O/Mn = 0.5 that indicates the predominance of Mn^{3+} after complete re-oxidation. For this sample, the O_2-consumption profile vs. temperature would be more representative of the re-oxidation of a single Mn^{2+} species while for stoichiometric and La-deficient compositions Mn^{2+} could coexist in different chemical environments. This explanation seems in agreement with H_2-TPR experiment on $La_{1.3}MnO_3$-C800 showing a less intense low-temperature reduction step assigned to the reduction of Mn^{4+} (see Fig. 4.9.).

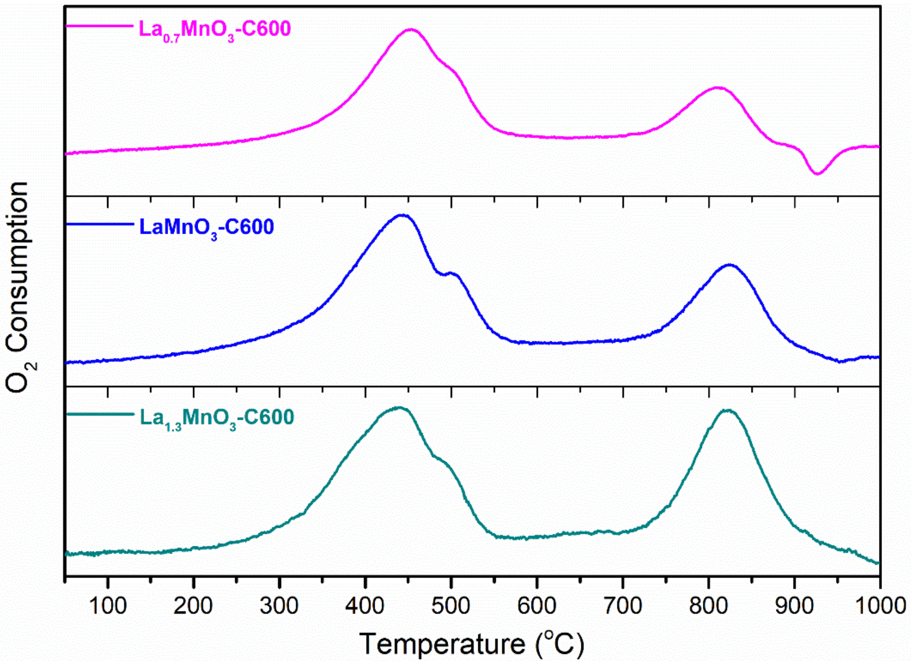

Fig.4.15. O_2-TPO profiles:

(Pink) $La_{0.7}MnO_3$-C600; (Blue) $LaMnO_3$-C600; (Cyan) $La_{1.3}MnO_3$-C600.

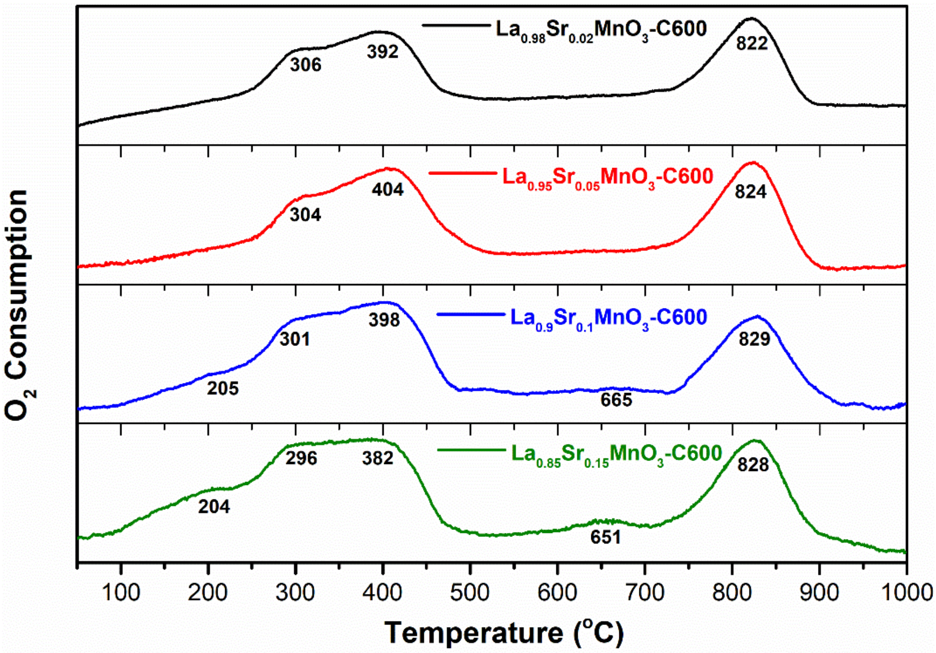

Fig.4.16. O_2-TPO profiles: (Black) $La_{0.98}Sr_{0.02}MnO_3$-C600; (Red) $La_{0.95}Sr_{0.05}MnO_3$-C600; (Blue) $La_{0.9}Sr_{0.1}MnO_3$-C600; (Olive) $La_{0.85}Sr_{0.15}MnO_3$-C600 in overall temperature range.

Let us examine now the $La_{1-x}Sr_xMnO_3$-600 series. The same two-step re-oxidation process in Fig.4.16 takes place and the restoration of the perovskite structure would start above 720°C. As exemplified in this figure, the high-temperature re-oxidation process seems to be weakly dependent to Sr-addition and mimics that earlier discussed on undoped compositions. According to previous observations on stoichiometric compositions, no negative signal appears above 900°C. The most important changes are observable at low temperature as strontium addition induces the formation of more re-oxidizable manganese species. It is obvious the re-oxidation occurs more readily and this observation is accentuated with a rise in strontium content. As strontium and lanthanum are not reducible, then O/Mn ratio in Table 4.3 is only sensitive to change in the oxidation state of manganese. As seen, the values for $x = 0.02$ near 0.8 > 0.5, taking the margin of error into account, emphasize the presence of Mn^{4+}.

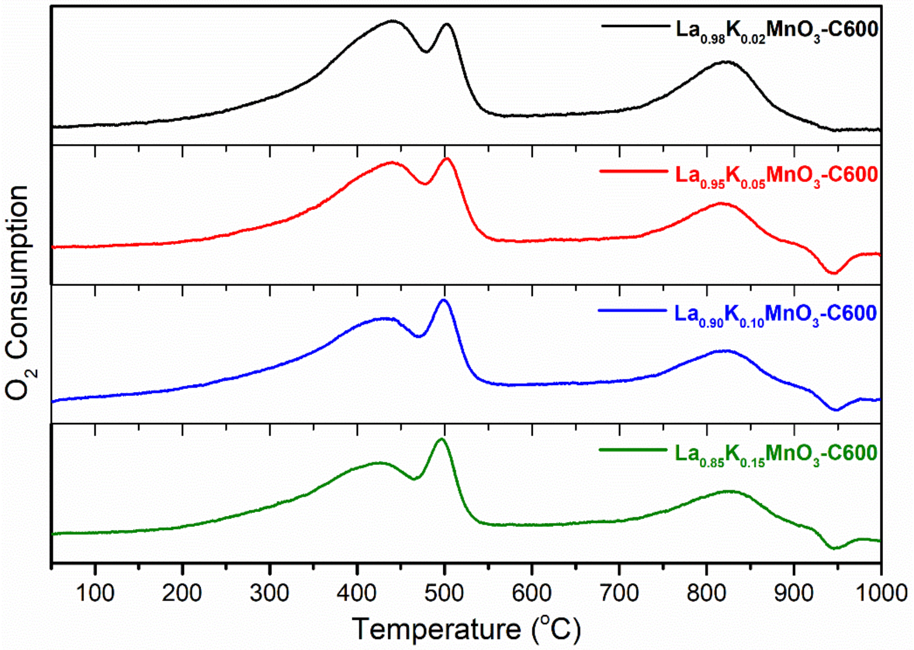

Fig.4.17. O_2-TPO profiles: (Black) $La_{0.98}K_{0.02}MnO_3$-C600; (Red) $La_{0.95}K_{0.05}MnO_3$-C600; (Blue) $La_{0.9}K_{0.1}MnO_3$-C600; (Olive) $La_{0.85}K_{0.15}MnO_3$-C600 in overall temperature range.

Interestingly, the O/Mn values gradually decrease with a rise in Sr content reaching 0.5 for the composition $x = 0.15$. Again, there is no discrepancy with H_2-TPR experiments for which we observed a decrease of the H/Mn ratio with an increase in Sr loading corresponding to less stabilization of Mn^{4+}. Nonetheless, these observations emphasize that the restoration of the electroneutrality after La^{3+} substitution by Sr^{2+} does not proceed through the adjustment of the oxidation state of manganese but would occur more likely through the oxygen stoichiometry. We have also to keep in mind that

Sr^{2+} insertion could also induce more structural constraints that would limit its insertion particularly at high concentration inducing segregation.

The O_2-consumption profiles vs T recorded on $La_{1-x}K_xMnO_3$ in Fig. 4.17 differ from those obtained on Sr-doped samples and seems more representative of phenomena taking place on La_xMnO_3 except at high temperature above 900°C. Indeed, the negative signal earlier discussed on $La_{0.7}MnO_3$ is restored for composition $x \geq 0.05$. In contrast to strontium, K-addition does not promote the oxidability of manganese species. Clearly the low-temperature reduction process disappears. It is also worth to note that the O/Mn ratio remains constant irrespective of the K composition. This observation could be jointly related to the growth of $K_{1.4}Mn_3O_6$. The remaining question lies in the relationship existing between this new phase and the appearance of the negative signal previously assigned to O_2 desorption.

Table 4.3. Amount of oxygen consumption from O_2-TPO.

Catalyst	Total O_2 Consumption (mmol/g)	O_2 Consumption (< 600 °C) (mmol/g)	Ratio of O_2 Consumption (< 600 °C)/%	O/Mn
$La_{0.7}MnO_3$-C800	1.7	1.4	82.4	0.7
$LaMnO_3$-C800	1.4	0.9	64.3	0.7
$La_{1.3}MnO_3$-C800	0.9	0.7	77.8	0.5
$La_{0.7}MnO_3$-C600	1.5	1.1	73.3	0.6
$LaMnO_3$-C600	1.5	1.0	66.7	0.7
$La_{1.3}MnO_3$-C600	0.8	0.5	62.5	0.5
$La_{0.98}Sr_{0.02}MnO_3$-C600	1.6	1.1	68.8	0.8
$La_{0.95}Sr_{0.05}MnO_3$-C600	1.4	0.8	57.1	0.6
$La_{0.9}Sr_{0.1}MnO_3$-C600	1.2	0.8	66.7	0.6
$La_{0.85}Sr_{0.15}MnO_3$-C600	1.1	0.7	63.6	0.5
$La_{0.98}K_{0.02}MnO_3$-C600	1.1	0.8	71.8	0.5
$La_{0.95}K_{0.05}MnO_3$-C600	1.0	0.8	77.8	0.5
$La_{0.9}K_{0.1}MnO_3$-C600	1.0	0.8	75.7	0.5
$La_{0.85}K_{0.15}MnO_3$-C600	1.1	0.8	74.5	0.5

2.2.5. Oxygen desorption (O_2-TPD/MS)

Oxygen desorption properties were treated following the two-step program (pretreatment under pure O_2 flow and then the desorption test during heating) Fig.4.18 with the measurements of thermal programmed desorption combined with mass spectroscopy (O_2-TPD/MS) in order to avoid the O_2 and CO_2 signals overlap.

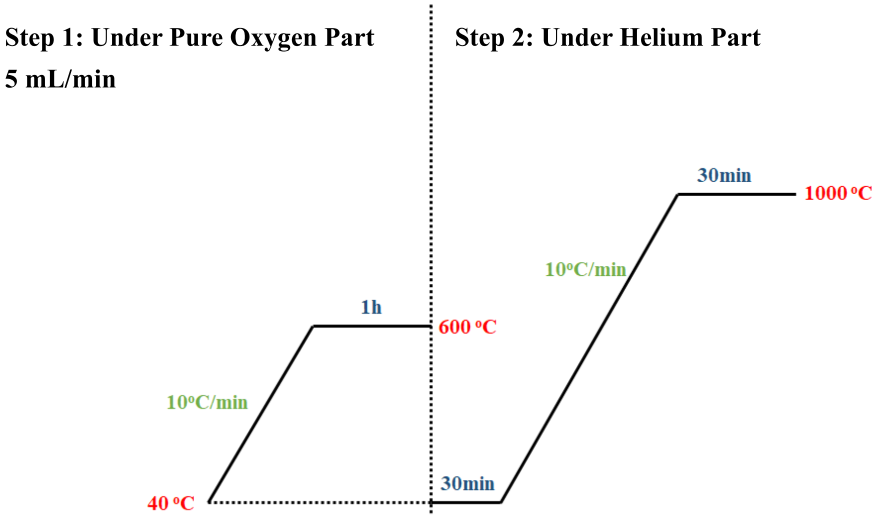

Fig.4.18. O_2-TPD/MS operation program.

Perovskite oxides with oxygen vacancies can produce/convert different oxygen species that should play a crucial role in the reaction of oxygen-containing substances. Therefore, it is essential to determine the quantity and strength of surface or sub-surface oxygen species available in perovskite oxides to manage properly the oxygen storage capacity of these materials typically near the stoichiometry in three-way catalysis and/or other catalytic applications [17].

In practice, perovskites were subjected to a ramp of temperature at constant heating rate as described in the experimental section. Outlet gas mixture was analyzed by Mass Spectrometry by selecting appropriate m/z values. In our case, the value m/z = 32 (O_2) was recorded allowing to substract extra processes which cannot be simply differentiated by analyzing only the TCD signal from chromatography analysis. The oxygen desorption profiles within the heating temperature from 100 to 1000 °C are described in Figs. 4.18, 4.19, 4.20 and 4.21.

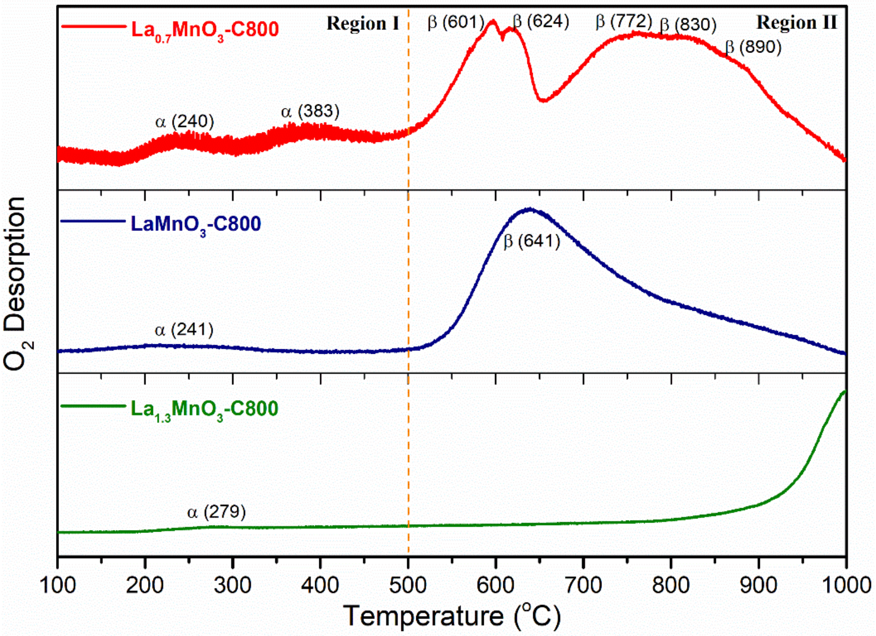

Fig.4.19. O_2-TPD/MS profiles: (Red) $La_{0.7}MnO_3$-C800; (Navy) $LaMnO_3$-C800; (Olive) $La_{1.3}MnO_3$-C800 in overall temperature range.

For the La_xMnO_3 series calcinated at 800 °C (Fig.4.19), the oxygen species desorbed in the low temperature region-I can be attributed to the weak molecular physisorbed and/or chemisorbed oxygen, which is described by α-oxygen, on perovskite surface. β-oxygen can be ascribed to oxygen species generated from oxygen vacancies on the surface or in the subsurface (500-700 °C) [18] and to lattice oxygen of perovskite bulk (above 700 °C) [10].

As to La deficient sample $La_{0.7}MnO_3$-C800 with obviously various oxygen species, two α-oxygen peaks attribute to surface adsorbed oxygen species [19] indicating that La deficiency promotes surface adsorbed oxygen types. The oxygen region-II described as β-oxygen from the deficient A-site sample bulk generates multistep oxygen desorption due to structural distortion caused by La defect. With more La content, samples seem to have a trend to weaken oxygen desorption, especially on La excess sample $La_{1.3}MnO_3$-C800 with the suppression of α-desorption and sharp delay of β-desorption (Table 4.4.).

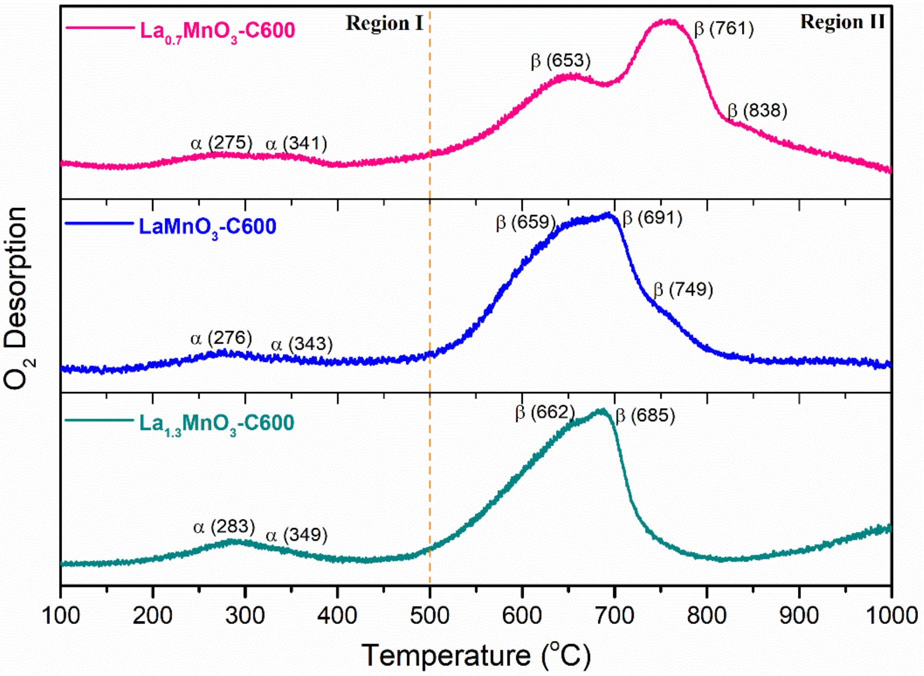

Fig.4.20. O_2-TPD MS profiles: (Pink) $La_{0.7}MnO_3$-C600; (Blue) $LaMnO_3$-C600; (Cyan) $La_{1.3}MnO_3$-C600 in overall temperature range.

With regard to lower calcination temperature at 600 °C of La_xMnO_3-C600 series (Fig. 4.20), both α-oxygen and β-oxygen present more evident profiles although the corresponding amounts of desorbed oxygen decrease compared to series calcinated at 800 °C. Consistent with the above examples, the increase in La content from defect to excess still limits the overall amount of oxygen desorption, but samples with excess La show more surface α-oxygen desorption and sharp improvement of β-desorption. Calculations of the amount of desorbed oxygen are resumed in Table 4.4. In contrast to previous observations from H_2-TPR experiments, calcination temperature does not influence the α-oxygen desorption process. On the other hand, it seems obvious that β-oxygen desorption is slightly improved on sample calcined at 800°C. Hence, improved crystallinity would favor bulk oxygen diffusion particularly on $La_{0.7}MnO_3$. The enhanced oxygen mobility from La-defect samples (Table.4.4.) than stoichiometric ones could be attributed to the oxygen vacancy generation, same as Y. Zhu et al. [35]. It is worthwhile to note that A-stoichiometry influences the β-oxygen desorption with a detrimental effect at increasing La concentration.

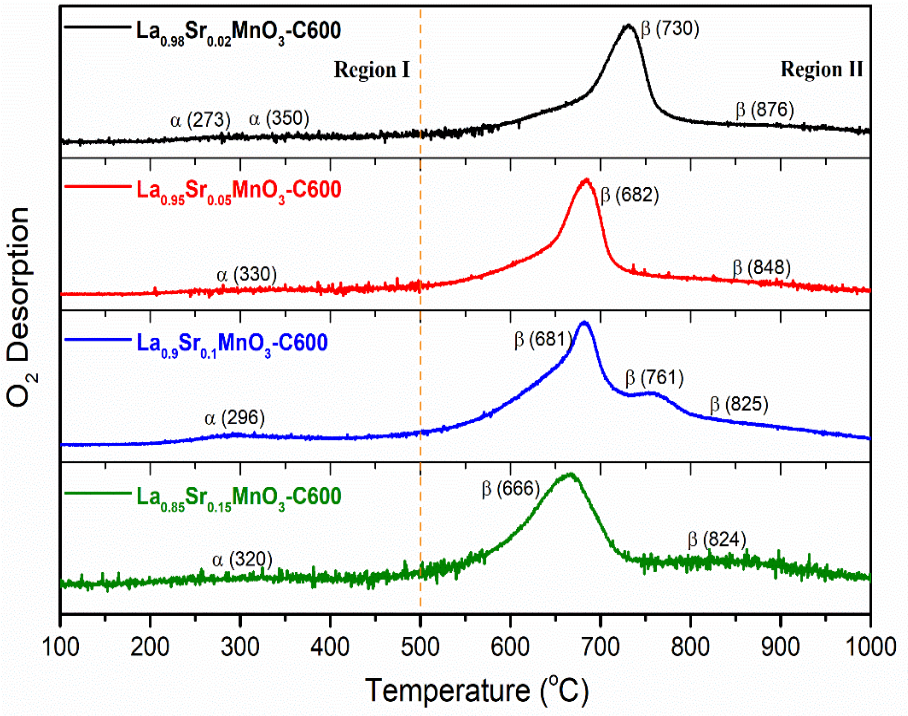

Fig.4.21. O_2-TPD MS profiles: (Black) $La_{0.98}Sr_{0.02}MnO_3$-C600; (Red) $La_{0.95}Sr_{0.05}MnO_3$-C600; (Blue) $La_{0.9}Sr_{0.1}MnO_3$-C600; (Olive) $La_{0.85}Sr_{0.15}MnO_3$-C600

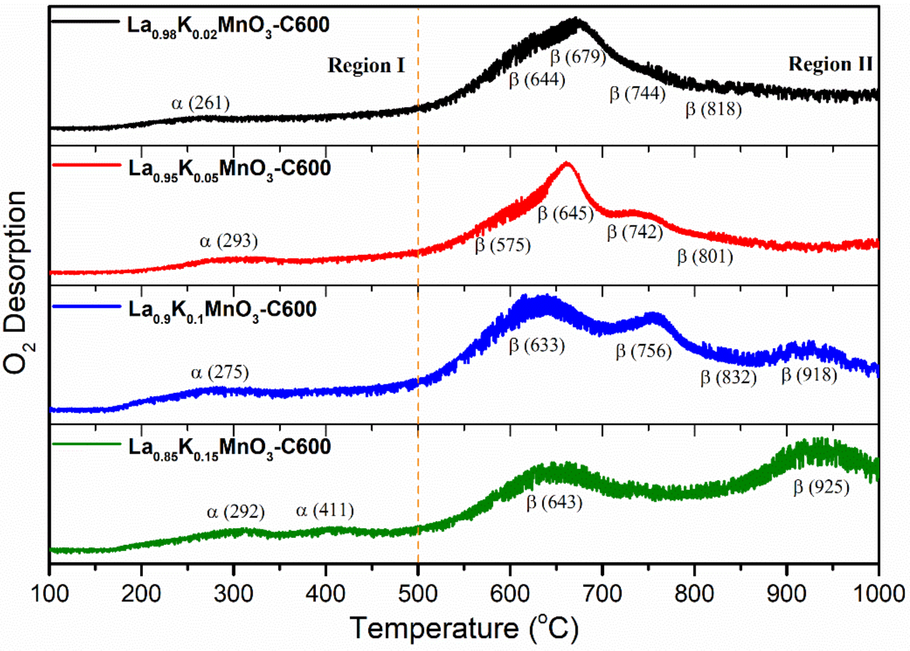

Fig.4.22. O_2-TPD MS profiles: (Black) $La_{0.98}K_{0.02}MnO_3$-C600; (Red) $La_{0.95}K_{0.05}MnO_3$-C600; (Blue) $La_{0.9}K_{0.1}MnO_3$-C600; (Olive) $La_{0.85}K_{0.15}MnO_3$-C600 in overall temperature range.

To stoichiometric Sr partially substituted samples, we still observed on O_2-TPD profile (Fig. 4.21) a weak α-desorption and the amount of O_2 desorbed are comparable with undoped samples according to the margin of error. By examining the β-desorption process, it seems to occur more readily with the increase of crystallization degree when Sr doping increases. By comparing the β-oxygen amounts with that recorded for the benchmark $LaMnO_3$-C600 (~0.56 mmol/g), a clear beneficial effect of Sr-doping on the amount of desorbed oxygen appears notably for the lowest Sr-composition. On the contrary, this available oxygen desorbs at much higher temperature. Then, an increase in strontium content is accompanied by a decrease in the amount of oxygen but which desorbs at lower temperature (Table 4.4.). Hence, two antagonistic effects appear as increasing amount of strontium inducing less available mobile oxygen species [32], but speed up their desorption at lower temperature. In fact, $LaMnO_3$-C600 and $La_{0.85}Sr_{0.15}Mn_{0.15}O_3$-C600 exhibit in some extent comparable O_2-desorption behavior.

Table 4.4. Amount of desorbed oxygen from O_2-TPD.

Catalyst	Amount of Desorbed Oxygen (mmol/g)		
	α-Oxygen	β-Oxygen	Total Amount
$La_{0.7}MnO_3$-C800	0.067	0.769	0.836
$LaMnO_3$-C800	0.052	0.722	0.774
$La_{1.3}MnO_3$-C800	-	-	0.669
$La_{0.7}MnO_3$-C600	0.052	0.723	0.775
$LaMnO_3$-C600	0.052	0.557	0.609
$La_{1.3}MnO_3$-C600	0.064	0.515	0.579
$La_{0.98}Sr_{0.02}MnO_3$-C600	0.014	0.701	0.715
$La_{0.95}Sr_{0.05}MnO_3$-C600	0.068	0.623	0.691
$La_{0.9}Sr_{0.1}MnO_3$-C600	0.020	0.600	0.620
$La_{0.85}Sr_{0.15}MnO_3$-C600	0.056	0.498	0.554
$La_{0.98}K_{0.02}MnO_3$-C600	0.022	0.522	0.544
$La_{0.95}K_{0.05}MnO_3$-C600	0.032	0.602	0.634
$La_{0.9}K_{0.1}MnO_3$-C600	0.041	0.492	0.533
$La_{0.85}K_{0.15}MnO_3$-C600	0.108	0.502	0.610

Remarkable observations when partial substitution strategy was applied to stoichiometric perovskite composition by potassium (Fig.4.22), *i.e.* $La_{1-x}K_xMnO_3$. Indeed, the α-desorption is improved and corresponds to higher amount of desorbed oxygen increasing gradually with a rise in K-doping to reach a maximum of 0.108 mmol/g on $La_{0.85}K_{0.15}MnO_3$ (Table 4.4.). For β-oxygen desorption, low amount of potassium does not drastically perturb oxygen behavior remaining comparable to that observed on the benchmark $LaMnO_3$. Contrarily to low temperature re-oxidation process, the amount of oxygen desorbed in independent of K-composition and no beneficial effect is discernible. In fact, the main observation is related to the occurrence of extra desorption processes taking place near 750°C and 920°C for $x \geq 0.05$. As a result, K-doping would delay the β-oxygen desorption in bulk to relatively higher temperature which could be attributed to the growth of growth of $K_{1.4}Mn_3O_6$. Let us note that this observation seems in relative agreement with O_2-TPO emphasizing a weak negative signal above 900°C previously assigned to oxygen desorption.

2.2. Textural Properties and surface composition

2.2.1 Textural properties

Nitrogen adsorption-desorption experiments provides an important route to characterize the textural properties of prepared perovskite catalysts, relative specific surface area (SSA), types of adsorption isotherms and pore size distributions depending on Brunauer–Emmett–Teller (BET) and Barrett-Joyner-Halenda (BJH) methods [20].

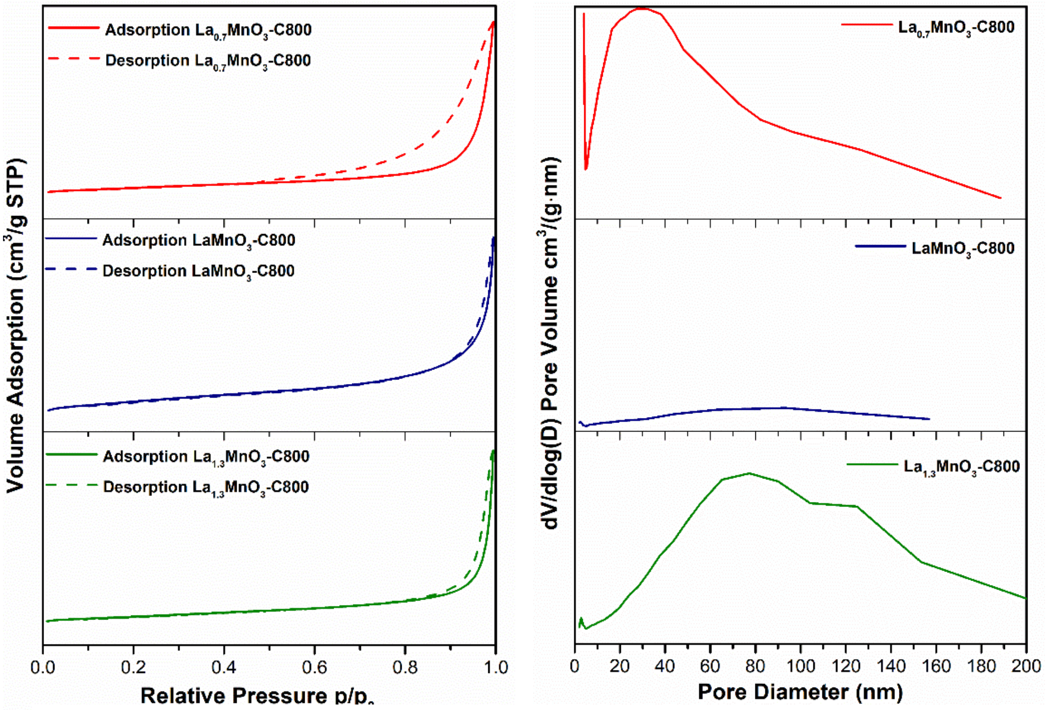

Fig.4.23. Textural properties: (Red) $La_{0.7}MnO_3$-C800; (Blue) $LaMnO_3$-C800; (Olive) $La_{1.3}MnO_3$-C800 in overall temperature range.

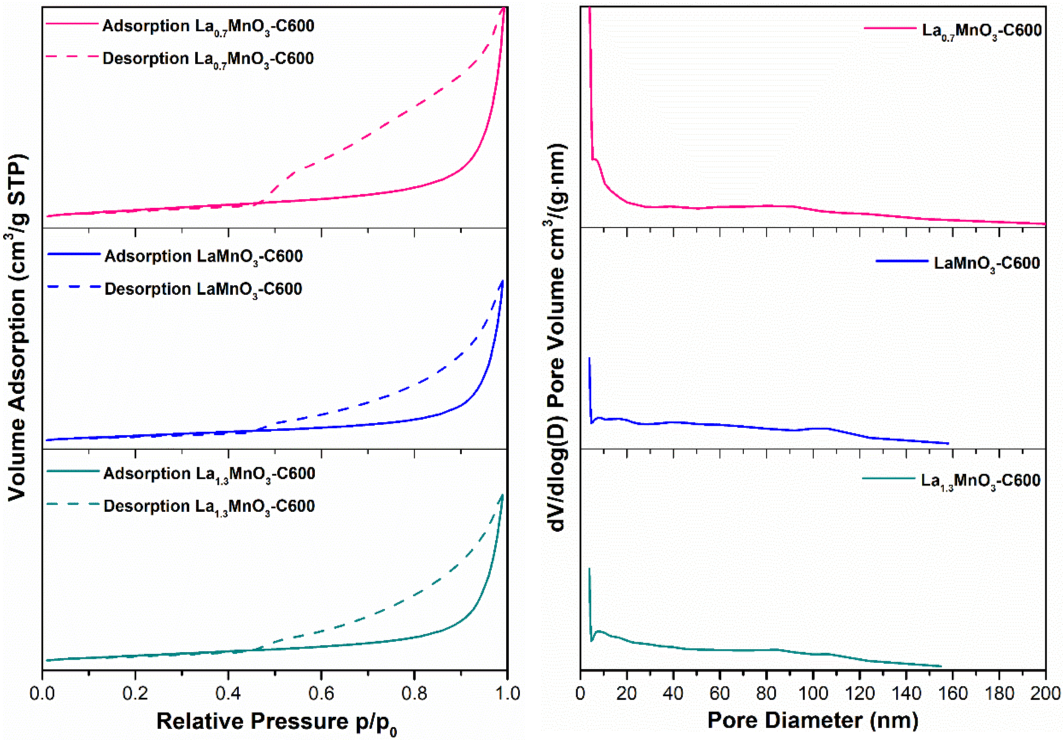

Fig.4.24. Textural properties: (Pink) $La_{0.7}MnO_3$-C600; (Blue) $LaMnO_3$-C600; (Cyan) $La_{1.3}MnO_3$-C600 in overall temperature range.

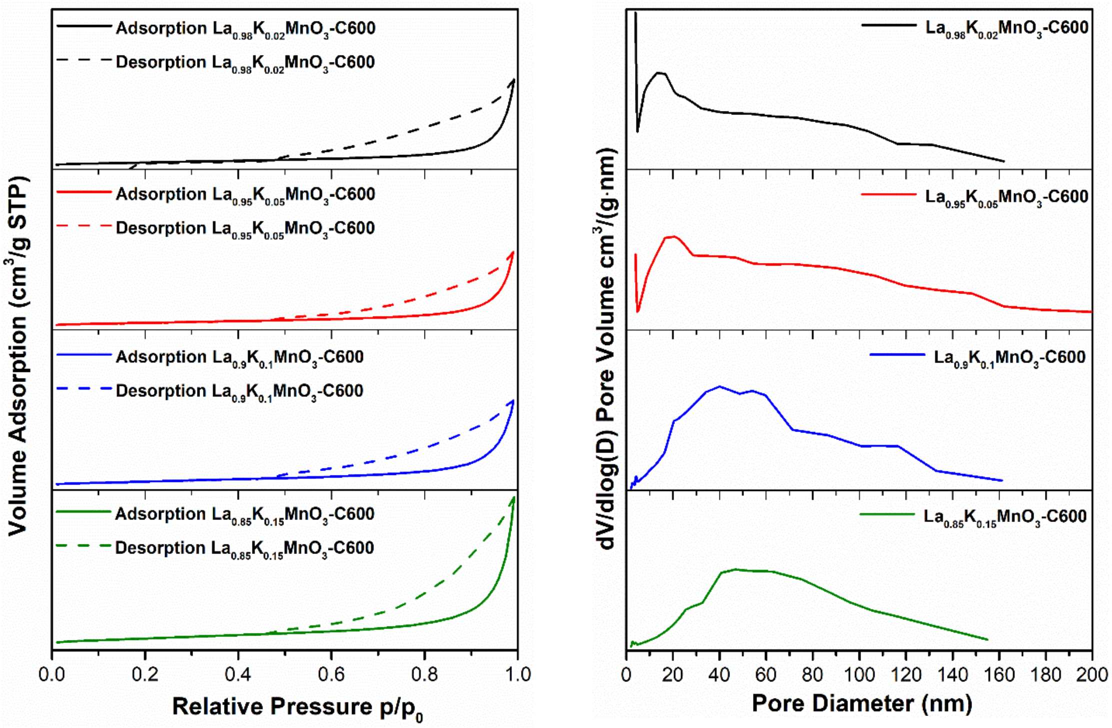

Fig.4.25. Textural properties: (Black) La$_{0.98}$K$_{0.02}$MnO$_3$-C600; (Red) La$_{0.95}$K$_{0.05}$MnO$_3$-C600; (Blue) La$_{0.9}$K$_{0.1}$MnO$_3$-C600; (Olive) La$_{0.85}$K$_{0.15}$MnO$_3$-C600 in overall temperature range.

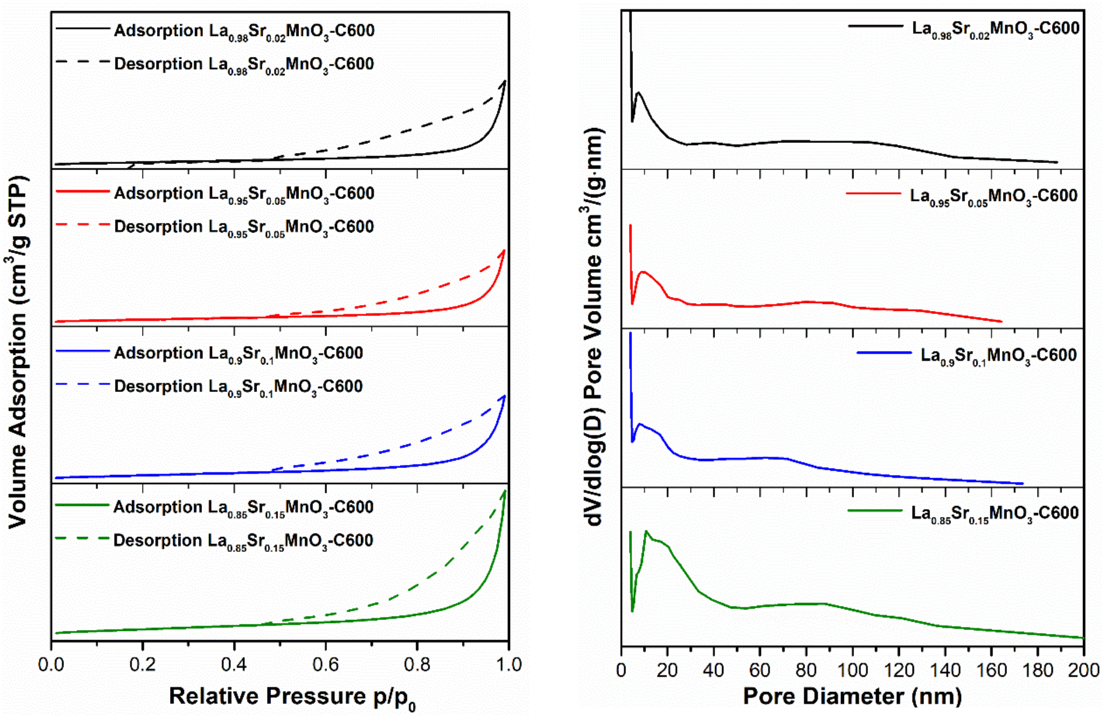

Fig.4.26. Textural properties: (Black) La$_{0.98}$Sr$_{0.02}$MnO$_3$-C600; (Red) La$_{0.95}$Sr$_{0.05}$MnO$_3$-C600; (Blue) La$_{0.9}$Sr$_{0.1}$MnO$_3$-C600; (Olive) La$_{0.85}$Sr$_{0.15}$MnO$_3$-C600 in overall temperature range.

Table 4.5. Textural properties of bulk perovskites.

Catalyst	SSA (m^2/g) [a]	Average Pore Diameter (nm) [b]	Pore Volume (cm^3/g)
$La_{0.7}MnO_3$-C800	26.4	16.3	0.17
$LaMnO_3$-C800	7.4	14.7	0.02
$La_{1.3}MnO_3$-C800	17.9	22.0	0.10
$La_{0.7}MnO_3$-C600	29.4	7.9	0.20
$LaMnO_3$-C600	21.7	10.8	0.14
$La_{1.3}MnO_3$-C600	23.7	10.1	0.14
$La_{0.98}K_{0.02}MnO_3$-C600	26.9	12.4	0.16
$La_{0.95}K_{0.05}MnO_3$-C600	22.8	17.4	0.16
$La_{0.9}K_{0.1}MnO_3$-C600	20.1	20.8	0.13
$La_{0.85}K_{0.15}MnO_3$-C600	16.6	21.4	0.09
$La_{0.98}Sr_{0.02}MnO_3$-C600	21.3	9.8	0.15
$La_{0.95}Sr_{0.05}MnO_3$-C600	21.1	11.0	0.12
$La_{0.9}Sr_{0.1}MnO_3$-C600	26.3	9.8	0.14
$La_{0.85}Sr_{0.15}MnO_3$-C600	36.9	12.4	0.23

Generally, the Y-axis deviation of the adsorption curve of the perovskite series of La_xMnO_3-C800 at the low pressure indicated that the materials had a strong effect on nitrogen. A physisorption isotherm type IV with a hysteresis loop type H2(b) reflected the complex pore structures and shapes, such as unevenly distributed tubular holes and densely packed spherical particle gap holes. In the state of complete crystallization from the XRD analysis, the specific surface area and the pore size distribution present significant differences among the three catalysts for different component strategies. Firstly, non-stoichiometric compositions show obviously higher specific surface areas (SSA), average pore diameters and pore volumes than the stoichiometric one (Table 4.5.). Besides, La-deficiency mainly presenting mesoporous pore distribution significantly increased the SSA than La-excess sample with principally macro-porous diameters. Stoichiometric $LaMnO_3$-C800 also weakly presented a mainly macro-porous feature.

With regard to the same composition La_xMnO_3 series calcinated at 600 ºC, all the series held larger SSA than the samples of high calcination temperature [21] and present also nitrogen isotherm type IV and type H2(b) of hysteresis loop. Different from the high temperature calcination series, the 600 ºC samples show a relative uniform distribution among micropore, mesopore and macropore types. La-deficient composition slightly shifted to macropore zone and La-excess sample held slightly more micropore and mesopore. As the 800 ºC series, La-deficiency still expressed the largest specific surface area and pore volume, but the differences with the other two samples reduced obviously. To the average pore diameter distribution, La-deficiency notably presented a negative influence to both calcination temperature series.

For the stoichiometric composition series of potassium substitution calcinated at 600 ºC, samples present type IV nitrogen isotherm and H2(b) hysteresis loop generally. And adding more potassium presented a negative impact on SSA (Table 4.5.) and a trend from mesoporous to microporous had been observed with potassium content increasing.

As the former series, Sr substitution series also held the type IV of nitrogen adsorption isotherms and H2(b) hysteresis loop in general. But unlike the K substitution stoichiometric series, Sr substitution samples showed a positive impact on SSA. Pore diameter distribution increased from mainly microporous state to relative larger mesoporous and macro-porous. Besides, with adding Sr content, the XRD results from amorphous state to crystal formation should be also taken into consideration.

2.2.2. Scanning electron microscopy / energy dispersive X-ray spectroscopy analysis

Textural analysis from nitrogen physisorption reveal samples with rather low specific surface area and total pore volume. SEM (Scanning electron microscopy) analysis can complement these previous observations. SEM analysis provides morphological information and also allow the observation of uniformity or heterogeneity. The combination with EDX (energy dispersive X-ray spectroscopy) analysis is useful to verify homogeneity in composition. But the relevance of this information is established if different zone can be examined.

SEM measurements were performed on La_xMnO_3 calcined at 600°C and 800°C and on K-substituted $LaMnO_3$ samples calcined at 600°C. For each sample different area were examined. As example, two regions are illustrated in Figs 4.29-4.33. In all cases, the absence of morphological organization is noticeable. For the stoichiometric $LaMnO_3$-C600 composition, a spongy structure is observed in some extent still observed on $LaMnO_3$-C800. Phase aggregation responsible of the loss of specific surface area is not correlated to the formation of large and densely packed aggregates. Regarding, the chemical composition, the elemental volume analyzed seems to be La-rich on $LaMnO_3$-C600 while the stoichiometry La/Mn = 1/1 matches with the expected composition on $LaMnO_3$-C800. An additional SEM-EDS experiment was performed on $La_{0.7}MnO_3$-C800 as contrarily to $LaMnO_3$-C800 no significant loss of specific surface area was observed. Fig. 4.47 reveal that the spongy structure, previously observed $LaMnO_3$-C600, is systematically observed and does not reveal aggregation in agreement with the preservation of the SSA.

It is also worth to note that irrespective of the zone analyzed homogeneous compositions are observable with the absence of strong segregation. Clearly the calculation of the La/Mn agrees with the expected composition $La_{0.7}MnO_3$. For the composition exhibiting an excess of lanthanum a calcination at 800°C induces a loss of SSA but in lower extent than on $LaMnO_3$-C800. SEM images reveals more densely packed structure compared to $La_{0.7}MnO_3$-C800. Similarly, a good reproducibility is observed on lanthanum and manganese compositions still demonstrating a good homogeneity in composition. It is also noticeable that the La/Mn ratio agree with the expected composition.

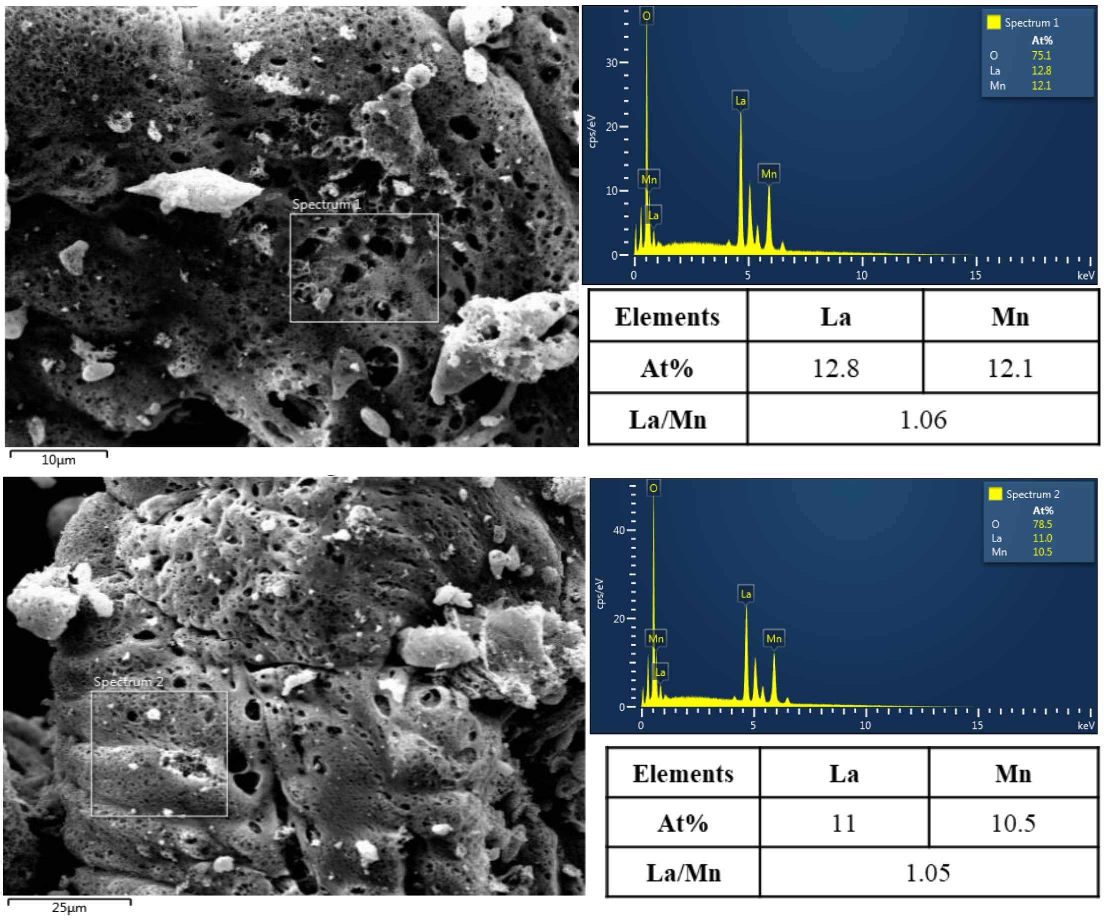

Elements	**La**	**Mn**
At%	12.8	12.1
La/Mn	1.06	

Elements	**La**	**Mn**
At%	11	10.5
La/Mn	1.05	

Fig.4.27. SEM-EDS analysis of $LaMnO_3$-C800.

A conclusion can be drawn by comparing data obtained from XRD, N_2-physisortion and SEM-EDX analysis on $LaMnO_3$, $La_{1.3}MnO_3$ and $La_{0.7}MnO_3$ revealing a higher thermal stability on La-deficient samples then preserving their textural properties.

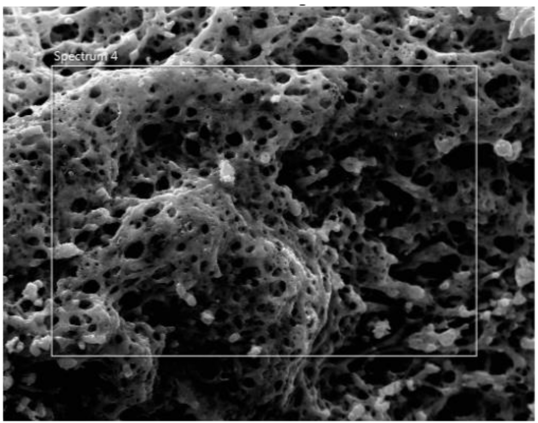

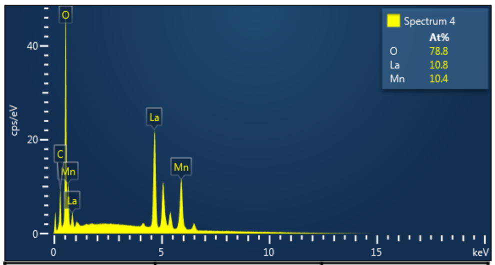

Elements	**La**	**Mn**
At%	12.6	8.6
La/Mn	1.46	

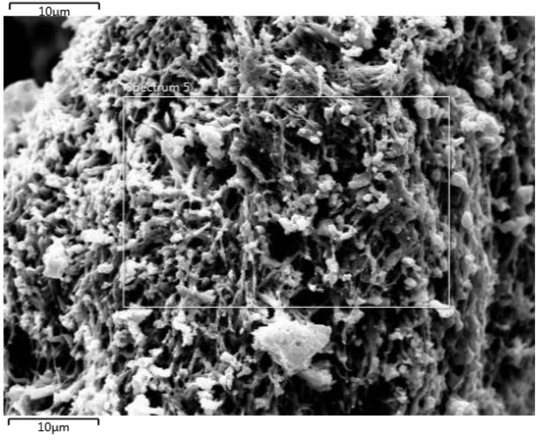

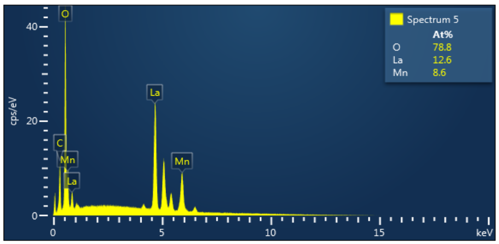

Elements	**La**	**Mn**
At%	12.6	8.6
La/Mn	1.46	

Fig.4.28. SEM-EDS analysis of $LaMnO_3$-C600.

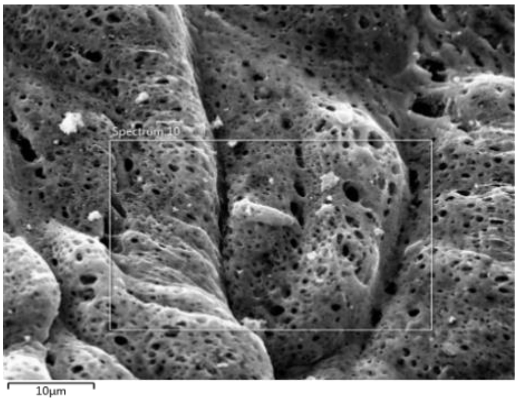

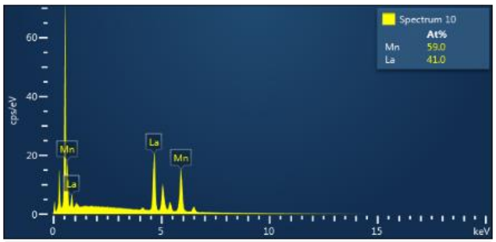

Elements	**La**	**Mn**
At%	41	59
La/Mn	0.69	

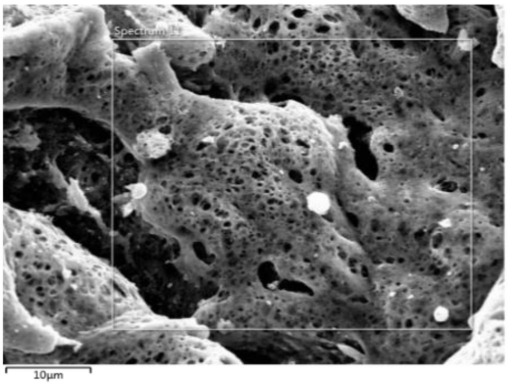

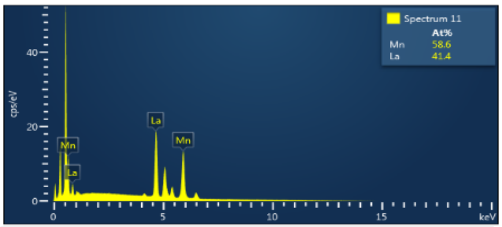

Elements	**La**	**Mn**
At%	41.4	58.6
Rapport	0.71	

Fig.4.29. SEM-EDS analysis of $La_{0.7}MnO_3$-C800.

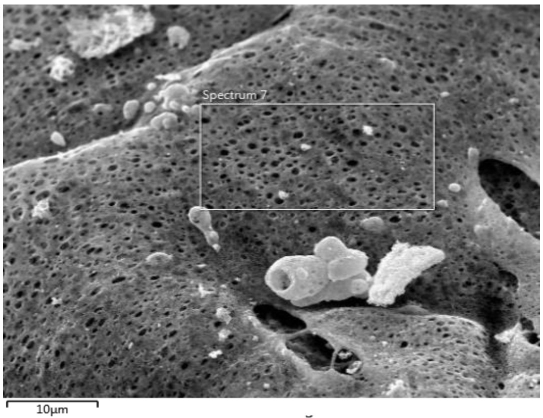

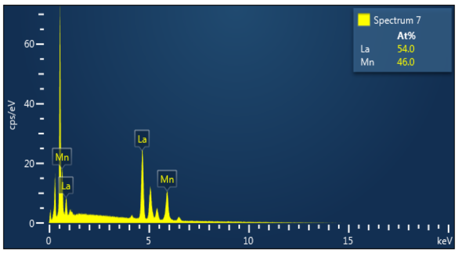

Elements	La	Mn
At%	54	46
La/Mn	1.17	

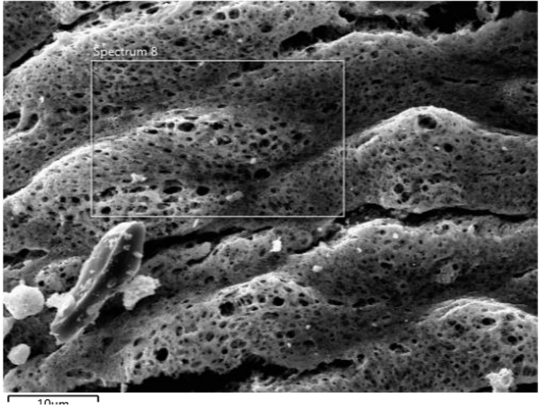

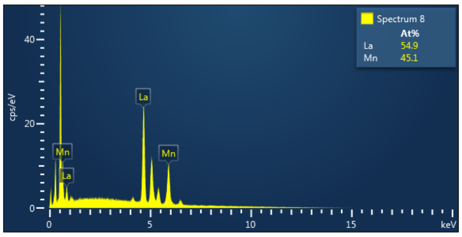

Elements	La	Mn
At%	54.9	45.1
La/Mn	1.22	

Fig.4.30. SEM-EDS analysis of $La_{1.3}MnO_3$-C800.

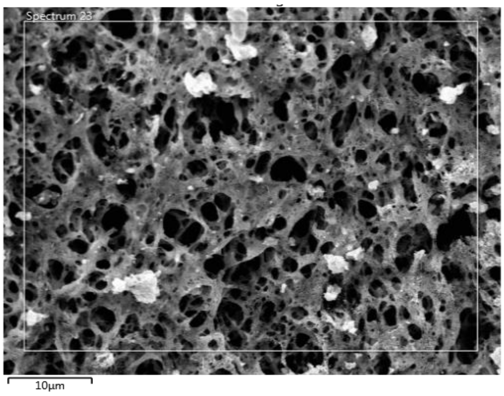

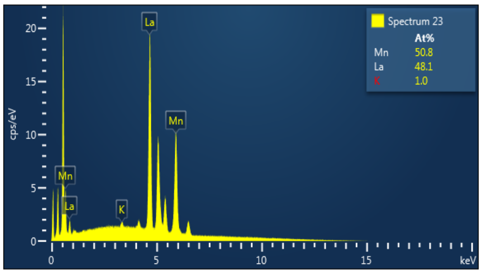

Elements	La	K	Mn
At%	48.1	1.0	50.8

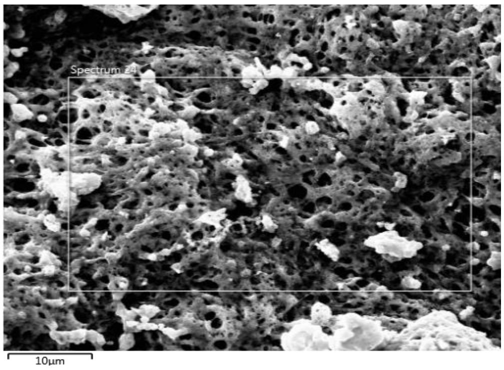

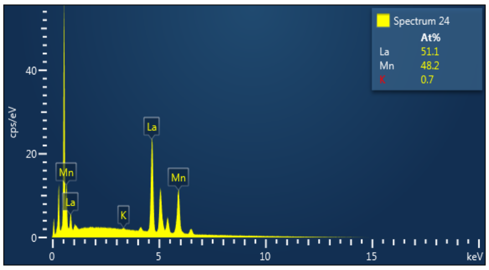

Elements	La	K	Mn
At%	51.1	0.7	48.2

Fig.4.31. SEM-EDS analysis of $La_{0.98}K_{0.02}MnO_3$-C600.

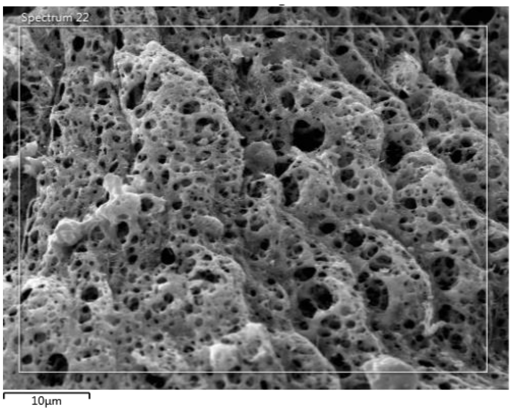

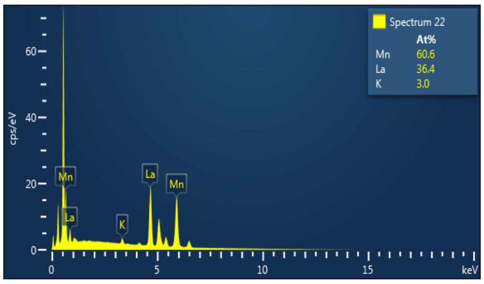

Elements	La	K	Mn
At%	36.4	3	60.6

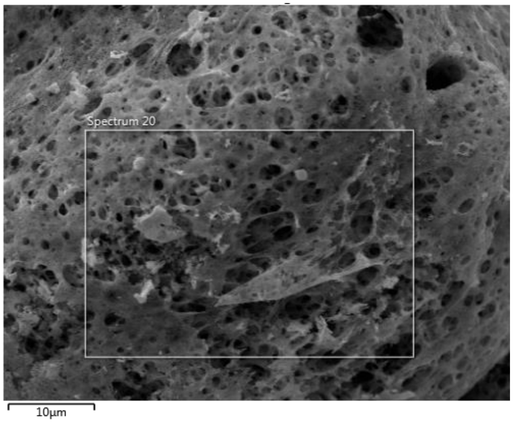

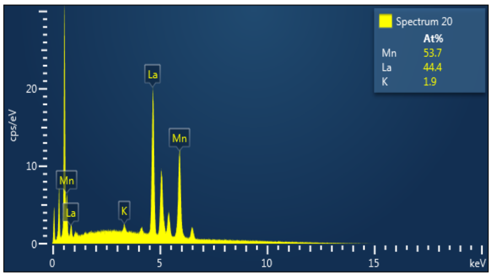

Elements	La	K	Mn
At%	44.4	1.9	53.7

Fig.4.32. SEM-EDS analysis of $La_{0.95}K_{0.05}MnO_3$-C600.

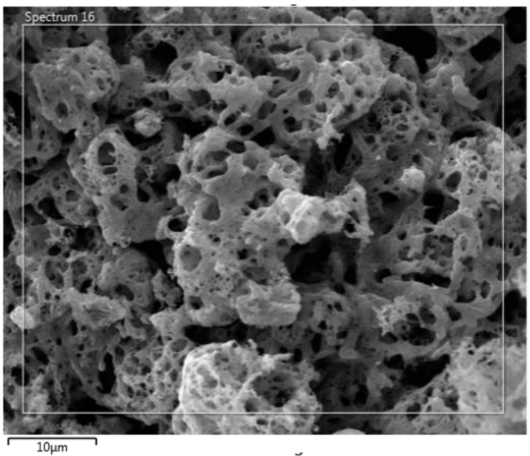

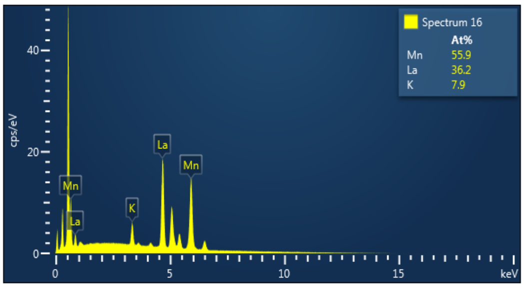

Elements	La	K	Mn
At%	36.2	7.9	55.9

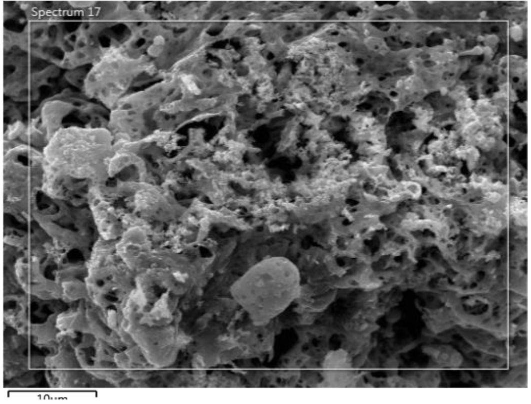

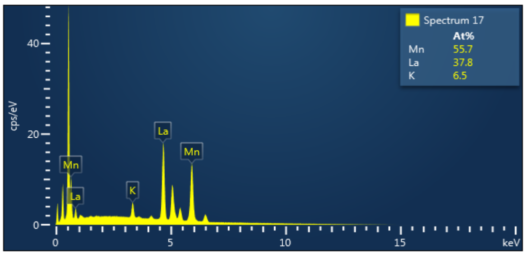

Elements	La	K	Mn
At%	37.8	6.5	55.7

Fig.4.33. SEM-EDS analysis of $La_{0.9}K_{0.1}MnO_3$-C600.

SEM coupled to EDX analysis was performed on $La_{1-x}K_xMnO_3$ compositions according to the same methodology. As seen in Fig. 4.49 the textural morphology differs from previous observations with a more open structure for the lowest K-composition, *i.e.* x = 0.02. This observation seems in rather good agreement with the gain observed in SSA compared to $LaMnO_3$-C600 (26.9 m^2/g vs. 21.7 m^2/g). For intermediate K-composition (x = 0.05 and 0.010) a different morphological structure is perceptible which tends to that observed on $LaMnO_3$-C600 with a characteristic sponge structure earlier described. Correlatively, a decrease in the specific surface area is observed then stabilizing at 20.1 m_2/g. Finally, for the highest composition (x = 0.15) the morphological structure changes and correspond to a subsequent loss in the SSA.

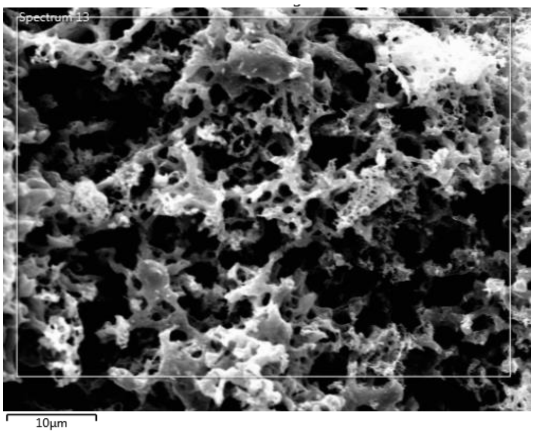

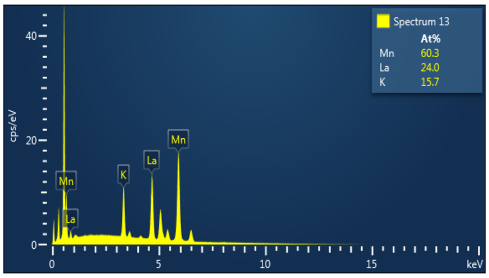

Elements	La	K	Mn
At%	24	15.7	60.3

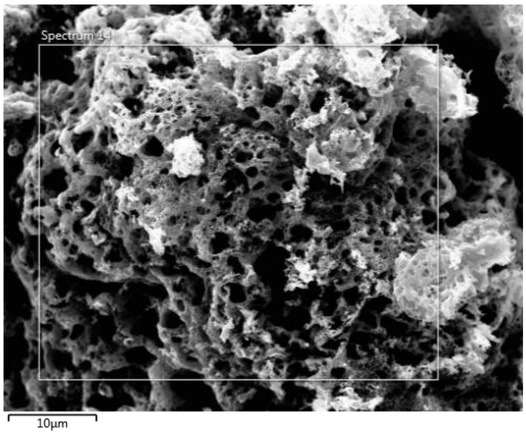

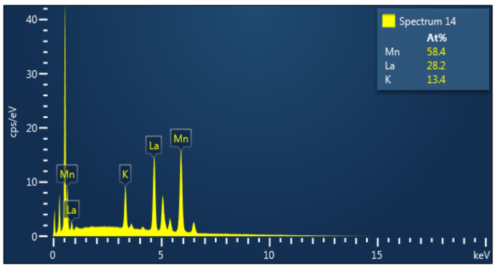

Elements	La	K	Mn
At%	28.2	13.4	58.4

Fig.4.34. SEM-EDS analysis of $La_{0.85}K_{0.15}MnO_3$-C600

Chemical composition reported for K-substituted sample did not reveal the same homogeneity in the distribution of La, K and Mn compared to $LaMnO_3$-C600 even though this latter sample reveals unexpectedly a La-rich composition. Chemical compositions are summarized in Table 4.6. Average composition from the different zone analyzed. The values for the atomic La/Mn, K/La and (La+K)/Mn ratios have been reported and can be compared to the theoretical stoichiometry.

Table 4.6. SEM-EDS atomic ratio.

Catalyst	Elemental composition (at.%)			A/B[a]	K/La	K/Mn
	La	Mn	K			
$LaMnO_3$-C600	11.6	9.4		1.23	-	-
$LaMnO_3$-C800	12.1	11.2		1.08	-	-
$La_{0.7}MnO_3$-C800	41.2	58.8		0.70	-	-
$La_{1.3}MnO_3$-C800	55.2	44.8		1.23	-	-
$La_{0.98}K_{0.02}MnO_3$-C600	49.6	49.5	0.9	1.02	0.02/0.02[b]	0.02/0.02[b]
$La_{0.95}K_{0.05}MnO_3$-C600	41.3	58.3	2.6	0.75	0.06/0.05[b]	0.04/0.05[b]
$La_{0.90}K_{0.10}MnO_3$-C600	37.8	55.3	6.9	0.81	0.18/0.11[b]	0.12/0.10[b]
$La_{0.85}K_{0.15}MnO_3$-C600	29.4	57.7	13	0.73	0.44/0.17[b]	0.23/0.15[b]

[a] A = La + K and B = Mn

[b] theoretical value

$LaMnO_3$-C600 can serve as benchmark for further comparisons with the series $La_{1-x}K_xMnO_3$-C600. For the reference, the La/Mn ratio exceeds the theoretical value reflecting rich La sample. On the other hand, the A/B values calculated for the K-substituted samples do not reveal A-rich sample. In fact, the opposite is observed with Mn rich samples at increasing K doping. Parallel to this observation, the K/La and K/Mn ratios deviate from the theoretical value emphasizing K-rich samples when the K loading increases. These tendencies could be related to the development of bulk $K_{1.39}Mn_3O_6$ phase characterizes from XRD analysis.

2.2.3. Surface composition from X-Ray photoelectron spectroscopy analysis

The role of surface reconstruction in tuning perovskite catalysts is an efficient route to methane activation. In order to further study the surface metal states and the related surface segregation influence of K and Sr partial substitution [22, 24], X-ray photoelectron spectroscopy (XPS) provides the main information related to the oxidation state of atoms and the related surface composition. The orbitals La 3d, K 2p, Sr 3d, Mn 2p, Mn 3s and O 1s were analyzed and compared to investigate the related impacts and properties on perovskite A-site adjustment involving stoichiometry and partial substitution based on $La_xA_{1-x}MnO_3$ formula.

As previous work breakdown structure, the XPS results are divided into two parts: influence of lanthanum stoichiometry and influence of A-site partial substitution of potassium and strontium incorporation in stoichiometric composition. Besides, the two calcination temperatures of La_xMnO_3 composition were discussed together considering the influences of calcination temperature and A-site lanthanum stoichiometry on surface metal valence. As to A-site stoichiometric partial substitution series, the surface properties were investigated together to discuss the changes in perovskite B-site metal valence states by the addition of potassium and strontium cation into basic composition. And the binding energy of C 1s were calibrated to 284.8 eV to all the samples [26]. In a word, the goals of two above-mentioned strategies are to study the perovskite B-site manganese cation valences changes aiming at improving the catalytic capacity of methane oxidation.

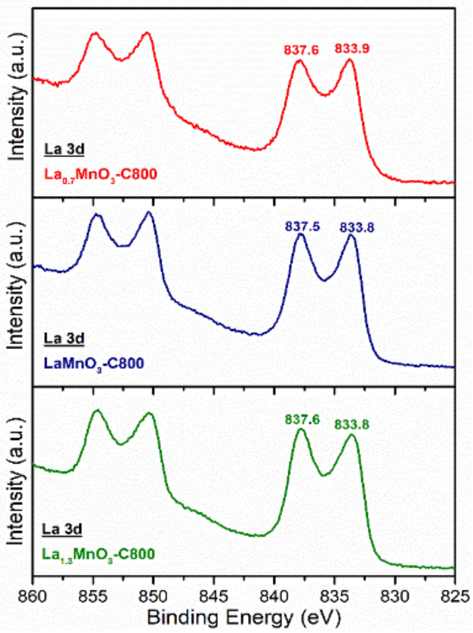

Fig.4.35 XPS spectrum of La 3d on La$_x$MnO$_3$-C800

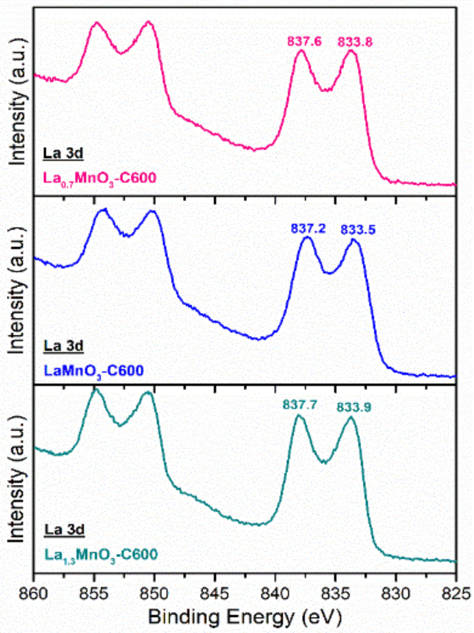

Fig.4.36 XPS spectrum of La 3d on La$_x$MnO$_3$-C600

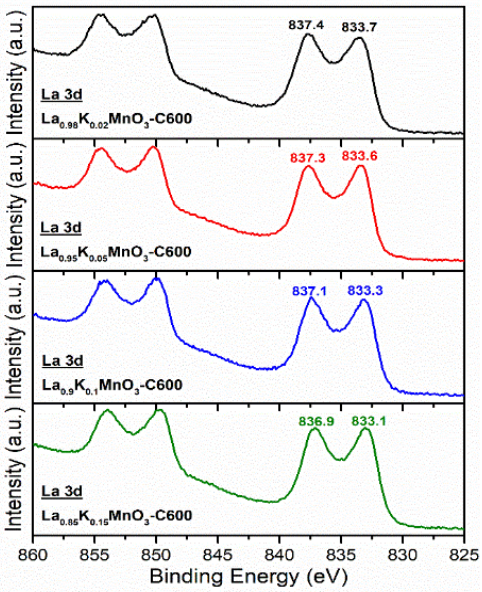

Fig.4.37. XPS spectrum of La 3d on La$_{1-x}$K$_x$MnO$_3$-C600

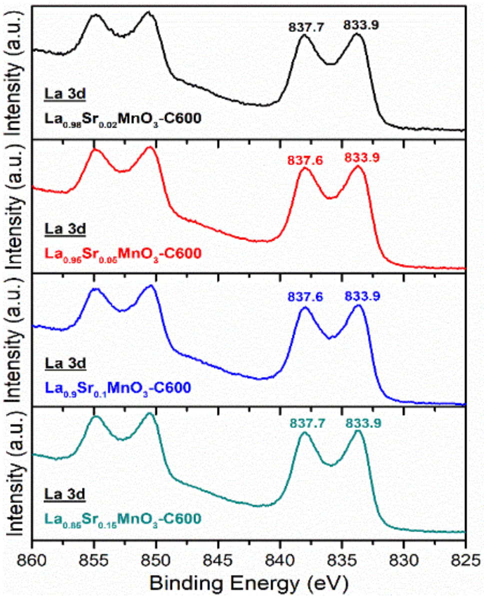

Fig.4.38. XPS spectrum of La 3d on La$_{1-x}$Sr$_x$MnO$_3$-C600

As to the series on the study of La-stoichiometry (Fig.4.35, Fig4.36), the XPS study on La 3d orbital also presented relatively stable binding energy positions (dual-peak binding energy range from 833 eV to 838 eV) and fixed difference value, which showed the stable La 3d orbital valence state. Besides, La_2O_3 as an unreducible metal oxide presented the high stability during the redox process in the range from room temperature to 1000 °C were already analyzed in the former investigations [11, 12, 14, 25].

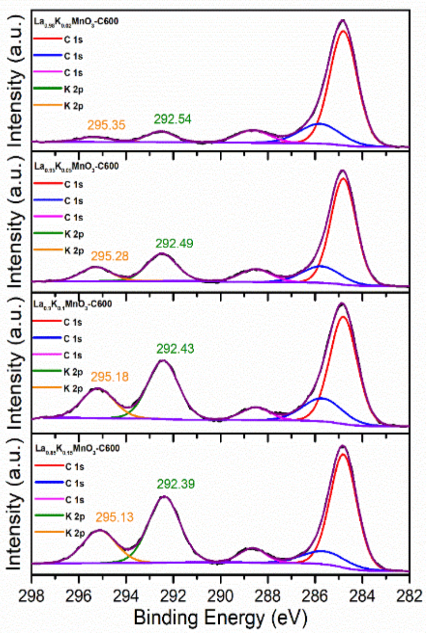

Fig.4.39. XPS spectrum of K 2p on $La_{1\_x}K_xMnO_3$-C600.

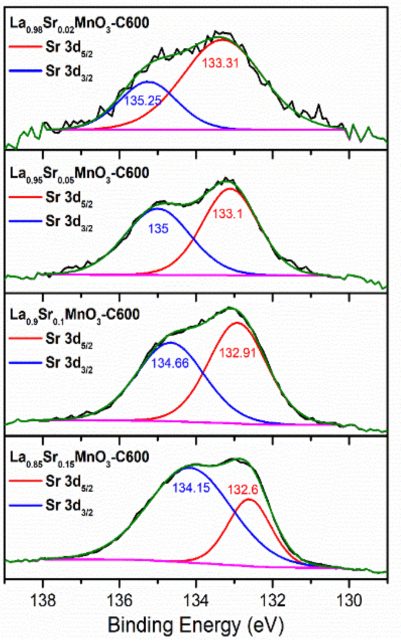

Fig.4.40. XPS spectrum of Sr 3d: $La_{1\_x}Sr_xMnO_3$-C600.

With regard to the A-site substituted series by K and Sr (Fig.4.37, Fig.4.38), the difference of binding energy located stable as the former observation. But an obvious difference on binding energy positions could be found: K substituted samples varied to relative lower binding energy (dual-peak from 292.54/295.35 eV to 292.39/295.13 eV) with adding increasingly potassium into perovskite composition; Sr substituted samples also varied to lower B.E. values with a progressive shift from 133.3 eV for $x = 0.02$ to 132.6 eV for $x = 0.15$. Considering the related XRD profile (Fig.4.7) in which the oxide of potassium $K_{1.39}Mn_3O_6$ appeared, the phenomenon could be attributed to phase separation of oxides and surface segregation [24] of potassium which influenced the La 3d signals. In the particular case of $La_{1-x}Sr_xMnO_3$ partial segregation of single oxide SrO could originate the observed changes in spectral features.

For K 2p and Sr 3d orbitals (Fig.4.39, Fig.4.40), the corresponding profiles became cumulatively intense as the content of potassium [26] and strontium increased. To the Sr-substituted series, the increasing photopeak intensity and integrated area indicated the increasing content of both surface and lattice strontium, which indicated probably the segregation of SrO when Sr increases. Besides, the binding energy of peaks presented the trend of moving to lower position indicating the generation of lattice strontium [27, 28] which corresponded to the related XRD result (Fig.4.8.) showing the formation of crystal perovskite while surface Sr becoming also intense due to surface segregation [36].

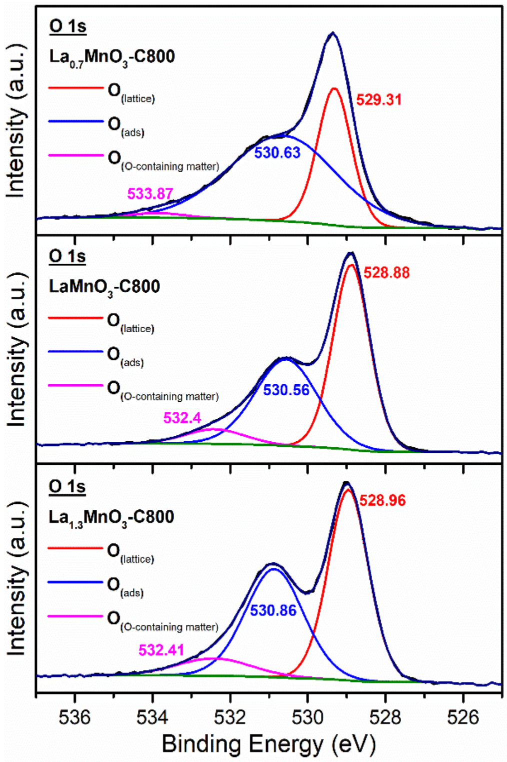

Fig.4.41. XPS spectrum of O 1s on La$_x$MnO$_3$-C800

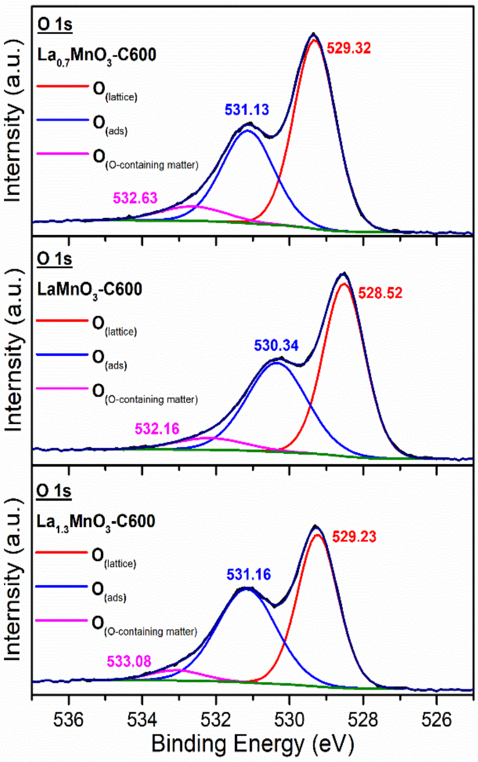

Fig.4.42. XPS spectrum of O 1s: La$_x$MnO$_3$-C600

The deconvolution of O 1s orbitals of samples could be attributed to lattice oxygen (Red line: O_{lat}), chemisorbed oxygen (Blue line: O_{ads}: O^{2-}, O^-, O_2^{2-}) and adsorbed hydroxyl and/or H_2O species containing oxygen matter (Pink line: O_w) respectively. The binding energy of non-stoichiometric composition samples generally situated at slightly higher position than two stoichiometric $LaMnO_3$ samples of different calcination temperatures (Fig.4.41, Fig.4.42). The molar ratio of O_{ads}/O_{lat} (Table.4.7.) from quantitative calculation of related peak areas presented the relative composition of surface oxygen species of samples on different calcination temperature and stoichiometry. To the 600 °C calcination samples, adsorbed oxygen species increased from La-defect to La-excess composition. However, as to the samples calcinated at 800 °C, La-defect sample - $La_{0.7}MnO_3$-C800 presented the high relative content of surface adsorbed oxygen species, which would be in touch with surface deficient structure of high crystallinity and was consistent with the result of N_2-physisorption (Fig.4.23.).

To the stoichiometric composition series of potassium and strontium on A-site (See Annexes Fig.4.43-S1, Fig.4.44-S2), the related O 1s binding energy and the molar ratio of O_{ads}/O_{lat} (Table.4.7.) from quantitative calculation of related peak areas were not consistent with the increasing content of K and Sr respectively.

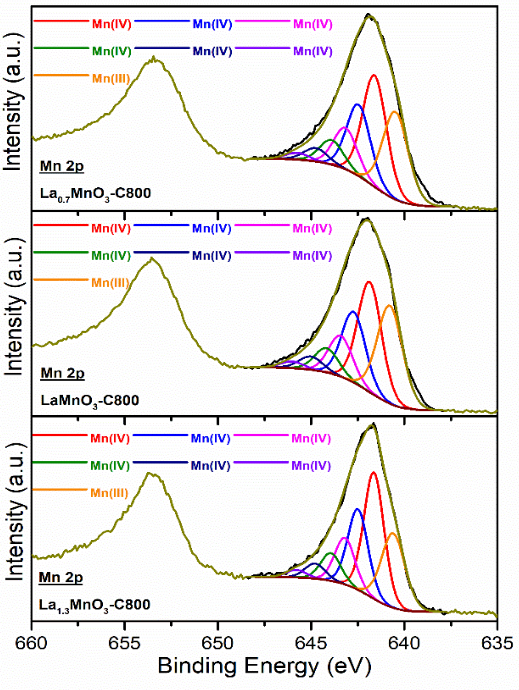

Fig.4.43. XPS spectrum of Mn 2p

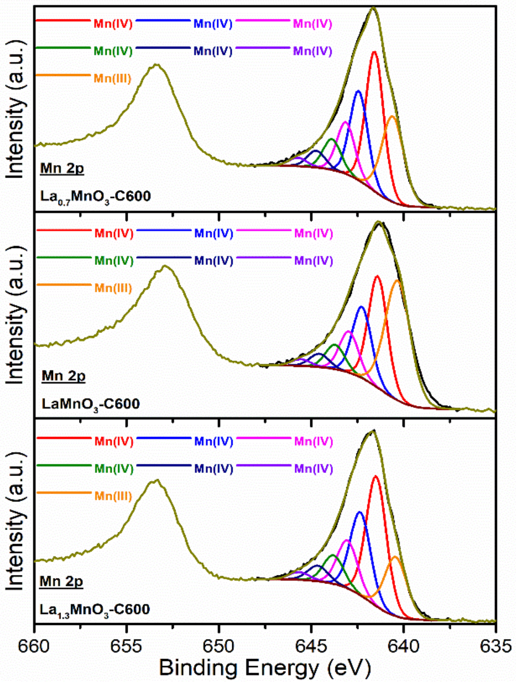

Fig.4.44. XPS spectrum of Mn 2p

Following the Mn 2p studies of M. Biesinger et al. [29], the Mn 2p orbitals of samples were analyzed into six peaks of Mn (IV) and one peak of Mn (III) in Fig.4.43, Fig.4.44, Fig.4.45 and Fig.4.46. The following quantitative calculation of Mn^{3+}/Mn^{4+} ratio [26, 30] depended on the related peak areas and globally both of the two stoichiometric samples presented relatively high Mn^{3+}/Mn^{4+} ratio in their respective series, which indicated that both of Mn-excess and La-excess of non-stoichiometric perovskites had the significant influence on modification of cation valence: La-excess samples showed relatively lower Mn (III) valence than La-deficient ones.

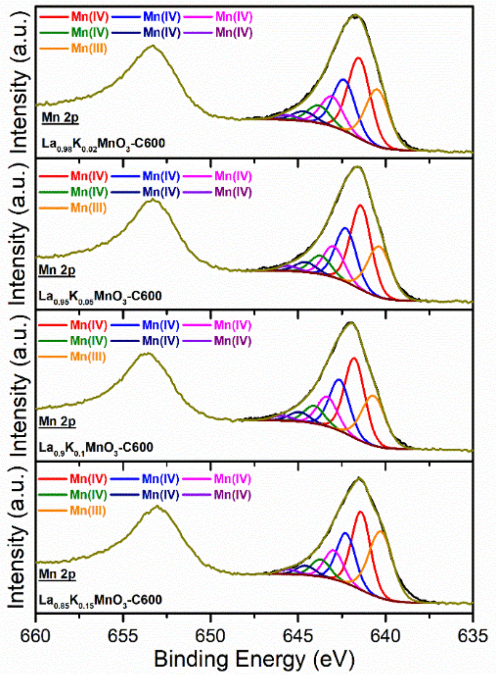

Fig.4.45. XPS spectrum of Mn 2p.

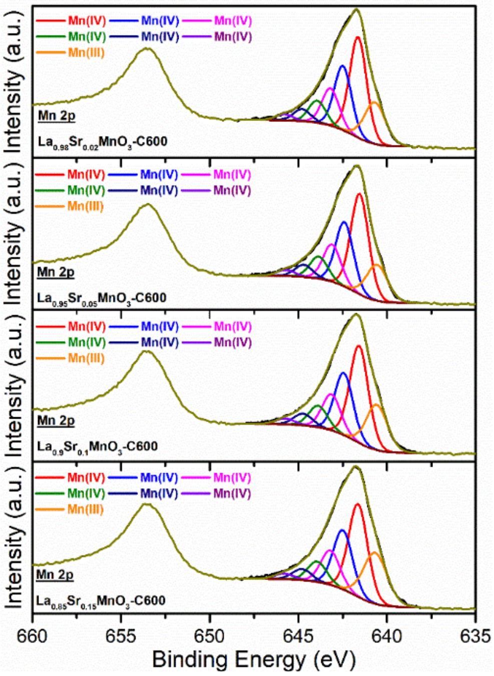

Fig.4.46. XPS spectrum of Mn 2p.

Mn 3s photopeak provides useful insights on the oxidation state of manganese [31]. multiplet splitting of Mn 3s peak results from the coupling of non-ionized Mn 3s electrons and 3d valence band electrons. Example of Mn 3s peak splitting is given in Fig.4.47. (See annexes Fig.4.47-S1, Fig.4.47-S2, Fig.4.47-S3)

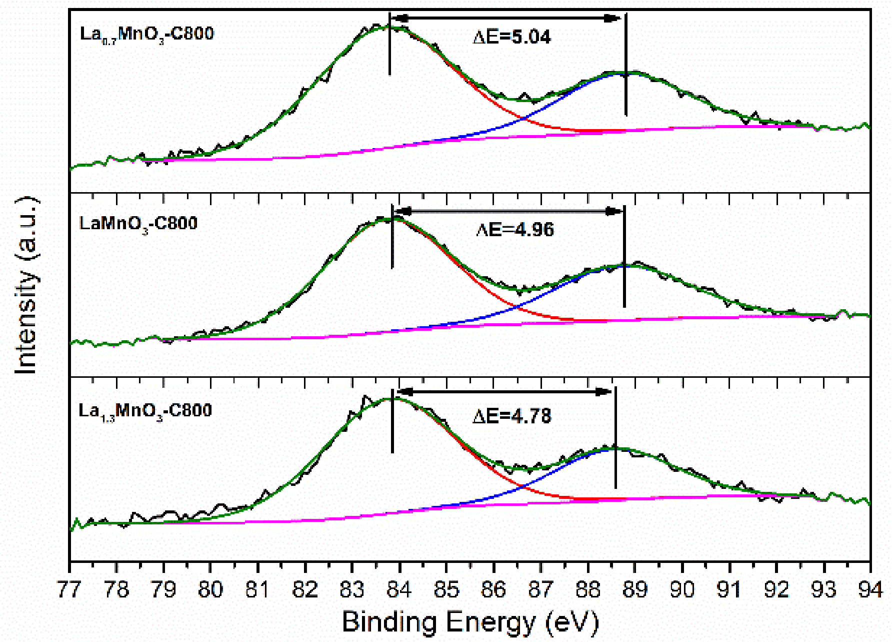

Fig.4.47. XPS spectrum of Mn 3s:
(Top) $La_{0.7}MnO_3$-C800; (Middle) $LaMnO_3$-C800; (Bottom) $La_{1.3}MnO_3$-C800.

Prominent multiplet splitting can be observed for Mn^{2+}, Mn^{3+} and Mn^{4+}. The average oxidation state (AOS) of manganese in the perovskite can be calculated according Eq. (4). [31]

$$\text{Average Oxidation State (AOS)} = 8.956 - 1.12\times\Delta E_{\text{splitting}}\ (\text{Mn 3s}) \qquad (5)$$

The numerical values for $\Delta E_{\text{splitting}}$ (Mn 3s) and the corresponding values calculated from Eq. (5) are reported in Table 4.7. The amplitude of variation for Mn^{3+}/Mn^{4+} from 0.18 to 0.59 is not easy to correlate to change on the AOS also varying in narrow range 3.28-3.65. In this latter case weak variation are observable. A good agreement is observed on La_xMnO_3-C800. In this case higher crystallization, in conformity with structural requirement, seems favorable. On the other hand, low crystallinity with partial segregation on La_xMnO_3-C600 could explain the absence of reliable comparison. Probably, more suitable comparison for K- and Sr-substitution was expected, as the substitution of trivalent by divalent and monovalent cation can create electronic imbalance. But we found that the restoration of the electroneutrality also involve the adjustment of oxygen stoichiometry. For $La_{1-x}K_xMnO_3$, clearly no relevant comparison appears. A discontinuity arises for $La_{0.85}K_{0.15}MnO_3$-C600 with a sharp increase in Mn^{3+}/Mn^{4+}. For the series For $La_{1-x}Sr_xMnO_3$, weak amplitude in the evolution of Mn^{3+}/Mn^{4+} and Mn AOS are observed but no discrepancy seems to appear.

With K and Sr molar content increasing, the two series calcinated at 600 °C presented generally fixed binding energy of main peak position and the lower Mn^{3+}/Mn^{4+} ratio [26, 30] than stoichiometric $LaMnO_3$-C600 composition indicating A-site substitution by lower valence cation K^+ and Sr^{2+} brought relatively higher Mn valence.

Table 4.7(a). XPS analysis on surface elements ratio of perovskites (%).

Catalyst	M (Site A) / M (Site B)			Mn^{3+}/Mn^{4+} [(a)]	$\Delta E_{splitting}$ (Mn 3s)	Mn (AOS) [(b)]	$O_{(ads)}/O_{(lat)}$ [(c)]
	La/Mn	Sr/Mn	K/Mn				
$La_{0.7}MnO_3$-C800	0.49	-	-	0.35	5.04	3.28	1.21
$LaMnO_3$-C800	0.76	-	-	0.39	4.96	3.37	0.79
$La_{1.3}MnO_3$-C800	1.11	-	-	0.28	4.78	3.57	0.82
$La_{0.7}MnO_3$-C600	0.40	-	-	0.31	4.92	3.42	0.61
$LaMnO_3$-C600	0.60	-	-	0.59	4.9	3.44	0.74
$La_{1.3}MnO_3$-C600	0.77	-	-	0.21	4.85	3.49	0.89

(a) *Mn^{3+}/Mn^{4+} ratio from Mn 2p orbital*

(b) *Mn average oxidation state (AOS) from Mn 3s orbital*

(c) *Oxygen adsorption species and lattice oxygen ratio from O 1s orbital*

Table 4.7(b). XPS analysis on surface elements ratio of perovskites (%).

Catalyst	M (Site A) / M (Site B)			Mn^{3+}/Mn^{4+} (a)	$\Delta E_{splitting}$ (Mn 3s)	Mn (AOS) (b)	$O_{(ads)}/O_{(lat)}$ (c)
	La/Mn	Sr/Mn	K/Mn				
$La_{0.98}K_{0.02}MnO_3$-C600	0.54	-	0.42	0.31	4.95	3.38	1.32
$La_{0.95}K_{0.05}MnO_3$-C600	0.44	-	0.91	0.29	4.89	3.45	0.69
$La_{0.9}K_{0.1}MnO_3$-C600	0.35	-	1.57	0.31	4.84	3.51	0.52
$La_{0.85}K_{0.15}MnO_3$-C600	0.53	-	2.41	0.45	4.91	3.43	1.07
$La_{0.98}Sr_{0.02}MnO_3$-C600	0.57	0.06	-	0.21	4.74	3.62	0.74
$La_{0.95}Sr_{0.05}MnO_3$-C600	0.77	0.12	-	0.18	4.71	3.65	0.81
$La_{0.9}Sr_{0.1}MnO_3$-C600	0.50	0.16	-	0.22	4.76	3.60	0.71
$La_{0.85}Sr_{0.15}MnO_3$-C600	0.59	0.25	-	0.28	4.78	3.57	0.77

(a) *Mn^{3+}/Mn^{4+} ratio from Mn 2p orbital*

(b) *Mn average oxidation state (AOS) from Mn 3s orbital*

(c) *Oxygen adsorption species and lattice oxygen ratio from O 1s orbital*

2.3. *In-situ* electrical conductivity: impacts of stoichiometry and substitution of lanthanum on A-site of perovskites

2.3.1. Introduction

Ionic conductivity measurements were performed in collaboration with Prof. I.-C. Marco at the Laboratory of Chemical Technology and Catalysis University of Bucharest (Romania).

As a matter of fact, these measurements are useful at least for two reasons. First, oxygen mobility and oxygen ionic conductivity are involved in OSC properties that broaden the operating window of TWC near stoichiometric conditions. The second reason comes from earlier study [37] which found that perovskite can activate alkane transformation thanks to their p-type semiconducting character. Hence, surface O-species could abstract hydrogen atoms. In practice, the behavior of semiconducting single or mixed oxides catalysts can be investigated by examining the evolution of their electrical conductivity in oxidative or reductive atmosphere. The following equilibrium can be established where h• and $O_{\bullet}^{\times}$ stand for a positive hole and a lattice oxygen anion of the solid respectively. This equilibrium will be displaced according the nature of the atmosphere.

$$O_2(gas) \leftrightarrows O_2^{-}(ads) + h^{\bullet} \leftrightarrows 2O^{-}(ads) + h^{\bullet} \leftrightarrows 2O^{2-}(ads) + 2h^{\bullet} \leftrightarrows O_{\bullet}^{\times}$$

The electrons trapped by the adsorbed oxygen leads to the creation of positive holes. On the other hand, under rich exposure in the presence of a reducing agent, such as methane, the consumption of lattice oxygen $O_{\bullet}^{\times}$ with the subsequent formation of oxygen vacancies is promoted and leads to lower concentration of the positive holes that induce a decrease of the electrical conductivity.

2.3.2. Principe and experimental considerations

Electrical conductivity measurements were carried out under air as a function of temperature. Steady-state measurement were also performed at 550°C at various partial pressure of oxygen. The following compositions have been studied La_xMnO_3-C600 and $La_xSr_{1-x}MnO_3$-C600 series compared to stoichiometric $LaMnO_3$-C800 sample. Experimental details are reported elsewhere [38]. Briefly, the perovskite samples into pellets to ensure good electrical contacts between the grains. The pellet was places between two platinum electrodes in a quartz tube reactor and exposed to controlled gas flowing. The electrical resistance was measured by a megaohm-meter (FLUKE 177 Digital Multimeter). The electrical conductivity σ was determined according to Eq. (6):

$$\sigma = \left(\frac{1}{R}\right)\frac{t}{S} \tag{6}$$

where R stands for the electrical resistance and t/S the geometrical factor of the pellet including the thickness *t* (ca. 3 mm) and the cross-section area S of the pellet.

2.3.3. Electrical measurement at different temperature in air

In the temperature range of this study, *i.e.* 60-600 °C, an exponential increase of the electrical conductivity is observed which obey to an Arrhenius law according to Eq. (7). The Arrhenius plots ln σ vs. the reciprocal temperature leads to the observation of straight lines as exemplified in Figs.4.48 which confirm that all samples analyzed are semiconducting oxides.

$$\sigma = \sigma_0 \cdot \exp\left(-\frac{E_c}{\mathrm{RT}}\right) \tag{7}$$

σ_0 is the pre-exponential factor which reflects the charge carrier concentration and can be determined from the intercept of the straight lines. E_c is the activation energy of conduction calculated from the slopes of the semi-log plots.

The behavior of $LaMnO_3$-C800 is noticeable as its semiconducting behavior is verified in a restricted domain of temperature below 200 °C. At higher temperatures, the electrical conductivity does not vary with temperature suggesting that the sample shift into a metallic conductivity state. Let us note that this behavior has been already pointed out on $LaCoO_3$ [38].

The difference observed on the electrical conductivity of $LaMnO_3$ calcined at 600°C and 800°C could be rationalized at first glance by a p-type semiconducting behavior for $LaMnO_3$-C800 with cationic vacancies (oxygen excess), as most the literature papers claim for $LaMnO_3$ calcined at temperatures higher than 750 °C, involving a polaron hoping mechanism in the Mn^{3+}–O^{2-}–Mn^{4+} network. In contrast, $LaMnO_3$-C600 would preferentially behave as a typical n-type semiconductor with, most likely, oxygen vacancies as main point defects involving an electron hoping conduction mechanism in the Mn^{3+}—O^{2}—Mn^{2+} network.

Table 4.8. Electrical conductivity as a function of temperature governed by the Arrhenius law.

Catalyst	E_c (eV)	σ_0 (Ω^{-1} cm^{-1})
$LaMnO_3$-C600	0.21	0.182
$La_{0.98}Sr_{0.02}MnO_3$-C600	0.56	1.470
$La_{0.95}Sr_{0.05}MnO_3$-C600	0.49	0.883
$La_{0.9}Sr_{0.1}MnO_3$-C600	0.32	0.265
$La_{0.85}Sr_{0.15}MnO_3$-C600	0.15	0.055
$La_{0.7}MnO_3$-C600	0.50	2.994
$La_{1.3}MnO_3$-C600	0.31	0.332
$LaMnO_3$-C800	0.09[a]	0.069[a]

[*] Determined from the low-temperature region.

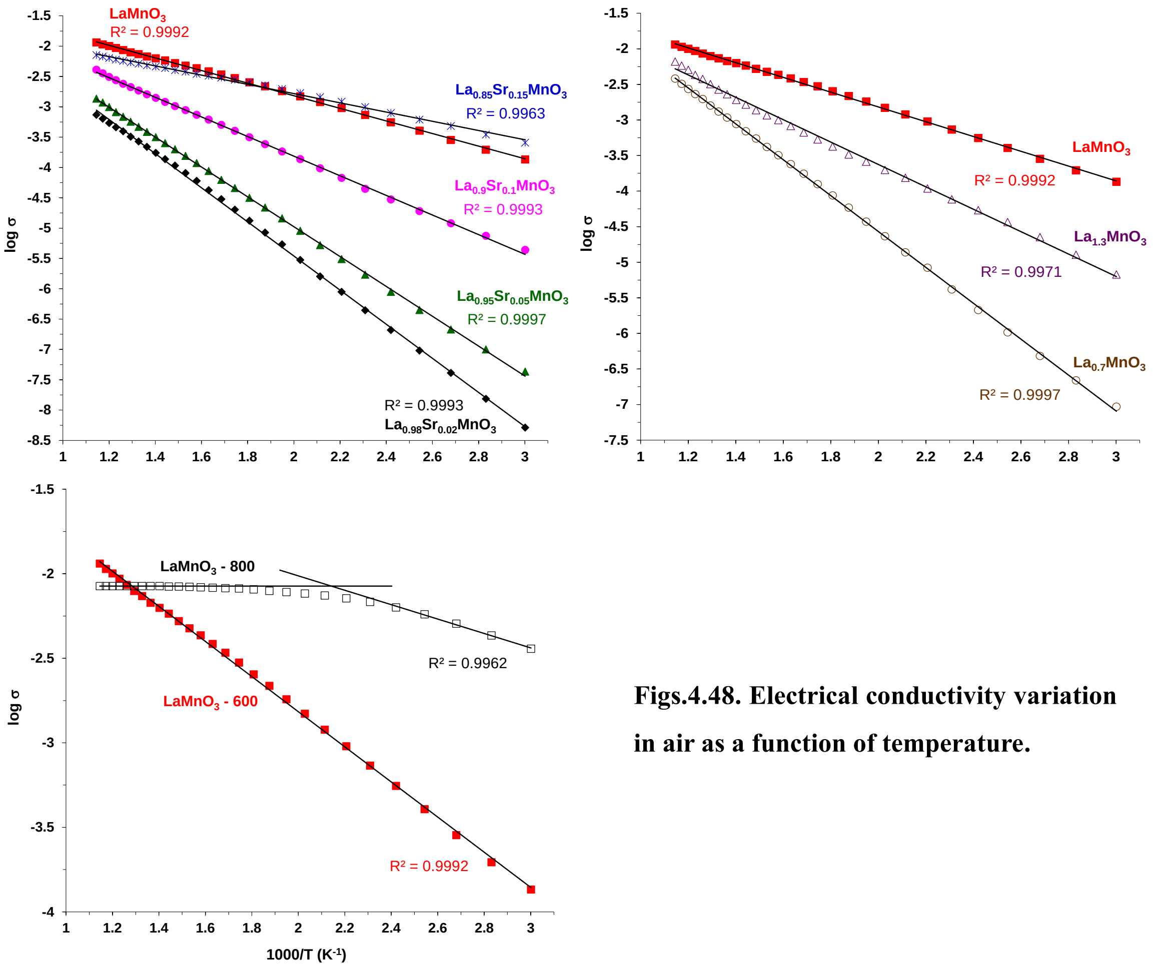

Figs.4.48. Electrical conductivity variation in air as a function of temperature.

The values for the pre-exponential factor σ_0 and the activation energy for conduction are reported in Table 4.8. As seen the lowest values for σ_0 is obtained on LaMnO$_3$-C800 while the highest one characterizes La$_{0.7}$MnO$_3$-C600 and in a lower extent La$_{0.98}$Sr$_{0.02}$MnO$_3$-C600. However, these latter two compositions also correspond to the highest values for E_c.

2.3.4. Oxygen partial dependency of electrical conductivity

Variation of σ as a function of the oxygen pressure was studied at 550 °C. Results are reported in Figs.4.49 in a log–log plot for all the materials studied. Although different, negative slopes, *i.e.* $\partial\sigma/\partial P_{O_2} < 0$, can be observed for all the solids calcined at 600 °C confirming their *n*-type behavior. For the solid calcined at 800 °C, no variation of σ as a function of the oxygen pressure was observed at 550 °C, in line with its metallic-like conductivity observed at this temperature. These observations emphasize the fact that the mechanism of conduction for the samples analyzed (except $LaMnO_3$-C800) would involve ionic oxygen vacancies.

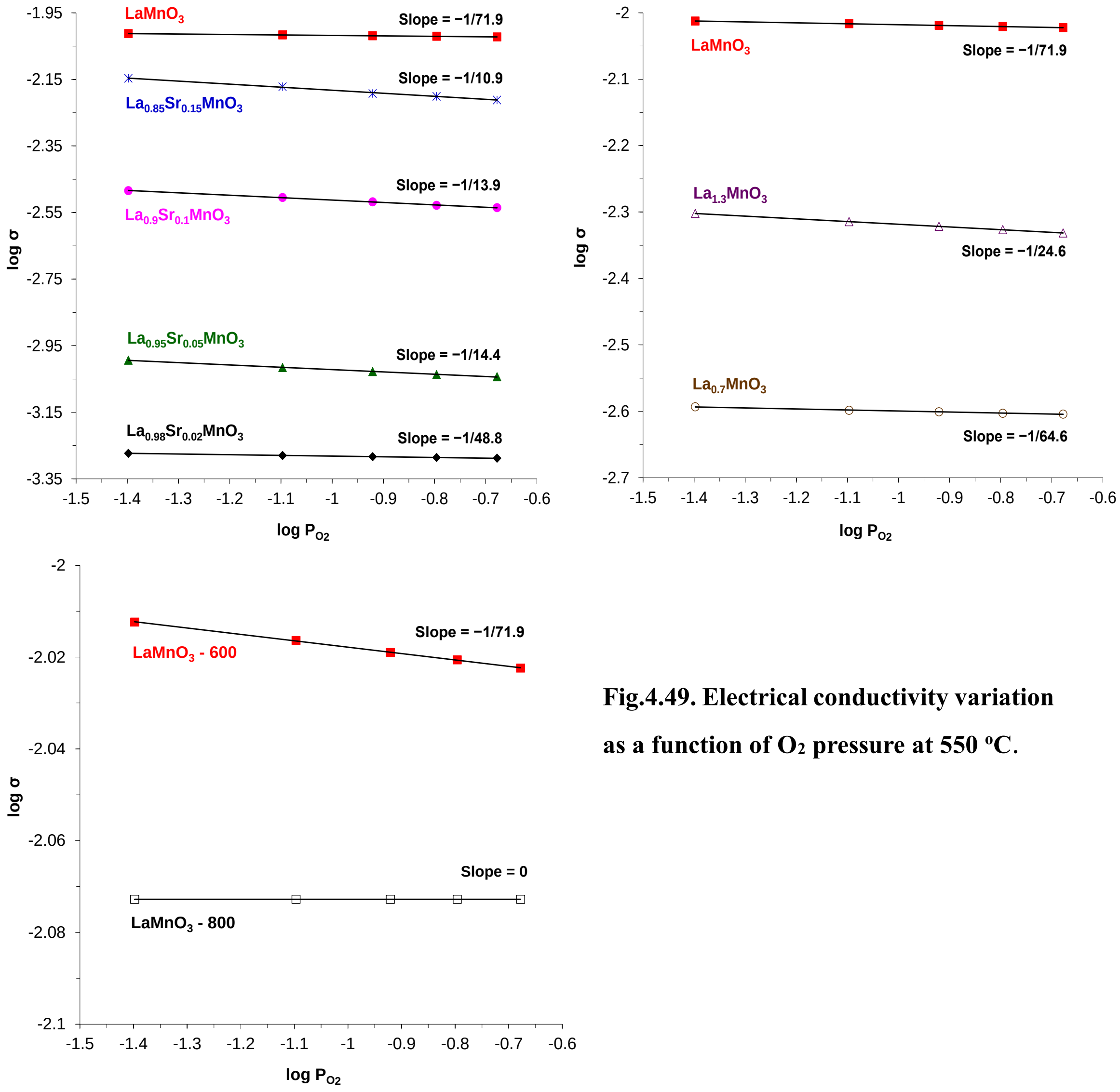

Fig.4.49. Electrical conductivity variation as a function of O_2 pressure at 550 °C.

3. Conclusion

This chapter was dedicated to the physicochemical characterization of bulk and surface properties of bare perovskite (in the absence of noble metal) prepared according to a classical citrate route. Particular attention was paid to the composition playing with the lanthanum stoichiometry and the nature and degree of substitution of La in the benchmark $LaMnO_3$ composition. The calcination temperature was taken into account only for the La_xMnO_3 series with x in the range 0.7-1.3. Two temperatures were selected, e.g. 600°C and 800°C, based on TGA-DSC analysis.

Regarding structural properties, the rhombohedral structure prevails irrespective of the calcination temperature. However, additional reflections on samples calcined at 600°C reveal the presence of MnO_x impurities. Calcination at 800°C leads to the pure rhombohedral structure with improved crystallinity and subsequent loss of specific surface area except on $La_{0.7}MnO_3$ with limited crystallite growth. Such observations have been confirmed from SEM-EDS analysis revealing the conservation of the morphological structure.

Potassium and strontium substitutions have been investigated on stoichiometric samples (with A/Mn = 1) calcined at 600°C. Substituted-Sr samples are more amorphous than the benchmark $LaMnO_3$ but crystallization occurs at increasing Sr-content. No bulk detectable impurity was detected from XRD analysis especially SrO segregation suggesting preferential inclusion in the perovskite lattice. A gain in specific surface area is noticeable for the highest Sr-substitution. Regarding K-substituted samples the opposite tendency is observed with a loss of specific surface area at increasing K content in conjunction with morphological changes and the appearance of stronger heterogeneity in composition with K-rich composition. All these changes have been related to the growth of $K_{1.4}Mn_3O_6$ phase besides the rhombohedral structure of the perovskite.

The reducibility of manganese species is also affected by these changes in structural properties as partial segregation of MnO_x species can lead to more reducible oxidic manganese species than those stabilized in the perovskite lattice in octahedral coordination. It has been found that oxidic manganese species can be already stabilized in different oxidation state in the benchmark $LaMnO_3$, *e.g.* Mn^{4+} and Mn^{3+} with a typical two-step reduction process until complete reduction to Mn^{2+}. La-stoichiometry was found to alter the reducibility with improved reducibility on $La_{0.7}MnO_3$ assigned to a greater formation of Mn^{4+}. A rather similar tendency characterized Sr-substituted samples. In contrast, potassium would preferentially stabilize Mn^{3+}.

The reactivity of oxygen towards desorption from O_2-TPD experiments reveals the existence of low-temperature process (a-desorption) assigned to the desorption of surface oxygen species and a high-temperature desorption process (β-desorption) assigned to subsurface and/or lattice oxygen species. Interestingly, (α-desorption is promoted on $La_{0.7}MnO_3$-C800 suggesting higher mobility due to defective sites at enhanced crystal organization. In contrast Sr- and K-substitutions have a detrimental effect. This is particularly true for the series $La_xK_{1-x}MnO_3$ characterizes by desorption above 900°C at increasing K content which could reflect the behavior of $K_{1.4}Mn_3O_6$.

Surface composition was studied from XPS analysis and provide useful information regarding the surface. Two information can be exploited regarding the mixed valence of manganese and related changes due to La-stoichiometry and K- and Sr-substitution and the surface composition. First, among the different series investigated the calculation of the Mn^{3+}/Mn^{4+} ratio emphasizes a greater stabilization of Mn^{4+} on $La_xSr_{1-x}MnO_3$ showing that the restoration of the electronic balance goes through changes in the oxidation state of manganese in the perovskite lattice. A priori this tendency was also expected on $La_xK_{1-x}MnO_3$ even more accentuated because of the substitution of trivalent by monovalent cation. However, the opposite tendency is observed with an increase of the Mn^{3+}/Mn^{4+} reaching its highest value on $La_{0.85}K_{0.15}MnO_3$ which emphasize a preferential stabilization of Mn^{3+}. This observation seems in rather agreement with a strong K-enrichment in connection with the formation of $K_{1.4}Mn_3O_6$.

Finally, electrical conductivity measurements emphasize different electrical conductivity mechanism on $LaMnO_3$ calcined at 600°C and 800°C. p-type semiconducting behavior involving in the Mn^{3+}–O^{2-}–Mn^{4+} network involving cationic vacancies (p type conductor) whereas $LaMnO_3$ calcined at 600°C would act as a typical n-type semiconductor involving oxygen vacancies in the Mn^{3+}–O^{2-}–Mn^{2+} network. Subsequent measurements on Sr-substituted samples confirm an anionic conductivity. The higher charge carriers are observed on $La_{0.7}MnO_3$ and $La_{0.98}Sr_{0.02}MnO_3$. However, a compensation effect is noticeable as a clear decrease in the activation barrier is observed at increasing Sr-content correcting to a lowering of the charge carriers.

References

1- V. Rives, Chapter 1, From Solid-State Chemistry to Soft Chemistry Routes. P. Granger, V. I. Parvulescu, S. Kaliaguine, W. Prellier, Perovskites and Related Mixed Oxides, Concepts and Applications. 2016 Wiley-VCH Verlag GmbH & Co. KGaA, Boschstr. 12, 69469 Weinheim, Germany. ISBN: 978-3-527-68661-2.

2- Perovskites as Substitutes of Noble Metals for Heterogeneous Catalysis: Dream or Reality. Sébastien Royer, Daniel Duprez, Fabien Can, Xavier Courtois, Catherine Batiot-Dupeyrat, Said Laassiri, and Houshang Alamdari. Chemical Reviews 2014 114 (20), 10292-10368. https://doi-org/10.1021/cr500032a.

3- Nicolas Bion, Fabien Can, Xavier Courtois, Daniel Duprez. Transition metal oxides for combustion and depollution processes. Jacques C. Védrine. Metal Oxides in Heterogeneous Catalysis, Elsevier, pp.287-353, 2018, Metal oxides series, ISBN: 978-0-12-811631-9. http://doi-org/10.1016/B978-0-12-811631-9.00006-5.

4- Pechini Processes: An Alternate Approach of the Sol–Gel Method, Preparation, Properties, and Applications. Lucangelo Dimesso. Springer International Publishing Switzerland 2016. L. Klein et al. (eds.), Handbook of Sol-Gel Science and Technology, http://doi-org/10.1007/978-3-319-19454-7_123-1.

5- J.P. Dacquin, M. Cabié, C.R. Henry, C. Lancelot, C. Dujardin, S.R. Raouf, P. Granger. Structural changes of nano-Pt particles during thermal ageing: Support-induced effect and related impact on the catalytic performances. Journal of Catalysis, Volume 270, Issue 2, 2010, Pages 299-309, ISSN 0021-9517, https://doi.org/10.1016/j.jcat.2010.01.006.

6- Wang, J., Cao, X., Liu, S., Guo, Y., Wang, Z., Li, X., Ren, Y., Xia, Z., Wang, H., Liu, C., Wang, N., Jiang, W., Ding, W., & Zhang, Z. (2020). Preparation, structural and sintering properties of AZO nanoparticles by sol-gel combustion method. Ceramics International, 46, 17659-17665. https://doi.org/10.1016/j.ceramint.2020.04.068.

7- Jawad Javaid Siddiqui, Kongjun Zhu, Jinhao Qiu, Hongli Ji, Sol–gel synthesis, characterization and microwave absorbing properties of nano sized spherical particles of $La_{0.8}Sr_{0.2}Mn_{0.8}Fe_{0.2}O_3$, Materials Research Bulletin, Volume 47, Issue 8, 2012, Pages 1961-1967, ISSN 0025-5408, https://doi.org/10.1016/j.materresbull.2012.04.017.

8- K. Rida, M.A. Peña, E. Sastre, A. Martínez-Arias. Effect of calcination temperature on structural properties and catalytic activity in oxidation reactions of LaNiO3 perovskite prepared by Pechini method. Journal of Rare Earths, Vol. 30, No. 3, Mar. 2012, P. 210. https://doi.org/10.1016/S1002-0721(12)60025-8.

9- Ahmad Gholizadeh. "X-ray peak broadening analysis in $LaMnO_{3+\delta}$ nano-particles with rhombohedral crystal structure". Journal of Advanced Materials and Processing, 3, 3, 2015, 71-83.

10- Chuanhui Zhang, Chao Wang, Wangcheng Zhan, Yanglong Guo, Yun Guo, Guanzhong Lu, Alexandre Baylet, Anne Giroir-Fendler, Catalytic oxidation of vinyl chloride emission over $LaMnO_3$ and $LaB_{0.2}Mn_{0.8}O_3$ (B=Co, Ni, Fe) catalysts, Applied Catalysis B: Environmental, Volume 129, 2013, Pages 509-516, ISSN 0926-3373, https://doi.org/10.1016/j.apcatb.2012.09.056.

11- Yuxi Liu, Hongxing Dai, Jiguang Deng, Yucheng Du, Xinwei Li, Zhenxuan Zhao, Yuan Wang, Baozu Gao, Huanggen Yang, Guangsheng Guo, In situ poly(methyl methacrylate)-templating generation and excellent catalytic performance of MnO_x/3DOM $LaMnO_3$ for the combustion of toluene and methanol, Applied Catalysis B: Environmental, Volumes 140–141, 2013, Pages 493-505, ISSN 0926-3373, https://doi.org/10.1016/j.apcatb.2013.04.051.

12- Fei Teng, Wei Han, Shuhui Liang, Buergen Gaugeu, Ruilong Zong, Yongfa Zhu, Catalytic behavior of hydrothermally synthesized $La_{0.5}Sr_{0.5}MnO_3$ single-crystal cubes in the oxidation of CO and CH_4, Journal of Catalysis, Volume 250, Issue 1, 2007, Pages 1-11, ISSN 0021-9517, https://doi.org/10.1016/j.jcat.2007.05.007.

13- Jianxiong Wu, Jean-Philippe Dacquin, Nora Djelal, Catherine Cordier, Christophe Dujardin, Pascal Granger, Calcium and copper substitution in stoichiometric and La-deficient $LaFeO_3$ compositions: A starting point in next generation of Three-Way-Catalysts for gasoline engines, Applied Catalysis B: Environmental, Volume 282, 2021, 119621, ISSN 0926-3373, https://doi.org/10.1016/j.apcatb.2020.119621.

14- Wenhao Yang, Yue Peng, Ya Wang, Yun Wang, Hao Liu, Zi'ang Su, Weinan Yang, Jianjun Chen, Wenzhe Si, Junhua Li, Controllable redox-induced in-situ growth of MnO_2 over Mn_2O_3 for toluene oxidation: Active heterostructure interfaces, Applied Catalysis B: Environmental, Volume 278, 2020, 119279, ISSN 0926-3373, https://doi.org/10.1016/j.apcatb.2020.119279.

15- A. Giroir-Fendler, S. Gil, A. Baylet. (La(0.8)A(0.2))MnO_3 (A = Sr, K) perovskite catalysts for NO and $C_{10}H_{22}$ oxidation and selective reduction of NO by C10H22. Chinese Journal of Catalysis, Elsevier, 2014, 35, pp.1299-1304. https://doi-org/10.1016/S1872-2067(14)60173-X.

16- Buciuman, F.C., Patcas, F. & Zsakó, J. TPR-study of Substitution Effects on Reducibility and Oxidative Non-stoichiometry of $La_{0.8}A'_{0.2}MnO_{3+\delta}$ Perovskites. Journal of Thermal Analysis and Calorimetry 61, 819–825 (2000). https://doi.org/10.1023/A:1010153331841.

17- Perovskite Oxides: Preparation, Characterizations, and Applications in Heterogeneous Catalysis. Junjiang Zhu, Hailong Li, Linyun Zhong, Ping Xiao, Xuelian Xu, Xiangguang Yang, Zhen Zhao, and Jinlin Li. ACS Catalysis 2014 4 (9), 2917-2940. http://doi-org/10.1021/cs500606g.

18- Hessam Ziaei-Azad, Abbasali Khodadadi, Parvaneh Esmaeilnejad-Ahranjani, Yadollah Mortazavi, Effects of Pd on enhancement of oxidation activity of $LaBO_3$ (B=Mn, Fe, Co and Ni) pervoskite catalysts for pollution abatement from natural gas fueled vehicles, Applied Catalysis B: Environmental, Volume 102, Issues 1–2, 2011, Pages 62-70, ISSN 0926-3373, https://doi.org/10.1016/j.apcatb.2010.11.025.

19- Shuhui Liang, Tongguang Xu, Fei Teng, Ruilong Zong, Yongfa Zhu, The high activity and stability of $La_{0.5}Ba_{0.5}MnO_3$ nanocubes in the oxidation of CO and CH_4, Applied Catalysis B: Environmental, Volume 96, Issues 3–4, 2010, Pages 267-275, ISSN 0926-3373, https://doi.org/10.1016/j.apcatb.2010.01.025.

20- Katie A. Cychosz, Remy Guillet-Nicolas, Javier Garcia-Martinez and Matthias Thommes, Recent advances in the textural characterization of hierarchically structured nanoporous materials, Chem. Soc. Rev., 2017, 46, 389, https://doi-org/10.1039/C6CS00391E.

21- Recent Advances of Lanthanum-Based Perovskite Oxides for Catalysis. Huiyuan Zhu, Pengfei Zhang, and Sheng Dai. ACS Catalysis 2015 5 (11), 6370-6385. http://doi-org/10.1021/acscatal.5b01667.

22- Understanding the Impact of Surface Reconstruction of Perovskite Catalysts on CH_4 Activation and Combustion. Felipe Polo-Garzon, Victor Fung, Xiaoming Liu, Zachary D. Hood, Elizabeth E. Bickel, Lei Bai, Hanjing Tian, Guo Shiou Foo, Miaofang Chi, De-en Jiang, and Zili Wu. ACS Catalysis 2018 8 (11), 10306-10315. http://doi-org/10.1021/acscatal.8b02307.

23- Perovskite Oxides: Preparation, Characterizations, and Applications in Heterogeneous Catalysis. Junjiang Zhu, Hailong Li, Linyun Zhong, Ping Xiao, Xuelian Xu, Xiangguang Yang, Zhen Zhao, and Jinlin Li. ACS Catalysis 2014 4 (9), 2917-2940. http://doi-org/10.1021/cs500606g.

24- Cation Size Mismatch and Charge Interactions Drive Dopant Segregation at the Surfaces of Manganite Perovskites. Wonyoung Lee, Jeong Woo Han, Yan Chen, Zhuhua Cai, and Bilge Yildiz. Journal of the American Chemical Society 2013 135 (21), 7909-7925. http://doi-org/10.1021/ja3125349.

25- S. Ponce, M.A. Peña, J.L. GFierro. Surface properties and catalytic performance in methane combustion of Sr-substituted lanthanum manganites. Applied Catalysis B: Environmental, Volume 24, Issues 3–4, 7 February 2000, Pages 193-205. https://doi.org/10.1016/S0926-3373(99)00111-3.

26- G. Abdallah, R. Bitar, S. K. P. Veerapandian, J-M. Giraudon, N. De Geyter, R. Morent, J-F. Lamonier. Acid treated Ce modified birnessite–type MnO_2 for ozone decomposition at low temperature: Effect of nitrogen containing co-pollutants and water. Applied Surface Science, Volume 571, 1 January 2022, 151240. https://doi.org/10.1016/j.apsusc.2021.151240.

27- Ethan J. Crumlin, Eva Mutoro, Wesley T. Hong, Michael D. Biegalski, Hans M. Christen, Zhi Liu, Hendrik Bluhm, and Yang Shao-Horn, In Situ Ambient Pressure X-ray Photoelectron Spectroscopy of Cobalt Perovskite Surfaces under Cathodic Polarization at High Temperatures. The Journal of Physical Chemistry C 2013 117 (31), 16087-16094. http://doi-org/10.1021/jp4051963.

28- Hf Deposition Stabilizes the Surface Chemistry of Perovskite Manganite Oxide. Roland Bliem, Dongha Kim, Jiayue Wang, Ethan J. Crumlin, and Bilge Yildiz. The Journal of Physical Chemistry C 2021 125 (6), 3346-3354. http://doi-org/10.1021/acs.jpcc.0c09707.

29- M.C. Biesinger, B.P. Payne, A.P. Grosvenor, L.W.M. Lau, A.R. Gerson, R.St.C. Smart., Resolving surface chemical states in XPS analysis of first row transition metals, oxides and hydroxides: Cr, Mn, Fe, Co and Ni., Applied Surface Science, Volume 257, Issue 7, 15 January 2011, Pages 2717-2730. https://doi.org/10.1016/j.apsusc.2010.10.051.

30- Abdallah, G.; Giraudon, J.-M.; Bitar, R.; Geyter, N.D.; Morent, R.; Lamonier, J.-F. Post-Plasma Catalysis for Trichloroethylene Abatement with Ce-Doped Birnessite Downstream DC Corona Discharge Reactor. Catalysts 2021, 11, 946. https://doi.org/10.3390/catal11080946.

31- H. Najjar, J-F. Lamonier, O. Mentré, J-M. Giraudon, H. Batis. Optimization of the combustion synthesis towards efficient $LaMnO_{3+y}$ catalysts in methane oxidation. Applied Catalysis B: Environmental, Volume 106, Issues 1–2, 21 July 2011, Pages 149-159. https://doi.org/10.1016/j.apcatb.2011.05.019.

32- Jon A. Onrubia-Calvo, B. Pereda-Ayo, U. De-La-Torre, Juan R. González-Velasco, Key factors in Sr-doped $LaBO_3$ (B = Co or Mn) perovskites for NO oxidation in efficient diesel exhaust purification. Applied Catalysis B: Environmental, Volume 213, 2017, Pages 198-210, ISSN 0926-3373, https://doi.org/10.1016/j.apcatb.2017.04.068.

33- Yin Xu, Jérémy Dhainaut, Jean-Philippe Dacquin, Anne-Sophie Mamede, Maya Marinova, Jean-François Lamonier, Hervé Vezin, Hui Zhang, Sébastien Royer. $La_{1-x}(Sr, Na, K)_xMnO_3$ perovskites for

HCHO oxidation: The role of oxygen species on the catalytic mechanism. Applied Catalysis B: Environmental, Volume 287, 2021, 119955, ISSN 0926-3373, https://doi.org/10.1016/j.apcatb.2021.119955.

34- Jirátová, K.; Pacultová, K.; Karásková, K.; Balabánová, J.; Koštejn, M.; Obalová, L. Direct Decomposition of NO over Co-Mn-Al Mixed Oxides: Effect of Ce and/or K Promoters. Catalysts 2020, 10, 808. https://doi.org/10.3390/catal10070808.

35- Yinlong Zhu, Wei Zhou, Jie Yu, Yubo Chen, Meilin Liu, and Zongping Shao, « Enhancing Electrocatalytic Activity of Perovskite Oxides by Tuning Cation Deficiency for Oxygen Reduction and Evolution Reactions », Chemistry of materials, 28, American Chemical Society, 2016, no 6, p. 1691-1697. https://doi-org/10.1021/acs.chemmater.5b04457.

36- R.M. García de la Cruz, H. Falcón, M.A. Peña, J.L.G. Fierro. Role of bulk and surface structures of $La_{1-x}Sr_xNiO_3$ perovskite-type oxides in methane combustion. Applied Catalysis B: Environmental, Volume 33, Issue 1, 2001, Pages 45-55, ISSN 0926-3373, https://doi.org/10.1016/S0926-3373(01)00157-6.

37- Study of the Catalytic Activity–Semiconductive Properties Relationship For $BaTiO_3$ and $PbTiO_3$ Perovskites, Catalysts for Methane Combustion. I. Popescu, I. Săndulescu, Á. Rédey, I.-C. Marcu, Catalysis Letters volume 141, pages 445–451 (2011), https://doi.org/10.1007/s10562-010-0538-2.

38- Ionel Popescu, Yihao Wu, Pascal Granger, Ioan-Cezar Marcu. An in situ electrical conductivity study of LaCoFe perovskite-based catalysts in correlation with the total oxidation of methane. Applied Catalysis A: General, Volume 485, 2014, Pages 20-27, ISSN 0926-860X, https://doi.org/10.1016/j.apcata.2014.07.025.

Annexes

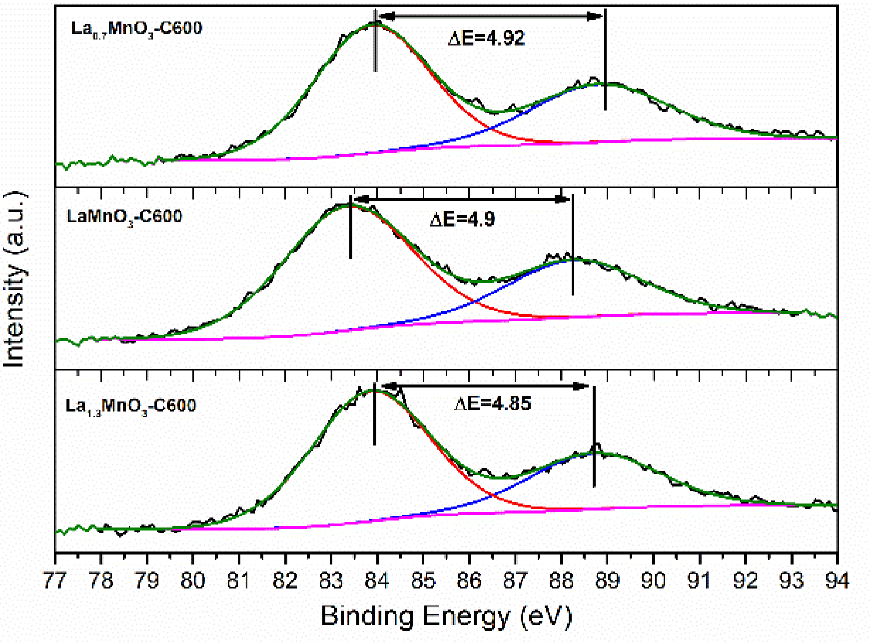

Fig.4.47-S1. XPS spectrum of Mn 3s:

(Top) $La_{0.7}MnO_3$-C600; (Middle) $LaMnO_3$-C600; (Bottom) $La_{1.3}MnO_3$-C600.

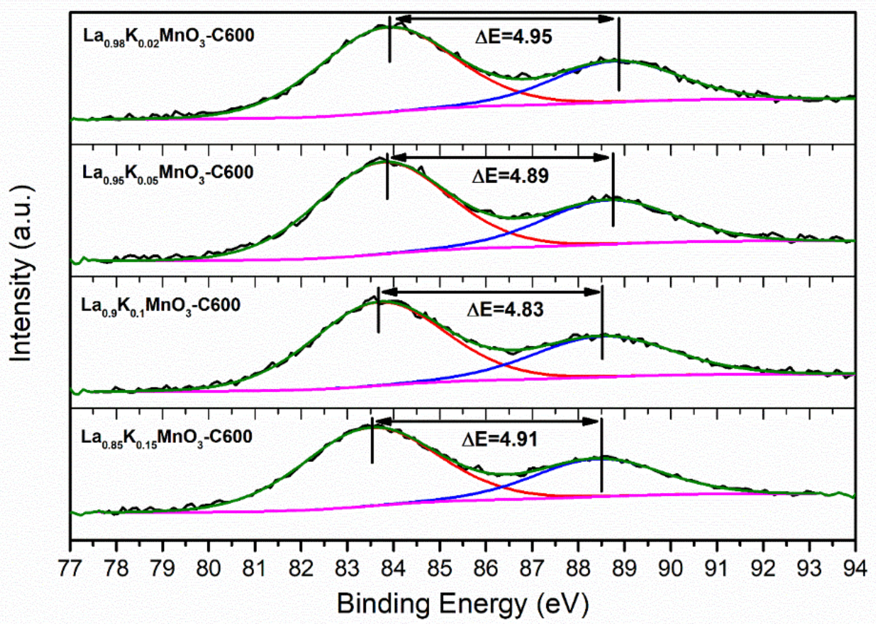

Fig.4.47-S2. XPS spectrum of Mn 2p:

$La_{0.98}K_{0.02}MnO_3$-C600; $La_{0.95}K_{0.05}MnO_3$-C600; $La_{0.9}K_{0.1}MnO_3$-C600; $La_{0.85}K_{0.15}MnO_3$-C600.

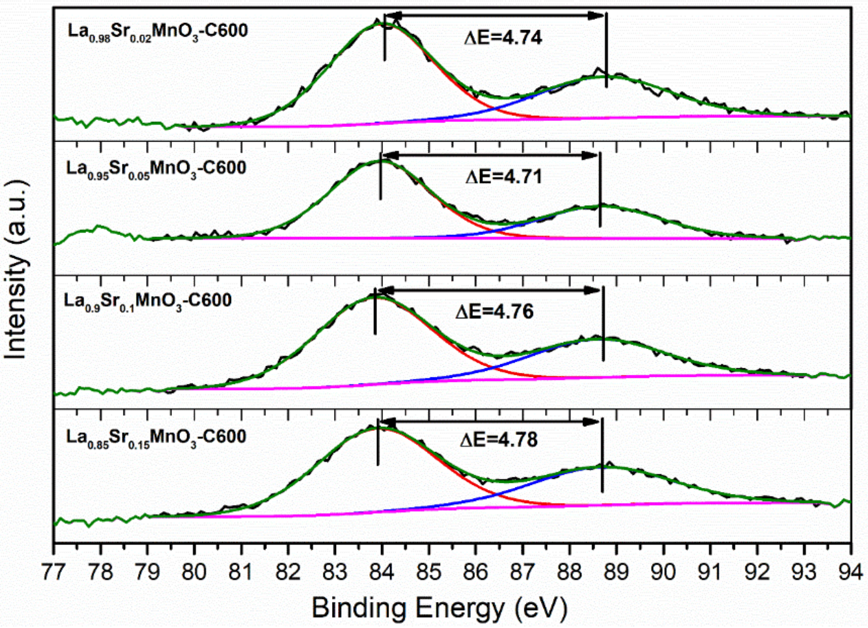

Fig.4.47-S3. XPS spectrum of Mn 2p:

$La_{0.98}K_{0.02}MnO_3$-C600; $La_{0.95}K_{0.05}MnO_3$-C600; $La_{0.9}K_{0.1}MnO_3$-C600; $La_{0.85}K_{0.15}MnO_3$-C600.

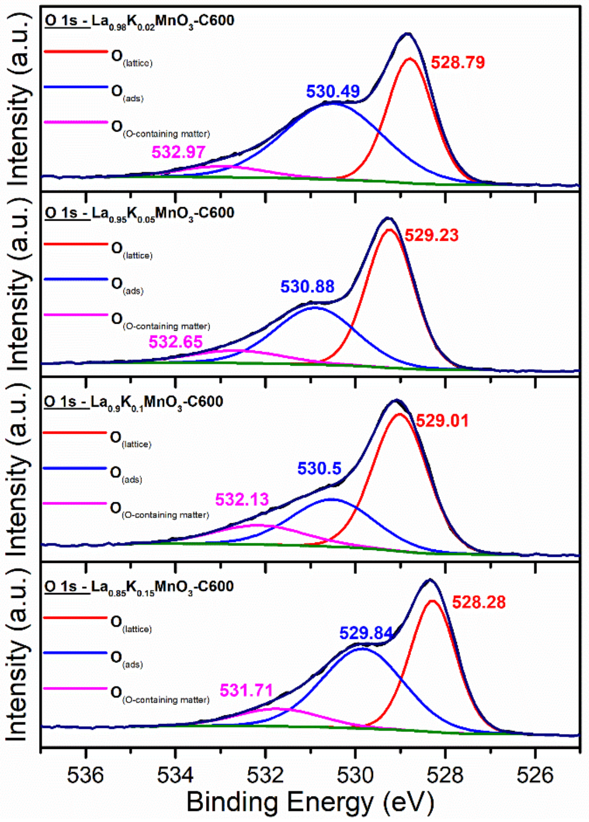

Fig.4.43-S1. XPS spectrum of O 1s:

$La_{0.98}K_{0.02}MnO_3$-C600; $La_{0.95}K_{0.05}MnO_3$-C600; $La_{0.9}K_{0.1}MnO_3$-C600; $La_{0.85}K_{0.15}MnO_3$-C600.

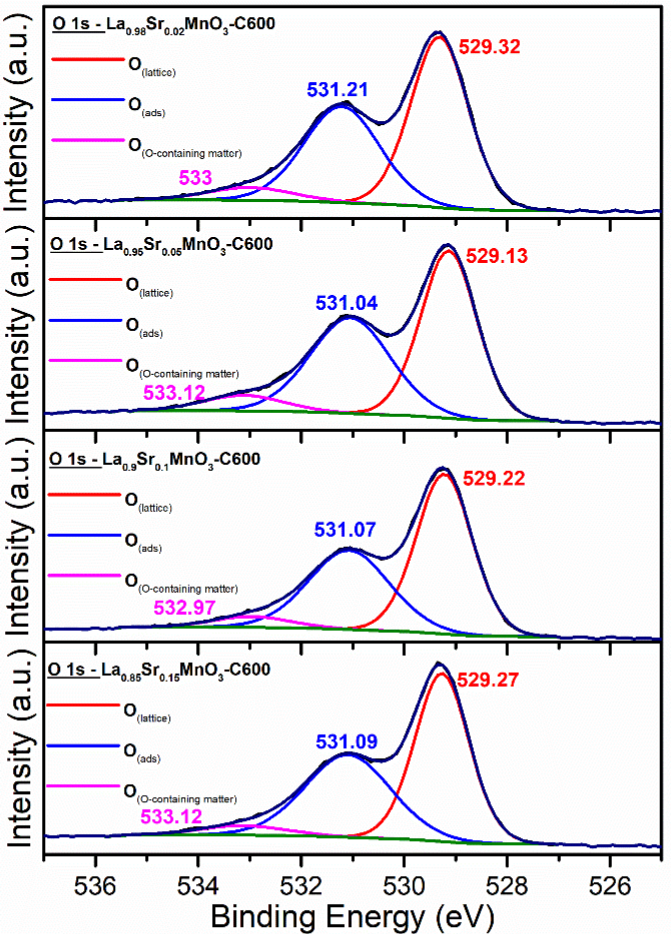

Fig.4.44-S2. XPS spectrum of O 1s:

$La_{0.98}Sr_{0.02}MnO_3$-C600; $La_{0.95}Sr_{0.05}MnO_3$-C600; $La_{0.9}Sr_{0.1}MnO_3$-C600; $La_{0.85}Sr_{0.15}MnO_3$-C600.

Chapter V. Palladium Incorporation on Bulk and Surface Properties of Perovskites

1. Introduction

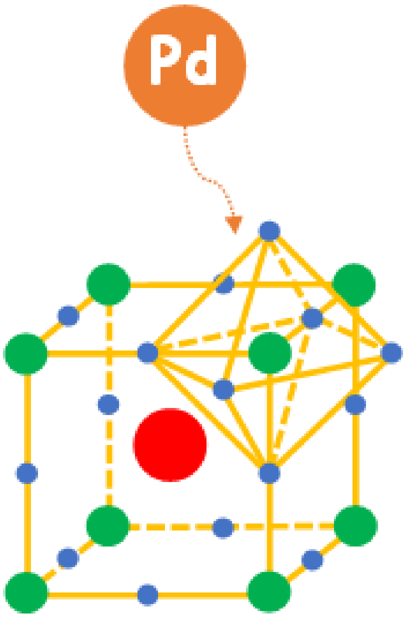

Fig.5.1.1 Schematic illustration of ideal Pd incorporated perovskite structure in the form of $Pd/ABO_{3+\delta}$ and $AB_xPd_{1-x}O_{3+\delta}$ formulation.
(Cation A: Red; Cation B: Green; Cation Pd: Orange; Anion O: Blue.)

Palladium is normally treated as the highly efficient noble metal to break C-H bond in methane catalytic combustion [39]. However, considering the high cost of palladium, perovskite materials are recognized as the attractive alternatives of noble metals [2] due to its flexible and modifiable ABO_3 formulation [1] influencing related structure and corresponding properties in bulk and on surface [40]. Hence, the combination of the precious metal and perovskite becomes an interesting topic and updated wide space worthy of further investigations which can avoid both shortcomings, such as thermal sintering of precious metals, catalysts poisoning and high temperature stability, as much as possible and play a bit better.

Nishihata et al. [41] firstly pointed the self-regeneration phenomenon of palladium located in B-site of perovskites and Tanaka et al. [42] then demonstrated that rhodium and platinum in B-site of perovskites also have the smart self-regeneration property in the research field of automobile emission control [43]. As a result, the property, which improves the catalytic performance of base metal, not only reduces the use of precious metal, but also effectively avoids the shortcomings of high temperature thermal sintering of noble metal. However, the concept developed by Nishihata et al. and Tanaka et al. also provoked strong debates of conflicting study regarding the self-regeneration of Pd/$LaFeO_3$ and $LaFe_{0.95}Pd_{0.05}O_{3-\delta}$ models in vehicle emission control area.

By way of illustration, Katz et al. [44] found that Pd particles at the surface of $LaFeO_3$ and subsequent dissolution of palladium into the perovskite lattice in lean conditions can be a limited process and would require a large number of defective sites which would not be available in $LaFeO_3$ exhibiting a crystalline nature [45]. Dynamic changes at the surface during three-way conditions are also subjected to prerequisite in terms of oxidability of the precious metal as well as the perovskite. This has been already emphasized [46, 47] that improved resistance to thermal sintering could not be strictly related to dynamic processes involving surface/sub-surface diffusion phenomena but more likely to the creation of strong metal-support interaction. Based on this, the key would be related to the method for palladium incorporation as well as the nature of the subsequent thermal treatment to activate the formation of metallic particle in strong interaction with the perovskite support.

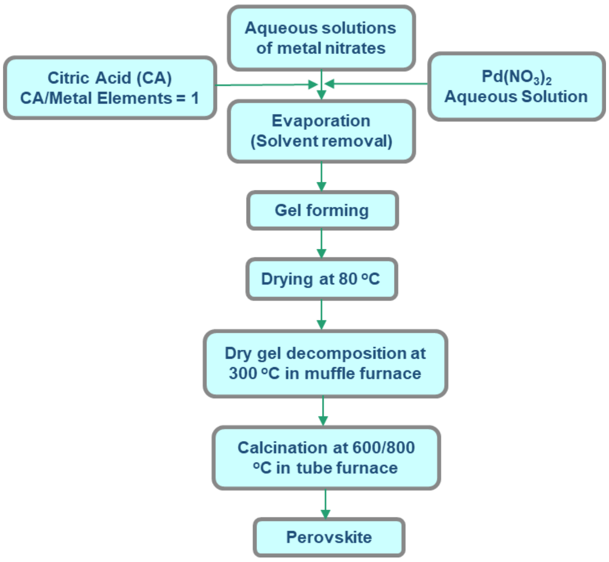

Fig.5.1.2. Pd incorporation by One-Pot Route.

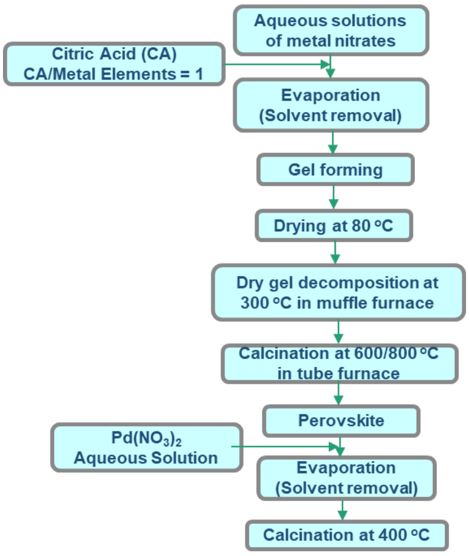

Fig.5.1.3 Pd incorporation by Sequential Route.

Two strategies have implemented for palladium addition according to a one-pot approach (Fig.5.1.2) consisting in incorporating palladium during the sol-gel synthesis and a sequential approach (Fig.5.1.3) which basically consists in adding palladium through a classical wet impregnation. The following scheme illustrate these two strategies.

Let us note that for the one pot route the precursor was calcined at two different temperatures in air, *i.e.* 600°C and 800°C corresponding to the stoichiometric composition labeled $LaMn_{0.98}Pd_{0.02}O_3$-C600 and $LaMn_{0.98}Pd_{0.02}O_3$-C800. For the samples prepared by sequential method, La_xMnO_3, calcined at 600°C or 800°C was further impregnated with the same amount of palladium (1 wt.% Pd). Impregnated precursors after drying were finally calcined in air at 400°C. The corresponding samples will be labeled Pd/La_xMnO_3-C600 and Pd/La_xMnO_3-C800 with $\boldsymbol{x}$ = 0.7, 1 and 1.3.

2. Impact of palladium incorporation mode on $La_xMnO_{3+\delta}$ perovskite: One-pot versus sequential method

2.1. Bulk and structural properties

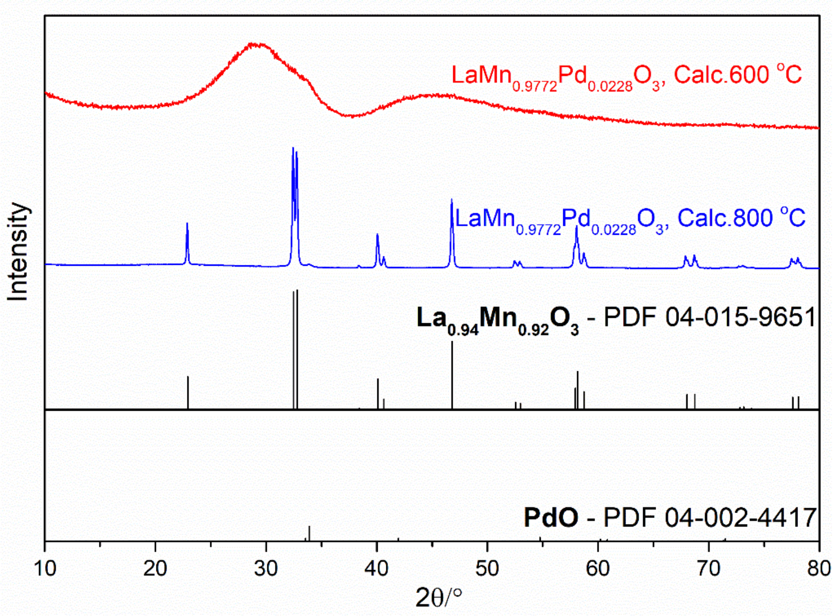

Fig.5.2.1. XRD profiles of 1% wt. Pd perovskites by One-Pot route: (Red) $LaMn_{0.9772}Pd_{0.0228}O_3$-C600 and (Blue) $LaMn_{0.9772}Pd_{0.0228}O_3$-C800.

XRD pattern recorded on $LaMn_{0.98}Pd_{0.02}O_3$-C600 in Fig.5.2.1. does not reveal distinct reflections which underline the amorphous structure of this sample. In contrast, narrow and intense reflections are observable for $LaMn_{0.98}Pd_{0.02}O_3$-C800 which reflect a high crystallinity as earlier discussed. The comparison with reference diffractograms shows a good agreement with the structure $La_{0.94}Mn_{0.92}O_3$ (PDF 04-015-9651). Because of rather low Pd content (1 wt.%), no reflection characteristic of PdO was detected notably on $LaMn_{0.98}Pd_{0.02}O_3$-C800 (ambiguous weak reflections of PdO, PDF 04-002-4417) which corresponds to the most severe calcination temperature.

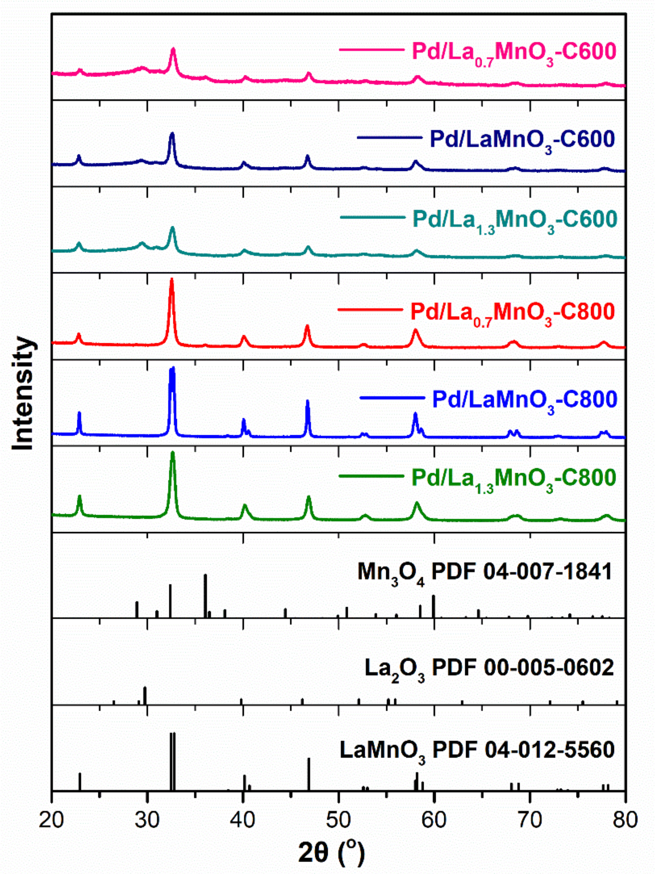

Fig.5.2.2. XRD profiles of 1% wt. Pd perovskites by Sequential

For impregnated samples (Fig.5.2.2), due to the very low doping content of palladium at 1 wt.% and the uneven distribution of Pd, the sensitivity of XRD cannot clearly reflect the characteristic peak of palladium species in the samples. Similar to the former perovskites without palladium impregnation process, all the samples showed the characteristic reflections of perovskite $LaMnO_3$ (PDF 04-012-5560). Higher calcination temperature till brought higher crystallinity, the lower temperature calcination samples presented the lower degree. In addition, calcination at 400 °C after impregnation of Pd nitrate solution seemed to have no obvious effect on the crystallization degree of perovskites.

2.2. Bulk reducibility from H_2-TPR

For the sample series with two different synthesis methods, H_2-Thermal-Programmed Reduction experiments can be useful to understand the reduction properties of palladium doped samples, and investigate the promotion effect of palladium on the perovskite reducibility. Accordingly, different impact can be expected as a function of the method used for Pd addition.

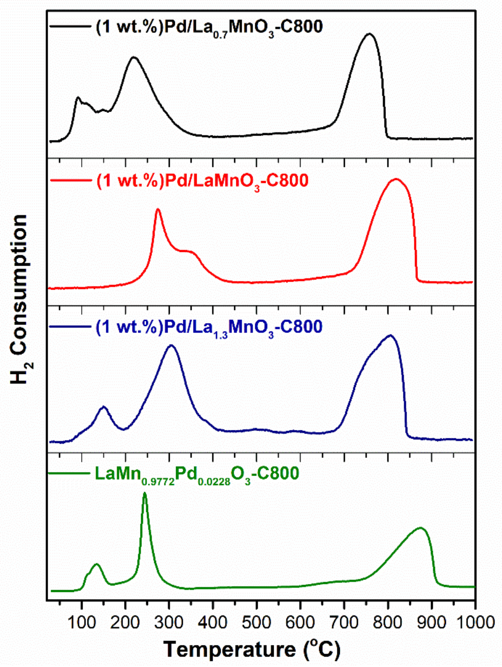

Fig.5.2.3. H_2-TPR profiles of 1% wt. Pd

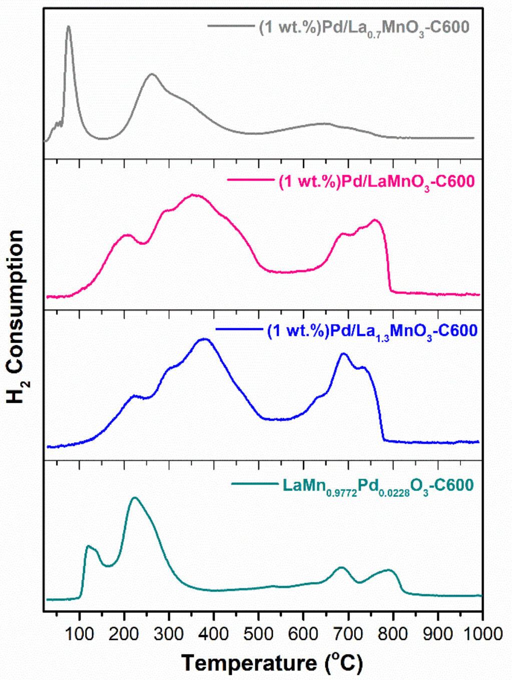

Fig.5.2.4. H_2-TPR profiles of 1% wt. Pd perovskites of C600 series.

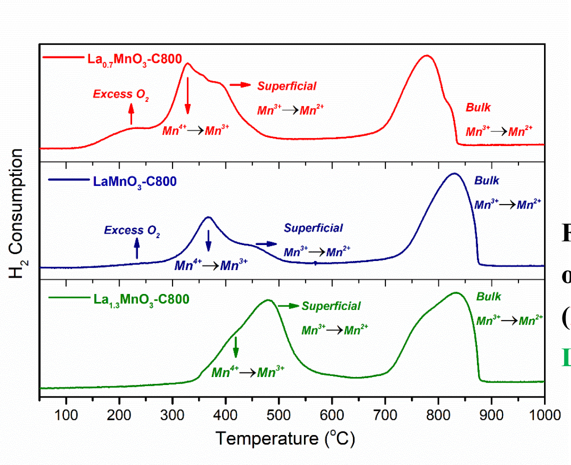

Fig.4.9. H_2 thermal-programmed reduction of La_xMnO_3 series calcinated at 800 °C ($La_{0.7}MnO_3$: Red; $LaMnO_3$: Navy; $La_{1.3}MnO_3$: Olive.)

Fig.5.2.3 earlier discussed in chapter 4 underlined a two-step reduction process starting from Mn^{4+} to Mn^{2+} with the intermediate formation of Mn^{3+}. Different contributions appear on the low-temperature reduction process assigned to the reduction of extra framework oxidic manganese species or stabilized in octahedral position in the perovskite lattice.

As seen in Figs. 5.2.3 and 5.2.4, the incorporation of palladium will essentially perturb the low-T reduction process inducing a sharp shift of the reduction of oxidic manganese species to lower temperature and the appearance of an extra H_2 consumption process below 150°C assigned to the reduction of oxidic PdO_x species into Pd^0 [48]. The different reduction processes can be resumed according to Eqs. (1)-(5):

$$LaMnPdO_3 + \frac{1}{2}H_2 = \frac{1}{2}La_2O_3 + MnO + Pd + \frac{1}{2}H_2O \text{ —— Eq. (1)}$$

$$PdO_x/LaMnO_3 + \frac{1}{2}H_2 = \frac{1}{2}La_2O_3 + MnO + Pd + \frac{x}{2}H_2O \text{ —— Eq. (2)}$$

$$Mn^{4+} \rightarrow Mn^{3+} \text{ —— Eq. (3)}$$

$$Mn^{3+} \rightarrow Mn^{2+} \text{ —— Eq. (4)}$$

$$Pd^{x+} \rightarrow Pd^0 \text{ —— Eq. (5)}$$

Hence, once reduced palladium will assist the reduction of the perovskite. It is remarkable that the reduction of PdO_x on Pd/$LaMnO_3$-C800 is not observed. For this sample the H_2 consumption profile mimic that observed on the bare sample even though a slight shift to lower temperature is observable. In fact, the reduction temperature of PdO particles is closely related to the composition of support materials which will govern the strength of interaction, the Pd dispersion and the particle size. Previous investigations found that well-dispersed PdO reduces above 100°C whereas the reduction of larger PdO particles in weaker interaction with the support would occur for T≤ 50°C [75, 76]. Based on this one can presume that a weaker interaction between Pd particles and the perovskite support would occur on Pd/$LaMnO_3$-C800.

A second peculiarity is observable on $LaMn_{0.98}Pd_{0.02}O_3$-C600. Beside the sharp low temperature reduction process starting at 100°C a shift of the high temperature reduction process to lower temperature is noticeable. Such a trend is in some extent noticeable on Pd/$LaMnO_3$-C600 and could reflect a much stronger interaction between Pd and the perovskite. In fact, it was expected on $LaMn_{0.98}Pd_{0.02}O_3$-C600 that the isolation of bulk cationic Pd^{n+} replacing Mn^{3+}/Mn^{4+} in octahedral coordination of the perovskite lattice can speed up the overall reduction process. For these two samples, it seems that a much greater Pd-perovskite interface could be obtained. In the contrast, a deterioration of such interface seems plausible on $LaMn_{0.98}Pd_{0.02}O_3$-C800 as the high temperature reduction process is partly restored and delayed.

Table 5.2.1. H_2-TPR profiles quantitative analysis.

Catalyst	Total H_2 Consumption (mmol/g)	H_2 Consumption < 550 °C (mmol/g)	Relative H_2 contribution (%) (< 550 °C)	H/M	SSA[1] (m²/g)	Nomalized Consumption (mmol/m²)
Pd/$La_{0.7}MnO_3$-C800	3.2	1.7	52.6	1.3	24.7	0.130
Pd/$LaMnO_3$-C800	2.9	1.0	35.4	1.4	7.2	0.403
Pd/$La_{1.3}MnO_3$-C800	2.6	1.3	49.8	1.5	16.7	0.156
$LaMn_{0.98}Pd_{0.02}O_3$-C800	6.3	4.4	70.8	1.5	6.4	0.984
Pd/$La_{0.7}MnO_3$-C600	3.7	3.2	86.4	1.5	28.9	0.128
Pd/$LaMnO_3$-C600	3.7	2.4	65.9	1.8	20.7	0.179
Pd/$La_{1.3}MnO_3$-C600	3.6	2.3	62.8	2.1	22.3	0.161
$LaMn_{0.98}Pd_{0.02}O_3$-C600	8.1	7.0	85.5	2.0	28.9	0.280

[1] SSA: Specific Surface Area.

As seen from the comparison of Table 4.2 in Chapter IV and Table 5.2.1, low content palladium incorporation obviously boosted the reduction capacities of catalysts, the synergetic Pd and Mn cations promoted the surface reduction activities to even lower temperature. Besides, generally, one-pot synthesis samples presented obviously more active properties than sequential samples depending on calculation results of the H/M ratio and unit hydrogen consumption (Table 5.2.1), which also reflected the importance of the synthesis method as a vital factor in catalyst design for stabilizing the palladium active sites.

2.3. Bulk reoxidation of reduced sampled from O_2-TPO

Similar to bare perovskites, reduced Pd-doped perovskites from H_2-TPR experiments were subjected to the same reoxidation process (Fig.4.14, Fig.4.15 in Chapter IV). As earlier explained, at 1000°C the perovskite is completely reduced according to Eq. (1). A key point during the reoxidation is related to: (i.) the restoration of the perovskite and (ii.) the possible reinsertion of oxidic palladium species inside the perovskite lattice and/or preferential segregation into PdO_x crystallites as described in Eq. (3.1.2):

$$Pd + La_2O_3 + 2\ MnO + (1+x)/2\ O_2 = PdO_x + 2\ LaMnO_3 \qquad \text{Eq. (3.1.2).}$$

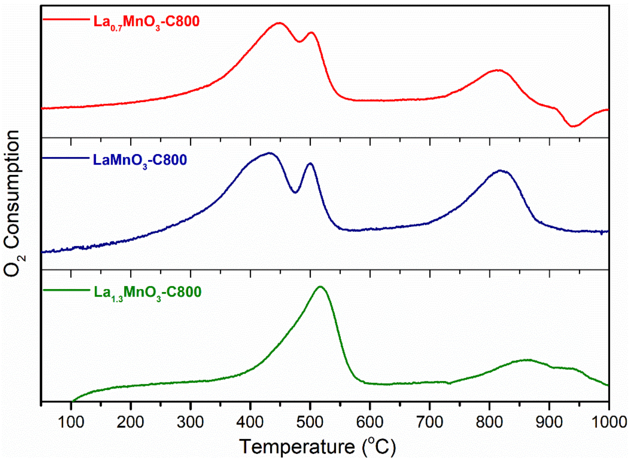

Fig.4.14. O_2-TPO profiles: (Red) $La_{0.7}MnO_3$-C800; (Navy) $LaMnO_3$-C800; (Olive) $La_{1.3}MnO_3$-C800.

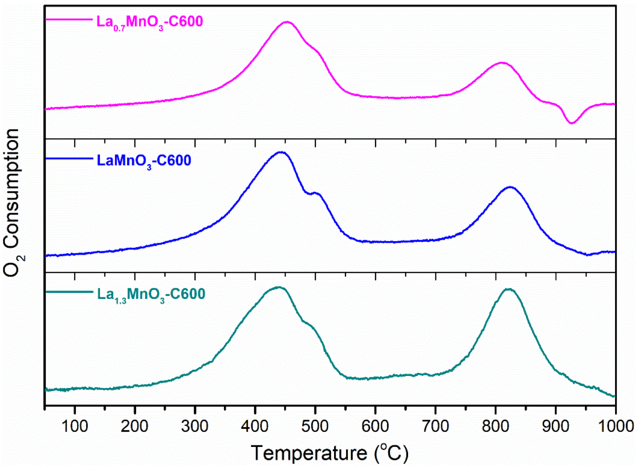

Fig.4.15. O_2-TPO profiles: (Pink) $La_{0.7}MnO_3$-C600; (Blue) $LaMnO_3$-C600; (Cyan) $La_{1.3}MnO_3$-C600.

In practice it was found that a two-steps reoxidation process takes place. A broad signal with two apparent maxima on $LaMnO_3$-C800 appears above 300°C.

In the presence of Pd, reoxidation was more complicated because Pd was oxidized to bivalent and higher valence states during the reversible $PdO_x \leftrightarrow Pd^0$ transformation and the interaction between Pd and MnO during oxidation should be taken into account.

According to previous studies about self-regeneration properties [41, 42, 43], a hypothesis could be inferred which may occur the oxygen release while surface high state Pd dissolving into the perovskite lattice. Thermal PdO_x stability and transformation depend on the interaction between Pd and the support [49].

On the whole, the splitting peak appeared in almost all samples at low temperature region. As the former bulk perovskites investigation on sequential synthesis series, a main two-steps re-oxidation process happened on reduced samples with 550 °C as the dividing line. However, both of the samples of one-pot route showed a nearly coherent reoxidation process, which could be inferred that different Pd incorporation methods presented different external profiles.

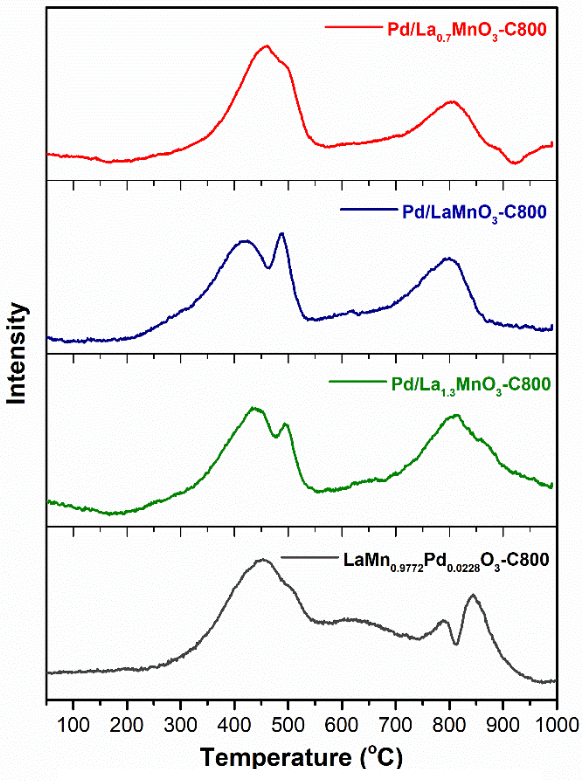

Fig.5.2.5. O_2-TPO profiles:
800 °C Calcination Samples.

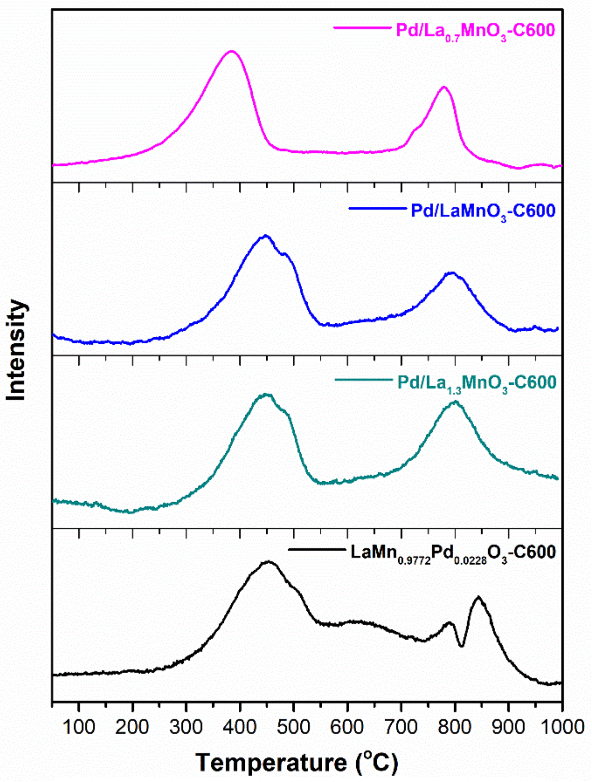

Fig.5.2.6. O_2-TPO profiles:
600 °C Calcination Samples.

In addition, the small negative peaks about 900 °C could be observed, which involved the release of oxygen. This situation was most pronounced and intense for the two non-stoichiometric sequential catalysts with Pd/$La_{0.7}MnO_3$ composition, especially on the sample calcined at 800°C. In the range of high temperature, the re-oxidation of

$Pd/La_{1.3}MnO_3$ composition did not seem to end at 1000 ºC that can be taken as the characteristic of La-excess composition. Moreover, one-pot series also presented the peak splitting at high temperature range due to different Pd doping technique, because PdO_x crystallites of different sizes exhibit different properties during redox process [50].

Table 5.2.2. Amount of oxygen consumption from O_2-TPO.

Catalyst	Total O_2 Consumption (mmol/g)	O/M
$Pd/La_{0.7}MnO_3$-C800	2.06996	0.84
$Pd/LaMnO_3$-C800	1.56335	0.76
$Pd/La_{1.3}MnO_3$-C800	1.42927	0.82
$LaMn_{0.98}Pd_{0.02}O_3$-C800	1.71431	0.83
$Pd/La_{0.7}MnO_3$-C600	1.06387	0.43
$Pd/LaMnO_3$-C600	1.42915	0.70
$Pd/La_{1.3}MnO_3$-C600	1.24320	0.71
$LaMn_{0.98}Pd_{0.02}O_3$-C600	1.92395	0.94

As a whole, compared to bulk perovskite without Pd doping (Fig.4.14, Fig.4.15 in Chapter IV) during the re-oxidation process, Pd incorporation route showed a significant difference in the re-oxidation process (Fig.5.2.5, Fig.5.2.6). Generally, the sequential method series maintained a two-step process similar to the perovskite without Pd doping, while the one-pot method showed a continuous oxidation process on the whole. From the calculation results (Table 5.2.2) of oxygen consumption and ratio of oxygen and metals (O/M), at first glance, one-pot samples consumed more oxygen overall from total O/M ratio. The high temperature calcined sequential samples showed overall higher O/M values than perovskite supports (Table 4.3 in Chapter IV) during the re-oxidation process, especially the $La_{0.7}MnO_3$-C800 showing the oxygen release at 900 ºC presented the same O/M ratio as the one-pot C800 sample. As to the sequential Pd doping C600 series, there was no significant change from Pd doping but the one-pot C600 sample consumed more oxygen due to its initial low degree of crystallinity.

2.4. Oxygen desorption (O_2-TPD / MS)

The oxygen desorption of palladium incorporated perovskite catalysts were also experimented by thermal programmed desorption combined with mass spectroscopy (O_2-TPD/MS) following the program as above Fig.4.18.

Palladium supported perovskite oxides with oxygen vacancies can produce/transform different kinds of oxygen species. Different from the single perovskite catalysts, Pd incorporated La_xMnO_3 type perovskites were investigated for the changes of these oxygen mobility and storage properties and oxygen bond strength in the reaction of oxygen-containing substances [51]. Therefore, measurements of the amount and intensity of surface or subsurface oxygen in palladium-supported perovskite oxides, in order to properly investigate the effect of palladium doping on the oxygen mobility and storage capacity, are usually performed in three-way catalysis and/or other catalytic applications near stoichiometry [17].

The related results of the MS on O_2-TPD are shown in the Fig.5.2.7 and Fig.5.2.8. The amount of O_2 released from perovskites was calculated after deconvolution of the O_2 desorption curve and are listed in Table 5.2.3. As the former oxygen desorption calculation in Table 4.4 in Chapter IV, the boundary between surface desorbed α-oxygen and β-oxygen from lattice [53] has been defined as previously at 500 °C. Only a little amount of O_2 desorbed from perovskites at $T < 500$ ˚C designated as α-O_2 and ascribed to oxygen species weakly bound to the surface of the perovskite and more O_2 desorption observed at $T > 500$ ◦C is referred to as β-O_2, which is removed from the lattice [52].

In general, sequential Pd incorporated perovskite samples presented the similar curves (Fig.5.2.7, Fig.5.2.8) as only perovskite cases (Fig.4.19, Fig.4.20 in Chapter IV) in accordance with previous study of Zhang et al. on Pd incorporation into perovskite [53], but with a reduced oxygen desorption capacity compared the results from Table 4.4 and Table 5.2.3. Among the samples with palladium incorporation method and stoichiometry as variables, the stoichiometric samples Pd/$LaMnO_3$ from sequential route showed the lower oxygen desorption than the one-pot $LaMn_{0.98}Pd_{0.02}O_3$ samples, implying poor molecular oxygen coverage and lattice oxygen reducibility of sequential ones. In addition, the lower calcination temperature brought the Pd/perovskites more oxygen desorption capacity. Both of above-mentioned results corresponded to the related hydrogen consumption from H_2-TPR measurements.

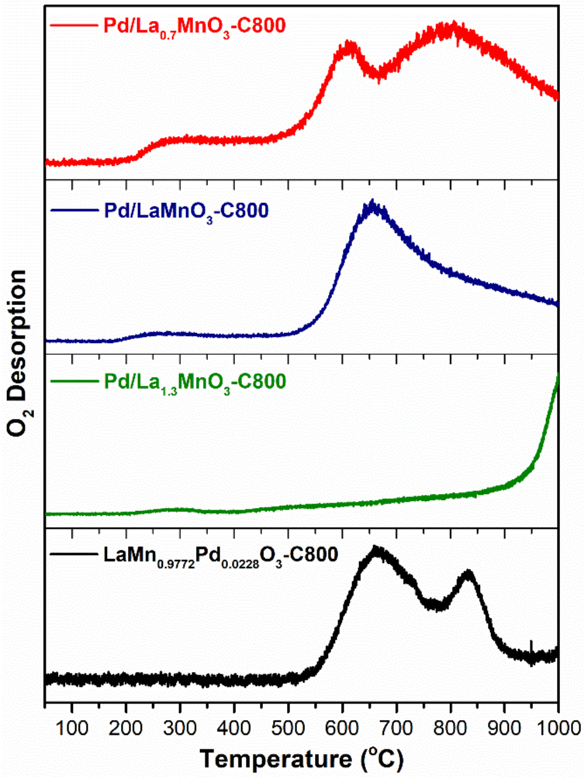

Fig.5.2.7. O_2-TPD-MS profiles: 800 °C Calcination Samples.

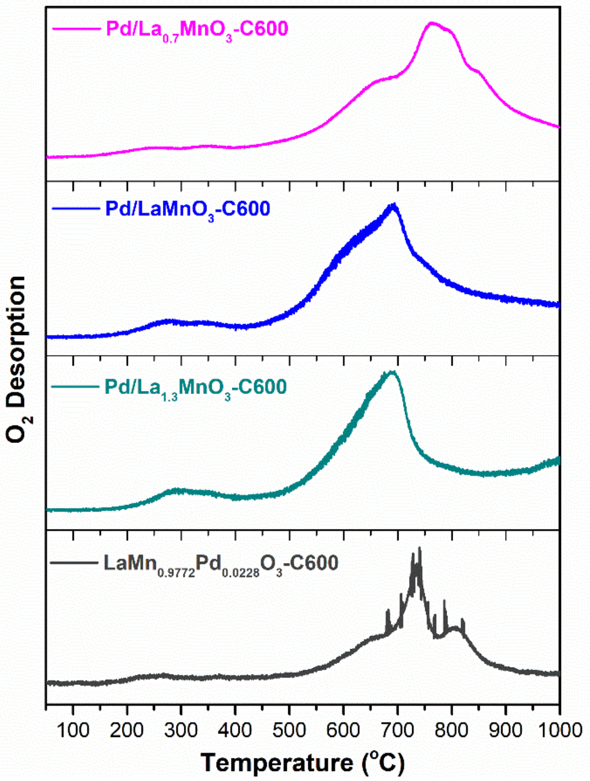

Fig.5.2.8. O_2-TPD-MS profiles: 600 °C Calcination Samples.

The same enhanced oxygen desorption effect was seen to the sequential Pd impregnated non-stoichiometric La-defect Pd/$La_{0.7}MnO_3$ composition, and the La-defect samples, especially the sample calcined at 800°C, still presented a broad flat α-O_2 desorption peak around 200 - 500 ◦C and without decay to the β-O_2 as desorption of Pd-free sample. Maintaining the significant enhancements of oxygen desorption was likely related to surface oxygen vacancies generated on Pd substitution and La-defect on surface and in structure. As to the La-excess ones, the C600 and C800 ones had the opposite results compared to stochiometric composition on oxygen desorption capacity.

Table 5.2.3. Amount of desorbed oxygen from O_2-TPD.

Catalyst	Amount of Desorbed Oxygen (mmol/g)		
	α-Oxygen[a]	β-Oxygen[b]	Total Amount
Pd/$La_{0.7}MnO_3$-C800	0.060	0.567	0.627
Pd/$LaMnO_3$-C800	0.012	0.320	0.332
Pd/$La_{1.3}MnO_3$-C800	-	-	0.521
$LaMn_{0.9772}Pd_{0.0228}O_3$-C800	-	0.497	0.497
Pd/$La_{0.7}MnO_3$-C600	0.130	0.720	0.850
Pd/$LaMnO_3$-C600	0.049	0.522	0.571
Pd/$La_{1.3}MnO_3$-C600	0.069	0.468	0.537
$LaMn_{0.9772}Pd_{0.0228}O_3$-C600	0.107	0.687	0.794

[a] T < 500 °C Oxygen desorption

[b] T > 500 °C Oxygen desorption

2.5. Surface analysis

For the study of surface properties, the measurements of XPS, H_2-chemisorption and N_2-physiosorption have been operated and the corresponding results have been summarized in the following Table 5.2.4. The Pd incorporation in tuning the surface properties of perovskite catalysts is an efficient route to methane activation in the low temperature range. In order to further study the impact of Pd doping methods, X-ray photoelectron spectroscopy (XPS) provides the two main results on the oxidation state of atoms and the related surface composition. The orbitals Pd 3d, La 3d, Mn 2p, Mn 3s and O 1s were analyzed and compared to investigate the related impacts and properties on palladium incorporation routes involving stoichiometry and Pd partial substitution based on La_xMnO_3 formula.

Besides, the dispersion and particle size of surface palladium species can be measured by hydrogen chemisorption method which provide a more convinced pathway to investigate the properties of surface precious metal. In addition, N_2-physisorption was used to analyze the surface construction of Pd/perovskite and their interaction micro-environments [54].

Generally, the calcination temperature, the Pd incorporation methods and the perovskite stoichiometry are the three vital variables that can affect the surface properties and bulk structure. For palladium species from Table 5.2.4 from both XPS and chemisorption results, the consistent trend showed the credibility of the double insurance. As a matter of fact, 1% low content Pd species of both synthesis routes were in the oxidation state PdO_x [55].

The examination of the specific surface area on impregnated samples does not reveal significant deviation compared to bare samples. As previously found calcination at 800°C has a strong detrimental effect with a loss of SSA except on La-deficient perovskites Pd/$La_{0.7}MnO_3$. Metallic palladium dispersion was estimated from H_2-chemisorption measurements performed at 100°C, taking a stoichiometric ratio H/Pd = 1. Prior chemisorption the catalysts were pre-reduced at 250°. Data in Table 4.14 reveals weak Pd dispersion on impregnated samples. Surprisingly, the highest metal dispersion is obtained on $LaMn_{0.98}Pd_{0.02}O_3$-C800 while $LaMn_{0.98}Pd_{0.02}O_3$-C600 exhibits Pd dispersion almost nil. These observations can be questionable in a certain extent as H_2-TPR experiment suggested a greater Pd-support interaction on this latter sample. HAAD-TEM analysis was performed to complement H_2-chemisorption.

High-angle annular dark-field imaging (HAADF) is an STEM/TEM technique which produces an annular dark field image formed by very high angle. This analysis was coupled to chemical analysis. Images were recorded in different scales from 600 nm to 7 nm. For $LaMn_{0.98}Pd_{0.02}O_3$-C600 (Fig.5.2.10) a very high Pd distribution is observed irrespective of the selective scales. In contrast, Fig.5.2.9 shows heterogeneous Pd distribution noticeable on $LaMn_{0.98}Pd_{0.02}O_3$-C800 with Pd-rich domain as exemplified coexisting with domains corresponding to homogeneous distribution.

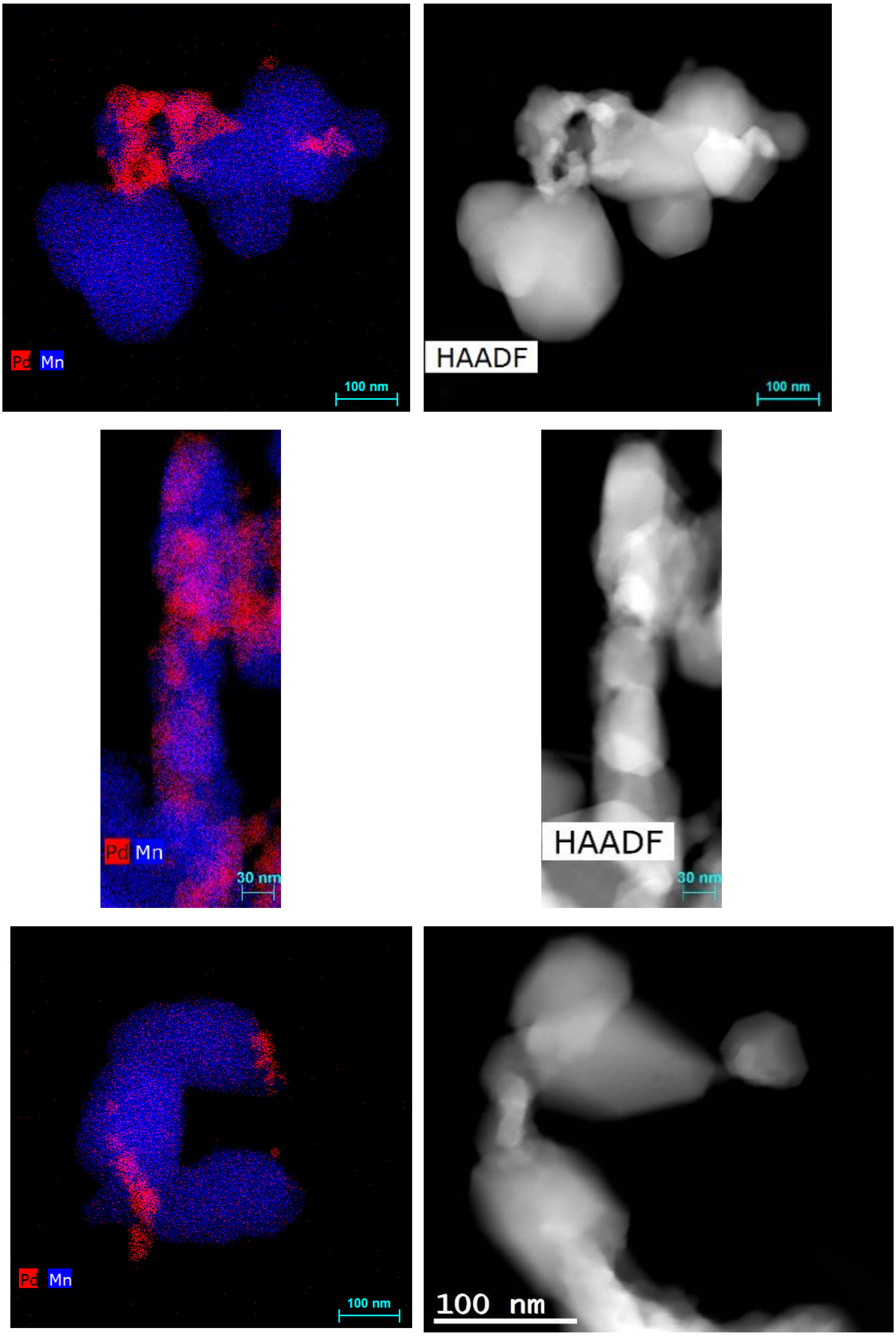

Fig.5.2.9. HAADF-S/TEM mapping of $LaMn_{0.98}Pd_{0.02}O_3$-C800.

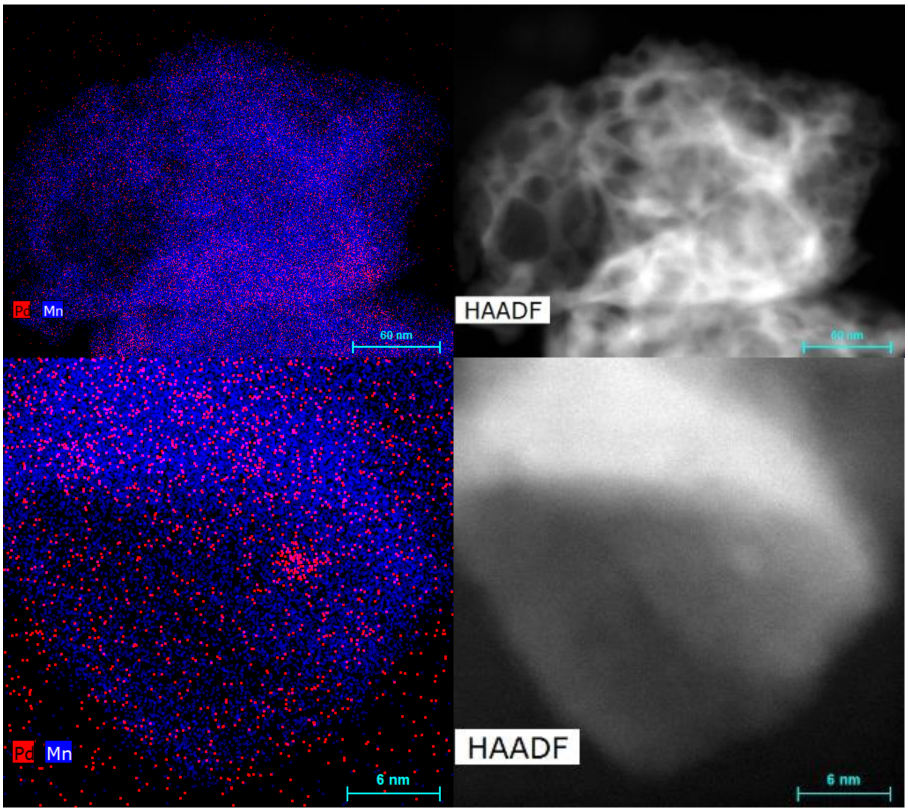

Fig.5.2.10. HAADF-S/TEM mapping of LaMn$_{0.98}$Pd$_{0.02}$O$_3$-C600.

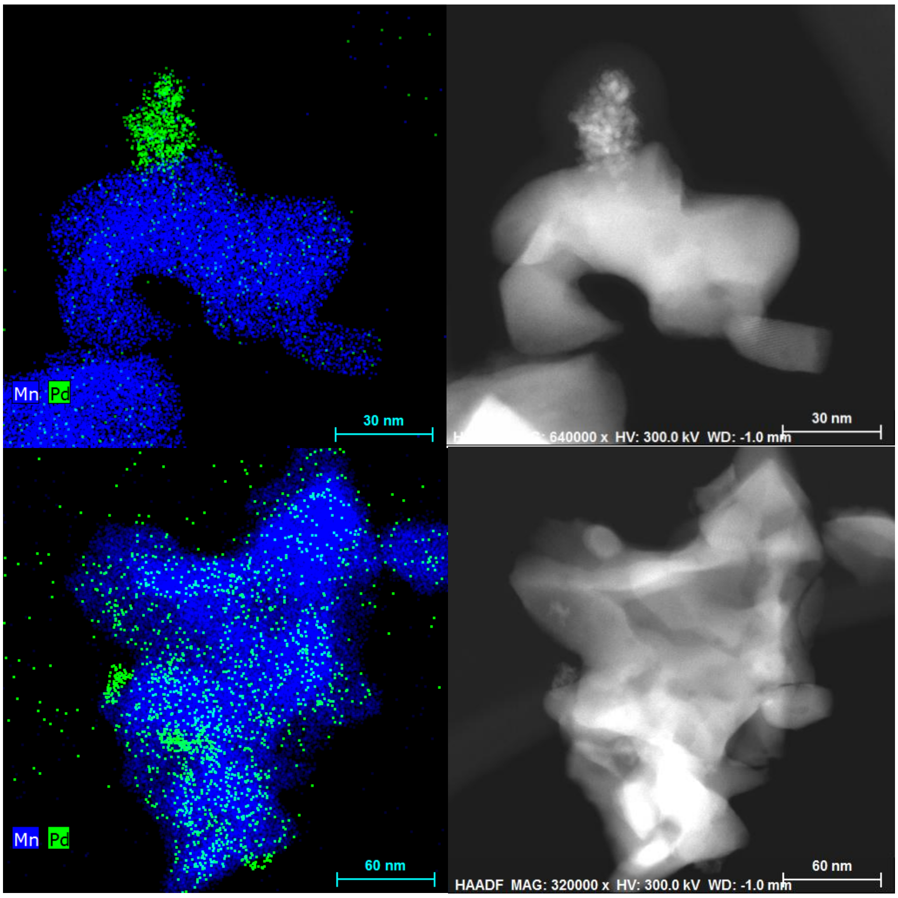

Fig.5.2.11. HAADF-S/TEM mapping of Pd/LaMnO$_3$-C600.

Regarding Pd/LaMnO$_3$-C600, it is obvious that Pd is more heterogeneously distributed in comparison with LaMn$_{0.98}$Pd$_{0.02}$O$_3$-C600. As exemplified in Fig.5.2.11, strong Pd aggregates form but coexist with domains characterized by a high Pd dispersion.

Returning to Pd dispersion some discrepancies appear with HAADF observation. However, those results can be reconciled by assuming that the pre-reduction temperature is not enough high to completely reduce Pd^{2+} species into metallic particles. This assertion seems to be acceptable at least for LaMn$_{0.98}$Pd$_{0.02}$O$_3$-C600 for which the very low metal dispersion does not fulfill the high degree of dispersion of oxidic Pd species on the calcined sample. Hence, one can expect a strong Pd-support interaction on LaMn$_{0.98}$Pd$_{0.02}$O$_3$-C600 which delays the reduction of oxidic palladium species. This conclusion could be also partly validated on Pd/LaMnO$_3$-C600 but in a certain extent as phase aggregation has been also characterized. Based on this the low Pd dispersion can account for the coexistence of unreduced PdO$_x$ species as well as large Pd particles. Now regarding the one-pot LaMn$_{0.98}$Pd$_{0.02}$O$_3$-C800 catalyst, it seems obvious that exsolution process may occur during the calcination but contrarily to impregnated Pd/LaMnO$_3$-C600 this ex-solution process is slow and avoid significant particle sintering.

Regarding XPS analysis, Pd 3d, La 3d, Mn 2p, Mn 3s and O 1s photo-peaks were analyzed. La 3d photopeak (see annexes Fig.5.2.S1) reveal similar spectral features as those already discussed on undoped samples. A dual-peak binding energy range from 833 eV to 838 eV is characteristic of La^{3+}. Semi quantitative analysis reveals a strong lanthanum enrichment on sample calcined at 600°C which tends to disappears when calcination proceeds at 800°C. The combination of Mn 2p (Fig.5.2.12) and Mn 3s (See Annexes Fig.5.2.S2) orbital studies provided the more convinced method to investigate the surface manganese. The Mn 2p spectra were deconvoluted following the previous studies of Biesinger et al. [29] and Abdallah et al. [26, 30]. From the figures of Mn 2p and the related calculation of Mn 3s from Table 5.2.4, the fact that lower calcination temperature can lead to higher surface Mn valence was confirmed. Interestingly, the

Mn^{3+}/Mn^{4+} ratio of Pd doped samples calcined at 800°C is higher than on undoped Pd samples. On the contrary, the Mn^{3+}/Mn^{4+} ratio showed the opposite trend for the series calcined at 600°C from comparison of Table 4.8 and Table 5.2.4. Such comparison suggests that calcination at 600°C is more favorable to stabilize Mn^{4+} species.

Oxygen species have been divided into three parts in Fig.5.2.13: lattice oxygen (O_{lat}: O^{2-}) in red curve, surface chemisorbed oxygen (O_{ads}: O^{2-}, O^{-}, O_2^{2-}) in blue and then adsorbed CO^{3-} and/or -OH containing oxygen matters in magenta [59]. The severe calcination temperature showed the positive effect on O_{ads}/O_{lat} ratio compared to lower sequential ones. And one-pot samples were generally high in value O_{ads}/O_{lat} ratio, but lower temperature one presented the highest level of chemisorbed surface oxygen (Table 5.2.4).

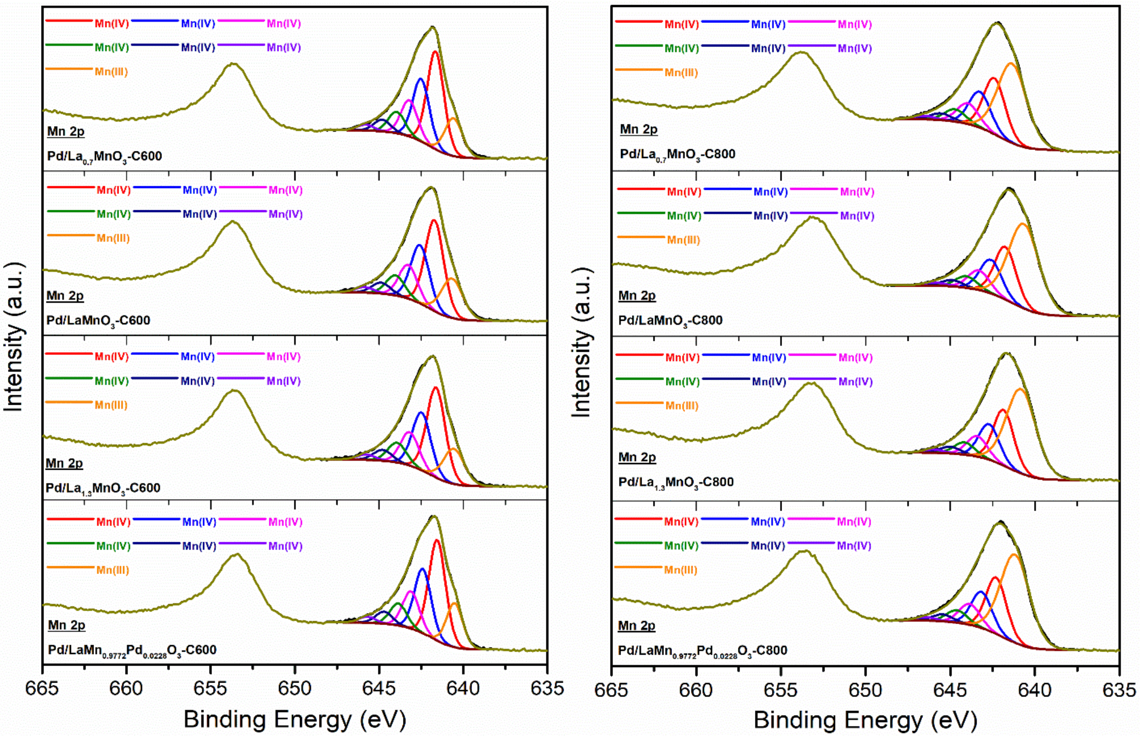

Fig.5.2.12. XPS spectrum of Mn 2p: One-pot and sequential samples.

XPS analysis can provide the Pd valence information, from Fig.5.2.14, Fig.5.2.15 and Fig.5.2.16, there is no Pd^0 species normally located around binding energy about 335 eV [56], PdO about 337 eV [57] and PdO_2 peak appeared around 339 eV [58]. The post-calcination samples were in the oxidation state globally, but the weak signals of

Pd/LaMnO3-C800 with high crystallinity and lowest specific surface area showed the almost only PdO.

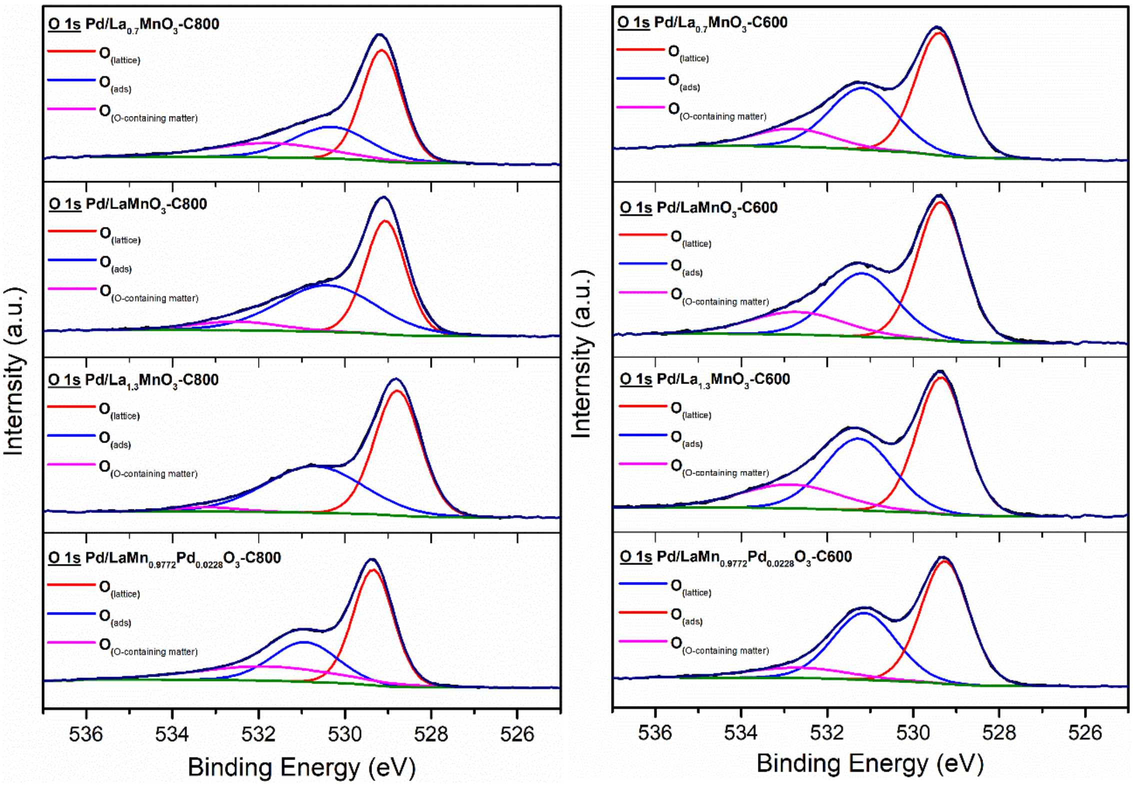

Fig.5.2.13. XPS spectrum of O 1s: One-pot and sequential samples.

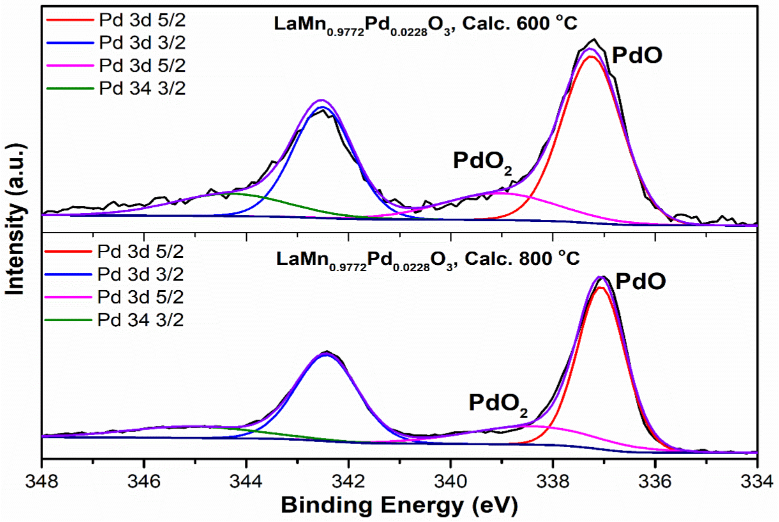

Fig.5.2.14. XPS spectrum of Pd 3d: One-Pot Calcination Samples.

Sample prepared by one-pot synthesis show that surface Pd/Mn ratio is sensitive to calcination temperature. The higher value obtained on $LaMn_{0.98}Pd_{0.02}MnO_3$-C800 seems to be in agreement with the segregation of more reducible PdO_x species coming from exsolution process and then responsible of higher H/Pd ratio from chemisorption measurements. In contrast, for $LaMn_{0.98}Pd_{0.02}MnO_3$-C600 the much lower Pd/Mn ratio reflects a minimization of ex-solution process with cationic palladium species less reducible in the perovskite lattice. There is no clear tendency if different coordination of extra-framework cationic Pd species would stabilize higher oxidation state. On the other hand, the stabilization of Mn^{4+} seems to be more favorable on samples calcined at 600°C. The 600 °C calcination samples held the higher SSA and manganese valences compared to severe 800 °C indicating a direct correlation among the calcination, specific surface area and Mn valences with the same variation trend between two valence orbitals of Mn 2p and Mn 3s.

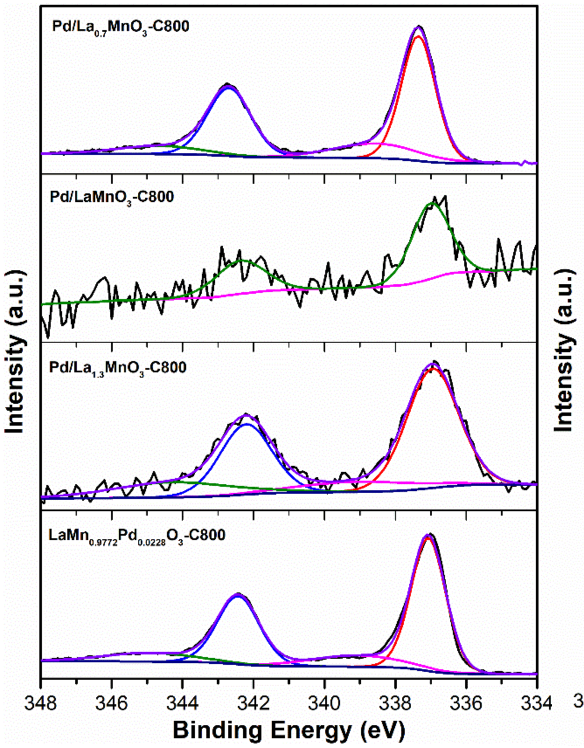

Fig.5.2.15. XPS spectrum of Pd 3d: 800 °C Calcination Samples.

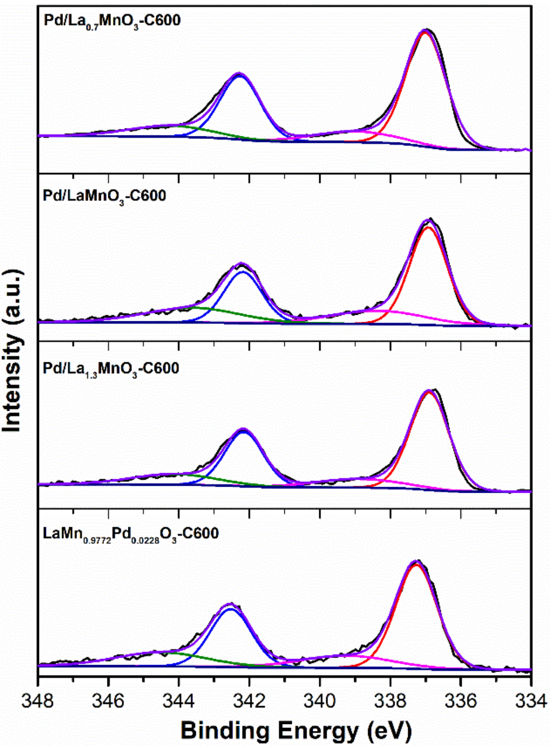

Fig.5.2.16. XPS spectrum of Pd 3d: 600 °C Calcination Samples.

Table 5.2.4. Summary of surface analysis of Pd incorporated perovskites.

Catalyst	XPS Analysis								Pd disp. (%) [g]	SSA[h] (m^2/g)
	Pd ratio (%)	Pd/La[a]	Mn/La[b]	Pd/Mn	Pd^{4+}/Pd^{2+} [c]	Mn^{3+}/Mn^{4+} [d]	Mn (AOS) [e]	$O_{(ads)}/O_{(lat)}$ [f]		
Pd/$La_{0.7}MnO_3$-C800	0.90	0.09	1.44	0.06	0.66	0.79	3.38	0.90	-	24.6
Pd/$LaMnO_3$-C800	0.07	0.01	0.86	0.01	-	0.94	3.45	0.99	5.4	7.4
Pd/$La_{1.3}MnO_3$-C800	0.44	0.03	0.61	0.05	0.31	0.91	3.65	0.79	-	17.6
$LaMn_{0.98}Pd_{0.02}O_3$-C800	2.01	0.14	0.75	0.19	0.40	0.92	3.48	0.81	28.2	6.4
Pd/$La_{0.7}MnO_3$-C600	2.44	0.22	1.04	0.21	0.14	0.17	3.62	0.71	6.2	29.4
Pd/$LaMnO_3$-C600	0.70	0.06	0.83	0.07	0.33	0.21	3.55	0.65	13	21.7
Pd/$La_{1.3}MnO_3$-C600	1.18	0.09	0.70	0.13	0.43	0.18	3.61	0.75	1	23.7
$LaMn_{0.98}Pd_{0.02}O_3$-C600	0.68	0.06	1.10	0.06	0.57	0.18	3.72	1.39	0.28	28.9

a. La/Pd ratio from XPS composition analysis

b. La/Mn ratio from XPS composition analysis

c. Pd^{4+}/Pd^{2+} ratio from XPS Pd 3d orbital

d. Mn^{3+}/Mn^{4+} ratio from XPS Mn 2p orbital

e. Mn average oxidation state (AOS) from XPS Mn 3s orbital

f. Oxygen adsorption species and lattice oxygen ratio from XPS O 1s orbital

g. Pd dispersion (%) from H_2-chemisorption measurements

h. Specific surface area from N_2-physisorption

3. Impact of palladium incorporation on the structural properties of Pd/$La_xA_{1-x}MnO_{3+\delta}$ catalysts (A=K, Sr)

3.1. Bulk reducibility from H_2-TPR

Following the same H_2-TPR/O_2-TPO experimental program (Fig.4.13), the reducibility of the 1wt.% Pd sequentially doped C600 samples were analyzed and the Fig.5.3.1 and Fig.5.3.2 showed the profiles of the K and Sr substituted series respectively and the quantitative results were calculated in Table 5.3.1.

In general, Pd impregnation obviously improved the reduction capacity of α-zone (T < 500 ºC) and the appearance of peak about 100 ºC could be attributed to the reduction signals of Pd species. Besides, the β-zone (T > 500 ºC) basically fixed in the same temperature positions. Quantitatively, the H/M ratio and hydrogen consumption decreased with increasing K and Sr substitution (Table 5.3.1).

Returning to bare $La_{1-x}K_xMnO_3$ and $La_{1-x}Sr_xMnO_3$ H_2-reduction profile (Fig.4.11, Fig.4.12) mainly underlined the two-step reduction process of Mn^{4+} to Mn^{2+}. A lower H_2 uptake recorded on $La_{1-x}K_xMnO_3$ emphasized a lower reducibility compared to $La_{1-x}K_xMnO_3$ and $La_{1-x}Sr_xMnO_3$ likely due to the growth of an extra composite material. XRD analysis also showed a greater crystallinity of K-substituted perovskite (Fig.4.1.7) with increasing K substitution. For Sr-substituted, a greater ability to stabilize Mn^{4+} was found.

The examination of Fig.5.3.1 and Fig.5.3.2 clearly shows a sharp shift of the low temperature reduction process on calcined Pd/$La_{1-x}K_xMnO_3$ while the high temperature does not seem to be significantly perturbated revealing comparable characteristics with the bare sample. It is not easy to distinguish the signal assigned to the reduction of PdO on this series which should occur at low T. In contrast PdO reduction appears more distinctly on Pd/$La_{1-x}Sr_xMnO_3$ with a weak contribution below 100°C. Surface and bulk reduction processed are also accelerated for Pd/$La_{1-x}Sr_xMnO_3$. A prominent reduction process takes place below 250°C with apparent maximum centered at lower temperature for x ≤ 0.05. The comparison of the total H_2-uptake reveals the same tendencies as on the undoped samples with lower values on Pd/$La_{1-x}K_xMnO_3$. Nonetheless, slight changes are noticeable on Pd/$La_{1-x}Sr_xMnO_3$ for x ≥ 0.1 with an increase in H_2-uptake.

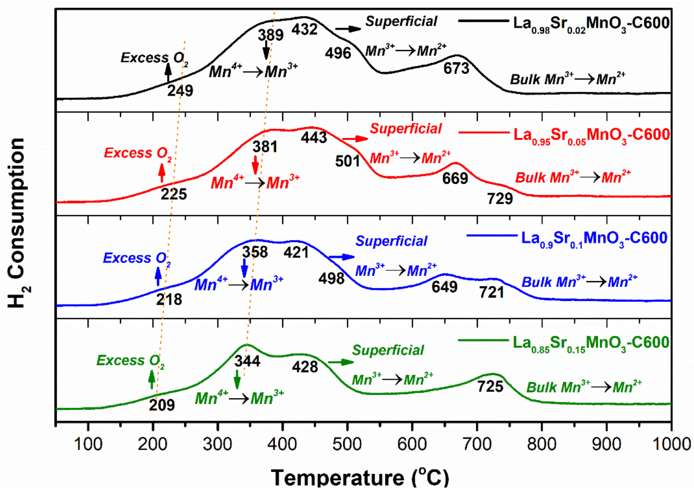

Fig.4.11. H_2-TPR profiles: (Black) $La_{0.98}Sr_{0.02}MnO_3$-C600; (Red) $La_{0.95}Sr_{0.05}MnO_3$-C600; (Blue) $La_{0.9}Sr_{0.1}MnO_3$-C600; (Olive)$La_{0.85}Sr_{0.15}MnO3$-C600 in overall temperature range.

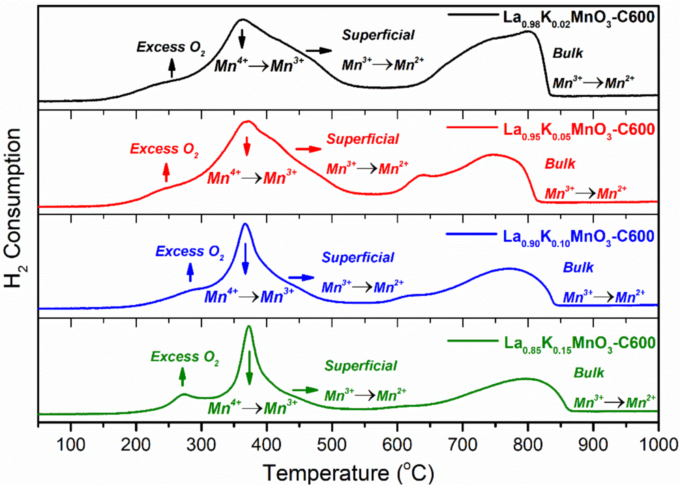

Fig.4.12. H_2-TPR profiles: (Black) $La_{0.98}K_{0.02}MnO_3$-C600; (Red) $La_{0.95}K_{0.05}MnO_3$-C600; (Blue) $La_{0.9}K_{0.1}MnO_3$-C600; (Olive)$La_{0.85}K_{0.15}MnO3$-C600 in overall temperature range.

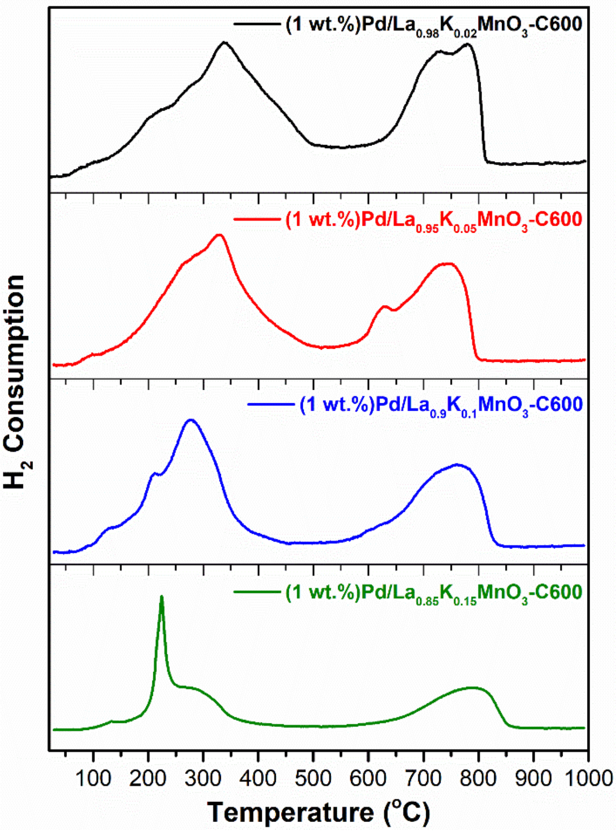

Fig.5.3.1 H_2-TPR of K substituted samples with Pd.

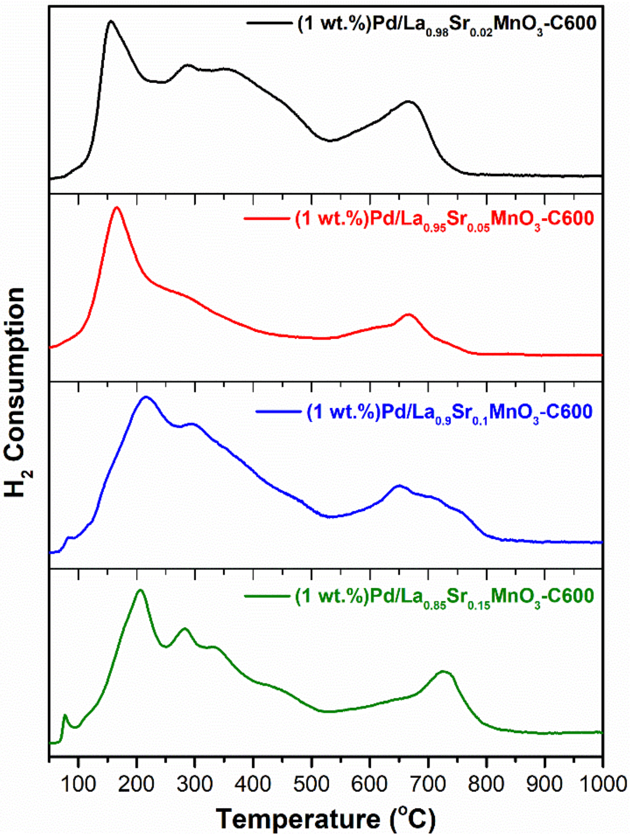

Fig.5.3.2 H_2-TPR of Sr substituted samples with Pd.

Table 5.3.1. H_2-TPR profiles quantitative analysis.

Catalyst	Total H_2 Consumption (mmol/g)	H_2 Consumption < 550 ºC (mmol/g)	Relative H_2 contribution (%) (< 550 ºC)	H/M [2]	SSA [1] (m^2/g)	Nomalized Consumption (mmol/m^2)
Pd/$La_{0.98}K_{0.02}MnO_3$-C600	3.7	2.2	59.1	1.8	26.3	0.14
Pd/$La_{0.95}K_{0.05}MnO_3$-C600	3.8	2.4	61.9	1.8	22.4	0.17
Pd/$La_{0.9}K_{0.1}MnO_3$-C600	3.3	2.0	59.4	1.5	19.8	0.17
Pd/$La_{0.85}K_{0.15}MnO_3$-C600	3.6	2.1	57.6	1.6	16.4	0.22
Pd/$La_{0.98}Sr_{0.02}MnO_3$-C600	4.5	2.8	62.1	2.2	21.0	0.21
Pd/$La_{0.95}Sr_{0.05}MnO_3$-C600	4.0	2.7	67.3	1.9	20.8	0.19
Pd/$La_{0.9}Sr_{0.1}MnO_3$-C600	4.1	2.6	63.3	2.0	25.7	0.16
Pd/$La_{0.85}Sr_{0.15}MnO_3$-C600	4.1	2.5	61.9	1.9	36.1	0.11

[1] SSA: Specific Surface Area.

[2] M = Pd + Mn

3.2. Bulk reoxidation of reduced sampled from O_2-TPO

Following the same H_2-TPR/O_2-TPO program (Fig.4.13), the re-oxidation ability of the 1wt.% Pd sequentially doped C600 samples followed the hydrogen reduction experiments. The Fig.5.3.3 and Fig.5.3.4 showed the profiles of the K and Sr substituted series respectively and the quantitative results were calculated in Table 5.3.2.

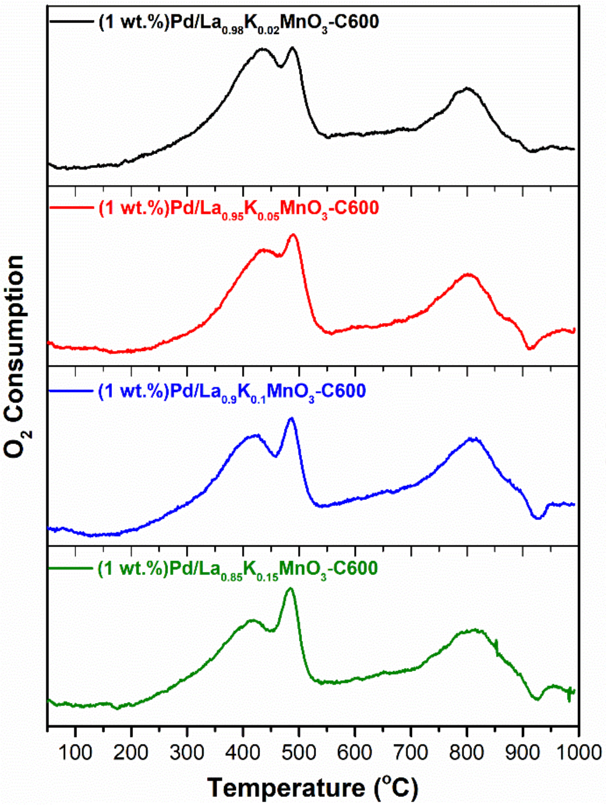

Fig.5.3.3 O_2-TPO of K substitution samples.

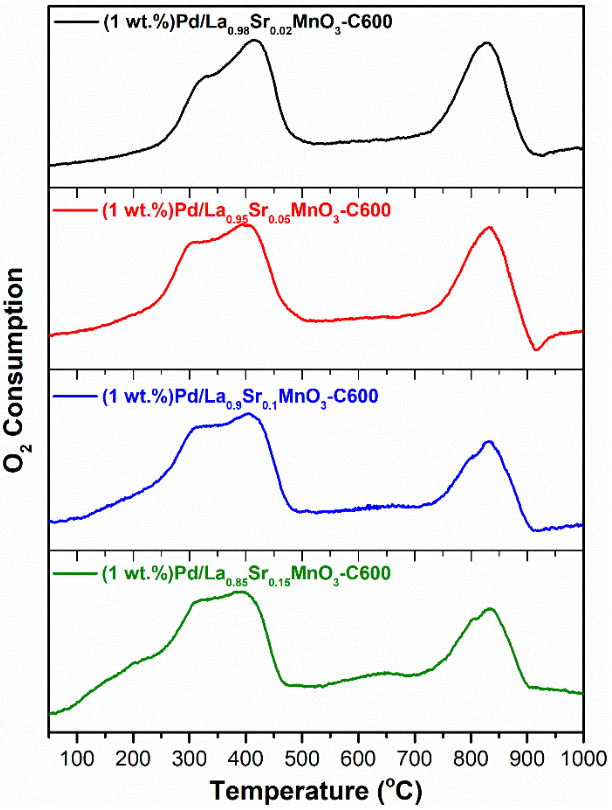

Fig.5.3.4 O_2-TPO of Sr substitution samples.

In general, Pd impregnation samples hold the same profiles (Fig.5.3.3, Fig.5.3.4) as the related perovskites without palladium doping (Fig.4.17, Fig.4.16) and two-step re-oxidation process took place and the restoration of the perovskite structure would start above 720°C. But the gas release appeared around 900 °C for the Sr substituted samples compared to the ones without Pd. And the K substituted samples showed the higher oxygen consumption values than the Sr substituted ones considering the oxygen consumption and O/M ratio (Table 5.3.2) which were the opposite of the previous reduction part (Table 5.3.1). This phenomenon was completely different from the perovskite series without palladium (Table 4.3), which showed that palladium impregnation brought a great impact on the redox process during perovskite reconstruction.

Table 5.3.2. Amount of oxygen consumption from O_2-TPO.

Catalyst	Total O_2 Consumption (mmol/g)	O/M [1]
Pd/$La_{0.98}K_{0.02}MnO_3$-C600	1.76	0.85
Pd/$La_{0.95}K_{0.05}MnO_3$-C600	1.62	0.78
Pd/$La_{0.9}K_{0.1}MnO_3$-C600	1.61	0.75
Pd/$La_{0.85}K_{0.15}MnO_3$-C600	1.62	0.74
Pd/$La_{0.98}Sr_{0.02}MnO_3$-C600	1.51	0.74
Pd/$La_{0.95}Sr_{0.05}MnO_3$-C600	1.68	0.81
Pd/$La_{0.9}Sr_{0.1}MnO_3$-C600	1.22	0.58
Pd/$La_{0.85}Sr_{0.15}MnO_3$-C600	1.22	0.58

[1] M = Pd + Mn

3.3. Oxygen desorption (O_2-TPD / MS)

The oxygen desorption was combined with mass spectrometry following the same protocol as former O_2-TPD program in order to avoid the overlap of oxygen and carbon dioxide and to calculate their quantitative study. Fig.5.3.5, Fig.5.3.6 and Table 5.3.3 showed the profiles and desorbed oxygen quantitative study of the K and Sr substitution series with 1wt.% Pd content impregnation. Let us notice that the catalyst was not pre-reduced prior to O_2-TPD experiments. Based on this, the impact of oxidic Pd species at the surface or sub-surface on the mobility of surface and sub-surface oxygen species can be examined.

The oxygen desorption of both presented the similar profiles as the series without Pd impregnation ones and the quantitative study showed more surface desorbed oxygen with Pd doping by wet-impregnation method indicating an improved surface oxygen mobility capacity. As to the total oxygen desorption amount (Table 5.3.3), Sr substitution samples increased while K substitution samples stayed stable with palladium incorporation, which could be attributed to the crystal formation to the Sr partially substituted samples. Hence, the oxygen desorption mainly depended on perovskite oxygen storage capacity. The deposition of palladium at the surface has no visible consequence on surface oxygen mobility.

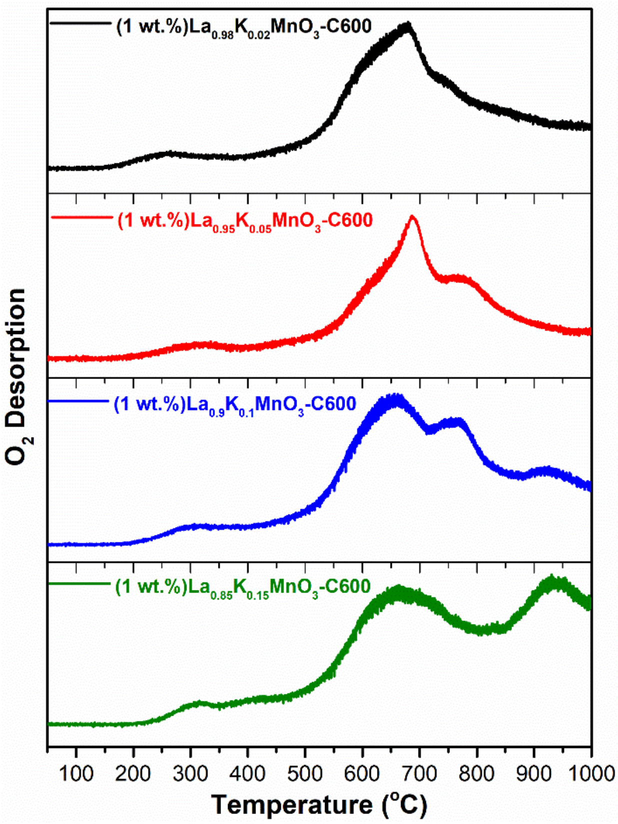

Fig.5.3.5 O_2-TPD of K substitution samples.

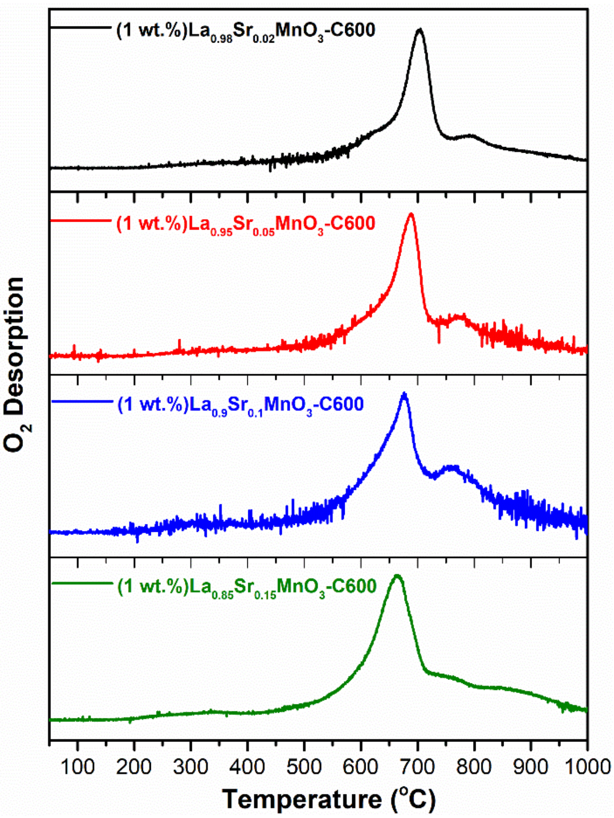

Fig.5.3.6 O_2-TPD of Sr substitution samples.

Table 5.3.3. Amount of desorbed oxygen from O_2-TPD.

Catalyst	Amount of Desorbed Oxygen (mmol/g)		
	α-Oxygen [a]	β-Oxygen [b]	Total Amount
Pd/$La_{0.98}K_{0.02}MnO_3$-C600	0.13	0.42	0.55
Pd/$La_{0.95}K_{0.05}MnO_3$-C600	0.16	0.39	0.55
Pd/$La_{0.9}K_{0.1}MnO_3$-C600	0.10	0.43	0.53
Pd/$La_{0.85}K_{0.15}MnO_3$-C600	0.11	0.46	0.57
Pd/$La_{0.98}Sr_{0.02}MnO_3$-C600	0.13	0.60	0.73
Pd/$La_{0.95}Sr_{0.05}MnO_3$-C600	0.14	0.61	0.75
Pd/$La_{0.9}Sr_{0.1}MnO_3$-C600	0.13	0.51	0.64
Pd/$La_{0.85}Sr_{0.15}MnO_3$-C600	0.12	0.51	0.63

[a] T < 500 °C Oxygen desorption

[b] T > 500 °C Oxygen desorption

3.4. Surface composition

The surface composition of the palladium incorporated catalysts based on K and Sr partially substituted perovskites was characterized by hydrogen chemisorption (H_2-Chemisorption), X-ray photoelectron spectroscopy (XPS) and N_2- physisorption, the combined study of the three methods can be used to study the surface properties of catalysts with more confidence on the impact of palladium incorporation (Table 5.3.4.) from the calculation of the A-site partial substitution catalysts (See annexes Fig.5.3.S1, Fig.5.3.S2, Fig.5.3.S3, Fig.5.3.S4 for XPS photo-peaks of A-site metals).

Firstly, the Pd species with the similar Pd 3d binding energy position (Fig.5.3.7, Fig.5.3.8) were in the oxidic state with Pd^{4+}/Pd^{2+} valences [55, 56, 57, 58] to all the partially substituted samples generally. And the surface Pd ratio and Pd dispersion indicated that slightly partial substitution by K and Sr seemed to be positive to the surface Pd state and stability (Table 5.3.4). Besides, the Pd dispersion from hydrogen chemisorption did not present the consistency with the specific surface areas of both of two substitution series.

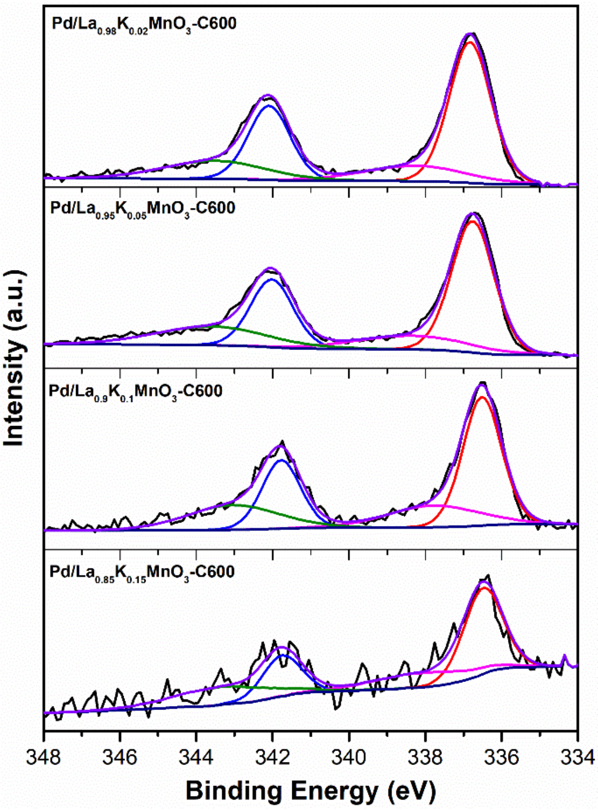

Fig.5.3.7 XPS analysis of Pd 3d orbital on K substitution samples.

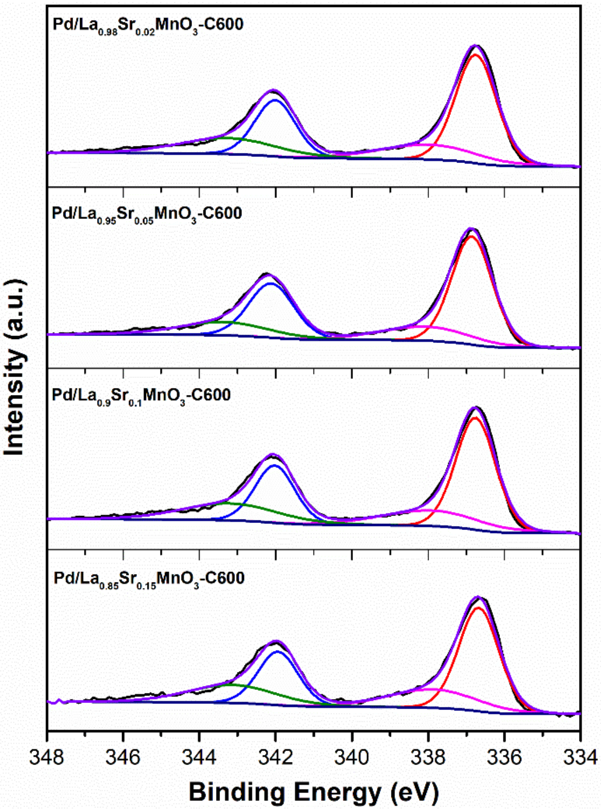

Fig.5.3.8 XPS analysis of Pd 3d orbital on K substitution samples.

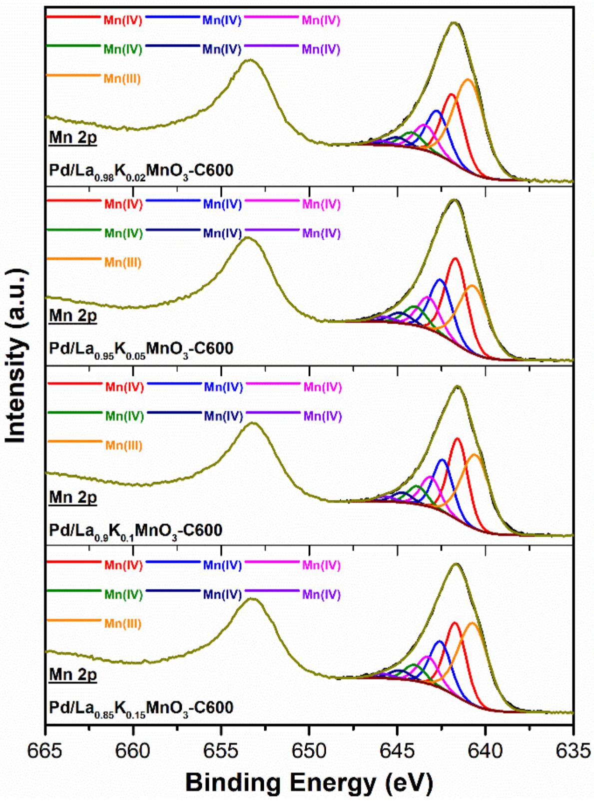

Fig.5.3.9 XPS analysis of Mn 2p orbital on K substitution samples.

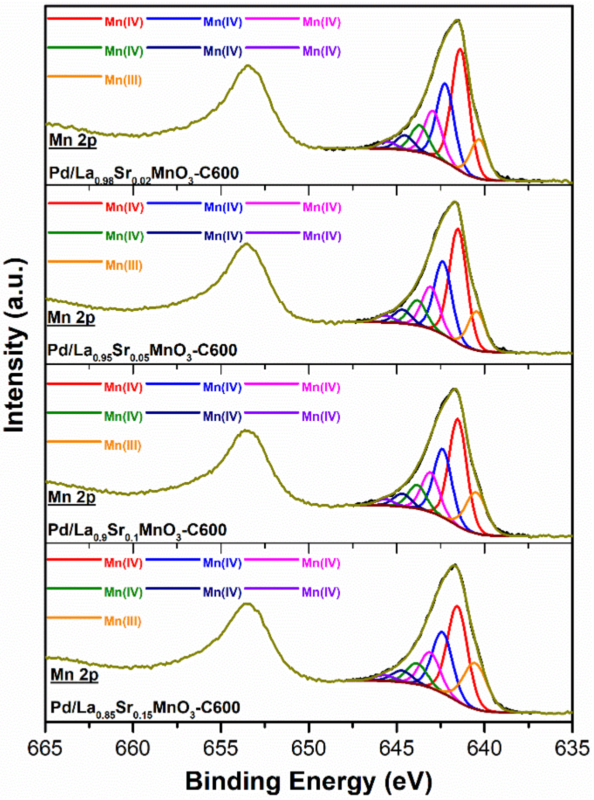

Fig.5.3.10 XPS analysis of Mn 2p orbital on Sr substitution samples.

The manganese valence states of the two series were investigated from Mn 2p and Mn 3s combination following the Mn 2p studies of M. Biesinger et al. [29] with six peaks of Mn (IV) and one peak of Mn (III) [26, 30] in Fig.5.3.9 and Fig5.3.10 and the Mn 3s orbitals analysis from multiplet splitting of Mn 3s peak [31] in Fig.5.3.11 and Fig.5.3.12. The related calculation was listed in Table 5.3.4 showing that Sr substituted samples presented higher valence state than K substituted ones on both Mn 2p and Mn 3s calculation in general.

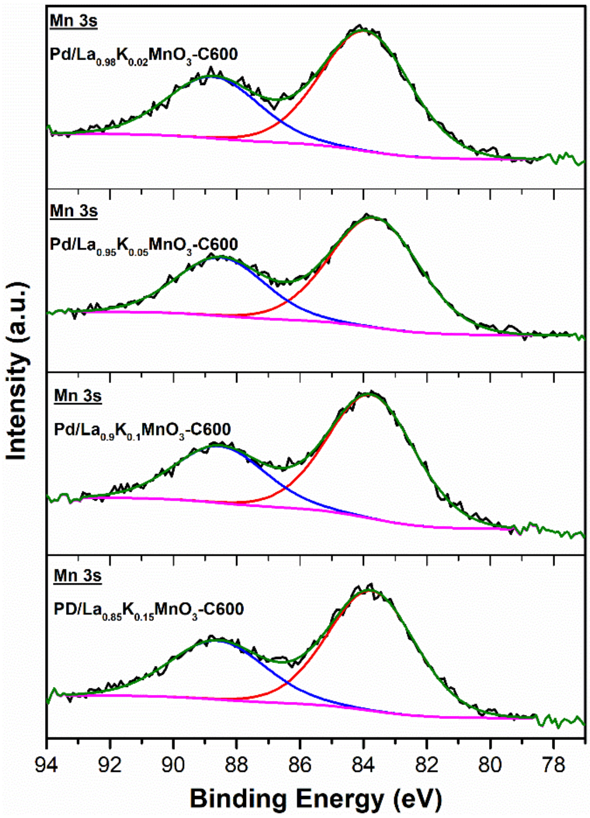

Fig.5.3.11 XPS analysis of Mn 3s orbital on K substitution samples.

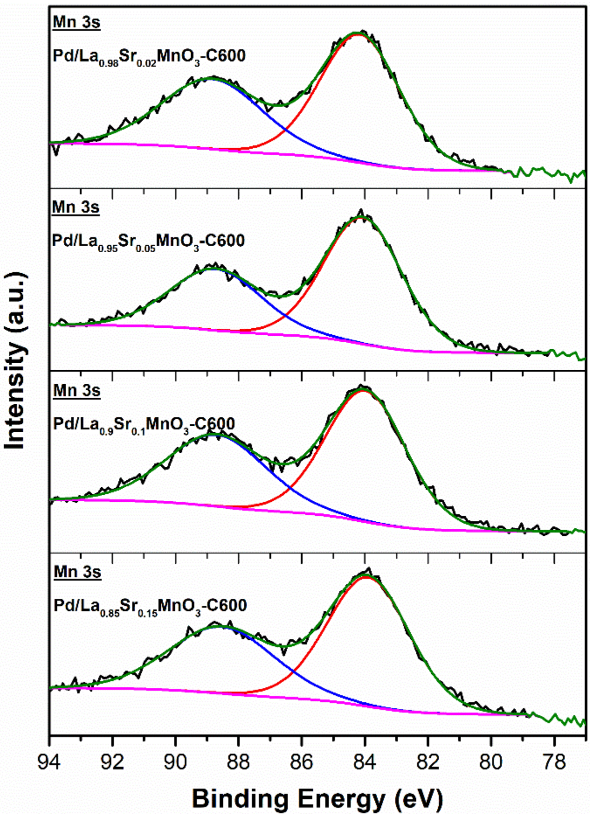

Fig.5.3.12 XPS analysis of Mn 3s orbital on Sr substitution samples.

In addition, K substitution samples hold the similar Mn valence state with all in crystal state, and the Sr substitution ones showed also the similar Mn valence state with the gradual formation of a crystalline state from XRD spectrum (Fig.4.8) indicating that the crystalline or amorphous state of perovskite seemed not strictly related to the nature of oxidic manganese species at the surface and the surface valence of manganese.

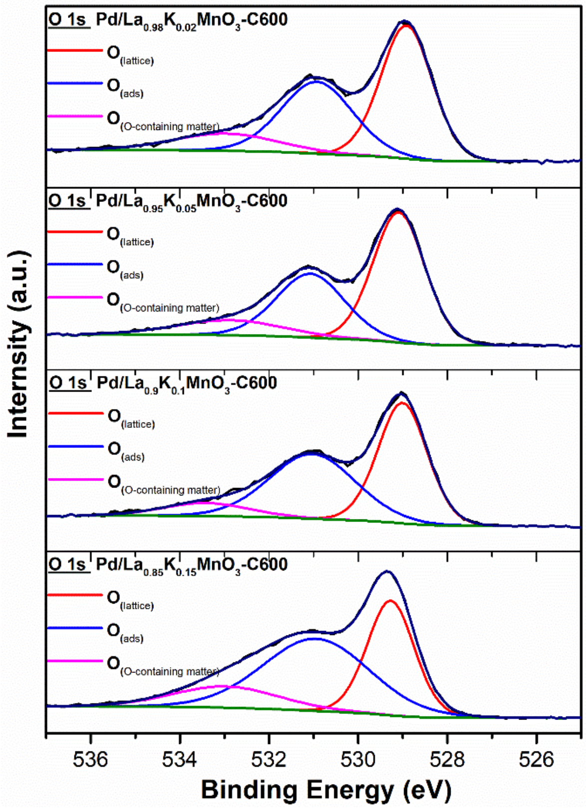

Fig.5.3.13 XPS analysis of O 1s orbital on K substitution samples.

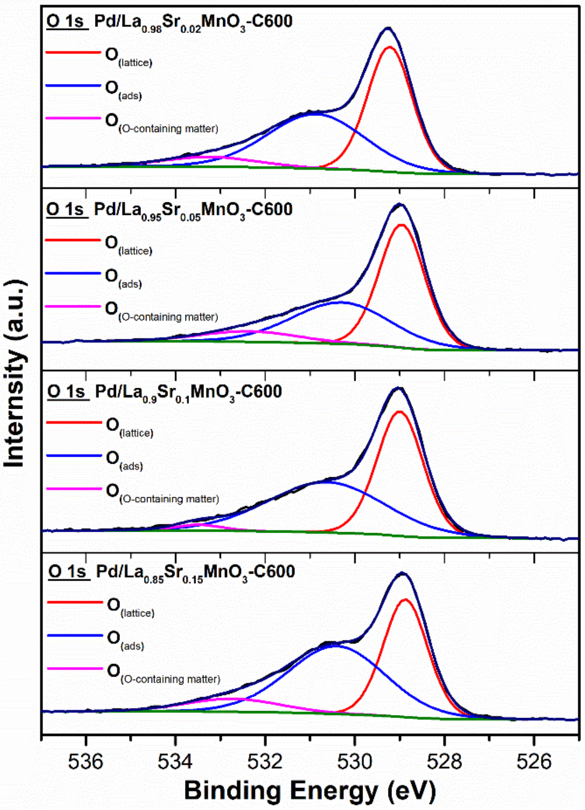

Fig.5.3.14 XPS analysis of O 1s orbital on Sr substitution samples.

The binding energy position and profiles of O 1s orbital of the samples were presented in Fig.5.3.13 and Fig.5.3.14 with mainly the lattice and surface adsorbed oxygen and little other oxygen-containing substances [59]. And the O_{ads}/O_{lat} ratio seemed rising with increasing both of K and Sr amount substitution showing that the surface (Table 5.3.4).

Table 5.3.4. Summary of surface analysis of Pd incorporated perovskites.

Catalyst	**XPS Analysis**								**Pd disp. (%) [e]**	**SSA[f] (m^2/g)**
	Pd ratio (%) [a]	$\frac{Pd}{\mathrm{La+K/Sr}}$	$\frac{Mn}{\mathrm{La+K/Sr}}$	$\frac{Pd}{\mathrm{Mn}}$	$\frac{Pd^{4+}}{Pd^{2+}}$	$\frac{Mn^{3+}}{Mn^{4+}}(b)$	**Mn (AOS) [c]**	$\frac{O_{ads}}{O_{lat}}(d)$		
Pd/$La_{0.98}K_{0.02}MnO_3$-C600	1.90	0.03	0.25	0.13	0.38	0.79	3.54	0.94	1.38	26.3
Pd/$La_{0.95}K_{0.05}MnO_3$-C600	2.41	0.05	0.40	0.12	0.43	0.44	3.48	0.73	0.08	22.4
Pd/$La_{0.9}K_{0.1}MnO_3$-C600	1.29	0.03	0.39	0.07	0.56	0.56	3.56	1.02	0.34	19.8
Pd/$La_{0.85}K_{0.15}MnO_3$-C600	0.32	0.01	0.28	0.02	0.63	0.67	3.48	1.27	0.02	16.4
Pd/$La_{0.98}Sr_{0.02}MnO_3$-C600	2.75	0.23	0.81	0.28	0.45	0.14	3.69	0.75	2.28	21.0
Pd/$La_{0.95}Sr_{0.05}MnO_3$-C600	1.94	0.15	0.81	0.19	0.36	0.14	3.70	0.64	12.4	20.8
Pd/$La_{0.9}Sr_{0.1}MnO_3$-C600	2.89	0.22	0.70	0.31	0.47	0.19	3.65	0.94	8.08	25.7
Pd/$La_{0.85}Sr_{0.15}MnO_3$-C600	1.37	0.10	0.68	0.14	0.52	0.24	3.71	1.42	2.02	36.1

a. Pd ratio (%) from XPS composition study

b. Mn^{3+}/Mn^{4+} ratio from XPS Mn 2p orbital

c. Mn average oxidation state (AOS) from XPS Mn 3s orbital

d. Oxygen adsorption species and lattice oxygen ratio from XPS O 1s orbital

e. Pd dispersion (%) from H_2-chemisorption measurements

f. Specific surface area from N_2-physisorption

4. Conclusion

Pd deposition has been investigated in this chapter according to two different procedures. The Pd was fixed at 1 wt.%. The first method was a classical sequential approach consisting in the impregnation of the perovskite substrates and then a calcination in air at 400°C. For the second one-pot method, palladium is introduced in the course of the sol gel procedure. In this latter case, the calcination was proceeded at much higher temperature to obtain the perovskite rhombohedral structure*, e.g.* 600°C or 800°C in air. One has to mention that calcination at 600°C led to more amorphous structure with residual bulk detectable impurities while at high temperature the formation of a well-crystallized pure structure was observed from XRD analysis. On the other hand, low calcination temperature preserves enough specific surface area needed for the dispersion of oxidic Pd species through the impregnation method.

According to above two protocols, drastic changes in the palladium distribution are expected as oxidic Pd species should segregate predominantly at the surface on the outermost layer of the perovskite on impregnated Pd/$LaMnO_3$ samples whereas Pd should be homogeneously distributed in the volume of the grain size for the sol gel $LaMn_{0.98}Pd_{0.02}O_3$ samples. Different techniques were implemented for the bulk and surface characterization. The reducibility of oxidic manganese species obeys to a two-step process starting from Mn^{4+} to Mn^{2+} and a more extensive reduction is observed when cationic palladium species are stabilized in the perovskite lattice in the series $LaMn_{0.98}Pd_{0.02}O_3$. O_2-TPD analysis also evidences improved oxygen desorption on one-pot samples. However, bulk oxygen mobility is deteriorated on well-crystallized perovskites, *e.g.* calcined at 800°C. As a matter of fact, the most prominent parameter which affects oxygen mobility seems to be the presence of defective sites due to La-deficiency with improved surface and bulk oxygen desorption.

Regarding oxidic palladium species their reducibility differs as isolated cationic palladium species in the perovskite are less reducible than extra-framework PdO_x species. Unexpectedly, H_2-chemisorption measurements on pre-reduced samples at

250°C revealed the highest Pd dispersion on $LaMn_{0.98}Pd_{0.02}O_3$ calcined at 800°C. At this reduction temperature the rhombohedral structure of the perovskite is conserved. In fact, HAADF-TEM measurements shows that Pd^{n+} species remains extremely dispersed and unreduced in this temperature conditions leading to very low H/Pd values from H_2-titration when $LaMn_{0.98}Pd_{0.02}O_3$ is calcined at 600°C. In contrast calcination at 800°C provokes Pd ex solution with the resulting segregation of small Pd particles at the surface which probably originates the high H/Pd ratio observed on this catalyst. Interestingly, HAADF-TEM also evidences highly dispersed Pd species coexisting with larger aggregates.

Finally, surface analysis from XPS agree with previous observations showing that Mn^{4+} species are better stabilized at the surface on samples calcined at 600°C. Except for $LaMn_{0.98}Pd_{0.02}O_3$ exhibiting low surface Pd concentration a surface Pd-enrichment is noticeable on sample calcined at 600°C. The high surface Pd concentration agree with exsolution process leading to more reducible PdO_x species and well-dispersed once reduced. Palladium oxide was found stabilized in +II and +IV oxidation. However, no discernible correlation was observed according to the dispersion of the chemical environment, e.g. lattice or extra lattice species.

Palladium has been incorporated to $La_{1-x}K_xMnO_3$ and $La_{1-x}Sr_xMnO_3$ by wet impregnation. It has been observed that bulk properties are weakly perturbated. As a general trend, no distinct evolution of the oxygen mobility is discernible. Pd dispersion are rather low exceptionally on $La_{1-x}K_xMnO_3$ despite comparable dispersion with $La_{1-x}Sr_xMnO_3$ but such observation seems to be in agreement with the lower surface concentration of palladium. For $La_{1-x}Sr_xMnO_3$ surface Mn enrichment takes place and correspond to a greater stabilization of Mn^{4+} compared to $La_{1-x}K_xMnO_3$. As a matter of fact, such a trend confirm previous observation as the formation of binary K/Mn structure would block the oxidation state of Mn^{3+}.

5. An attempt to optimize perovskite formulation on palladium incorporated $La_xSr_{0.15}MnO_{3+\delta}$ for methane catalytic combustion

5.1. Introduction

After nearly a century of mature development of the catalytic industry, single precious or base metal catalysts have been widely studied, breakthrough progress is becoming more and more difficult. Among them, noble metal catalysts are widely used in the fields of energy chemical industry and environmental protection, such as automobile exhaust purification, hydrogen fuel cells, petroleum refining, biomass and solid waste conversion and utilization, etc. Due to the high price and limited reserves of precious metals, reducing the amounts of precious metals in catalysts has been a major challenge in the field of catalysis. As to methane catalytic oxidation, Palladium as a precious metal, which is treated as the most efficient metal for the methane strong C-H bond breaking at low temperature, is particularly special for the remove of trace amounts of methane in the emission of natural gas vehicles (NGVs) [59]. In an era of diverse fuel sources with the huge world-wide resources of natural gas (much larger than crude oil), the study of Pd based catalyst for methane oxidation is of great practical and future significance [60].

In recent years, composite metal oxide catalyst more and more attracted the interests of the catalytic scientists in methane catalysis, such as perovskite materials [61], high entropy metal alloys (HEAs) [62], cerium oxide supported palladium [63] and spinel metal oxides [64] because their shape, structure and surface properties of composite metals influence each other, and the characteristics of various metal oxides can work together with surprising synergy effect and strengthened efficiency of methane catalysis. In the aforementioned study of methane catalysis, Pd is treated as the most efficient metal for the methane strong C-H bond breaking at low temperature [65], as a result, palladium is chosen as one of the candidate materials in this study. In the same time, the above-mentioned polymetallic oxide catalysts provided also the methods to protect the Pd species from poisoning and sintering. For example, the spinel metal oxide $MgAl_2O_4$ substrate, which is difficult to be reduced, can inhibit the excessive oxidation of Pd in the hyperoxic environment and maintain the catalytic active structure of Pd-PdO_x at temperatures as high as 800-1200°C [64]. And both of the perovskite and high entropy metal oxide have been reported for their noble metal self-regeneration property [41, 66], which is helpful to protect the interface of Pd, PdO_x and/or Pd/PdO_x with their unique advantages of noble metal protection from perovskite [74] in order to improve its high activity and hydrothermal stability for NGVs three-way catalyst.

M. Richard et al. pointed the ground state of free oxygen molecules could be activated by a sequential electron transfer leading to the formation of reactive superoxide (O^{2-}), peroxide (O_2^{2-}) and oxide species (O^{2-}) and the formation of reactive oxygen species could also occur without electron transfer by chemically active singlet oxygen (1Δg) formation with an obviously reduced the Pd content realized on dual-bed $LaMnO_3$-Pd/YSZ [67]. Depending on the drastic rate enhancement observed on the oxygen exchange which positively influences the rate of methane oxidation in connection with the creation of more reactive oxygen species, P. Granger proposed $LaMnO_3$ perovskite validation and interesting prospects regarding the feasibility of developing the former dual-bed catalytic systems for the abatement of methane at low temperature [68].

However, the factors affecting the catalytic effect have become more and more complex, the control of metal-support interactions is such significant to improve composite catalysts in heterogeneous catalysts to enhance activity and selectivity [69]. Hence, the content of various metals in the composite catalyst, temperature, location of active metals, catalyst structure and synthesis method, cost control and so on are all factors that need to be considered. Therefore, how to conduct research methodology efficiently becomes particularly important. Besides the impact of specific shape of noble metal [65], in particular, reducing the use of precious metals to low or even ultralow content appears to be of realistic and future significance. For example, traditionally, the distance between the two active sites of a catalyst is considered as "closer is better". In previous studies, the precious metal Pt is usually placed inside the support channel, and the distance between the two active sites is considered as "closer is better". Under the goal of reducing the content of precious metals, K. Chen et al. [70] studied the position of Pt metal in the composite catalyst and found that when 0.01% nano-scale Pt was located in the pore mouth of the support, the catalytic efficiency was increased by orders of magnitude and the cost advantage was extremely high, which is very instructive for the thesis work on combination of Pd and perovskite.

In the exhaust gas composition of NGVs, NO is a pollution gas that cannot be ignored. Kim et al. [71] studied Pd based Sr-substituted perovskite $La_{0.9}Sr_{0.1}CoO_3$ and $La_{0.9}Sr_{0.1}MnO_3$ for treating NO_x reduction with significant performance and pointed the potential of Pd/perovskite catalysts as a viable substitute in reducing the NO_x gas and the cost of three-way catalytic system.

Besides, our previous study on Pd/$La_{0.85}Sr_{0.15}MnO_3$-C600 perovskite (See later catalytic reaction part) had a significant methane oxidation performance among the 16 ones during the first time high-throughput reactions at RealCat Platform in Centrale Lille Engineering School. Therefore, the combination of low Pd content and Sr partially substituted $LaMnO_3$ perovskite has been chosen as our strategical formulation to methane catalytic combustion for methane exhaust trace. As a result, the combination of design of experiments (DOE) and high-throughput experiments (HTE) has been chosen as the efficient methodology to optimize the composition of multi-elemental composite while providing the interactions and impacts of factors among the huge amounts of data [72].

For the series of perovskite catalysts using a factorial reduced matrix, there are always two different factors between samples. However, the relevant analysis reports are not yet available from the DOE partners, we firstly studied the overview of this series from physicochemical properties in bulk and on surface. Besides, the post-reaction XPS analysis results from high throughput are listed in the annexes of this chapter and the methane catalytic measurements in real near-stoichiometric exhaust gas condition are analyzed in Chapter VII.

In conclusion, on the basis of the previous study of perovskite-based catalyst with 1wt.% Pd content for first high throughput methane catalytic oxidation measurements, 1%Pd/$La_{0.85}Sr_{0.15}MnO_3$-C600 was found the optimal catalyst. Hence, depending on the four factors: calcination temperature, palladium content, palladium incorporation method and perovskite A-site defect, the attempt to optimize perovskite formulation based on palladium incorporated $La_xSr_{0.15}MnO_{3+\delta}$ with DOE design was planned in the second high throughput methane catalytic oxidation. Considering the scientific and industrial significance of reducing Pd content, to investigate the internal synergy property between palladium incorporation and related perovskite factors, it is necessary as an efficient method to optimize the formulation of perovskite catalyst particularly in the three-way catalytic system of natural gas vehicle engines working in extreme environments.

5.2. Design of experiments

The design of experiments (DOE) method includes two parts: design of experiments and analysis of data. The first part contains variable selection, factor coding, spreadsheet and experimental operation; the latter part concerns statistic model, the relationship of data results and optimization [73]. Depending on the working situation and the suggestion from Prof. M. Bigan of Department of Chemistry in Lille University, the fractional factorial design become the choice.

Table 5.5.1. Factor choices for $La_xSr_{0.15}MnO_3$ formulation.

Factors (X)	Level -1	Level 0	Level +1
Calcination Temperature X1 (°C)	600	700	800
Pd content X2 (wt.%)	0,5	0.75	1
A-site stoichiometry (fixed $Sr_{0.15}$) X3	0,7	0.85	1
Incorporation mode X4	Sequential	Sequential	One-pot

For coding the 4 factors (Table 5.5.1), a full design needs 16 experiments, considering our working situation, a reduced matrix has been given with 8 experiments and 3 repetitions as the center of the statistical response surface in order to better understanding the impact proportion of every factor and their corresponding interaction.

Table 5.5.2. Factor coding for $La_xSr_{0.15}MnO_3$ formulation.

X1	X2	X3	X4
-1	-1	-1	-1
+1	-1	-1	+1
-1	+1	-1	+1
+1	+1	-1	-1
-1	-1	+1	+1
+1	-1	+1	-1
-1	+1	+1	-1
+1	+1	+1	+1
0	0	0	0
0	0	0	0
0	0	0	0

Then, the 4 factors above are substituted into the below Table 5.5.2 and Table 5.5.3 is obtained with the catalyst formulation that need to be prepared and then tested following the interested research fields. Besides, three impact concerned (methane oxidation conversion, palladium dispersion, specific surface area) are chosen as our interested studies. And one bare perovskite ($La_{0.7}Sr_{0.15}MnO_3$–C700) without Pd doping is added into this framework as a reference.

Table 5.5.3. Catalyst design for $La_xSr_{0.15}MnO_3$ formulation.

Factor	X1	X2	X3	X4	Catalysts to test
Exp. No	T °C	Pd	Metal (La/Sr)	Pd-Incorporation mode	
1	600	0,5	0,7(0.55/0.15)	sequential	0.5%Pd/($La_{0.55}Sr_{0.15}MnO_3$ - C600)
2	800	0,5	0,7(0.55/0.15)	one pot	$La_{0.55}Sr_{0.15}Mn_{0.9909}Pd_{0.0091}O_3$ - C800
3	600	1	0,7(0.55/0.15)	one pot	$La_{0.55}Sr_{0.15}Mn_{0.9818}Pd_{0.0182}O_3$ - C600
4	800	1	0,7(0.55/0.15)	sequential	1%Pd/($La_{0.55}Sr_{0.15}MnO_3$ - C800)
5	600	0,5	1(0.85/0.15)	one pot	$La_{0.85}Sr_{0.15}Mn_{0.9890}Pd_{0.0110}O_3$ - C600
6	800	0,5	1(0.85/0.15)	sequential	0.5%Pd/($La_{0.85}Sr_{0.15}MnO_3$ - C800)
7	600	1	1(0.85/0.15)	sequential	1%Pd/($La_{0.85}Sr_{0.15}MnO_3$ - C600)
8	800	1	1(0.85/0.15)	one pot	$La_{0.85}Sr_{0.15}Mn_{0.9779}Pd_{0.0221}O_3$ - C800
9	700	0.75	0.85(0.7/0.15)	sequential	0.75%Pd/($La_{0.7}Sr_{0.15}MnO_3$ – C700)
9	700	0.75	0.85(0.7/0.15)	sequential	0.75%Pd/($La_{0.7}Sr_{0.15}MnO_3$ – C700)
9	700	0.75	0.85(0.7/0.15)	sequential	0.75%Pd/($La_{0.7}Sr_{0.15}MnO_3$ – C700)

5.3. Bulk properties

5.3.1. X-ray diffraction

X-ray diffraction (XRD) is used to study the perovskite crystalline states (Fig.5.5.1), in general, crystal formation depends on the calcination temperature and preparation method, and palladium content and A-site lanthanum defect have no obvious effect on the structure of perovskite crystal. These samples basically conformed to the crystal reflections of the reference strontium partially substituted perovskite ($La_{0.8}Sr_{0.2}MnO_3$ PDF 01-075-3215).

The two 600 °C calcinated sequential samples (0.5%Pd/$La_{0.55}Sr_{0.15}MnO_3$-C600, 1%Pd/$La_{0.85}Sr_{0.15}MnO_3$-C600) do not present the crystalline state compared to the other samples. Among the 600 °C samples (black, dark yellow, cyan and magenta), one-pot method seemed to contribute to forming perovskite crystal structure regardless of Pd content or A-site defect, which means one-pot palladium incorporation seemed to be helpful to form perovskite crystals compared to the sequential wet-impregnated ones.

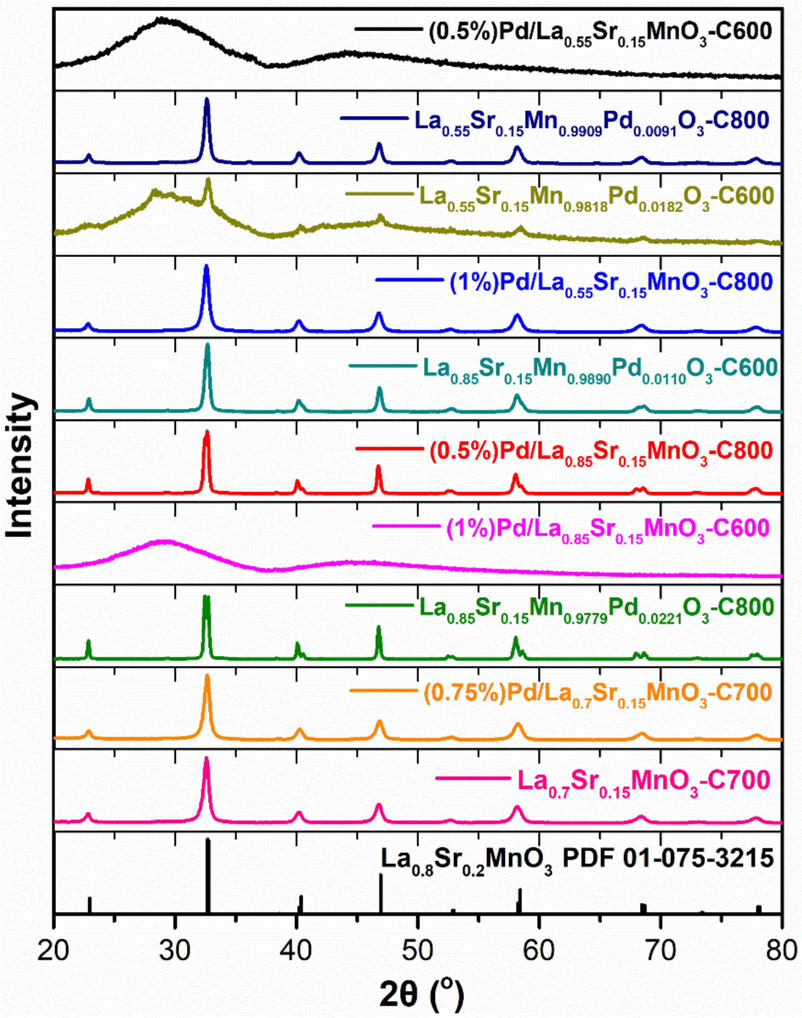

Fig.5.5.1 XRD spectrums of 9 Pd/perovskites and 1 support.

In addition, the XRD spectrum of 0.75%Pd/($La_{0.7}Sr_{0.15}MnO_3$-C700) perovskite did not show a significant difference with spectrum shift from the bare $La_{0.7}Sr_{0.15}MnO_3$ one indicating that powder XRD was insufficient to detect ultralow content palladium. For other samples with different compositions, the perovskite structure containing strontium is also maintained on the whole, which also indicates that the homogeneous or heterogeneous distribution of trace palladium on the surface has little influence on the XRD signal characteristic patterns.

5.3.2. Bulk reducibility and reoxidation capacity from combination of H_2-TPR and O_2-TPO

The evaluation of reducibility and reoxidation ability of the catalytic series has been experienced by H_2 and O_2 consumption of combined thermal-programmed experiments following the same protocol as former chapters (Fig.4.13). The Fig.5.5.2 and Fig.5.5.3 presented the reduction and reoxidation profiles of the nine Pd incorporated perovskites and one support.

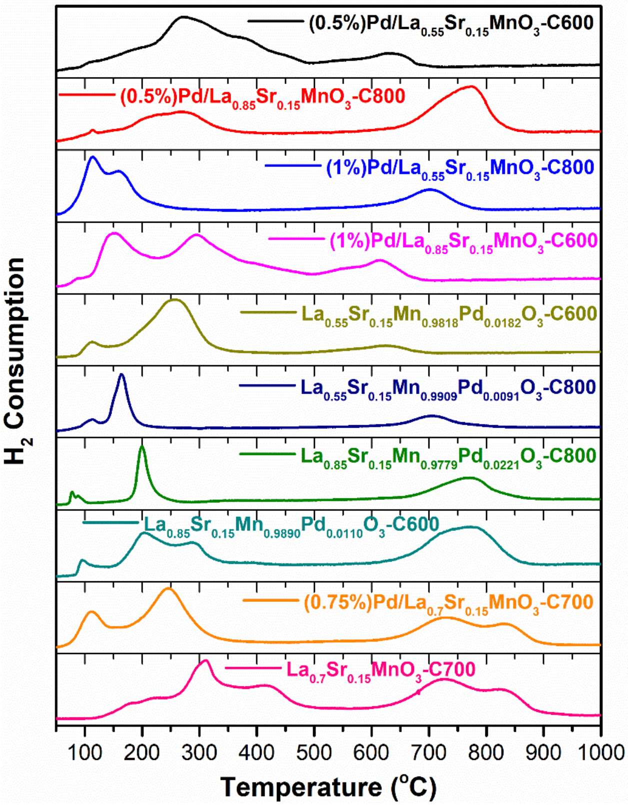

Fig.5.5.2 H_2-TPR of 9 Pd/perovskites and 1 support.

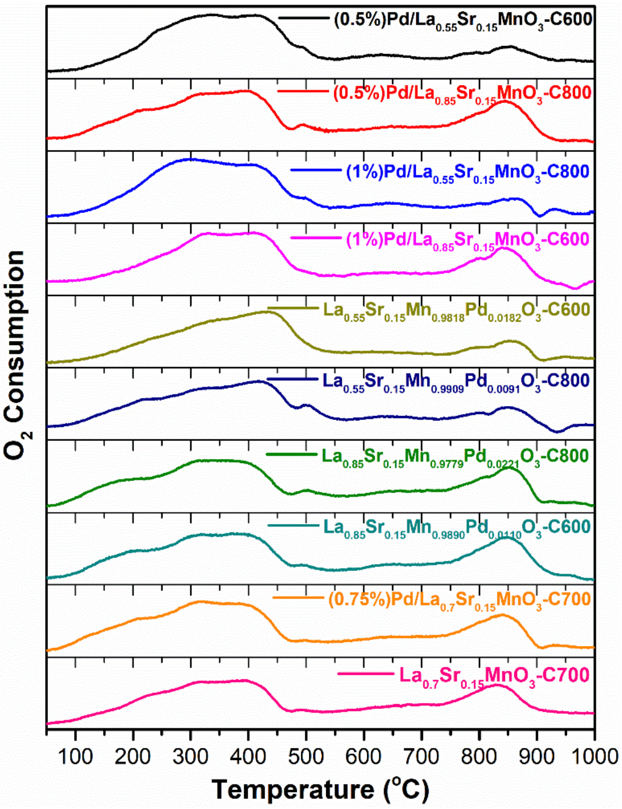

Fig.5.5.3 O_2-TPO of 9 Pd/perovskites and 1 support.

This series of profiles shows that it has all the characteristics of previous materials in terms of the overall reduction and then oxidation process, such as three characteristic interval reduction peaks, palladium reduction peak around 100 °C, surface and bulk reduction peaks and oxygen release negative peak above 900 °C oxidation part.

Table 5.5.4. Amount of hydrogen consumption from H_2-TPR with specific surface and specific consumption.

Catalyst	Total H_2 Consumption (mmol/g)	H_2 Consumption < 550 ºC (mmol/g)	Relative H_2 contribution (%) < 550 ºC	H/M [a]	SSA [b] (m^2/g)	Nomalized Consumption ($mmol/m^2$)
0.5%Pd/($La_{0.55}Sr_{0.15}MnO_3$ - C600)	4.4	3.2	73.8	1.7	27.9	0.16
$La_{0.55}Sr_{0.15}Mn_{0.9909}Pd_{0.0091}O_3$ - C800	2.4	1.6	66.8	0.9	30.3	0.08
$La_{0.55}Sr_{0.15}Mn_{0.9818}Pd_{0.0182}O_3$ - C600	4.5	3.5	78.8	1.7	32.6	0.14
1%Pd/($La_{0.55}Sr_{0.15}MnO_3$ - C800)	3.2	1.8	56.2	1.2	45.6	0.07
$La_{0.85}Sr_{0.15}Mn_{0.9890}Pd_{0.0110}O_3$ - C600	3.0	1.4	45.4	1.4	26.4	0.11
0.5%Pd/($La_{0.85}Sr_{0.15}MnO_3$ - C800)	2.9	1.2	39.1	1.4	11.8	0.25
1%Pd/($La_{0.85}Sr_{0.15}MnO_3$ - C600)	5.0	3.9	78.5	2.4	36.9	0.14
$La_{0.85}Sr_{0.15}Mn_{0.9779}Pd_{0.0221}O_3$ - C800	2.1	0.9	42.6	1.0	7	0.3
0.75%Pd/($La_{0.7}Sr_{0.15}MnO_3$ – C700)	3.3	1.8	53.7	1.4	49.0	0.07
$La_{0.7}Sr_{0.15}MnO_3$ – C700	3.1	1.4	46.1	1.3	51.3	0.06

[a] M = Mn + Pd

[b] SSA: Specific surface area

During the reduction in hydrogen gas flow, both La^{3+} and Sr^{2+} are nonreducible under the H_2-TPR condition, the reduction peaks should only root in the reduction of Pd and Mn species the perovskites, and La_2O_3, SrO, MnO and Pd metal states are the states in the end of reduction [23]. Same as former studies on Pd incorporation, two main impacts could be observed: one was Pd species reduction peak appeared about 100 ºC, the other was that Pd doping obviously boosted the surface Mn species (Mn^{4+} and surface Mn^{3+} situated in a highly unsaturated coordination micro-environment [32]) reduction (zone < 500 ºC) to even lower temperature area. Besides, the higher the calcination temperature led to an increasingly clear surface and lattice reduction interval which could be connected with their different crystallinity from XRD spectrum (Fig.5.5.1). In addition, from the quantitative study (Table 5.5.4), the factors of palladium doping, low temperature calcination and A-site defects appeared to have positive effects on the overall and surface consumption of hydrogen and the calculation of H/M ratio.

Table 5.5.5. Amount of hydrogen consumption from O_2-TPO.

Catalyst	Total O_2 Consumption (mmol/g)	O/M [(a)]	Nomalized Consumption (mmol/m^2)
0.5%Pd/($La_{0.55}Sr_{0.15}MnO_3$-C600)	1.1	0.4	0.04
$La_{0.55}Sr_{0.15}Mn_{0.9909}Pd_{0.0091}O_3$-C800	1.7	0.7	0.06
$La_{0.55}Sr_{0.15}Mn_{0.9818}Pd_{0.0182}O_3$-C600	1.4	0.5	0.04
1%Pd/($La_{0.55}Sr_{0.15}MnO_3$-C800)	1.3	0.5	0.03
$La_{0.85}Sr_{0.15}Mn_{0.9890}Pd_{0.0110}O_3$-C600	1.3	0.6	0.05
0.5%Pd/($La_{0.85}Sr_{0.15}MnO_3$-C800)	1.4	0.7	0.12
1%Pd/($La_{0.85}Sr_{0.15}MnO_3$-C600)	1.2	0.6	0.03
$La_{0.85}Sr_{0.15}Mn_{0.9779}Pd_{0.0221}O_3$-C800	1.3	0.6	0.19
0.75%Pd/($La_{0.7}Sr_{0.15}MnO_3$–C700)	1.4	0.6	0.03
$La_{0.7}Sr_{0.15}MnO_3$–C700	1.4	0.6	0.03

[a] M = Pd + Mn

In addition, the A-site defect samples showed the deeper the defect in A site, the deeper the binding degree of Pd and surface manganese reduction peaks regardless of the synthesis methods and calcination temperatures. In other words, the A-site defect promoted the redox capacity of palladium species and manganese oxides on the perovskite surface.

The following reoxidation from O_2-TPO reflected the ability and the stability to form the perovskite structure again. At 500 °C, the reoxidation process can still be divided into two parts and the differences of reoxidation profiles mainly depended on the A-site defect especially in α-zone (< 500 °C). From the $La_{0.7}Sr_{0.15}MnO_3$ series, Pd incorporation seemed to lead to gas release about 900 °C. Besides, the quantitative calculation (Table 5.5.5) on oxygen consumption and their quantity per unit metal (O/M) showed no significant difference on all samples.

5.3.3. Oxygen desorption (O_2-TPD/MS)

The oxygen desorption was combined with mass spectrometry following the same protocol as former oxygen desorption program (Fig.4.18). Mass spectrometry was combined with thermal programmed desorption analysis in order to avoid the overlap of oxygen and carbon dioxide and to calculate related oxygen desorbed quantity. Fig.5.5.4 and Table 5.5.6 showed the profiles and quantitative study of the fixed Sr substitution series.

In principle, the A-site deficiency and low calcination temperature presented the positive impacts on the oxygen desorption indicating stronger oxygen mobility, storage capacity and the ability to produce/convert different oxygen species [35]. Besides, the Pd incorporation to $La_{0.7}Sr_{0.15}MnO_3$ sample brought a positive impact on the capacity of oxygen desorption. In addition, the synthesis methods of perovskites seemed to have no obvious impact on the desorption capacity of oxygen.

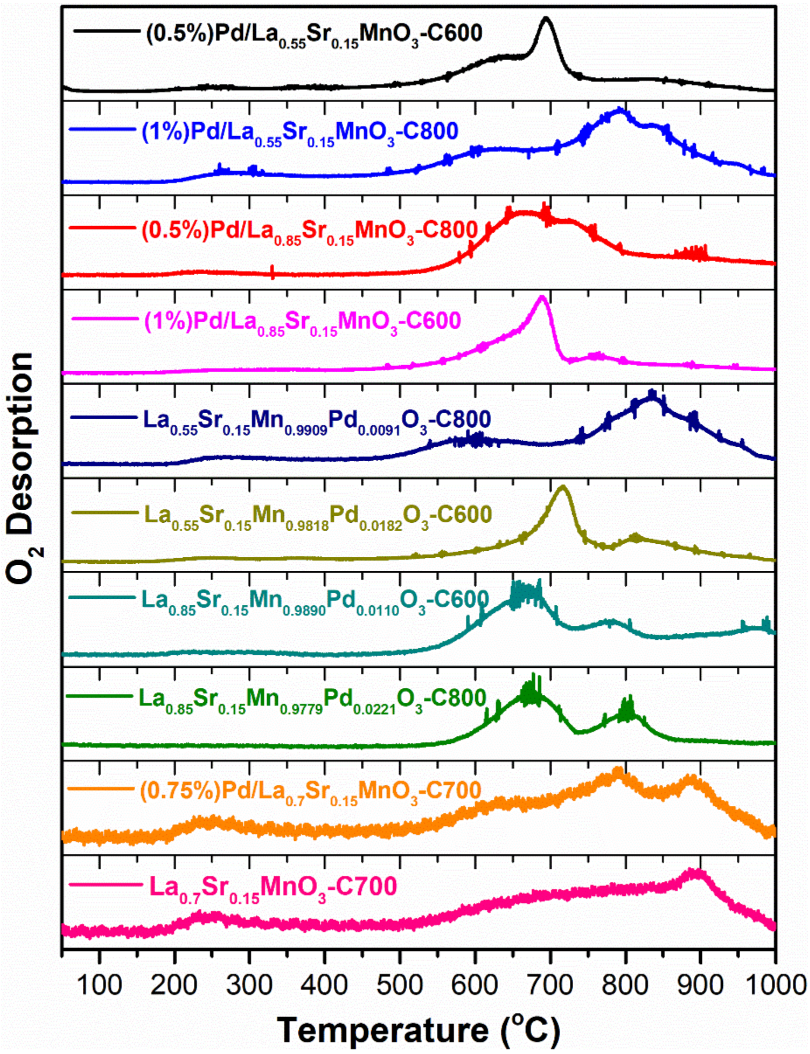

Fig.5.5.4 Oxygen desorption from O_2-TPD of 9 Pd/perovskites and 1 support.

Table 5.5.6. Amount of desorbed oxygen from O_2-TPD.

Catalyst	Amount of Desorbed Oxygen (mmol/g)		
	α-Oxygen [a]	β-Oxygen [b]	Total Amount
0.5%Pd/($La_{0.55}Sr_{0.15}MnO_3$ - C600)	0.14	0.66	0.80
$La_{0.55}Sr_{0.15}Mn_{0.9909}Pd_{0.0091}O_3$ - C800	0.09	0.34	0.43
$La_{0.55}Sr_{0.15}Mn_{0.9818}Pd_{0.0182}O_3$ - C600	0.13	0.69	0.82
1%Pd/($La_{0.55}Sr_{0.15}MnO_3$ - C800)	0.10	0.48	0.58
$La_{0.85}Sr_{0.15}Mn_{0.9890}Pd_{0.0110}O_3$ - C600	0.07	0.31	0.38
0.5%Pd/($La_{0.85}Sr_{0.15}MnO_3$ - C800)	0.06	0.29	0.35
1%Pd/($La_{0.85}Sr_{0.15}MnO_3$ - C600)	0.12	0.63	0.75
$La_{0.85}Sr_{0.15}Mn_{0.9779}Pd_{0.0221}O_3$ - C800	0.06	0.24	0.30
0.75%Pd/($La_{0.7}Sr_{0.15}MnO_3$ – C700)	0.11	0.33	0.44
$La_{0.7}Sr_{0.15}MnO_3$ – C700	0.10	0.30	0.40

[a] Desorbed oxygen < 500 °C

[b] Desorbed oxygen > 500 °C

5.3.4. Inductive coupled plasma atomic emission spectroscopy

The elemental composition analysis was proceeded by inductively coupled plasma atomic emission spectroscopy (ICP-AES) at RealCat Platform in Centrale Lille engineering school in order to more accurately measure the elemental composition ratio of the perovskite catalysts as a whole.

In general, the composition of the eight catalysts basically conformed to the initially theoretical design, especially the Pd content of 0.5%wt. and 1%wt. states. (Table 5.5.7). This overall composition of the elements presented the different results compared to the surface composition studies from XPS analysis (Table 5.5.8), which indicated that there was the elemental segregation on the samples surface.

Table 5.5.7. Elemental composition analysis from ICP/MS spectroscopy.

Catalyst	La	Sr	Mn	Pd
0.5%Pd/($La_{0.85}Sr_{0.15}MnO_3$ - C800)	52.65%	5.99%	24.70%	0.56%
0.5%Pd/($La_{0.55}Sr_{0.15}MnO_3$ - C600)	39.57%	8.92%	28.26%	0.61%
1%Pd/($La_{0.85}Sr_{0.15}MnO_3$ - C600)	45.57%	5.45%	20.47%	1.02%
1%Pd/($La_{0.55}Sr_{0.15}MnO_3$ - C800)	39.51%	8.97%	28.03%	1.02%
$La_{0.85}Sr_{0.15}Mn_{0.9890}Pd_{0.0110}O_3$ - C600	50.07%	5.73%	22.86%	0.50%
$La_{0.55}Sr_{0.15}Mn_{0.9909}Pd_{0.0091}O_3$ - C800	42.98%	7.65%	30.76%	0.57%
$La_{0.85}Sr_{0.15}Mn_{0.9779}Pd_{0.0221}O_3$ - C800	50.41%	5.73%	23.00%	0.90%
$La_{0.55}Sr_{0.15}Mn_{0.9818}Pd_{0.0182}O_3$ - C600	38.43%	6.75%	27.02%	1.02%

5.4. Surface composition

The surface composition of the nine palladium incorporated catalysts and one perovskite support have been characterized by chemisorption (H_2-Chemisorption), X-ray photoelectron spectroscopy (XPS) and N_2- physisorption, the combined study of the three methods can be used to study the surface properties of catalysts with more confidence on the impact of palladium incorporation (Table 5.5.8.). The results of surface properties of nine catalysts can be taken into the matrix of design of experiments, and the influence of four factors on surface properties, especially the palladium impacts can be obtained through analysis.

The binding energy position and profiles of Pd 3d orbital from the nine Pd doped samples were showed in the Fig.5.5.5 and Pd valences were mainly in Pd^0, Pd^{2+} and Pd^{4+} states [55, 56, 57, 58], and the state of Pd does not seem to be related to the method of synthesis or the calcination temperature. The quantitative study of Pd ratio on surface from XPS analysis showed that the samples of sequential preparation route generally presented higher surface Pd content than the one-pot ones and the Pd dispersion presented also the same trend from the H_2-chemisorption analysis.

The binding energy position and profiles of O 1s orbital of the samples were presented in Fig.5.5.6 with mainly the lattice and surface adsorbed oxygen and little other oxygen-containing substances [59]. And the O_{ads}/O_{lat} ratio seemed no coherence with stoichiometry, calcination temperature and sequential/one-pot preparation route.

As previous work breakdown structure on A-site metals, the XPS results are divided into two parts: influence of lanthanum stoichiometry and influence of A-site partial substitution of strontium incorporation in stoichiometric composition. The binding energy of La 3d generally stayed the same position for all samples indicating homogenization state of lanthanum. But the Sr 3d binding energy profiles and position varied due to the degree of crystallization from the different calcination temperature and Sr surface segregation [27, 28, 36].

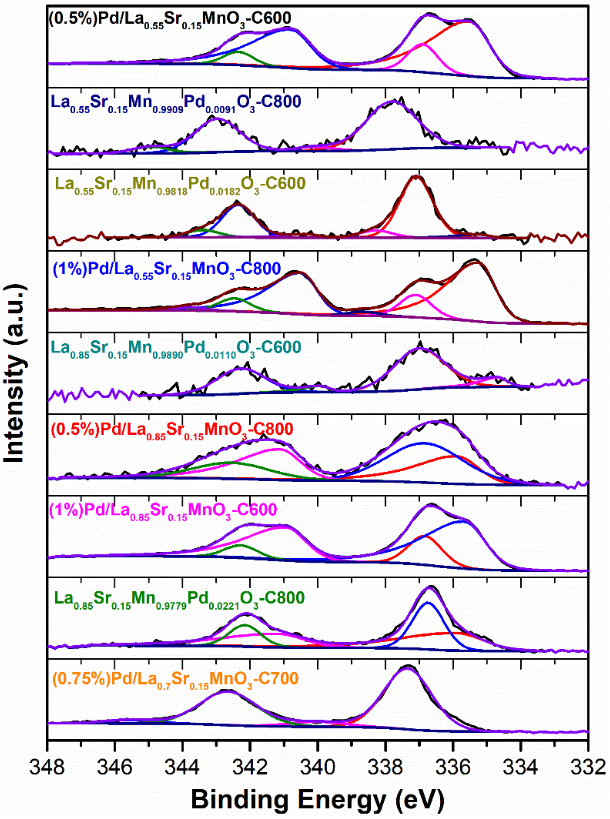

Fig.5.5.5 Pd 3d XPS analysis.

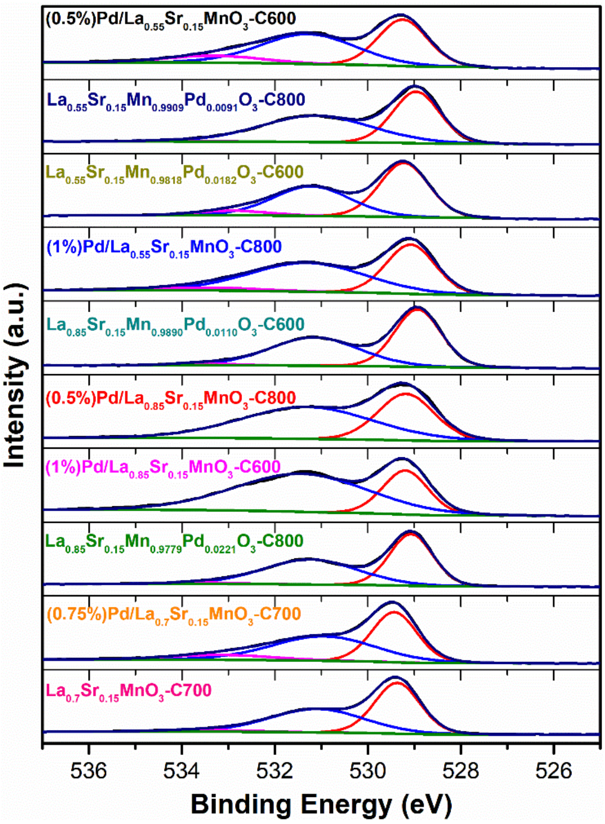

Fig.5.5.6 O 1s XPS analysis.

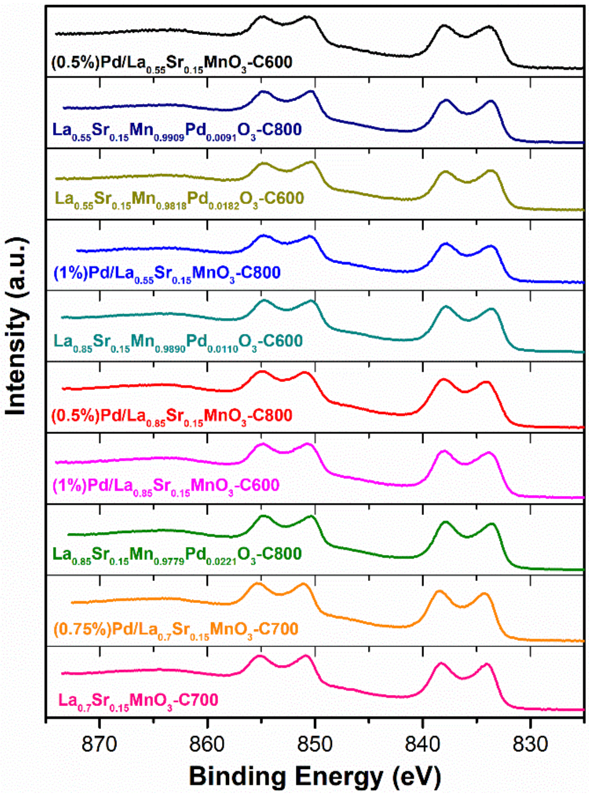

Fig.5.5.7 La 3d XPS analysis.

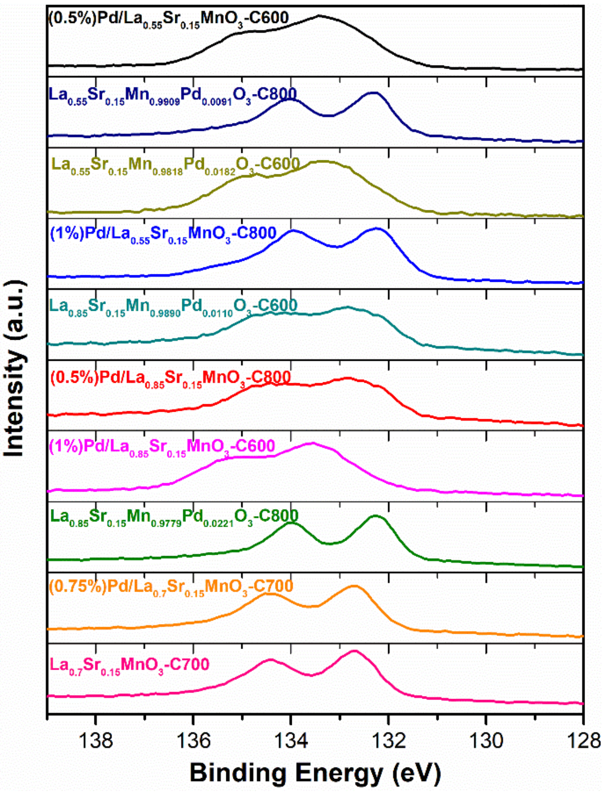

Fig.5.5.8 Sr 3d XPS analysis.

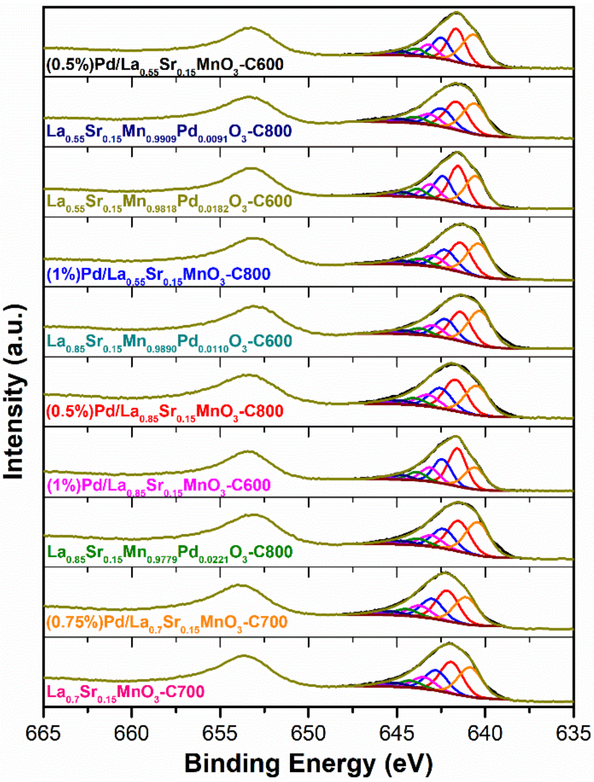

Fig.5.5.9 Mn 2p XPS analysis.

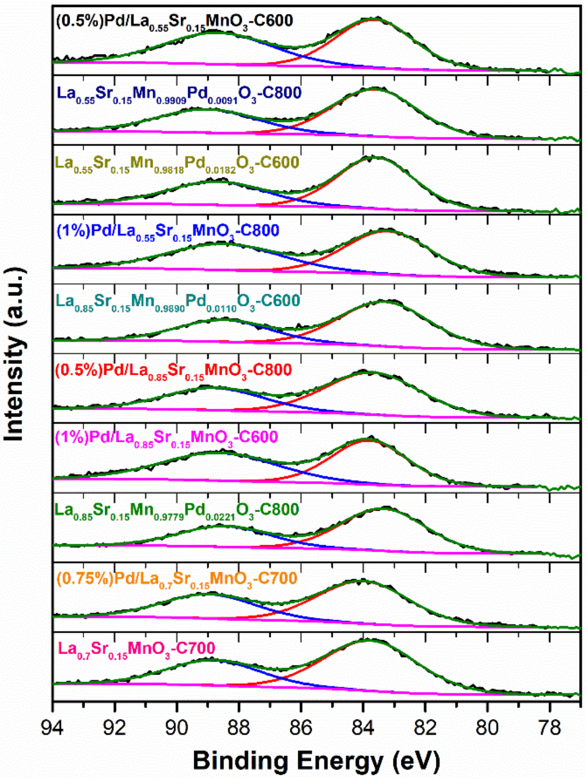

Fig.5.5.10 Mn 3s XPS analysis.

The manganese XPS study was investigated as the former analysis by Mn 2p and Mn 3s together to analyze the Mn valence state following the Mn 2p studies of M. Biesinger et al. [29] in Fig.5.4.9. The lower calcination temperature and the A-site defect showed the positive impacts leading to higher Mn valence state depending on the quantitative study from Mn 2p orbitals of samples with six peaks of Mn (IV) and one peak of Mn (III) [26, 30] and Mn 3s from multiplet splitting of Mn 3s peak [31] in Fig.5.4.10.

Prominent multiplet splitting can be observed for Mn^{2+}, Mn^{3+} and Mn^{4+}. The average oxidation state (AOS) of manganese from Mn 3s orbital of perovskite can be calculated as Chapter IV according Eq. (5.5.1). [31]

$$\text{Average Oxidation State (AOS)} = 8.956 - 1.12\times\Delta E_{\text{splitting}} \qquad \text{(Eq.5.5.1)}$$

In addition, as to the $La_{0.7}Sr_{0.15}MnO_3$-C700 sample, Pd impregnation led to higher surface Mn valence state which have the same tend of hydrogen consumption as H_2-TPR results (Fig.5.5.2, Table 5.5.4).

Table 5.5.8. Summary of surface analysis of 9 fresh palladium incorporated perovskites and 1 support after calcination.

Catalyst	XPS Analysis									H_2-Chemisorption	N_2- physisorption
	Pd ratio (%) [(a)]	$\frac{Pd}{\text{La + Sr}}$	$\frac{Mn}{\text{La + Sr}}$	$\frac{Pd}{\text{Mn}}$	$\frac{Pd^{2+}}{Pd^{0}}$	$\frac{Pd^{4+}}{Pd^{2+}}$	$\frac{Mn^{3+}}{Mn^{4+}}(b)$	Mn (AOS) [(c)]	$\frac{O_{ads}}{O_{lat}}(d)$	Pd disp. (%) [(e)]	SSA[(f)] (m^2/g)
0.5%Pd/($La_{0.55}Sr_{0.15}MnO_3$-C600)	4.92	0.50	1.21	0.42	0.20	-	0.52	3.35	2.04	4.6	27.9
$La_{0.55}Sr_{0.15}Mn_{0.9909}Pd_{0.0091}O_3$-C800	0.16	0.01	1.27	0.01	-	0.10	0.42	2.88	1.17	2.8	30.3
$La_{0.55}Sr_{0.15}Mn_{0.9818}Pd_{0.0182}O_3$-C600	0.23	0.02	1.27	0.02	11.03	0.16	0.41	3.25	0.85	3.6	32.6
1%Pd/($La_{0.55}Sr_{0.15}MnO_3$-C800)	4.0	0.39	1.34	0.29	0.21	0.21	0.53	3.08	1.06	4.8	45.6
$La_{0.85}Sr_{0.15}Mn_{0.9890}Pd_{0.0110}O_3$-C600	0.13	0.01	0.66	0.01	6.97	-	0.56	3.19	0.95	5.6	26.4
0.5%Pd/($La_{0.85}Sr_{0.15}MnO_3$-C800)	0.53	0.04	0.70	0.05	1.05	-	0.41	3.27	1.59	3.8	11.8
1%Pd/($La_{0.85}Sr_{0.15}MnO_3$-C600)	4.26	0.37	0.83	0.45	0.26	-	0.28	3.56	2.56	8.4	36.9
$La_{0.85}Sr_{0.15}Mn_{0.9779}Pd_{0.0221}O_3$-C800	0.53	0.03	0.67	0.05	0.78	-	0.48	3.22	1.06	0.4	7
0.75%Pd/($La_{0.7}Sr_{0.15}MnO_3$–C700)	1.20	0.09	0.95	0.10	-	0.10	0.39	3.38	0.78	16.8	49.0
$La_{0.7}Sr_{0.15}MnO_3$–C700	-	-	0.87	-	-	-	0.42	3.29	0.96	-	51.3

a. Pd ratio (%) from XPS composition study

b. Mn^{3+}/Mn^{4+} ratio from XPS Mn 2p orbital

c. Mn average oxidation state (AOS) from XPS Mn 3s orbital

d. Oxygen adsorption species and lattice oxygen ratio from XPS O 1s orbital

e. Pd dispersion (%) from H_2-chemisorption measurements

f. Specific surface area from N_2-physisorption

5.5. Conclusion

In this part, the fractional factorial matrix of design of experiments, which includes a selected subset of a full factorial design, was dedicated to design the formulation of nine palladium incorporated samples in order to understand the proportion of the impact of each factor and the relevant synergetic correlation by efficiently building the relationships between factors and related requirements of natural gas engine emission, such as methane conversion, NO reduction, palladium dispersion, oxygen storage capacity, specific surface area, etc. Once the framework matrix of experimental design is established, the above parameters of interest can be substituted into the matrix responses by relevant computer software to form correlation surface diagram readily. The methodology can effectively guide the catalyst design of complex system.

Regarding the bulk analysis from XRD, the spectrums maintained the reference strontium substituted perovskite structure except two sequential C600 samples in amorphous state. As to the reduction capacity from H_2-TPR experiments, interestingly, the more the defect, the closer the reduction peaks of palladium species and surface manganese among the three different A-site stoichiometric compositions. The low calcination temperature and the perovskite A-site deficiency contributed to stronger oxygen desorption capacity. Elemental analysis by ICP/MS spectroscopy confirmed the whole elemental composition corresponding to designed perovskite formulation, which could be referred to surface composition investigation.

The XPS analysis of lanthanum and strontium as A-site metals reflected the totally different properties: lanthanum showed the stability but the state of strontium depended on calcination temperature. Although there were always two different factors in each pair of catalyst combination comparison, without receiving the results of cooperation partner, it could still be seen that the surface defects seem to promote the existence of metallic palladium species of which binding energy at 335 eV. In addition to the main divalent palladium, a trace amount of tetravalent palladium could also be detected. Within the same discussion as former study on poor palladium dispersion from one-pot sample of high calcination temperature, surface deficiency and low calcination temperature presented the positive impacts on palladium dispersion and specific surface area. In addition, these samples were both measured both in high throughput reactions for kinetic study in Chapter VI and in real exhaust gas composition of natural gas engine catalytic reaction in Chapter VII. Ultimately, the specific systematic DOE study needs to wait for the analysis report from statistic partner before the final conclusion of this section on impact factors aiming at reducing palladium content can be given.

References

1. V. Rives, Chapter 1, From Solid-State Chemistry to Soft Chemistry Routes. P. Granger, V. I. Parvulescu, S. Kaliaguine, W. Prellier, Perovskites and Related Mixed Oxides, Concepts and Applications. 2016 Wiley-VCH Verlag GmbH & Co. KGaA, Boschstr. 12, 69469 Weinheim, Germany. ISBN: 978-3-527-68661-2.
2. Sébastien Royer, Daniel Duprez, Fabien Can, Xavier Courtois, Catherine Batiot-Dupeyrat, Said Laassiri, and Houshang Alamdari., Perovskites as Substitutes of Noble Metals for Heterogeneous Catalysis: Dream or Reality., Chemical Reviews 2014 114 (20), 10292-10368. https://doi-org/10.1021/cr500032a.
3. Nicolas Bion, Fabien Can, Xavier Courtois, Daniel Duprez. Transition metal oxides for combustion and depollution processes. Jacques C. Védrine. Metal Oxides in Heterogeneous Catalysis, Elsevier, pp.287-353, 2018, Metal oxides series, ISBN: 978-0-12-811631-9. http://doi-org/10.1016/B978-0-12-811631-9.00006-5.
4. Pechini Processes: An Alternate Approach of the Sol–Gel Method, Preparation, Properties, and Applications. Lucangelo Dimesso. Springer International Publishing Switzerland 2016. L. Klein et al. (eds.), Handbook of Sol-Gel Science and Technology, http://doi-org/10.1007/978-3-319-19454-7_123-1.
5. J.P. Dacquin, M. Cabié, C.R. Henry, C. Lancelot, C. Dujardin, S.R. Raouf, P. Granger. Structural changes of nano-Pt particles during thermal ageing: Support-induced effect and related impact on the catalytic performances. Journal of Catalysis, Volume 270, Issue 2, 2010, Pages 299-309, ISSN 0021-9517, https://doi.org/10.1016/j.jcat.2010.01.006.
6. Wang, J., Cao, X., Liu, S., Guo, Y., Wang, Z., Li, X., Ren, Y., Xia, Z., Wang, H., Liu, C., Wang, N., Jiang, W., Ding, W., & Zhang, Z. (2020). Preparation, structural and sintering properties of AZO nanoparticles by sol-gel combustion method. Ceramics International, 46, 17659-17665. https://doi.org/10.1016/j.ceramint.2020.04.068.
7. Jawad Javaid Siddiqui, Kongjun Zhu, Jinhao Qiu, Hongli Ji, Sol–gel synthesis, characterization and microwave absorbing properties of nano sized spherical particles of $La_{0.8}Sr_{0.2}Mn_{0.8}Fe_{0.2}O_3$, Materials Research Bulletin, Volume 47, Issue 8, 2012, Pages 1961-1967, ISSN 0025-5408, https://doi.org/10.1016/j.materresbull.2012.04.017.

8. K. Rida, M.A. Peña, E. Sastre, A. Martínez-Arias. Effect of calcination temperature on structural properties and catalytic activity in oxidation reactions of $LaNiO_3$ perovskite prepared by Pechini method. Journal of Rare Earths, Vol. 30, No. 3, Mar. 2012, P. 210. https://doi.org/10.1016/S1002-0721(12)60025-8.
9. Ahmad Gholizadeh. "X-ray peak broadening analysis in $LaMnO_{3+\delta}$ nano-particles with rhombohedral crystal structure". Journal of Advanced Materials and Processing, 3, 3, 2015, 71-83.
10. Chuanhui Zhang, Chao Wang, Wangcheng Zhan, Yanglong Guo, Yun Guo, Guanzhong Lu, Alexandre Baylet, Anne Giroir-Fendler, Catalytic oxidation of vinyl chloride emission over $LaMnO_3$ and $LaB_{0.2}Mn_{0.8}O_3$ (B=Co, Ni, Fe) catalysts, Applied Catalysis B: Environmental, Volume 129, 2013, Pages 509-516, ISSN 0926-3373, https://doi.org/10.1016/j.apcatb.2012.09.056.
11. Yuxi Liu, Hongxing Dai, Jiguang Deng, Yucheng Du, Xinwei Li, Zhenxuan Zhao, Yuan Wang, Baozu Gao, Huanggen Yang, Guangsheng Guo, In situ poly(methyl methacrylate)-templating generation and excellent catalytic performance of MnO_x/3DOM $LaMnO_3$ for the combustion of toluene and methanol, Applied Catalysis B: Environmental, Volumes 140–141, 2013, Pages 493-505, ISSN 0926-3373, https://doi.org/10.1016/j.apcatb.2013.04.051.
12. Fei Teng, Wei Han, Shuhui Liang, Buergen Gaugeu, Ruilong Zong, Yongfa Zhu, Catalytic behavior of hydrothermally synthesized $La_{0.5}Sr_{0.5}MnO_3$ single-crystal cubes in the oxidation of CO and CH_4, Journal of Catalysis, Volume 250, Issue 1, 2007, Pages 1-11, ISSN 0021-9517, https://doi.org/10.1016/j.jcat.2007.05.007.
13. Jianxiong Wu, Jean-Philippe Dacquin, Nora Djelal, Catherine Cordier, Christophe Dujardin, Pascal Granger, Calcium and copper substitution in stoichiometric and La-deficient $LaFeO_3$ compositions: A starting point in next generation of Three-Way-Catalysts for gasoline engines, Applied Catalysis B: Environmental, Volume 282, 2021, 119621, ISSN 0926-3373, https://doi.org/10.1016/j.apcatb.2020.119621.
14. Wenhao Yang, Yue Peng, Ya Wang, Yun Wang, Hao Liu, Zi'ang Su, Weinan Yang, Jianjun Chen, Wenzhe Si, Junhua Li, Controllable redox-induced in-situ growth of MnO_2 over Mn_2O_3 for toluene oxidation: Active heterostructure interfaces, Applied Catalysis B: Environmental, Volume 278, 2020, 119279, ISSN 0926-3373, https://doi.org/10.1016/j.apcatb.2020.119279.
15. Giroir-Fendler, S. Gil, A. Baylet. $(La(0.8)A(0.2))MnO_3$ (A = Sr, K) perovskite catalysts for NO and $C_{10}H_{22}$ oxidation and selective reduction of NO by $C_{10}H_{22}$. Chinese Journal of Catalysis, Elsevier,

2014, 35, pp.1299-1304. https://doi-org/10.1016/S1872-2067(14)60173-X.

16. Buciuman, F.C., Patcas, F. & Zsakó, J. TPR-study of Substitution Effects on Reducibility and Oxidative Non-stoichiometry of $La_{0.8}A'_{0.2}MnO_{3+\delta}$ Perovskites. Journal of Thermal Analysis and Calorimetry 61, 819–825 (2000). https://doi.org/10.1023/A:1010153331841.
17. Perovskite Oxides: Preparation, Characterizations, and Applications in Heterogeneous Catalysis. Junjiang Zhu, Hailong Li, Linyun Zhong, Ping Xiao, Xuelian Xu, Xiangguang Yang, Zhen Zhao, and Jinlin Li. ACS Catalysis 2014 4 (9), 2917-2940. http://doi-org/10.1021/cs500606g.
18. Hessam Ziaei-Azad, Abbasali Khodadadi, Parvaneh Esmaeilnejad-Ahranjani, Yadollah Mortazavi, Effects of Pd on enhancement of oxidation activity of $LaBO_3$ (B=Mn, Fe, Co and Ni) pervoskite catalysts for pollution abatement from natural gas fueled vehicles, Applied Catalysis B: Environmental, Volume 102, Issues 1–2, 2011, Pages 62-70, ISSN 0926-3373, https://doi.org/10.1016/j.apcatb.2010.11.025.
19. Shuhui Liang, Tongguang Xu, Fei Teng, Ruilong Zong, Yongfa Zhu, The high activity and stability of $La_{0.5}Ba_{0.5}MnO_3$ nanocubes in the oxidation of CO and CH_4, Applied Catalysis B: Environmental, Volume 96, Issues 3–4, 2010, Pages 267-275, ISSN 0926-3373, https://doi.org/10.1016/j.apcatb.2010.01.025.
20. Katie A. Cychosz, Remy Guillet-Nicolas, Javier Garcia-Martinez and Matthias Thommes, Recent advances in the textural characterization of hierarchically structured nanoporous materials, Chem. Soc. Rev., 2017, 46, 389, https://doi-org/10.1039/C6CS00391E.
21. Recent Advances of Lanthanum-Based Perovskite Oxides for Catalysis. Huiyuan Zhu, Pengfei Zhang, and Sheng Dai. ACS Catalysis 2015 5 (11), 6370-6385. http://doi-org/10.1021/acscatal.5b01667.
22. Understanding the Impact of Surface Reconstruction of Perovskite Catalysts on CH_4 Activation and Combustion. Felipe Polo-Garzon, Victor Fung, Xiaoming Liu, Zachary D. Hood, Elizabeth E. Bickel, Lei Bai, Hanjing Tian, Guo Shiou Foo, Miaofang Chi, De-en Jiang, and Zili Wu. ACS Catalysis 2018 8 (11), 10306-10315. http://doi-org/10.1021/acscatal.8b02307.
23. Perovskite Oxides: Preparation, Characterizations, and Applications in Heterogeneous Catalysis. Junjiang Zhu, Hailong Li, Linyun Zhong, Ping Xiao, Xuelian Xu, Xiangguang Yang, Zhen Zhao, and Jinlin Li. ACS Catalysis 2014 4 (9), 2917-2940. http://doi-org/10.1021/cs500606g.
24. Cation Size Mismatch and Charge Interactions Drive Dopant Segregation at the Surfaces of

Manganite Perovskites. Wonyoung Lee, Jeong Woo Han, Yan Chen, Zhuhua Cai, and Bilge Yildiz. Journal of the American Chemical Society 2013 135 (21), 7909-7925. http://doi-org/10.1021/ja3125349.

25. S. Ponce, M.A. Peña, J.L. GFierro. Surface properties and catalytic performance in methane combustion of Sr-substituted lanthanum manganites. Applied Catalysis B: Environmental, Volume 24, Issues 3–4, 7 February 2000, Pages 193-205. https://doi.org/10.1016/S0926-3373(99)00111-3.
26. G. Abdallah, R. Bitar, S. K. P. Veerapandian, J-M. Giraudon, N. De Geyter, R. Morent, J-F. Lamonier. Acid treated Ce modified birnessite–type MnO_2 for ozone decomposition at low temperature: Effect of nitrogen containing co-pollutants and water. Applied Surface Science, Volume 571, 1 January 2022, 151240. https://doi.org/10.1016/j.apsusc.2021.151240.
27. Ethan J. Crumlin, Eva Mutoro, Wesley T. Hong, Michael D. Biegalski, Hans M. Christen, Zhi Liu, Hendrik Bluhm, and Yang Shao-Horn, In Situ Ambient Pressure X-ray Photoelectron Spectroscopy of Cobalt Perovskite Surfaces under Cathodic Polarization at High Temperatures. The Journal of Physical Chemistry C 2013 117 (31), 16087-16094. http://doi-org/10.1021/jp4051963.
28. Hf Deposition Stabilizes the Surface Chemistry of Perovskite Manganite Oxide. Roland Bliem, Dongha Kim, Jiayue Wang, Ethan J. Crumlin, and Bilge Yildiz. The Journal of Physical Chemistry C 2021 125 (6), 3346-3354. http://doi-org/10.1021/acs.jpcc.0c09707.
29. M.C. Biesinger, B.P. Payne, A.P. Grosvenor, L.W.M. Lau, A.R. Gerson, R.St.C. Smart., Resolving surface chemical states in XPS analysis of first row transition metals, oxides and hydroxides: Cr, Mn, Fe, Co and Ni., Applied Surface Science, Volume 257, Issue 7, 15 January 2011, Pages 2717-2730. https://doi.org/10.1016/j.apsusc.2010.10.051.
30. Abdallah, G.; Giraudon, J.-M.; Bitar, R.; Geyter, N.D.; Morent, R.; Lamonier, J.-F. Post-Plasma Catalysis for Trichloroethylene Abatement with Ce-Doped Birnessite Downstream DC Corona Discharge Reactor. Catalysts 2021, 11, 946. https://doi.org/10.3390/catal11080946.
31. H. Najjar, J-F. Lamonier, O. Mentré, J-M. Giraudon, H. Batis. Optimization of the combustion synthesis towards efficient $LaMnO_{3+y}$ catalysts in methane oxidation. Applied Catalysis B: Environmental, Volume 106, Issues 1–2, 21 July 2011, Pages 149-159. https://doi.org/10.1016/j.apcatb.2011.05.019.
32. Jon A. Onrubia-Calvo, B. Pereda-Ayo, U. De-La-Torre, Juan R. González-Velasco, Key factors in Sr-doped $LaBO_3$ (B = Co or Mn) perovskites for NO oxidation in efficient diesel exhaust

purification. Applied Catalysis B: Environmental, Volume 213, 2017, Pages 198-210, ISSN 0926-3373, https://doi.org/10.1016/j.apcatb.2017.04.068.

33. Yin Xu, Jérémy Dhainaut, Jean-Philippe Dacquin, Anne-Sophie Mamede, Maya Marinova, Jean-François Lamonier, Hervé Vezin, Hui Zhang, Sébastien Royer. $La_{1-x}(Sr, Na, K)_xMnO_3$ perovskites for HCHO oxidation: The role of oxygen species on the catalytic mechanism. Applied Catalysis B: Environmental, Volume 287, 2021, 119955, ISSN 0926-3373, https://doi.org/10.1016/j.apcatb.2021.119955.
34. Jirátová, K.; Pacultová, K.; Karásková, K.; Balabánová, J.; Koštejn, M.; Obalová, L. Direct Decomposition of NO over Co-Mn-Al Mixed Oxides: Effect of Ce and/or K Promoters. Catalysts 2020, 10, 808. https://doi.org/10.3390/catal10070808.
35. Yinlong Zhu, Wei Zhou, Jie Yu, Yubo Chen, Meilin Liu, and Zongping Shao, « Enhancing Electrocatalytic Activity of Perovskite Oxides by Tuning Cation Deficiency for Oxygen Reduction and Evolution Reactions », Chemistry of materials, 28, American Chemical Society, 2016, no 6, p. 1691-1697. https://doi-org/10.1021/acs.chemmater.5b04457.
36. R.M. García de la Cruz, H. Falcón, M.A. Peña, J.L.G. Fierro. Role of bulk and surface structures of $La_{1-x}Sr_xNiO_3$ perovskite-type oxides in methane combustion. Applied Catalysis B: Environmental, Volume 33, Issue 1, 2001, Pages 45-55, ISSN 0926-3373, https://doi.org/10.1016/S0926-3373(01)00157-6.
37. Study of the Catalytic Activity–Semiconductive Properties Relationship For $BaTiO_3$ and $PbTiO_3$ Perovskites, Catalysts for Methane Combustion. I. Popescu, I. Săndulescu, Á. Rédey, I.-C. Marcu, Catalysis Letters volume 141, pages 445–451 (2011), https://doi.org/10.1007/s10562-010-0538-2.
38. Ionel Popescu, Yihao Wu, Pascal Granger, Ioan-Cezar Marcu. An in situ electrical conductivity study of LaCoFe perovskite-based catalysts in correlation with the total oxidation of methane. Applied Catalysis A: General, Volume 485, 2014, Pages 20-27, ISSN 0926-860X, https://doi.org/10.1016/j.apcata.2014.07.025.
39. Huang, Cenyan & Shan, Wenpo & Lian, Zhihua & Zyme, Hi & He, Hong. (2020). Recent advances in three-way catalysts of natural gas vehicles. Catalysis Science & Technology. https://doi-org/10.1039/D0CY01320J.
40. J.P. Dacquin, C. Lancelot, C. Dujardin, P. Da Costa, G. Djega-Mariadassou, P. Beaunier, S. Kaliaguine, S. Vaudreuil, S. Royer, P. Granger. Influence of preparation methods of $LaCoO_3$ on the

catalytic performances in the decomposition of N_2O. Applied Catalysis B: Environmental, Volume 91, Issues 3–4, 2009, Pages 596-604, ISSN 0926-3373, https://doi.org/10.1016/j.apcatb.2009.06.032.

41. Y. Nishihata, J. Mizuki, T. Akao, H. Tanaka, M. Uenishi, M. Kimura, T. Okamoto & N. Hamada. Self-regeneration of a Pd-perovskite catalyst for automotive emissions control. Nature 418, 164–167 (2002). https://doi.org/10.1038/nature00893.
42. Tanaka, H., Taniguchi, M., Uenishi, M., Kajita, N., Tan, I., Nishihata, Y., Mizuki, J., Narita, K., Kimura, M. and Kaneko, K. (2006), Self-Regenerating Rh- and Pt-Based Perovskite Catalysts for Automotive-Emissions Control. Angewandte Chemie International Edition, 45: 5998-6002. https://doi-org/10.1002/anie.200503938.
43. Hirohisa Tanaka, Mari Uenishi, Masashi Taniguchi, Isao Tan, Keiichi Narita, Mareo Kimura, Kimiyoshi Kaneko, Yasuo Nishihata, Jun'ichiro Mizuki. The intelligent catalyst having the self-regenerative function of Pd, Rh and Pt for automotive emissions control. Catalysis Today, Volume 117, Issues 1–3, 2006, Pages 321-328, ISSN 0920-5861, https://doi.org/10.1016/j.cattod.2006.05.029.
44. Michael B. Katz, George W. Graham, Yingwen Duan, Hong Liu, Carolina Adamo, Darrell G. Schlom, and Xiaoqing Pan, « Self-Regeneration of Pd–$LaFeO_3$ Catalysts: New Insight from Atomic-Resolution Electron Microscopy », *Journal of the American Chemical Society*, 133, American Chemical Society, 2011, nº 45, p. 18090-18093. https://doi-org/10.1021/ja2082284.
45. Granger, P., Renème, Y., Lahougue, A. et al. Thermal Aging of Perovskite Based Natural Gas Vehicle Catalysts: Dependency of the Mode of Pd Incorporation. Top Catal 63, 1474–1484 (2020). https://doi.org/10.1007/s11244-020-01331-x.
46. Y. Wu, C. Dujardin, C. Lancelot, J.P. Dacquin, V.I. Parvulescu, M. Cabié, C.R. Henry, T. Neisius, P. Granger, Catalytic abatement of NO and N_2O from nitric acid plants: A novel approach using noble metal-modified perovskites, Journal of Catalysis, Volume 328, 2015, Pages 236-247, ISSN 0021-9517, https://doi.org/10.1016/j.jcat.2015.02.001.
47. J.P. Dacquin, C. Lancelot, C. Dujardin, C. Cordier-Robert, and P. Granger, Support-Induced Effects of $LaFeO_3$ Perovskite on the Catalytic Performances of Supported Pt Catalysts in $DeNO_x$ Applications, The Journal of Physical Chemistry C 2011 115 (5), 1911-1921, http://doi.org/10.1021/jp1069779.

48. J.-M. Giraudon, A. Elhachimi, F. Wyrwalski, S. Siffert, A. Aboukaïs, J.-F. Lamonier, G. Leclercq, Studies of the activation process over Pd perovskite-type oxides used for catalytic oxidation of toluene, Applied Catalysis B: Environmental, Volume 75, Issues 3–4, 2007, Pages 157-166, ISSN 0926-3373, https://doi.org/10.1016/j.apcatb.2007.04.005.
49. Xiaoyin Chen, Johannes W. Schwank, Galen B. Fisher, Yisun Cheng, Mark Jagner, Robert W. McCabe, Michael B. Katz, George W. Graham, Xiaoqing Pan, Nature of the two-step temperature-programmed decomposition of PdO supported on alumina, Applied Catalysis A: General, Volume 475, 2014, Pages 420-426, ISSN 0926-860X, https://doi.org/10.1016/j.apcata.2014.01.056.
50. Jianjun Chen, Yang Wu, Wei Hu, Pengfei Qu, Guochen Zhang, Pascal Granger, Lin Zhong, Yaoqiang Chen, New insights into the role of Pd-Ce interface for methane activation on monolithic supported Pd catalysts: A step forward the development of novel PGM Three-Way Catalysts for natural gas fueled engines, Applied Catalysis B: Environmental, Volume 264, 2020, 118475, ISSN 0926-3373, https://doi.org/10.1016/j.apcatb.2019.118475.
51. Lars Giebeler, Dieter Kießling, Gerhard Wendt, $LaMnO_3$ Perovskite Supported Noble Metal Catalysts for the Total Oxidation of Methane, Chem. Eng. Technol. 2007, 30, No. 7, 889–894, http://doi.org/10.1002/ceat.200600306.
52. Jianxiong Wu, Yuanshuang Zheng, Jean-Philippe Dacquin, Nora Djelal, Catherine Cordier, Christophe Dujardin, Pascal Granger, Impact of dual calcium and manganese substitution of La-deficient perovskites on structural and related catalytic properties: Future opportunities in next three-way-catalyst generation?, Applied Catalysis A: General, Volume 619, 2021, 118137, ISSN 0926-860X, https://doi.org/10.1016/j.apcata.2021.118137.
53. Runduo Zhang, Adrian Villanueva, Houshang Alamdari, Serge Kaliaguine, Cu- and Pd-substituted nanoscale Fe-based perovskites for selective catalytic reduction of NO by propene, Journal of Catalysis, Volume 237, Issue 2, 2006, Pages 368-380, ISSN 0021-9517, https://doi.org/10.1016/j.jcat.2005.11.019.
54. Ye Lu, Katarzyna A. Michalow, Santhosh Kumar Matam, Alexander Winkler, Alexandra E. Maegli, Songhak Yoon, Andre Heel, Anke Weidenkaff, Davide Ferri, Methane abatement under stoichiometric conditions on perovskite-supported palladium catalysts prepared by flame spray synthesis, Applied Catalysis B: Environmental, Volume 144, 2014, Pages 631-643, ISSN 0926-3373, https://doi.org/10.1016/j.apcatb.2013.08.001.

55. Xinwei Yang, Qin Gao, Zhenyang Zhao, Yanglong Guo, Yun Guo, Li Wang, Yunsong Wang, Wangcheng Zhan, Surface tuning of noble metal doped perovskite oxide by synergistic effect of thermal treatment and acid etching: A new path to high-performance catalysts for methane combustion, Applied Catalysis B: Environmental, Volume 239, 2018, Pages 373-382, ISSN 0926-3373, https://doi.org/10.1016/j.apcatb.2018.08.038.
56. Xingang Li, Cheng Chen, Cheng Liu, Hui Xian, Li Guo, Jiaolong Lv, Zheng Jiang, and Philippe Vernoux, Pd-Doped Perovskite: An Effective Catalyst for Removal of NOx from Lean-Burn Exhausts with High Sulfur Resistance, ACS Catalysis 2013 3 (6), 1071-1075, http://doi.org/10.1021/cs400136t.
57. Yuan Wang, Hamidreza Arandiyan, Jason Scott, Mandana Akia, Hongxing Dai, Jiguang Deng, Kondo-Francois Aguey-Zinsou, and Rose Amal, High Performance Au–Pd Supported on 3D Hybrid Strontium-Substituted Lanthanum Manganite Perovskite Catalyst for Methane Combustion, ACS Catalysis 2016 6 (10), 6935-6947, http://doi-org/10.1021/acscatal.6b01685.
58. Lidiya S. Kibis, Alexander A. Simanenko, Andrey I. Stadnichenko, Vladimir I. Zaikovskii, and Andrei I. Boronin, Probing of Pd^{4+} Species in a PdO_x–CeO_2 System by X-Ray Photoelectron Spectroscopy, Lidiya S. Kibis, Alexander A. Simanenko, Andrey I. Stadnichenko, Vladimir I. Zaikovskii, and Andrei I. Boronin, The Journal of Physical Chemistry C 2021 125 (38), 20845-20854, http://doi-org/10.1021/acs.jpcc.1c04646.
59. Jihui Wang, Hong Chen, Zhicheng Hu, Mingfa Yao & Yongdan Li (2015) A Review, on the Pd-Based Three-Way Catalyst, Catalysis Reviews: Science and Engineering, 57:1, 79-144, http://doi-org/10.1080/01614940.2014.977059.
60. Patrick Gélin, Michel Primet, Complete oxidation of methane at low temperature over noble metal-based catalysts: a review, Applied Catalysis B: Environmental, Volume 39, Issue 1, 2002, Pages 1-37, ISSN 0926-3373, https://doi.org/10.1016/S0926-3373(02)00076-0.
61. Sangwook Joo, Arim Seong, Ohhun Kwon, Kyeounghak Kim, Jong Hoon Lee, Raymond J. Gorte, John M. Vohs, Jeong Woo Han, Guntae Kim. Highly active dry methane reforming catalysts with boosted in situ grown Ni-Fe nanoparticles on perovskite via atomic layer deposition. Science Advances. 2020-08-28. http://doi-org/10.1126/sciadv.abb1573.
62. Tangyuan Li, Yonggang Yao, Zhennan Huang, Pengfei Xie, Zhenyu Liu, Menghao Yang, Jinlong Gao, Kaizhu Zeng, Alexandra H. Brozena, Glenn Pastel, Miaolun Jiao, Qi Dong, Jiaqi Dai, Shuke

Li, Han Zong, Miaofang Chi, Jian Luo, Yifei Mo, Guofeng Wang, Chao Wang, Reza Shahbazian-Yassar & Liangbing Hu. Denary oxide nanoparticles as highly stable catalysts for methane combustion. Nat Catal 4, 62–70 (2021). https://doi.org/10.1038/s41929-020-00554-1.

63. M. Cargnello, J. J. Delgado Jaén, J. C. Hernández Garrido, K. Bakhmutsky, T. Montini, J. J. Calvino Gámez, R. J. Gorte, P. Fornasiero, Exceptional Activity for Methane Combustion over Modular Pd@CeO_2 Subunits on Functionalized Al_2O_3, Science 337, 713 (2012), https://doi.org/10.1126/science.1222887.

64. J. Yang, M. Peng, G. Ren, H. Qi, X. Zhou, J. Xu, F. Deng, Z. Chen, J. Zhang, K. Liu, X. Pan, W. Liu, Y. Su, W. Li, B. Qiao, D. Ma, T. Zhang, A Hydrothermally Stable Irreducible Oxide-Modified Pd/$MgAl_2O_4$ Catalyst for Methane Combustion, Angew. Chem. Int. Ed. 2020, 59, 18522. https://doi-org/10.1002/anie.202009050.

65. Weixin Huang, Aaron C. Johnston-Peck, Trenton Wolter, Wei-Chang D. Yang, Lang Xu, Jinwon Oh, Benjamin A. Reeves, Chengshuang Zhou, Megan E. Holtz, Andrew A. Herzing, Aaron M. Lindenberg, Manos Mavrikakis, Matteo Cargnello, Steam-created grain boundaries for methane C–H activation in palladium catalysts, Science 373, 1518–1523 (2021), https://doi.org/10.1126/science.abj5291.

66. Sun Y, Dai S. High-entropy materials for catalysis: A new frontier. Science Advances, 2021, 7(20), https://doi.org/10.1126/sciadv.abg1600.

67. Richard, M., Can, F., Duprez, D., Gil, S., Giroir-Fendler, A. and Bion, N. (2014), Remarkable Enhancement of O_2 Activation on Yttrium-Stabilized Zirconia Surface in a Dual Catalyst Bed. Angew. Chem. Int. Ed., 53: 11342-11345. https://doi-org/10.1002/anie.201403921.

68. P. Granger, Challenges and breakthroughs in post-combustion catalysis: how to match future stringent regulations, Catal. Sci. Technol., 2017, 7, 5195. http://doi-org/10.1039/c7cy00983f.

69. van Deelen, T.W., Hernández Mejía, C. & de Jong, K.P. Control of metal-support interactions in heterogeneous catalysts to enhance activity and selectivity. Nat Catal 2, 955–970 (2019). https://doi.org/10.1038/s41929-019-0364-x.

70. Cheng, K., Smulders, L. C., van der Wal, L. I., Oenema, J., Meeldijk, J. D., Visser, N. L., ... & de Jong, K. P. (2022). Maximizing noble metal utilization in solid catalysts by control of nanoparticle location. Science, 377(6602), 204-208. https://doi.org/10.1126/science.abn8289.

71. C. H. Kim, G. Qi, K. Dahlberg, W. Li, Strontium-Doped Perovskites Rival Platinum Catalysts for

Treating NO_x in Simulated Diesel Exhaust, pp. 1624-1627, Vol 327, Issue 597, 26 Mar 2010, Science. https://doi.org/10.1126/science.1184087.

72. Yao, Y., Dong, Q., Brozena, A., Luo, J., Miao, J., Chi, M., ... & Hu, L. (2022). High-entropy nanoparticles: Synthesis-structure-property relationships and data-driven discovery. Science, 376(6589), https://doi.org/10.1126/science.abn3103.
73. Davis R, John P. Application of Taguchi-based design of experiments for industrial chemical processes. Statistical approaches with emphasis on design of experiments applied to chemical processes, 2018, 137. http://doi-org/10.5772/intechopen.69501.
74. Kothari, M., Jeon, Y., Miller, D.N. et al. Platinum incorporation into titanate perovskites to deliver emergent active and stable platinum nanoparticles. Nat. Chem. 13, 677–682 (2021). https://doi.org/10.1038/s41557-021-00696-0.
75. Hideaki Muraki, Koji Yokota, Yoshiyasu Fujitani, Nitric oxide reduction performance of automotive palladium catalysts, Applied Catalysis, Volume 48, Issue 1, 1989, Pages 93-105, ISSN 0166-9834, https://doi.org/10.1016/S0166-9834(00)80268-7.
76. Istvan Halasz, Alan Brenner, Mordecai Shelef, K.Y. Simon Ng, Preparation and characterization of $PdO\text{-}MoO_3/\gamma\text{-}Al_2O_3$ catalysts, Applied Catalysis A: General, Volume 82, Issue 1, 1992, Pages 51-63, ISSN 0926-860X, https://doi.org/10.1016/0926-860X(92)80005-W.

Annexes

XPS analysis for Pd/La$_x$MnO$_3$, Pd/La$_x$K$_{1-x}$MnO$_3$, Pd/La$_x$Sr$_{1-x}$MnO$_3$ series before high throughput reaction

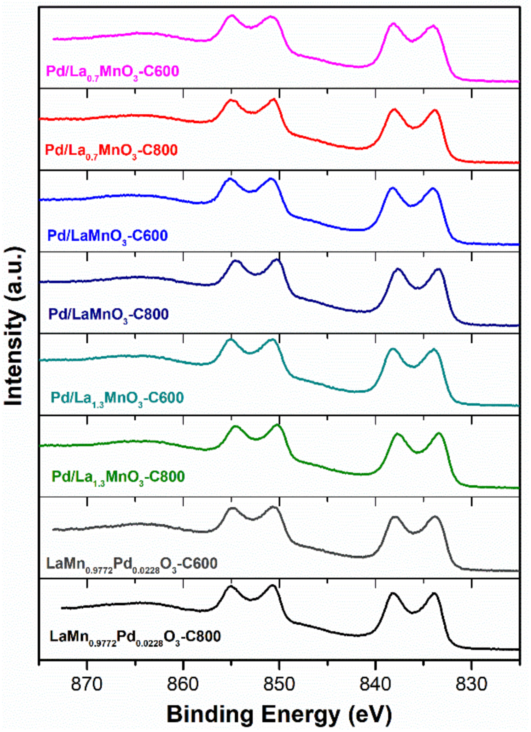

Fig.5.2.S1. XPS spectrum of La 3d: One-pot and sequential samples.

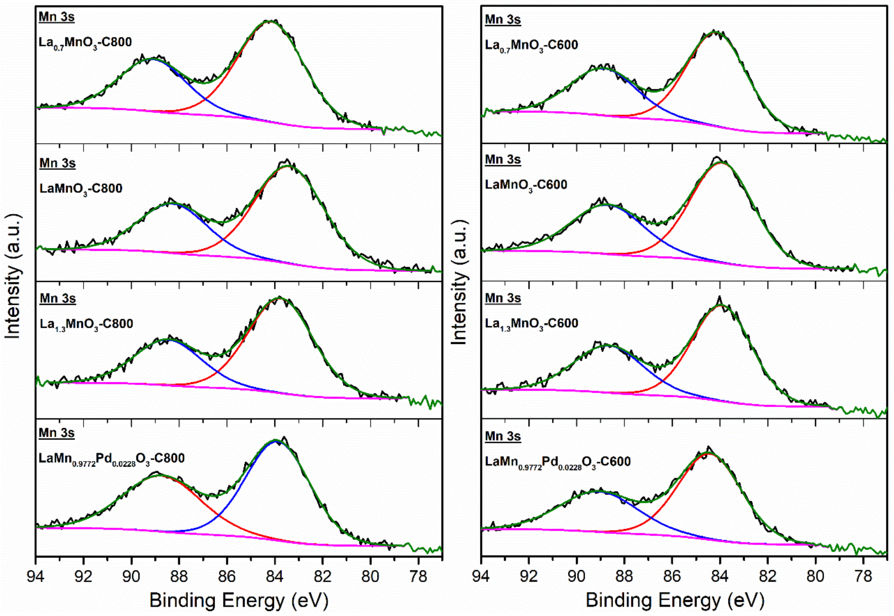

Fig.5.2.S2. XPS spectrum of Mn 3s: One-pot and sequential samples.

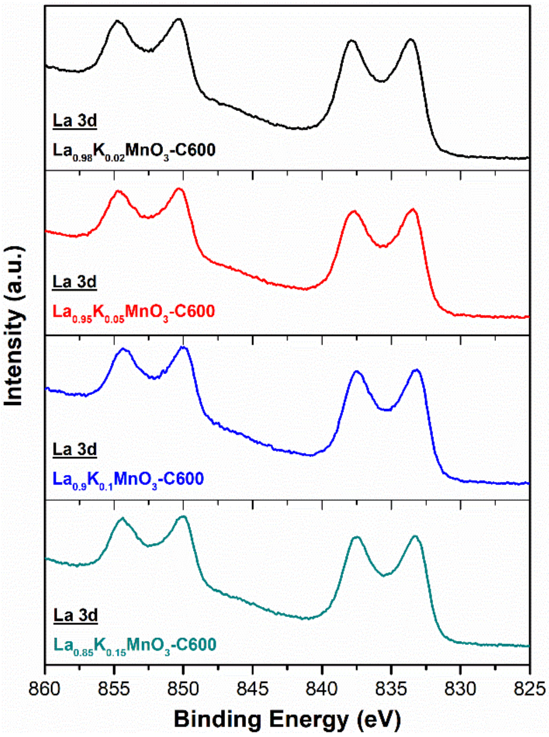

Fig.5.3.S1 XPS analysis of La 3d orbital on K substitution samples.

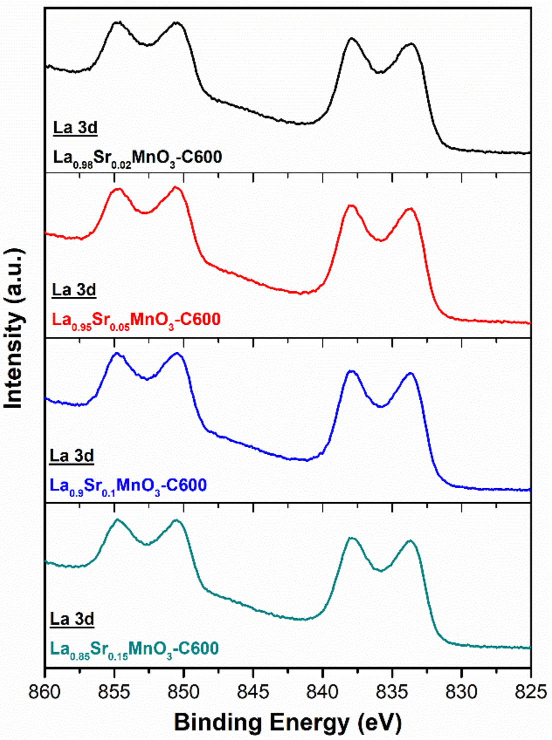

Fig.5.3.S2 XPS analysis of La 3d orbital on Sr substitution samples.

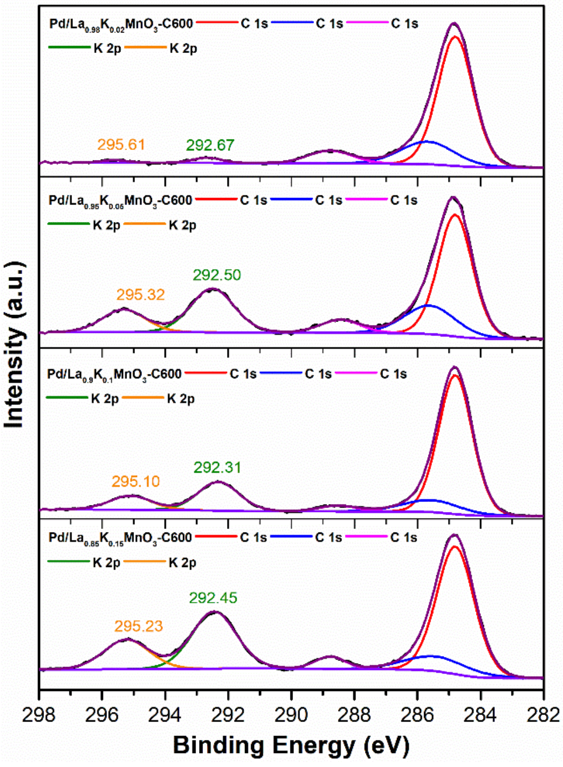

Fig.5.3.S3 XPS analysis of K 2p orbital on K substitution samples.

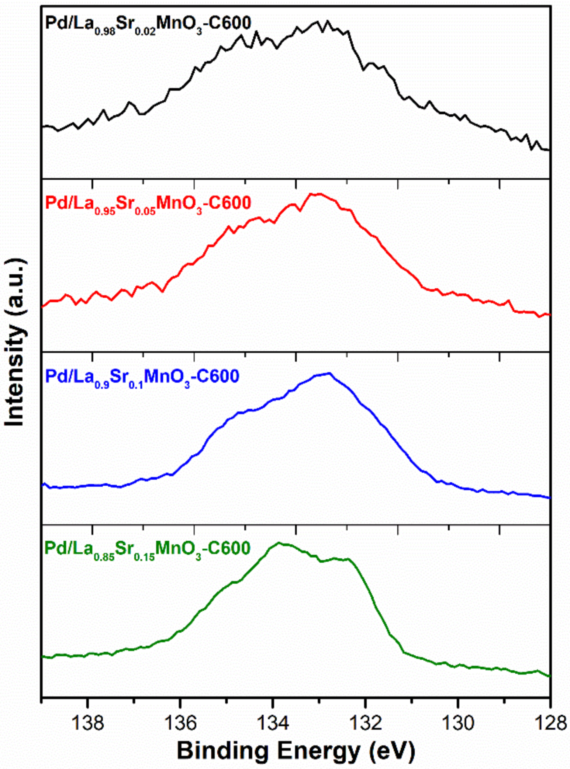

Fig.5.3.S4 XPS analysis of Sr 3d orbital on Sr substitution samples.

XPS analysis for Pd/La$_x$MnO$_3$, Pd/La$_x$K$_{1-x}$MnO$_3$, Pd/La$_x$Sr$_{1-x}$MnO$_3$ series after high throughput reaction

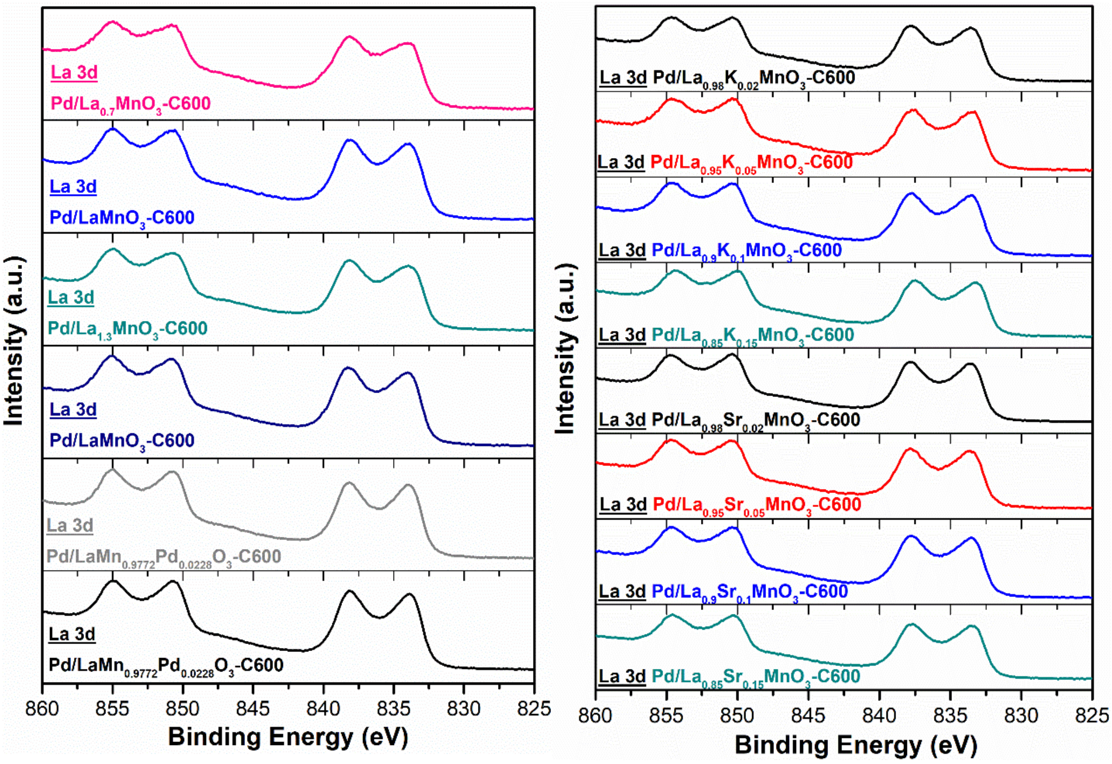

Fig.S5.3.1 XPS spectrum of post-reaction La 3d: One-pot and sequential

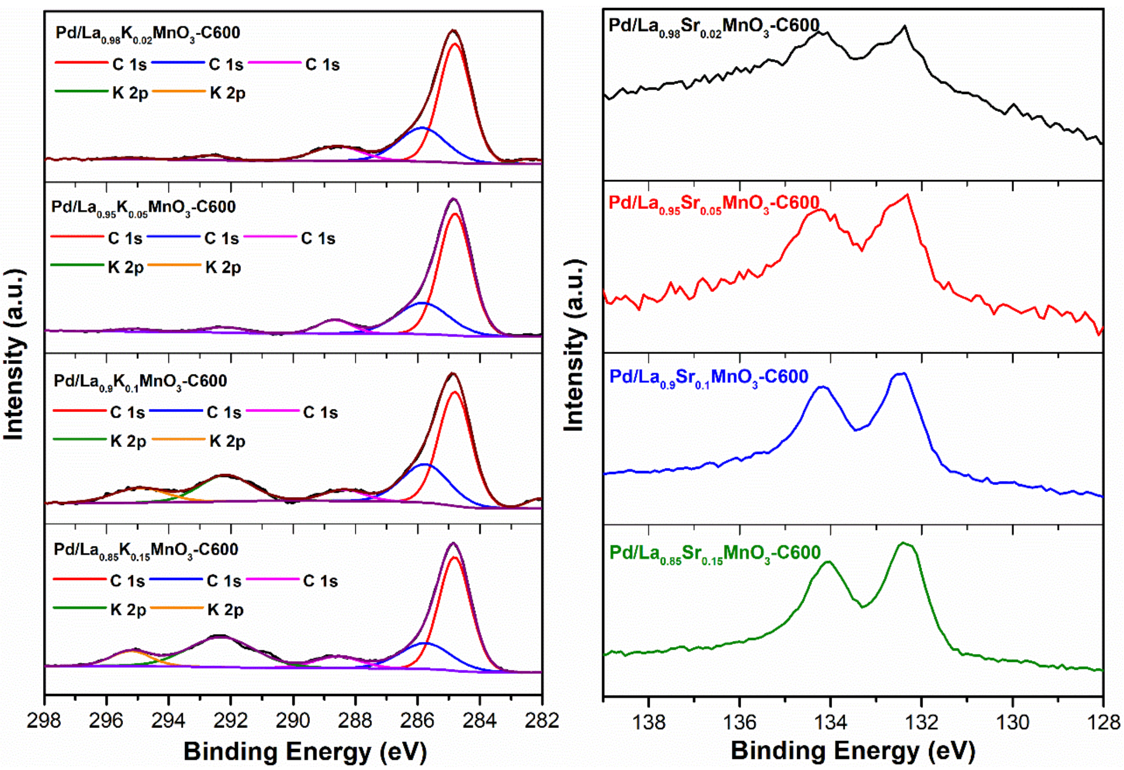

Fig.S5.3.2 XPS spectrum of post-reaction K 2p and Sr 3d: Sequential samples.

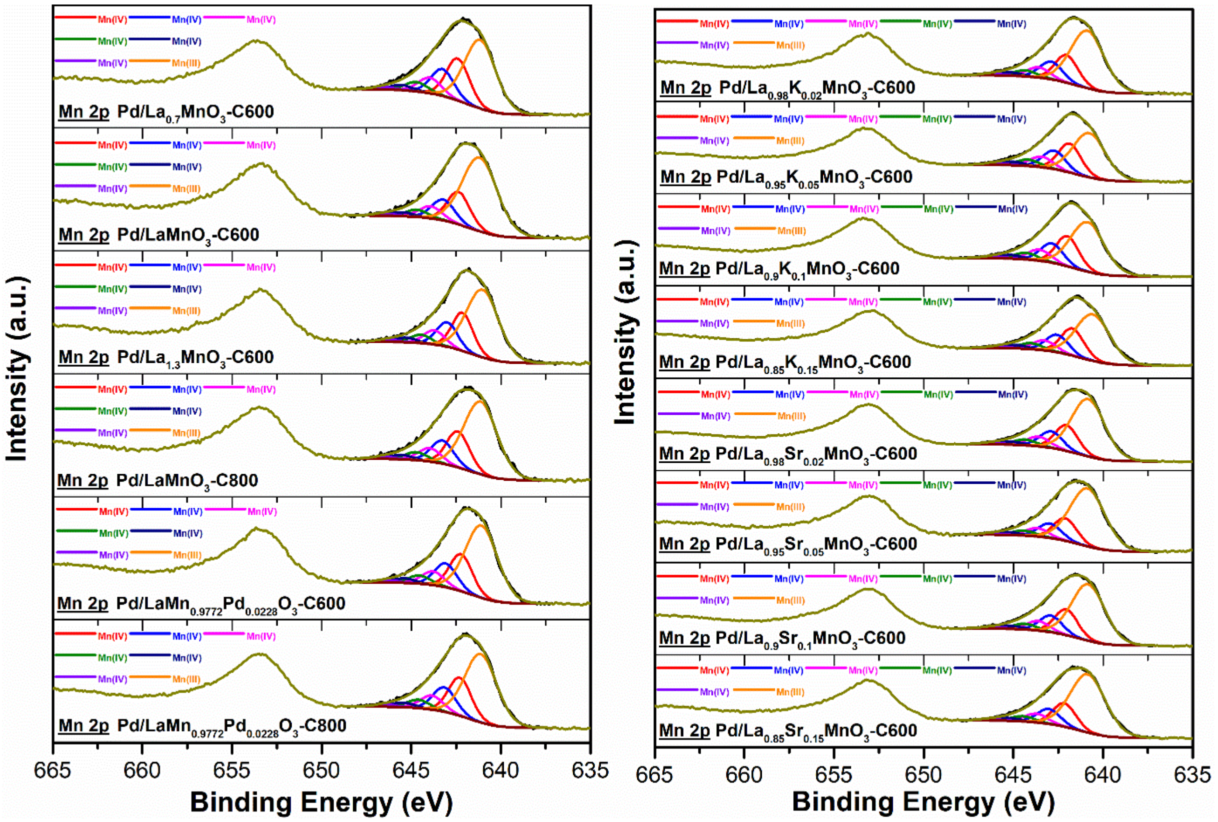

Fig.S5.3.3 XPS spectrum of post-reaction Mn 2p: One-pot and sequential

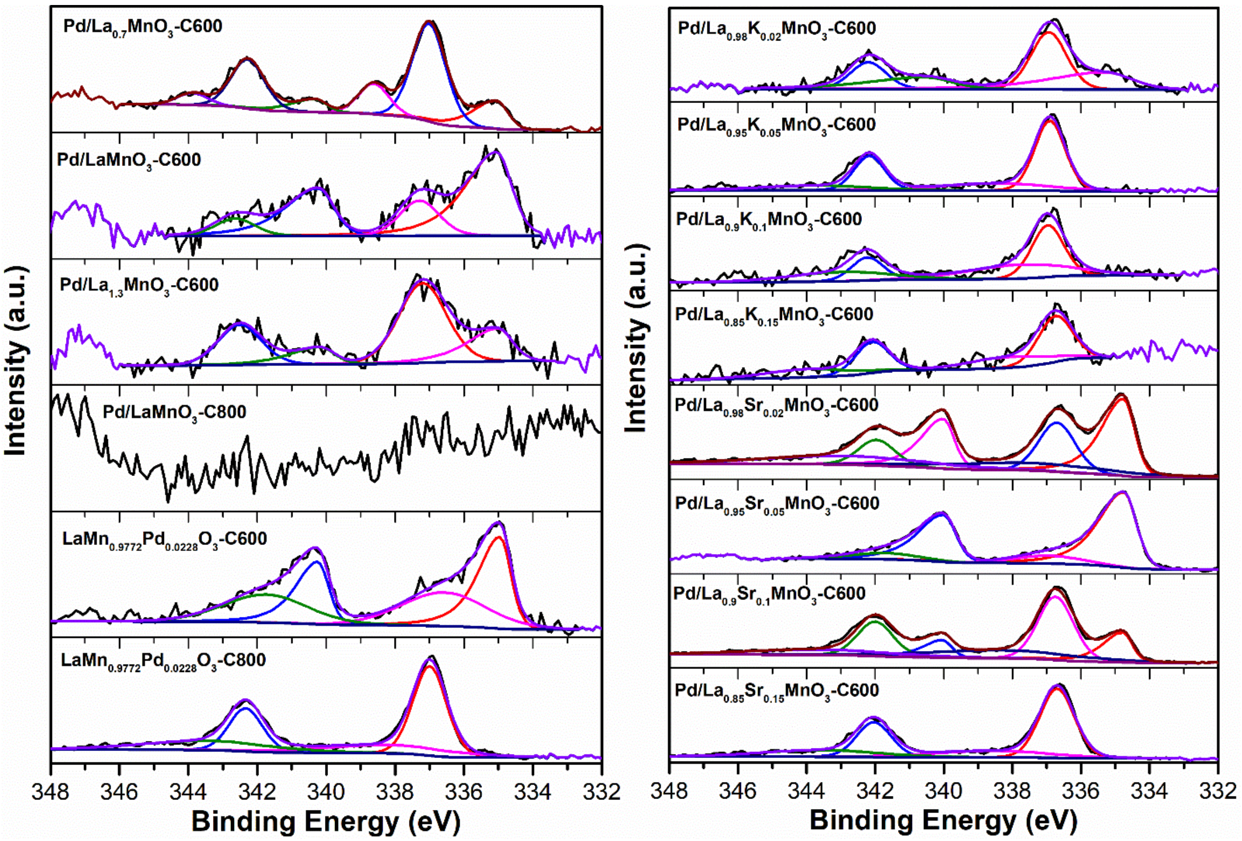

Fig.S5.3.4 XPS spectrum of post-reaction Pd 3d: One-pot and sequential

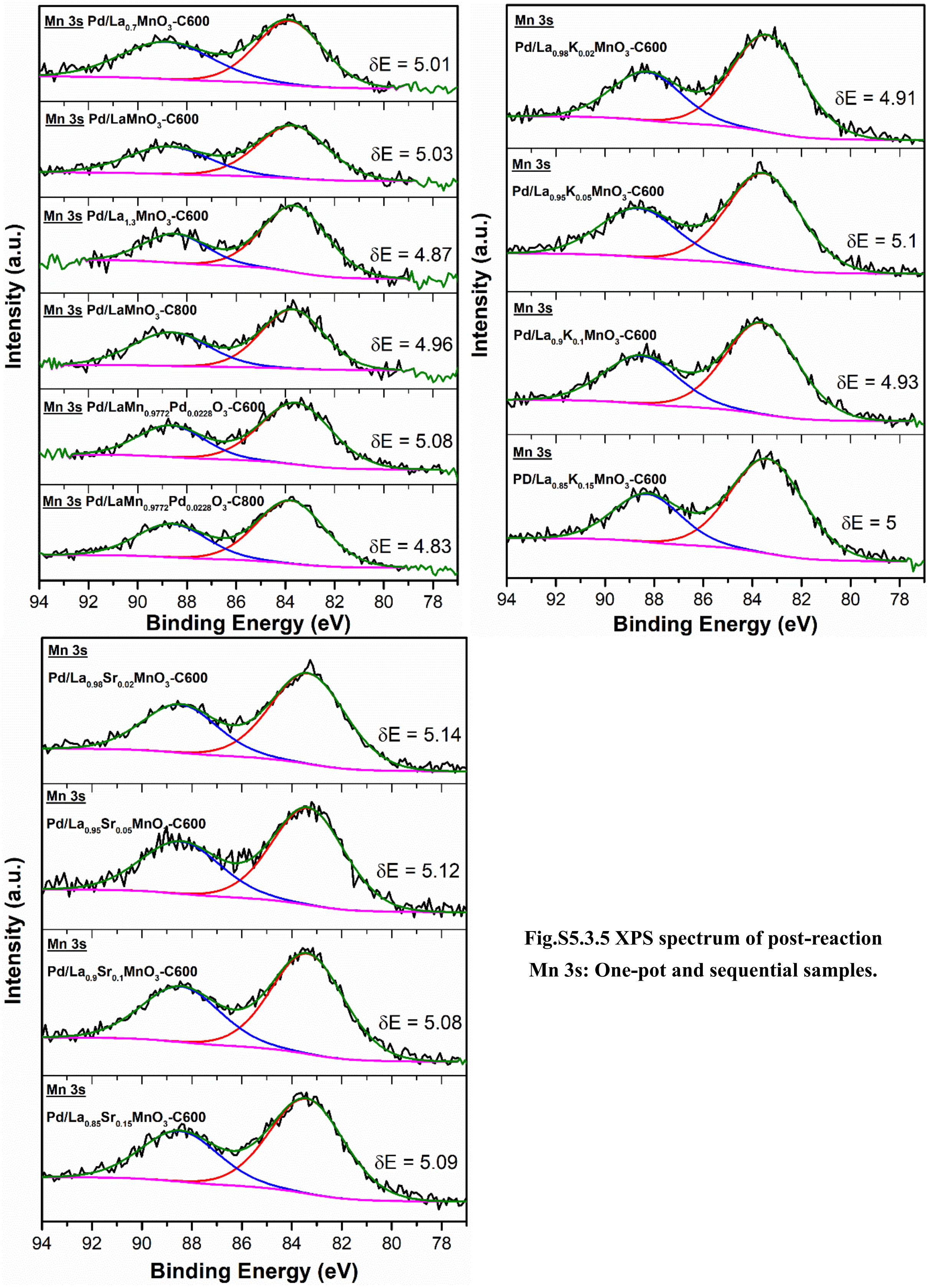

Fig.S5.3.5 XPS spectrum of post-reaction Mn 3s: One-pot and sequential samples.

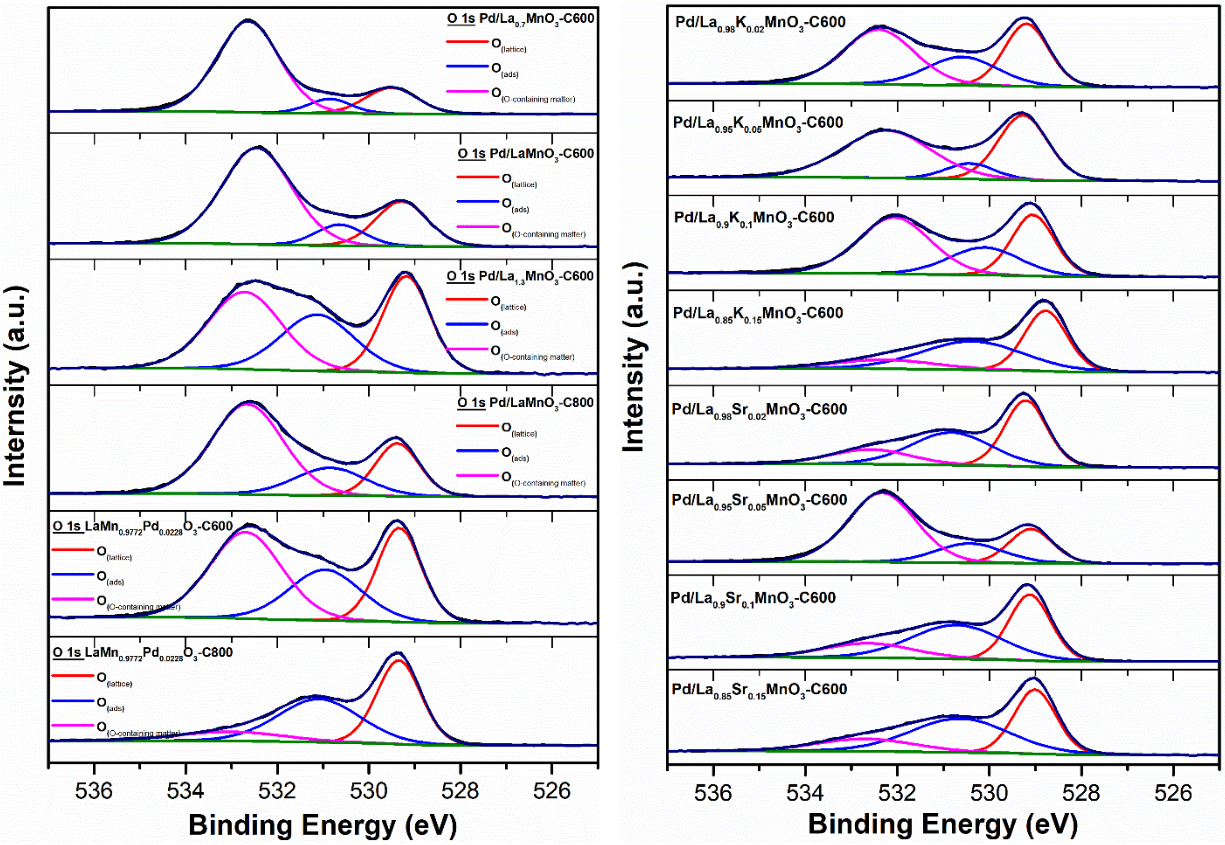

Fig.S5.3.6 XPS spectrum of post-reaction O 1s: One-pot and sequential samples.

Table S5.3.1. Impact of Pd incorporation into perovskite, post-reaction of high throughput, on the surface properties of Pd-based perovskite catalysts

Catalysts	XPS analysis after high throughput reaction for Pd/La$_x$MnO$_3$, Pd/La$_x$K$_{1-x}$MnO$_3$, Pd/La$_x$Sr$_{1-x}$MnO$_3$ series.								
	Pd ratio (At%) [a]	$\frac{Pd}{\text{La}(+\text{k}/\text{Sr})}$	$\frac{Pd^{4+}}{Pd^{2+}}$	$\frac{Pd^{2+}}{Pd^{0}}$	$\frac{Pd}{\text{Mn}}$	$\frac{Mn^{3+}}{Mn^{4+}}(b)$	**Mn（AOS）** [c]	$\frac{O_{ads}}{O_{lat}}$	O_{Suf} **Ratio (%)** [d]
Pd/LaMnO$_3$(C600)	0.14	0.02	-	1.75	0.03	1.45	3.29	0.44	66.95
Pd/LaMnO$_3$(C800)	-	-	-	-	-	1.22	3.37	0.86	59.92
Pd/La$_{0.7}$MnO$_3$(C600)	0.32	0.10	0.24	3.63	0.06	0.93	3.31	0.46	74.27
Pd/La$_{1.3}$MnO$_3$(C600)	0.58	0.01	-	2.27	0.06	1.14	3.47	0.91	39.46
LaMn$_{0.98}$Pd$_{0.02}$O$_3$(C600)	0.68	0.08	-	0.92	0.11	1.16	3.24	0.89	44.62
LaMn$_{0.98}$Pd$_{0.02}$O$_3$(C800)	1.29	0.11	1.91	-	0.14	1.04	3.52	0.96	12.10
Pd/La$_{0.98}$K$_{0.02}$MnO$_3$(C600)	0.25	0.02	-	1.12	0.03	1.27	3.53	0.73	44.74
Pd/La$_{0.95}$K$_{0.05}$MnO$_3$(C600)	0.22	0.04	0.42	-	0.04	0.91	3.21	0.24	51.54
Pd/La$_{0.9}$K$_{0.1}$MnO$_3$(C600)	0.20	0.01	0.99	-	0.01	1.00	3.40	0.76	46.77
Pd/La$_{0.85}$K$_{0.15}$MnO$_3$(C600)	0.10	0.003	0.60	-	0.01	1.06	3.44	1.13	14.22
Pd/La$_{0.98}$Sr$_{0.02}$MnO$_3$(C600)	1.19	0.10	0.99	0.58	0.21	1.34	3.21	0.94	17.86
Pd/La$_{0.95}$Sr$_{0.05}$MnO$_3$(C600)	0.65	0.09	-	0.18	0.12	1.63	3.24	0.89	62.72
Pd/La$_{0.9}$Sr$_{0.1}$MnO$_3$(C600)	1.15	0.08	0.58	2.26	0.12	1.32	3.24	1.12	18.31
Pd/La$_{0.85}$Sr$_{0.15}$MnO$_3$(C600)	0.80	0.06	0.44	-	0.08	1.59	3.22	1.25	16.96

[a] from Pd dispersion ratio (%) from XPS

[b] from XPS Mn 2p orbital

[c] average oxidation state

[d] ratio of hydroxyl, calcium carbonate and other oxygen-containing substances in total oxygen amount (within lattice oxygen and adsorbed oxygen species)

XPS analysis for palladium incorporated $La_xSr_{0.15}MnO_3$ series after high throughput reaction

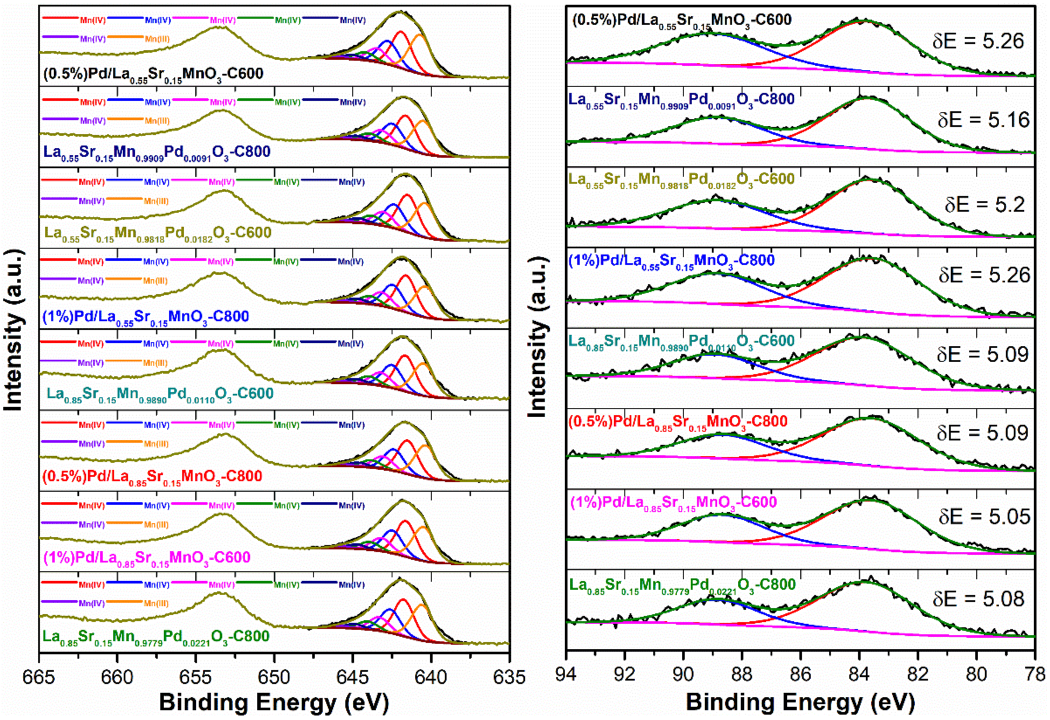

Fig.S5.3.7 XPS spectrum of post-reaction Mn 2p and Mn 3s: One-pot and sequential

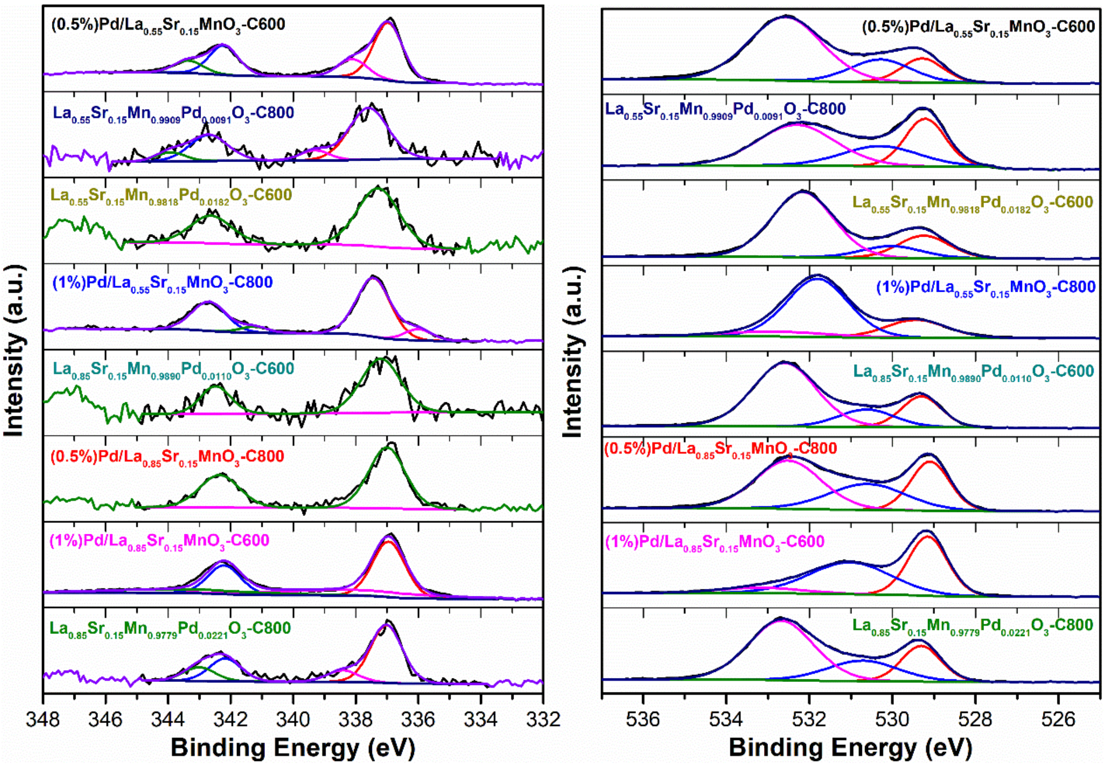

Fig.S5.3.8 XPS spectrum of post-reaction Pd 3d and O 1s: One-pot and sequential

Table S5.3.1. Impact of Pd incorporation into perovskite, post-reaction of high throughput, on the surface properties of Pd-based perovskite catalysts

Catalysts	**XPS analysis after high throughput reaction for Pd/La$_x$MnO$_3$, Pd/La$_x$K$_{1-x}$MnO$_3$, Pd/La$_x$Sr$_{1-x}$MnO$_3$ series.**								
	Pd ratio (At%) [a]	$\frac{Pd}{\mathrm{La+Sr}}$	$\frac{Pd^{4+}}{Pd^{2+}}$	$\frac{Pd^{2+}}{Pd^{0}}$	$\frac{Pd}{\mathrm{Mn}}$	$\frac{Mn^{3+}}{Mn^{4+}}(b)$	**Mn（AOS）** [c]	$\frac{O_{ads}}{O_{lat}}$	O_{Suf} **Ratio (%)** [d]
0.5%Pd/(La$_{0.55}$Sr$_{0.15}$MnO$_3$-C600)	1.28	0.22	0.88	-	0.16	0.47	3.03	1.37	65.99
La$_{0.55}$Sr$_{0.15}$Mn$_{0.9909}$Pd$_{0.0091}$O$_3$-C800	0.10	0.01	0.19	-	0.01	0.44	3.15	0.81	47.73
La$_{0.55}$Sr$_{0.15}$Mn$_{0.9818}$Pd$_{0.0182}$O$_3$-C600	0.10	0.02	0	-	0.01	0.41	3.10	0.64	67.90
1%Pd/(La$_{0.55}$Sr$_{0.15}$MnO$_3$-C800)	0.62	0.12	-	6.16	0.12	0.37	3.03	3.27	10.25
La$_{0.85}$Sr$_{0.15}$Mn$_{0.9890}$Pd$_{0.0110}$O$_3$-C600	0.06	0.01	0	-	0.01	0.40	3.22	0.80	64.53
0.5%Pd/(La$_{0.85}$Sr$_{0.15}$MnO$_3$-C800)	0.19	0.02	0	-	0.03	0.43	3.22	1.05	44.67
1%Pd/(La$_{0.85}$Sr$_{0.15}$MnO$_3$-C600)	1.17	0.08	0.52	-	0.12	0.42	3.27	1.13	8.49
La$_{0.85}$Sr$_{0.15}$Mn$_{0.9779}$Pd$_{0.0221}$O$_3$-C800	0.19	0.02	0.31	-	0.03	0.43	3.24	1.04	57.45

[a] from Pd dispersion ratio (%) from XPS

[b] from XPS Mn 2p orbital

[c] average oxidation state

[d] ratio of hydroxyl, calcium carbonate and other oxygen-containing substances in total oxygen amount (within lattice oxygen and adsorbed oxygen species)

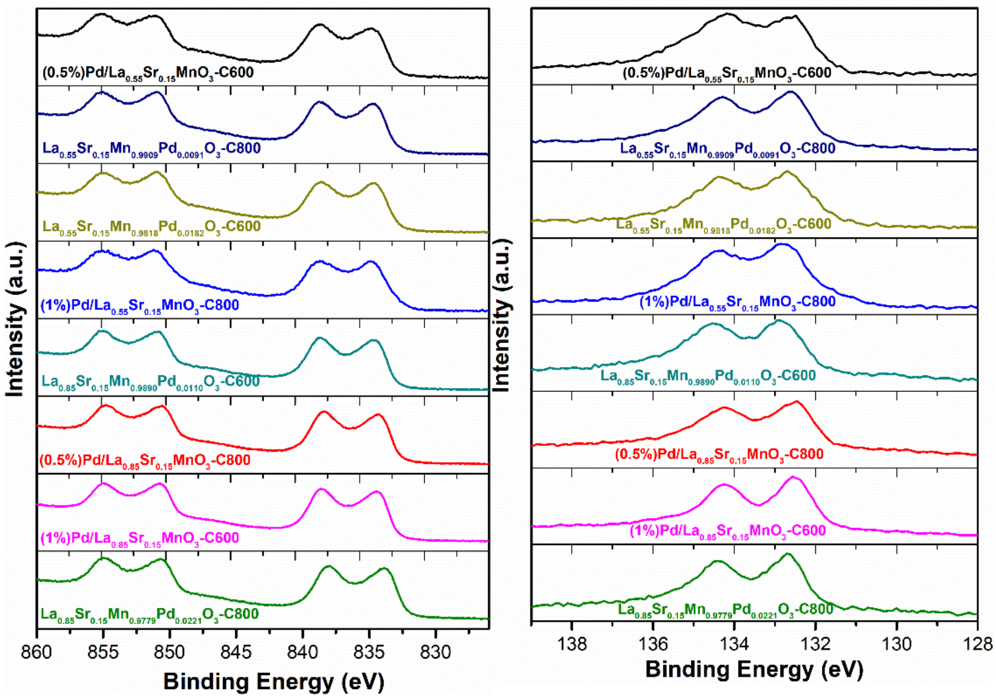

Fig.S5.3.9 XPS spectrum of post-reaction La 3d and Sr 3d: One-pot and sequential

Chapter VI. Theoretical and Experimental Combination from High Throughput Experimentations of Methane Oxidation in Lean and Stoichiometric Conditions

1. Introduction

As previously discussed, the substitution of liquid fuels by natural gas engines is envisioned at short terms and complies with more stringent regulations on atmospheric pollutant emissions with lower NO_x and nearly zero particulate emissions. However, more efficient three-way catalytic technologies are required to avoid unburnt methane emission recognized as potent greenhouse gas. One of the key issues lies in their weak efficacy near the stoichiometry or under slight rich exposure typically under three-way catalytic operating conditions. Up to now, the kinetics of catalytic methane combustion and related model prediction have been investigated essentially in lean conditions on benchmark supported palladium catalysts [1-5]. Numerical simulations near stoichiometric conditions from relevant microkinetic analysis are scarce [6,7]. A critical factor is the preservation of the dispersion of PdO_x species recognized as the active sites [8,9]. At high temperature typically encountered in three-way operating conditions, the decomposition of PdO_x into less active nanometric metallic Pd^0 species cannot be strictly ruled out causing a loss of efficiency. [8]. Presently, there is no clear consensus on the nature and architecture of active sites in typical three-way operating conditions. Miller and Malatpure [10] assumed a pair of sites composed of PdO and Pd^0. New generation of three-way catalysts has arisen in the past two decades able for stabilizing the dispersion of precious metals in a broader temperature range under switching lean/rich exposure thanks to strong interactions with perovskite structures [11-13]. The development of such supported catalysts has also opened up debate over the consensus that PdO_x is the active site of the reaction. For instance, Lu et al. [14] synthesized hexagonal $Pd\text{-}YFeO_{3\pm\delta}$ structure by flame-spray-pyrolysis, with preferential formation of supported Pd^0 and Pd^{2+} species instead of solid solution. They observed a strong rate enhancement in methane conversion after cycling up to 850°C under reaction conditions assigned to the formation of metallic particles and the phase transition to orthorhombic $YFeO_{3\pm\delta}$. Besides, Gonzáles-Marcos et al. [15] also observed the coexistence of two kinetic regimes from light-off curves on Pd supported on $Ce_{0.68}Zr_{0.32}O_2$ explained by the involvement of Pd(+I)-like species at low temperature while metallic Pd^0 species would act as active sites at high temperature. Different kinetic regimes have been also identified on Pd/Al_2O_3-CeO_2 assigned to the prevalence of the Pd-Ce or Pd-PdO interface accompanied with higher TOF values and lower activation barrier in the former case [16]. The nature of the active site-related reaction mechanisms is also disputed over the presence or the absence of water in the feed gas. Steam has currently a detrimental effect [17] by hindering oxygen mobility on the support and suppressing the oxygen exchange process at the metal support interface [18]. In addition, water can originate deactivation because the large accumulation of water can weaken the strength of Pd nanoparticles on support material, and then become more sensitive to coalescence process, leading to changes in the particle size and morphology.

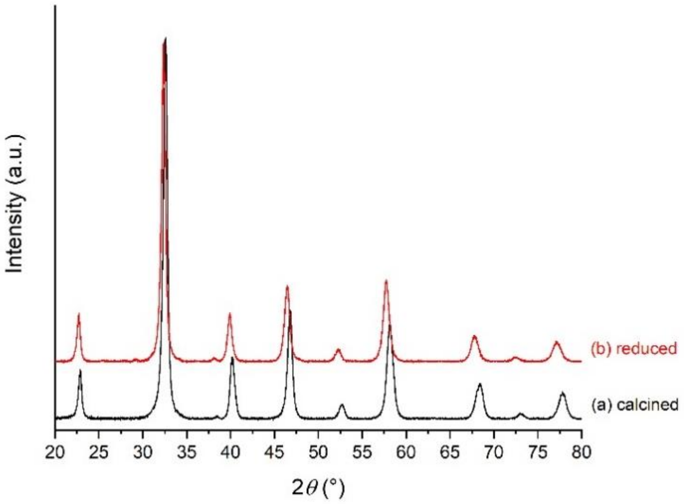

Fig 6.1 XRD patterns recorded on calcined $Pd/La_{0.7}MnO_3$(SOL) catalyst (a) and after pre-reduction in H_2 at 250°C (b).

This chapter reports a kinetic study of the catalytic CH_4/O_2 reaction on Pd-based catalysts in the presence and absence of steam. Different parameters have been investigated related to the lanthanum composition, the methodology for Pd incorporation and the Pd content. Two different richness for the inlet gas mixture have been investigated in the presence of an excess of oxygen and near stoichiometric conditions. Based on combined theoretical and experimental approaches, the different reaction mechanisms, accounting for single and dual sites involving surface reactive oxygen species form the perovskite, have been compared.

Prior to reaction, the catalyst samples were *in situ* reduced at 250°C. As example, XRD analysis on ex situ pre-reduced Pd/$La_{0.7}MnO_3$ catalyst (Fig 6.1) shows that the rhombohedral perovskite structure is conserved after reduction in moderate temperature conditions, *i.e.* 250°C in a flow containing 5 vol.% H_2 in He. The characteristic reflections of the rhombohedral $La_{0.7}MnO_3$ structure persist after reduction. A slight shift on to lower 2θ values is noticeable which reflects an expansion of the cell volume due to the reduction of Mn^{4+} to Mn^{3+}.

2. Theoretical approach on model Pd (111) surface

The unity bond index-quadratic exponential potential (UBI-QEP) is a theoretical method suited for straightforward calculations of heat and activation energies for elementary steps involved in a catalytic reaction according to a thermodynamic approach briefly described in Scheme 6.1. This method can be considered as a generalization of the bond order conservation Morse potential method as described elsewhere [21]. Calculations of activation barrier E and enthalpy of reaction ΔH were performed on a closed-packed Pd (111) surface with preferred three-fold hollow sites corresponding to n = 3. A set of elementary steps representative of adsorption steps and surface reactions in the course of methane oxidation has been selected. In all cases forward and reverse transformation have been envisioned characterized by activation energies respectively E_f and E_r such as $\Delta H = E_f - E_r$. Only gas phase total bond energy D and atomic heat of chemisorption (Q) are needed [22] for the calculation of activation barrier as described in Table 6.1. Oxygen and methane adsorptions were assumed none activated.

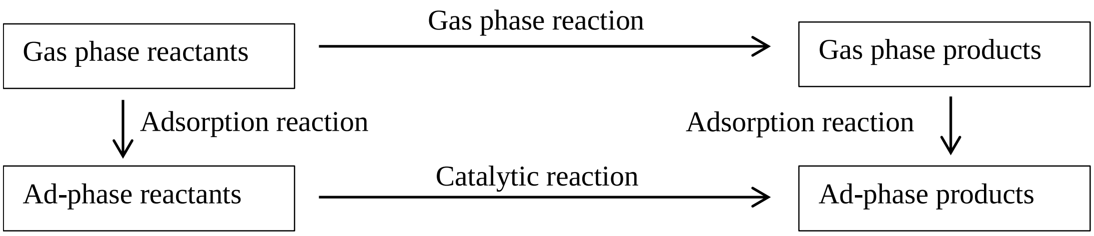

Scheme 6.1. Methodology for the calculation of activation barrier for forwards and reverse elementary steps and enthalpies $\Delta H = E_f - E_r$..

Table 6.1. Equation for the calculation of activation energy for various elementary steps described in the unity bond index-quadratic exponential potential method (UBI-QEP).

Elementary step	Equation
Heat of adsorption of dissociated atom with Q_{0A} the heat of adsorption for metal-atom bonding	$Q_A = Q_{0A}\left(2 - \frac{1}{n}\right)$
Heat of adsorption strongly bonded diatomic AB molecules	$Q_{AB} = \frac{Q_A^2}{Q_A + D_{AB}}$
Activation energy $E_{AB,g}$ for the dissociation of diatomic gas phase species $AB_g \rightarrow A_* + B_*$	$E_{AB,g} = \frac{1}{2}\left(D_{AB} + \frac{Q_A Q_B}{Q_A + Q_B} - Q_{AB} - Q_A - Q_B\right)$
Activation energy $E_{AB,ads}$ in case of dissociation of adsorbed diatomic AB molecules	$E_{AB,ads} = E_{AB,g} + Q_{AB}$
Activation energy for the recombination $A_* + B_* \rightarrow AB_g$	$E_{AB,g} = Q_A + Q_B - D_{AB}$
Activation energy for the recombination $A_* + B_* \rightarrow AB_*$	$E_{AB,ads} = Q_A + Q_B - D_{AB} - E_{AB,g}$

Numerical values are listed in Table 6.2 and account for a typical accuracy of 5-15 kJ/mol. These values correspond to the zero-coverage limit when free sites are largely available, which is rarely the case when catalytic measurements are performed near atmospheric pressure. The heat of adsorptions for none activated adsorption processes, *i.e.* dissociative and molecular adsorption respectively for O_2 and CH_4, reveal a much higher exothermicity of oxygen adsorption reflecting a stronger adsorption. Subsequent surface reactions have been considered with two different scenarios for the dissociation of chemisorbed methane molecules involving a nearest-neighbor vacant Pd site or occupied by chemisorbed O atoms.

Slightly lower activation barrier is obtained in the former case (97 kJ/mol vs. 117 kJ/mol) which emphasizes that chemisorbed O atom would not *a priori* favor the C-H bond breaking in $CH_{4,ads}$ molecules in these coverage conditions. Previous DFT calculations on PdO(101) surface [23] differ from these conclusions showing that hydrogen abstraction from methane would occur more readily over a Pd_{cus}-O_{cus} site pair. As a matter of fact, such differences were expected as already pointed out by Zhu et al [3] who found significant change of the activation energy on Pd metal and PdO for methane combustion suggesting different reaction mechanisms and we must also keep in mind the borderline case for $\theta = 0$ which does not reflect the adsorbate composition in our operating conditions.

The intermediate production of CO can be discussed near stoichiometric conditions when the surface is oxygen depleted because similarly to O_{ads} and OH_{ads}, CO_{ads} species could potentially act as inhibitor preventing methane dissociation. Let us note the low activation barrier for the following step: $CO_* + O_* \leftrightarrows CO_2 + 2_*$ which presumes a fast CO oxidation to CO_2. Results near zero-coverage *a priori* suggest a detrimental effect of oxygen related to inhibiting effect. However, the adsorbate coverage dependency of the activation barrier assigned to the C-H bond breaking step must be envisioned.

Table 6.2. Heat of reaction and activation barrier calculated on Pd(111) at $\theta = 0$ from the UBI-QEP method.

Reaction	**ΔH (kJ/mol)**	**$E_f^{\,a}$ (kJ/mol)**	**$E_r^{\,b}$ (kJ/mol)**
$O_2 + 2* \leftrightarrows 2O*$	-232	0	232
$CH_4 + * \leftrightarrows CH_4*$	-90	0	90
$CH_4* + * \leftrightarrows CH_3* + H*$	88	97	9
$CH_3* + * \leftrightarrows CH_2* + H*$	66	104	38
$CH_2* + * \leftrightarrows CH* + H*$	35	99	64
$CH* + * \leftrightarrows C* + H*$	-145	21	166
$C* + O* \leftrightarrows CO* + *$	-174	31	205
$CO* \leftrightarrows CO + *$	134	134	0
$CO* + O* \leftrightarrows CO_2 + 2*$	-36	20	56
$O* + H* \leftrightarrows OH* + *$	29	90	61
$OH* + H* \leftrightarrows H_2O + 2*$	-114	0	114
$2\,OH* \leftrightarrows H_2O + O* + *$	144	144	0
$CH_4* + O* \leftrightarrows CH_3* + OH*$	117	117	0
$CH_3* + O* \leftrightarrows CH_2* + OH*$	95	102	7
$CH_2* + O* \leftrightarrows CH* + OH*$	64	93	29
$CH* + O* \leftrightarrows C* + OH*$	-116	42	158

More representative energy data can be calculated using the UBI-QEP method upon addition of co-adsorbates resulting from the fact that the surface metal atoms interact with more than one adsorbate. The usual decrease in the heat of adsorption while increasing oxygen and methane coverage due to repulsive interactions is correctly predicted by the UBI-QEP method. This effect becomes significant when the adsorbed species occupied more than 40% adsorption sites with a sharp weakening effect of Pd-O adsorption bond. The effect of coverage adsorbate can be also quantified on the activation barrier.

Particular attention has been paid to the following step $CH_4* + O* \leftrightarrows CH_3* + OH*$ (step 6b in mechanism I(b)) characterized by an activation barrier higher than step corresponding to C-H bond breaking on a nearest-neighbour vacant site at zero coverage. Chemisorbed O atom and OH groups appear as reactant and product respectively. Evolution of the activation with respect to θ_O and θ_{OH} is a key information.

Some restrictions in the UBI-QEP method lies in the lack of possibility to consider the mutual interactions between adsorbed O and OH. Figs 6.2 (a) and (b) only take the repulsive interactions between the same adsorbate, *i.e.* O_{ads} or OH_{ads}, into account. As seen, antagonistic evolutions appear as increasing O-coverage induces a lowering of the activation barrier for θ_O above 0.4. This tendency emphasizes a clear assistance of oxygen in the C-H bond scission and seems to reconcile previous investigations which privileged a cooperative effect of Pd^0 and PdO [10].

On the contrary, an increase of the activation barrier is observable with a rise of θ_{OH} which clearly shows a detrimental effect. On the basis of these theoretical calculations, the classical beneficial effect of nearest neighbour O atoms is restored at increasing coverage while he did not appear formally at nil coverage.

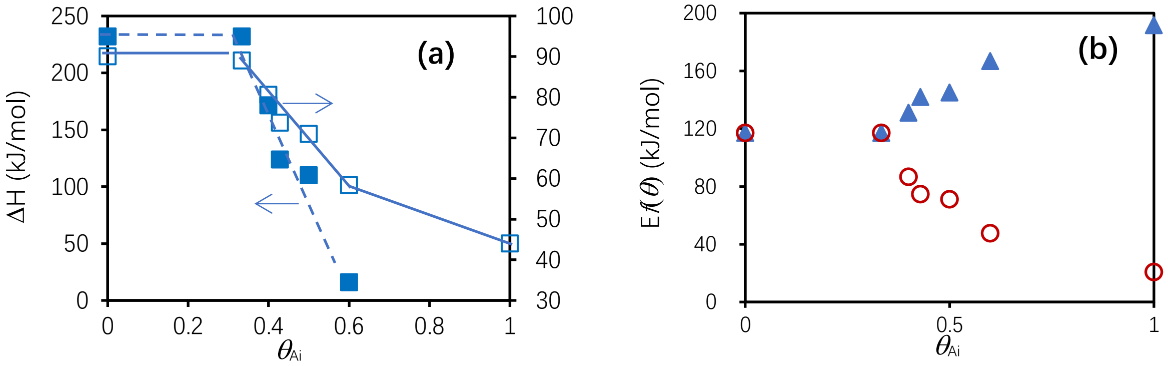

Fig. 6.2. Coverage dependency of enthalpy of adsorption for gaseous O_2 (■) and methane (□) (b) surface oxygen and OH coverage dependency of activation barrier of step (6b) O coverage (○) and OH coverage (▲)

3. Mechanistic insights on reaction mechanism for methane oxidation on polycrystalline Pd-based catalyst in lean conditions

3.1. Experimental methodology

In this chapter, the kinetic behavior of Pd-based catalysts has been investigated in steady state conditions at 400°C with partial pressure of methane in the range $(0.75\text{-}3.0)\times10^{-3}$ atm and an excess of 0.05 atm O_2. The temperature dependence of the reaction rate has been examined at constant $p(CH_4) = 1.0\times10^{-3}$ atm in the temperature range 350-400°C. After a first series of kinetic measurements, catalysts samples were *in situ* aged at 750°C in the presence of 10 vol% H_2O and 5 vol.% O_2.

Afterwards, the aged samples were subjected to the same protocol for a second series of steady-state kinetic measurements. For all experiments the space velocity was maintained constant at 60 $L.h^{-1}.g^{-1}$. As indicated in the experimental section the specific reaction rate can be calculated by assuming CSTR assumption in case of very low CH_4 conversion. In most case the mass balance for a plug flow reactor has been considered leading to Eqs. (1) and (2) respectively for the calculation the overall rate constant k and the specific rate constant r. F_0, $F_{CH_{4,0}}$, $[CH_4]_0$, and W stand for the total inlet volume flow rate, the inlet molar flow rate of methane, the inlet molar concentration of methane and the weight sample.

$$k = \frac{F_0}{W}\ln\frac{1}{1-X_{CH_4}} \qquad (1)$$

$$r = k[CH_4]_0\left(1-X_{CH_4}\right) = \frac{F_{CH_{4,0}}}{W}\left(1-X_{CH_4}\right)\ln\frac{1}{1-X_{CH_4}} \qquad (2)$$

The occurrence of mass transfer phenomena was verified from the calculation of the Weisz-Prater criterion in Eq. (3) which accounts for the observed reaction rate (r_{obs}, $mol.m^3.s^{-1}$), the observed concentration of methane in the gas phase (C_{obs}, $mol.m^{-3}$), the effective diffusivity of CH_4 ($D_{eff,CH4}$, $m^2.s^{-1}$), and the characteristic length representing the volume to surface ratio (L, m). The results obtained from those calculations taking methane conversion in the range 0.01-0.3 into account strictly fulfill the boundary conditions given by Eq. (3) with numerical values lower than 4×10^{-3}.

$$\frac{r_{obs}\,L^2}{C_{obs}\,D_{eff,CH_4}} < 1 \qquad (3)$$

16 catalysts samples were investigated with composition listed in Table 5.3. The main parameters that characterize these samples are:

(i) the A-stoichiometry taking La-deficient and stoichiometric ABO_3 composition;

(ii) the substitution of lanthanum by strontium and potassium;

(iii) the methodology developed for palladium incorporation directly during the sol-gel synthesis (one pot method) or by wet impregnation of the calcined perovskite (sequential method);

(iv) the temperature for the thermal treatment to build up the perovskite structure on sol-gel samples.

As emphasized in Table 6.3, these different parameters have significant impact both on structural properties as described earlier and also on the surface properties. Indeed, one can observe significant change on the specific surface area, the palladium dispersion and the valance state of key element stabilized in some extent in unusual oxidation state such as Pd(+IV) species.

$Pd/La_{0.7}MnO_3$ catalysts served as benchmark to illustrate the methodology implemented for obtaining experimental kinetic features, *i.e.* specific rate, TOF, pre-exponential factor and apparent activation energy from the Arrhenius plot and the calculation of rate constant and adsorption enthalpies predicted from rate expression derived from a representative reaction mechanism scheme.

The subsequent discussion lies in the interpretation that can be given to the changes observed in the predicted values of these thermodynamic and kinetic constants, in particular after ageing, with regard to the surface properties of the catalysts, the main characteristics of which are summarized in Table 6.4.

The apparent reaction order for methane can be deduced from the slope ln r vs. ln CH_4 concentration in Fig.6.3 while the preexponential factor and the apparent activation energy can be calculated from the intercept and the slope of the Arrhenius plot in Fig.6.4. The numerical values are reported in Table 6.5.

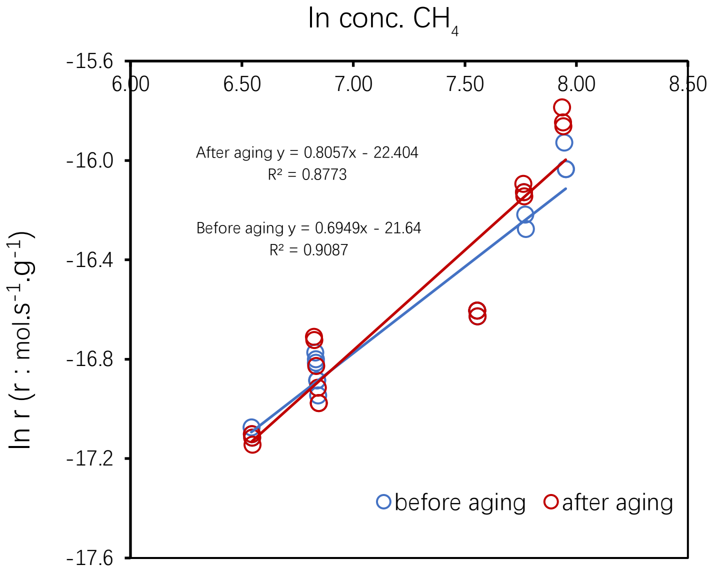

Fig. 6.3. Apparent reaction order with respect to methane on pre-reduced and aged Pd/$La_{0.7}MnO_3$.

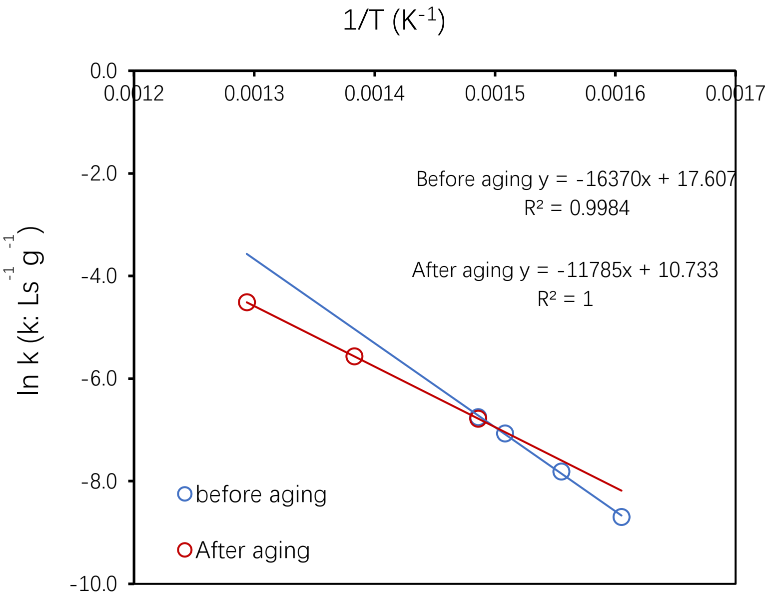

Fig. 6.4. Arrhenius plots on pre-reduced and aged Pd/$La_{0.7}MnO_3$.

Table 6.3. Impact of palladium incorporation into perovskites, i.e. wet impregnation vs sol gel (One-Pot) method, on the surface properties of Pd-based perovskite catalysts

Catalysts	Thermal treatment	Method for Pd incorporation	SSA (m^2/g)	Pd dispersion [a] (%)	XPS analysis			
					Pd/Mn	Mn^{3+}/Mn^{4+} [b]	Mn（AOS) [c]	Pd^{x+}/Pd^{2+} ($x > 2$)
$Pd/LaMnO_3$(C600)	Calc. in air 400°C	wet impregnation	21.7	13.0	0.039	0.22	3.58	0.33
$Pd/LaMnO_3$(C800)	Calc. in air 400°C	wet impregnation	7.4	5.4	0.010	0.94	3.46	0.44
$Pd/La_{0.7}MnO_3$(C600)	Calc. in air 400°C	wet impregnation	29.4	6.2	0.130	0.18	3.63	0.14
$Pd/La_{1.3}MnO_3$(C600)	Calc. in air 400°C	wet impregnation	23.7	1.0	0.075	0.18	3.62	0.43
$LaMn_{0.98}Pd_{0.02}O_3$(C600)	Calc. in air 600°C	Sol-gel (One Pot)	28.9	0.2	0.04	0.19	3.48	0.57
$LaMn_{0.98}Pd_{0.02}O_3$(C800)	Calc. in air 800°C	Sol-gel (One Pot)	6.4	28.0	0.102	0.91	3.72	0.40
$Pd/La_{0.98}K_{0.02}MnO_3$(C600)	Calc. in air 400°C	wet impregnation	26.9	1.4	0.042	0.79	3.54	0.38
$Pd/La_{0.95}K_{0.05}MnO_3$(C600)	Calc. in air 400°C	wet impregnation	22.8	0.08	0.041	0.44	3.48	0.29
$Pd/La_{0.9}K_{0.1}MnO_3$(C600)	Calc. in air 400°C	wet impregnation	20.1	0.4	0.024	0.56	3.56	0.32
$Pd/La_{0.85}K_{0.15}MnO_3$(C600)	Calc. in air 400°C	wet impregnation	16.6	0.02	0.007	0.67	3.48	0.63
$Pd/La_{0.98}Sr_{0.02}MnO_3$(C600)	Calc. in air 400°C	wet impregnation	21.3	2.2	0.147	0.14	3.69	0.14
$Pd/La_{0.95}Sr_{0.05}MnO_3$(C600)	Calc. in air 400°C	wet impregnation	21.1	12.4	0.107	0.16	3.70	0.12
$Pd/La_{0.9}Sr_{0.1}MnO_3$(C600)	Calc. in air 400°C	wet impregnation	26.3	8	0.158	0.19	3.65	0.14
$Pd/La_{0.85}Sr_{0.15}MnO_3$(C600)	Calc. in air 400°C	wet impregnation	36.9	2.0	0.078	0.28	3.71	0.28

[a] from H_2 chemisorption at 100°C on prereduced catalyst at 250°C

[b] from XPS Mn 2p orbital

[c] average oxidation state

Table 6.4. Kinetic parameters for the CH_4/O_2 and $CH_4/O_2/H_2O$ reaction on $Pd/La_{0.7}MnO_3$ respectively in lean and near stoichiometric conditions

Catalyst	Thermal treatment	*p*(CH_4)/10^{-3} (atm)	*p*(O_2)/10^{-3} (atm)	*p*(H_2O)/10^{-3} (atm)	T (°C)	Preexponential factor A (s^{-1})	E_{app} (kJ/mol)	Reaction order			Specif. rate $mol.s^{-1}g^{-1}$	TOF (s^{-1})	Reference
								CH_4	O_2	H_2O			
1 wt.%$Pd/La_{0.7}MnO_3$	Pre-reduced/250°C	0.75-3.0	50	-	400	6.2×10^{11}	136.0	0.7	-	-	4.5×10^{-8}	0.015	This study
		1	50	100	400	-	-	-	-	-	0.9×10^{-8}	0.003	This study
	Aged[a]	0.75-3.0	50	-	400	6.4×10^{8}	97.9	0.8	-	-	4.4×10^{-8}	0.015	This study
		1	50	100	400	-	-	-	-	-	2.1×10^{-8}	0.007	This study
	Pre-reduced/250°C	0.75-3.0	2.0-6.0	5.0-20.0	460	2.6×10^{8}	87.6	0.8	0.14	~ -1.0	17.4×10^{-8}	0.088	This study
0.86 wt.% Pd/ZrO_2	Calc./air, 500°C	20	200	1-150	280	-	-	1.1	0.1	-1.0		0.015	[5]
7.7 wt.%Pd/Si-Al_2O_3	Calc./air, 500°C	20	200	-	280	-	85					0.012	[4]
Pd foil	under reaction mixture/500°C	0.2	200	0.0125	280	-	125	0.7	0.2	-0.9		0.59	[24]

[a] in 10 vol.% H_2O in O_2 vol.% at 750°C

Table 6.5. Kinetic and thermodynamic constants optimized from a least square method at 400°C on $Pd/La_{0.7}MnO_3$

Thermal treatment	T(reaction) (°C)	k_{6c}[c]	k_{12}[c]	K_{CH4}[d]	K_O[d]
Reduced[a]	400	$(2.5\pm0.3)\times10^{-6}$	$(5.2\pm0.6)\times10^{-2}$	17.2 ± 0.9	$(5.0\pm0.3)\times10^{-2}$
Aged[b]	400	$(11.6\pm0.2\times10^{-6}$	$(2.3\pm0.6)\times10^{-2}$	5.7 ± 0.3	$(8.0\pm0.4)\times10^{-1}$

[a] pre-reduction at 250°C

[b] aging at 750°C in air with 10 vol.% H_2O

[c] $mol.min^{-1}g^{-1}$ - [d] atm^{-1}

The comparison of calculated reaction rates, TOF and kinetic parameters, i.e. reaction order, pre-exponential factors and apparent activation energy can be compared with previous data obtained either on metallic or oxidic Pd surface. As a matter of fact, they did not reveal significant discrepancies [4,5,24]. Indeed, an increase of the activation energy on metallic surface is noticeable and the kinetics obeys to a positive reaction order with respect to methane. The lowering of TOF values in the presence of 10 vol.% H_2O is also consistent with a strong inhibiting effect of water on the reaction rate. Let us note that comparable specific rates and TOF values are measured on aged catalyst still in the absence of water. This observation does not show significant detrimental effect of the aging process in the presence of steam. As a matter of fact, previous investigations revealed that the alteration of the metal-support interaction may depend on the nature of the pretreatment and the richness of the reactant mixture with an alteration accentuated in reducing atmosphere by using perovskite as substrate [25,26]. Indeed, pre-reduction at moderate temperature, *i.e.* 250°C would in principle preserve the metal support interface as the structural properties have not been deteriorated.

3.2. Kinetic modeling

In first approximation, two reaction mechanisms (I(a) and I(b)) have been examined based on the UBI-QEP method which account for metallic Pd sites stabilized on $La_{0.7}MnO_3$. Mechanism I(b) can be supported due to a combined effect related to a weaker oxygen inhibiting effect associated to a lowering of the heat of adsorption and a lowering of the activation energy of step (3b) at increasing O-coverage as expected in large excess of oxygen.

Mechanism I(a)

(4) $O_2(g) + 2\ast \leftrightarrows 2O_{\ast}$
(5) $CH_4(g) + \ast \leftrightarrows CH_{4\ast}$
(6a) $CH_{4\ast} + \ast \rightarrow CH_{3\ast} + H_{\ast}$
(7a) $CH_{3\ast} + \ast \rightarrow CH\ast + H\ast$
(8a) $CH_{\ast} + \ast \rightarrow CH\ast + H\ast$
(9a) $CH_{\ast} + \ast \rightarrow C\ast + H\ast$
(10) $C_{\ast} + O_{\ast} \rightarrow CO_{\ast} + \ast$
(11) $CO_{\ast} + O\ast \rightarrow CO_2 + 2\ast$
(12) $2OH_{\ast} \rightarrow H_2O + O_{\ast} + 2\ast$

Mechanism II

(4) $O_2(g) + 2\ast \leftrightarrows 2O_{\ast}$
(5) $CH_4(g) + \ast \leftrightarrows CH_{4\ast}$
(6c) $CH_{4\ast}$ + ‘O’ → $CH_{3\ast}$ + ‘OH’
(7c) $CH_{3\ast}$ + ‘O’ → $CH_{2\ast}$ + ‘OH’
(8c) $CH_{2\ast}$ + ‘O’ → $CH_{\ast}$ + ‘OH’
(9c) $CH_{\ast}$ + ‘O’ → $C_{\ast}$ + ‘OH’
(10) $C_{\ast} + O_{\ast} \rightarrow CO_{\ast} + \ast$
(11) $CO_{\ast} + O_{\ast} \rightarrow CO_2 + 2\ast$
(12) 2‘OH’ → H_2O + ‘O’

Mechanism I(b)

(4) $O_2(g) + 2\ast \leftrightarrows 2O_{\ast}$

(5) $CH_4(g) + \ast \leftrightarrows CH_{4\ast}$

(6b) $CH_{4\ast} + O_{\ast} \rightarrow CH_{3\ast} + OH_{\ast}$

(7b) $CH_{3\ast} + O_{\ast} \rightarrow CH_{2\ast} + OH_{\ast}$

(8b) $CH_{2\ast} + O_{\ast} \rightarrow CH_{\ast} + OH_{\ast}$

(9b) $CH_{\ast} + O_{\ast} \rightarrow C_{\ast} + OH_{\ast}$

(10) $C_{\ast} + O_{\ast} \rightarrow CO_{\ast} + \ast$

(11) $CO_{\ast} + O_{\ast} \rightarrow CO_2 + 2\ast$

(12) $2OH_{\ast} \rightarrow H_2O + O_{\ast} + 2\ast$

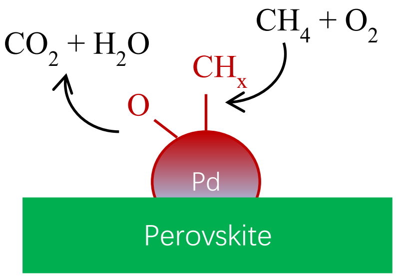

Scheme corresponding to mechanism I(b)

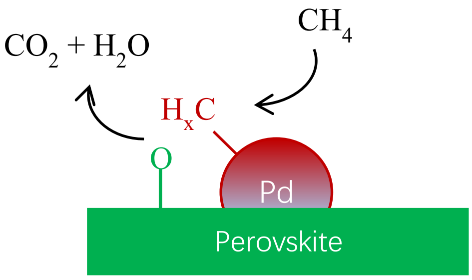

Scheme corresponding to mechanism II

In fact, the aforementioned elementary steps closely mimic those already reported in the literature on PdO [13] even though the nature of oxygen can be questioned coming from dissociative adsorption into chemisorbed O species on PdO/Pd and/or surface oxygen lattice species. Mechanism I(a) and I(b) agree with a single site mechanism only composed of Pd atoms with competitive adsorptions of O_2 and methane. The positive reaction order for CH_4 concentration (see Table 6.4) accounts for the kinetic limiting effect of the first C-H bond dissociation [27]. Fujimoto et al. [5] also suggested that subsequent C-H bond breaking are kinetically insignificant. By assuming the first C-H bond breaking slow, then all the other step would occur much faster and reversible adsorptions can be assumed quasi equilibrated leading to Eqs. (13) and (14) corresponding to surface coverages of adsorbed methane molecules and O atoms on Pd, *i.e.* $\theta^{*}_{CH_4}$ and $\theta^{*}_{O}$with θ^{*}_{v} corresponding to the fraction of vacant sites based on the hypothesis that O_{ads}, and $CH_{4,ads}$ are the most abundant intermediates at the surface.

$$\theta_O^* = \sqrt{K_O P_{O_2}}\,\theta_v^* \qquad (13)$$

$$\theta_{CH_4}^* = K_{CH_4} P_{CH_4}\,\theta_v^* \qquad (14)$$

$$\text{with } \theta_v^* = \frac{1}{1+K_{CH_4}P_{CH_4}+\sqrt{K_O P_{O_2}}} \qquad (15)$$

The expression of the reaction rate in Eqs. (16) and (17) respectively for mechanism I(a) and I(b) can be easily derived in agreement with this set of assumptions.

$$r = k_{6a}\theta_{CH_4}^*\theta_v^* = \frac{k_{6a}K_{CH_4}P_{CH_4}}{\left[1+K_{CH_4}P_{CH_4}+\sqrt{K_O P_{O_2}}\right]^2} \qquad (16)$$

$$r = k_{6b}\theta_{CH_4}^*\theta_O^* = \frac{k_{6b}K_{CH_4}P_{CH_4}\sqrt{K_O P_{O_2}}}{\left[1+K_{CH_4}P_{CH_4}+\sqrt{K_O P_{O_2}}\right]^2} \qquad (17)$$

The linear transformed of the reaction rate Eqs. (16) and (17) allow a graphical discrimination. In practice, the set of assumptions for their establishment is valid if the plots $\sqrt{P_{CH_4}/r}$ and $\sqrt{P_{CH_4}\sqrt{P_{O_2}}/r}$ vs. P_{CH_4} is linear with a positive slope.

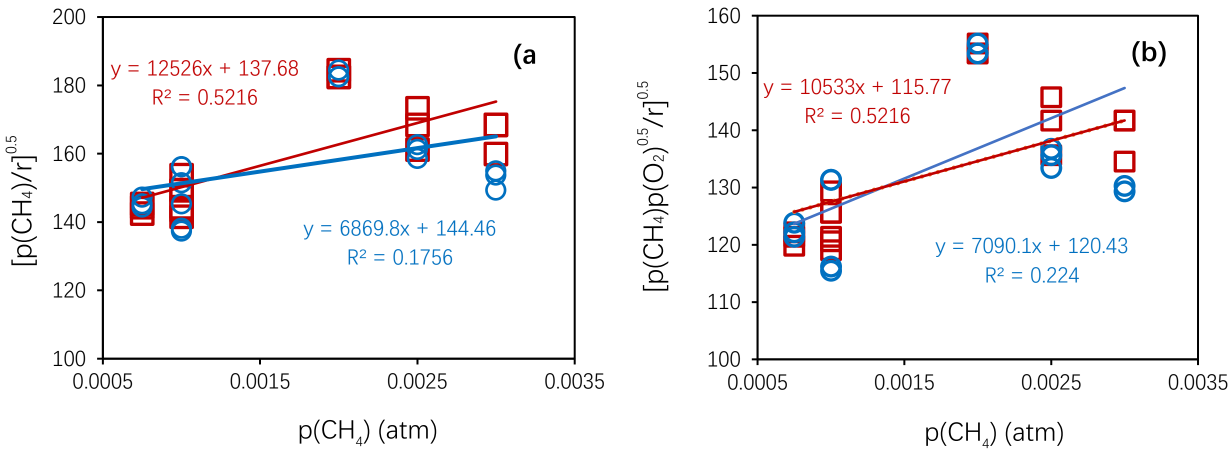

Fig. 6.5. Plot of $\sqrt{\frac{P_{CH_4}}{r}}$ vs. $p(P_{CH_4})$ (a) and $\sqrt{\frac{P_{CH_4}\sqrt{P_{O_2}}}{r}}$ vs. $p(P_{CH_4})$ (b) from reaction rate values measured on pre-reduced (☐)and aged Pd/$La_{0.7}MnO_3$ (○) at 400°C.

As observed in Fig.6.5, the plots reveal a poor agreement. On the basis of these observations, a dual site mechanism II has been examined as alternative which differs from Mechanism I(a) and I(b) by the nature of reactive oxygen species. Indeed, they would no longer come from the direct gaseous O_2 dissociative adsorption on metallic Pd sites but from surface lattice oxygen of the perovskite support at the Pd-$La_{0.7}MnO_3$ interface. Let us note that one cannot strictly rule out reactive oxygen species coming from PdO at the vicinity of Pd^0 site even though it is accepted that oxidation of metallic Pd particle is a slow process [2].

The reaction rate from Mechanism II can be expressed according to Eq. (18) as follow:

$$r = k_{6c}\theta^{*}_{CH_4}\theta_O \qquad (18),$$

where k_{3c} stands for the rate constant related to step (6c) in mechanism II, $\theta^{*}_{CH_4}$ the methane coverage on metallic Pd sites ($*$) and θ_O the coverage reactive 'O' supplied from the support materials and/or PdO. Similarly, oxygen and methane adsorption steps on Pd are still assumed at quasi-equilibrium in agreement with Eqs. (13) and (14). As reactive 'O' species are converted to 'OH' species the mass balance given Eq. (19) which accounts for θ_O and the θ_{OH} representative of 'O' and 'HO' coverage on the support can be established.

$$\theta_O + \theta_{OH} = 1 \qquad (19)$$

By applying steady-state approximation to 'O' species then

$$\frac{d\theta_O}{dt} = r_{12} - 4r_{6c} = k_{12}\theta_{OH}^2 - 4k_{6c}\theta^{*}_{CH_4}\theta_O = 0 \qquad (20)$$

By substituting θ_{OH} by 1-θ_O from Eq. (19), subsequent resolution leads to Eq. (21) :

$$\theta_O = \frac{(2k_{12}+4k_{6c}\theta^{*}_{CH_4})}{2k_{12}}\left[1 \pm \sqrt{1-\left(\frac{2k_{12}}{2k_{12}+4k_{6c}\theta^{*}_{CH_4}}\right)^2}\right] \qquad (21)$$

Finally, the reaction rate Eq. (22) can be obtained by replacing the expression of θ_O given in Eq. (21).

$$r = k_{6c}\theta^{*}_{CH_4}\theta_O = \frac{k_{6c}\theta^{*}_{CH_4}(2k_{12}+4k_{6c}\theta^{*}_{CH_4})}{2k_{12}}\left[1 \pm \sqrt{1-\left(\frac{2k_{12}}{2k_{12}+4k_{6c}\theta^{*}_{CH_4}}\right)^2}\right] \qquad (22)$$

By assuming step (6c) as slow step, *i.e.* $k_{12} \gg k_{6c}$, then $\frac{2k_{12}}{2k_{12}+4k_{6c}\theta^{*}_{CH_4}} \sim 1$, and one can simplify Eq. (22) leading to Eq. (23).

$$r = \frac{k_{6c}\theta^{*}_{CH_4}(2k_{12}+4k_{6c}\theta^{*}_{CH_4})}{2k_{12}} = k_{6c}\theta^{*}_{CH_4}\left(1+\frac{2k_{6c}\theta^{*}_{CH_4}}{k_{12}}\right) \tag{23}$$

$$r = \frac{k_{6c}K_{CH_4}P_{CH_4}}{(1+K_{CH_4}P_{CH_4}+\sqrt{k_O P_{O_2}})}\left[1+\frac{2k_{6c}K_{CH_4}P_{CH_4}}{k_{12}(1+K_{CH_4}P_{CH_4}+\sqrt{k_O P_{O_2}})}\right] \tag{24}$$

Kinetic and thermodynamic constants in Table 6.5 have been estimated from a least square method through the minimization of the sum of the square difference between predicted and experimental reaction rates $\sum(r_{exp.} - r_{predic.})^2$. Only Eq. (24) has been considered for the adjustment. The comparison of optimized values obtained on pre-reduced catalyst and after aging at 750°C in steam agree with mechanism II. They corroborate previous conclusions emphasizing the supply of reactive oxygen from the support [17,18]. The rate constant k_{3c} for methane dissociation increases significantly on the aged catalyst which agrees with the decrease of the apparent activation energy from 136 kJ/mol to 97.9 kJ/mol on aged sample (Table 6.4). Such evolution could suggest a strengthening of the metal support interface. This assumption is supported by comparable values for k_{12} which still indicate a fast restoration of 'O' reactive species.

Such changes also coincide with an alteration of the adsorptive properties of palladium because adsorption competition on aged sample becomes more in favor of oxygen with sharp increase in O-coverage at the expense of methane coverage as illustrated in Fig.6.6. Hence, statistically the probability to find adsorbed methane on Pd at the vicinity of reactive O species from perovskite would lessen. This inhibiting effect would exert a diluting effect and counterbalance the increase observed on the reaction rate constant k_{6c} which could potentially explain unchanged specific reaction rate and TOF values on aged Pd/$La_{0.7}MnO_3$. Nevertheless, the most prominent information given by those data is related to the absence of significant deterioration of the Pd-support interface when the catalyst is exposed to 5 vol.% O_2 and 10 vol.% H_2O at 750°C as mechanism II still prevails.

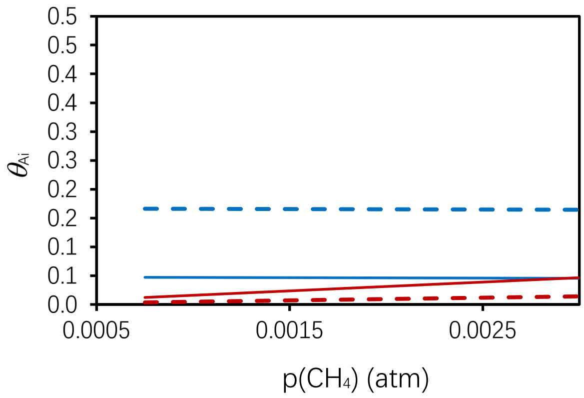

Fig. 6.6. Evolution of surface coverage θ_{Ai} for methane (red curve), oxygen (blue curve) vs. methane partial pressure during the CH_4/O_2 reaction on pre-reduced $Pd/La_{0.7}MnO_3$ (bold line), on aged catalyst (- - - -) in the absence of steam and on pre-reduced catalyst.

3.3. Impact of lanthanum stoichiometry, lanthanum substitution by strontium and potassium on the catalytic properties of supported palladium

In this chapter, the perovskite structure has been obtained by heating the precursor at 600°C in air for obtaining the rhombohedral structure. Pd has been systematically added through a sequential wet impregnation and the Pd-doped precursor was ultimately calcined at 400°C. As summarized in Table 6.6, changes in perovskite composition induces modifications of the textural properties in connection with structural changes previously discussed in Chapter 4 as the substitution of La^{3+} by Sr^{2+} an K^{+} can lead to amorphous structure and segregation in the particular case of K-doped perovskite materials. All these changes can also lead to change in the reducibility of oxidic Pd species related to the strength of interaction with the perovskite structure then influencing the palladium dispersion measured on reduced samples at 250°C.

First examination of kinetic features reported in Table 6.4 reveals different trends according to the perovskite composition. related insight and comparison contributed to following comments:

1. The addition of 1 vol.% H_2O has a strong detrimental effect ascribed to significant inhibiting effect of water adsorption on the reaction rate of methane combustion on pre-reduced and aged catalysts. Even so, such sensibility seems to be attenuated on $Pd/La_{1-x}K_xMnO_3$ series.
2. It seems obvious that thermal aging leads to different behavior by comparing pre-reduced and aged samples operating in similar dried conditions. Indeed, on the series Pd/La_xMnO_3 the deactivation accentuates when La composition x increases. La-deficiency would minimize the deactivation. In contrast, K-substitution lower the thermal stability with an

accentuation of the deactivation especially for low K content. Strontium behaves differently as the reverse tendency is observable on Sr-substituted with improved activity after aging at low Sr content, *i.e.* for $x \leq 0.5$.

3. For the apparent order for methane, there is no distinction on pre-reduced sample with a positive value as reported elsewhere [27]. On the other hand, accurate determination of reaction order on aged samples was not easy because the reaction order may vary in the partial pressure range of methane of this study.
4. Let us now examine the evolution observed on the pre-exponential factor and on the apparent activation energy. As a matter of fact, their comparison reveals opposite tendencies: (i) On Pd/La_xMnO_3 and Pd/$La_{1-x}K_xO_3$ lower specific reaction rate values on aged catalysts are clearly governed by a decrease in the pre-exponential factor as the parallel lowering of E_{app} values should in principle induces an increase of the reaction rate. (ii) On Pd/$La_{1-x}Sr_xO_3$, at low Sr content, a rate enhancement is clearly noticeable. Similarly, such evolution can be explained by an increase of the pre-exponential factor while E_{app} also increase. On the other hand, at high Sr content, *i.e.* $x = 0.15$, strontium substitution induces a loss of activity which is mainly explained by an increase in E_{app} despite an increase on pre-exponential factor A.
5. Finally, among the different support composition, the highest reaction rate value is obtained on Pd/$LaMn_{0.85}Sr_{0.15}O_3$, *i.e.* 13.2×10^{-8} mol.s^{-1}.g^{-1} vs. 5.5×10^{-8} mol.s^{-1}.g^{-1} on the benchmark Pd/$LaMnO_3$ which underline the beneficial effect of strontium at low concentration.

For sake of clarity, the main trends from the abovementioned comparisons are related to the high thermal stability of Pd/$La_{0.7}MnO_3$: A compensation effect on the aged sample is noticeable related to a decrease in E_{app} jointly with a lowering of A. For Sr-substituted samples, a gain in activity is observed on aged Pd/$LaMn_{0.98}Sr_{0.02}O_3$ despite unfavorable increase in E_{app} compensated by a joint increase of A. In terms of reaction rates, pre-reduced Pd/$LaMn_{0.85}Sr_{0.15}O_3$ outperforms all others compositions. Let us note that these kinetics features cannot be easily explained by the prevalence of unique parameter from the physicochemical characterization reported in Table 6.3.

Clearly, changes in SSA, Pd dispersion and evolutions from semi-quantitative XPS analysis, *i.e.* surface atomic Pd/Mn, Mn^{3+}/Mn^{4+}, Pd^{x+}/Pd^{2+} ratios cannot provide relevant comparisons. This suggests that cooperative effects between the support, developing oxygen storage properties, and nano-sized Pd particles would remain the most prominent arguments for the interpretation of kinetic measurements and would be still in favor of dual site mechanism II earlier described at least for pre-reduced catalysts.

Similarly, the least-square method earlier described has been profitably used for the optimization of the reaction rate constants k_{6c} and k_{12} related to methane dissociation assisted by neighbor reactive surface oxygen from the perovskite and their restoration respectively. The equilibrium constants K_{CH_4} and K_O correspond to methane and dissociative oxygen adsorption on Pd sites. Results are reported in Table 6.7. As seen, $k_{12} >> k_{6c}$ which means that the previous assumption to obtain Eq. (24) is still verified.

Clearly the evolution of k_{6c} is independent of the Pd dispersion which agrees with the fact that the density of active sites would depend on preferentially the extent of Pd-support interface involving both the reactivity of surface oxygen species from ceria and the reactivity of methane adsorbed of Pd sites. Regarding, methane adsorption, the values of K_{CH_4} reflect the strength of methane adsorption which can be in some extent related to the physicochemical properties of nano-sized Pd particles in terms of structural (size and morphology) and electronic properties. Both effects can be driven by the support (SSA and composition).

This strength in methane adsorption can modulate the competition for adsorption between methane and O_2. Methane and oxygen coverages can be calculated from Eqs. (13) and (14) and plotted as a function of $p(CH_4)$ as illustrated in Figs. 6.7-6.9. The tendencies observed can be discussed globally. K-substitution favors oxygen adsorption and this tendency accentuates on aged samples. The competition is also in favor of oxygen on pre-reduced Sr-substituted samples except on $Pd/La_{0.85}Sr_{0.15}O_3$ which exhibits the highest reaction rate. Based on these comparisons, in most cases, adsorbed oxygen species would act as inhibitor.

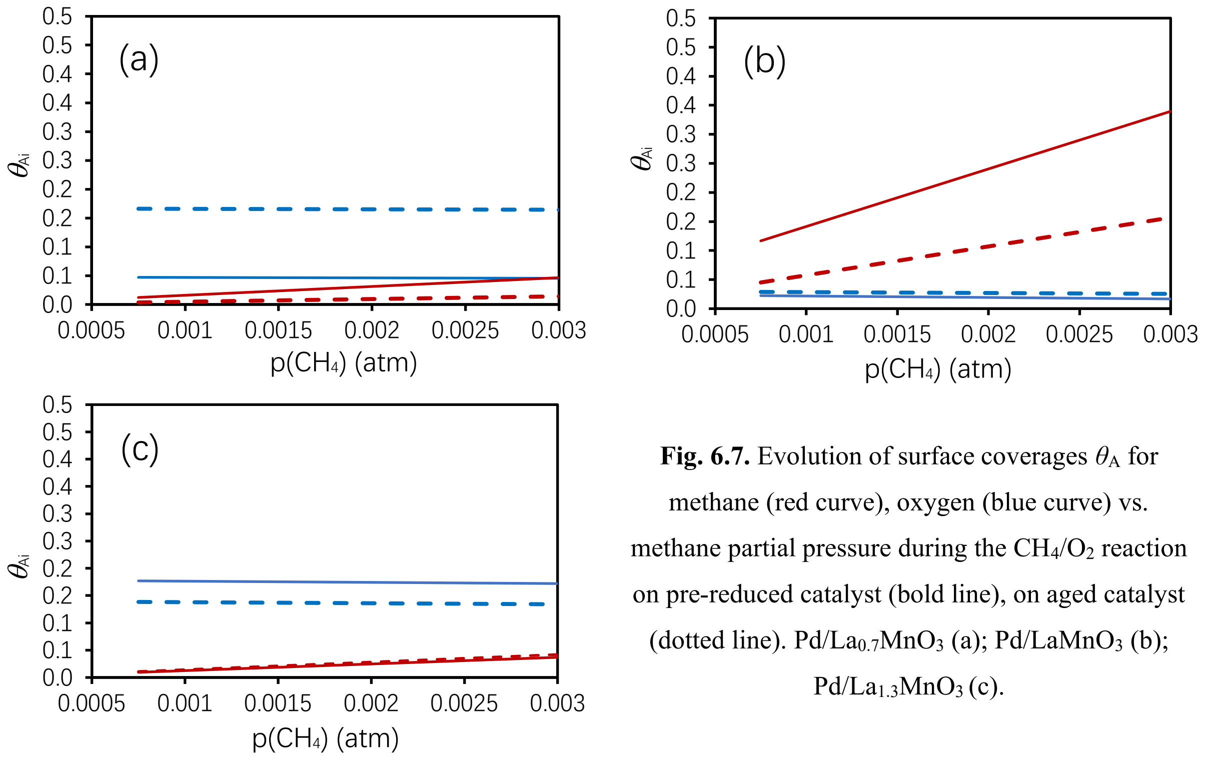

Fig. 6.7. Evolution of surface coverages θ_A for methane (red curve), oxygen (blue curve) vs. methane partial pressure during the CH_4/O_2 reaction on pre-reduced catalyst (bold line), on aged catalyst (dotted line). Pd/$La_{0.7}MnO_3$ (a); Pd/$LaMnO_3$ (b); Pd/$La_{1.3}MnO_3$ (c).

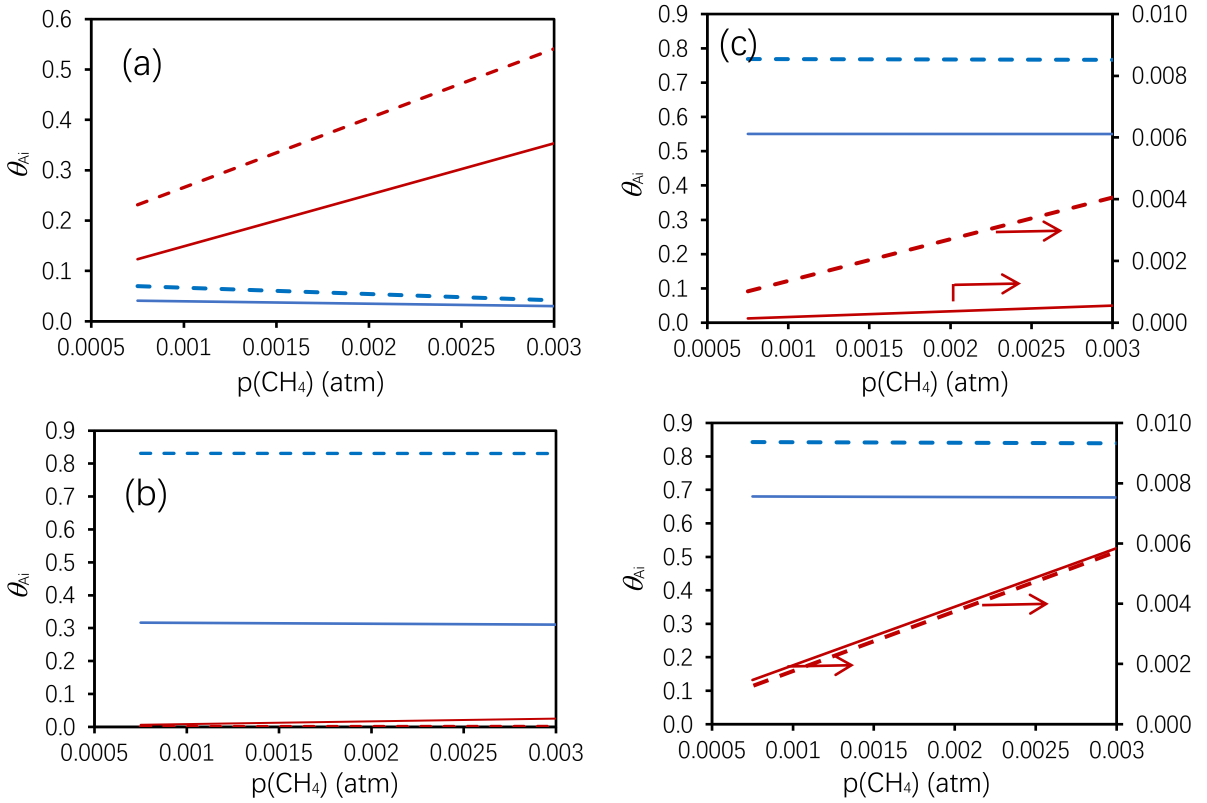

Fig. 6.8. Evolution of surface coverages θ_{Ai} for methane (red curve), oxygen (blue curve) vs. methane partial pressure during the CH_4/O_2 reaction on pre-reduced catalyst (bold line), on aged catalyst (dotted line). Pd/$La_{0.98}K_{0.02}MnO_3$ (a); Pd/$La_{0.95}K_{0.05}MnO_3$ (b); Pd/$La_{0.90}K_{0.10}MnO_3$ (c); Pd/$La_{0.85}K_{0.15}MnO_3$ (c).

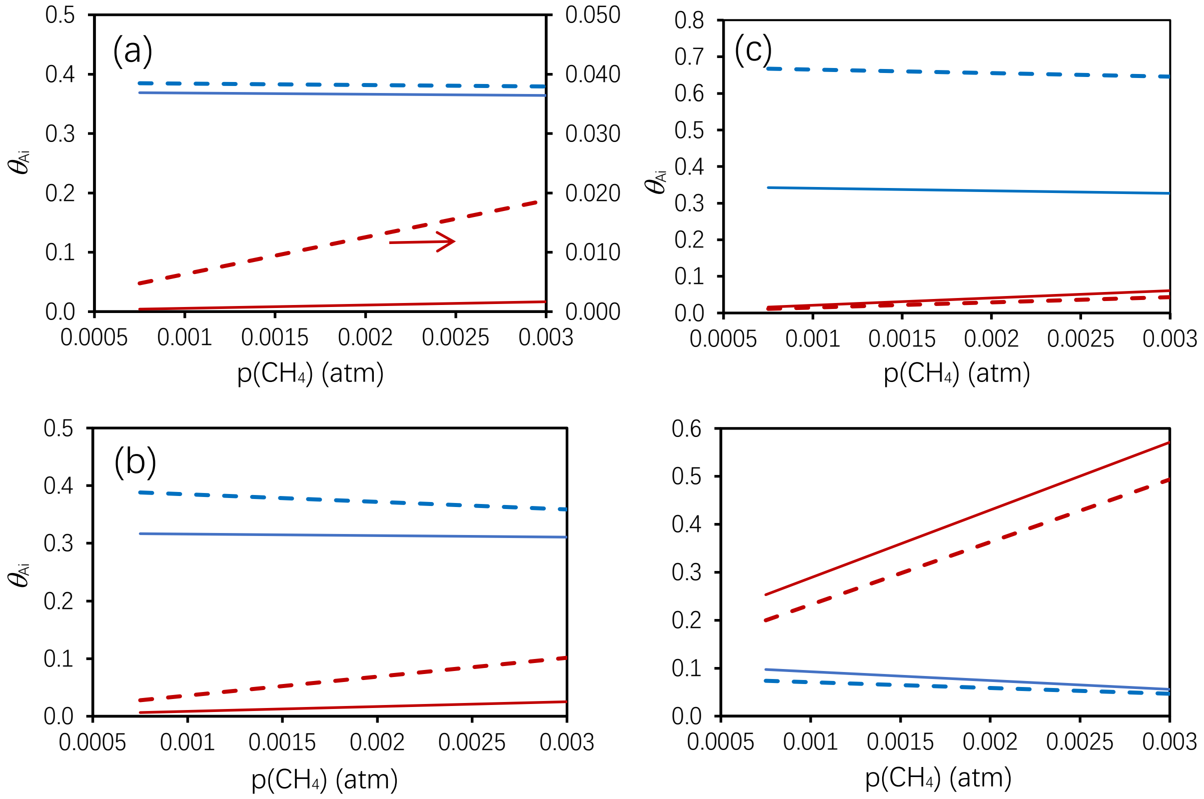

Fig. 6.9. Evolution of surface coverages θ_{Ai} for methane (red curve), oxygen (blue curve) vs. methane partial pressure during the CH_4/O_2 reaction on pre-reduced catalyst (bold line), on aged catalyst (dotted line). $Pd/La_{0.98}Sr_{0.02}MnO_3$ (a); $Pd/La_{0.95}Sr_{0.05}MnO_3$ (b); $Pd/La_{0.90}Sr_{0.10}MnO_3$ (c); $Pd/La_{0.85}Sr_{0.15}MnO_3$ (c).

Table 6.6(a). Kinetic parameters for the CH_4/O_2 reaction at 400°C in lean conditions over pre-reduced and aged Pd/perovskite catalyst.

Catalyst	Thermal treatment	$p(CH_4)/10^{-3}$ (atm)	$p(O_2)/10^{-3}$ (atm)	$p(H_2O)/10^{-3}$ (atm)	Pre-exponential factor A (s^{-1})	E_{app} (kJ/mol)	CH_4 order	Specif. Rate ($mol.s^{-1}g^{-1}$)	TOF (s^{-1})
$Pd/La_{0.7}MnO_3$	Pre-reduced/250°C	0.75-3.0	50	-	6.2×10^{11}	136.0	0.7	4.5×10^{-8}	0.015
		1	50	100	-	-	-	0.9×10^{-8}	0.003
	Aged[a]	0.75-3.0	50	-	6.4×10^{8}	97.9	0.8	4.4×10^{-8}	0.015
		1	50	100	-	-	-	2.1×10^{-8}	0.007
$Pd/LaMnO_3$	Pre-reduced/250°C	0.75-3.0	50	-	1.2×10^{8}	140.5	0.7	5.5×10^{-8}	
		1	50	100	-	-	-	1.1×10^{-8}	
	Aged[a]	0.75-3.0	50	-	1.8×10^{3}	119.1	n.d	4.6×10^{-8}	
		1	50	100	-	-	-	1.6×10^{-8}	
$Pd/La_{1.3}MnO_3$	Pre-reduced/250°C	0.75-3.0	50	-	8.4×10^{6}	127.7	0.7	4.1×10^{-8}	
		1	50	100	-	-	-	0.5×10^{-8}	
	Aged[a]	0.75-3.0	50	-	4.5×10^{6}	128.4	n.d	1.9×10^{-8}	
		1	50	100	-	-	-	0.7×10^{-8}	

Table 6.6(b). Kinetic parameters for the CH_4/O_2 reaction at 400°C in lean conditions over pre-reduced and aged Pd/perovskite catalyst.

Catalyst	Thermal treatment	$p(CH_4)/10^{-3}$ (atm)	$p(O_2)/10^{-3}$ (atm)	$p(H_2O)/10^{-3}$ (atm)	Pre-exponential factor A (s^{-1})	E_{app} (kJ/mol)	CH_4 order	Specif. Rate ($mol.s^{-1}g^{-1}$)	TOF (s^{-1})
$Pd/LaMn_{0.98}K_{0.02}O_3$	Pre-reduced/250°C	0.75-3.0	50	-	1.7×10^{7}	128.8	0.7	6.5×10^{-8}	
		1	50	100	-	-	-	1.2×10^{-8}	
	Aged[a]	0.75-3.0	50	-	7.5×10^{5}	117.0	1.0	2.5×10^{-8}	
		1	50	100	-	-	-	1.5×10^{-8}	
$Pd/LaMn_{0.95}K_{0.05}O_3$	Pre-reduced/250°C	0.75-3.0	50	-	4.8×10^{4}	99.1	0.8	3.8×10^{-8}	
		1	50	100	-	-	-	0.8×10^{-8}	
	Aged[a]	0.75-3.0	50	-	4.4×10^{4}	102.2	1.1	2.1×10^{-8}	
		1	50	100	-	-	-	1.5×10^{-8}	
$Pd/LaMn_{0.9}K_{0.1}O_3$	Pre-reduced/250°C	0.75-3.0	50	-	1.6×10^{7}	132.3	0.9	3.7×10^{-8}	
		1	50	100	-	-	-	1.0×10^{-8}	
	Aged[a]	0.75-3.0	50	-	2.0×10^{5}	112.5	1.1	1.4×10^{-8}	
		1	50	100	-	-	-	1.4×10^{-8}	
$Pd/LaMn_{0.85}K_{0.15}O_3$	Pre-reduced/250°C	0.75-3.0	50	-	2.8×10^{5}	111.2	0.9	2.8×10^{-8}	
		1	50	100	-	-	-	1.0×10^{-8}	
	Aged[a]	0.75-3.0	50	-	2.8×10^{4}	99.6	1.4	1.7×10^{-8}	
		1	50	100	-	-	-	1.4×10^{-8}	
$Pd/LaMn_{0.98}Sr_{0.02}O_3$	Pre-reduced/250°C	0.75-3.0	50	-	4.4×10^{6}	123.4	0.7	4.2×10^{-8}	
		1	50	100	-	-	-	1.4×10^{-8}	
	Aged[a]	0.75-3.0	50	-	3.1×10^{6}	119.2	n.d.	6.6×10^{-8}	
		1	50	100	-	-	-	1.9×10^{-8}	
$Pd/LaMn_{0.95}Sr_{0.05}O_3$	Pre-reduced/250°C	0.75-3.0	50	-	1.2×10^{6}	116.6	0.7	4.5×10^{-8}	
		1	50	100	-	-	-	1.3×10^{-8}	
	Aged[a]	0.75-3.0	50	-	5.8×10^{6}	123.5	n.d.	4.7×10^{-8}	
		1	50	100	-	-	-	2.0×10^{-8}	
$Pd/LaMn_{0.9}Sr_{0.1}O_3$	Pre-reduced/250°C	0.75-3.0	50		2.4×10^{6}	116.3	0.7	6.4×10^{-8}	
		1	50		-	-	-	0.6×10^{-8}	
	Aged[a]	0.75-3.0	50		3.8×10^{6}	121.9	n.d	5.5×10^{-8}	
		1	50		-	-	-	1.5×10^{-8}	
$Pd/LaMn_{0.85}Sr_{0.15}O_3$	Pre-reduced/250°C	0.75-3.0	50	-	3.6×10^{6}	116.1	0.6	13.2×10^{-8}	
		1	50	100	-	-	-	3.0×10^{-8}	
	Aged[a]	0.75-3.0	50	-	7.5×10^{6}	123.4	n.d.	7.5×10^{-8}	
		1	50	100	-	-	-	2.9×10^{-8}	

Table 6.7 Kinetic and thermodynamic constants optimized in lean conditions at 400°C on pre-reduced and aged supported Pd catalyst on perovskite support material.

Catalyst	Thermal treatment	k_{6c}[c]	k_{12}[c]	K_{CH4}[d]	K_O[d]
$Pd/La_{0.7}MnO_3$	Reduced[a]	(2.5±0.3)´10-6	(5.2±0.6)´10-2	17.2±0.9	(5.0±0.3)´10-2
	Aged[b]	(11.6±0.2´10-6	(2.3±0.6)´10-2	5.7±0.3	(8.0±0.4)´10-1
$Pd/LaMnO_3$	Reduced[a]	(2.5±0.3)´10-5	0.59±0.06	170±20	(1.3±0.2)´10-2
	Aged[b]	(4.4±0.5´10-5	0.20±0.02	63±7	(1.9±0.2)´10-2
$Pd/La_{1.3}MnO_3$	Reduced[a]	(1.5±0.2)´10-4	(8.9±0.1)´10-2	16±2	0.94±0.09
	Aged[b]	(9.8±0.1´10-5	0.50±0.06	17±2	0.53±0.07
$Pd/LaMn_{0.98}K_{0.02}O_3$	Reduced[a]	(2.4±0.3)´10-5	0.58±0.06	185±20	(4.8±0.5)´10-2
	Aged[b]	(1.9±0.2´10-5	0.90±0.09	404±41	0.20±0.02
$Pd/LaMn_{0.95}K_{0.05}O_3$	Reduced[a]	(7.5±0.8)´10-5	0.43±0.05	38±4	3±0.3
	Aged[b]	(1.0±0.1)´10-3	1.3±0.02	3.8±0.4	49±5
$Pd/LaMn_{0.9}K_{0.1}O_3$	Reduced[a]	(4.1±0.4)´10-3	0.61±0.06	0.42±0.04	30±3
	Aged[b]	(2.7±0.3)´10-3	0.30±0.03	5.6±0.6	223±23
$Pd/LaMn_{0.85}K_{0.15}O_3$	Reduced[a]	(8.4±0.9)´10-4	0.60±0.06	6.1±0.7	(91±9)
	Aged[b]	(2.7±0.3)´10-3	0.18±0.02	12±2	587±60
$Pd/LaMn_{0.98}Sr_{0.02}O_3$	Reduced[a]	(3.6±0.4)´10-4	0.56±0.06	9.0±0.9	6.9±0.7
	Aged[b]	(4.5±0.5´10-4	0.51±0.06	10.4±2	7.9±0.8
$Pd/LaMn_{0.95}Sr_{0.05}O_3$	Reduced[a]	(2.4±0.3)´10-4	0.60±0.06	13±2	4.3±0.5
	Aged[b]	(8.2±0.9)´10-5	0.86±0.09	62±6	8.8±0.9
$Pd/LaMn_{0.9}Sr_{0.1}O_3$	Reduced[a]	(1.2±0.2)´10-4	0.80±0.08	33±4	5.7±0.6
	Aged[b]	(1.7±0.3)´10-4	0.80±0.09	46±5	8.6±0.9
$Pd/LaMn_{0.85}Sr_{0.15}O_3$	Reduced[a]	(2.6±0.3)´10-5	0.88±0.09	473±48	0.45±0.05
	Aged[b]	(1.9±0.2)´10-5	0.90±0.09	337±40	0.20±0.2

[a] reduced at 250°C - [b] aged at 750°C in 10 vol.% H_2O with 5 vol% O_2

[c] mol.min^{-1}.g^{-1} - [d] atm^{-1}

3.4. Impact of palladium incorporation and calcination temperature

Similar mathematical resolution was implemented to exploit kinetics measurements performed on supported Pd/$LaMnO_3$(C600) and Pd/$LaMnO_3$(C800) as well as sol-gel $LaMn_{0.98}Pd_{0.02}O_3$(C600) and $LaMn_{0.98}Pd_{0.02}O_3$(C600). As earlier explained, C600 refer to the calcination temperature of the perovskite performed at 600°C and 800°C.

First kinetic parameters reported in Table 6.8 did not reveal sharp changes in comparison with data in Table 6.6 regarding the detrimental effect of water on the reaction rate both on pre-reduced and aged samples. It appears that this effect is more accentuated in comparison with K- and Sr-substituted perovskite support materials. The reaction order remains unchanged on pre-reduced catalysts.

Nevertheless, different evolutions appear on the apparent activation energy compared to previous changes observed revealing a decrease in E_{app} recorded on aged samples. As exemplified in Table 6.8, thermal aging induces a sharp increase in E_{app} notably on aged $LaMn_{0.98}Pd_{0.02}O_3$. Interestingly, the reverse tendency is observed on Pd/$LaMnO_3$. The highest specific rate on pre-reduced sample is observed on $LaMn_{0.98}Pd_{0.02}O_3$(C800) while the lowest one is recorded on Pd/$LaMnO_3$(C800) which also exhibits the lowest thermal stability likely due to enhanced Pd particle sintering.

Optimized value for the reaction rate and equilibrium constant at 400°C are reported in Table 6.9. The rate constant reflects the reactivity of intermediates while the equilibrium constant reflects the strength of adsorption both are connected in some extent because the activation process take place if the strength of adsorption is enough important to weaken intramolecular bonds and facilitate the cleavage of a C-H bond.

No clear correlation appears by comparing the numerical values ok k_{6c} and K_{CH4} which seems consistent with a dual-site mechanism in which Pd can activate vicinal reactive oxygen species from the perovskite support. Based on this, the competition for adsorption of methane and oxygen could not be a determining parameter but this assertion could not be no longer valid in case of competition of mechanism I(b) and II as in case of optimal O-coverage leading to a weaking of the Pd-O_{ads} adsorption bond and a lowering of the rate constant k_{6b} depending on θ_O as the description in Fig.6.2.

By examining plots in Fig.6.10 clearly two different adsorption behaviors appear by comparing pre-reduced and aged Pd/$LaMnO_3$(C600) and $LaMn_{0.98}Pd_{0.02}O_3$(C600) catalysts. In the former case, aging has only a weak impact on the adsorption competition with a surface predominantly covered by methane molecular. Pre-reduced $LaMn_{0.98}Pd_{0.02}O_3$(C600) and Pd/$LaMnO_3$(C600) exhibit comparable adsorption behavior but this one sharply deviates after aging because the competition become largely in favor of oxygen on aged $LaMn_{0.98}Pd_{0.02}O_3$(C600).

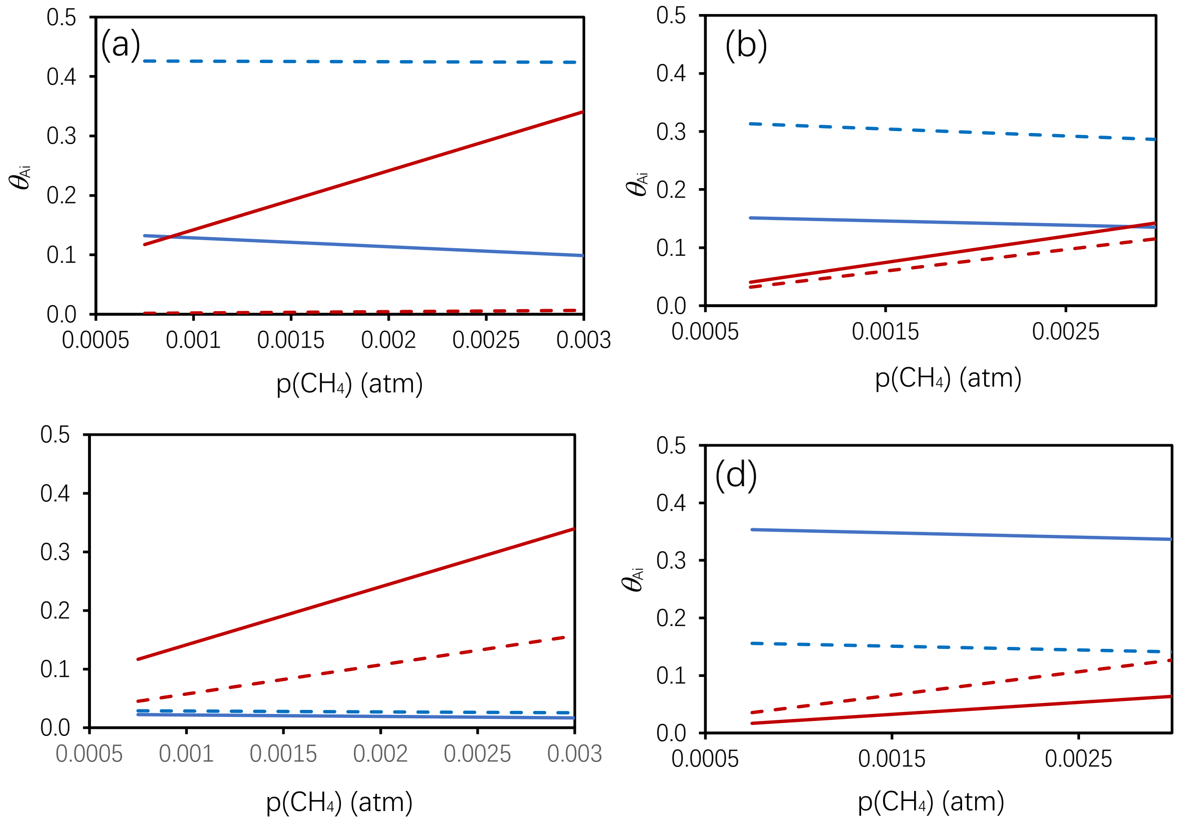

Fig. 6.10. Evolution of surface coverages θ_{Ai} for methane (red curve), oxygen (blue curve) vs. methane partial pressure during the CH_4/O_2 reaction on pre-reduced catalyst (bold line), on aged catalyst (dotted line). $LaMn_{0.98}Pd_{0.02}O_3$(C600) (a); $LaMn_{0.98}Pd_{0.02}O_3$(C800) (b); Pd/$LaMnO_3$(C600) (c); Pd/$LaMnO_3$(C800) (d).

Such behavior correspond to antagonistic evolution on the apparent activation energy values (E_{app}) as aging induces a lowering of E_{app} on Pd/$LaMnO_3$(C600) whereas an increase in E_{app} is characterized on aged $LaMn_{0.98}Pd_{0.02}O_3$(C600). It is worthwhile to note that this latter catalyst exhibits comparable adsorption behavior as Pd/$LaMnO_3$(C800) which could suggest that exsolution process could take place during aging leading to the segregation of larger Pd particles predominantly formed on pre-reduced Pd/$LaMnO_3$(C800) which could strengthen O_2 adsorption.

The affinity of pre-reduced Pd/$LaMnO_3$(C800) is much higher than that of Pd/$LaMnO_3$(C600). However, it seems obvious that aging will have lesser impact as in this typical case to O-adsorption will be slightly weaken which means that surface reconstruction taking place during aging would have different consequence according to the procedure for Pd incorporation.

Finally, the competition for O_2 adsorption seems more accentuated on pre-reduced $LaMn_{0.98}Pd_{0.02}O_3$(C800) than on $LaMn_{0.98}Pd_{0.02}O_3$(C600) likely due to the fact that calcination at 800°C will favor Pd exsolution from the bulk to the surface. Nonetheless, aged samples converge toward rather comparable behavior as Pd ex solution will occur during aging and probably will affect more extensively $LaMn_{0.98}Pd_{0.02}O_3$(C600).

In order to get more insight into surface changes induces by thermal aging additional HAADF-TEM measurements were achieved on aged $LaMn_{0.98}Pd_{0.02}O_3$(C600) and $LaMn_{0.98}Pd_{0.02}O_3$(C800) (Fig.6.11, Fig.6.12). Indeed, contrarily to calcined $LaMn_{0.98}Pd_{0.02}O_3$(C600) aging leads to the coexistence of small Pd particles as well as larger clusters (Fig.6.11). For $LaMn_{0.98}Pd_{0.02}O_3$(C800), ex solution process originally provokes the formation of larges Pd particles leading to a greater stabilization. Aging, leads to particles sintering but in lower extent which emphasizes the fact that both samples lead to more comparable surface properties.

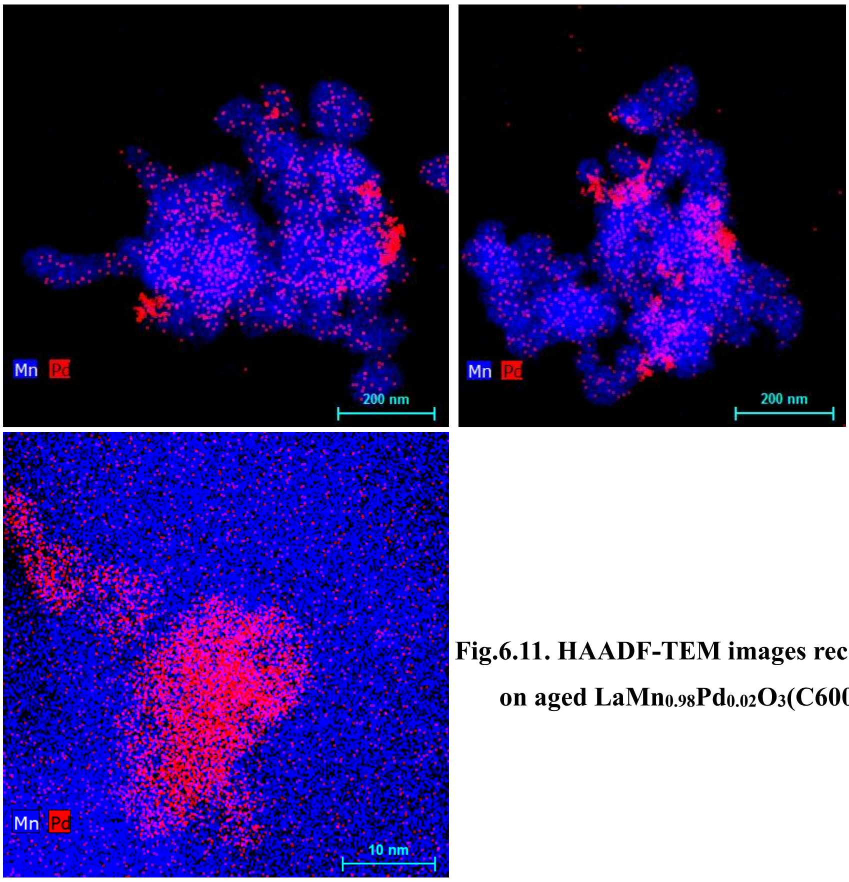

Fig.6.11. HAADF-TEM images recorded on aged $LaMn_{0.98}Pd_{0.02}O_3$(C600).

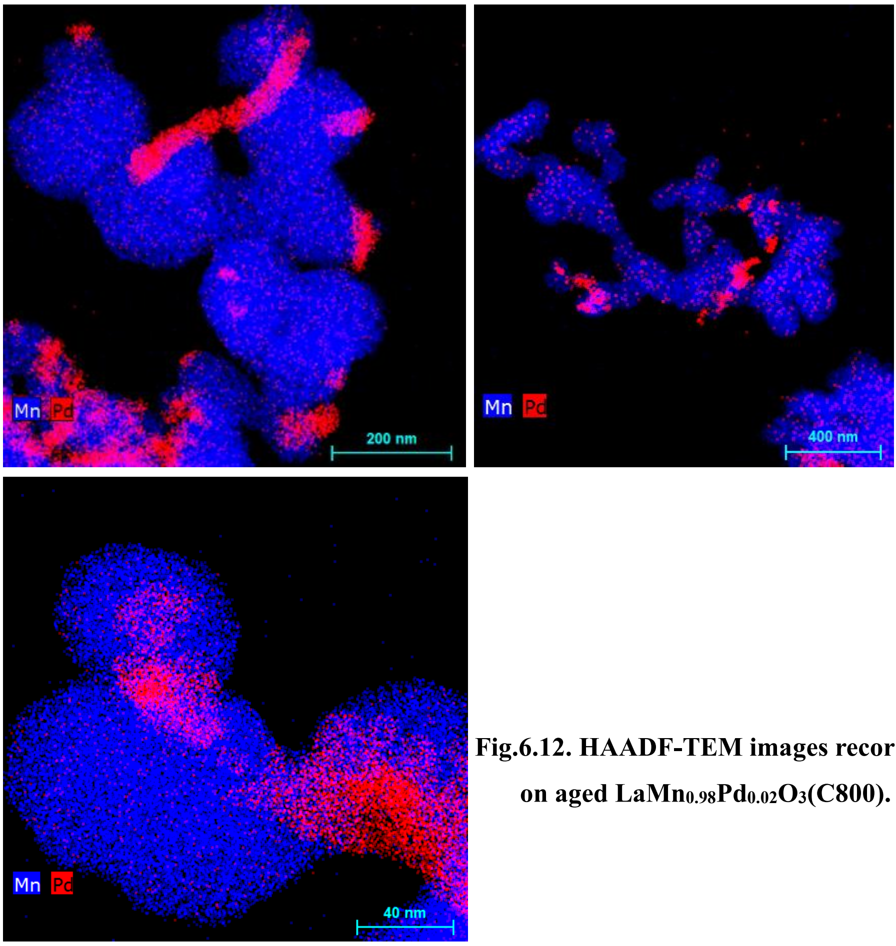

Fig.6.12. HAADF-TEM images recorded on aged $LaMn_{0.98}Pd_{0.02}O_3$(C800).

Table 6.8. Kinetic parameters for the CH_4/O_2 reaction at 400°C in lean conditions over pre-reduced and aged Pd/perovskite catalyst.

Catalyst	Thermal treatment	$p(CH_4)/10^{-3}$ (atm)	$p(O_2)/10^{-3}$ (atm)	$p(H_2O)/10^{-3}$ (atm)	Pre-exponential factor A (s^{-1})	E_{app} (kJ/mol)	CH_4 order	Specif. Rate ($mol.s^{-1}g^{-1}$)	TOF (s^{-1})
$Pd/LaMnO_3$(C600)	Pre-reduced/250°C	0.75-3.0	50	-	1.2×10^{8}	140.5	0.7	5.5×10^{-8}	
		1	50	100	-	-	-	1.1×10^{-8}	
	Aged[a]	0.75-3.0	50	-	1.8×10^{3}	119.1	n.d	4.6×10^{-8}	
		1	50	100	-	-	-	1.6×10^{-8}	
$Pd/LaMnO_3$(C800)	Pre-reduced/250°C	0.75-3.0	50	-	1.3×10^{7}	129.4	0.6	4.8×10^{-8}	
		1	50	100	-	-	-	0.6×10^{-8}	
	Aged[a]	0.75-3.0	50	-	3.1×10^{6}	122.7	n.d	3.6×10^{-8}	
		1	50	100	-	-	-	1.7×10^{-8}	
$LaMn_{0.98}Pd_{0.02}O_3$(C600)	Pre-reduced/250°C	0.75-3.0	50	-	7.6×10^{5}	111.8	0.7	6.3×10^{-8}	
		1	50	100	-	-	-	1.4×10^{-8}	
	Aged[a]	0.75-3.0	50	-	8.4×10^{6}	127.3	n.d	4.2×10^{-8}	
		1	50	100	-	-	-	1.6×10^{-8}	
$LaMn_{0.98}Pd_{0.02}O_3$(C800)	Pre-reduced/250°C	0.75-3.0	50	-	5.2×10^{4}	94.7	0.7	8.9×10^{-8}	
		1	50	100	-	-	-	0.5×10^{-8}	
	Aged[a]	0.75-3.0	50	-	1.4×10^{7}	131.9	n.d	3.1×10^{-8}	
		1	50	100	-	-	-	1.6×10^{-8}	

Table 6.9 Kinetic and thermodynamic constants optimized in lean conditions at 400°C on pre-reduced and aged supported Pd catalyst on perovskite support material.

Catalyst	Thermal treatment	k_{6c}^{c}	k_{12}^{c}	K_{CH4}^{d}	K_{O}^{d}
Pd/LaMnO$_3$(C600)	Reduced^{a}	$(2.5\pm0.3)\times10^{-5}$	0.59±0.06	170±20	$(1.3\pm0.2)\times10^{-2}$
	Aged^{b}	$(4.4\pm0.5\times10^{-5}$	0.20±0.02	63±7	$(1.9\pm0.2)\times10^{-2}$
Pd/LaMnO$_3$(C800)	Reduced^{a}	$(8.9\pm0.9)\times10^{-5}$	1.50±0.20	35±4	6.3±0.7
	Aged^{b}	$(5.4\pm0.6\times10^{-5}$	0.80±0.10	57±6	0.8±0.1
LaMn$_{0.98}$Pd$_{0.02}$O$_3$(C600)	Reduced^{a}	$(2.6\pm0.3)\times10^{-5}$	0.80±0.10	196±20	0.6±0.1
	Aged^{b}	$(9.8\pm0.1\times10^{-4}$	0.50±0.06	4±1	11±2
LaMn$_{0.98}$Pd$_{0.02}$O$_3$(C800)	Reduced^{a}	$(1.6\pm0.2)\times10^{-5}$	0.80±0.10	65±7	0.7±0.1
	Aged^{b}	$(1.9\pm0.2\times10^{-5}$	1.0±0.1	64±7	5.0±0.6

3.5. Discussion and conclusion

Lanthanum substitution: impact on the catalytic Pd properties of Pd particles

Kinetic behavior of Pd-doped perovskite can be reasonably modeled according to a dual site mechanism which account the creation of dual sites at the Pd-support interface. At first glance this conclusion is supported by the intrinsic catalytic properties of perovskite in methane combustion [28-30]. Indeed, Gao et al explained the catalytic behavior of on $La_{1-x}Sr_xCoO_{3-\delta}$ in methane combustion by the cooperation of surface lattice oxygen vacancy with surrounding cationic cobalt species stabilized in lower oxidation state. These authors clearly identified a beneficial effect of Sr which manifests preferentially at low composition $x \leq 0.1$ which differ from our observations as best performance were obtained on the perovskite corresponding to the higher Sr content. Such apparent discrepancy is expected as palladium is intrinsically more active than perovskite but can originate support effect.

Strontium has been already pointed out as a potential promoter for supported palladium catalysts enhancing Pd dispersion. The basicity of the support material can be also improved inducing electronic effects with an increase of the electron density of Pd particles [31]. Let us note that the K-substitution can also lead to the same effect with electron donation to Pd particles [32,33]. Hence, a strengthening of the metallic character of Pd particles could be *a priori* provoked by the K- and Sr-substitution. Related competition for methane and oxygen adsorption on Pd particles could be in principle altered in some extent.

Nevertheless, divergent observations are noticeable as oxygen would compete more in favor of oxygen on $Pd/La_{1-x}K_xMnO_3$ while a strengthening of methane adsorption prevail on $Pd/La_{1-x}Sr_xMnO_3$. This divergency proves that the Pd itself cannot explained the evolution observed on the catalytic properties. They would also account for the textural and structural properties of the perovskite support which can govern oxygen mobility and the production of reactive oxygen species. Hence, while Sr-substitution does not alter the perovskite structure, XRD analysis clearly evidence phase segregation induced by K-substitution lowering oxygen mobility.

By way of illustration, Alifanti et al. [30] studied methane and propane combustion on lanthanum transition metal perovskite. They investigated the role played by oxygen mobility on $La_{1-x}Sr_xM_{1-y}M'_yO_{3-\delta}$ which combines the texture of the catalyst and the structure. They found that high activity of perovskite depends on the SSA. Interestingly, the loss of activity on aged catalyst due to the loss of SSA is compensated by a faster bulk oxygen mobility at high temperature.

Based on these arguments, neither Pd alone nor perovskite alone would explain the catalytic properties. In fact, they would result from the transfer of oxygen from the perovskite to the palladium particle as reported elsewhere on Pd doped hexaaluminate catalysts [34]. It has been found that this oxygen mobility would be directly related to the Mn^{3+}/Mn^{2+} redox properties.

XPS study had been applied on the 16 samples recovered after high throughput reaction, the related metal properties were listed in the Table 6.10 as reasonable reference. Compared with the former results of fresh calcinated samples in Chapter V, the most obvious facts were the manganese valence decreased from the Mn 2p and Mn 3s orbitals indicating that the Mn cation participated the methane reduction, and the surface Pd ratio decreased sharply for sequential samples rather than one-pot samples which contained also the closed Pd ratio as before. For the Pd doped $LaMnO_3$ series, both of the above effects indicated the different mechanisms for sequential and one-pot samples during aging process, one-pot doped samples changed but sequential remained the same.

Strategy for Pd incorporation combined with calcination temperature

Let us move to Pd-doped $LaMnO_3$ with two different methods for palladium addition according to a two-step process involving wet impregnation of $LaMnO_3$ calcined at 600°C and 800°C and a one pot method where palladium is added during the sol. Afterward the same steps for the sol gel route were conserved till the calcination at 600°C or 800°C to obtain $LaMn_{1-x}Pd_xO_3$(C600) and $LaMn_{1-x}Pd_xO_3$(C600). As previously discussed, the calcination of the perovskite changes the textural properties but the subsequent loss of specific surface area could be *a priori* compensated by improved bulk diffusion. The method for palladium incorporation is also a critical parameter as the surface density can drastically changes as well as the strength of interaction according to the method itself but also to the importance of the specific surface area.

As seen in Table 6.7, impregnated samples are surface Pd-rich sample while sol gel samples exhibit much lower surface Pd density as Pd is expected to be randomly distributed in the bulk with the absence of significant gradient. Incorporation of palladium in the perovskite lattice is recognize to improve the stability of 3DOM $La_{0.6}Sr_{0.4}Mn_{1-x}Pd_xO_3$ [35].

However, jointly to a greater stabilization inside the perovskite lattice, the surface density can sharply drop underlined by an extremely low Pd dispersion almost nil. The dispersion on supported Pd catalyst is also rather low but could has different origin as Pd rich surface could signifies the segregation of large Pd particles. $LaMn_{0.98}Pd_{0.02}O_3$(C800) exhibit the highest Pd dispersion and also the lowest specific surface area which highlight exsolution process taking place when the calcination temperature is high. Hence, diffusion from the bulk to the surface could lead to surface Pd enrichment jointly to the segregation of reducible PdO_x species.

Prior catalytic measurements in methane combustion, the authors reduced the catalyst at 500°C which leaded to partial deterioration of the perovskite structure while cationic Pd^{2+} species in octahedral coordination are extracted from their initial position and segregated at the surface into nanosized metallic Pd^0 particles. Zao et al. found in this configuration a high thermal stability and improved tolerance to CO_2, H_2O and SO_2 poisoning effects likely related to a much stronger metal-support interaction than that obtained simply by impregnation [36]. Let us note in our case that the pre-reduction performed at 250°C did not alter the structural properties of the perovskite. On the other hand, extensive reduction of oxidic to metallic Pd species should.

Under reaction conditions, it is not easy to identify the valence state of Pd active site as re-oxidation cannot be completely ruled out even though this process is slow and likely depend on the size and the strength of interaction with the support. Hicks et al. [37] found that that oxidation over palladium was structure-sensitive, small particles being less active than larger ones. The authors assigned this structure-sensitivity to the reactivity of adsorbed oxygen and concluded that palladium oxide dispersed over alumina is much less active than oxide clusters covering metallic crystallites.

By examining the range of variation of TOF and the rate constant k_{6c} no clear dependency with Pd dispersion appears this is highlighted on $LaMn_{0.98}Pd_{0.02}O_3$ exhibiting the highest Pd dispersion but the lowest value for k_{6c}. As a matter of fact, the highest value for k_{6c} has been obtained on aged $LaMn_{0.98}Pd_{0.02}O_3$(C600) which jointly suffer from a strong oxygen adsorption likely inhibiting methane adsorption. However, this effect is moderate as only slight changes observed on the specific rate. All these observations seem to emphasized that Pd sites themselves would not be the driving force in determining the catalytic properties but take the extent of interface with the support materials.

Table 6.10. Impact of palladium incorporation into perovskite, i.e. wet impregnation vs sol gel (One-Pot) method on the surface properties of Pd-based perovskite catalysts

Catalysts	Method for Pd incorporation	XPS analysis after high throughput reaction						
		Pd ratio (%) [a]	$\frac{Pd}{\mathrm{La(+k/Sr)}}$	$\frac{Pd^{4+}}{Pd^{2+}}$	$\frac{Pd^{2+}}{Pd^{0}}$	$\frac{Pd}{\mathrm{Mn}}$	$\frac{Mn^{3+}}{Mn^{4+}}(b)$	Mn（AOS) [c]
Pd/LaMnO$_3$(C600)	wet impregnation	0.14	0.02	-	1.75	0.03	1.45	3.29
Pd/LaMnO$_3$(C800)	wet impregnation	-	-	-	-	-	1.22	3.37
Pd/La$_{0.7}$MnO$_3$(C600)	wet impregnation	0.32	0.10	0.24	3.63	0.06	0.93	3.31
Pd/La$_{1.3}$MnO$_3$(C600)	wet impregnation	0.58	0.01	-	2.27	0.06	1.14	3.47
LaMn$_{0.98}$Pd$_{0.02}$O$_3$(C600)	Sol-gel (One-Pot)	0.68	0.08	-	0.92	0.11	1.16	3.24
LaMn$_{0.98}$Pd$_{0.02}$O$_3$(C800)	Sol-gel (One-Pot)	1.29	0.11	1.91	-	0.14	1.04	3.52
Pd/La$_{0.98}$K$_{0.02}$MnO$_3$(C600)	wet impregnation	0.25	0.02	-	1.12	0.03	1.27	3.53
Pd/La$_{0.95}$K$_{0.05}$MnO$_3$(C600)	wet impregnation	0.22	0.04	0.42	-	0.04	0.91	3.21
Pd/La$_{0.9}$K$_{0.1}$MnO$_3$(C600)	wet impregnation	0.20	0.01	0.99	-	0.01	1.00	3.40
Pd/La$_{0.85}$K$_{0.15}$MnO$_3$(C600)	wet impregnation	0.10	0.003	0.60	-	0.01	1.06	3.44
Pd/La$_{0.98}$Sr$_{0.02}$MnO$_3$(C600)	wet impregnation	1.19	0.10	0.99	0.58	0.21	1.34	3.21
Pd/La$_{0.95}$Sr$_{0.05}$MnO$_3$(C600)	wet impregnation	0.65	0.09	-	0.18	0.12	1.63	3.24
Pd/La$_{0.9}$Sr$_{0.1}$MnO$_3$(C600)	wet impregnation	1.15	0.08	0.58	2.26	0.12	1.32	3.24
Pd/La$_{0.85}$Sr$_{0.15}$MnO$_3$(C600)	wet impregnation	0.80	0.06	0.44	-	0.08	1.59	3.22

[a] from Pd ratio (%) from XPS

[b] from XPS Mn 2p orbital

[c] average oxidation state

4. Mechanistic insights on reaction mechanism for methane oxidation on polycrystalline Pd-based catalyst near-stoichiometric conditions in the presence of steam

In this section the reaction has been studied in experimental conditions that mimic three-way operating conditions. The presence of steam has been considered but in much lower concentration: 1-2 vol.% instead of ~ 10 vol.% in real exhaust conditions. An additional important feature is also related to much lower oxygen concentrations. In practice, we should expect that the supply of reactive oxygen species from the perovskite support should attenuate the negative impact of low oxygen concentration on the kinetics of methane combustion. In contrast, these operating conditions could originate the occurrence of extra parallel reactions such as steam reforming or successive water gas shift reaction [38] even though the concentration of water has been lowered. Formally, palladium is not a benchmark as nickel or rhodium generally recognized more reactive for steam reforming reaction. However, perovskite structure was found active to catalyze such reaction, particularly Sr-doped perovskite structure [38]. Let us note that the reaction mechanism should not be more complex as most of intermediates and elementary steps are common to total or partial oxidation. Indeed, the slow steps still remains the C-H bond breaking.

As the previous kinetic study in lean conditions revealed the superiority of Sr-doped catalysts especially the composition Pd/$LaMn_{0.85}Sr_{0.15}O_3$(C600). In order to implement minimum experimental data to investigate the impact of various factors: (i.) calcination temperature, (ii.) Pd content, (iii.) Pd incorporation strategies: one pot vs. sequential impregnation method, (iv.) lanthanum deficiency on perovskite A-site. This part has been discussed in a former separate Sub-Chapter 5.5. The beneficial of strontium has been already pointed out as Sr-doping favors oxygen vacancies which eases the migration of oxygen from the bulk to the surface. An interesting effect also lies in joint effects with palladium and La-deficiency. Physicochemical properties on these series are resumed in Table 6.11. The operating conditions selected for steady-state kinetic measurements are reported in Table 6.12. The same procedure has been repeated with kinetic measurements performed on pre-reduced samples. A second set of kinetic measurements were performed on aged samples after exposure 4h at 750°C in 10 vol.% H_2O and 5 vol.% O_2 diluted in He.

Table 6.11. Impact of perovskite $La_xSr_{0.15}MnO_{3+\delta}$ composition and palladium incorporation route, i.e. wet impregnation vs sol gel (One-Pot) method, on the surface properties of Pd-based perovskite catalysts

Catalysts	Pd content (wt.%)	Method for Pd incorporation	SSA (m^2/g)	Pd dispersion [a] (%)	XPS analysis				
					Pd/Mn	Mn^{3+}/Mn^{4+} [b]	Mn（AOS）[c]	Pd^{x+}/Pd^{2+} ($x > 2$)	Pd^{2+}/Pd^0
$Pd/La_{0.55}Sr_{0.15}MnO_3$(C600)	0.5	Sequential	27.9	4.6	0.214	0.52	3.3	-	0.20
$La_{0.55}Sr_{0.15}Pd_{0.01}Mn_{0.99}O_3$(C800)	0.5	One-pot	30.3	2.8	0.06	0.42	2.9	0.10	-
$La_{0.55}Sr_{0.15}Pd_{0.02}Mn_{0.98}O_3$(C600)	1.0	One-pot	32.6	3.6	0.011	0.41	3.3	0.16	12.74
$Pd/La_{0.55}Sr_{0.15}MnO_3$(C800)	1.0	Sequential	45.7	4.8	0.157	0.53	3.1	0.04	0.25
$La_{0.85}Sr_{0.15}Pd_{0.01}Mn_{0.99}O_3$(C600)	0.5	One-pot	24.6	5.6	0.008	0.56	3.2	-	6.97
$Pd/La_{0.85}Sr_{0.15}MnO_3$(C800)	0.5	Sequential	11.8	3.8	0.032	0.41	3.3	-	1.05
$Pd/La_{0.85}Sr_{0.15}MnO_3$(C600)	1.0	Sequential	36.9	8.4	0.257	0.28	3.6	-	0.26
$La_{0.85}Sr_{0.15}Pd_{0.02}Mn_{0.98}O_3$(C800)	1.0	One-pot	7	0.4	0.035	0.48	3.2	-	0.78

[a] from H_2 chemisorption at 100°C on prereduced catalyst at 250°C

[b] from XPS Mn 2p orbital

[c] average oxidation state

Table 6.12. Inlet partial pressures conditions during steady-state rate tests at 460°C.

$p(CH_4)_0$	$p(O_2)_0$	$p(H_2O)_0$
0.001	0.002	0.01
0.003	0.002	0.01
0.00075	0.002	0.01
0.002	0.002	0.01
0.001	0.006	0.01
0.001	0.005	0.01
0.001	0.002	0.005
0.001	0.002	0.02
0.001	0.002	0.01

Physicochemical characterization of the samples has been already discussed and can be resumed as follow regarding the main trends:

- Calcination at 800°C has a detrimental effect on the specific surface area except on Sr-doped sampled exhibiting La-deficiency.
- Pd dispersion are low with no strong deviations. The weak dispersion reflects equally particle sintering and/or the stabilization of unreducible palladium species in the perovskite lattice remaining oxidic after prereduction at 250°C.
- Sharp difference is noticeable on the surface Pd/Mn ratio. Hence, the high value on sample prepared via the sequential method would agree with preferential aggregation due to weak Pd-perovskite interaction and low dispersion. In contrast, the low Pd/Mn ratio would reflect homogeneous bulk distribution of oxidic Pd species in strong interaction with the perovskite lattice.
- In agreement with abovementioned comments, the detection of metallic Pd^0 species, mainly on impregnated samples, would reflect the presence of highly-reducible oxidic likely in weak interaction with the perovskite support. This species would reduce under X-ray irradiation during XPS measurements.

4.1. Steady-state rate measurements

The influence of the temperature of the reaction rates has been investigated in the range 400-480°C and 460-540°C respectively for pre-reduced and aged catalysts. One can observe that aging leads to deactivation (see Fig. 6.13(a)). A classical Arrhenius behavior is observed on 0.5 wt.% Pd/$La_{0.85}Sr_{0.15}MnO_3$(C800).

The intercept and the slope of the straight line can lead to the calculation of the pre-exponential factor A and the apparent activation energy E_{app}. The value of E_{app} shifts from 145.7 kJ/mol to 128.4 kJ/mol after aging. A compensation effect is observed with a sharp decrease of the pre-exponential factor from 9.1×10^7 to 2.9×10^6 $L.s^{-1}.g^{-1}$. Hence, deactivation would result from a loss of density of active sites. While no significant comparison can be drawn with the same catalyst for the combustion of methane in lean and dry conditions, a tentative comparison can be achieved with 1 wt.% Pd/ $La_{0.85}Sr_{0.15}MnO_3$(C600). It is remarkable that aging induces different kinetic behavior because in this specific case an opposite trend is observed with an increase in E_{app} on the aged catalysts.

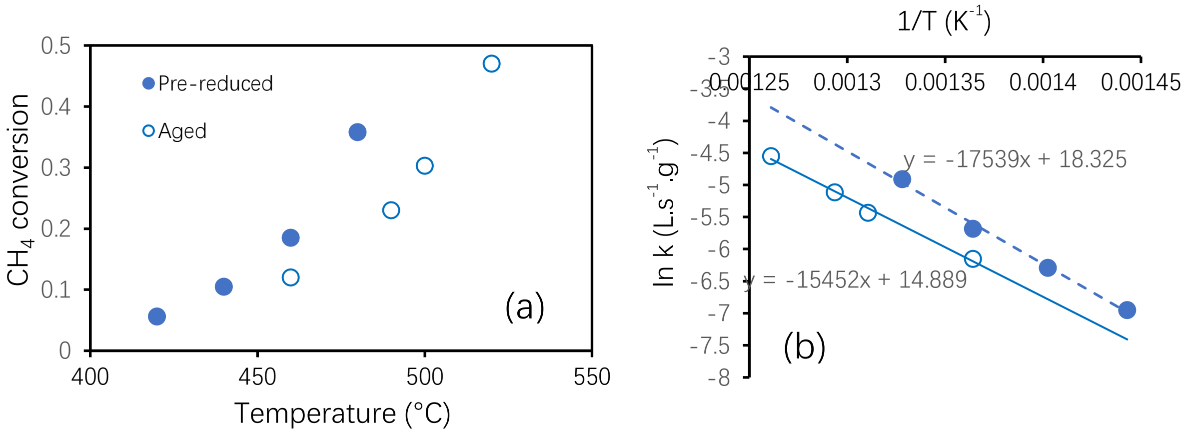

Fig.6.13. Influence of temperature on methane conversion recorded on pre-reduced and aged 0.5 wt.% Pd/$La_{0.85}Sr_{0.15}MnO_3$(C800) (a) – corresponding Arrherius plots (b): 0.03 g. catalyst, 0.1 vol.% CH_4, 0.2 vol.% O_2, 1.0 vol.% H_2O.

Surprisingly, for the others catalysts samples, the Arrhenius behavior was no longer observed as exemplified in Fig.6.14. Two ranges of conversion are observed differentiated by a minimum as indicated in the figure. In most cases, when this minimum can be identified, a shift to higher temperature is noticeable on the aged samples. It is also noticeable that aging does not equally lead to the same trends as gain in conversion is sometimes observed instead of deactivation.

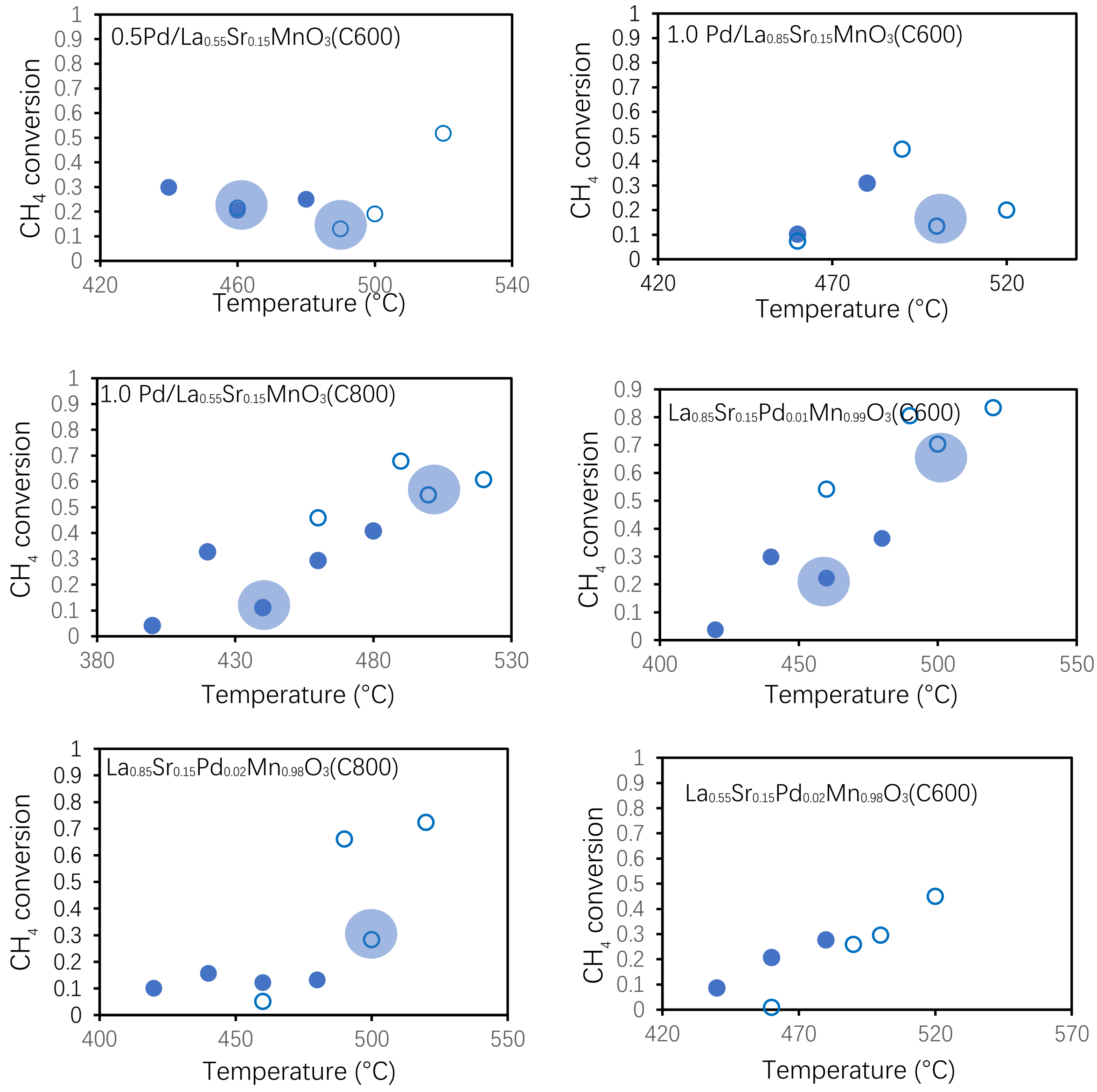

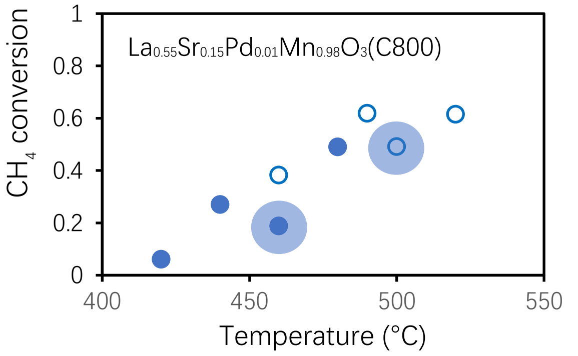

Fig. 6.14. Influence of temperature on methane conversion recorded on pre-reduced (●) and aged (○) support Pd catalysts.

Subsequent comparisons can be done with homologues free of strontium. Their preparation is similar. The same two protocols for Pd addition were used and they also differ from the La-stoichiometry. As general trend, it appears that strontium addition improves the resistance to deactivation. Indeed, deactivation is significantly delayed compared to Sr-free benchmark systems. As observed in Table 6.13 a gain in methane conversion is sometimes observed. On the other hand, strontium has a detrimental effect on the catalytic activity as Sr-free samples are usually more active below 400°C.

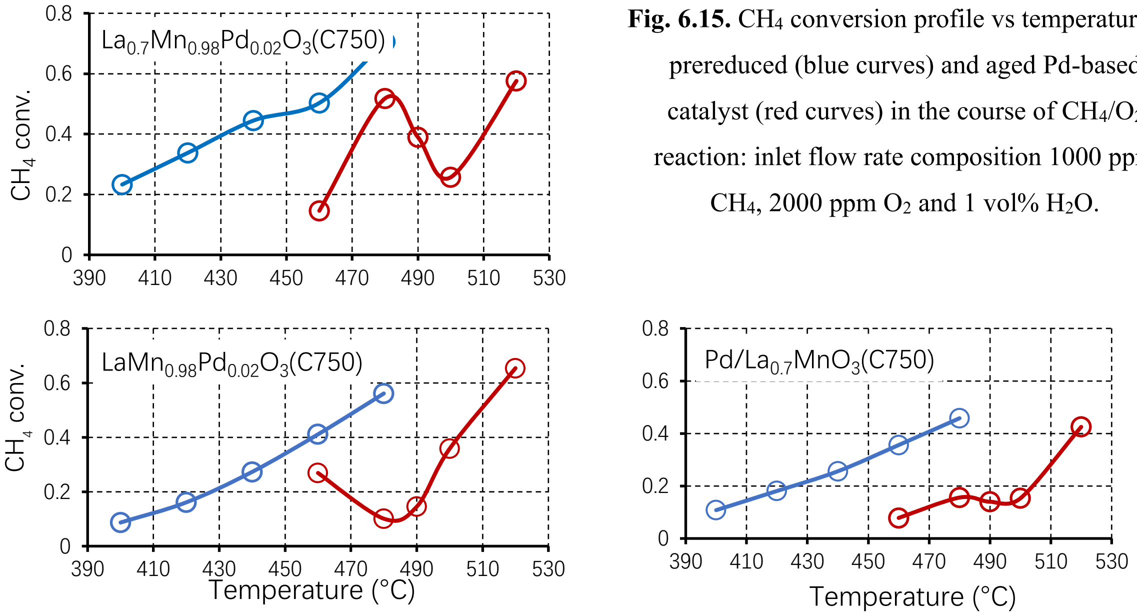

Fig. 6.15. CH_4 conversion profile vs temperature on prereduced (blue curves) and aged Pd-based catalyst (red curves) in the course of CH_4/O_2 reaction: inlet flow rate composition 1000 ppm CH_4, 2000 ppm O_2 and 1 vol% H_2O.

Table 6.13. Impact of thermal aging on CH_4 conversion measured at 460°C in the presence of 0.1 vol.% CH_4, 0.2 vol.% O_2 and 1.0 vol.% H_2O.

Catalyst	Before Aging Conversion (%)	After Aging Conversion (%)
0.5%Pd/$La_{0.55}Sr_{0.15}MnO_3$(C600)	20.64	22.41
0.5%Pd/($La_{0.85}Sr_{0.15}MnO_3$(C800)	20.79	11.79
1%Pd/($La_{0.55}Sr_{0.15}MnO_3$(C800)	25.59	49.05
1%Pd/($La_{0.85}Sr_{0.15}MnO_3$(C600)	0.44	7.09
$La_{0.55}Sr_{0.15}Mn_{0.01}Pd_{0.99}O_3$(C800)	21.89	41.34
$La_{0.55}Sr_{0.15}Mn_{0.02}Pd_{0.98}O_3$(C600)	12.62	9.33
$La_{0.85}Sr_{0.15}Mn_{0.99}Pd_{0.01}$O3(C600)	20.98	53.1
$La_{0.85}Sr_{0.15}Mn_{0.98}Pd_{0.02}O_3$(C800)	15.97	17.01

The partial pressure dependencies of methane, oxygen and water of the reaction rate have been studied at 460°C. Particular attention was paid to kinetic measurements on pre-reduced samples. Results obtained on aged samples will not be presented and discussed.

Table 6.14. Kinetic parameters for the CH_4/O_2 reaction at 460°C according to the operating conditions described in Table 6.12

Catalyst	CH_4 order	O_2 order	H_2O order	Specif. Rate[a] (mol.$s^{-1}g^{-1}$)
0.5%Pd/$La_{0.55}Sr_{0.15}MnO_3$(C600)	1.9	0.42	0.38	0.26×10^{-7}
0.5%Pd/($La_{0.85}Sr_{0.15}MnO_3$(C800)	0.85	0.03	-0.31	1.43×10^{-7}
1%Pd/($La_{0.55}Sr_{0.15}MnO_3$(C800)	0.89	-0.46	-0.47	1.47×10^{-7}
1%Pd/($La_{0.85}Sr_{0.15}MnO_3$(C600)	-	-	-	-
$La_{0.55}Sr_{0.15}Mn_{0.99}Pd_{0.01}O_3$(C800)	>0	>0	>0	0.54×10^{-7}
$La_{0.55}Sr_{0.15}Mn_{0.98}Pd_{0.02}O_3$(C600)	0.76	0.24	0	5.5×10^{-8}
$La_{0.85}Sr_{0.15}Mn_{0.99}Pd_{0.01}$O3(C600)	0.98	0.17	0.07	1.30×10^{-8}
$La_{0.85}Sr_{0.15}Mn_{0.98}Pd_{0.02}O_3$(C800)	0.96	0.23	-0.96	5.5×10^{-8}
$LaMn_{0.98}Pd_{0.02}O_3$(C750)	0.72	0.09	-0.97-	2.03×10^{-7}
$La_{0.7}Mn_{0.98}Pd_{0.02}O_3$(C750)	0.86	0.04	-0 .39	2.40×10^{-7}
1%Pd/$La_{0.7}MnO_3$(C750)	0.79	0.14	-0.72	1.73×10^{-7}

[a] measured at 460°C in presence of 0.1 vol% CH_4, 0.2 vol.% O_2 and 1.0 vol.% H_2O.

As seen in Table 6.14, apparent reaction orders and specific reaction rates at 460°C on Sr-doped samples are compared with Sr free samples. The evolutions observed on the reaction rate values corroborate previous comments emphasizing the detrimental effect of strontium. This effect accentuates at low Pd content and on sample prepared according to the one-pot method. Regarding the benchmark composition (in the absence of strontium) a positive value is obtained for methane and oxygen while the negative order with respect to water reflect a strong inhibiting effect earlier reported [35]. By examining the values obtained on Sr-doped samples some discrepancies clearly appear in some extent contradict observations on benchmarks according to the following comments:

- The first order kinetics with methane concentration is confirm except on 0.5% Pd/$La_{0.85}Sr_{0.15}MnO_3$(C800) obeying to a second order kinetics.
- The beneficial effect of oxygen is verified except on 1%Pd/$La_{0.55}Sr_{0.15}MnO_3$(C800) characterized by a negative reaction order.
- The strong inhibiting effect of water disappears on $La_{0.55}Sr_{0.15}Mn_{0.98}Pd_{0.02}O_3$(C600). A positive value is even observed $La_{0.85}Sr_{0.15}Mn_{0.99}Pd_{0.01}O_3$(C600) and 0.5%Pd/$La_{0.55}Sr_{0.15}MnO_3$(C600).

4.2. Kinetic modeling

The kinetics has been studied near stoichiometric conditions in the 1-2 vol.% H_2O with lower partial pressure of methane and O_2 (see Table 6.12). Consequently, water adsorption must be considered according to the following step (23):

$$H_2O + O_* + * \leftrightarrows 2OH_* \qquad (23)$$

By assuming this step quasi at equilibrium then the OH-coverage expression can be expressed according to Eq. (24):

$$\theta_{OH}^* = \left[\mathrm{K}_{H_2O}\mathrm{P}_{\mathrm{H}_2O}\sqrt{\mathrm{K_O P_{O_2}}}\right]^{0.5}\theta_v^* \qquad (24)$$

$$\text{with } \theta_v^* = \frac{1}{1+\mathrm{K}_{CH_4}\mathrm{P_{CH_4}}+\sqrt{\mathrm{K_O P_{O_2}}}+\left[\mathrm{K}_{H_2O}\mathrm{P}_{\mathrm{H}_2O}\sqrt{\mathrm{K_O P_{O_2}}}\right]^{0.5}} \qquad (25)$$

Regarding the reaction rate Eqs. (16), (17) and (24) their expressions only differ from the denominator which includes the following additional terms $\left[\mathrm{K}_{H_2O}\mathrm{P}_{\mathrm{H}_2O}\sqrt{\mathrm{K_O P_{O_2}}}\right]^{0.5}$. Hence, the following set of Eqs. (26)-(28) can be established.

$$r_1 = k_{6a}\theta_{CH_4}^*\theta_v^* = \frac{k_4 K_{CH_4} P_{CH_4}}{\left[1+\mathrm{K}_{CH_4}\mathrm{P_{CH_4}}+\sqrt{\mathrm{K_O P_{O_2}}}+\left[\mathrm{K}_{OH}\mathrm{P}_{\mathrm{H}_2O}\sqrt{\mathrm{K_O P_{O_2}}}\right]^{0.5}\right]^2} \qquad (26)$$

$$r_2 = k_{6b}\theta_{CH_4}^*\theta_O^* = \frac{k_{15} K_{CH_4} P_{CH_4}\sqrt{\mathrm{K_O P_{O_2}}}}{\left[1+\mathrm{K}_{CH_4}\mathrm{P_{CH_4}}+\sqrt{\mathrm{K_O P_{O_2}}}+\left[\mathrm{K}_{OH}\mathrm{P}_{\mathrm{H}_2O}\sqrt{\mathrm{K_O P_{O_2}}}\right]^{0.5}\right]^2} \qquad (27)$$

$$r_3 = k_{6c}\theta_{CH_4}^*\theta_O = \frac{k_{6c} K_{CH_4} P_{CH_4}}{D}\left[1+\frac{2k_{6c} K_{CH_4} P_{CH_4}}{k_{12} D}\right] \qquad (28)$$

$$\text{with } \mathrm{D} = \left[1+\mathrm{K}_{CH_4}\mathrm{P_{CH_4}}+\sqrt{\mathrm{K_O P_{O_2}}}+\left[\mathrm{K}_{OH}\mathrm{P}_{\mathrm{H}_2O}\sqrt{\mathrm{K_O P_{O_2}}}\right]^{0.5}\right]$$

In a first approach steady-state rate measurements on the Sr-free catalyst will be exploited. By examining the reaction order, the positive value with respect to the partial pressure of oxygen would *a priori* invalidate Eqs. (26) and (28) which would mean that reaction rate Eq. (27) would be suitable for the modeling of reaction rate. As a matter of fact, a graphical discrimination cannot be easily implemented as Eqs. (27) cannot be strictly linearized by applying a simple mathematical function: the reciprocal 1/*x*. Based on this, the least square method has been preferentially used. For sake of clarity, we conserved previous conclusions which ruled out mechanism I(a) corresponding to Eq. (26). In contrast, mechanism I(c), involving the Pd-perovskite interface, and mechanism I(b) involving adsorbed O species on Pd as intermediates have been considered in the optimization method. Hence, experimental and predicted reaction rate according to Eq. (29) have been compared for the adjustment of the rate constants and the equilibrium adsorption constants. The description of the procedure is schematized in Fig.6.16.

$$r = r_2 + r_3 = k_{6b}\theta^*_{CH_4}\theta^*_O + k_{6c}\theta^*_{CH_4}\theta_O =$$

$$\frac{k_{6b}K_{CH_4}P_{CH_4}\sqrt{\mathrm{K_O P_{O_2}}}}{\left[1+\mathrm{K}_{CH_4}\mathrm{P_{CH_4}}+\sqrt{\mathrm{K_O P_{O_2}}}+\left[\mathrm{K}_{OH}\mathrm{P}_{\mathrm{H_2}O}\sqrt{\mathrm{K_O P_{O_2}}}\right]^{0.5}\right]^2} + \frac{k_{6c}K_{CH_4}P_{CH_4}}{D}\left[1 + \frac{2k_{6c}K_{CH_4}P_{CH_4}}{k_{12}D}\right] \qquad (29)$$

As described, the different kinetic and thermodynamic constants have been optimized when the sum of the square difference between predicted and experimental rates tend to a minimum value. As seen a good consistency is observed by examining the plot predicted data vs. experimental data. Based on this the contribution of each mechanism can be estimated revealing on $La_{0.7}Mn_{0.98}Pd_{0.02}O_3$ still the predominance of mechanism I(c) with step (6c) slow.

p (CH$_4$)$_0$	p (O$_2$)$_0$	p (H$_2$O)$_0$	Experimental r (mol/s/g)	Predicted r (mol/s/g)	Criteria	Contribution mech. Ib	Relative Contribution
0.001	0.002	0.01	2.39E-07	2.07E-07	9.75583E-16	6.05E-08	0.29
0.001	0.002	0.01	2.38E-07	2.07E-07	9.5093E-16	6.05E-08	0.29
0.001	0.002	0.01	2.38E-07	2.07E-07	9.26256E-16	6.05E-08	0.29
0.003	0.002	0.01	6.08E-07	6.22E-07	1.81501E-16	1.81E-07	0.29
0.003	0.002	0.01	6.09E-07	6.22E-07	1.53948E-16	1.81E-07	0.29
0.003	0.002	0.01	6.02E-07	6.22E-07	3.9718E-16	1.81E-07	0.29
0.00075	0.002	0.01	1.87E-07	1.55E-07	9.87102E-16	4.54E-08	0.29
0.00075	0.002	0.01	1.87E-07	1.55E-07	9.8311E-16	4.54E-08	0.29
0.00075	0.002	0.01	1.86E-07	1.55E-07	9.44168E-16	4.54E-08	0.29
0.002	0.002	0.01	4.54E-07	4.15E-07	1.55373E-15	1.21E-07	0.29
0.002	0.002	0.01	4.50E-07	4.15E-07	1.27219E-15	1.21E-07	0.29
0.002	0.002	0.01	4.48E-07	4.15E-07	1.08337E-15	1.21E-07	0.29
0.001	0.006	0.01	2.49E-07	2.26E-07	5.06481E-16	1.05E-07	0.46
0.001	0.006	0.01	2.49E-07	2.26E-07	5.14513E-16	1.05E-07	0.46
0.001	0.006	0.01	2.49E-07	2.26E-07	5.2231E-16	1.05E-07	0.46
0.001	0.005	0.01	2.47E-07	2.21E-07	6.7439E-16	9.57E-08	0.43
0.001	0.005	0.01	2.48E-07	2.21E-07	7.31731E-16	9.57E-08	0.43
0.001	0.005	0.01	2.47E-07	2.21E-07	6.4986E-16	9.57E-08	0.43
0.001	0.002	0.005	2.39E-07	2.79E-07	1.5873E-15	6.06E-08	0.22
0.001	0.002	0.005	2.40E-07	2.79E-07	1.52725E-15	6.06E-08	0.22
0.001	0.002	0.005	2.39E-07	2.79E-07	1.5873E-15	6.06E-08	0.22
0.001	0.002	0.02		1.49E-07	2.22338E-14	6.04E-08	0.41
0.001	0.002	0.02		1.49E-07	2.22338E-14	6.04E-08	0.41
0.001	0.002	0.02		1.49E-07	2.22338E-14	6.04E-08	0.41
0.001	0.002	0.01	2.40E-07	2.07E-07	1.06148E-15	6.05E-08	0.29
0.001	0.002	0.01	2.38E-07	2.07E-07	9.6326E-16	6.05E-08	0.29
0.001	0.002	0.01	2.28E-07	2.07E-07	4.1929E-16	6.05E-08	0.29
				Target to be minimized	**8.78555E-14**		

Adjustable parameters	
k_{6c}	0.004356775
k_{12}	5.90E-01
K_{CH4}	0.09791896
K_{O2}	5.60913E-06
K_{OH}	18517.81033
k_{6b}	5.845004031

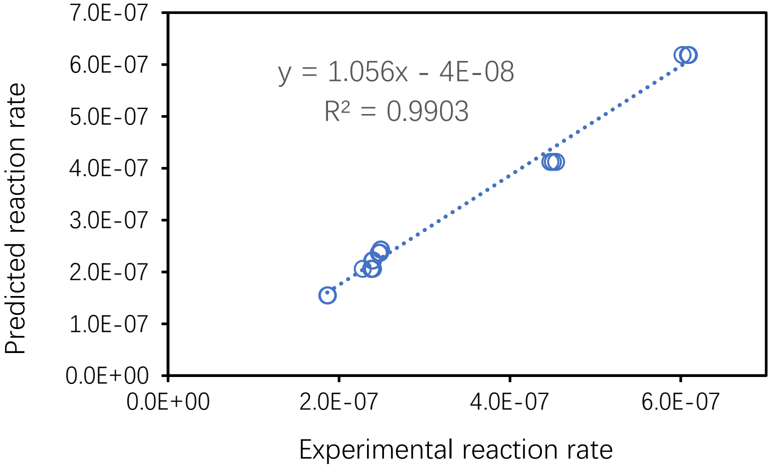

Fig. 6.16. Description of the adjustment routine by considering the minimum value reached for the sum of the square difference between experimental and predicted reaction rate according to Eq. (29) leading to optimized values for the rate constants k_n and the equilibrium constant K_i on La$_{0.7}$Mn$_{0.98}$Pd$_{0.02}$O$_3$.

The same methodology has been repeated for $LaMn_{0.98}Pd_{0.02}O_3$ and 1%Pd/$La_{0.7}MnO_3$. For the former catalyst mixed kinetic regimes is still observed. However, 1%Pd/$La_{0.7}MnO_3$ behaves differently as the adjustment routine leads to an optimized k_{6c} value almost nil with no longer contribution of mechanism I(c).

In this particular case, only mechanism I(b) involving Pd as active sites would occur and Eq. (27) would be the most representative. This equation agrees with an increase of the order value for oxygen. Let us note that the numerical values of K_{OH} higher than those estimated for the equilibrium constant of methane and oxygen suggests a significant inhibiting effect of water adsorption.

This assertion can be easily verified by the calculation of the coverage of O-, OH and adsorbed methane species. As illustrated in Fig.6.17, the methane coverage (not represented) is extremely low while adsorbed O and OH group predominate showing competitive adsorptions largely in favor of these two ad-species. This particularly true for dissociative water adsorption on Pd with high coverage reflecting a strong inhibiting effect. The detrimental effect of water could also affect the rate constant k_{6b}.

Indeed, theoretical calculations pointed out that the activation barrier related to step (6(b)) depends on θ_O and θ_{OH} (see Fig. 6.2). This effect is markedly observed when the site occupancy exceeds 40%. As seen in Fig.6.16, oxygen coverage on the benchmark catalysts never reached this limit and θ_O suggesting a weak impact on the C-H bond breaking. In contrast, θ_{OH} exceed 40% which would provoke an increase in the activation barrier. Hence, the predominance of adsorbed OH group would also induce a decrease of k_{6b}.

$$r_2 = k_{6b}\theta^*_{CH_4}\theta^*_O = \frac{k_{15}K_{CH_4}P_{CH_4}\sqrt{K_O P_{O_2}}}{\left[1+K_{CH_4}P_{CH_4}+\sqrt{K_O P_{O_2}}+\left[K_{OH}P_{H_2O}\sqrt{K_O P_{O_2}}\right]^{0.5}\right]^2} \qquad (27)$$

Consequently, near the stoichiometry, in the presence of steam, mechanism I(b) would prevail at the expense of mechanism I(c). This means that the Pd-perovskite interface would be strongly altered even suppressed for Pd/$La_{0.7}MnO_3$ and only Pd active sites would run in these operating conditions. This could be explained by a strong OH group accumulation onto the support in the presence of steam in the inlet gas mixture blocking mobility and reactivity of surface oxygen lattice. Indeed, Shwartz et al. found on Pd-based catalyst that OH groups accumulation on the support hinders oxygen mobility and provokes deactivation [17,18].

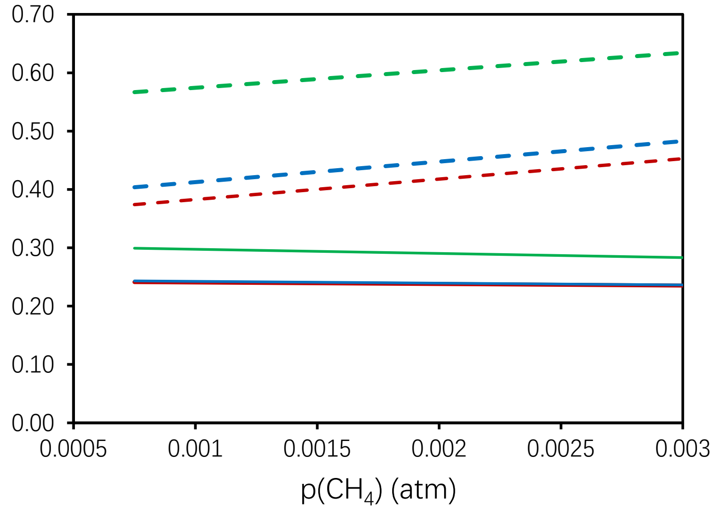

Fig.6.17. Evolution of surface coverages θ_{Ai} for oxygen (bold line) and OH species (dotted line) vs. methane partial pressure during the CH_4/O_2 reaction on pre-reduced $La_{0.7}Mn_{0.98}Pd_{0.02}O_3$ (red), $LaMn_{0.98}Pd_{0.02}O_2$ (blue) and $Pd/La_{0.7}MnO_3$ (green).

Table 6.15 Kinetic and thermodynamic constants optimized near the stoichiometry in the presence of steam at 460°C on pre-reduced Pd catalyst on perovskite support material. Predicted values were derived from Eq. (29).

Catalyst	k_{6c} (mol.s-1.g-1)	k_{6b} (mol.s-1.g-1)	k_{12} (mol.s-1.g-1)	K_{CH4} (atm-1)	K_O (atm-1)	K_{OH} (atm-1)	Contribution mech. I(b) (%)
$La_{0.7}Mn_{0.98}Pd_{0.02}O_3$	$(5.2\pm0.3)\times10^{-3}$	$(3.4\pm0.4)\times10^{-2}$	0.59±0.06	0.030±0.003	10±1	121±12	59
$LaMn_{0.98}Pd_{0.02}O_2$	0	$(3.6\pm0.4)\times10^{-2}$	0.50±0.50	0.043±0.005	11±1	127±13	58
$Pd/La_{0.7}MnO_3$	0	$(1.4\pm0.2)\times10^{-2}$	0.71±0.10	0.23±0.03	21±3	133±14	100
$0.5\%Pd/La_{0.85}Sr_{0.15}MnO_3$(C800)	0	$(3.3\pm0.4)\times10^{-2}$	0.71±0.10	0.018±0.002	80±8	6.3±0.7	100
$1\%Pd/La_{0.55}Sr_{0.15}MnO_3$(C800)	$(8.9\pm0.9)\times10^{-3}$	$(3.1\pm0.4)\times10^{-1}$	8.0±0.08	0.010±0.02	108±11	10±1	56
$La_{0.55}Sr_{0.15}Mn_{0.98}Pd_{0.02}O_3$(C600)	0	$(1.0\pm0.1)\times10^{-1}$	0.93±0.12	0.014±0.002	4.0±0.4	negligible	100

4.3. Particular case of Sr-doped catalysts

As discussed in Table 6.14, the kinetic behavior of Sr-doped deviate from benchmark systems. Tentative predictions by using Eq. (29) fail to described the partial pressure dependency of the reaction rate in most cases. Only, 0.5%Pd/$La_{0.85}Sr_{0.15}MnO_3$(C800), 1%Pd/$La_{0.55}Sr_{0.15}MnO_3$(C800) and $La_{0.55}Sr_{0.15}Mn_{0.98}Pd_{0.02}O_3$(C600) lead to a reasonable agreement. Based on such discrepancies no relevant conclusion can be *a priori* drawn as no consensus on the reaction mechanism appears from this first optimization routine.

In a second attempt, the following mechanism I(d) has been assumed. This mechanism proposal lies in the high OH coverage calculated and can agree with positive value for the reaction order for water. The same set of hypotheses can be taken into account to establish the reaction rate Eq. (30).

Mechanism I(d)

(4) $O_2(g) + 2* \leftrightarrows 2O*$

(5) $CH_4(g) + * \leftrightarrows CH_4*$

(6d) $CH_4* + OH* \rightarrow CH_3* + * + H_2O$

(7d) $CH_3* + O* \rightarrow CH_2* + * + H_2O$

(8d) $CH_2* + O* \rightarrow CH* + + * + H_2O$

(9d) $CH* + O* \rightarrow C* + + * + H_2O$

(10) $C* + O* \rightarrow CO* + *$

(11) $CO* + O* \rightarrow CO_2 + 2*$

(12) $2OH* \leftrightarrows H_2O + O* + 2*$

$$r_4 = k_{6d}\theta^*_{CH_4}\theta^*_{OH} = \frac{k_{6d}K_{CH_4}P_{CH_4}\left[\mathrm{K}_{OH}\mathrm{P}_{\mathrm{H}_2O}\sqrt{\mathrm{K_O P_{O_2}}}\right]^{0.5}}{\left[1+\mathrm{K}_{CH_4}\mathrm{P_{CH_4}}+\sqrt{\mathrm{K_O P_{O_2}}}+\left[\mathrm{K}_{OH}\mathrm{P}_{\mathrm{H}_2O}\sqrt{\mathrm{K_O P_{O_2}}}\right]^{0.5}\right]^2} \quad (30)$$

For the adjustment routine, we have adopted the same strategy taking for prediction Eq. (31) into account.

$$r = r_4 + r_3 = k_{6d}\theta^*_{CH_4}\theta^*_{OH} + k_{6c}\theta^*_{CH_4}\theta_O =$$

$$\frac{k_{6d}K_{CH_4}P_{CH_4}\left[\mathrm{K}_{OH}\mathrm{P}_{\mathrm{H}_2O}\sqrt{\mathrm{K_O P_{O_2}}}\right]^{0.5}}{\left[1+\mathrm{K}_{CH_4}\mathrm{P_{CH_4}}+\sqrt{\mathrm{K_O P_{O_2}}}+\left[\mathrm{K}_{OH}\mathrm{P}_{\mathrm{H}_2O}\sqrt{\mathrm{K_O P_{O_2}}}\right]^{0.5}\right]^2} + \frac{k_{6c}K_{CH_4}P_{CH_4}}{D}\left[1 + \frac{2k_{6c}K_{CH_4}P_{CH_4}}{k_{12}D}\right] \quad (31)$$

Unfortunately, no improvement from this second attempt was obtained leading to inconclusive arguments on the effective role of strontium on the kinetics.

4.4. Brief conclusion

Kinetic measurements in lean and dried conditions led to a reaction mechanism which illustrate a cooperation between Pd and the perovskite support. Improved surface properties on Sr-doped samples have been assigned to stronger methane adsorption in dry conditions. As already mentioned, strontium can also improve bulk oxygen mobility which could create synergy effect.

In this sub-chapter, Sr-doped catalysts were studied in different operating conditions near the stoichiometry and in wet conditions. Their catalytic properties were compared to benchmark systems free of strontium. Kinetic exploitation was feasible on Sr-free samples revealing in that case a mixed regimes with the coexistence of a dual site mechanisms and a single site mechanism involving only palladium. It appears that this latter mechanism prevails on Pd/$La_{0.7}MnO_3$ assigned to a significant deterioration of the Pd-support interface likely due to significant OH accumulation on the perovskite blocking oxygen mobility. Subsequent optimization of kinetic and thermodynamic constants also reveals a weakening of methane adsorption with competition for adsorption becoming largely in favor of oxygen and water.

In the presence of strontium, more complex kinetic features were observed. First, the classical Arrhenius behavior is no longer observed. The reaction order estimated differ from those obtained on Sr-free samples. Optimization of the different kinetic and thermodynamic constants was only possible on three catalysts, *i.e.* 0.5%Pd/$La_{0.85}Sr_{0.15}MnO_3$(C800), 1%Pd/$La_{0.55}Sr_{0.15}MnO_3$(C800) and $La_{0.55}Sr_{0.15}Mn_{0.98}Pd_{0.02}O_3$(C600). By examining the equilibrium constant similar tendencies reproduce with a weak methane adsorption. In contract, a strengthening of oxygen adsorption and a weakening of water adsorption is discernible.

References

1. Jacky Au-Yeung, Kaidong Chen, Alexis T. Bell, Enrique Iglesia, Isotopic Studies of Methane Oxidation Pathways on PdO Catalysts, Journal of Catalysis, Volume 188, Issue 1, 1999, Pages 132-139, ISSN 0021-9517, https://doi.org/10.1006/jcat.1999.2643.
2. H. Stotz, L. Maier, A. Boubnov, A.T. Gremminger, J.-D. Grunwaldt, O. Deutschmann, Surface reaction kinetics of methane oxidation over PdO, Journal of Catalysis, Volume 370, 2019, Pages 152-175, ISSN 0021-9517, https://doi.org/10.1016/j.jcat.2018.12.007.
3. G. Zhu, J. Han, D.Y. Zemlyanov, F.H. Ribeiro, Temperature Dependence of the Kinetics for the Complete Oxidation of Methane on Palladium and Palladium Oxide, J. Phys. Chem. B 109 (2005) 2331-2337. https://doi-org/10.1021/jp0488665.
4. F.H. Ribeiro, M. Chow, R.A. Dallabetta, Kinetics of the Complete Oxidation of Methane over Supported Palladium Catalysts, Journal of Catalysis, Volume 146, Issue 2, 1994, Pages 537-544, ISSN 0021-9517, https://doi.org/10.1006/jcat.1994.1092.
5. Ken-ichiro Fujimoto, Fabio H. Ribeiro, Miguel Avalos-Borja, Enrique Iglesia, Structure and Reactivity of PdO_x/ZrO_2 Catalysts for Methane Oxidation at Low Temperatures, Journal of Catalysis, Volume 179, Issue 2, 1998, Pages 431-442, ISSN 0021-9517, https://doi.org/10.1006/jcat.1998.2178.
6. Fan Zeng, Keith L. Hohn, Modeling of three-way catalytic converter performance with exhaust mixture from natural gas-fueled engines, Applied Catalysis B: Environmental, Volume 182, 2016, Pages 570-579, ISSN 0926-3373, https://doi.org/10.1016/j.apcatb.2015.10.004.
7. Johan Nilsson, Per-Anders Carlsson, Natalia M. Martin, Emma C. Adams, Giovanni Agostini, Henrik Grönbeck, Magnus Skoglundh, Methane oxidation over Pd/Al_2O_3 under rich/lean cycling followed by operando XAFS and modulation excitation spectroscopy, Journal of Catalysis, Volume 356, 2017, Pages 237-245, ISSN 0021-9517, https://doi.org/10.1016/j.jcat.2017.10.018.
8. M. Santhosh Kumar, A. Eyssler, P. Hug, N. van Vegten, A. Baiker, A. Weidenkaff, D. Ferri, Elucidation of structure–activity relationships of model three-way catalysts for the combustion of methane, Applied Catalysis B: Environmental, Volume 94, Issues 1–2, 2010, Pages 77-84, ISSN 0926-3373, https://doi.org/10.1016/j.apcatb.2009.10.023.
9. Alexander Winkler, Panayotis Dimopoulos, Roland Hauert, Christian Bach, Myriam Aguirre,

10. Catalytic activity and aging phenomena of three-way catalysts in a compressed natural gas/gasoline powered passenger car, Applied Catalysis B: Environmental, Volume 84, Issues 1–2, 2008, Pages 162-169, ISSN 0926-3373, https://doi.org/10.1016/j.apcatb.2008.03.013.
11. James B. Miller, Manaswita Malatpure, Pd catalysts for total oxidation of methane: Support effects, Applied Catalysis A: General, Volume 495, 2015, Pages 54-62, ISSN 0926-860X, https://doi.org/10.1016/j.apcata.2015.01.044.
12. Granger, P., Renème, Y., Lahougue, A. et al. Thermal Aging of Perovskite Based Natural Gas Vehicle Catalysts: Dependency of the Mode of Pd Incorporation. Top Catal 63, 1474–1484 (2020). https://doi.org/10.1007/s11244-020-01331-x.
13. Nishihata, Y., Mizuki, J., Akao, T. et al. Self-regeneration of a Pd-perovskite catalyst for automotive emissions control. Nature 418, 164–167 (2002). https://doi.org/10.1038/nature00893.
14. Mari Uenishi, Masashi Taniguchi, Hirohisa Tanaka, Mareo Kimura, Yasuo Nishihata, Junichiro Mizuki, Tetsuhiko Kobayashi, Redox behavior of palladium at start-up in the Perovskite-type $LaFePdO_x$ automotive catalysts showing a self-regenerative function, Applied Catalysis B: Environmental, Volume 57, Issue 4, 2005, Pages 267-273, ISSN 0926-3373, https://doi.org/10.1016/j.apcatb.2004.11.011.
15. Ye Lu, Katarzyna A. Michalow, Santhosh Kumar Matam, Alexander Winkler, Alexandra E. Maegli, Songhak Yoon, Andre Heel, Anke Weidenkaff, Davide Ferri, Methane abatement under stoichiometric conditions on perovskite-supported palladium catalysts prepared by flame spray synthesis, Applied Catalysis B: Environmental, Volume 144, 2014, Pages 631-643, ISSN 0926-3373, https://doi.org/10.1016/j.apcatb.2013.08.001.
16. M. Pilar González-Marcos, Beñat Pereda-Ayo, Asier Aranzabal, José A. González-Marcos, Juan R. González-Velasco, On the effect of reduction and ageing on the TWC activity of $Pd/Ce_{0.68}Zr_{0.32}O_2$ under simulated automotive exhausts, Catalysis Today, Volume 180, Issue 1, 2012, Pages 88-95, ISSN 0920-5861, https://doi.org/10.1016/j.cattod.2011.04.035.
17. Jianjun Chen, Yang Wu, Wei Hu, Pengfei Qu, Guochen Zhang, Pascal Granger, Lin Zhong, Yaoqiang Chen, New insights into the role of Pd-Ce interface for methane activation on monolithic supported Pd catalysts: A step forward the development of novel PGM Three-Way Catalysts for natural gas fueled engines, Applied Catalysis B: Environmental, Volume 264, 2020, 118475, ISSN 0926-3373, https://doi.org/10.1016/j.apcatb.2019.118475.

18. W.R. Shwartz, L.D. Pfefferle, Combustion of Methane over Palladium-Based Catalysts: Catalytic Deactivation and Role of the Support, J. Phys. Chem C 116 (2012) 8571-8579, https://doi-org/10.1021/jp212236e.
19. Yuanshuang Zheng, Amaury Decoster, Andrea Osti, Antonella Glisenti, Jean-Philippe Dacquin, Fabien Dhainaut, Svetlana Heyte, Pascal Granger, Combined theoretical and experimental kinetic approach for methane conversion on model supported Pd/$La_{0.7}MnO_3$ NGV catalyst: Sensitivity to inlet gas composition and consequence on the Pd-support interface, Applied Catalysis A: General, Volume 641, 2022, 118687, ISSN 0926-860X, https://doi.org/10.1016/j.apcata.2022.118687.
20. Jianxiong Wu, Jean-Philippe Dacquin, Nora Djelal, Catherine Cordier, Christophe Dujardin, Pascal Granger, Calcium and copper substitution in stoichiometric and La-deficient $LaFeO_3$ compositions: A starting point in next generation of Three-Way-Catalysts for gasoline engines, Applied Catalysis B: Environmental, Volume 282, 2021, 119621, ISSN 0926-3373, https://doi.org/10.1016/j.apcatb.2020.119621.
21. Anke Schön, Jean-Philippe Dacquin, Pascal Granger, Christophe Dujardin, Non stoichiometric $La_{1-y}FeO_3$ perovskite-based catalysts as alternative to commercial three-way-catalysts? – Impact of Cu and Rh doping, Applied Catalysis B: Environmental, Volume 223, 2018, Pages 167-176, ISSN 0926-3373, https://doi.org/10.1016/j.apcatb.2017.06.026.
22. Evgeny Shustorovich, Harrell Sellers, The UBI-QEP method: A practical theoretical approach to understanding chemistry on transition metal surfaces, Surface Science Reports, Volume 31, Issues 1–3, 1998, Pages 1-119, ISSN 0167-5729, https://doi.org/10.1016/S0167-5729(97)00016-2.
23. Evgeny Shustorovich, Alexis T. Bell, Decomposition and reduction of NO on transition metal surfaces: bond order conservation Morse potential analysis, Surface Science, Volume 289, Issues 1–2, 1993, Pages 127-138, ISSN 0039-6028, https://doi.org/10.1016/0039-6028(93)90892-N.
24. Domenica R. Fertal, Matteo Monai, Laura Proaño, Maxim P. Bukhovko, Jihyeon Park, Yong Ding, Bert M. Weckhuysen, Anil C. Banerjee, Calcination temperature effects on Pd/alumina catalysts: Particle size, surface species and activity in methane combustion, Catalysis Today, Volume 382, 2021, Pages 120-129, ISSN 0920-5861, https://doi.org/10.1016/j.cattod.2021.08.005.
25. R.S Monteiro, D Zemlyanov, J.M Storey, F.H Ribeiro, Turnover Rate and Reaction Orders for the Complete Oxidation of Methane on a Palladium Foil in Excess Dioxygen, Journal of Catalysis, Volume 199, Issue 2, 2001, Pages 291-301, ISSN 0021-9517,

https://doi.org/10.1006/jcat.2001.3176.

26. Y. Wu, C. Dujardin, C. Lancelot, J.P. Dacquin, V.I. Parvulescu, M. Cabié, C.R. Henry, T. Neisius, P. Granger, Catalytic abatement of NO and N_2O from nitric acid plants: A novel approach using noble metal-modified perovskites, Journal of Catalysis, Volume 328, 2015, Pages 236-247, ISSN 0021-9517, https://doi.org/10.1016/j.jcat.2015.02.001.
27. J.P. Dacquin, C. Lancelot, C. Dujardin, P. Granger, Support-Induced Effects of $LaFeO_3$ Perovskite on the Catalytic Performances of Supported Pt Catalysts in $DeNO_x$ Applications, J. Phys. Chem. C 115 (2011) 1911-1921. https://doi-org/10.1021/jp1069779.
28. M. Van den Bossche, H. Grönbeck, Methane Oxidation over PdO(101) Revealed by First-Principles Kinetic Modeling, J. Am. Chem. Soc. 2015, 137, 12035-12044. https://doi-org/10.1021/jacs.5b06069.
29. Kwang Sup Song, Danilo Klvana, Jitka Kirchnerova, Kinetics of propane combustion over $La_{0.66}Sr_{0.34}Ni_{0.3}Co_{0.7}O_3$ perovskite, Applied Catalysis A: General, Volume 213, Issue 1, 2001, Pages 113-121, ISSN 0926-860X, https://doi.org/10.1016/S0926-860X(00)00884-X.
30. M Alifanti, J Kirchnerova, B Delmon, D Klvana, Methane and propane combustion over lanthanum transition-metal perovskites: role of oxygen mobility, Applied Catalysis A: General, Volume 262, Issue 2, 2004, Pages 167-176, ISSN 0926-860X, https://doi.org/10.1016/j.apcata.2003.11.024.
31. Zhiming Gao, Ruiyan Wang, Catalytic activity for methane combustion of the perovskite-type $La_{1-x}Sr_xCoO_{3-\delta}$ oxide prepared by the urea decomposition method, Applied Catalysis B: Environmental, Volume 98, Issues 3–4, 2010, Pages 147-153, ISSN 0926-3373, https://doi.org/10.1016/j.apcatb.2010.05.023.
32. Unnikrishnan R. Pillai, Endalkachew Sahle-Demessie, Strontium as an efficient promoter for supported palladium hydrogenation catalysts, Applied Catalysis A: General, Volume 281, Issues 1–2, 2005, Pages 31-38, ISSN 0926-860X, https://doi.org/10.1016/j.apcata.2004.11.009.
33. Tomohiro Majima, Eugene Kono, Shuhei Ogo, Yasushi Sekine, Pre-reduction and K loading effects on noble metal free Co-system catalyst for water gas shift reaction, Applied Catalysis A: General, Volume 523, 2016, Pages 92-96, ISSN 0926-860X, https://doi.org/10.1016/j.apcata.2016.05.025.
34. Eugene Kono, Sakurako Tamura, Keisuke Yamamuro, Shuhei Ogo, Yasushi Sekine, Pd/K/Co-oxide catalyst for water gas shift, Applied Catalysis A: General, Volume 489, 2015, Pages 247-254, ISSN 0926-860X, https://doi.org/10.1016/j.apcata.2014.10.016.

35. A. Baylet, S. Royer, P. Marécot, J.M. Tatibouët, D. Duprez, High catalytic activity and stability of Pd doped hexaaluminate catalysts for the CH_4 catalytic combustion, Applied Catalysis B: Environmental, Volume 77, Issues 3–4, 2008, Pages 237-247, ISSN 0926-3373, https://doi.org/10.1016/j.apcatb.2007.07.031.

36. Xingtian Zhao, Ran Zhang, Yuxi Liu, Jiguang Deng, Peng Xu, Jun Yang, Zhuo Han, Zhiquan Hou, Hongxing Dai, Chak-Tong Au, In-situ reduction-derived Pd/3DOM $La_{0.6}Sr_{0.4}MnO_3$: Good catalytic stability in methane combustion, Applied Catalysis A: General, Volume 568, 2018, Pages 202-212, ISSN 0926-860X, https://doi.org/10.1016/j.apcata.2018.10.011.

37. Robert F. Hicks, Haihua Qi, Michael L. Young, Raymond G. Lee, Structure sensitivity of methane oxidation over platinum and palladium, Journal of Catalysis, Volume 122, Issue 2, 1990, Pages 280-294, ISSN 0021-9517, https://doi.org/10.1016/0021-9517(90)90282-O.

38. Xianglei Yin, Laihong Shen, Shen Wang, Baoyi Wang, Cheng Shen, Double adjustment of Co and Sr in $LaMnO_{3+\delta}$ perovskite oxygen carriers for chemical looping steam methane reforming, Applied Catalysis B: Environmental, Volume 301, 2022, 120816, ISSN 0926-3373, https://doi.org/10.1016/j.apcatb.2021.120816.

Chapter VII. Catalytic Measurements in Real Exhaust Gas Composition from NGVs Engines

1. Introduction

This last chapter is focused on the performance of Pd-doped samples in more realistic operating conditions which account for the presence of NO and CO in the inlet gas mixture. Catalytic measurements were performed in wet conditions but the steam composition has been lowered as the expected composition should normally tend to 10 vol.% in real exhaust gas compositions. Catalytic measurements were performed on catalysts in powder form with a space velocity of 100 $L.h^{-1}g^{-1}$. The feed gas composition in stoichiometric conditions was the following:

Table 1. Composition of the inlet feed gas mixture during catalytic measurements.

Gas	CH_4	CO	NO	O_2	CO_2	He	H_2O
Conc. Vol.%	0.1	0.05	0.2	0.125	8.0	Balance	1.0

Aging process has been also envisioned and described in the experimental section and the catalytic properties were also evaluated on aged samples. While Rh is a benchmark for NO_x removal because of a much faster N-O bond scission, the development of Rh-free Three-Way-Catalysts or the replacement of Rh by palladium started long time ago is still an interesting issue [1].

Particular attention was paid to the Pd content, the strategy for Pd deposition and the composition of the support on the catalytic properties. As exemplified, kinetic measurements in chapter 6 revealed that the support material can play a key role in methane combustion supplying reactive oxygen species but mostly in lean and dry conditions. A cooperative effect was observed which can be modeled by a dual site reaction mechanism. In contrast, the presence of steam can lead to significant detrimental effect as strong accumulation of OH group at the surface of the perovskites can suppress the contribution of the support. Nonetheless, the composition of the support still remains an outstanding parameter as it can govern Pd dispersion and alter the electron density in nanosized Pd particles. La and Ba are recognized to stabilize Pd dispersion becoming more resistant to thermal sintering during thermal aging, resulting in improved dispersion of Pd [2]. Improved resistance to deactivation has been also explained by electron transfer from electronegative La to PdO. As the consequence, the decomposition of PdO would be delayed [3]. Wang et al. [4] also found that doping with basic materials, *e.g.* Sr and Ba, increases in electron density of nanosized Pd particles on Sr and Ba materials which leads to CO-poisoning effect. Perovskite itself can exhibit remarkable catalytic performances in three-way operating conditions. This potentiality is related to the ease to accommodate transition metals in B-site [5]. In the particular case of $LaMnO_3$ composition, Giannakas et al. [6] suggested that the fraction of Mn^{3+}–O–Mn^{4+} pairs could be another critical parameter which could influence the catalytic activity.

In agreement we our previous conclusions, the Pd-$LaMnO_3$ interface is expected to govern the catalytic efficiency in NO reduction. Indeed, Mohammadi et al. [**7**] investigated NO/CO reaction in presence of water and tried to optimize the interface through different preparation methods. Interestingly, they found that the CO-inhibiting effect can be modulated by the Pd-perovskite interface and can be lowered in the presence of water. In case of deteriorated interface, strong CO adsorption prevails then suppressing adsorption/dissociation of NO. Optimal performance were related to the involvement of lattice oxygen for CO oxidation and subsequent replenishment from NO dissociation at the Pd-perovskite boundary. On the other hand, the occurrence of the Water gas shift reaction enhances NH_3 formation [12-15].

The composition of the catalyst is not the unique parameter for the explanation of the catalytic reaction. The composition of the reaction mixture and the range of temperature can lead to different behaviors. At low temperature, generally methane is not activated, the competition between the CO/NO and CO/O_2 reactions will predominantly prevail. The absence of trace of hydrogen in our inlet composition mixture should avoid the undesired formation of ammonia [7]. However, the water-gas-shift reaction can supply hydrogen. A rise in temperature can lead to sharp changes in the products distribution as the presence of steam and CO_2 can originate extra reactions involving methane activation. In principle, the expected reactions are the direct combustion of methane and/or NO/CH_4 reaction. However, dry and steam reforming reactions cannot be no longer neglected and can originate sharp changes in the selectivity of NO reduction as related production hydrogen can change the selectivity in favor of ammonia production [12-15].

Table 2. summarizes the possible reaction that can occur at low and high temperature.

Reaction	Low T	High T
$CO + 1/2O_2 = CO_2$	×	
$2CO + 2NO = N_2 + 2CO_2$	×	
$2NO + H_2 = N_2 + H_2O$	×	
$CH_4 + 2NO = N_2 + 2H_2O$		×
$CH_4 + 2O_2 = CO_2 + 2H_2O$		×
$CH_4 + CO_2 = 2CO + 2H_2$		×
$CH_4 + H_2O = CO + 3H_2$		×
$CO + H_2O = CO_2 + H_2$	×	
$CO_2 + H_2 = CO + H_2O$	×	

2. Catalytic measurements for palladium incorporated $La_xMnO_{3+\delta}$ series

The 1wt.% palladium doped La_xMnO_3 samples consist in 5 samples which differ from the method used for Pd incorporation, *e.g.* sequential route and one-pot method, the lanthanum stoichiometry (x = 0.7 and 1) and the calcination temperature. Prior to reaction, all samples were pre-reduced in hydrogen at 250°C. Temperature-programmed conversion profiles vs. temperature are reported in Figs. 7.2.1-7.2.4.

2.1. Methane conversion

Understanding the methane activation and oxidation under real exhaust conditions is of great importance and methane is the main emission gas component in exhaust gas of stoichiometric NGV engines [8], the related methane conversion was discussed for the heating process (Fig.7.2.1) and the reaction temperature of 550 ° C (Fig.7.2.2).

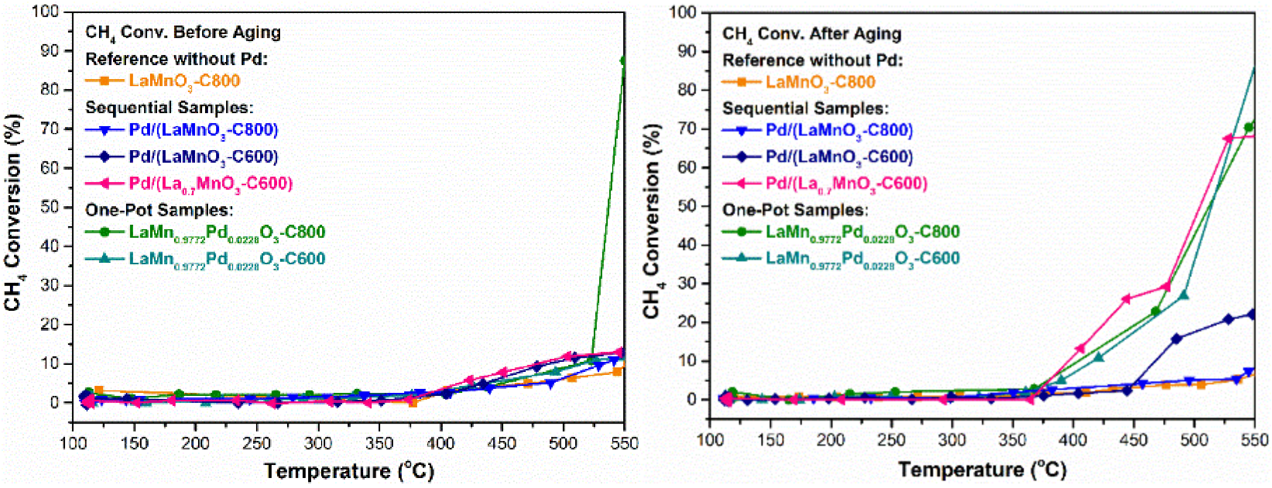

Fig.7.2.1. Methane conversion before/after aging in temperature range from 120 to 550 °C.

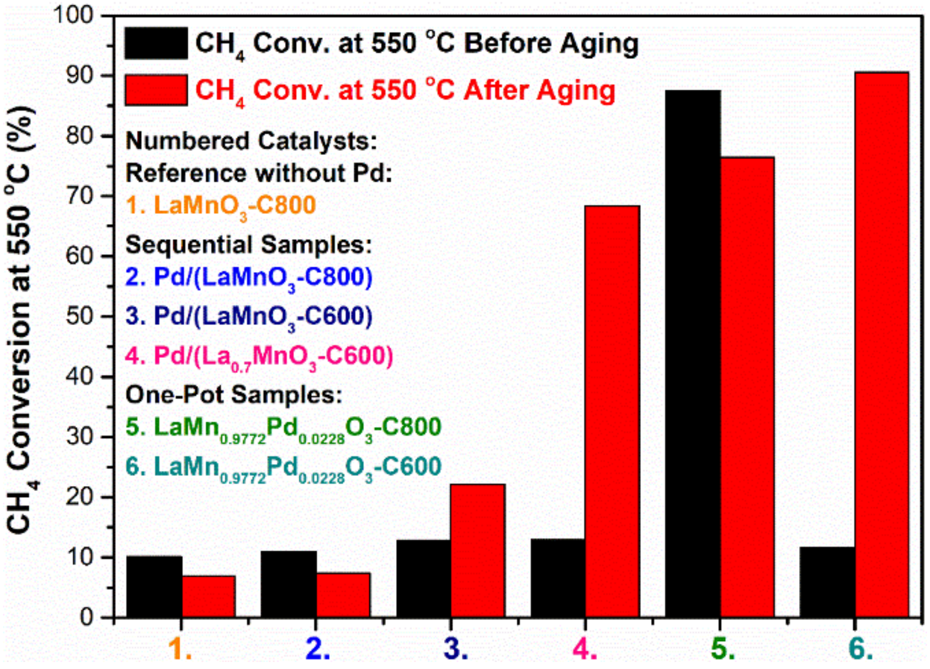

Fig.7.2.2. Methane conversion at 550 °C before/after aging.

Table 7.2.1. Summary of methane conversion of calcinated Pd incorporated $LaMnO_3$ series.

Catalyst	Calc.T ^{a} (°C)	SSA ^{b} (m^2/g)	Pd disp. (%) ^{c}	Pd ratio (%) ^{d}	550 °C Conv. % BA ^{e}	550 °C Conv. % AA ^{f}
Pd/$LaMnO_3$-C800	800, 400	7.4	2.7	0.07	8	5
$LaMn_{0.9772}Pd_{0.0228}O_3$-C800	800	6.4	14.1	2.01	88	77
Pd/$La_{0.7}MnO_3$-C600	600, 400	29.4	3.1	2.44	12	68
Pd/$LaMnO_3$-C600	600, 400	21.7	6.5	0.7	12	21
$LaMn_{0.9772}Pd_{0.0228}O_3$-C600	600	28.9	0.14	0.68	11	91

a. Calcination temperature of one-pot and sequential methods
b. Specific surface area
c. Pd dispersion from H_2-chemisorption
d. Surface Pd ratio of fresh catalysts from XPS analysis
e. Methane conversion before aging process
f. Methane conversion after aging process

Bare $LaMnO_3$-C800 perovskite served as benchmark exhibiting a very weak conversion in the whole range of temperature. Palladium addition has only a weak effect on the conversion of methane on impregnated samples and $LaMn_{0.98}Pd_{0.02}O_3$-C600 with conversion remaining below 15% at 550°C. The development of a significant conversion is only observed on $LaMn_{0.98}Pd_{0.02}O_3$-C800 reaching ~88% at 550°C. At first glance, this behavior can be *a priori* explained by the highest density of palladium at the surface corresponding to a high Pd dispersion. An obvious difference is observed after aging with a remarkable activation except on aged Pd/$LaMnO_3$-C800 which mimics the behavior of $LaMnO_3$-C800 and corresponds to a slight deactivation. The gain in conversion on aged $LaMn_{0.98}Pd_{0.02}O_3$-C600 can be explained by the segregation at the surface of palladium through exsolution process which has been found more accentuated on $LaMn_{0.98}Pd_{0.02}O_3$-C600. Nonetheless, HAADF-TEM did not reveal strong particle sintering with a high Pd dispersion remaining and a moderate formation of large Pd particles.

2.2. Carbon monoxide conversion

Carbon monoxide (CO) emissions, as the main pollution gas of automobile exhaust gas, from uncontrolled stoichiometric NGV engines were twice that of uncontrolled diesel vehicles [9]. Therefore, it is of great significance to investigate the CO removal efficiency of palladium incorporated perovskites as an index of catalyst evaluation. Fig. 7.2.3 shows that CO conversion starts at much lower temperature, below 150°C, and occurs more slowly on undoped Pd sample with complete conversion above 350°C instead of 250°C for the less active Pd-doped sample. Clearly, palladium recognized as a metal of choice for the CO/O_2 reaction improves the conversion especially on $LaMn_{0.98}Pd_{0.02}O_3$-C800 and Pd/$La_{0.7}MnO_3$-C800. The conversion is not drastically amplified after aging as reported for methane. In most cases a slight deactivation occurs except on $LaMn_{0.98}Pd_{0.02}O_3$-C600 for which the activity in conversion develops. Hence, this catalyst exhibits remarkable thermal stability which can be related to slower exsolution process which likely limit extensive Pd aggregation. Based on this, a greater Pd-interaction could growth and slower particle sintering. As discussed in the introduction, at low temperature changes in conversion could be related to the occurrence of CO-inhibiting effect that can occur on electron-rich Pd particles. The growth of large Pd particle would likely occur on supported catalysts even though Pd/$La_{0.7}MnO_3$ seems to be remarkably stable at high temperature. A stronger Pd-perovskite interaction could be expected in case of well-dispersed Pd particles which could be a favorable configuration for stabilizing electron deficient Pd particles.

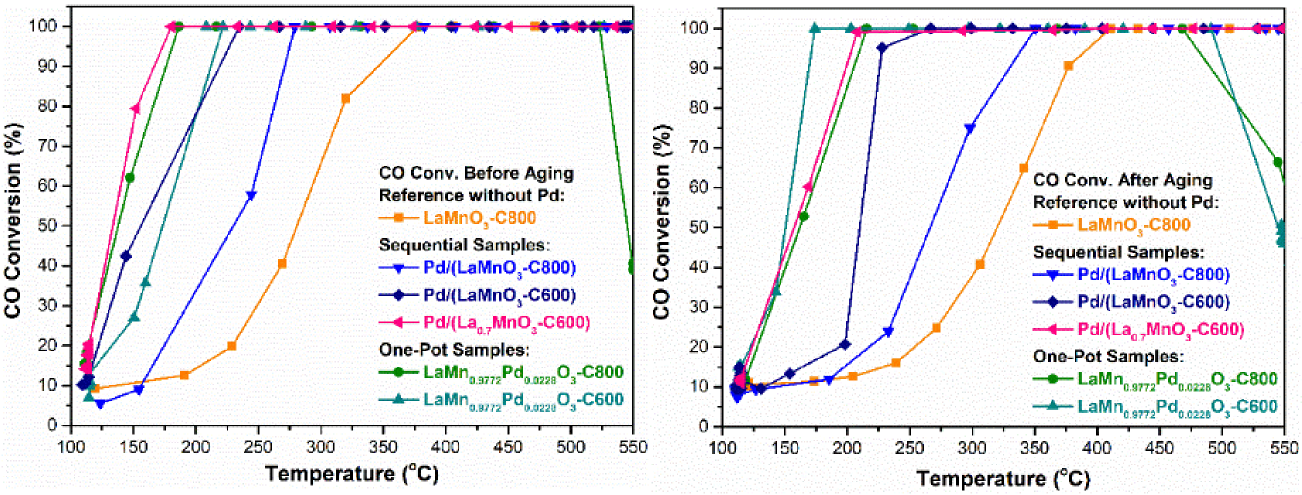

Fig.7.2.3. Carbon monoxide conversion before/after aging in temperature range from 120 to 550 °C.

At high temperature, interesting observations are related to a loss of CO conversion taking place above 525°C. This observation is only noticeable on pre-reduced $LaMn_{0.98}Pd_{0.02}O_3$-C800. In brief, such observation is usually assigned to an extra formation of CO. This coincides with the sharp increase in methane conversion, consequently, can be explained by the involvement of methane reforming reactions coupled to the Reverse Water Gas Shift reaction. It is remarkable that this tendency accentuates after aging starting at lower temperature on aged $LaMn_{0.98}Pd_{0.02}O_3$-C800 and appearing on aged $LaMn_{0.98}Pd_{0.02}O_3$-C600.

2.3. Nitric oxide conversion

Nitric oxide (NO) emissions, as main pollution exhaust gas, could be eliminated efficiently near-zero levels by three-way catalytic technology of stoichiometric natural gas engines [9]. The target for nitric oxide reduction is nitrogen, but the by-products NH_3 [10] and N_2O are generated during TWCs reduction. In addition, the aging process could influence the catalyst oxygen storage and mobility properties leading to NH_3 and N_2O generation [11].

Following the above-mentioned equations and formulas, the figures of NO conversion, N_2, N_2O yields (Fig.7.2.5 to Fig.7.2.7) presented the related results during heating from 120 to 550 °C and the conversion at 550 °C before/after aging showed the properties in the working temperature (Fig.7.2.4).

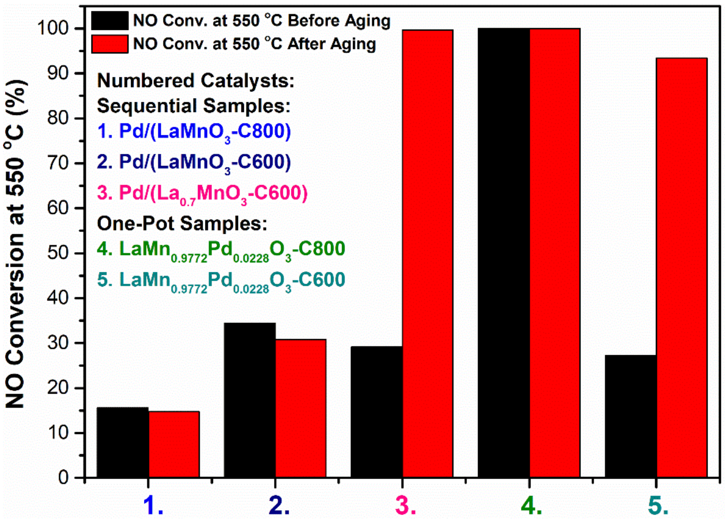

Fig.7.2.4. Nitric oxide conversion at 550 °C before/after aging.

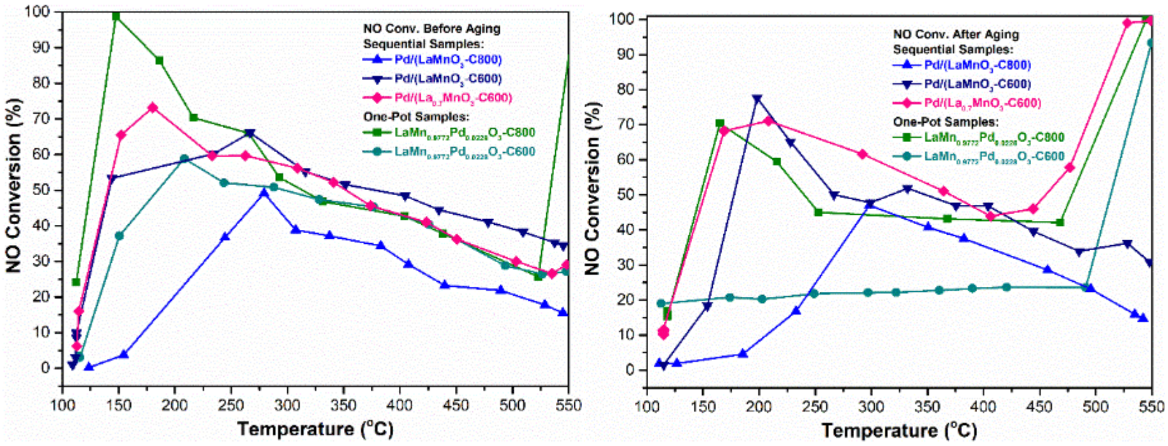

Fig.7.2.5. Nitric oxide conversion before/after aging in temperature range from 120 to 550 °C.

A broad range of temperature is observed for NO conversion with maximum conversion reached in the temperature range 150-200°C on pre-reduced catalyst (see Fig. 7.2.5). A complete conversion is obtained on $LaMn_{0.98}Mn_{0.02}O_3$-C800 which also coincides with a high CO conversion in this temperature domain. At low temperature the following reactivity sequence can be established:

$LaMn_{0.98}Mn_{0.02}O_3$-C800 > Pd/$La_{0.7}MnO_3$-C600 > $LaMn_{0.98}Mn_{0.02}O_3$-C600 > Pd/$LaMnO_3$-C600> Pd/$LaMnO_3$-C800

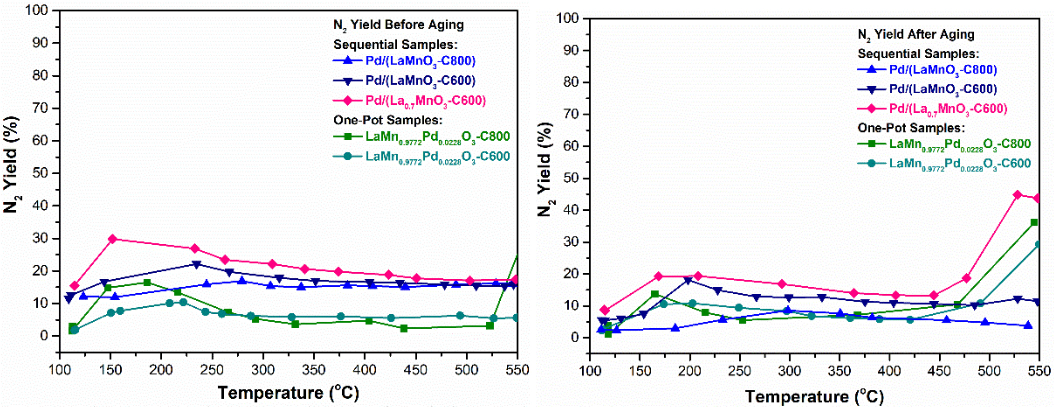

Fig.7.2.6. Nitrogen yield before/after aging in temperature range from 120 to 550 °C.

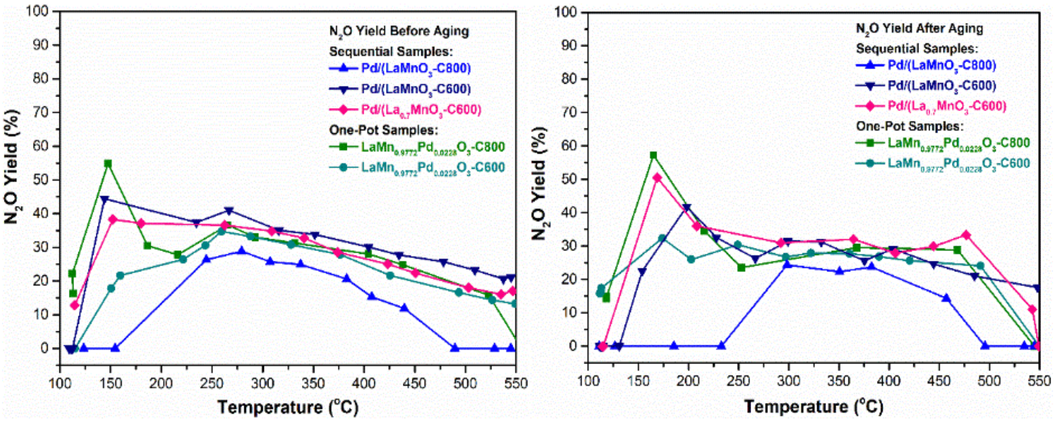

Fig.7.2.7. Nitrous oxide yield before/after aging in temperature range from 120 to 550 °C.

Based on these observations the competition between the CO/NO and the CO/O_2 reaction would be more in favor of the former one. On the other hand, a rise in temperature leads to a progressive and continuous decrease of NO conversion while CO conversion remains complete which emphasizes the weak selectivity of CO as reducing agent reacting preferentially with O_2 when the temperature increases. A peculiar behavior characterizes $LaMn_{0.98}Mn_{0.02}O_3$-C800 at high temperature with a sharp increase in NO conversion reaching 85% at 550°C. It is also remarkable that this sharp gain in conversion coincides with a sharp decrease in CO conversion because of the occurrence of reforming and WGS reactions.

After aging the behavior of $Pd/LaMnO_3$-C800 remains unchanged suggesting a stabilized surface. On the other hand, the low NO conversion range recorded on the other samples attenuates and slightly shifts to higher temperature. This deactivation seems to affect more strongly $LaMn_{0.98}Mn_{0.02}O_3$-C800 and $LaMn_{0.98}Mn_{0.02}O_3$-C600. In contrast, the reverse trend is observed at high temperature with a sharp gain in NO conversion and a quasi-complete conversion of NO on $Pd/La_{0.7}MnO_3$-C600, $LaMn_{0.98}Mn_{0.02}O_3$-C800 and $LaMn_{0.98}Mn_{0.02}O_3$-C600.

The examination of the product distribution provides more insights. As indicated in Figs 7.2.6-7.2.8, N_2, N_2O. At high temperature when NO dissociate more easily, the production of ammonia can occur thank to the occurrence of reforming reaction

$$2NO + 2CO = N_2 + CO_2 \qquad (1)$$
$$2NO + CO = N_2O + CO_2 \qquad (2)$$
$$2NO + 2H_2 = N_2 + 2H_2O \qquad (3)$$
$$2NO + H_2 = N_2O + H_2O \qquad (4)$$
$$2NO + 5H_2 = 2NH_3 + 2H_2O \qquad (5)$$

At low temperature, N_2O forms more extensively on pre-reduced samples compared to N_2 irrespective of the catalyst composition. $LaMn_{0.98}Mn_{0.02}O_3$-C800 and $LaMn_{0.98}Mn_{0.02}O_3$-C600 exhibit also an exceptional high production of NH_3. The production of N_2O decreases with a rise in temperature while nitrogen production remains unchanged. A sharp production of ammonia takes place on $LaMn_{0.98}Mn_{0.02}O_3$-C800 at 550°C in agreement with the aforementioned discussion. After aging the same trends are perceptible. However, an improved production of nitrogen is noticeable at high temperature particularly on $LaMn_{0.98}Mn_{0.02}O_3$-C800, $Pd/La_{0.7}MnO_3$-C600 $LaMn_{0.98}Mn_{0.02}O_3$-C800 and $Pd/La_{0.7}MnO_3$-C600. Let us note that the production of ammonia intensifies on these three catalysts.

Generally, on three-way catalysts containing Rh, the selectivity and product distributions from NO reduction are governed by the strength of NO adsorption on the metal. In our case, it seems obvious that additional parameters occur as high production of N_2O should correspond to low NO conversion and reversely. In practice, we observed the opposite trend at low temperature which emphasizes the existence of competitive reactions and inhibiting effects. At high temperature, NO conversion is complete corresponding to low adsorbate coverages with higher fraction of vacant sites available for NO dissociation and H_2 dissociative adsorption. Hence, resulting chemisorbed N atoms would recombine must faster to produce N_2 as well as their probability to react with chemisorbed H atoms to produce NH_3 would increase. Interestingly, the production of nitrogen is enhanced on aged Pd/$La_{0.7}MnO_3$-C600 $LaMn_{0.98}Mn_{0.02}O_3$-C800 and Pd/$La_{0.7}MnO_3$-C600 above 450°C.

3. Catalytic measurements for palladium incorporated $La_xSr_{0.15}MnO_{3+\delta}$ series

In this chapter the main changes are related to Sr-substitution and the reduction of palladium content from 1 wt.% to 0.5 wt.%. The parameters examined in the previous chapter have been also conserved, *e.g.* A-stoichiometry, method for Pd incorporation and calcination temperature in order to optimized a catalyst composition. As Sr acts as basic materials, it can alter the electronic properties of metallic Pd particles increasing their electron density. Strictly speaking, it is not easy to predict the consequence in terms of catalytic properties as this effect can be detrimental in case of strengthening of the CO bond adsorption or beneficial at low temperature as NO could dissociate more readily. This effect likely depends on the close proximity of Sr and Pd and would depend on the method used for Pd addition. In principle, a closer and stronger interaction is expected on samples prepared according to the one-pot method.

3.1. Methane conversion

As the main emission reduction target in this investigation, methane conversion is the most direct catalyst evaluation parameter. Fig.7.3.1 showed the global methane conversion at 550 ºC of working condition, and the catalysts promotion by aging process occurred again on 600 ºC.

Figs. 7.3.1 and 7.3.2 show the conversion profiles vs. temperature et compared methane conversion at 550°C. As previously shown, methane activation needs high temperature and the presence of water near stoichiometric conditions. Interestingly, a gain in conversion was observed on undoped Sr-samples after aging. On the series prepared by sequential method improved performances in methane conversion are obtained on 1 wt.%Pd/$La_{0.55}Sr_{0.15}MnO_3$-C800 and 0.5 wt.% Pd/$La_{0.85}Sr_{0.15}MnO_3$-C800. Calcination at high temperature leads generally to higher crystallinity with lower amounts of impurities. In contrast, a loss of specific surface area is generally observed except in the particular case of A-deficiency. Based on this, two antagonistic behaviors can occur related to improved bulk oxygen mobility and OSC properties on well-crystallized samples but lower Pd dispersion are expected when the specific surface area reduces. Obviously bulk oxygen mobility could be the most prominent parameter at high temperature. After aging, 1 wt.% Pd/$La_{0.55}Sr_{0.15}MnO_3$-C800 and 0.5 wt.% Pd/$La_{0.85}Sr_{0.15}MnO_3$-C800 lose their performance while a gain in activity in methane conversion is observed on 0.5 wt.%Pd/$La_{0.55}Sr_{0.15}MnO_3$-C600 and 1 wt.%Pd/$La_{0.85}Sr_{0.15}MnO_3$-C600.

Let us now examine the catalysts prepared by the one-pot method. Similarly, the samples calcined at 800°C initially outperform the series calcined at 600°C. However, while the activity develops on aged $La_{0.55}Sr_{0.15}Mn_{0.98}Pd_{0.02}O_3$-C600, the reverse tendency is observed for the other aged samples even though a moderate loss of conversion is observed on $La_{0.85}Sr_{0.15}Mn_{0.98}Pd_{0.02}O_3$-C800. This global comparison reveals that the structural properties, driven by the calcination temperature of the perovskite and the aging temperature, would be the most important criteria in compared to A-stoichiometry, Pd content and dispersion. Hence, improved oxygen mobility would be dependent on structural requirement fulfilled when the catalyst is subjected to high temperature. The catalytic performance seemed having no coherence with surface palladium ratio and dispersion from XPS analysis and hydrogen chemisorption (Table 7.3.1) indicating the interaction of surface metals was of significance, which corresponded to the kinetic study of combination of palladium species and perovskite in former chapter.

Table 7.3.1. Summary of CH_4 conversion of calcinated Pd incorporated $La_xSr_{0.15}MnO_3$ series.

Catalyst	Calc.T [a] (°C)	SSA [b] (m^2/g)	Pd disp. (%) [c]	Pd ratio (%) [d]	550 °C Conv. BA [e]	550 °C Conv. AA [f]
0.5%Pd/($La_{0.55}Sr_{0.15}MnO_3$-C600)	600, 400	27.9	2.3	4.92	7.5	26.9
$La_{0.55}Sr_{0.15}Mn_{0.9909}Pd_{0.0091}O_3$-C800	800	30.3	1.4	0.16	35	32.2
$La_{0.55}Sr_{0.15}Mn_{0.9818}Pd_{0.0182}O_3$-C600	600	32.6	1.8	0.23	6.5	36.8
1%Pd/($La_{0.55}Sr_{0.15}MnO_3$-C800)	800, 400	45.6	2.4	4.0	92	84.6
$La_{0.85}Sr_{0.15}Mn_{0.9890}Pd_{0.0110}O_3$-C600	600	26.4	2.8	0.13	1.4	5.3
0.5%Pd/($La_{0.85}Sr_{0.15}MnO_3$-C800)	800, 400	11.8	1.9	0.53	72.5	67.2
1%Pd/($La_{0.85}Sr_{0.15}MnO_3$-C600)	600, 400	36.9	4.2	4.26	6.8	66.2
$La_{0.85}Sr_{0.15}Mn_{0.9779}Pd_{0.0221}O_3$-C800	800	7	0.2	0.53	70.4	56.3

a. Calcination temperature of one-pot and sequential methods
b. Specific surface area
c. Pd dispersion from H_2-chemisorption
d. Surface Pd ratio of fresh catalysts from XPS analysis
e. Methane conversion before aging process
f. Methane conversion after aging process

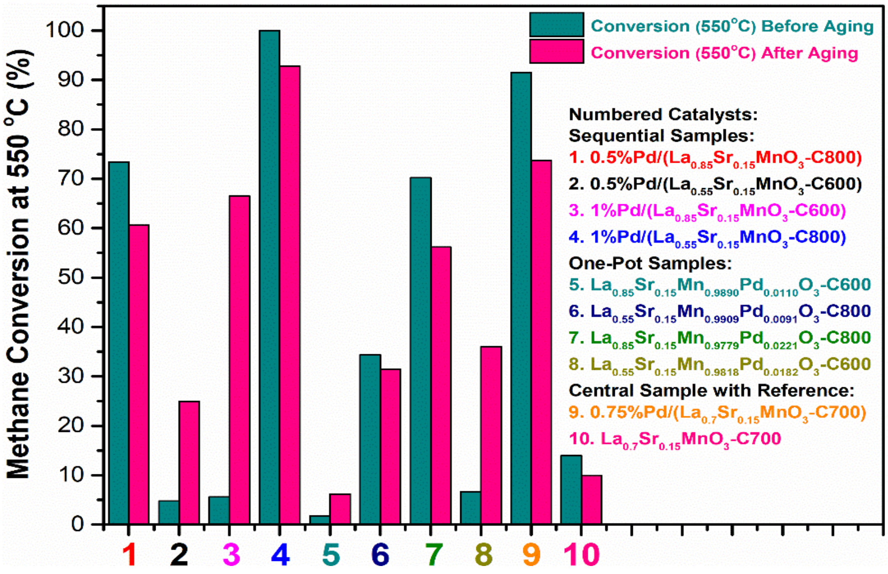

Fig.7.3.1. Methane conversion at 550 °C before/after aging.

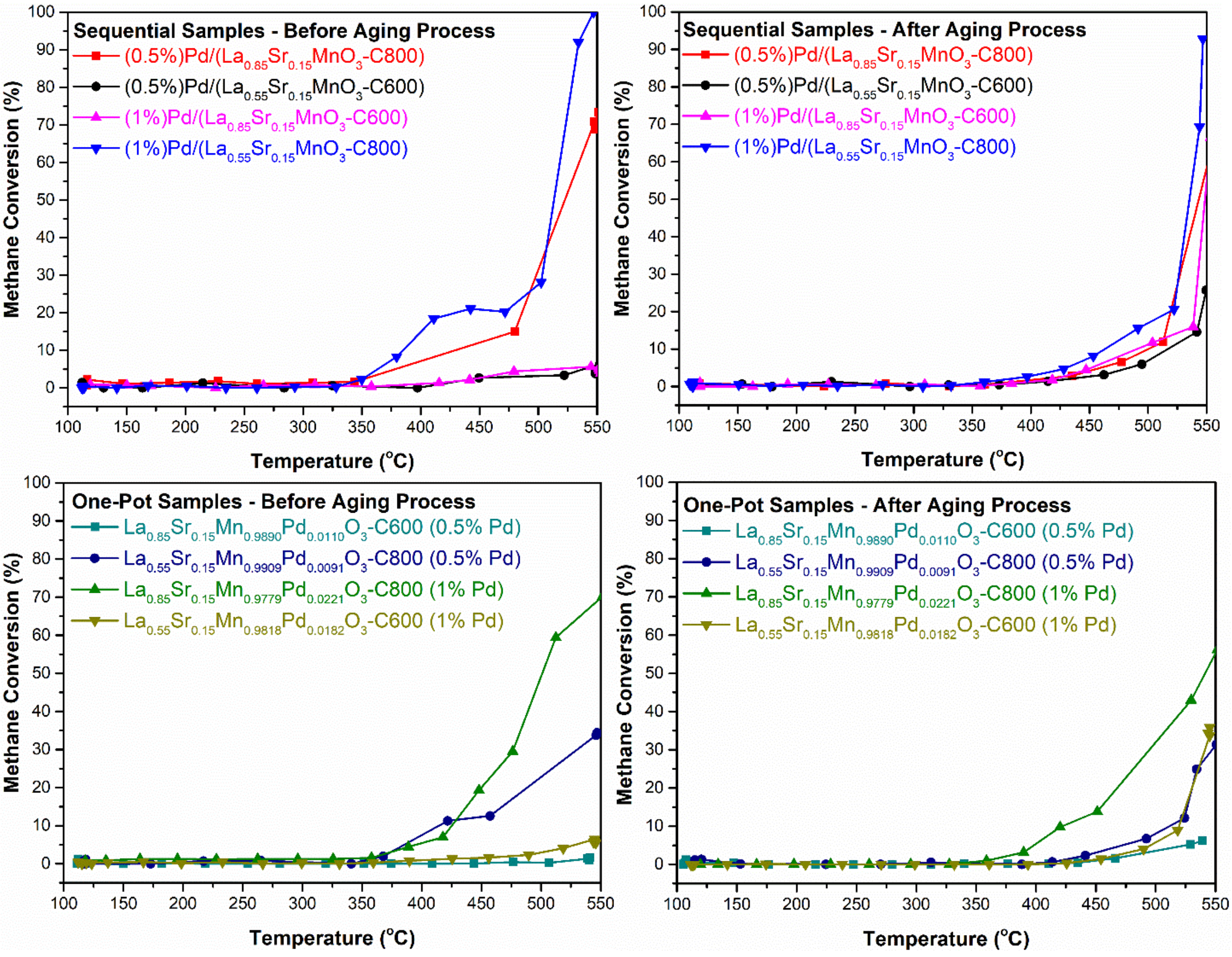

Fig.7.3.2. Methane conversion before/after aging during heating from 120 to 550 °C.

3.2. Carbon monoxide conversion

In principle at low temperature, palladium originates a high activity in the CO/O_2 reaction and the support should play a negligible role reactive oxygen species being supplied from gaseous O_2 adsorption. Once pre-reduced, impregnated samples exhibit superior performance compared to one pot samples likely due to the fact that a large fraction of palladium is imbedded in the perovskite structure according to this latter method.

The better activity on impregnated samples is also related to the higher density of Pd sites on the highly loaded samples. Aging leads globally to a loss of activity on impregnated sample presumably due to Pd particle sintering. In contrast exsolution process leads to surface Pd enrichment. This process already demonstrated can originate improved performances with highest conversion measured on $La_{0.55}Sr_{0.15}Mn_{0.98}Pd_{0.01}O_3$-C800. Typically, on this sample, A-deficiency and lower Pd content should minimize the loss of specific surface area and stabilize a good Pd dispersion.

Sr partial substitution into perovskite could bring more porous material and oxygen vacancies, and J. Yang et al. reported that O^- as a primary oxygen species as well as its origin over perovskite oxides for CO oxidation, and the oxygen vacancy offered a feasible defect strategy from Sr doping in perovskite for high-performance heterogeneous-structured catalysts [16].

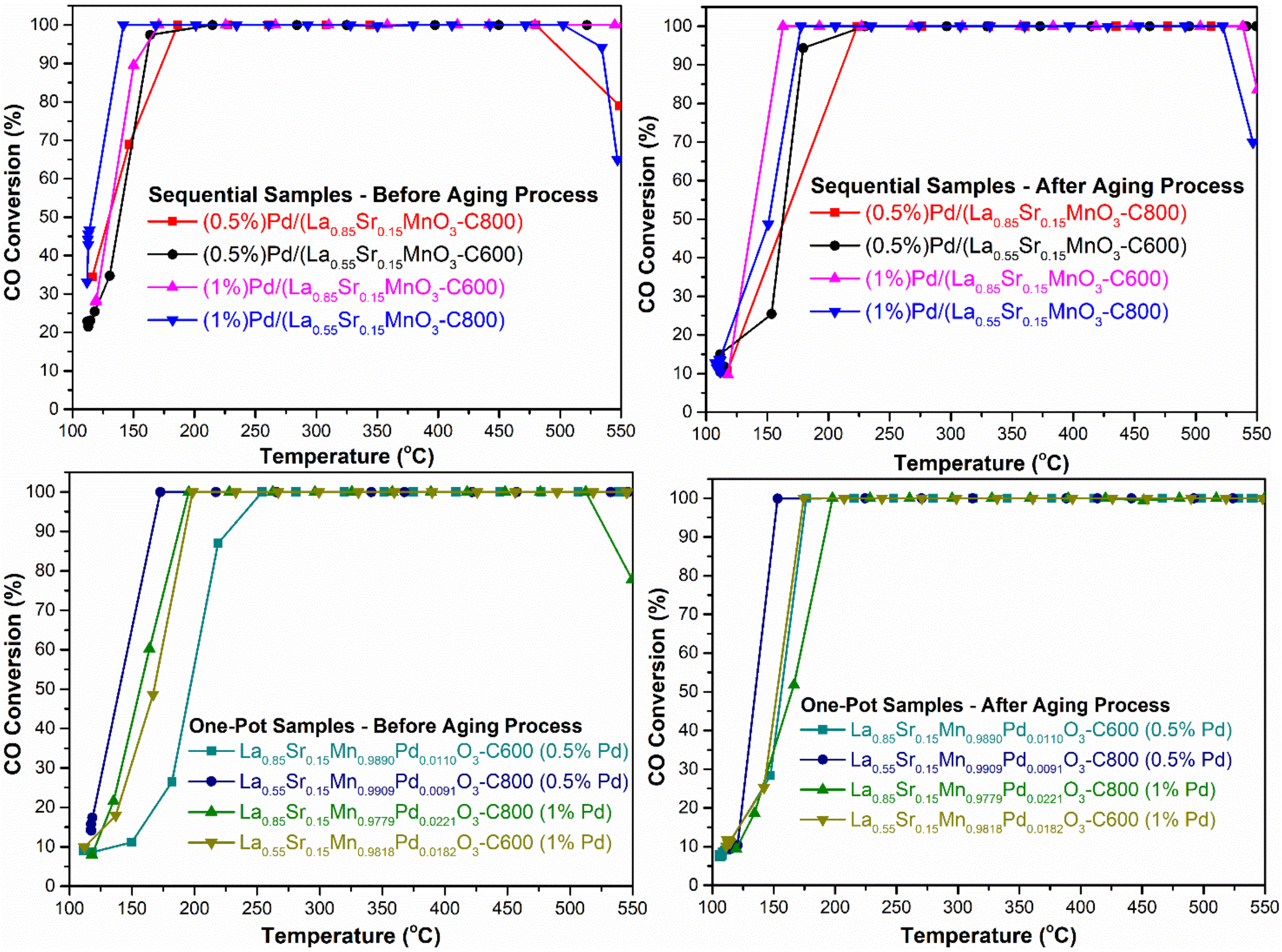

Fig.7.3.3. Carbon monoxide conversion before/after aging during heating from 120 to 550 °C.

3.3. Nitric oxide conversion

Sr doped perovskites were widely used for NO removal [17] and NO conversion because Sr substitution into $LaMnO_3$ type perovskite changed the related structure, transition metal oxidation state and oxygen vacancies generation [18].

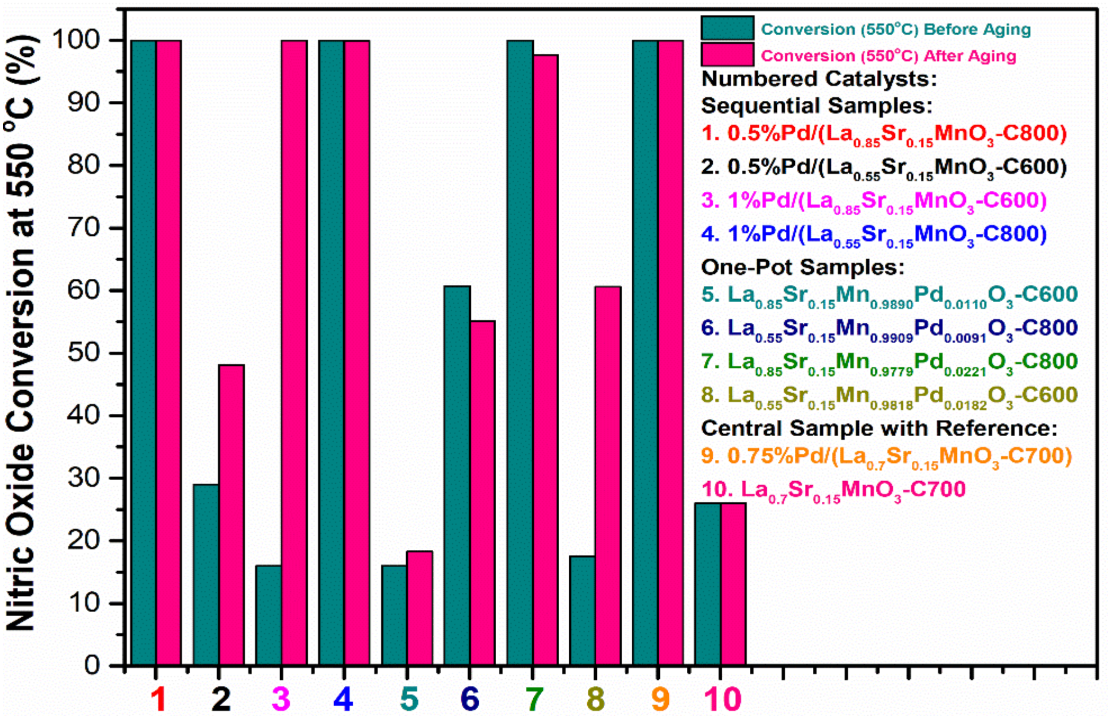

Fig.7.3.4. Nitric oxide conversion at 550 °C before/after aging.

The NO conversion profile vs. temperature (Fig. 7.3.5) are rather comparable to those previously discussed on undoped Sr-samples. On pre-reduced catalysts a low temperature conversion is observed with a maximum in the range 150-200°C.

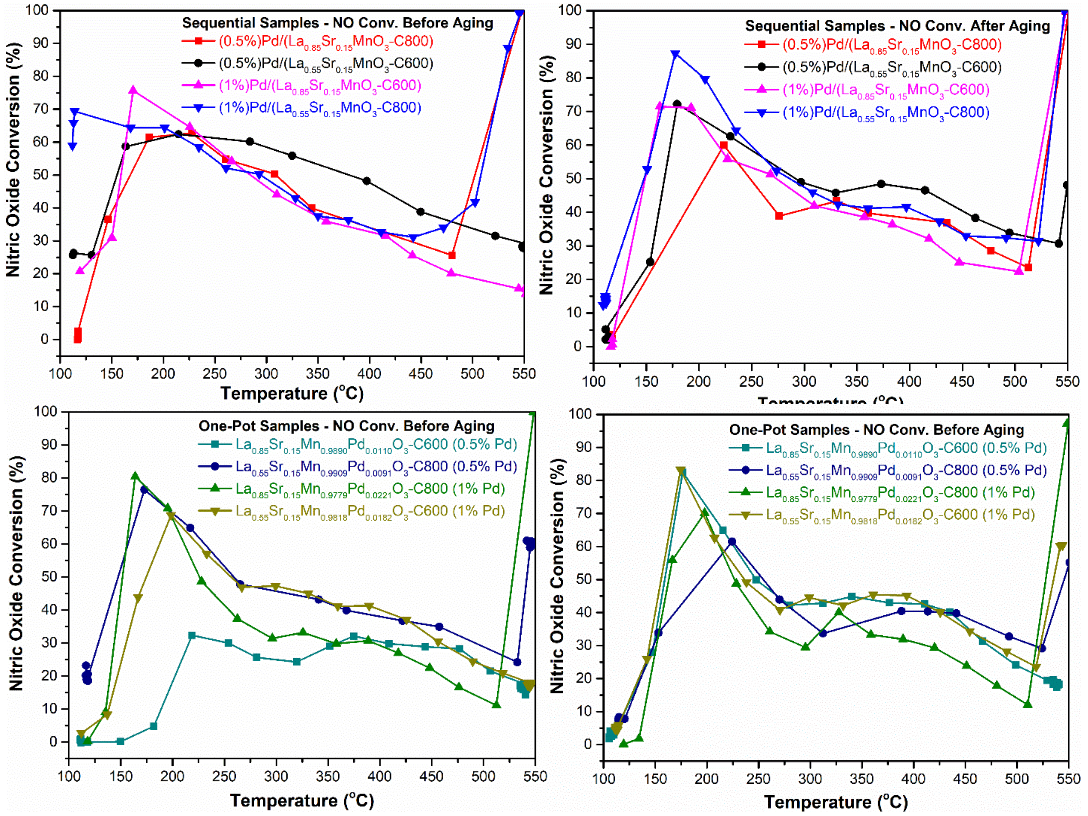

Fig.7.3.5. Nitric oxide conversion during heating from 120 to 550 ºC.

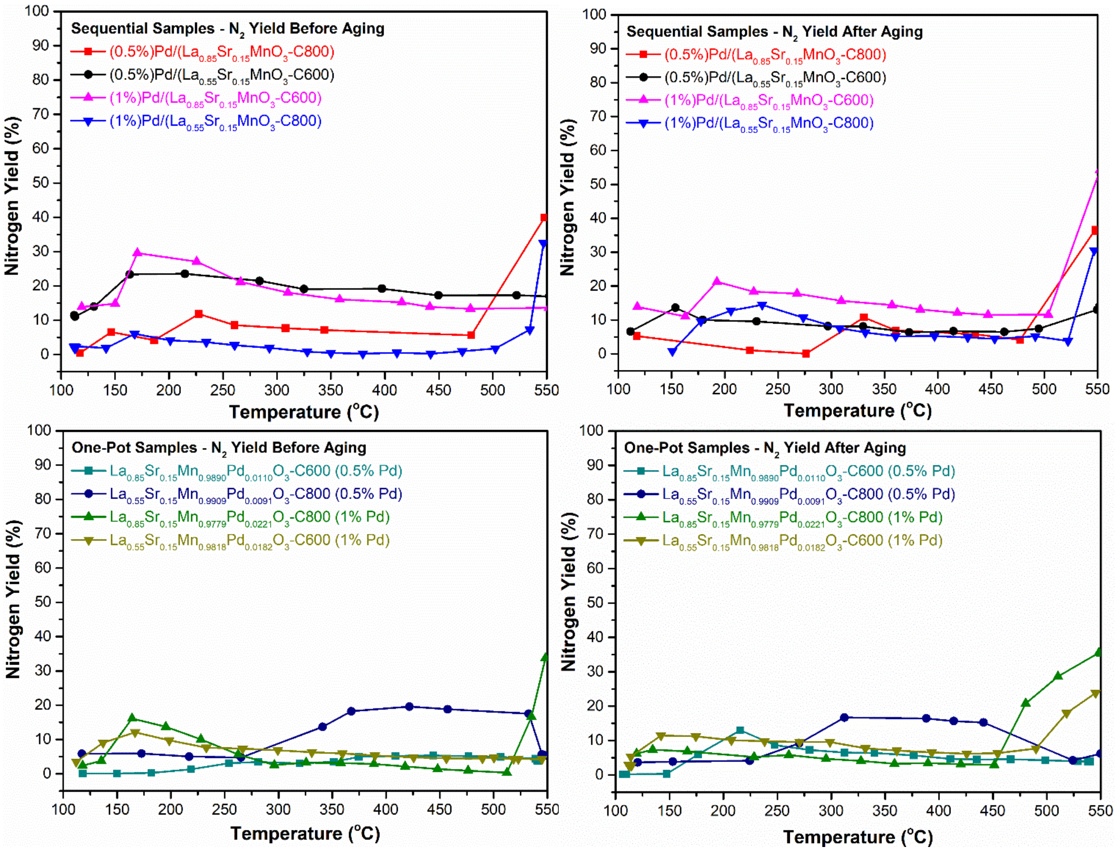

Fig.7.3.6. Nitrogen yield during heating from 120 to 550 ºC.

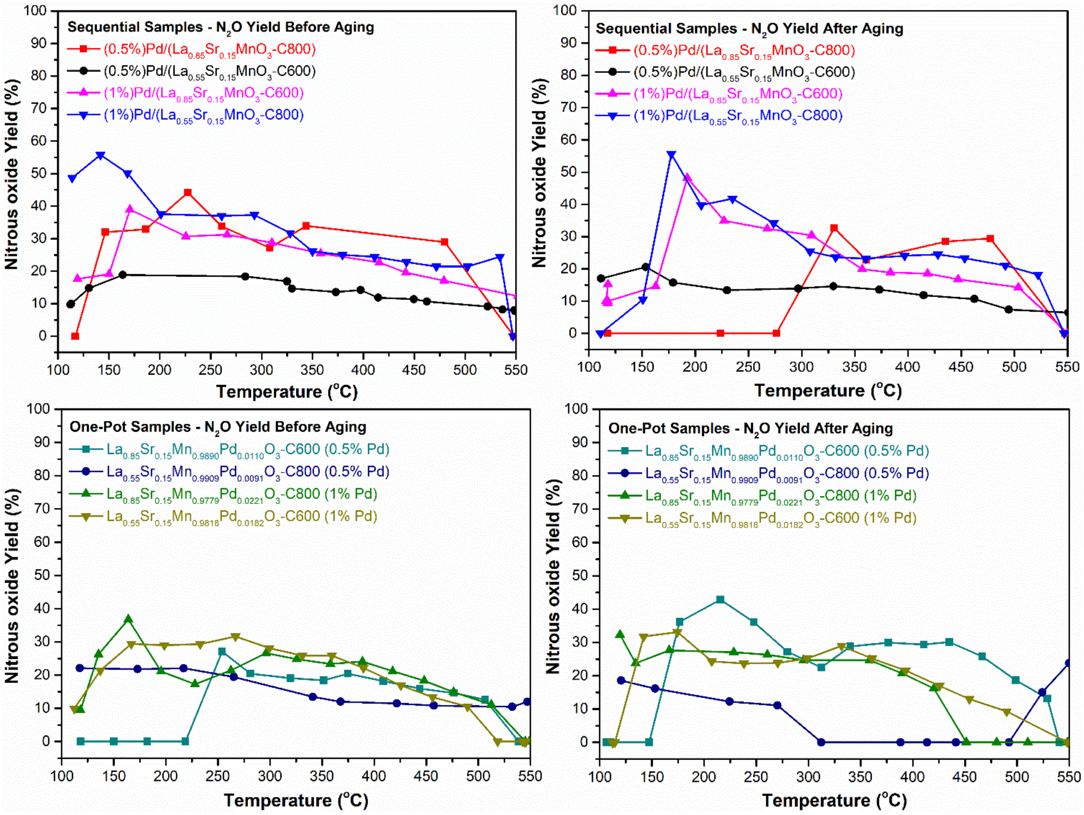

Fig.7.3.7. Nitrous oxide yield during heating from 120 to 550 °C.

Subsequent increase in temperature is accompanied with a gradual decrease in NO conversion. Finally, a sharp increase is often observed above 500°C. Such tendency reproduces irrespectively on impregnated or one pot samples before and after aging. Hence, Sr-doping does not seem to lead to remarkable changes. On impregnated samples, slightly improved conversions are discernible for highly Pd loaded samples both on pre-reduced and aged samples. Higher density of Pd sites would be more favorable.

Such tendency can be in some extent verified on one-pot samples as the highest conversion at low temperature are recorded on the two catalysts calcined at 800°C. Based on this, the Pd loading will not be the determining parameter in that case as the residual Pd concentration at the surface will be governed by exsolution process, *e.g.* Pd extraction from the lattice to the surface. As explained thermal aging will favor such process which can explain improved activity recorded on the two samples originally calcined at 600°C.

Yields for N_2, N_2O vs temperature are reported in Figs 7.3.6-7.3.7. Globally, changes observed are comparable to previous observation. At low temperature, there is no clear correlation between the evolutions of the yields in N_2O and the conversion that could explain that they would be mostly governed by the strength of NO adsorption. In fact, this behavior seems to be most representative of the evolution observed at high temperature when NO desorbs and/or dissociates.

Nitrogen yields are globally lower on the one-pot samples and aging did not induce discernible changes except on $La_{0.85}Sr_{0.15}Mn_{0.98}Pd_{0.02}O_3$-C800. The highest nitrogen yield is obtained on 1 wt.% Pd/ $La_{0.85}Sr_{0.15}MnO_3$-C600 stabilizing in the range 0.25-0.4 and increasing above 525°C to reach 0.5.

N_2O production is still significant and Sr seems to have no effect. The mode of Pd incorporation seems to also have a weak effect. In most often cases, N_2O declines at high temperature as aforementioned.

4. Conclusion

This chapter reports the catalytic properties of three-way Pd-based catalysts in more representative compositions of exhaust NGVs engines. Palladium interacts with perovskite substrate. Different parameters affect the perovskite composition, *e.g.* calcination temperature, A-deficiency, A-stoichiometry, Sr-substitution. Regarding palladium two methods have been implemented for their incorporation according to a classical wet impregnation leading to extra framework PdO aggregates or during the sol-gel synthesis with preferential isolated cationic Pd species stabilized inside the perovskite lattice. Palladium content has been investigated by reducing the composition by half. Catalysts were pre-reduced at 250°C. These temperature conditions did not affect the structural properties of the rhombohedral structure but can induce the reduction of Mn^{4+} to Mn^{3+}. Regarding the reducibility of oxidic palladium species, extra framework PdO species were found more reducible than cationic Pd^{n+} inside the perovskite lattice.

Multiple reactions take place in different temperature regimes near stoichiometric conditions. At low temperature, CO conversion prevails. It was found and suggested that Pd could be involved in the CO/O_2, CO/NO and CO/H_2O reaction. The involvement of the latter reaction has a detrimental impact as the production of hydrogen can originate the production of ammonia in large extent. Methane conversion is obviously strongly delayed taking place above 450°C. The presence of steam and large amount of CO_2 eases the methane conversion thanks to the involvement of reforming reactions. However, this reaction is also accompanied with a significant production of ammonia.

The results for methane conversion on undoped Sr-catalysts can be resumed in the following Table 7.2.1. and can be compared to surface properties in terms of SSA, surface Pd concentration et metallic Pd dispersion. The highest conversion recorded on pre-reduced $LaMn_{0.98}Pd_{0.02}O_3$-C800 cannot be explained by the specific surface area but more probably by the high surface concentration of palladium.

Aging leads to Pd exsolution process improving the conversion on aged $LaMn_{0.9772}Pd_{0.0228}O_3$-C600. The rate enhancement in methane conversion on aged Pd/$La_{0.7}MnO_3$-C600 also provides additional insights as this catalyst is characterized by a high surface and bulk oxygen mobility assisted by the presence of palladium. Hence, both of observation suggests that cooperative effect between Pd and surface reactive oxygen from the perovskite would be the driving force in determining the catalytic performance.

Strontium substitution leads to rate enhancement on pre-reduced samples. In contrast aging has a detrimental impact on impregnated sample. One-pot sample leads to marginal changes after aging which suggests a weak impact of strontium.

Table 7.2.1. Summary of methane conversion of calcinated Pd incorporated $LaMnO_3$ series.

Catalyst	Calc.T [a] (°C)	SSA [b] (m^2/g)	Pd disp.[c] (%)	Pd ratio[d] (%)	Conv. %[e] reduced	Conv. %[f] aged
$Pd/LaMnO_3$-C800	400	7.4	2.7	0.07 [f]	8	5
$LaMn_{0.9772}Pd_{0.0228}O_3$-C800	800	6.4	14.1	2.01[f]	88	77
$Pd/La_{0.7}MnO_3$-C600	600	29.4	3.1	2.44 [f]	12	68
$Pd/LaMnO_3$-C600	400	21.7	6.5	0.7 [f]	12	21
$LaMn_{0.9772}Pd_{0.0228}O_3$-C600	600	28.9	0.14	0.68 [f]	11	91

a. Calcination temperature of Pd-doped catalysts
b. Specific surface area
c. Pd dispersion from H_2-chemisorption
d. Surface Pd ratio of fresh catalysts from XPS analysis
e. Recorded at 550°C for fresh samples
f. On aged catalysts

As explained CO conversion is likely involved in various competitive reactions. There is no strong argument in favor of a strong CO inhibiting effect on CO conversion after Sr-substitution especially on impregnated samples. Indeed, it is expected that Sr is mainly stabilized in the perovskite structure. At high Sr-substitution surface, Sr enrichment cannot be strictly ruled out. Nonetheless, no perceptible loss of CO conversion assigned to a strengthening of CO adsorption bond has been observed neither on impregnated samples nor on samples prepared according to the one-pot method. As a matter of fact, the presence of water could contribute to clean the surface avoiding this detrimental effect. As explained, structural and surface changes during aging mainly occur on one-pot sample as Pd exsolution. This is particular true for $La_{0.85}Sr_{0.15}Mn_{0.99}Pd_{0.01}O_3$-C600. In that case by reducing half the palladium composition inside the perovskite lattice, exsolution process could be slower and then minimizing possible aggregation process when Pd segregates at the surface.

Finally, the examination and the conversion curves of NO and product distribution clearly show high performance in NO reaction notably at low temperature thank to CO and indirectly to H_2 produced from the WGS reaction. However, a volcano-type curves is usually observed emphasizing the weak selectivity of these two reducing agents which will react preferentially with oxygen with a rise in temperature. At high temperature the NO conversion is restored lowering the production of N_2O but in this temperature domain a significant production of ammonia is obtained coexisting with nitrogen.

It seems not easy to distinguish between impregnated and one pot sample which variety is the most sensitive to deactivation and the real impact of strontium. On undoped samples prepared according to the one pot method aging induce a loss of performance in NO conversion in the low temperature range while the activity is promoted at high temperature. Such tendency does not appear distinctly on aged samples. It seems that strontium would attenuate the effect of deactivation.

References

1. Summers, J. C., J. J. White, and W. B. Williamson. "Durability of Palladium Only Three-Way Automotive Emisson Control Catalysts." SAE Transactions 98 (1989): 360–75. http://www.jstor.org/stable/44472036.
2. M. Takahashi, S. Kikuchi, K. Iwachido, M. Ikeda, H. Goto, Development of New Three-way Catalyst Technologies to Improve Purification Performance for Exhaust Emission after Severe Thermal Aging, Trans. Soc. Automot. Eng. Jpn. 44 (2013) 15–20. https://doi.org/10.11351/jsaeronbun.45.197.
3. Dal Young Yoon, Young Jin Kim, Ji Hyun Lim, Byong K. Cho, Suk Bong Hong, In-Sik Nam, Jin Woo Choung, Thermal stability of Pd-containing $LaAlO_3$ perovskite as a modern TWC, Journal of Catalysis, Volume 330, 2015, Pages 71-83, ISSN 0021-9517, https://doi.org/10.1016/j.jcat.2015.07.013.
4. Yuan Jing, Gang Wang, Kah Wei Ting, Zen Maeno, Kazumasa Oshima, Shigeo Satokawa, Shuhei Nagaoka, Ken-ichi Shimizu, Takashi Toyao, Roles of the basic metals La, Ba, and Sr as additives in Al_2O_3-supported Pd-based three-way catalysts, Journal of Catalysis, Volume 400, 2021, Pages 387-396, ISSN 0021-9517, https://doi.org/10.1016/j.jcat.2021.06.016.
5. H He, H.X Dai, C.T Au, An investigation on the utilization of perovskite-type oxides $La_{1-x}Sr_xMO_3$ (M = $Co_{0.77}Bi_{0.20}Pd_{0.03}$) as three-way catalysts, Applied Catalysis B: Environmental, Volume 33, Issue 1, 2001, Pages 65-80, ISSN 0926-3373, https://doi.org/10.1016/S0926-3373(01)00159-X.
6. A.E Giannakas, A.K Ladavos, P.J Pomonis, Preparation, characterization and investigation of catalytic activity for NO+CO reaction of $LaMnO_3$ and $LaFeO_3$ perovskites prepared via microemulsion method, Applied Catalysis B: Environmental, Volume 49, Issue 3, 2004, Pages 147-158, ISSN 0926-3373, https://doi.org/10.1016/j.apcatb.2003.12.002.
7. Asghar Mohammadi, Ali Farzi, Christoph Thurner, Bernhard Klötzer, Sabine Schwarz, Johannes Bernardi, Aligholi Niaei, Simon Penner, Tailoring the metal-perovskite interface for promotional steering of the catalytic NO reduction by CO in the presence of H_2O on Pd-lanthanum iron manganite composites, Applied Catalysis B: Environmental, Volume 307, 2022, 121160, ISSN 0926-3373, https://doi.org/10.1016/j.apcatb.2022.121160.
8. Dong Jiang, Konstantin Khivantsev, and Yong Wang, Low-Temperature Methane Oxidation for Efficient Emission Control in Natural Gas Vehicles: Pd and Beyond., ACS Catalysis 2020 10 (23), 14304-14314, http://doi.org/10.1021/acscatal.0c03338.
9. Arvind Thiruvengadam, Marc Besch, Vishnu Padmanaban, Saroj Pradhan, Berk Demirgok, Natural gas vehicles in heavy-duty transportation-A review, Energy Policy, Volume 122, 2018, Pages 253-259, ISSN 0301-4215, https://doi.org/10.1016/j.enpol.2018.07.052.
10. Kang Sun, Lei Tao, David J. Miller, Da Pan, Levi M. Golston, Mark A. Zondlo, Robert J. Griffin, H. W. Wallace, Yu Jun Leong, M. Melissa Yang, Yan Zhang, Denise L. Mauzerall, and Tong Zhu., Vehicle Emissions as an Important Urban Ammonia Source in the United States and China., Environmental Science & Technology 2017 51 (4), 2472-2481. http://doi.org/10.1021/acs.est.6b02805.
11. Pauliina Nevalainen, Niko M. Kinnunen, Anna Kirveslahti, Kauko Kallinen, Teuvo Maunula, Matthew Keenan, Mika Suvanto, Formation of NH_3 and N_2O in a modern natural gas three-way catalyst designed for heavy-duty vehicles: the effects of simulated exhaust gas composition and ageing, Applied Catalysis A: General, Volume 552, 2018, Pages 30-37, ISSN 0926-860X, https://doi.org/10.1016/j.apcata.2017.12.017.

12. Zhonghui Cui, Song Song, Huibin Liu, Yingtian Zhang, Fei Gao, Tong Ding, Ye Tian, Xiaobin Fan, Xingang Li, Synergistic effect of Cu^+ single atoms and Cu nanoparticles supported on alumina boosting water-gas shift reaction, Applied Catalysis B: Environmental, Volume 313, 2022, 121468, ISSN 0926-3373, https://doi.org/10.1016/j.apcatb.2022.121468.
13. Ching-Shiun Chen, Jarrn-Horng Lin, Tzu-Wen Lai, Bao-Hui Li, Active sites on Cu/SiO_2 prepared using the atomic layer epitaxy technique for a low-temperature water–gas shift reaction, Journal of Catalysis, Volume 263, Issue 1, 2009, Pages 155-166, ISSN 0021-9517, https://doi.org/10.1016/j.jcat.2009.02.004.
14. Gold, Copper, and Platinum Nanoparticles Dispersed on $CeO_x/TiO_2(110)$ Surfaces: High Water-Gas Shift Activity and the Nature of the Mixed-Metal Oxide at the Nanometer Level, Joon B. Park, Jesus Graciani, Jaime Evans, Dario Stacchiola, Sanjaya D. Senanayake, Laura Barrio, Ping Liu, Javier Fdez. Sanz, Jan Hrbek, and José A. Rodriguez, Journal of the American Chemical Society 2010 132 (1), 356-363 http://doi-org/10.1021/ja9087677.
15. Sara Aranifard, Salai Cheettu Ammal, Andreas Heyden, On the importance of metal–oxide interface sites for the water–gas shift reaction over Pt/CeO_2 catalysts, Journal of Catalysis, Volume 309, 2014, Pages 314-324, ISSN 0021-9517, https://doi.org/10.1016/j.jcat.2013.10.012.
16. Ji Yang, Siyu Hu, Yarong Fang, Son Hoang, Li Li, Weiwei Yang, Zhenfeng Liang, Jian Wu, Jinpeng Hu, Wen Xiao, Chuanqi Pan, Zhu Luo, Jun Ding, Lizhi Zhang, and Yanbing Guo, Oxygen Vacancy Promoted O_2 Activation over Perovskite Oxide for Low-Temperature CO Oxidation, ACS Catalysis 2019 9 (11), 9751-9763 http://doi.org/10.1021/acscatal.9b02408.
17. Junjiang Zhu, Arne Thomas, Perovskite-type mixed oxides as catalytic material for NO removal, Applied Catalysis B: Environmental, Volume 92, Issues 3–4, 2009, Pages 225-233, ISSN 0926-3373, https://doi.org/10.1016/j.apcatb.2009.08.008.
18. Jon A. Onrubia-Calvo, B. Pereda-Ayo, U. De-La-Torre, Juan R. González-Velasco, Key factors in Sr-doped $LaBO_3$ ($B = Co$ or Mn) perovskites for NO oxidation in efficient diesel exhaust purification, Applied Catalysis B: Environmental, Volume 213, 2017, Pages 198-210, ISSN 0926-3373, https://doi.org/10.1016/j.apcatb.2017.04.068.

Annexes

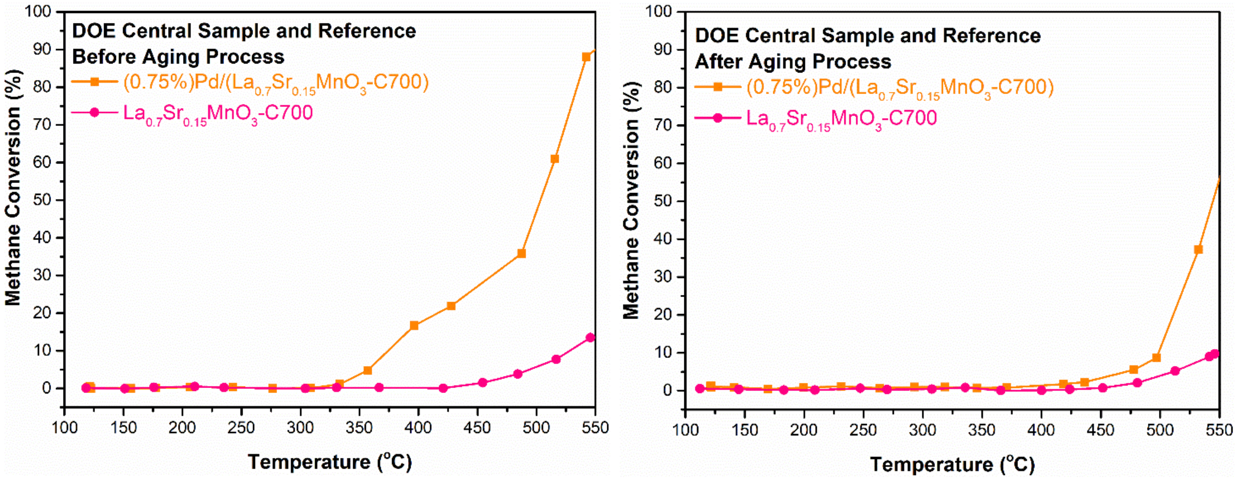

Fig.S7.3.2. Methane conversion during heating from 120 to 550 °C before/after aging.

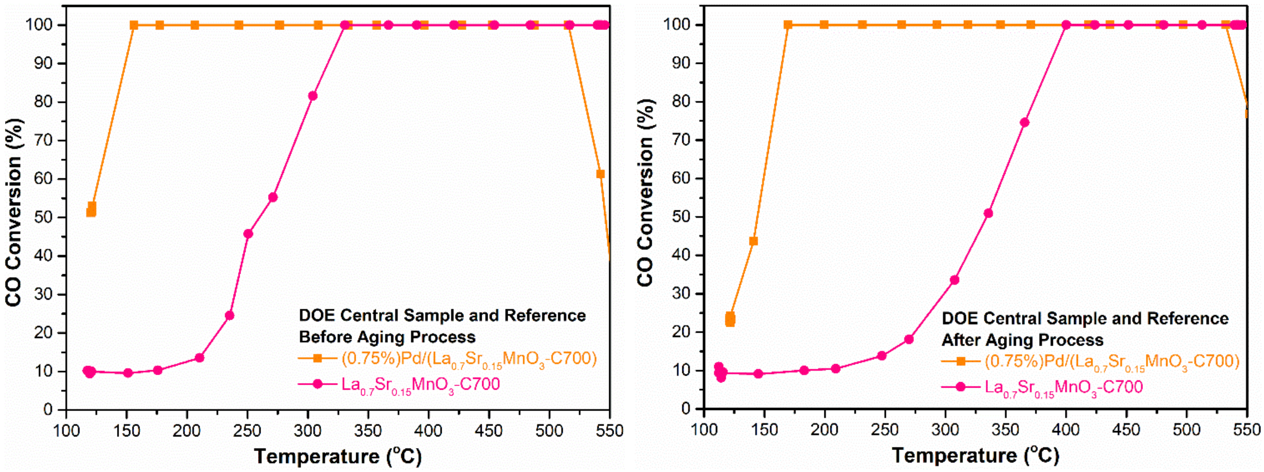

Fig.S7.3.2. Carbon monoxide conversion during heating from 120 to 550 °C before/after aging.

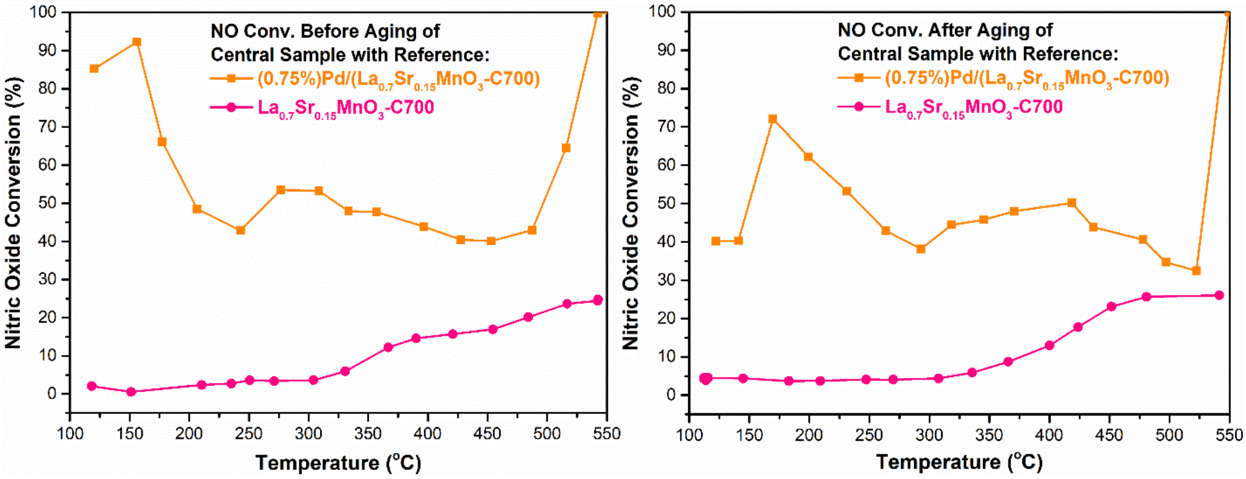

Fig.S7.3.3. Nitric oxide conversion during heating from 120 to 550 °C before/after aging.

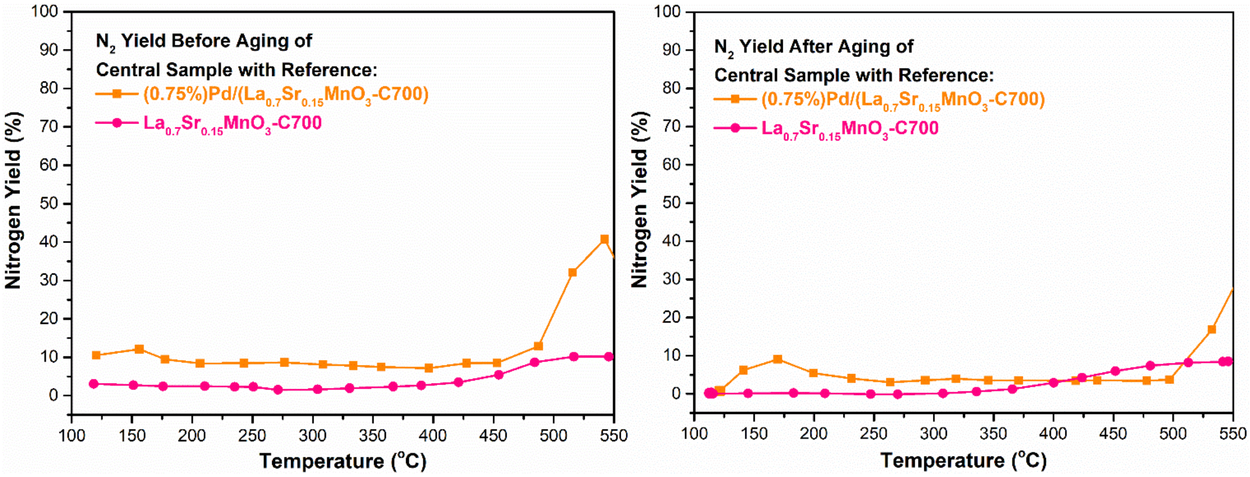

Fig.S7.3.4. Nitrogen yield during heating from 120 to 550 °C before/after aging.

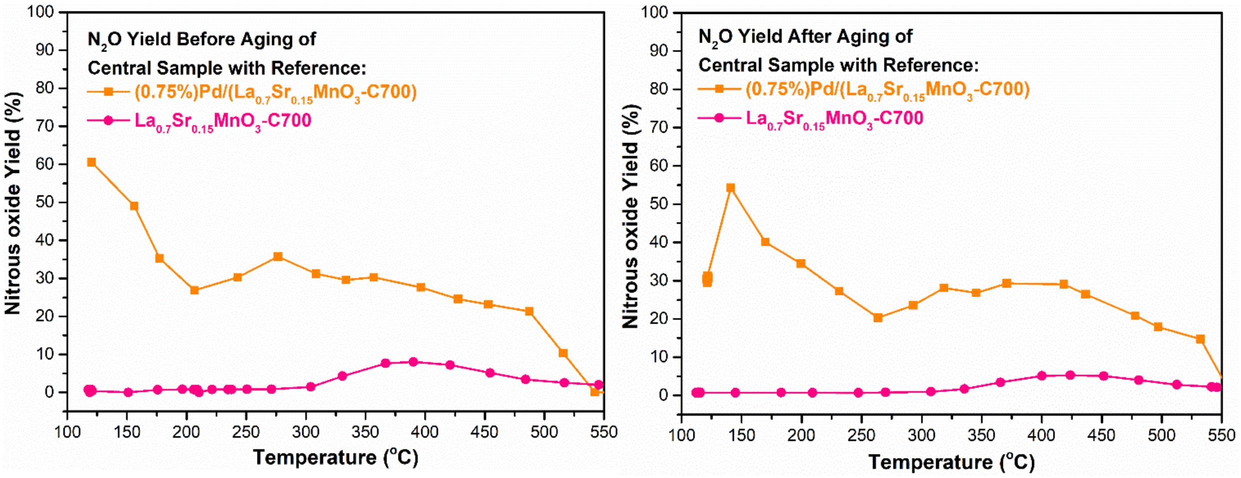

Fig.S7.3.5. Nitrous oxide yield during heating from 120 to 550 °C before/after aging.

Chapter VIII. General Conclusion and Outlook

1. General conclusion

The general objective of this thesis work was to develop Three Way Catalysts based on perovskite and palladium for the treatment of traces of methane from vehicles running on natural gas, which is treated as the alternative and renewable energy sources to traditional liquid fossil fuels. Perovskite with the general formula ABO_3 is treated as the potential alternative materials to the noble metal and could partially replace palladium based three-way catalysts for exhaust gas of natural gas engine.

In more detail, the state-of-art investigation is based on the combination of two kind of active catalysts, each having a role in the targeted reaction – the catalytic combustion of methane. Perovskites based on $LaMnO_3$ composition are used as active support of precious metal palladium because of the excellent methane oxidation activity during high temperature. Among them, the perovskite A-site study of non-stoichiometric lanthanum and the partial substitutions of lanthanum by potassium and strontium have been used to modify the structure of perovskite to generate structural distortions for better catalytic activity and mobility of the oxygen. Besides, palladium, recognized as a noble metal with excellent low temperature methane catalytic performance, has been incorporated into perovskite catalysts by different strategies (i.e. one-pot method and sequential method by synthesis of the sol-gel method of citric acid). Structure determines properties, different palladium doping methods and the differences of perovskite bulk preparation have the significant impacts on physiochemical and catalytic properties of catalysts. Therefore, the above chapters presented the catalysts from different standpoints: i.) A-site defect and substituted perovskite bulk properties in chapter 4, ii.) the evaluation of two palladium incorporation methods based on former bulk physiochemical study in chapter 5, iii.) the kinetic investigation for understanding the dual-active-site mechanisms in chapter 6 and iv.) the catalytic measurement in real exhaust gas flow to research the ability to handle multiple polluting gases simultaneously in chapter 7.

Given the consideration of cost control and palladium as an expensive precious metal, the aim of the study was also to provide new insights in order to reduce the use of palladium starting from 1 wt.% Pd and then shifting to 0.5 wt.% as ultimate goal.

The first chapter mainly concerned the bulk and surface properties of perovskite compositions. The lanthanum stoichiometry as well as Sr- and K-substitution have been investigated. The calcination temperature used for obtaining the typical rhombohedral structure appears as key parameter. Indeed, a pre-requisite is to obtain samples developing high specific surface area and oxygen mobility to enhance their oxygen storage capacity. As a general trend calcination at 600°C led to higher specific surface area but bulk impurities corresponding to single oxides have been detected. At high calcination temperature the pure structure can be obtained with improved bulk oxygen mobility. In contrast a loss of specific surface area is generally observed on stoichiometric composition. The best compromise was obtained on La-deficient $La_{0.7}MnO_3$ composition with the conservation of small crystallites than preserving high specific surface area.

Potassium and strontium substitutions were subsequently studied on stoichiometric samples (with A/Mn = 1) calcined at 600°C. Subsequent potassium substitutions do not lead to improved properties essentially due to phase segregation with the appearance of monoclinic lattice structure $K_{1.39}Mn_3O_6$ exhibiting weak oxygen mobility. Strontium substitution led to more amorphous structures with improved crystallization at increasing Sr content. No phase segregation appears distinctly from XRD analysis, but surface strontium enrichment slightly appears at increasing Sr content. XPS analysis also revealed a larger fraction of Mn^{4+} stabilized on Sr-substituted samples which emphasizes the fact that strontium in different chemical environment would coexist in dodecahedral environment in the perovskite lattice and as extra framework species. Let us note that these changes did not induce improved surface and bulk oxygen mobility. Nonetheless, the mixed valence Mn^{4+}/Mn^{3+} with increasing amount of Mn^{4+} on Sr-doped samples has been considered as a relevant descriptor for methane activation.

Palladium has been previously recognized as a benchmark for methane combustion. Despite numerous investigations, the nature of active sites is still debated. Most of the investigations performed in lean conditions pointed out that PdO_x could be active but alternative explanations have arisen suggesting the involvement of dual sites involving Pd^0/PdO interface or metallic Pd species in strong interaction with a substrate developing OSC properties. All these suggestions can be taken into consideration especially in operating TWC conditions where PdO_x is potentially unstable and can decompose into metallic particles. Based on this, two different strategies have been implemented for Pd incorporation according to a classical wet impregnation or one-pot method consisting in adding palladium during the sol gel process. In this latter case, calcination at 600°C or 800°C led to significant changes evidenced from HAADF-TEM analysis emphasizing significant ex solution process leading to more reducible extra framework PdO_x at the surface when the catalyst is calcined at 800°C. On the other hand, oxidic Pd species remains well-dispersed on $LaMn_{0.98}Pd_{0.02}O_3$-C600 calcined at 600°C. For impregnated samples, lower dispersion is observed related to surface Pd-rich sample. However, Pd/$LaMnO_3$-C600 acts as an exception because palladium was found highly dispersed. K- and Sr-doped perovskite compositions were only impregnated at this stage and for Sr-doped samples the higher fraction at the surface of Mn^{4+} was still observed. XPS also showed surface Pd enriched surface. It was also found that the presence of palladium has a beneficial effect on the oxygen desorption suggesting improved OSC properties compared to the bare samples.

The catalytic properties of Pd-doped perovskite samples have been investigated on pre-reduced samples at 250°C. In these moderate reduction temperature conditions, the rhombohedral perovskite structure is conserved and extra framework PdO_x species are reduced. For isolated oxidic Pd^{n+} species stabilized in octahedral coordination of $LaMn_{0.98}Pd_{0.02}O_3$ partial extraction may occur leading to well-dispersed nano-sized metallic Pd species. However, H_2-chemisorption measurements revealed that a significant fraction could remain stabilized as cations inside the perovskite lattice on sample calcined at 600°C. The catalyst functionalities for methane combustion were evaluated from high-through-put experiments on model inlet gas composition composed of 750-3000 ppm CH_4 with 5 vol.% O_2. Kinetic measurements were discussed based on 3 different reaction mechanisms involving only palladium in the composition of the active site and a dual site mechanism involving Pd and surface reactive oxygen species from the support. In the derivation of a rate expression the first C-H bon breaking in adsorbed methane molecules has been assumed by considering a vacant nearest-neighbor site or the assistance of chemisorbed O atoms. While the first proposal was invalidated only a weak agreement was observed with the second mechanism proposal which led to consider reactive oxygen species from the perovskite instead of gaseous O_2. A rather good agreement is obtained according to a dual site mechanism. The calculation of rate constants and equilibrium constants for adsorption led to interesting discussion relative to the strength of adsorption of methane and O_2 on palladium which can be differently modulated according to the composition of the composition of the perovskite. Aging at 750°C in the presence of 10 vol.% H_2O and 5 vol.% O_2 did not deteriorate the Pd-support interface and it was still verified that the dual site mechanism prevails. In some extent this interface can be strengthened and can lead to gain in methane conversion especially on Sr-doped catalysts. On the other hand, near stoichiometric conditions in the presence of steam, kinetic measurement led to the conclusion that strong water adsorption on the perovskite with OH accumulation suppress the OSC properties and the metal-support interface.

Finally, the catalysts were evaluated in more realistic exhaust gas composition near the stoichiometry in the presence of NO and CO from 100°C to 550°C that simulated le catalytic performance during cold start engine. In the temperature range conditions, several competitive and successive reactions take place and can predominate at low or high temperature. As a general trend, CO is quickly converted below 200°C. The occurrence of competitive CO/O_2, CO/NO and CO/H_2O reactions can explain the sudden CO conversion leading to complex evolution notably in the product distribution of the NO reduction. Indeed, the CO/NO reaction lead unexpectedly to the production of ammonia which emphasizes the fact that H_2 would be necessarily supplied and can be only explained to the Water-Gas-Shift reaction. The tendency shows that this reaction would be more pronounced on catalysts prepared by the sol-gel method. Hence, more defective site promoted on these samples could a priori favor the dissociation of water. At high temperature the involvement of reforming reaction would be more responsible of methane conversion as in this temperature range a loss of CO conversion is often observed. Among the products from NO reduction the formation of N_2O is quasi suppressed, both nitrogen and ammonia produce predominantly. Aging induces changes in the catalytic behavior as Pd exsolution process enhance the conversion of methane on aged $LaMn_{0.9772}Pd_{0.0228}O_3$-C600 likely explained by a increase of surface Pd concentration. The rate enhancement in methane conversion on aged Pd/$La_{0.7}MnO_3$-C600 also provides additional insights as this catalyst is characterized by a high surface and bulk oxygen mobility assisted by the presence of palladium. Hence, cooperative effect between Pd and surface reactive oxygen from the perovskite would be favored.

A tentative optimization of the catalyst composition led to various attempts which account for A-deficiency and a reduction of the Pd content. The comparison of the results did not previous a good convergence towards an optimized composition. For CO conversion the best selection in terms of activity and thermal stability correspond to $La_{0.85}Sr_{0.15}Mn_{0.99}Pd_{0.01}O_3$-C800 (0.5 wt.% Pd) but this catalyst is not enough selective to convert efficiently NO. Finally, the better consensus can be obtained on 1 wt.% Pd/$La_{0.85}Sr_{0.15}MnO_3$-C600. The superiority of this latter catalyst is also related to a much lower production of ammonia in favor of nitrogen in the whole range of temperature.

2. Outlook

For the further investigation on the project in the future, the first task is to continue the part of design of experiments to understand the ratio of the importance of the four factors for each physicochemical and catalytic property. On the basis of the intrinsic connection between four factors and interested property parameters, such as methane conversion, palladium distribution, NO conversion with N_2 and N_2O yield, specific surface area, etc., the design of experiments results, which contribute to future palladium incorporated perovskite design, will be obtained from collaboration with chemically statistical partner. With the help of the analysis of four factors, the catalyst formulation for the next stage will be designed with the goal of reducing Pd content.

Furthermore, because of large amount water existence in the real condition, increasing steam amount should be taken into consideration. And the sulfur and phosphorus resistance of the catalyst should also be scheduled for testing as well.

In addition, considering the CO production from methane reforming above 500 ^{o}C and the N_2O and NH_3 generation from NO conversion, an effective solution should be taken into account within the limits of emission regulations, for instance, by adding another reaction bed of base metal perovskite in a double-bed concept specially for CO, NO, N_2O and NH_3 reduction.

All the above experimental operations were measured in lab-scale, therefore, scale-up experiments with catalyst deposition in the honeycomb of three-way catalytic convertor of natural gas engines should be scheduled in the future experiments.

The above-mentioned objectives are aimed at converting the state-of-art dual-active-site three-way catalysts into reality of natural gas engine exhaust purification. Under the strategic prospect of natural gas as an alternative, clean and renewable energy, the study of this thesis has a realistic instructive significance in the case of cost control and resource saving.

Acknowledgements

This thesis was finished in the “Unité de Catalyse et Chimie du Solide” (UMR CNRS 8181) under the framework of “Smartcat” project (No. ANR-18-CE07-0040) funded by “Agence Nationale de la Recherche”. I would like to thank the funding support from “Agence Nationale de la Recherche” that the project and my thesis can be completed in the context of the Covid-19 pandemic lasting three years.

In the beginning, I am very grateful to my thesis director Mr. Pascal GRANGER who is such a great professor with an unshakable place in my life and guided me in a new direction in my life and influenced the depth and breadth of possibilities of my career choices. I was impressed by his seriousness, professionalism and passion for his work, and I learnt the definition of excellence from him who has brought me from a narrow specialty of materials formulation to a broader environmental science.

Besides, I would like to thank distinguished members of my defense jury, Dr. Valérie KELLER from Strasbourg, Dr. Philippe VERNOUX from Lyon, Prof. Catherine ESPECEL and Dr. Xavier COURTOIS from Poitiers, for their hard work with suggestions and corrections on the revision and progress of my thesis.

The Project “Smartcat” has been completed with the efforts of three units: Unité de Catalyse et Chimie du Solide (UMR CNRS 8181) in University of Lille, Institut de Chimie des Milieux et Matériaux de Poitiers (UMR CNRS 7285) in University of Poitiers and Laboratoire de Synthèse et Fonctionnalisation des Céramiques (UMR CNRS 3080) of Saint-Gobain. Even though we could not discuss the progress of the project face-to-face as initially planned for a long time due to the Covid-19 pandemic that lasted for three years, the project was successfully concluded in October 2022 with the joint efforts of everyone. Hence, I would thank to the professors from Lille: Mr. Christophe DUJARDIN, Mr. Jean-Philippe DACQUIN and Mrs. Mélissandre RICHARD, the professors from Poitiers: Mr. Nicolas BION, Mr. Fabien CAN, Mr. Xavier COURTOIS from Poitiers, Dr. Helena KAPER from Saint-Gobain and Mr.

Olivier MARCHAND from Center Research Machinery Thermiques, it is because of your broad vision and rich knowledge that you have given me a lot of insight and very meaningful work suggestions which guide Maxime DELPORTE and me to satisfactorily finish our thesis work.

I mostly worked in UCCS during my nearly four years of doctoral studies, hence, I got to know many excellent colleagues. Mr. Olivier GARDOLL, as a professional and enthusiastic engineer, I appreciate your patience for taking the time to answer because I always had a large number of samples for requests. Mrs. Barbara DECLERCK-BOULANGER as our secretary-general, always helped me deal with many complicated administrative procedures. Dr. Pardis SIMON, as our research engineer of XPS, because I have too many samples, thank you for helping me to test a lot of XPS experiments in your busy work. Mr. David PORIER, our secretary in charge of CNRS affairs, thanks for your patience and professionalism to help me with all the administrative procedures. Prof. Franck DUMEIGNIL and Prof. Jean-François PAUL, I met you during my interview and every review after that, thank you for your kind guidance and advice. As the design of experiments is one of the innovative highlights in the thesis, I give many thanks to Prof. Muriel BIGAN for all statistical analysis. I would thank to Prof. Jean-François LAMONIER, as team-leader of REMCAT group and heterogeneous catalysis, his guidance that I received during work and XPS was very impressive. Mrs. Svetlana HEYTE, such a passional research engineer in Realcat platform, thank you very much for teaching and guiding me to obtain the knowledge and practice for the high throughput heterogeneous catalytic reaction, I have benefited a lot from your enthusiasm and professionalism. Thanks to Dr. Maya MARINOVA for your serious guidance and professional explication to help us better understand our catalysts. In addition, I would thank to Prof. Véronique RATAJ, Prof. Sébastien ROYER, Mrs. Martine TRENTESAUX, Mr. Stéphane CHAMBREY, Prof. Carole LAMONIER, Dr. Christine LANCELOT, Dr. Alain RIVES, Mrs. Sandrine BERTON, Prof. Edmond PAYEN, Prof. Claude MIRODATOS and all the other professors who guided and helped me during my study in Villeneuve d’Ascq. And I appreciate the half

year work with Prof. Jing ZHANG (Dean of School of New Energy, Nanjing University of Science and Technology), as a great woman scientist, who taught me not only the scientific knowledge and serious altitude with passion, but also the responsibility to family.

In addition, I want to thank my friend who graduated from the "Université de Lyon 1 Claude Beranrd/IRCE-Lyon", Dr. Junjie PU, ex-student of Dr. Dorothée LRURENTI, who introduced me this thesis opportunity after my graduation from CPE Lyon Engineering School. Besides, I met many nice friends and cute colleagues during the past years, many thanks to Dr. Bang GU, Dr. Xiang YU, Dr. Dan WU, Dr. Grêce ABDALLAH, Dr. Shilpa SONAR, Miss Yujie WANG, Dr. Tanushree KANE, Dr. Jianxiong WU, Dr. Yong ZHOU, Dr. Shuo CHEN, Dr. Di HU, Dr. Hanyu HU, Mr. Victor DEBOOS, Mr. Ibrahim HATOUM, Mr. Amaury DECOSTER, Dr. Jianying DENG, Miss Paola ARANGO, Dr. Hermann SIAKA, Dr. Quyang LIN, Dr. Nassim BOUCHOUL, Dr. Carmen CIOTONEA, Dr. Shreya NANDI, Dr. Taha ELGAYYAR, Dr. Nicolas MONTROUSSIER, Mr. Lei JIANG, Mr. Julien DUPONT, Miss. Bertha FARAH, Dr. Chunyang DONG, Dr. Dichao SHI, Dr. Jingpeng ZHAO, Dr. Feng NIU, Dr. Qiyan WANG and everyone else I've ever got alone with.

In the end, I would also thank to my family and friends in China although the distance is more than eight thousand kilometers, your encouragement, support and expectation for my soul is the source of my power to carry on. I would also thank to myself, I never thought to give up although this long march was such hard. And I feel very happy to combine my former formulation study with palladium boosted perovskite catalysts in environmental catalysis.

Le vent se lève, il faut tenter de vivre !

Scientific Productions

Publications

1. Jianxiong Wu, **Yuanshuang Zheng**, Jean-Philippe Dacquin, Nora Djelal, Catherine Cordier, Christophe Dujardin, Pascal Granger*, Impact of dual calcium and manganese substitution of La-deficient perovskites on structural and related catalytic properties: Future opportunities in next three-way-catalyst generation?, Applied Catalysis A: General, Volume 619, **2021**, 118137, ISSN 0926-860X, https://doi.org/10.1016/j.apcata.2021.118137.

2. **Yuanshuang Zheng**, Amaury Decoster, Andrea Osti, Antonella Glisenti, Jean-Philippe Dacquin, Fabien Dhainaut, Svetlana Heyte, Pascal Granger*, Combined theoretical and experimental kinetic approach for methane conversion on model supported Pd/$La_{0.7}MnO_3$ NGV catalyst: Sensitivity to inlet gas composition and consequence on the Pd-support interface, Applied Catalysis A: General, Volume 641, **2022**, 118687, ISSN 0926-860X, https://doi.org/10.1016/j.apcata.2022.118687.

3. Decoster, A., **Zheng, Y.**, Dhainaut, F. et al. Rh/$Ce_xZr_{1-x}O_2$ as NGV Catalyst: Impact of the Preparation of Ceria-Zirconia Support on the Catalytic Performance. Top Catal (2022). https://doi.org/10.1007/s11244-022-01717-z.

Conferences

1. **Yuanshuang ZHENG**, Svetlana HEYTE, Pascal GRANGER*.
   Oral Presentation: *"High throughput approach for optimizing three-way-catalyst for natural gas engine: importance of the metal-support interface".*
   First international symposium on High-Throughput Catalysis, 2021.
   University of Lille, Villeneuve d'Ascq, France.

2. **Yuanshuang ZHENG**, Pascal GRANGER*.
   Oral Presentation: *"Model Pd-perovskite three-way catalysts for natural gas engines: Impact of Pd incorporation on the kinetics"*
   12th International Conference on Environmental Catalysis (ICEC), 2022.
   Osaka University and Kansai University, Osaka, Japan.

“ Le vent se lève, il faut tenter de vivre ! ”

« Le Cimetière marin (1920) »

Paul Valéry